

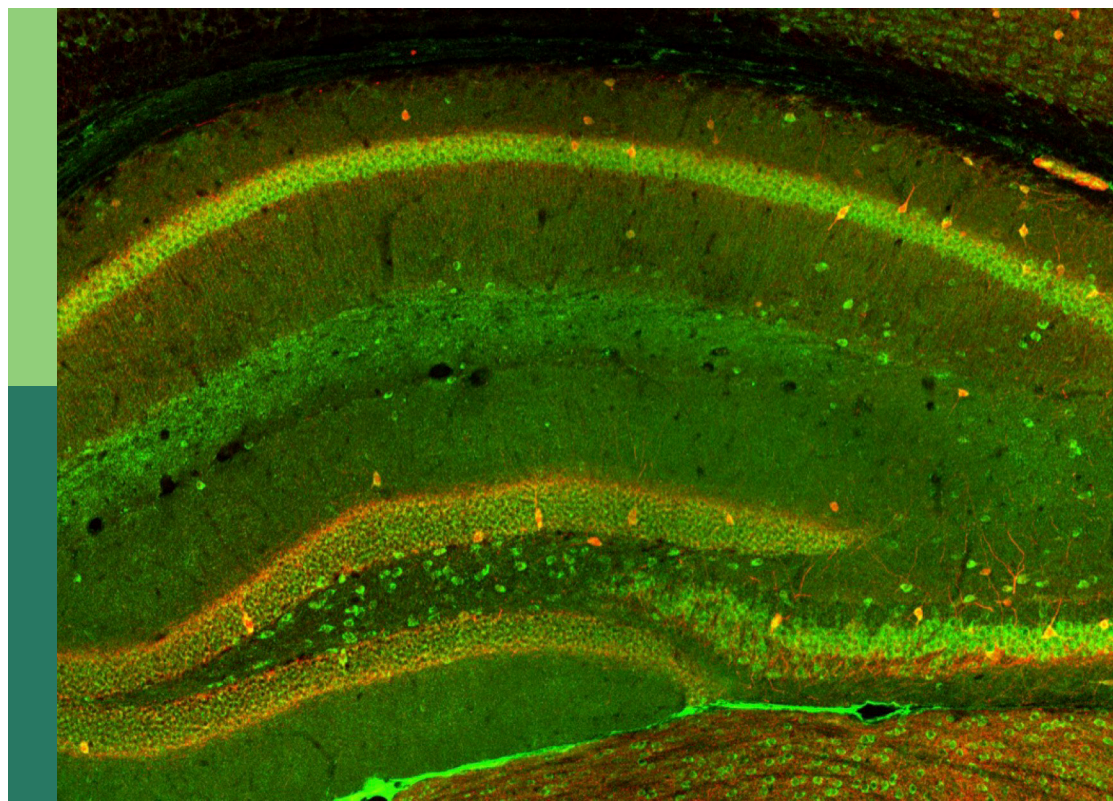
Neuromodulation and neural technologies for sight restoration

Edited by

Maesoon Im, Leanne Chan, Shelley Fried, Diego Ghezzi
and Günther Zeck

Published in

Frontiers in Cellular Neuroscience
Frontiers in Medical Technology
Frontiers in Neuroscience
Frontiers in Cell and Developmental Biology



FRONTIERS EBOOK COPYRIGHT STATEMENT

The copyright in the text of individual articles in this ebook is the property of their respective authors or their respective institutions or funders. The copyright in graphics and images within each article may be subject to copyright of other parties. In both cases this is subject to a license granted to Frontiers.

The compilation of articles constituting this ebook is the property of Frontiers.

Each article within this ebook, and the ebook itself, are published under the most recent version of the Creative Commons CC-BY licence. The version current at the date of publication of this ebook is CC-BY 4.0. If the CC-BY licence is updated, the licence granted by Frontiers is automatically updated to the new version.

When exercising any right under the CC-BY licence, Frontiers must be attributed as the original publisher of the article or ebook, as applicable.

Authors have the responsibility of ensuring that any graphics or other materials which are the property of others may be included in the CC-BY licence, but this should be checked before relying on the CC-BY licence to reproduce those materials. Any copyright notices relating to those materials must be complied with.

Copyright and source acknowledgement notices may not be removed and must be displayed in any copy, derivative work or partial copy which includes the elements in question.

All copyright, and all rights therein, are protected by national and international copyright laws. The above represents a summary only. For further information please read Frontiers' Conditions for Website Use and Copyright Statement, and the applicable CC-BY licence.

ISSN 1664-8714
ISBN 978-2-8325-3826-5
DOI 10.3389/978-2-8325-3826-5

About Frontiers

Frontiers is more than just an open access publisher of scholarly articles: it is a pioneering approach to the world of academia, radically improving the way scholarly research is managed. The grand vision of Frontiers is a world where all people have an equal opportunity to seek, share and generate knowledge. Frontiers provides immediate and permanent online open access to all its publications, but this alone is not enough to realize our grand goals.

Frontiers journal series

The Frontiers journal series is a multi-tier and interdisciplinary set of open-access, online journals, promising a paradigm shift from the current review, selection and dissemination processes in academic publishing. All Frontiers journals are driven by researchers for researchers; therefore, they constitute a service to the scholarly community. At the same time, the *Frontiers journal series* operates on a revolutionary invention, the tiered publishing system, initially addressing specific communities of scholars, and gradually climbing up to broader public understanding, thus serving the interests of the lay society, too.

Dedication to quality

Each Frontiers article is a landmark of the highest quality, thanks to genuinely collaborative interactions between authors and review editors, who include some of the world's best academicians. Research must be certified by peers before entering a stream of knowledge that may eventually reach the public - and shape society; therefore, Frontiers only applies the most rigorous and unbiased reviews. Frontiers revolutionizes research publishing by freely delivering the most outstanding research, evaluated with no bias from both the academic and social point of view. By applying the most advanced information technologies, Frontiers is catapulting scholarly publishing into a new generation.

What are Frontiers Research Topics?

Frontiers Research Topics are very popular trademarks of the *Frontiers journals series*: they are collections of at least ten articles, all centered on a particular subject. With their unique mix of varied contributions from Original Research to Review Articles, Frontiers Research Topics unify the most influential researchers, the latest key findings and historical advances in a hot research area.

Find out more on how to host your own Frontiers Research Topic or contribute to one as an author by contacting the Frontiers editorial office: frontiersin.org/about/contact

Neuromodulation and neural technologies for sight restoration

Topic editors

Maesoon Im — Brain Science Institute, Korea Institute of Science and Technology (KIST), Republic of Korea

Leanne Chan — City University of Hong Kong, Hong Kong, SAR China

Shelley Fried — Massachusetts General Hospital, Harvard Medical School, United States

Diego Ghezzi — Hôpital ophtalmique Jules-Gonin, Switzerland

Günther Zeck — Vienna University of Technology, Austria

Citation

Im, M., Chan, L., Fried, S., Ghezzi, D., Zeck, G., eds. (2023). *Neuromodulation and neural technologies for sight restoration*. Lausanne: Frontiers Media SA. doi: 10.3389/978-2-8325-3826-5

Table of contents

- 05 **Editorial: Neuromodulation and neural technologies for sight restoration**
Maesoon Im, Günther M. Zeck, Leanne Lai Hang Chan, Diego Ghezzi and Shelley I. Fried
- 09 **Block Phenomena During Electric Micro-Stimulation of Pyramidal Cells and Retinal Ganglion Cells**
Sogand Sajedi, Andreas Fellner, Paul Werginz and Frank Rattay
- 22 **Transcorneal Electrical Stimulation Induces Long-Lasting Enhancement of Brain Functional and Directional Connectivity in Retinal Degeneration Mice**
Stephen K. Agadagba, Abdelrahman B. M. Eldaly and Leanne Lai Hang Chan
- 38 **Correlated Activity in the Degenerate Retina Inhibits Focal Response to Electrical Stimulation**
Jungryul Ahn, Seongkwang Cha, Kwang-Eon Choi, Seong-Woo Kim, Yongseok Yoo and Yong Sook Goo
- 56 **Artificial Visual Information Produced by Retinal Prostheses**
Sein Kim, Hyeonhee Roh and Maesoon Im
- 64 **Progress on Designing a Chemical Retinal Prosthesis**
Jiajia Wu, Corey M. Rountree, Sai-Siva Kare, Pradeep Kumar Ramkumar, John D. Finan and John B. Troy
- 72 **Stage-Dependent Changes of Visual Function and Electrical Response of the Retina in the *rd10* Mouse Model**
Seongkwang Cha, Jungryul Ahn, Yurim Jeong, Yong Hee Lee, Hyong Kyu Kim, Daekee Lee, Yongseok Yoo and Yong Sook Goo
- 91 **Ultrasound stimulation for non-invasive visual prostheses**
Jaya Dilip Badadhe, Hyeonhee Roh, Byung Chul Lee, Jae Hun Kim and Maesoon Im
- 100 **Retinal ganglion cell desensitization is mitigated by varying parameter constant excitation pulse trains**
Wennan Li, Dorsa Haji Ghaffari, Rohit Misra and James D. Weiland
- 112 **Factors affecting two-point discrimination in Argus II patients**
Ezgi I. Yücel, Roksana Sadeghi, Arathy Kartha, Sandra Rocio Montezuma, Gislin Dagnelie, Ariel Rokem, Geoffrey M. Boynton, Ione Fine and Michael Beyeler
- 132 **Multichannel stimulation module as a tool for animal studies on cortical neural prostheses**
Yuki Hayashida, Seiji Kameda, Yuichi Umehira, Shinnosuke Ishikawa and Tetsuya Yagi
- 153 **High spatial resolution artificial vision inferred from the spiking output of retinal ganglion cells stimulated by optogenetic and electrical means**
Andreea Elena Cojocaru, Andrea Corna, Miriam Reh and Günther Zeck

- 166 **Toward a personalized closed-loop stimulation of the visual cortex: Advances and challenges**
Fabrizio Grani, Cristina Soto-Sánchez, Antonio Fimia and Eduardo Fernández
- 175 **Electrically-evoked responses for retinal prostheses are differentially altered depending on ganglion cell types in outer retinal neurodegeneration caused by *Crb1* gene mutation**
Hyeonhee Roh, Yanjinsuren Otgondemberel, Jeonghyeon Eom, Daniel Kim and Maesoon Im
- 191 **Functional optimization of light-activatable Opto-GPCRs: Illuminating the importance of the proximal C-terminus in G-protein specificity**
Siri Leemann and Sonja Kleinlogel
- 205 **Computational analysis of efficient organic solar cell-based retinal prosthesis using plasmonic gold nanoparticles**
Ali Rahmani and Kyungsik Eom



OPEN ACCESS

EDITED AND REVIEWED BY
Arianna Maffei,
Stony Brook University, United States

*CORRESPONDENCE

Maesoon Im
✉ maesoon.im@kist.re.kr
Günther M. Zeck
✉ guenther.zeck@tuwien.ac.at
Leanne Lai Hang Chan
✉ leanne.chan@cityu.edu.hk
Diego Ghezzi
✉ info@ghezzilab.org
Shelley I. Fried
✉ fried.shelley@mgh.harvard.edu

RECEIVED 30 September 2023
ACCEPTED 03 October 2023
PUBLISHED 17 October 2023

CITATION

Im M, Zeck GM, Chan LLH, Ghezzi D and
Fried SI (2023) Editorial: Neuromodulation and
neural technologies for sight restoration.
Front. Cell. Neurosci. 17:1304872.
doi: 10.3389/fncel.2023.1304872

COPYRIGHT

© 2023 Im, Zeck, Chan, Ghezzi and Fried. This
is an open-access article distributed under the
terms of the [Creative Commons Attribution
License \(CC BY\)](#). The use, distribution or
reproduction in other forums is permitted,
provided the original author(s) and the
copyright owner(s) are credited and that the
original publication in this journal is cited, in
accordance with accepted academic practice.
No use, distribution or reproduction is
permitted which does not comply with these
terms.

Editorial: Neuromodulation and neural technologies for sight restoration

Maesoon Im^{1,2,3*}, Günther M. Zeck^{4*}, Leanne Lai Hang Chan^{5*},
Diego Ghezzi^{6*} and Shelley I. Fried^{7,8*}

¹Brain Science Institute, Korea Institute of Science and Technology (KIST), Seoul, Republic of Korea, ²Division of Bio-Medical Science & Technology, KIST School, University of Science and Technology (UST), Seoul, Republic of Korea, ³KHU-KIST Department of Converging Science and Technology, Kyung Hee University, Seoul, Republic of Korea, ⁴Institute of Biomedical Electronics, TU Wien, Vienna, Austria, ⁵Department of Electrical Engineering, City University of Hong Kong, Kowloon, Hong Kong SAR, China, ⁶Ophthalmic and Neural Technologies Laboratory, Department of Ophthalmology, Hôpital Ophtalmique Jules-Gonin, Fondation Asile des Aveugles, University of Lausanne, Lausanne, Switzerland, ⁷Boston VA Medical Center, Boston, MA, United States, ⁸Department of Neurosurgery, Massachusetts General Hospital, Harvard Medical School, Boston, MA, United States

KEYWORDS

artificial vision, sight restoration, neuromodulation, neural technologies, visual prosthesis, retinal prosthesis

Editorial on the Research Topic

Neuromodulation and neural technologies for sight restoration

The ability to restore vision to the blind with artificial stimulation remains one of the tantalizing goals of neural engineering and many new technological developments offer ongoing advances in support of this effort. Nevertheless, clinical test results remain sub-optimal, i.e., most approaches continue to elicit light percepts (phosphenes) but the reliable creation of more complex visual patterns remains elusive. In this Frontiers Research Topic entitled “*Neuromodulation and neural technologies for sight restoration*,” 11 Original Research articles, 3 Mini Review and one Perspective describe efforts ranging from an in-depth analysis of clinical test results focused on better understanding existing limitations to development of novel strategies for driving the retina to fundamental modeling and physiological studies focused on the development of more effective stimulation strategies.

In the first study, Yücel et al. examined the factors underlying high thresholds and poor spatial resolution in users of the Argus II epiretinal implant and found that inadvertent activation of passing axons, lift of the device off the retinal surface, and retinal damage all played a role. Although the Argus II is no longer commercially available, the analysis and discussion of the 3 individual components provide insights that will be relevant to many other devices.

Current research focuses on therapeutic strategies to restore vision in retinal degeneration (RD) patients. However, there is limited investigation into neural activities in the brain following retinal electrical stimulation. Additionally, the neuromodulatory changes resulting from prolonged electrical stimulation in the brains of retinitis pigmentosa (RP) patients have not been studied. Agadagba et al. studied the effects of transcorneal retinal electrical stimulation on functional and directional connectivity in visual and non-visual brain cortices of RD mice. The results showed that transient stimulation did not significantly alter brain connectivity, but 1-week post-stimulation revealed increased theta-gamma coupling and enhanced coherence and connectivity in theta, alpha, and beta

oscillations. Notably, 2-weeks post-stimulation demonstrated long-lasting enhancements in network coherence and connectivity between visual and non-visual cortices. These findings suggest that transcorneal retinal electrical stimulation can modulate brain connectivity and may have implications for higher cortical functions.

Rapid fading of artificial visual percepts has been reported in clinical studies. To explore this, Li et al. investigated how desensitization of mouse retinal ganglion cells (RGCs) can be mitigated by changing stimulation parameters. They reported the RGC desensitization is not related to stimulus amplitude but stimulation frequency, suggesting the fading may be partially addressed by optimizing the stimulation conditions. In past retinal prosthetic studies, the various genotypes of retinal degenerative diseases have not been well considered. For example, more than 80 different genes have been identified to cause RP. Roh et al. compared phenotypes of the retinas of *rd8* and *rd10* mice which have *Crb1* and *Pde6b* mutations, respectively. They also systematically examined electrically-evoked network-mediated spiking responses of RGCs (Im and Fried, 2015; Roh et al., 2022) of the *rd8* retinas by first classifying the types of RGCs into non-direction selective ON, non-direction selective OFF, or direction selective ON-OFF (Im and Fried, 2016; Otgondemberel et al., 2021). Then, they compared the electric responses of those cells with their own visually-evoked responses and found the correlation levels of those two responses (i.e., electric and visual responses) are differentially altered even at the early stage of degeneration caused by the *Crb1* gene. Spiking patterns of the electrically-evoked responses of *rd8* retinas seem to be similar to those of early-stage *rd10* retinas (Yoon et al., 2020).

Ahn et al. study retinal ganglion cell activity in photoreceptor-degenerated *ex vivo* mice and macaque *ex vivo* retinæ upon electrical stimulation. They identified a spatially extended activation (>800 μm) to short and strong electrical stimulation of the RD retina. This activity was mediated by stimulation of the electrically coupled bipolar-amacrine network. The authors suggest that such wide-spread activation may have limited the outcome of retinal prosthetics. Indeed, the use of brief, strong stimulus currents may represent a challenge for photoreceptor-degenerated retinæ, where a more localized activation has been reported for lower current amplitudes in previous studies (Ryu et al., 2017; Corna et al., 2021). Future work may identify if the aberrant activity presynaptic to the RGCs across large retinal portions persist if time-varying, non-stationary stimuli with variable amplitude (Chenais et al., 2021) or waveforms (Höfling et al., 2020) are applied.

The degree of degeneration and preserved responsiveness is of importance in restoration of artificial vision. Cha et al. investigated stage-dependent changes of visual function and electrical responsiveness in *rd10* mice. The authors report light-induced activity in RGCs in the *ex vivo* retina up to postnatal day 70, and interestingly, a longer preservation of the ON response. Previously, it was thought that OFF-type RGCs would survive longer (Stasheff, 2008) in the rod-degenerated mouse retina. Future work may clarify if preservation of RGC classes is specific to certain strains. The study by Cha et al. also shows that for certain pulsatile stimuli presented by one electrode in epiretinal configuration

activates only a small portion of RGCs. The spatial confinement, however, remained unclear.

High resolution discrimination of grating-like electrodes has been reported by Cojocaru et al. They applied electrical stimulation in rod-photoreceptor degenerated retinæ in epiretinal configuration using high-density electrode arrays. Here, stimulation was performed using sinusoidal waveforms presented continuously at 40 Hz, i.e., a stimulus duration of 25 ms. The authors demonstrated localized activation of RGCs with fine electrode gratings, down to 32 μm . They demonstrated avoidance of axonal stimulation using these waveforms—a long lasting, open question in retinal prosthetics. In agreement with previous work using point-like electrodes it appears that sinusoidal waveforms locally stimulate ganglion cells. Cojocaru et al. furthermore compared their results in the same retina with optogenetic stimulation of either bipolar cells transduced with ChR2 or with optogenetic stimulation of RGCs transduced with ChR2. Interestingly, they could not identify any significant differences regarding the spatial resolution, which was even higher than with electrical stimulation. Based on support vector machine classifier Cojocaru et al. estimated an optimal resolution with optogenetic stimulation of ~ 3 cycles/degree, corresponding to 20/200, in line with previous *ex vivo* work (McGregor et al., 2020; Gauvain et al., 2021; Reh et al., 2022).

A major concern using optogenetics for vision restoration in the retina had been the high light intensity, and efficacy of coupling. The concern with high light intensities has been solved by using optogenetic transducers coupled to G-protein receptors (van Wyk et al., 2015), with mGluR6 expressed in the retina by ON bipolar cells. Specific targeting of chimeric transducers, i.e., OptoGPCR chimeras between light gated G-protein coupled receptors (opsins) and ligand-gated G-protein coupled receptors. The study by Leeman and Kleinlogel sheds light on the expression efficacy of these chimeras.

Advancement in interfacing electronics would be essential for the enhanced performance of prosthetic systems. In this Research Topic, Hayashida et al. presented an advanced multichannel stimulation module for intracortical micro-stimulation in preclinical animal studies. They introduced a scalable 64-channel stimulation module, allowing for a deeper understanding of the relationship between the spatiotemporal patterns of stimuli and the resulting neural responses through pre-clinical animal studies. An application-specific integrated circuit (ASIC) chip was designed and implemented as the primary current output device, while a field-programmable gate array (FPGA) served as the controller. *In-vivo* experiments demonstrated the stimulation effect with a temporal resolution in the millisecond range. The multichannel stimulation module enabled control over not only the shape of each biphasic current pulse but also the degree of charge imbalance and the temporal order of pulse among multiple channels. These features are considered valuable for intracortical micro-stimulation in preclinical animal studies.

Computational approaches also can deepen our understanding of neuromodulation effects as well as expedite the development processes. For example, Sajedi et al. used computer simulation to examine the blocking phenomenon which may be caused by electric stimulation above an upper threshold of nerve cells. They

investigated the effect of overstimulation for layer 5 pyramidal cells and alpha RGCs and suggested the importance of an appropriate stimulation window for the reliable activation of target neurons for neural prosthetic applications. Also, Rahmani and Eom used computational analysis of an organic solar cell that has spherical gold nanoparticles (AuNPs) for retinal prosthetic applications. Their analysis indicated the incorporation of AuNPs can enhance the photoconversion efficiency, thereby lowering the required light intensity for photovoltaic activation of retinal neurons. These studies suggest the efficiency of the computational approaches which can be experimentally verified in the follow-up studies.

The 3 Mini Reviews recapitulate three different topics in the field of visual prosthetics. In the first one by Wu et al., implanted devices that use a chemical stimulus (instead of electrical or optical ones) to reactivate the retina are discussed including the components of a chemical retinal prosthesis, the potential spatial and temporal resolution, and the possibility of achieving naturalistic stimulation. The biocompatibility and excitotoxicity of these kinds of implants are reviewed as well. The next logical step for chemical retinal prostheses is validation in *in-vivo* animals. In the second review article of Badadhe et al., the authors summarized the current status of ultrasound stimulation, a modality for sight restoration that is much less invasive than most existing approaches. Although several studies have demonstrated somewhat promising results of the acoustic prosthesis, Badadhe et al. pointed out that the working principle behind this modality is yet to be completely understood for more accurate neuromodulation.

The third review offered a new aspect of artificially-created neural activity for vision restoration by recapitulating computational neuroscience approaches to quantify neural information. In the work of Kim et al., the authors claim that there have been very few efforts such as the study of Kang et al. (2021) to understand the quality of neural spiking activities in the field of visual prosthetics, particularly in terms of the amount of neural information generated by any form of artificial stimulation. They briefly introduced the two different methods (i.e., direct and reconstruction methods) that can calculate information rates from the recorded spike trains. Lastly, in a Perspective article, Grani et al. argued that closed-loop stimulation strategies can substantially improve the effectiveness of cortical visual prostheses. They have succinctly summarized previous examples of closed-loop strategies applied in various neural prostheses and several challenges to be overcome in future research.

Taken together, the 15 articles in the present Research Topic describe many of the aspects that need to be considered as new and ongoing efforts strive to improve performance of retinal and other visual prostheses. While progress toward the goal of near-normal

vision with an implant remains limited, such efforts continue to offer hope to the millions of people who are blind.

Author contributions

MI: Writing—original draft, Writing—review and editing. GZ: Writing—original draft, Writing—review and editing. LC: Writing—original draft, Writing—review and editing. DG: Writing—original draft, Writing—review and editing. SF: Writing—original draft, Writing—review and editing.

Funding

The author(s) declare financial support was received for the research, authorship, and/or publication of this article. This work was supported by the National Research Foundation of Korea (NRF) Grant 2020R1C1C1006065, 2021M3F3A2A01037366, and Grant 2022M3E5E8017395 funded by the Korean Government (MSIT).

Acknowledgments

The authors are thankful to the contributors to this Research Topic and the editorial support of the journal.

Conflict of interest

The authors declare that the research was conducted in the absence of any commercial or financial relationships that could be construed as a potential conflict of interest.

The author(s) declared that they were an editorial board member of Frontiers, at the time of submission. This had no impact on the peer review process and the final decision.

Publisher's note

All claims expressed in this article are solely those of the authors and do not necessarily represent those of their affiliated organizations, or those of the publisher, the editors and the reviewers. Any product that may be evaluated in this article, or claim that may be made by its manufacturer, is not guaranteed or endorsed by the publisher.

References

- Chenais, N. A. L., Airaghi Leccardi, M. J. I., and Ghezzi, D. (2021). Naturalistic spatiotemporal modulation of epiretinal stimulation increases the response persistence of retinal ganglion cell. *J. Neural Eng.* 18, 016016. doi: 10.1088/1741-2552/abcd6f
- Corna, A., Ramesh, P., Jetter, F., Lee, M. J., Macke, J. H., and Zeck, G. (2021). Discrimination of simple objects decoded from the output of retinal ganglion cells upon sinusoidal electrical stimulation. *J. Neural Eng.* 18, 046086. doi: 10.1088/1741-2552/ac0679
- Gauvain, G., Akolkar, H., Chaffiol, A., Arcizet, F., Khoei, M. A., Desrosiers, M., et al. (2021). Optogenetic therapy: high spatiotemporal resolution and pattern discrimination compatible with vision restoration in non-human primates. *Commun. Biol.* 4, 1–15. doi: 10.1038/s42003-020-01594-w
- Höfling, L., Oesterle, J., Berens, P., and Zeck, G. (2020). Probing and predicting ganglion cell responses to smooth electrical stimulation in healthy and blind mouse retina. *Sci. Rep.* 10, 5248. doi: 10.1038/s41598-020-61899-y

- Im, M., and Fried, S. I. (2015). Indirect activation elicits strong correlations between light and electrical responses in ON but not OFF retinal ganglion cells. *J. Physiol.* 593, 3577–3596. doi: 10.1113/JP270606
- Im, M., and Fried, S. I. (2016). Directionally selective retinal ganglion cells suppress luminance responses during natural viewing. *Sci. Rep.* 6, 35708. doi: 10.1038/srep35708
- Kang, J. H., Jang, Y. J., Kim, T., Lee, B. C., Lee, S. H., and Im, M. (2021). Electric stimulation elicits heterogeneous responses in ON but not OFF retinal ganglion cells to transmit rich neural information. *IEEE Trans. Neural Syst. Rehabil. Eng.* 29, 300–309. doi: 10.1109/TNSRE.2020.3048973
- McGregor, J. E., Godat, T., Dhakal, K. R., Parkins, K., Strazzeri, J. M., Bateman, B. A., et al. (2020). Optogenetic restoration of retinal ganglion cell activity in the living primate. *Nat. Commun.* 11, 1–9. doi: 10.1038/s41467-020-15317-6
- Otgondemberel, Y., Roh, H., Fried, S. I., and Im, M. (2021). Spiking characteristics of network-mediated responses arising in direction-selective ganglion cells of rabbit and mouse retinas to electric stimulation for retinal prostheses. *IEEE Trans. Neural Syst. Rehabil. Eng.* 29, 2445–2455. doi: 10.1109/TNSRE.2021.3128878
- Reh, M., Lee, M.-J., and Zeck, G. (2022). Expression of channelrhodopsin-2 in rod bipolar cells restores ON and OFF responses at high spatial resolution in blind mouse retina. *Adv. Therapeutics.* 5, 2100164. doi: 10.1002/adtp.202100164
- Roh, H., Otgondemberel, Y., and Im, M. (2022). Short pulses of epiretinal prostheses evoke network-mediated responses in retinal ganglion cells by stimulating presynaptic neurons. *J. Neural Eng.* 19, 055006. doi: 10.1088/1741-2552/ac8ed7
- Ryu, S. B., Choi, J. W., Ahn, K. N., Goo, Y. S., and Kim, K. H. (2017). Amplitude modulation-based electrical stimulation for encoding multipixel spatiotemporal visual information in retinal neural activities. *J. Korean Med. Sci.* 32, 900–907. doi: 10.3346/jkms.2017.32.6.900
- Stasheff, S. F. (2008). Emergence of sustained spontaneous hyperactivity and temporary preservation of OFF responses in ganglion cells of the retinal degeneration (rd1) mouse. *J. Neurophysiol.* 99, 1408–1421. doi: 10.1152/jn.00144.2007
- van Wyk, M., Löwel, S., and Kleinlogel, S. (2015). Restoring the ON switch in blind retinas: Opto-mGluR6, a next-generation, cell-tailored optogenetic tool. *PLoS Biol.* 13, e1002143. doi: 10.1371/journal.pbio.1002143
- Yoon, Y. J., Lee, J. I., Jang, Y. J., An, S., Kim, J. H., Fried, S. I., et al. (2020). Retinal degeneration reduces consistency of network-mediated responses arising in ganglion cells to electric stimulation. *IEEE Trans. Neural Syst. Rehabil. Eng.* 28, 1921–1930. doi: 10.1109/TNSRE.2020.3003345



Block Phenomena During Electric Micro-Stimulation of Pyramidal Cells and Retinal Ganglion Cells

Sogand Sajedi*, Andreas Fellner, Paul Werginz† and Frank Rattay†

Institute for Analysis and Scientific Computing, Vienna University of Technology, Vienna, Austria

OPEN ACCESS

Edited by:

Maesoon Im,
Brain Science Institute, Korea Institute
of Science and Technology (KIST),
South Korea

Reviewed by:

Javad Paknahad,
University of Southern California,
United States
Tatiana Kameneva,
Swinburne University of Technology,
Australia

*Correspondence:

Sogand Sajedi
sogand.sajedi@tuwien.ac.at

†These authors have jointly
supervised this work

Specialty section:

This article was submitted to
Cellular Neurophysiology,
a section of the journal
Frontiers in Cellular Neuroscience

Received: 06 September 2021

Accepted: 08 November 2021

Published: 26 November 2021

Citation:

Sajedi S, Fellner A, Werginz P and
Rattay F (2021) Block Phenomena
During Electric Micro-Stimulation
of Pyramidal Cells and Retinal
Ganglion Cells.
Front. Cell. Neurosci. 15:771600.
doi: 10.3389/fncel.2021.771600

Electric micro-stimulation of the nervous system is a means to restore various body functions. The stimulus amplitude necessary to generate action potentials, the lower threshold (LT), is well characterized for many neuronal populations. However, electric overstimulation above an upper threshold (UT) prevents action potential generation and therefore hinders optimal neuro-rehabilitation. Previous studies demonstrated the impact of the UT in micro-stimulation of retinal ganglion cells (RGCs). The observed phenomenon is mostly explained by (i) reversed sodium ion flow in the soma membrane, and (ii) anodal surround block that hinders spike conduction in strongly hyperpolarized regions of the axon at high stimulus intensities. However, up to now, no detailed study of the nature of these phenomena has been presented, particularly for different cell types. Here, we present computational analyses of LT and UT for layer 5 pyramidal cells (PCs) as well as alpha RGCs. Model neurons were stimulated in close vicinity to the cell body and LTs and UTs as well as the ratio UT/LT were compared. Aside from a simple point source electrode and monophasic stimuli also realistic electrode and pulse configurations were examined. The analysis showed: (i) in RGCs, the soma contributed to action potential initiation and block for small electrode distances, whereas in PCs the soma played no role in LTs or UTs. (ii) In both cell types, action potential always initiated within the axon initial segment at LT. (iii) In contrast to a complete block of spike conductance at UT that occurred in RGCs, an incomplete block of spiking appeared in PC axon collaterals. (iv) PC axon collateral arrangement influenced UTs but had small impact on LTs. (v) Population responses of RGCs change from circular regions of activation to ring-shaped patterns for increasing stimulus amplitude. A better understanding of the stimulation window that can reliably activate target neurons will benefit the future development of neuroprostheses.

Keywords: pyramidal cell, retinal ganglion cell, axon initial segment, neural stimulation, computer simulation, upper threshold, block, compartment model

INTRODUCTION

Selective micro-stimulation of single neurons and, even more provoking, their subcellular structures such as the axon initial segment (AIS), soma or axon terminals are challenging for modern neuroprostheses. In the last decade, miniaturization of electronic components has enabled efficient stimulation of individual cells. For example, high-density micro-electrode arrays with a pixel pitch down to 25 μm have been developed for inner eye (retinal) prostheses

(Mathieson et al., 2012). Penetrating electrodes might be even more successful for focal stimulation of the retina (Chen et al., 2020), the visual cortex, or other brain structures (Schmidt et al., 1996; Middlebrooks and Snyder, 2008; Nguyen et al., 2016).

In most cases of extracellular stimulation, cathodic stimulation requires less current amplitude to elicit a spike in a target cell than anodic stimulation (Ranck, 1975; Rattay, 1986, 1999). Therefore, cathodic pulses are often used for electric stimulation or, in order to avoid charge accumulation within the tissue, pseudo-monophasic cathodic pulses with a weak second anodic balancing phase are applied. However, for cathodic stimulation there is an intensity window with a lower threshold (LT) and an upper threshold (UT) for spike initiation and propagation. High-intensity cathodic stimulation of a nerve fiber causes strongly hyperpolarized regions on both sides of the electrode, blocking the propagation of an action potential (AP) generated in the central region close to the electrode. This phenomenon is called the anodal surround block or cathodic block (Katz and Miledi, 1965; Jankowska and Roberts, 1972; Roberts and Smith, 1973; Rattay and Aberham, 1993).

An intensity window for successful cathodic stimulation was also observed on cultured neurons before they developed neurites (Buitenweg et al., 2002). Moreover, stimulation of retinal ganglion cells (RGCs) with a micro-electrode close to the soma revealed an UT during high-amplitude stimulation with cathodic pulses (Boinagrov et al., 2012). A simplified computational model supported the hypothesis that the UT is caused by a reversal of sodium current flow in the soma when the transmembrane voltage exceeds the Nernst potential E_{Na} of sodium ions. Using a more detailed RGC model including dendrites, soma and axon, Rattay found cases in which the UT occurred in the soma while an AP was elicited in the axon which further propagated one-sided along the optic nerve (Rattay, 2014). This asymmetric firing is important for the interpretation of experiments, as the UT observation in the soma does not exclude spike conduction. The axonal activation during the somatic UT was also reported by Meng et al. (2018). In addition to the sodium reversal current, two crucial mechanisms were identified to cause the UT in the soma, namely the impact of strong potassium currents and the inactivation of sodium channels (Fellner et al., 2019).

In this modeling study, we used detailed three-dimensional geometries of two cell types representative for cortical and retinal stimulation: rat pyramidal cells (PCs) from the somatosensory cortex and mouse alpha RGCs. Our analysis aimed to identify the somatic contribution to AP generation at LT as well as blockage of spikes at UT during micro-stimulation close to the cell body. We examined AP initiation with a focus on the AIS and spike propagation in light of complex axon collateral structures. Finally, we studied realistic electrode and pulse properties as well as the impact of electrode positioning.

MATERIALS AND METHODS

Model Neurons

Eight reconstructed morphologies of layer 5 pyramidal neurons of rat somatosensory cortex were downloaded from an online

database¹ (Ascoli, 2006; Hay et al., 2013; Cohen et al., 2020); a model cell is shown in **Figure 1A**. Soma diameter was set to 20 μm in all model PCs. Axonal trees were split into hillock, AIS, unmyelinated axon, nodes of Ranvier, and myelinated axon (see **Table 1**). The hillock ($L = 0\text{--}2\ \mu\text{m}$) was attached to the soma followed by the AIS ($L = 35\text{--}48\ \mu\text{m}$) and an unmyelinated axon section up to the first axonal bifurcation (100–150 μm from the soma). Following axonal branches were split into nodes of Ranvier (0.5–1 μm) and internodes ($L = 100 \times$ section diameter; Rushton, 1951). Nodes of Ranvier were placed at the beginning of each branch as well as at the end of myelin sections except at terminal branches. The length of each node of Ranvier was dependent on the length of the adjacent myelin section; this was done to prevent self-spiking that could result from a too large nodal area.

34 reconstructed morphologies of mouse alpha RGCs were taken from a previous study (Werginz et al., 2020); **Figure 1B** shows a representative model cell. Each model neuron was divided into dendrites, soma ($D = 14\text{--}24\ \mu\text{m}$), hillock ($L = 10\text{--}47\ \mu\text{m}$), AIS ($L = 12\text{--}33\ \mu\text{m}$), and distal (unmyelinated) axon ($L \sim 1000\ \mu\text{m}$).

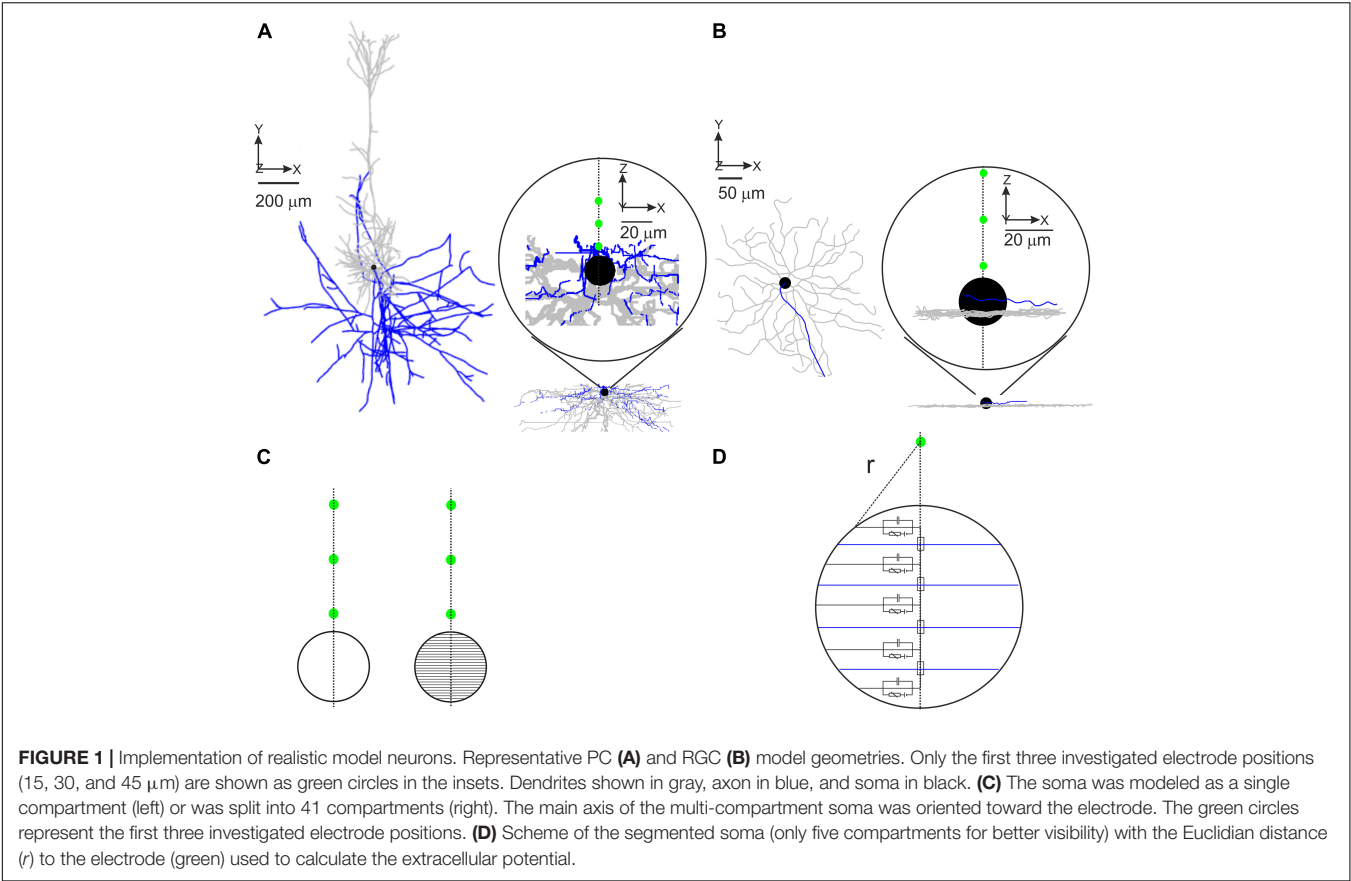
For each cell, the soma was either modeled as a single spherical compartment or as a sphere approximated by 41 cone-shaped compartments. For the multi-compartment soma approach (**Figure 1C**), the main axis of the soma was always pointing toward the stimulating electrode to study the gradient of the applied electric field across the soma (Fellner et al., 2019). Responses to intracellular and extracellular stimulation in both cell types were performed in NEURON 7.8 (Carnevale and Hines, 2006); Python 3.8² was used to control the simulations. Compartment length was between 1 and 2 μm in the axon and below 10 μm in dendritic sections. Extracellular stimulation was modeled *via* NEURON's "extracellular" mechanism. A monophasic cathodic pulse with a duration of 0.1 ms was used in the majority of all experiments. Charge-balanced biphasic pulses with different cathodic/anodic ratios were used in a subset of simulations.

Biophysical Properties

For PCs, the biophysical properties (i.e., ion channel kinetics and densities, **Table 1**) of the soma and dendrites were specified based on experimental data (see Table 1 and cell 5 data of Almog and Korngreen, 2014) and the axon kinetics were adapted from Mainen and Sejnowski (1996). Leak conductivity, intracellular resistivity, and specific membrane capacitance were set to 0.39 pS/ μm^2 , 120 $\Omega\cdot\text{cm}$, and 0.6 $\mu\text{F}/\text{cm}^2$, respectively, except for the myelinated part of the axon. The nodes of Ranvier had an increased leak conductivity of 200 pS/ μm^2 , whereas the myelinated internode had a lowered membrane capacitance of 0.04 $\mu\text{F}/\text{cm}^2$. Model temperature was set to 34°C. Model baseline function, including action potential initiation and (back)propagation as well as spike shape, was tested by intracellular current injections into the PC soma and compared to Almog and Korngreen (2014).

¹<http://neuromorpho.org/>

²<https://www.python.org>



Biophysical properties of RGCs were slightly modified from previous studies (Fohlmeister et al., 2010; Werginz et al., 2020; **Table 2**) without changing baseline function, i.e., AP initiation in the AIS, forward and backward propagation of spikes into the distal axon and somatodendritic compartment, respectively. Leak conductivity, intracellular resistivity, and specific membrane capacitance were set to 2.5 pS/ μm^2 , 143 $\Omega\cdot\text{cm}$, and 1 $\mu\text{F}/\text{cm}^2$, respectively. Model temperature was set to 33°C.

Extracellular Potentials

Stimulating electrodes were placed in close vicinity of the soma within distances of 15, 30, 45, 60, 100, and 200 μm to the soma center (**Figures 1A,B**, green circles). The extracellular potential V_e was calculated for a point source in a homogeneous infinite medium. In addition, disk electrode stimulation was applied to RGCs in a semi-infinite medium. The extracellular resistivity ρ_e was smaller for cortical tissue (300 $\Omega\cdot\text{cm}$; Rattay and Wenger, 2010) than for retinal tissue (1000 $\Omega\cdot\text{cm}$; Werginz and Rattay, 2016).

For point source stimulation the extracellular potential was calculated as (Rattay, 1999)

$$V_e = \frac{\rho_e I_{stim}}{4\pi r}$$

with I_{stim} being the stimulus current applied to the electrode and r representing the Euclidian distance from the compartment

center to the electrode. In the multi-compartment soma configuration, r was computed as the distance to the compartment surface (**Figure 1D**).

TABLE 1 | Ionic current densities along the neural membrane for PC models based on data from Mainen and Sejnowski (1996) and Almog and Korngreen (2014).

	Unit	SOMA	DEND	AXON				
				Hill	AIS	Unmy	Node	Inter
g_{Na}	pS/ μm^2	352	56	6000	30000	1000	30000	352
$g_{K,fast}$	pS/ μm^2	332	28	1000	1000	332	1000	332
$g_{K,slow}$	pS/ μm^2	206	3.79	1500	1500	206	1500	206
g_H	pS/ μm^2	2.51	118					
g_{bK}	pS/ μm^2	0.64	1.23					
g_{sK}	pS/ μm^2	3.18	0.52					
P_{HVA}	$\mu\text{m}/\text{s}$	0.93	1.56					
P_{MVA}	$\mu\text{m}/\text{s}$	31.5	4.9					

g_{Na} , $g_{K,fast}$, $g_{K,slow}$, g_H , g_{bK} , and g_{sK} represent the maximum conductivities of sodium, fast inactivating potassium, slow inactivating potassium, hyperpolarization-activated cation, small-conductance Ca^{2+} -gated potassium, and large-conductance Ca^{2+} -gated potassium channels, respectively. P_{HVA} and P_{MVA} are the permeabilities of the Ca^{2+} high- and medium voltage-gated channels. The dendritic conductivities decreased with increasing distance from the soma, for more details see Almog and Korngreen (2014).

The electric potential generated by a disk electrode was calculated as (Newman, 1966; Wiley and Webster, 1982; Rattay, 1988)

$$V_e = \frac{\rho_e I_{stim}}{2\pi a} \arcsin\left(\frac{2a}{\sqrt{(r-a)^2 + z^2} + \sqrt{(r+a)^2 + z^2}}\right)$$

with a , r , and z being the electrode radius, the radial, and the axial distance to the electrode, respectively.

Statistical Analysis

Comparison between two groups were performed by the Kruskal-Wallis test. Significance levels were set as follows: $p < 0.05$ *, $p < 0.01$ **, $p < 0.001$ ***. Boxplots use standard notation (1st Quartile, Median, 3rd Quartile). All statistical analyses were performed in Python 3.8.

RESULTS

Somatic Contribution to Lower and Upper Thresholds

To examine the contribution of the soma to LT and UT, model neurons were either equipped with a soma consisting of a single sphere or of 41 truncated cone compartments (Figures 1C, 2A left). The right part of Figure 2A shows the activating function, a predictor for excitation along the neural membrane (Rattay, 1999), for a cathodic electrode current of 1 μ A. For the multi-compartment soma, the activating function is positive (red, indicating depolarization) in compartments close to the electrode, whereas compartments further away from the electrode have a negative activating function (blue) indicating hyperpolarization. In contrast, for the single-compartment soma, the activating function is small (white), resulting from no reflection of the extracellular potential gradient across the soma.

LTs and UTs in PCs ($n = 8$) and RGCs ($n = 34$) were computed at point source distances of 15, 30, 45, 60, 100, and 200 μ m to the soma center (Figures 2B,C). As expected LTs and UTs increased with electrode distance; LTs were in similar ranges in RGCs and PCs for small distances (~ 1 μ A for 15 μ m distance). However, in PCs LTs were higher but still within an order of magnitude

compared to RGCs for larger distances. In contrast, UTs were almost 10-fold larger in PCs vs. RGCs.

No significant difference between both soma configurations, neither in LTs nor in UTs, was observed in PCs for all distances indicating little contribution of the *trans*-somatic electric field to UTs (Figure 2B, orange vs. gray). In contrast, for RGCs, LTs in the multi-compartment configuration were significantly lower than in the single-compartment soma model for electrode distances ≤ 60 μ m. Also, UTs were significantly lower in the multi-compartment soma configuration for electrode distances of 15 and 30 μ m (Figure 2C, orange vs. gray).

Threshold ratios (UT/LT) in PCs were calculated for the single- and multi-compartment soma configuration (Figure 2D). The ratios were smallest for the shortest investigated electrode distance, increased for distances up to 60 μ m and decreased again for electrode-to-soma distances of 100 and 200 μ m. No significant difference was found in ratios between both soma configurations at any examined electrode distance. Figure 2E displays threshold ratios for RGCs for single and multi-compartment soma configurations, respectively. Threshold ratios increased monotonically with electrode distance and a significant difference between both soma configurations could be observed in RGCs for the closest electrode distance suggesting a significant contribution of the soma in determining the stimulus window.

We were also interested in whether single morphological features influence LTs, UTs as well as threshold ratios for a given distance. We computed linear correlations between single anatomical parameters (e.g., AIS length, soma diameter, etc.); r^2 values for each correlation are shown in Supplementary Tables 1, 2. We did not observe a clear trend for any feature tested, with an exception of PC dendritic area vs. LT that resulted in r^2 values > 0.4 for all distances (Supplementary Table 1). Additionally, AIS length was somewhat correlated to thresholds and threshold ratios for small electrode distances, similar to results obtained by previous studies that showed a correlation between AIS length and LTs (Jeng et al., 2011; Werginz et al., 2020). These results indicate that LTs, UTs as well as threshold ratios are not dependent on single anatomical properties but to a combination of anatomy, biophysics as well as axonal geometry relative to the electrode location.

In summary, we found up to 300-times higher UTs in PCs compared to their LTs whereas threshold ratios were below 50 for all electrode distances in RGCs. A significant soma contribution was observed in both LTs and UTs for RGCs, particularly for small electrode distances, in contrast to a negligible soma contribution in PCs regardless of electrode distance.

Partial Upper Threshold in Pyramidal Cells

In our initial experiments, spiking activity was detected in the distal axon in RGCs as it is the sole output pathway in these cells. PCs, however, have complex axons with numerous collaterals, and we decided to detect APs at the first node of Ranvier approximately 100–150 μ m distant to the soma where the axon starts to bifurcate. In a second set of simulations, we questioned whether partial spiking, i.e., APs in one part of the axon but

TABLE 2 | Ionic current densities along the neural membrane for RGC models based on data from Fohlmeister et al. (2010) and Werginz et al. (2020).

	Unit	SOMA	DEND	AXON		
				Hill	AIS	Unmy
$g_{Na1.2}$	pS/ μ m ²	650	650	1625	0	1000
$g_{Na1.6}$	pS/ μ m ²	0	0	0	1625	0
$g_{K1.2}$	pS/ μ m ²	350	350	625	0	700
$g_{K1.6}$	pS/ μ m ²	0	0	0	625	0
g_{Ca}	pS/ μ m ²	15	15	15	15	15
$g_{K,Ca}$	pS/ μ m ²	1.5	1.5	1.5	1.5	1.5

$g_{Na1.2}$, $g_{Na1.6}$, $g_{K1.2}$, $g_{K1.6}$, g_{Ca} , and $g_{K,Ca}$ represent the maximum conductivities of sodium $Na_v1.2/1.6$, their corresponding potassium, calcium, and Ca^{2+} -activated potassium channels, respectively.

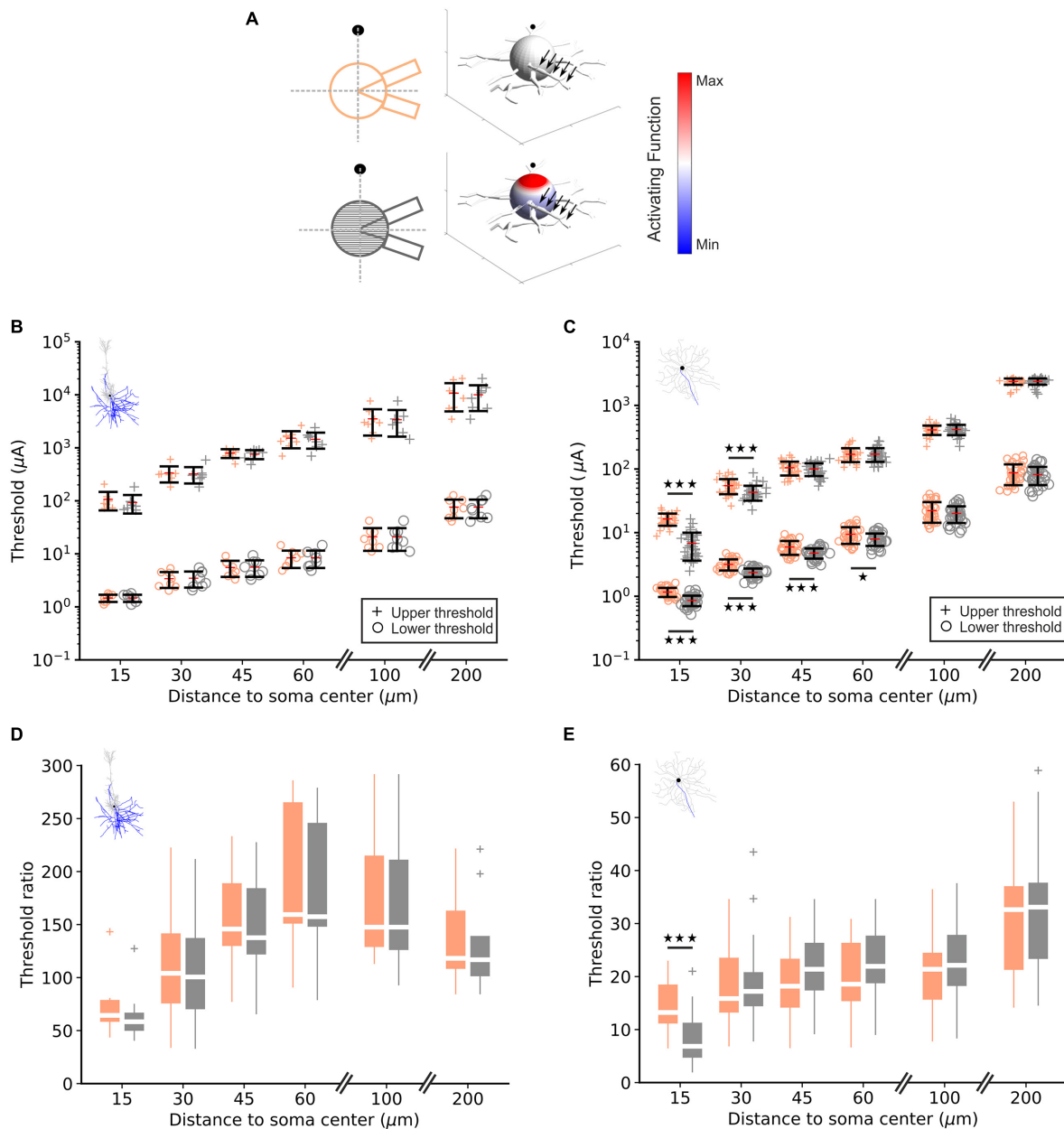


FIGURE 2 | Lower and upper threshold in RGC and PC models. **(A)** For one RGC and both soma configurations (left), each compartment is color-coded by its activating function in response to a 1 μA cathodic pulse (right). The point source electrode is shown as filled black circle/sphere, black arrows indicate the axon. **(B)** Computed lower ("o") and upper ("+") thresholds for the single- (orange) and multi-compartment soma (gray) in eight PCs for different electrode distances. **(C)** Same as panel (B) for 34 RGCs. **(D)** Threshold ratio UT/LT for PCs at different electrode distances. **(E)** Same as panel (D) for RGCs; note the different y-scales in panels (D,E).

no spiking in other portions of the cell, could occur in PCs. Surprisingly, a complete block did not occur in any of the eight investigated PCs, but depending on the electrode distance to the soma, at least small portions of the cell generated an AP, even at amplitudes above previously determined UTs. **Figure 3** demonstrates this partial block phenomenon for one model cell (PC7) when the electrode was at a distance of 15 μm . At LT, the axon and soma generated an AP which actively backpropagated

into the dendritic tree [**Figure 3A**, note the broad dendritic calcium spike (Almog and Korngreen, 2014)]. When the pulse amplitude was set to 50% of the UT the axonally initiated AP did not propagate across the soma and backpropagation into the dendrites failed (**Figure 3B**). At stimulus levels equal to and higher than UT, some parts along the axon still generated APs while most portions of the cell were in a blocking condition (**Figures 3C,D**).

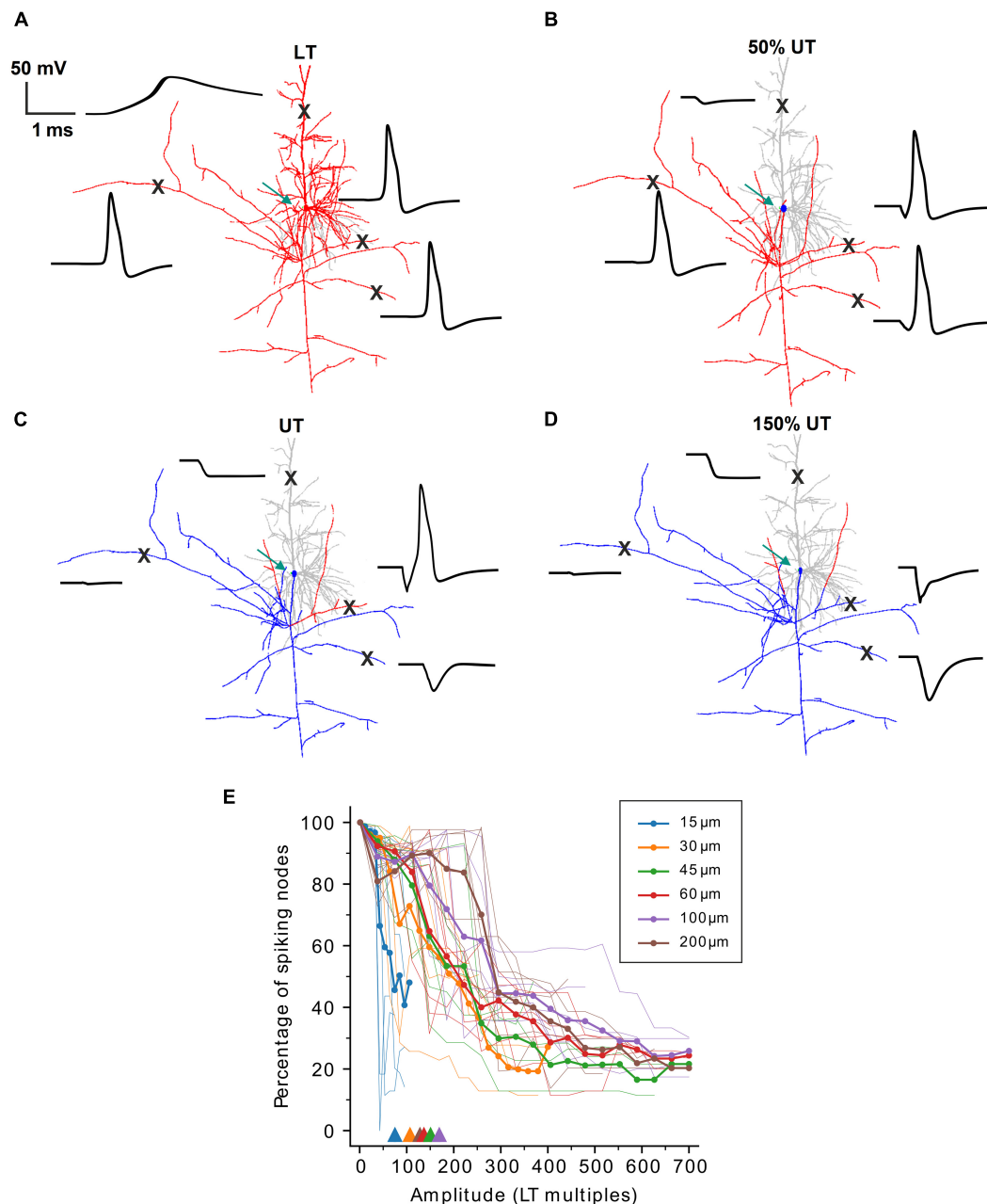


FIGURE 3 | Partial spiking activity during high-amplitude stimulation in PCs. **(A)** Neuron shape plot showing portions along the neural membrane which generated an AP (red) and that were not excited (gray) when stimulated at LT. Membrane voltage over time (black) is shown for four locations ("X") along the PC. **(B–D)** Similar as panel **(A)** but for amplitudes of 50% UT **(B)**, UT **(C)**, and 150% UT **(D)**, respectively. Regions with an AP are shown in red, regions without an AP in gray (dendrites) or blue (axon and soma). Green arrows indicate the electrode location 15 μ m distant to the soma. **(E)** The percentage of spiking nodes of Ranvier is plotted against stimulus amplitude (in multiples of LT) for all six investigated electrode distances. Thin lines indicate the spiking node percentage for single cells, thick lines indicate population means. Triangles show the mean thresholds ratios from **Figure 2D** for different electrode distances.

To quantify the partial spiking in axon collaterals, we computed the percentage of spiking nodes of Ranvier at stimulus amplitudes above LT (**Figure 3E**). For the smallest electrode distance of 15 μ m, similar to the results from **Figure 2D** (see **Figure 3E**, triangles), the percentage of spiking nodes dropped rapidly when stimulus amplitude exceeded $\sim 50 \times$ LT. For

larger distances the spiking percentage decreased but eventually plateaued at approximately 25% indicating partial spiking even at stimulus amplitudes $> 500 \times$ LT.

Taken together, no complete block was observed in PCs for all examined distances and AP blockage was mostly observed in regions with strong hyperpolarization in response

to high-amplitude stimulation. The partial block is mostly specific to extracellular stimulation of the cell and originates from an inhomogeneous reflection of electric field on the transmembrane voltage of axon collaterals and inhomogeneous activating function.

Axon Initial Segment-Induced Spiking During Micro-Stimulation

In the next set of experiments, we were interested in the location where APs are initiated during stimulation close to the soma. The site of spike initiation (SSI) was defined as the compartment whose membrane voltage first crossed 0 mV. The SSI was examined in the multi-compartment soma configuration. When applying a monophasic cathodic pulse close to the soma (15 μm distance), following the activating function (cf. **Figure 2A**), a distinct polarization pattern of the somatic compartments could be observed. For both cell types, somatic compartments close to the stimulating electrode were strongly depolarized during the pulse whereas compartments on the far side of the soma were hyperpolarized (**Figures 4A,C**, red and blue arrows). Interestingly, the strong depolarization at the soma did not result in an AP directly but compartments along the proximal axon initiated the spike (**Figures 4A,C**, light blue). This region is called the axon initial segment and, due to its high density of sodium channels, has been shown to be the SSI during a variety of stimulation conditions in both PCs and RGCs (Rattay and Wenger, 2010; Werginz et al., 2014). The AIS-induced AP subsequently propagated bidirectionally into the distal axon as well as backward into the soma and dendrites (**Figures 4A,C**, thick black line).

The experiment was repeated for all model neurons at electrode distances of 15, 30, 45, 60, 100, and 200 μm . The SSI was confined to the AIS in all cases, with small variations for different electrode distances. This is shown by plotting the distance between the SSI and the soma vs. the sum of the distance between the AIS and the soma and the length of the AIS (**Figures 4B,D**). The solid gray lines show the best-fit logistic functions with r^2 values of 0.74 and 0.91 for RGCs and PCs, respectively.

Our results show that APs are always initiated within the AIS for micro-stimulation in the vicinity of the soma, regardless of electrode-to-soma distance. For short AIS lengths, the AP initiated close to the distal end of the AIS, whereas in cells with longer AIS which are located far from the soma the SSI was shifted to the center of the AIS.

Stimulus Parameters Affect Threshold Ratios

So far, our simulations were restricted to stimulation with a point source and monophasic pulses from defined electrode locations. However, parameters such as electrode size and pulse duration cannot be chosen freely in neural implants due to hardware, software, and energy constraints. The placement of stimulating electrodes is also limited by constraints of the surrounding biological tissue. In the retina, for example, implants can be placed on the epiretinal surface to stimulate RGCs directly. In such implants an array of disk electrodes interfaces with the

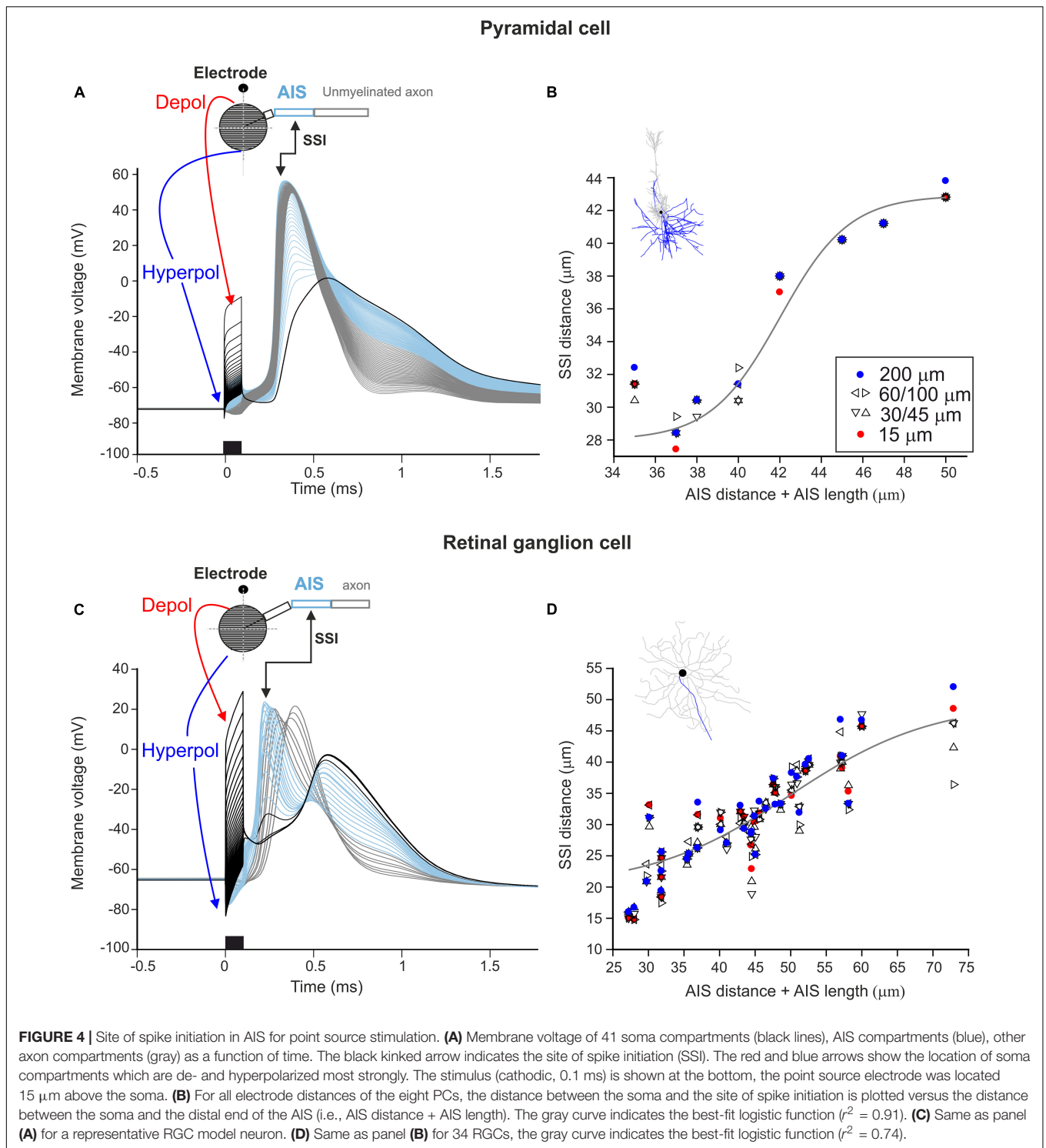
targeted RGCs. Therefore, the impact of the size of disk electrodes on LTs, UTs and the UT/LT ratios was examined. The electrode-to-soma distance was set to 15 μm as in our previous simulations as the strongest effect of the *trans*-somatic electric field on LTs and UTs was observed at smallest distances. **Figure 5A** shows UT/LT ratios for electrode diameters ranging from 10 to 200 μm and compares them to the point source electrode results. For electrode diameters in the range of 10–50 μm threshold ratios increased, however, for the largest electrode tested we found decreasing threshold ratios that were in a similar range as for point source stimulation.

To prevent potentially tissue damage due to charge accumulation, most studies use charge-balanced biphasic pulses. Therefore, we studied threshold ratios when a biphasic cathodic-first pulse was applied. The cathodic phase duration was held constant at 0.1 ms, whereas the following anodic pulse duration was varied from 0.1 up to 1 ms with its amplitude adjusted for charge-neutral stimulation. Threshold ratios are shown for phase duration ratios ($D_{\text{cat}}/D_{\text{ano}}$) ranging from 0.1 to 1 and compared with the monophasic pulse used in our previous simulations (**Figure 5B**). Our results indicate up to threefold higher threshold ratios for symmetric and close to symmetric pulse shapes (pulse ratio > 0.6), whereas this effect decreased for longer charge balancing pulses. For the longest anodic pulse of 1 ms the biphasic stimulus became pseudo-monophasic and its UT/LT ratio was close to the monophasic case.

Targeted stimulation of PCs with neural implants is challenging as the precise electrode location cannot be determined during surgery. The inserted micro-electrodes are placed within the targeted cortical layer(s) and thus can be located randomly in space relative to PC somata. In order to quantify the effect of the electrode-to-soma positioning, LTs, UTs as well as threshold ratios were calculated in the eight PC model neurons for six electrode locations around the soma. Electrode distance was set to 15 μm to the center of the multi-compartment soma (**Figure 6A**). LTs and UTs for all investigated positions are shown for each cell in **Figure 6B**. Interestingly, for each of the eight model neurons tested, one electrode location resulted in significantly lower LTs and UTs (outliers in **Figure 6B**). More detailed analysis revealed that these outliers were linked to the electrode distance to the hillock (**Figure 6C**). Similar LTs and UTs were observed for all positions, except for the closest electrode location to the axon hillock, which resulted in the lowest LTs and UTs (red ellipse). **Figure 6D** shows threshold ratios of the six investigated electrode locations for each cell. Median ratios ranged from 40 to 80 similar to threshold ratios for an electrode distance of 15 μm (cf. **Figure 2D**).

Population Response of Retinal Ganglion Cells to Supra-Threshold Stimulation

In a final set of experiments, we explored how the UT affects the activation pattern of a population of RGCs. **Figure 7A** shows the transition from LT to UT for 100 RGCs distributed on the epiretinal surface when stimulated by a 50 μm disk electrode. The pulse was biphasic with a pulse ratio of 0.1, i.e., a 0.1 ms cathodic stimulus followed by a 1 ms balancing pulse. Small



amplitudes led to focal activation of RGCs which were located slightly offset from the stimulating electrode (Figure 7A, 1 and 2 μA). This can be explained by the low-threshold region at the distal AIS in RGCs (Fried et al., 2009; Jeng et al., 2011; Werginz et al., 2020). Increasing the stimulus amplitude led to an enlarged region of activation (Figure 7A, 4 and 8 μA). At high amplitudes

the UT resulted in a different activation pattern with RGCs that had lowest thresholds being prevented from firing APs first (Figure 7A, 1 vs. 16 μA). Highest amplitudes generated a ring of activated RGCs around the stimulating electrode creating a non-responding region around the stimulating electrode (Figure 7, 32 and 64 μA). We were also interested in the total number

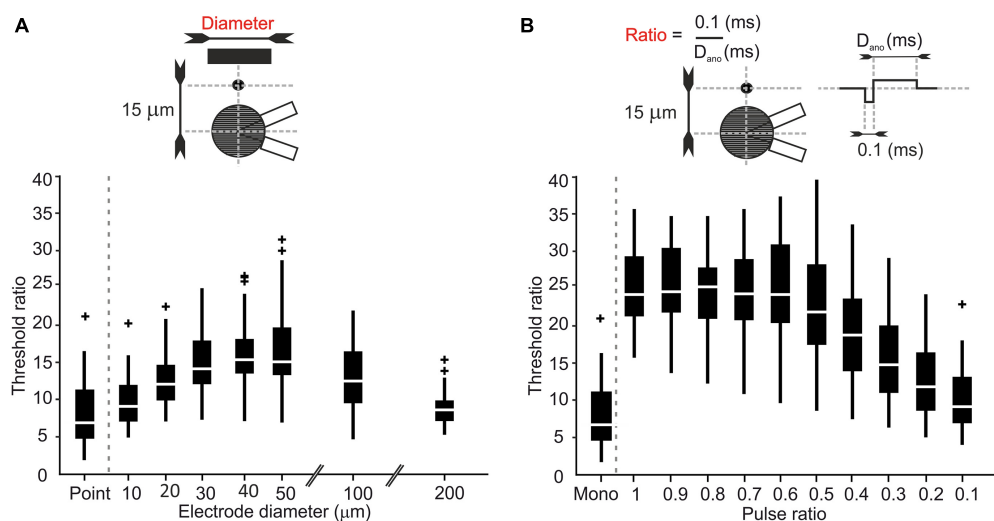


FIGURE 5 | Electrode size and pulse configuration affect threshold ratios in RGCs. **(A)** Threshold ratio vs. electrode diameters ranging from 10 to 200 μm . **(B)** Threshold ratio of monophasic and charge balanced biphasic pulses plotted vs. the ratio $0.1/D_{\text{ano}}$.

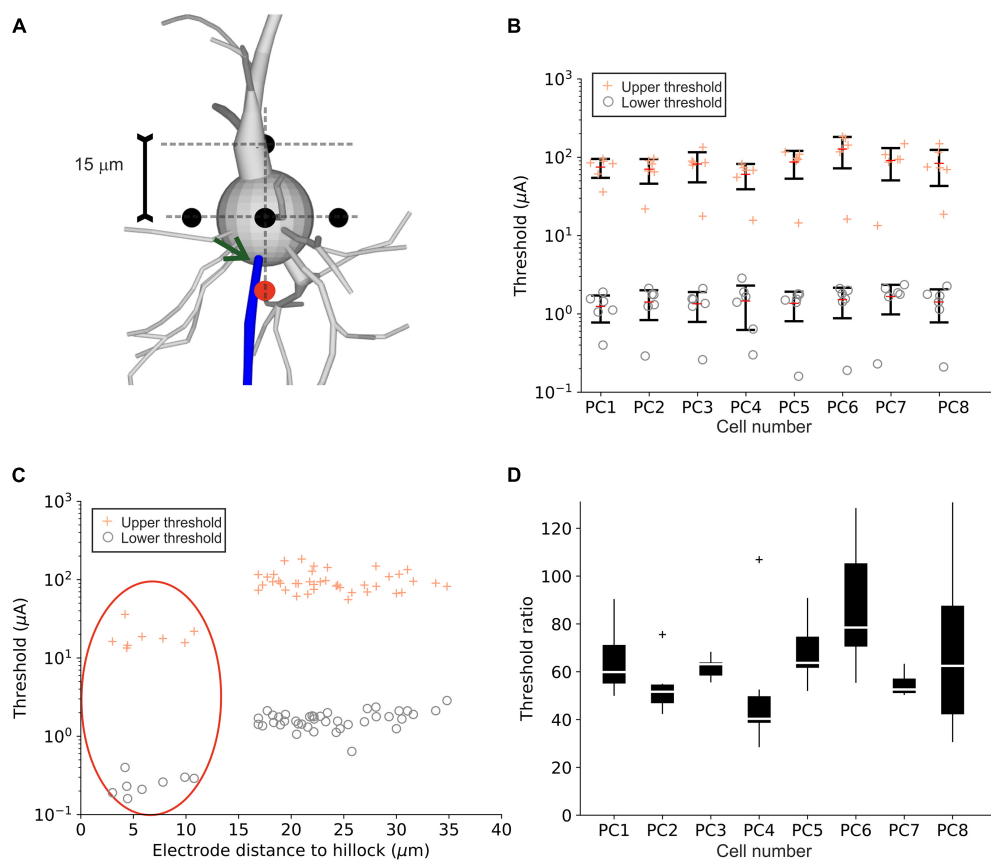


FIGURE 6 | Upper and lower threshold for different point source locations close to the PC soma. **(A)** Six electrode positions (black and red circles) in a distance of 15 μm to the soma center were investigated for the eight PC model neurons. The red circle indicates the electrode positions closest to the hillock (indicated by arrow). **(B)** LTs ("o") and UTs ("+") are shown for individual cells. **(C)** LTs ("o") and UTs ("+") plotted as a function of electrode distance to the hillock. Points within the red ellipse correspond to the red electrode location in panel **(A)**. **(D)** Threshold ratios for all eight PCs for all electrode locations.

of activated RGCs for different stimulus amplitudes. **Figure 7B** shows a monotonic increase of activated cells when the stimulus amplitude was increased from 1 to 64 μA . Interestingly, the number of activated cells still increased when RGCs close to the electrode were already blocked (gray shading). However, despite a larger number of activated cells at higher amplitudes, the different activation pattern (circular versus ring-shaped, **Figure 7B**, top) is not expected to generate well-defined visual percepts.

DISCUSSION

During extracellular electric stimulation axons are the most sensitive elements of a neuron for spike initiation (Porter, 1963; Nowak and Bullier, 1998; Rattay and Wenger, 2010). Typically, axon stimulation requires about five times lower intensities for cathodic versus anodic pulses (BeMent and Ranck, 1969; Rattay, 1990). Consequently, to save energy, cathodic stimulation is often preferred in neuroprosthetics, e.g., as pseudo-monophasic pulses in deep brain and spinal cord stimulation. The existence of an upper limit/threshold (UT) for cathodic axon stimulation was detected and quantified by a ratio UT/LT of about 3 (Katz and Miledi, 1965) and a ratio of 8–10 during micro-stimulation of myelinated fibers in the spinal cord (Roberts and Smith, 1973; Ranck, 1975).

Spike initiation in dendrites is demanding because of their low sodium channel density (Gasparini et al., 2004; Rattay and Wenger, 2010; Rattay et al., 2012). An increased sodium channel density in the soma (**Table 2**) makes it a potential candidate (i) to play a role in spike initiation as the depolarized region of the soma activates the low threshold sodium channels in the AIS, and (ii) for influencing the UT because of the strong gradient of the electric field across the soma during micro-stimulation. A large gradient of the applied electric field is needed to depolarize portions of the somatic membrane and the primarily depolarized region is smaller than half of the somatic surface (**Figure 2A**; Fellner et al., 2019). Such large gradients are expected in the vicinity of micro-electrodes.

As shown by experiments, a micro-electrode in a distance of about 25 μm from an RGC soma resulted in a LT of 3 μA and an UT at 18 μA , i.e., an UT/LT ratio of 6, if both LT and UT are defined by the rule 50% of the pulses elicit spikes, whereas the ratio is about 10 for stronger limits, e.g., rare spiking similar to spontaneous firing at LT and UT (Boinagrov et al., 2012). We obtained comparable UT/LT ratios in the investigated model RGCs which increased with electrode distance (**Figure 2E**). In order to see the contribution of the soma to spike generation, the simulations were executed with a single- and a multi-compartment model of the soma. The difference in the statistical plots of both evaluations is an indicator that the soma contributes to spike generation and suppression. This difference was significant in RGCs for LTs and UTs when electrode distance was smaller than 60 and 30 μm , respectively (**Figure 2D**). In contrast, no significant difference was found in PCs between both soma configurations, neither in LTs nor in UTs (**Figure 2B**).

As no experimental UT studies are available for PCs, we speculate that the small impact of the PC soma to LTs and

UTs is based on anatomical differences in comparison to RGCs, these are (i) a larger number of dendrites has to be maintained by the PC soma with intracellular current flow during somatic excitation and (ii) the PC axon has many branches in various directions (**Figure 1**). The complex cell geometry of PCs hinders the complete block in all axon branches (**Figure 3**) and reduces the UT/LT ratio slightly if certain axon branches are removed (not shown).

Some of our observations are in line with previous results showing that during extracellular stimulation of cortical neurons axonal firing could be observed while the soma, dendrites, AIS, as well as the first node of Ranvier were blocked artificially (Nowak and Bullier, 1996). For stimulation of PCs around the soma (up to 200 μm away in our case) we observed that partial UTs are related to the arrangement of axonal branches and their distance to the stimulating electrode, which affected UTs, whereas it had little impact on LTs. In RGCs, on the other hand, a complete UT always arises from either a somatic UT for close electrode distances with smaller threshold ratios (up to 15) or an anodal surround UT of the axon for larger electrode distances with higher threshold ratios (up to 60).

We show that at LT, APs always initiated within the AIS in both cell types as in agreement with various studies using intracellular stimulation or synaptic excitation (Palmer and Stuart, 2006; Shu et al., 2007; Yu et al., 2008; Bender and Trussell, 2012). This is also in line with previous studies showing the AIS is the most sensitive region for electric stimulation (Fried et al., 2009; Jeng et al., 2011; Werginz et al., 2020); however, in our study, stimulation was always applied close to the soma and not directly above the AIS. The somatic polarization leads to axial currents depolarizing the AIS, which subsequently initiate the AP because of its high density of sodium channels. In contrast to an experimental study that shows the distal end of the AIS ($\sim 35 \mu\text{m}$) to be the site of AP initiation in layer 5 PCs (Palmer and Stuart, 2006), we demonstrate that with increasing the AIS length, the site of AP initiation was shifted toward the center of AIS in both cell types (**Figure 4**).

For RGCs, we also tested realistic electrode geometries as well as pulse parameters and how these affect LTs and UTs. Our findings suggest that small micro-electrodes up to 50 μm in diameter increase the stimulation window as UTs become larger. On the other hand, the largest electrode diameter tested (200 μm) resulted in low threshold ratios. In retinal implants, the optimal electrode size is still under debate; however, our results indicate that UTs are not likely to play a significant role during stimulation, independent of electrode size. Similarly, symmetric charge-balanced pulses, as mostly applied in current retinal implants, increase the threshold ratio up to 25. Pseudo-monophasic pulses, on the other hand, resulted in (low) threshold ratios similar to monophasic pulses. In PCs, LTs and UTs but not threshold ratios were highly dependent on the relative arrangement between electrode and target neuron with electrode locations close to the axon hillock leading to both lowest LTs and UTs (**Figures 6B,C**). In cortex, the large number of PCs surrounding a stimulating electrode can therefore have different LTs and UTs but similar threshold ratios.

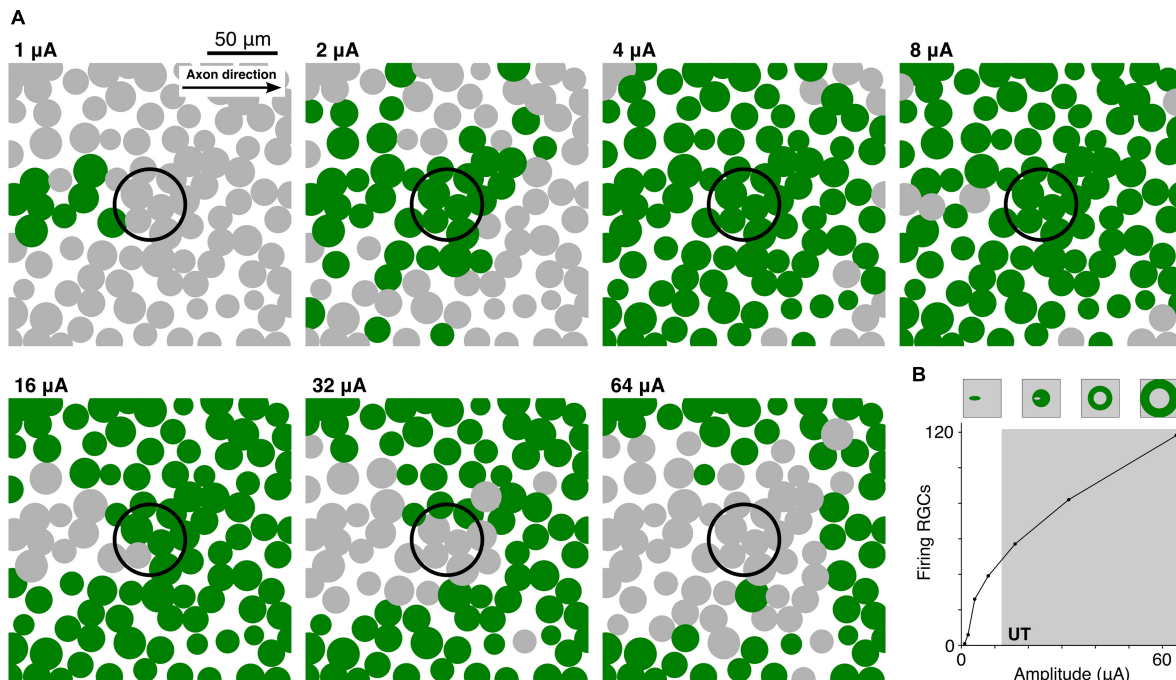


FIGURE 7 | High-amplitude stimulation results in distorted RGC activation patterns. **(A)** Top view of 100 RGC somas (filled circles) within a $200 \times 200 \mu\text{m}$ patch of the retina. Each RGC was rotated so that its axon pointed toward the right. RGCs were stimulated by a $50 \mu\text{m}$ disk electrode (black unfilled circle) located $15 \mu\text{m}$ from the epiretinal surface at amplitudes ranging from 1 to $64 \mu\text{A}$. For a given amplitude, green circles indicate cells which fired an action potential whereas gray RGCs did not respond. **(B)** 200 RGCs were stimulated within a region of interest $1 \times 1 \text{ mm}$ in size. The number of RGCs that fired an action potential is plotted versus the stimulus amplitude. Schematics on top indicate the transition of the activation pattern with increasing amplitude.

For actual applications of electric stimulation in neuroprosthetics, the question arises which stimulation configuration maximizes the stimulation window, i.e., the amplitude range which can elicit an AP. In RGCs, our results suggest that stimulation from a large distance ($200 \mu\text{m}$) with an intermediate electrode size ($50 \mu\text{m}$) and biphasic symmetric charge balanced pulses (pulse ratio = 1) will maximize the stimulation window. However, stimulation from a relatively large distance from the epiretinal surface will not achieve high spatial resolution and therefore limit clinical outcome. For PCs, on the other hand, stimulation from intermediate distances ($60 \mu\text{m}$) resulted in highest threshold ratios, however, our results show a strong dependency of thresholds and threshold ratios from the axonal geometry in PCs. Therefore, we cannot make a general statement for PCs which stimulus configuration maximizes threshold ratios.

The models used in this study include assumptions that simplify the underlying mechanisms. Although our presented models are detailed descriptions of the anatomy and biophysics of RGCs and PCs, there are still several shortcomings that should be mentioned. In all our computations, the extracellular medium, i.e., retinal or cortical tissue, was assumed to be homogeneous. In reality, however, neural tissue was shown to be non-homogeneous which will lead to distorted electric field within the tissue. For small electrode-to-cell distances, we assume that the non-homogeneity will not have a strong influence on

our results, however, we cannot rule out that for large distances this effect will alter our results moderately. The majority of the results shown in this study were computed with a simplified point source approach which does not accurately mimic the clinical situation for retinal and cortical stimulation. However, electric fields generated by a point source become similar to fields generated by a disk electrode for cases when the distance between target neuron and the electrode is larger than the electrode diameter (see Werginz et al., 2020). Therefore, in the retina the point source approach is comparable to stimulation with small disk electrodes [$<20 \mu\text{m}$, (Grosberg et al., 2017)] even when the electrode-to-cell distance is small. The retina as well as the brain consist of a large number of cell types which a single study cannot investigate. We chose two major cell types of the retina and cortex, however, cannot rule out that other cell types will respond differently to high-amplitude stimulation and therefore will have different threshold ratios than we report here.

Overall, our results indicate that an upper threshold exists during electric micro-stimulation in PCs and RGCs. The practical implications of an upper threshold are still under debate, especially because of the lack of experimental and clinical data. Here, we show that in RGCs UTs are at least as high as five times LTs for smallest electrode distances (Figure 1). Our simulations of population responses with realistic electrodes and pulse configurations resulted in UTs of approximately $15 \times \text{LT}$ (Figure 7). Based on these results it is unlikely that

UTs will have strong practical implications in retinal implants. However, in this study we only investigated one class of cells (alpha RGCs); whether other classes of cells will have different responses to high-amplitude stimulation and/or lower UTs is unknown and therefore requires additional experimental and computational studies. PCs were shown to have higher threshold ratios than RGCs in the range of 50–200 (**Figure 1**). Therefore, our results suggest that UTs will not have practical implications in stimulation of cortical tissue. However, we show that the arrangement of axon collaterals is prone to generate partial firing of APs (**Figure 3**) which makes it more difficult to derive general statements about the outcome of high-amplitude stimulation in the cortex based on computational analyses.

DATA AVAILABILITY STATEMENT

The original contributions presented in the study are included in the article/**Supplementary Material**, further inquiries can be directed to the corresponding author/s.

REFERENCES

- Almog, M., and Korngreen, A. (2014). A quantitative description of dendritic conductances and its application to dendritic excitation in layer 5 pyramidal neurons. *J. Neurosci.* 34, 182–196. doi: 10.1523/JNEUROSCI.2896-13.2014
- Ascoli, G. A. (2006). Mobilizing the base of neuroscience data: the case of neuronal morphologies. *Nat. Rev. Neurosci.* 7, 318–324. doi: 10.1038/nrn1885
- BeMent, S. L., and Ranck, J. B. Jr. (1969). A quantitative study of electrical stimulation of central myelinated fibers. *Exp. Neurol.* 24, 147–170. doi: 10.1016/0014-4886(69)90012-0
- Bender, K. J., and Trussell, L. O. (2012). The physiology of the axon initial segment. *Annu. Rev. Neurosci.* 35, 249–265. doi: 10.1146/annurev-neuro-062111-150339
- Boinagrov, D., Pangratz-Fuehrer, S., Suh, B., Mathieson, K., Naik, N., and Palanker, D. (2012). Upper threshold of extracellular neural stimulation. *J. Neurophysiol.* 108, 3233–3238. doi: 10.1152/jn.01058.2011
- Buitenweg, J. R., Rutten, W. L. C., and Marani, E. (2002). Extracellular stimulation window explained by a geometry-based model of the neuron-electrode contact. *IEEE Trans. Biomed. Eng.* 49, 1591–1599. doi: 10.1109/TBME.2002.804504
- Carnevale, N. T., and Hines, M. L. (2006). *The NEURON Book*. Cambridge: Cambridge University Press.
- Chen, J., Poulaki, V., Kim, S.-J., Eldred, W. D., Kane, S., Gingerich, M., et al. (2020). Implantation and extraction of penetrating electrode arrays in minipig retinas. *Transl. Vis. Sci. Technol.* 9:19. doi: 10.1167/tvst.9.5.19
- Cohen, C. C. H., Popovic, M. A., Klooster, J., Weil, M.-T., Möbius, W., Nave, K.-A., et al. (2020). Saltatory conduction along myelinated axons involves a periaxonal nanocircuit. *Cell* 180, 311–322. doi: 10.1016/j.cell.2019.11.039
- Fellner, A., Stiennon, I., and Rattay, F. (2019). Analysis of upper threshold mechanisms of spherical neurons during extracellular stimulation. *J. Neurophysiol.* 121, 1315–1328. doi: 10.1152/jn.00700.2018
- Fohlmeister, J. F., Cohen, E. D., and Newman, E. A. (2010). Mechanisms and distribution of ion channels in retinal ganglion cells: using temperature as an independent variable. *J. Neurophysiol.* 103, 1357–1374. doi: 10.1152/jn.00123.2009
- Fried, S. I., Lasker, A. C. W., Desai, N. J., Eddington, D. K., and Rizzo, J. F. III (2009). Axonal sodium-channel bands shape the response to electric stimulation in retinal ganglion cells. *J. Neurophysiol.* 101, 1972–1987. doi: 10.1152/jn.91081.2008
- Gasparini, S., Migliore, M., and Magee, J. C. (2004). On the initiation and propagation of dendritic spikes in CA1 pyramidal neurons. *J. Neurosci.* 24, 11046–11056. doi: 10.1523/JNEUROSCI.2520-04.2004

AUTHOR CONTRIBUTIONS

SS contributed to the conception and design of the study, implementation of computational models as well as data analysis, visualization, and writing of the manuscript. AF contributed to the implementation of computational models. PW and FR contributed to the conception and design of the study as well as data analysis and writing of the manuscript.

FUNDING

This work was supported by Austrian Science Fund (FWF) Grant No. 29650.

SUPPLEMENTARY MATERIAL

The Supplementary Material for this article can be found online at: <https://www.frontiersin.org/articles/10.3389/fncel.2021.771600/full#supplementary-material>

- Grosberg, L. E., Ganesan, K., Goetz, G. A., Madugula, S. S., Bhaskhar, N., Fan, V., et al. (2017). Activation of ganglion cells and axon bundles using epiretinal electrical stimulation. *J. Neurophysiol.* 118, 1457–1471. doi: 10.1152/jn.00750.2016
- Hay, E., Schürmann, F., Markram, H., and Segev, I. (2013). Preserving axosomatic spiking features despite diverse dendritic morphology. *J. Neurophysiol.* 109, 2972–2981. doi: 10.1152/jn.00048.2013
- Jankowska, E., and Roberts, W. J. (1972). An electrophysiological demonstration of the axonal projections of single spinal interneurons in the cat. *J. Physiol.* 222, 597–622. doi: 10.1113/jphysiol.1972.sp009817
- Jeng, J., Tang, S., Molnar, A., Desai, N. J., and Fried, S. I. (2011). The sodium channel band shapes the response to electric stimulation in retinal ganglion cells. *J. Neural Eng.* 8:36022. doi: 10.1088/1741-2560/8/3/036022
- Katz, B., and Miledi, R. (1965). Propagation of electric activity in motor nerve terminals. *Proc. R. Soc. London. Ser. B. Biol. Sci.* 161, 453–482. doi: 10.1098/rspb.1965.0015
- Mainen, Z. F., and Sejnowski, T. J. (1996). Influence of dendritic structure on firing pattern in model neocortical neurons. *Nature* 382, 363–366. doi: 10.1038/382363a0
- Mathieson, K., Loudin, J., Goetz, G., Huie, P., Wang, L., Kamins, T. I., et al. (2012). Photovoltaic retinal prosthesis with high pixel density. *Nat. Photonics* 6, 391–397. doi: 10.1038/nphoton.2012.104
- Meng, K., Fellner, A., Rattay, F., Ghezzi, D., Meffin, H., Ibbotson, M. R., et al. (2018). Upper stimulation threshold for retinal ganglion cell activation. *J. Neural Eng.* 15:46012. doi: 10.1088/1741-2552/aabb7d
- Middlebrooks, J. C., and Snyder, R. L. (2008). Intraneural stimulation for auditory prosthesis: modiolar trunk and intracranial stimulation sites. *Hear. Res.* 242, 52–63. doi: 10.1016/j.heares.2008.04.001
- Newman, J. (1966). Resistance for flow of current to a disk. *J. Electrochem. Soc.* 113, 501–502.
- Nguyen, H. T., Tangutooru, S. M., Rountree, C. M., Kantzos, A. J., Tarlochan, F., Yoon, W. J., et al. (2016). Thalamic visual prosthesis. *IEEE Trans. Biomed. Eng.* 63, 1573–1580. doi: 10.1109/TBME.2016.2567300
- Nowak, L. G., and Bullier, J. (1996). Spread of stimulating current in the cortical grey matter of rat visual cortex studied on a new in vitro slice preparation. *J. Neurosci. Methods* 67, 237–248. doi: 10.1016/0165-0270(96)00065-9
- Nowak, L. G., and Bullier, J. (1998). Axons, but not cell bodies, are activated by electrical stimulation in cortical gray matter II. Evidence from selective inactivation of cell bodies and axon initial segments. *Exp. Brain Res.* 118, 489–500. doi: 10.1007/s002210050305

- Palmer, L. M., and Stuart, G. J. (2006). Site of action potential initiation in layer 5 pyramidal neurons. *J. Neurosci.* 26, 1854–1863. doi: 10.1523/JNEUROSCI.4812-05.2006
- Porter, R. (1963). Focal stimulation of hypoglossal neurones in the cat. *J. Physiol.* 169:630. doi: 10.1113/jphysiol.1963.sp007285
- Ranck, J. B. (1975). Which elements are excited in electrical stimulation of mammalian central nervous system: a review. *Brain Res.* 98, 417–440. doi: 10.1016/0006-8993(75)90364-9
- Rattay, F. (1986). Analysis of Models for External Stimulation of Axons. *IEEE Trans. Biomed. Eng.* 33, 974–977. doi: 10.1109/TBME.1986.325670
- Rattay, F. (1988). Modeling the excitation of fibers under surface electrodes. *IEEE Trans. Biomed. Eng.* 35, 199–202. doi: 10.1109/10.1362
- Rattay, F. (1990). *Electrical Nerve Stimulation: Theory, Experiments, and Applications*. Vienna: Springer.
- Rattay, F. (1999). The basic mechanism for the electrical stimulation of the nervous system. *Neuroscience* 89, 335–346. doi: 10.1016/S0306-4522(98)00330-3
- Rattay, F. (2014). On the upper threshold phenomenon of extracellular neural stimulation. *J. Neurophysiol.* 112, 2664–2665. doi: 10.1152/jn.00323.2014
- Rattay, F., and Aberham, M. (1993). Modeling Axon Membranes for Functional Electrical Stimulation. *IEEE Trans. Biomed. Eng.* 40, 1201–1209. doi: 10.1109/10.250575
- Rattay, F., and Wenger, C. (2010). Which elements of the mammalian central nervous system are excited by low current stimulation with microelectrodes?. *Neuroscience* 170, 399–407. doi: 10.1016/j.neuroscience.2010.07.032
- Rattay, F., Paredes, L. P., and Leao, R. N. (2012). Strength–duration relationship for intra-versus extracellular stimulation with microelectrodes. *Neuroscience* 214, 1–13. doi: 10.1016/j.neuroscience.2012.04.004
- Roberts, W. J., and Smith, D. O. (1973). Analysis of Threshold Currents during Myostimulation of Fibres in the Spinal Cord. *Acta Physiol. Scand.* 89, 384–394. doi: 10.1111/j.1748-1716.1973.tb05533.x
- Rushton, W. A. H. (1951). A theory of the effects of fibre size in medullated nerve. *J. Physiol.* 115, 101–122. doi: 10.1113/jphysiol.1951.sp004655
- Schmidt, E. M., Bak, M. J., Hambrecht, F. T., Kufta, C. V., O'Rourke, D. K., and Vallabhanath, P. (1996). Feasibility of a visual prosthesis for the blind based on intracortical micro stimulation of the visual cortex. *Brain* 119, 507–522. doi: 10.1093/brain/119.2.507
- Shu, Y., Duque, A., Yu, Y., Haider, B., and McCormick, D. A. (2007). Properties of action-potential initiation in neocortical pyramidal cells: evidence from whole cell axon recordings. *J. Neurophysiol.* 97, 746–760. doi: 10.1152/jn.00922.2006
- Werginz, P., and Rattay, F. (2016). The impact of calcium current reversal on neurotransmitter release in the electrically stimulated retina. *J. Neural Eng.* 13:46013. doi: 10.1088/1741-2560/13/4/046013
- Werginz, P., Fried, S. I., and Rattay, F. (2014). Influence of the sodium channel band on retinal ganglion cell excitation during electric stimulation—a modeling study. *Neuroscience* 266, 162–177. doi: 10.1016/j.neuroscience.2014.01.067
- Werginz, P., Raghuram, V., and Fried, S. I. (2020). The relationship between morphological properties and thresholds to extracellular electric stimulation in α RGCs. *J. Neural Eng.* 17:45015. doi: 10.1088/1741-2552/abab47
- Wiley, J. D., and Webster, J. G. (1982). Analysis and control of the current distribution under circular dispersive electrodes. *IEEE Trans. Biomed. Eng.* 29, 381–385. doi: 10.1109/TBME.1982.324910
- Yu, Y., Shu, Y., and McCormick, D. A. (2008). Cortical action potential backpropagation explains spike threshold variability and rapid-onset kinetics. *J. Neurosci.* 28, 7260–7272. doi: 10.1523/JNEUROSCI.1613-08.2008

Conflict of Interest: The authors declare that the research was conducted in the absence of any commercial or financial relationships that could be construed as a potential conflict of interest.

Publisher's Note: All claims expressed in this article are solely those of the authors and do not necessarily represent those of their affiliated organizations, or those of the publisher, the editors and the reviewers. Any product that may be evaluated in this article, or claim that may be made by its manufacturer, is not guaranteed or endorsed by the publisher.

Copyright © 2021 Sajedi, Fellner, Werginz and Rattay. This is an open-access article distributed under the terms of the Creative Commons Attribution License (CC BY). The use, distribution or reproduction in other forums is permitted, provided the original author(s) and the copyright owner(s) are credited and that the original publication in this journal is cited, in accordance with accepted academic practice. No use, distribution or reproduction is permitted which does not comply with these terms.



Transcorneal Electrical Stimulation Induces Long-Lasting Enhancement of Brain Functional and Directional Connectivity in Retinal Degeneration Mice

Stephen K. Agadagba¹, Abdelrahman B. M. Eldaly^{1,2} and Leanne Lai Hang Chan^{1*}

¹ Department of Electrical Engineering, City University of Hong Kong, Kowloon, Hong Kong SAR, China, ² Electrical Engineering Department, Faculty of Engineering, Minia University, Minia, Egypt

OPEN ACCESS

Edited by:

Arianna Maffei,
Stony Brook University, United States

Reviewed by:

Christianne E. Strang,
University of Alabama at Birmingham,
United States

Qi Fang,
University of Southern California,
United States

*Correspondence:

Leanne Lai Hang Chan
leanne.chan@cityu.edu.hk

Specialty section:

This article was submitted to
Cellular Neurophysiology,
a section of the journal
Frontiers in Cellular Neuroscience

Received: 28 September 2021

Accepted: 14 January 2022

Published: 07 February 2022

Citation:

Agadagba SK, Eldaly ABM and
Chan LLH (2022) Transcorneal
Electrical Stimulation Induces
Long-Lasting Enhancement of Brain
Functional and Directional
Connectivity in Retinal Degeneration
Mice.

Front. Cell. Neurosci. 16:785199.
doi: 10.3389/fncel.2022.785199

To investigate neuromodulation of functional and directional connectivity features in both visual and non-visual brain cortices after short-term and long-term retinal electrical stimulation in retinal degeneration mice. We performed spontaneous electrocorticography (ECoG) in retinal degeneration (rd) mice following prolonged transcorneal electrical stimulation (pTES) at varying currents (400, 500 and 600 μ A) and different time points (transient or day 1 post-stimulation, 1-week post-stimulation and 2-weeks post-stimulation). We also set up a sham control group of rd mice which did not receive any electrical stimulation. Subsequently we analyzed alterations in cross-frequency coupling (CFC), coherence and directional connectivity of the primary visual cortex and the prefrontal cortex. It was observed that the sham control group did not display any significant changes in brain connectivity across all stages of electrical stimulation. For the stimulated groups, we observed that transient electrical stimulation of the retina did not significantly alter brain coherence and connectivity. However, for 1-week post-stimulation, we identified enhanced increase in theta-gamma CFC. Meanwhile, enhanced coherence and directional connectivity appeared predominantly in theta, alpha and beta oscillations. These alterations occurred in both visual and non-visual brain regions and were dependent on the current amplitude of stimulation. Interestingly, 2-weeks post-stimulation demonstrated long-lasting enhancement in network coherence and connectivity patterns at the level of cross-oscillatory interaction, functional connectivity and directional inter-regional communication between the primary visual cortex and prefrontal cortex. Application of electrical stimulation to the retina evidently neuromodulates brain coherence and connectivity of visual and non-visual cortices in retinal degeneration mice and the observed alterations are largely maintained. pTES holds strong possibility of modulating higher cortical functions including pathways of cognition, awareness, emotion and memory.

Keywords: electrocorticography (ECoG), retinal degeneration, transcorneal electrical stimulation, theta-gamma coupling, brain coherence, brain connectivity analysis

INTRODUCTION

The human brain is a dynamic organ that produces large scale coordinated electrophysiological activities in billions of neurons. These activities are represented as repetitive patterns of brain oscillations. Brain oscillations are capable of interacting with each other at different frequencies; a concept called cross-frequency coupling (CFC). This rhythmic interaction between synchronous neural oscillations is a known fingerprint of functional coupling. CFC has been reported to occur in various brain regions including deep brain structures such as the hippocampus (Michaels et al., 2018), amygdala (Zheng et al., 2019), cortical areas of the prefrontal cortex (Helfrich et al., 2017), motor cortex (De Hemptinne et al., 2013) and visual cortex (Sokoliuk and VanRullen, 2012). Notwithstanding the area of occurrence, CFC often features an interaction where the phase of low frequency oscillations such as theta (5–10 Hz) or alpha (10–15 Hz) has been demonstrated to couple or modulate the amplitude of high frequency gamma oscillations (30–100 Hz) (Zhang et al., 2019). This phase amplitude coupling (PAC) of the associated brain rhythms has been severally proven to play important roles in higher cognitive functions of the brain including visual functions (Sokoliuk and VanRullen, 2012), working memory (Lega et al., 2014) and behavioral functions (Ohki et al., 2020) amongst others.

When more than one brain region is considered, brain coherence may be established owing to a high degree of association or similarity in neural activities between the associated brain regions. Apart from interpreting only the similarity in neural activities between brain sites, the directional connectivity between the brain regions must also be taken into account. For example, visual recognition of letters in the human brain specifically involves connectivity networks arising from the occipital lobe in the brain posterior to the anterior regions of the brain (Garagnani et al., 2017). Similar to CFC, both coherence and directional connectivity measures are also used to infer a functional relationship between different regions of the brain. In essence, coherence and directional connectivity between brain regions are of paramount importance in establishing coordinated network activities for physiological brain functionality.

Evidence from scientific research has shown that the pathogenesis of neurodegeneration is linked to progressive and wide spread changes in neural networks of the brain (McMackin et al., 2019). Furthermore, it has been demonstrated that drastically reduced brain coherence and connectivity are key features of several neurological and neurodegenerative disorders such as schizophrenia, Parkinson's disease, epilepsy, autism and Alzheimer's disease (Nakamura et al., 2017; Bazzigaluppi et al., 2018; Salimpour and Anderson, 2019). Consequently, electrical stimulation strategies have been studied to modulate neural oscillations and ultimately re-adjust dysfunctional brain connectivity networks (Salimpour and Anderson, 2019). Indeed, it has been reported that transcranial alternating current (Vossen et al., 2015) and transcranial direct current (Jamil et al., 2017) stimulation paradigm modulates percepts in the brain and the aftereffects outlast the electrical stimulation period. At this juncture, it is crucial to mention that the neural

information that originates from the retina is integrated by systems that are in active communication with one another including motor, cognitive and emotional systems (Mulckhuyse, 2018; Song et al., 2019; Costumero et al., 2020). With research progress in retinal signaling pathways, it is now becoming clearer that multiple coherence and connectivity pathways exist between the retina and other non-visual brain regions such as the prefrontal cortex, motor cortex, hippocampus and the amygdala (Preston and Eichenbaum, 2013; Turk-Browne, 2019). A typical example is the fear-emotional system which has been reported to involve a conglomeration of neural inputs from the retina, the prefrontal cortex, the hippocampus, the amygdala and the motor cortex (McFadyen et al., 2019). These inputs are both excitatory and inhibitory and occur *via* feedforward and feedback mechanisms in the associated brain regions (Suzuki and Amaral, 1994).

Similar to the aforementioned diseases, retinitis pigmentosa is also a neurodegeneration disease that involves progressive degeneration of light sensitive photoreceptor retina neurons and ultimately leads to vision loss or blindness. It has been reported that despite retinal degeneration, the retinotopic map is largely preserved (Xie et al., 2010). Consequently, several approaches are being studied for vision restoration in RP patients including retina electrical stimulation *via* invasive and non-invasive routes (Chow, 2013; Rahmatnejad et al., 2016; Beyeler et al., 2019; Chenais et al., 2021). Arising from this and from the clear evidence that the retina of the eye forms a neural-link with the brain (Murphy et al., 2016; Varadarajan and Huberman, 2018), it is therefore crucial to understand the short-term and long-term implication of retina electrical stimulation on different brain regions. Currently, there is no systematic study about the short-term and long-term neurophysiological effects of prolonged retinal stimulation in visual and non-visual regions of the brain. Furthermore, retinal prostheses are designed to treat diseases of the outer retina, such as Age-related Macular Degeneration (AMD) and Retinitis Pigmentosa (RP), which blind hundreds of thousands each year. These visual devices are implanted to electrically stimulate the retina circuitry with the aim of providing partial or complete vision restoration. Nonetheless, because retinal prostheses need to be turned on continuously to aid the daily life activities of the implant recipients, the long-term use of these devices is hypothesized to unavoidably trigger neuromodulation in both visual and non-visual regions of the brain. In our previous studies, we demonstrated that repetitive prolonged transcorneal electrical stimulation (pTES) is able to modulate the resting state brain activity of retinal degeneration (rd) mice in a frequency (Agadagba and Chan, 2020; Agadagba et al., 2020) and pulse duration-dependent manner (Agadagba and Chan, 2021). We also observed that the awake brain was more responsive to the effect of retinal electrical stimulation in comparison to the anesthetized brain (Agadagba et al., 2020). This finding about brain states has also been corroborated by other authors and it has been linked to variations in cortical processing between the two brain states (Keller et al., 2012; Durand et al., 2016). From the foregoing, in our present study we have exclusively used the retinal degeneration (rd) mice model of the human blinding disease retinitis pigmentosa to decipher the

effect of a prolonged electrical stimulation of the retina from a brain-wide perspective.

Brain coherence and connectivity indices have been previously studied in the resting brain state by techniques that analyze continuous electrophysiological signals such as local field potential (LFP), electrocorticogram (ECoG) and electroencephalogram (EEG) (Young and Eggermont, 2009). Specifically, ECoG is unique in approach and has high spatio-temporal resolution which allows tracking of neural oscillatory coherence and connectivity that occurs in the CNS. In the present study we therefore used resting state ECoG to investigate neuromodulation of functional and directional brain connectivity in both visual and non-visual cortices of rd mice after short-term stimulation (transient or 1-day post-stimulation) and long-term stimulation (1-week post-stimulation and 2-weeks post-stimulation), respectively.

MATERIALS AND METHODS

Animals and Surgery

In all experiments, retinal degeneration 10 (rd10) mice were used as animal models of human RP. The mice were bred in Laboratory Animal Research Unit (LARU) at City University of Hong Kong. All procedures for animal handling and animal experimentation were reviewed and approved by the Animal Research Ethics Sub-Committee at City University of Hong Kong (A-0249) and were carried out in compliance with the Animals (Control of Experiments) Ordinance at Department of Health, Hong Kong SAR (20–162 in DH/HT&A/8/2/5 Pt.3). A total of forty rd10 mice (20 males and 20 females) of post-natal age P60–P90 were used in this study. All surgical steps were same as described in our previous research (Agadagba et al., 2019). To summarize the surgical procedures, rd10 mice were first injected with ketamine-xylazine anesthesia (ketamine: 100 mg/kg, Xylazine: 10 mg/kg), followed by administration of mixed anesthesia [isoflurane (1.5%) and medical oxygen (0.4%)] to maintain the sleep state during the surgery. Each mouse was head fixed on a stereotaxic (Stoelting, CA, United States) and after surgical craniotomy, four stainless steel bone-screw recording electrodes of shaft diameter 2.4 mm were implanted subdurally (Model# EDP81912; Decorah LLC, GEC, United States). For the visual region, we implanted the recording electrode bilaterally over the primary visual cortex (Anterior–Posterior: –3.5 mm, Midline: 2.5 mm) (Figures 1A–C). For the non-visual region, we implanted the recording electrode bilaterally over the general region of the frontal cortex (Anterior–Posterior: 2 mm, Midline: 1 mm) in the vicinity of the medial prefrontal cortex (mPFC) and the frontal association region (Figures 1A–C). Henceforth, we refer to this region as the prefrontal cortex of the rd10 animals. It is important to state here that in the present study we used the term “non-visual region” exclusively in the context that the prefrontal cortex although involved in image interpretation, however, it does not receive direct visual signals from the receptive fields of the retinal neurons compared to the primary visual cortex. Following implantation in the regions of interest, the reference bone-screw was positioned in the cerebellar region

(Figure 1C). Heart rate of all mice was carefully monitored and their body temperature was kept constant with a heat pad (Model # TP702; Gaymar Industries, Inc., NY, United States) at 38°C. To prevent mice eyes from drying out during surgery and recording sessions, lubrical eye gel was applied. After surgery, all animals were allowed to recover for 1 week (7 days) before further experimentation.

Retinal Stimulation

Following anesthesia administration with mixture of isoflurane (1.5%) and medical oxygen (0.4%), all mice were mounted on the stereotaxic (Stoelting, CA, United States) in preparation for retinal stimulation. Retinal stimulation of rd10 mice was done by transcorneal electrical stimulation (TES). Similar to our previous studies (Agadagba et al., 2019, 2020; Agadagba and Chan, 2021), we used TES in the present study because the mouse eye is small in size (approximately 3 mm in diameter) thus no commercially available retinal implants for stimulation of the mouse eye. TES therefore provided a readily applicable non-invasive stimulation approach for the mouse eye with no known post-surgical complications. The procedure of TES was similar to our previous studies (Agadagba et al., 2020; Agadagba and Chan, 2021). Briefly, a silver wire electrode used as the stimulating electrode (impedance: 0.143 k Ω at 1 kHz) was initially connected at one end to an electrical pulse generator (Multichannel Systems STG stimulator, Model # 4004; Baden-Württemberg, Germany). The other end of the silver wire electrode was positioned on the right cornea of rd10 mice (Figure 1C). A needle reference electrode was positioned subcutaneously in close proximity to the right eye. TES was applied for a prolonged period of 30 min (hence we dubbed the stimulation as “pTES”) and repeated over the course of 7 days. Both short-term and long-term effects of pTES were investigated as described in section “Electrocorticography Signal Acquisition.”

Three test groups (with ten rd10 mice per group) were set up. Each test group was injected with charge balanced biphasic square-wave pulses of varied current intensity (400, 500, and 600 μ A, respectively), at 10 Hz stimulation frequency and 2 ms/phase pulse width. In this regard, the charge injected per phase for each test group was 0.8 μ C, 1 μ C and 1.2 μ C, respectively. A sham control group of rd10 mice ($n = 10$) was also set up and treated in the same manner as the test groups but without retinal electrical stimulation. All mice were closely monitored during and after all experimental procedures. All mice showed no sign of discomfort or emotional stress.

Electrocorticography Signal Acquisition

ECoG was used to record spontaneous electrophysiological activity over the cortical surface of awake rd10 mice. The ECoG signal was acquired and amplified by connecting an active transfer cable from the recording electrode to a data acquisition system (Model # Micro 1401-3; Cambridge Electronic Design, United Kingdom). During the process of signal acquisition, ECoG signal was sampled at 5 kHz from 0.3 to 300 Hz. A signal gain function of 1 K and 50 Hz notch filter was applied (Model # 3600; A-M Systems, Washington, United States) for signal amplification and noise cancellation. ECoG signal recording time

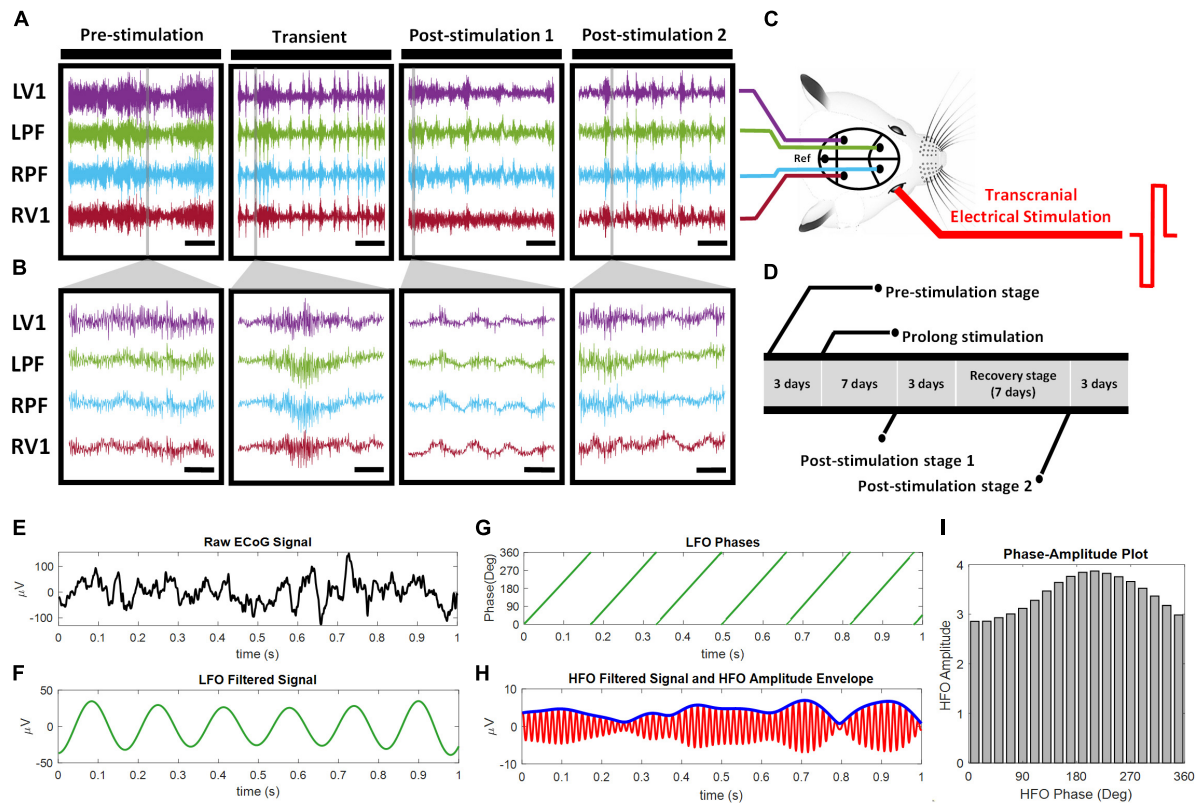


FIGURE 1 | ECoG Experimental design and steps taken to compute cross-frequency phase-amplitude coupling. **(A,B)** Represent ECoG signal traces from one rd10 mouse. ECoG signal was recorded from the four brain sites: the left primary visual cortex (LV1), the left prefrontal cortex (LPF), the right prefrontal cortex (RPF) and the right primary visual cortex (RV1) across four stages of stimulation (pre-stimulation, transient, post-stimulation 1 and post-stimulation 2) **(A)** scale bar, 5 s, **(B)** Scale bar, 100 ms. **(C)** Pictorial representation of the ECoG recording positions in the mouse brain and biphasic transcranial electrical stimulation applied to the right eye. Ref: reference electrode position. **(D)** Timeline of experimental design. Transient stage ECoG recording was performed on the first day of the 7 days prolonged stimulation. The raw ECoG signal **(E)** was filtered into phase of LFO **(F)** and amplitude (thin line) of HFO **(G)**. The time series of LFO phase and amplitude envelope of HFO (thick line) was computed from the respective filtered ECoG signals via Hilbert transformation **(H)**. The phase amplitude plot **(I)** was constructed and used to calculate the mean distribution of amplitudes over the phase bins.

was 10 min in duration. In order to investigate the short-term and long-term effects of pTES, we acquired data from ECoG recording for four stimulation stages namely pre-stimulation, transient stage, post-stimulation stage 1 and post-stimulation stage 2 (**Figures 1A,B**). For the short-term effects of pTES, transient stage ECoG activity was recorded only on day 1 of pTES while for the long-term effects of pTES, post-stimulation stage 1 ECoG activity was recorded 1-week after the start of pTES and post-stimulation stage 2 was recorded at 2-weeks after the start of the 7-days pTES (from day 17). Hence, we also refer to transient stage as day-1 post-stimulation, post-stimulation stage 1 as 1-week post-stimulation and post-stimulation stage 2 as 2-weeks post-stimulation (**Figures 1A,B,D**).

Signal Pre-processing and Signal Analysis

ECoG signal from this study was pre-processed by de-noising and down-sampling. As mentioned previously during online data sampling, 50 Hz notch filter was applied to the data

amplifier system to remove interfering 50 Hz and its super-harmonics originating from the alternating current (AC) line. Following data acquisition, a fair amount of 50 Hz noise observed was eliminated by an infinite impulse response comb (IIR-comb) filter in MATLAB algorithm (MathWorks, Inc., R2018b, Natick, Massachusetts, United States). There were approximately 3×10^6 data points obtained from each recording electrode channel which was very large and had the potential to increase computation time. To solve this problem and reduce computation time during data analysis, the ECoG signal was down-sampled from 5 to 1 kHz with MATLAB algorithm (MathWorks, Inc., R2018b, Natick, Massachusetts, United States).

Analysis of Cross-Frequency Coupling

CFC between low frequency oscillations (LFOs) and high frequency oscillations (HFOs) was analyzed for the left (contralateral) prefrontal cortex and the left (contralateral) primary visual cortex channels by PAC method (**Figures 1E-I**). Estimation of modulation index (*MI*) was used to quantify the

degree of coupling between associated brain oscillations based on Kullback-Leibler method (Tort et al., 2010). Briefly, linear finite impulse response (FIR) filter was used to filter the raw data into LFOs (1–29 Hz) for phase and HFOs (10–295 Hz) for amplitude. The phases and amplitudes of the LFOs and HFOs, respectively, were extracted by Hilbert transform from the time series of each filtered signal, followed by coupling into one composite. Next, the phases were binned into eighteen intervals (from 0° to 360° with step 20°).

The mean of the amplitude envelope over each phase bin was calculated to quantify amplitude distribution over phase bins. *MI* was computed by normalizing *H* (the entropy measure of the normalized amplitude distribution over phase bins) via the maximum achievable entropy value; $H_{\max} = \log(N)$, where *N* equals to the number of phase bins (equation 1).

$$MI = (H_{\max} - H) / H_{\max} \quad (1)$$

To test the statistical significance of the *MI* values, a distribution of 50 surrogate *MI* values was created by randomly shuffling the composite time series of high-frequency amplitude envelope and phases of a low-frequency signal after segmenting equally into 20 blocks. Assuming the surrogate *MI* values are normally distributed, the *MI* value of the original signal was considered significant depending on whether it reached the top 5% of this surrogate data distribution, otherwise it was ignored and replaced with zero. Thus, in comodulogram plots, any *MI* value greater than zero was statistically significant. For a particular channel, the averaged *MI* was calculated for all trials in each group. The comodulogram plots were obtained by representing the average *MI* values of multiple phase and pairs of amplitude frequency, computed in steps of 1 Hz with 2 Hz phase bandwidths and in steps of 5 Hz with 10 Hz amplitude bandwidths.

Analysis of Coherence

The coherence between ECoG channels of the left prefrontal cortex and the left primary visual cortex was estimated by using the *mscohere.m* function in MATLAB (MathWorks, Inc., R2018b, Natick, Massachusetts, United States). Specifically, this gives the magnitude squared coherence $C_{xy}(f)$. The magnitude squared coherence is a coherence estimate of two signals *x* and *y* based on their frequencies. $C_{xy}(f)$ uses Welch's averaged modified periodogram to assess the degree of association between input signals *x* and *y*.

$$C_{xy}(f) = \frac{|P_{xy}(f)|^2}{P_{xx}(f)P_{yy}(f)}, 0 \leq C_{xy}(f) \leq 1, \quad (2)$$

In equation 2 above, P_{xx} and P_{yy} represent the power spectral density of the signals *x* and *y*, respectively; P_{xy} represents the cross-power spectrum spectral density. For each stimulation group in the present study, the mean coherence among a pair of two EEG channels (left prefrontal cortex and the left primary visual cortex) was calculated. Over the whole ECoG recording, ECoG signal was segmented into epochs of 2 s with 1 s overlap. Over the entire frequency range (0.5 Hz–300 Hz), C_{xy} was computed at each frequency bin and epoch for each mouse.

Subsequently, the mean coherence and standard error of the mean (SEM) were then computed for all mice across the four stages (pre-stimulation, transient, post-stimulation stage 1 and post-stimulation stage 2).

Analysis of Directional Connectivity

The directional connectivity between the ECoG channels of the left prefrontal cortex and left primary visual cortex was assessed by normalized symbolic transfer entropy (NSTE), which is a non-linear method for estimating directional functional connectivity on the basis of information theory. STE quantifies the dominating direction of information flow between time series from structurally or functionally coupled systems by estimating the amount of information between the future of the target signal and the past of the source signal given the knowledge delivered from the history of the target signal in the model, which is described as follows:

$$\begin{aligned} STE_{X \rightarrow Y} &= I(Y^F; X^P | Y^P) \\ &= H(Y^F | Y^P) - H(Y^F | X^P, Y^P), \end{aligned} \quad (3)$$

where, X^P , Y^P , and Y^F represent the past of source and target signals; and the future of the target signal, respectively. $H(Y^F | Y^P)$ is the entropy of the process Y^F , that is dependent on its past. In the present study, EEGlab version 15 (Swartz Center for Computational Neuroscience, CA) and EEGapp (BIAPT lab, McGill University) toolboxes were integrated with MATLAB (MathWorks, Inc., R2018b, Natick, Massachusetts, United States) in order to estimate the NSTE. Briefly, the ECoG signal was first filtered into eight frequency bands (delta, theta, alpha, beta, low gamma, medium-gamma, high-gamma and ultra-gamma) and then segmented the filtered data into 10-s-long ECoG epochs without overlapping. The potential bias of STE was eliminated with a shuffled data by subtracting the original STE and then dividing by the entropy of the target signal, $H(Y^F | Y^P)$ (equation 4).

$$NSTE_{X \rightarrow Y} = \frac{STE_{X \rightarrow Y} - STE_{X \rightarrow Y}^{\text{Shuffled}}}{H(Y^F | Y^P)} \in [0, 1], \quad (4)$$

The feedforward (FF) NSTE and feedback (FB) NSTE between the left prefrontal cortex and the left primary visual cortex was sequentially computed in each epoch for the 10 min recording duration. The directional connectivity between the left prefrontal cortex and the left primary visual cortex was defined by the average NSTE in each stimulation group across the four stimulation stages.

Statistical Analysis

All statistical analyses were performed by using the software Origin (Pro) (Version 2015, Origin Lab Corporation, Northampton, MA, United States). To test the statistical significance of the change in PAC, coherence and NSTE across the four stages of stimulation, one-way ANOVA and Tukey's multi-comparison tests were carried out for the eight frequency bands. The adjusted *P*-values by Tukey's correction was $*P < 0.025$.

RESULTS

Medium-Gamma Oscillations Are Coupled to Theta Waves in the Primary Visual Cortex Following Retinal Electrical Stimulation

It has been demonstrated that CFC between the phases of LFOs and the amplitudes of HFOs play important roles in visual-related activities (Spaak et al., 2012). Thus, in the left primary visual cortex we analyzed the effect of varying the stimulation current (400, 500, and 600 μ A) on the coupling characteristics between the phase of delta, theta and alpha waves and the amplitude of a range of gamma oscillations (low gamma γ_l , medium gamma γ_m , high gamma γ_h and ultra-gamma γ_u). The results obtained at each stage of pTES (transient, post-stimulation 1 and post-stimulation 2) were compared with the corresponding baseline (pre-stimulation) PAC results in rd10 mice. As shown in **Figures 2A,B**, for the transient stage all stimulation groups (400, 500, and 600 μ A) yielded no significant change ($P = 0.778$, 0.997 , and 0.918) in PAC of all assessed LFOs and HFOs compared to the corresponding pre-stimulation PAC. However, for 1-week post-stimulation (post-stimulation stage 1), all stimulation groups (400, 500, and 600 μ A) displayed prominent increase ($P = 0.009$, 0.004 , and 0.003) in theta medium-gamma PAC compared with the theta-medium gamma PAC at the pre-stimulation stage (**Figures 2A,B**).

Two weeks after the start of the 7-days pTES (2-weeks post-stimulation or post-stimulation stage 2), there was maintained elevated increase in theta-medium gamma PAC of rd10 mice stimulated with 400 μ A ($P = 0.010$), 500 μ A ($P = 0.011$), and 600 μ A ($P = 0.011$), respectively, compared with theta-medium gamma PAC at the pre-stimulation stage (**Figures 2A,B**). Despite, the long-lasting enhancement in theta-medium gamma PAC among all stimulation groups, 400 μ A stimulation appeared to elicit a stronger long-lasting enhancement in theta medium-gamma PAC compared with the 500 and 600 μ A stimulations, respectively. This was evident because stimulation with 400 μ A showed no significant change ($P = 0.107$) in the enhanced theta-medium gamma PAC between post-stimulation stage 1 and post-stimulation stage 2 compared to the significant change that occurred in the theta-medium gamma PAC between post-stimulation stage 1 and post-stimulation stage 2 with both 500 μ A ($P = 0.019$) and 600 μ A ($P = 0.019$) stimulations (**Figure 2B**). Meanwhile the left primary visual cortex of the sham control group displayed no significant changes in theta medium-gamma PAC across the three stimulation stages (transient $P = 0.131$, post-stimulation 1 $P = 0.056$ and post-stimulation 2 $P = 0.061$) (**Supplementary Figures 1A,B**).

Both Medium-Gamma and High-Gamma Oscillations Are Coupled to Theta Waves in the Prefrontal Cortex Following Retinal Electrical Stimulation

PAC characteristics of LFOs and HFOs have been demonstrated to play major roles in cognitive neuronal networks of the

prefrontal cortex (Andino-Pavlovsky et al., 2017). This prompted us to analyze the changes in PAC of the left prefrontal cortex of rd10 mice in response to varying the stimulation current of TES. Similar to the left primary visual cortex, we monitored PAC features during different stages of TES (transient, post-stimulation 1 and post-stimulation 2) in all experimental groups (400, 500, and 600 μ A and sham control), subsequently we compared the results with the corresponding baseline (pre-stimulation stage) PAC of rd10 mice. Unlike the left primary visual cortex for the transient stage, the left prefrontal cortex revealed significant increase for both theta medium-gamma ($P = 0.012$, $P = 0.01$, and $P = 0.007$) and high-gamma ($P = 0.019$, 0.013 , and 0.007) PAC in 400, 500, and 600 μ A stimulation groups, respectively, compared with the corresponding pre-stimulation PAC results (**Figures 2C,D**). Furthermore, for 1-week post-stimulation (post-stimulation stage 1), the left prefrontal cortex displayed significantly enhanced theta medium-gamma ($P = 0.001$, 0.002 , and 0.005) and high-gamma ($P = 0.01$, 0.011 , and 0.006) PAC, respectively, across all stimulation groups (400, 500, and 600 μ A) compared with the corresponding PAC results at the pre-stimulation stage (**Figures 2C,D**).

We observed that for 2-weeks post-stimulation (post-stimulation stage 2), only rd10 mice stimulated with 400 μ A maintained the significant increase in both theta medium-gamma ($P = 0.01$) and theta high-gamma PAC ($P = 0.014$) compared with the corresponding pre-stimulation PAC results (**Figures 2C,D**). In this regard rd10 mice stimulated with 500 and 600 μ A, respectively, showed no significant change in theta-medium gamma (500 μ A $P = 0.486$; 600 μ A $P = 0.213$) and high-medium gamma (500 μ A $P = 0.455$; 600 μ A $P = 0.526$) PAC compared with the corresponding pre-stimulation PAC results (**Figures 2C,D**). Similar to the left primary visual cortex, in the left prefrontal cortex of rd10 mice stimulated with 400 μ A, there was no significant change (**Figure 2D**) in theta medium-gamma ($P = 0.172$) and theta high-gamma ($P = 0.683$) PAC between post-stimulation stage 1 and post-stimulation stage 2. However, for both 500 and 600 μ A groups, theta medium-gamma (500 μ A $P = 0.002$; 600 μ A $P = 0.001$) and theta high-gamma (500 μ A $P = 0.011$; 600 μ A $P = 0.001$) PAC in post-stimulation stage 2 was significantly reduced when compared to the corresponding PAC results in post-stimulation stage 1 (**Figure 2D**). Similar to the left primary visual cortex all stimulation stages, the left prefrontal cortex of the sham control group displayed no significant changes in theta medium-gamma (transient $P = 0.197$, post-stimulation 1 $P = 0.035$ and post-stimulation 2 $P = 0.026$) and theta high-gamma (transient $P = 0.03$, post-stimulation 1 $P = 0.935$ and post-stimulation 2 $P = 0.985$) PAC (**Supplementary Figures 1C,D**).

Prolonged Transcorneal Electrical Stimulation Stimulates a Marked Increase of Coherence Between the Prefrontal Cortex and Primary Visual Cortex

In addition to prominent increase in PAC, a large increase of coherence across theta, alpha and beta frequency band, respectively, was detected between the left prefrontal cortex

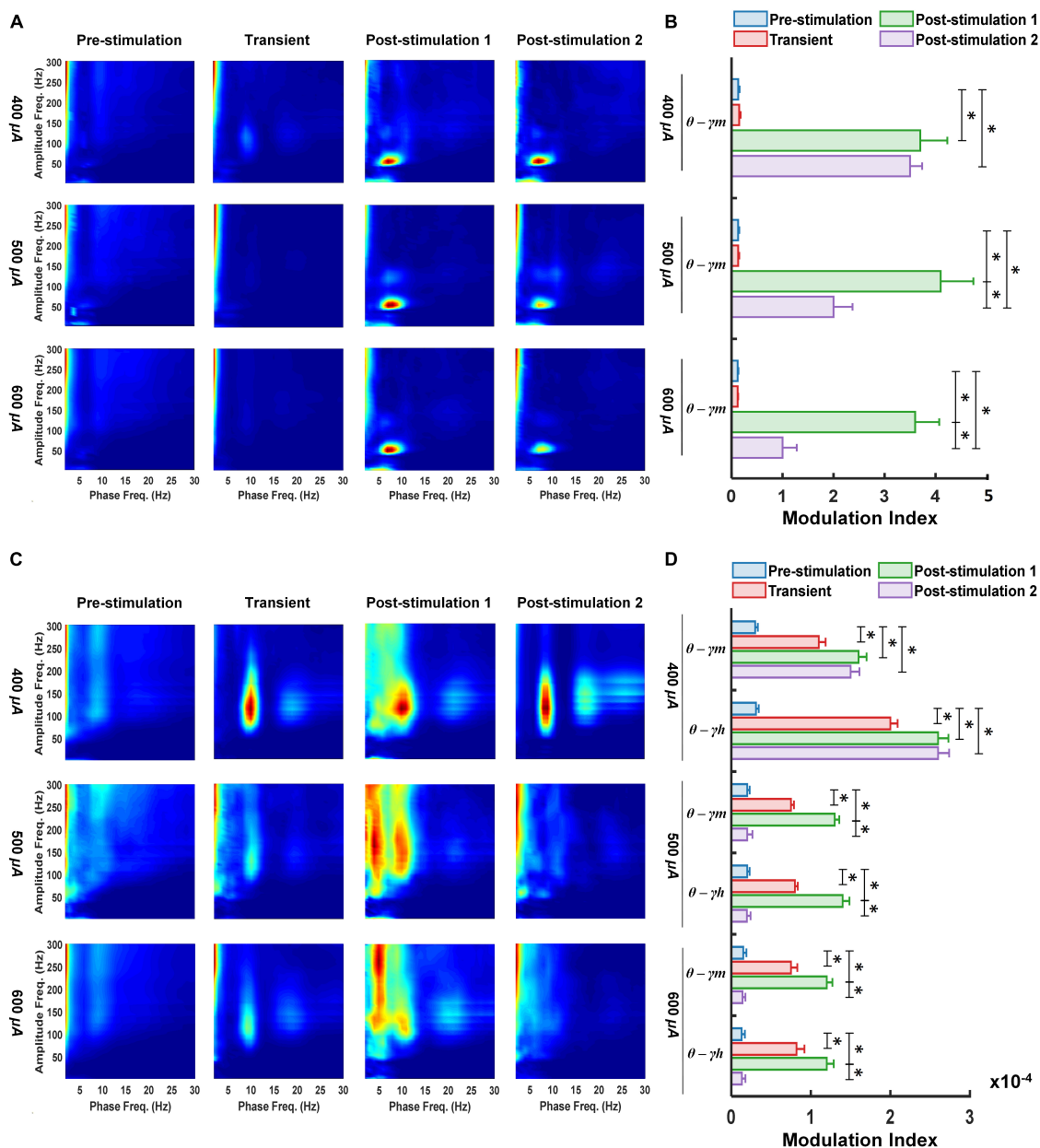


FIGURE 2 | Following retinal electrical stimulation theta waves modulates medium-gamma oscillations in the left primary visual cortex (A,B) while modulating both medium-gamma and high-gamma oscillations in the left prefrontal cortex (C,D). (A) Phase-amplitude comodulograms was computed for ECoG signals from 400 μ A stimulation ($n = 6$), 500 μ A stimulation ($n = 6$), 600 μ A stimulation ($n = 6$) during pre-stimulation (baseline), transient stimulation, post-stimulation stage 1 and post-stimulation stage 2. (B) Mean MI values for phases of slow theta waves (5.5–10 Hz) and amplitudes of fast medium-gamma oscillations (60–115 Hz) in the left primary visual cortex. (C) Phase-amplitude comodulograms computed for ECoG signals from 400 μ A stimulation ($n = 6$), 500 μ A stimulation ($n = 6$), 600 μ A stimulation ($n = 6$) during pre-stimulation (baseline), transient stimulation, post-stimulation stage 1 and post-stimulation stage 2. (D) Mean MI values for phases of slow theta waves (5.5–10 Hz) and amplitudes of fast medium-gamma (60–115 Hz) and high-gamma oscillations (125–175 Hz) in the left prefrontal cortex. Twelve types of cross-frequency coupling were investigated between the three phase frequency bands [delta (0.5–5 Hz), theta (5–10 Hz) and alpha (10–15 Hz)], and four amplitude frequency bands [low gamma (30–55 Hz), medium-gamma (60–115 Hz), high-gamma (125–175 Hz), and ultra-gamma (185–300 Hz)]. $\theta - \gamma_m$, Theta medium-gamma coupling; $\theta - \gamma_h$, Theta high-gamma coupling. * Significant ($P < 0.025$); Error bar denotes SEM.

and left primary visual cortex at various stimulation stages and current amplitudes of retinal stimulation (Figure 3A). For 1-week post-stimulation (post-stimulation stage 1), rd10 mice stimulated with 400, 500, and 600 μ A all displayed significantly enhanced

mean coherence in theta ($P < 0.001$, $P < 0.001$, and $P < 0.001$) alpha ($P < 0.001$, $P = 0.001$, and $P = 0.017$) and beta ($P < 0.001$, $P < 0.001$, and $P = 0.001$) oscillations between the left prefrontal cortex and left primary visual cortex (Figure 3B). This high

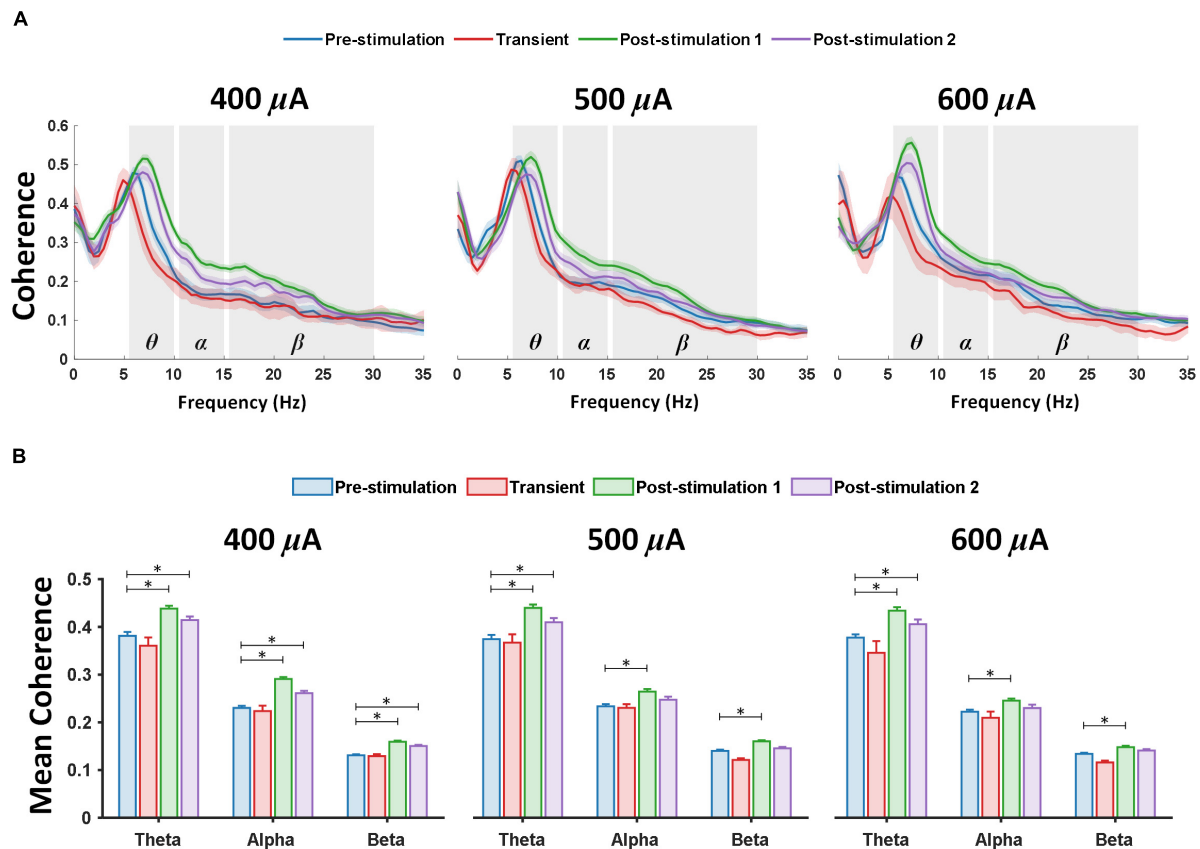


FIGURE 3 | Theta, alpha and beta coherence is markedly elevated between the left prefrontal cortex and left primary visual cortex after retinal electrical stimulation. **(A)** Coherence spectrum showed prominent enhancement in theta, alpha and beta frequency bands; the shaded area depicts SEM. **(B)** Mean coherence values over two ECoG channels (left prefrontal cortex and primary visual cortex) from 400 μA stimulation ($n = 6$), 500 μA stimulation ($n = 6$), 600 μA stimulation ($n = 6$) during pre-stimulation (baseline), transient stimulation, post-stimulation stage 1 and post-stimulation stage 2. * Significant ($P < 0.025$); Error bar denotes SEM.

coherence between the left prefrontal cortex and left primary visual cortex was maintained in theta ($P = 0.014$, $P = 0.019$, and $P < 0.016$) oscillations across all stimulation groups (400, 500, and 600 μA) for 2-weeks post-stimulation (post-stimulation stage 2) (**Figure 3B**). Furthermore, during the same period (post-stimulation stage 2) only rd10 mice stimulated with 400 μA significantly maintained the enhanced mean coherence between the left prefrontal cortex and left primary visual cortex in alpha ($P < 0.001$) and beta ($P < 0.001$) waves but this long-lasting enhancement was not seen in the alpha and beta waves of both 500 μA ($P = 0.304$, $P = 0.494$) and 600 μA ($P = 0.768$, $P = 0.253$) stimulation groups (**Figure 3B**).

It is worth noting that transient pTES did not elicit significant changes in theta, alpha and beta mean coherence between the left prefrontal cortex and left primary visual cortex across 400 μA ($P = 0.510$, $P = 0.895$, and $P = 0.983$), 500 μA ($P = 0.974$, $P = 0.992$, and $P = 0.372$), 600 μA ($P = 0.266$, $P = 0.666$, and $P = 0.441$) of rd10 mice (**Figure 3B**). Again, across the three stimulation stages (transient, post-stimulation stage 1 and post-stimulation stage 2) 400 μA stimulation showed no significant change in mean coherence of delta ($P = 0.985$, $P = 0.378$, and $P = 0.835$), low gamma ($P = 0.961$, $P = 0.657$, and $P = 0.248$), medium gamma

($P = 0.349$, $P = 0.659$, and $P = 0.321$), high gamma ($P = 0.348$, $P = 0.144$, and $P = 0.166$) and ultra-high gamma ($P = 0.325$, $P = 0.224$, and $P = 0.543$) compared with the corresponding pre-stimulation results (**Supplementary Figure 2**). Similarly, across the three stimulation stages (transient, post-stimulation stage 1 and post-stimulation stage 2) 500 μA stimulation showed no significant change in mean coherence of delta ($P = 0.563$, $P = 0.957$, and $P = 0.995$), low gamma ($P = 0.403$, $P = 0.311$, and $P = 0.921$), medium gamma ($P = 0.827$, $P = 0.935$, and $P = 0.731$), high gamma ($P = 0.924$, $P = 0.716$, and $P = 0.692$) and ultra-high gamma ($P = 0.932$, $P = 0.618$, and $P = 0.602$) compared with the corresponding pre-stimulation results (**Supplementary Figure 2**). 600 μA stimulation followed the same trend as 400 and 500 μA stimulations with no significant change in mean coherence of delta ($P = 0.601$, $P = 0.538$, and $P = 0.667$), low gamma ($P = 0.237$, $P = 0.285$, and $P = 0.156$), medium gamma ($P = 0.701$, $P = 0.084$, and $P = 0.061$), high gamma ($P = 0.322$, $P = 0.46$, and $P = 0.221$) and ultra-high gamma ($P = 0.467$, $P = 0.578$, and $P = 0.528$) across the three stimulation stages (transient, post-stimulation stage 1 and post-stimulation stage 2), respectively, compared with the corresponding pre-stimulation results (**Supplementary Figure 2**). For sham control

group, there was no significant change in mean coherence of delta ($P = 0.984$, $P = 0.722$, and $P = 0.273$), theta ($P = 0.998$, $P = 0.991$, and $P = 0.147$), alpha ($P = 0.988$, $P = 0.986$, and $P = 0.0723$) beta ($P = 0.909$, $P = 0.681$, and $P = 0.317$), low gamma ($P = 0.861$, $P = 0.937$, and $P = 0.318$), medium gamma ($P = 0.981$, $P = 0.341$, and $P = 0.07$), high gamma ($P = 0.410$, $P = 0.068$, and $P = 0.093$) and ultra-high gamma ($P = 0.035$, $P = 0.08$, and $P = 0.049$) oscillations across the three stimulation stages (transient, post-stimulation stage 1 and post-stimulation stage 2) (Supplementary Figure 3).

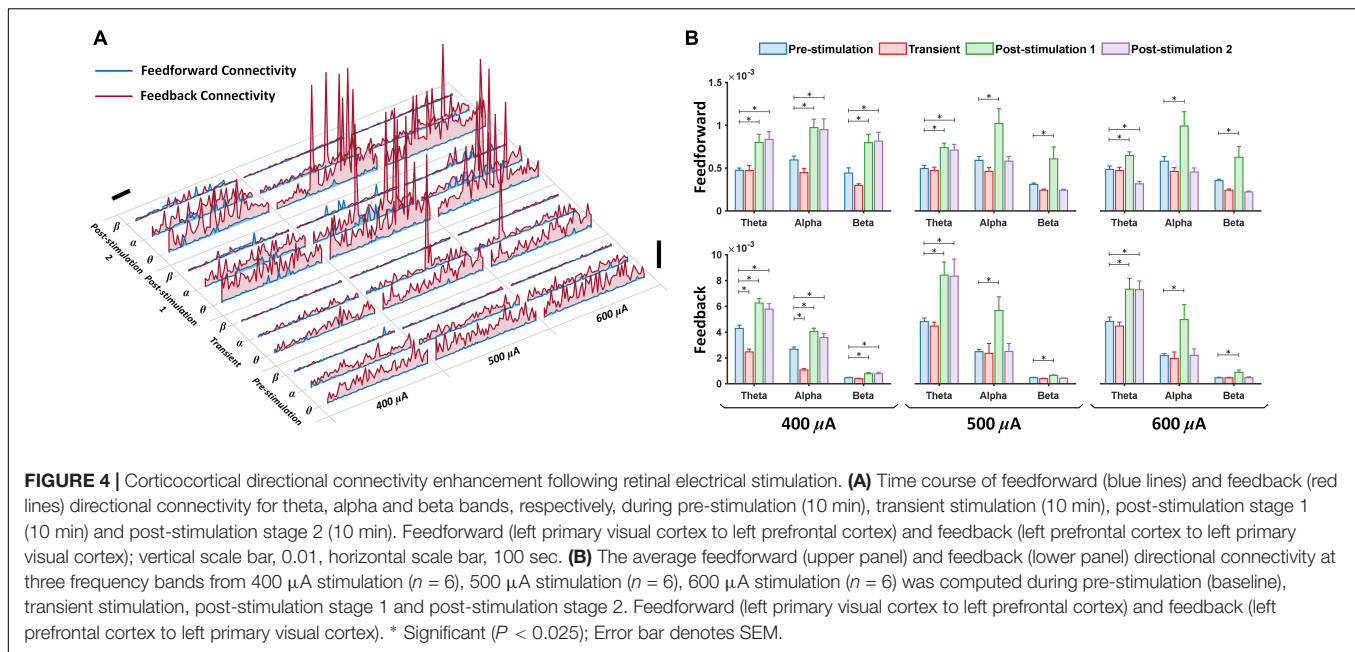
Prefrontal Cortex-Primary Visual Cortex Connectivity of Theta, Alpha and Beta Waves After Prolonged Transcorneal Electrical Stimulation Exceed Baseline Feedforward and Feedback Directional Connectivity

Presence of brain oscillations in the awake state has been associated with feedforward and feedback connectivity, portraying directional flow of neuronal information (Michalareas et al., 2016). Feedforward (left primary visual cortex to left prefrontal cortex) and feedback (left prefrontal cortex to left primary visual cortex) connectivity analyses were applied to the eight frequency bands under various stimulation current amplitudes (400, 500, and 600 μA) and different stages of stimulation (pre-stimulation, transient, post-stimulation stage 1 and post-stimulation stage 2) (Figures 4A,B). In the time series plot, we observed that all test experimental groups (400, 500, and 600 μA) displayed changes in feedforward (blue lines) and feedback (red lines) directional connectivity for theta, alpha and beta bands at different stages of stimulation (Figure 4A). For the feedforward direction, transient pTES largely showed no significant change in theta, alpha and beta oscillations of 400 μA ($P = 0.771$, $P = 0.628$, and $P = 0.563$), 500 μA ($P = 0.987$, $P = 0.781$, and $P = 0.905$), and 600 μA ($P = 0.994$, $P = 0.809$, and $P = 0.592$) stimulations, respectively, compared with the corresponding pre-stimulation directional connectivity (Figure 4B upper panel). This same trend was observed in the respective theta, alpha and beta feedback directional connectivity of rd10 mice stimulated with 500 μA ($P = 0.992$, $P = 0.939$, and $P = 0.362$), and 600 μA ($P = 0.974$, $P = 0.996$, and $P = 0.916$) compared to the corresponding pre-stimulation directional connectivity (Figure 4B lower panel). For 400 μA stimulation group, transient pTES yielded no significant change in beta ($P = 0.909$) feedback directional connectivity while simultaneously causing significant decreased theta ($P < 0.001$) and alpha ($P < 0.001$) feedback directional connectivity, respectively, compared with the corresponding pre-stimulation directional connectivity (Figure 4B lower panel).

At 1-week post-stimulation (post-stimulation stage 1), we observed striking significant increase in feedforward direction connectivity of theta, alpha and beta oscillations for 400 μA ($P = 0.009$, $P = 0.013$, $P = 0.008$), 500 μA ($P = 0.004$, $P = 0.01$, $P = 0.017$), and 600 μA ($P = 0.014$, $P = 0.012$, $P = 0.015$)

stimulations, respectively, compared with the corresponding pre-stimulation directional connectivity (Figure 4B upper panel). Similar significant increase was also observed in the feedback direction of theta, alpha and beta oscillations for 400 μA ($P < 0.001$, $P < 0.001$, $P < 0.001$), 500 μA ($P = 0.017$, $P = 0.013$, $P < 0.001$), and 600 μA ($P = 0.015$, $P = 0.021$, $P = 0.02$) stimulations, respectively, compared with the corresponding pre-stimulation directional connectivity (Figure 4B lower panel). This analysis also uncovered that at 2-weeks after the start of the 7-days pTES (post-stimulation stage 2), rd10 mice stimulated with 400 μA maintained significant increase in feedforward connectivity of theta ($P = 0.003$), alpha ($P = 0.022$) and beta ($P = 0.005$) oscillations, respectively, and also feedback connectivity of theta ($P = 0.006$), alpha ($P = 0.02$) and beta ($P = 0.021$) oscillations, respectively, compared with the corresponding pre-stimulation connectivity (Figure 4B upper and lower panels). In comparison to the pre-stimulation stage, we additionally observed that at the post-stimulation stage 2, both 500 and 600 μA stimulation groups significantly maintained the elevated increase in both feedforward (for 500 μA stimulation $P = 0.014$, for 600 μA stimulation $P = 0.01$) and feedback theta connectivity (for 500 μA stimulation $P = 0.021$, for 600 μA stimulation $P = 0.017$). However, this feature was lost in the feedforward direction of both alpha (for 500 μA stimulation $P = 0.9$, for 600 μA stimulation $P = 0.782$) and beta (for 500 μA stimulation $P = 0.953$, for 600 μA stimulation $P = 0.445$) and the feedback directions of both alpha (for 500 μA stimulation $P = 0.91$, for 600 μA stimulation $P = 0.9$) and beta (for 500 μA stimulation $P = 0.748$, for 600 μA stimulation $P = 0.95$) (Figure 4B upper and lower panels).

For analysis of the other brain oscillations, across the three stimulation stages (transient, post-stimulation stage 1 and post-stimulation stage 2) 400 μA stimulation showed no significant change in feedforward connectivity of delta ($P = 0.996$, $P = 0.768$ and $P = 0.985$), low gamma ($P = 0.738$, $P = 0.213$, and $P = 0.232$), medium gamma ($P = 0.91$, $P = 0.95$, and $P = 0.982$), high gamma ($P = 0.763$, $P = 0.8012$, and $P = 0.708$) and ultra-high gamma ($P = 0.6$, $P = 0.077$, and $P = 0.116$) compared with the corresponding pre-stimulation results (Supplementary Figure 4 upper panel). In the feedback direction there was also no significant change in the connectivity of delta ($P = 0.904$, $P = 0.961$, and $P = 0.973$), low gamma ($P = 0.26$, $P = 0.433$, and $P = 0.301$), medium gamma ($P = 0.703$, $P = 0.751$, and $P = 0.71$), high gamma ($P = 0.234$, $P = 0.218$, and $P = 0.281$) and ultra-high gamma ($P = 0.071$, $P = 0.045$, and $P = 0.031$) compared with the corresponding pre-stimulation results (Supplementary Figure 4 lower panel). For 500 μA stimulation feedforward connectivity also displayed no significant change across the three stimulation stages (transient, post-stimulation stage 1 and post-stimulation stage 2) of delta ($P = 0.607$, $P = 0.917$, and $P = 0.919$), low gamma ($P = 0.948$, $P = 0.395$, and $P = 0.803$), medium gamma ($P = 0.741$, $P = 0.052$, and $P = 0.071$), high gamma ($P = 0.982$, $P = 0.972$, and $P = 0.98$) and ultra-high gamma ($P = 0.687$, $P = 0.736$, and $P = 0.497$) compared with the corresponding pre-stimulation results (Supplementary Figure 4 upper panel). In this regard, feedback connectivity for 500 μA stimulation also achieved no significant change



in delta ($P = 0.949$, $P = 0.968$, and $P = 0.980$), low gamma ($P = 0.957$, $P = 0.98$, and $P = 0.981$), medium gamma ($P = 0.969$, $P = 0.967$, and $P = 0.933$), high gamma ($P = 0.961$, $P = 0.875$, and $P = 0.952$) and ultra-high gamma ($P = 0.826$, $P = 0.372$, and $P = 0.464$) oscillations compared with the corresponding pre-stimulation results (**Supplementary Figure 4** lower panel). 600 μ A stimulation followed the same trend as 400 and 500 μ A stimulations with no significant change in feedforward connectivity and feedback connectivity compared with the corresponding pre-stimulation results (**Supplementary Figure 4** upper and lower panels). The following P -values were obtained across the three stimulation stages for 600 μ A stimulation in the feedforward direction; Delta ($P = 0.994$, $P = 0.833$, and $P = 0.908$), low gamma ($P = 0.947$, $P = 0.968$, and $P = 0.952$), medium gamma ($P = 0.486$, $P = 0.707$, $P = 0.264$), high gamma ($P = 0.702$, $P = 0.615$, $P = 0.185$) and ultra-high gamma ($P = 0.967$, $P = 0.366$, and $P = 0.346$). Meanwhile in the feedback direction the P -values across the three stimulation stages for 600 μ A stimulation were Delta ($P = 0.981$, $P = 0.904$, and $P = 0.971$), low gamma ($P = 0.913$, $P = 0.9$, and $P = 0.983$), medium gamma ($P = 0.977$, $P = 0.948$, $P = 0.906$), high gamma ($P = 0.904$, $P = 0.878$, $P = 0.969$) and ultra-high gamma ($P = 0.929$, $P = 0.766$, $P = 0.766$).

Meanwhile rd10 mice that received no pTES (sham control group) showed no significant difference in feedforward connectivity across all assessed oscillations and three stages of stimulation compared to the corresponding pre-stimulation results (**Supplementary Figures 5, 6**) (Delta $P = 0.979$, $P = 0.931$, and $P = 0.972$; Theta $P = 0.971$, $P = 0.833$ and $P = 0.958$; Alpha $P = 0.903$, $P = 0.511$, and $P = 0.283$; Beta $P = 0.947$, $P = 0.843$, and $P = 0.968$; Low gamma $P = 0.815$, $P = 0.754$, and $P = 0.341$; Medium gamma $P = 0.477$, $P = 0.195$, and $P = 0.26$; High gamma $P = 0.382$, $P = 0.199$, and $P = 0.374$; Ultra-high gamma $P = 0.828$, $P = 0.858$, and $P = 0.967$). Similarly, this feature was also observed

in the feedback direction of the sham control group across all assessed oscillations and across the three stages of stimulation compared to the corresponding pre-stimulation results (Delta $P = 0.971$, $P = 0.983$, and $P = 0.961$; Theta $P = 0.409$, $P = 0.98$, and $P = 0.901$; Alpha $P = 0.449$, $P = 0.912$, and $P = 0.904$; Beta $P = 0.953$, $P = 0.9234$, and $P = 0.9524$; Low gamma $P = 0.663$, $P = 0.695$, and $P = 0.352$; Medium gamma $P = 0.921$, $P = 0.464$, and $P = 0.724$; High gamma $P = 0.781$, $P = 0.876$, and $P = 0.984$; Ultra-high gamma $P = 0.342$, $P = 0.987$, and $P = 0.417$).

DISCUSSION

Electrocorticography Recording in Awake Mice and Circadian Impacts

Previous ECoG studies have reported that modulations in time of the day affect cognitive performance as well as neurophysiological activities of the brain (Blatter and Cajochen, 2007; García et al., 2012; Chellappa et al., 2018; Facer-Childs et al., 2018; Fisk et al., 2018). In other words, circadian rhythm plays a key role in biological functioning in living systems. Intrinsic factors such as sleep-wake cycle and external factors such as lighting conditions also play unique roles in controlling circadian rhythm of biological systems (Waterhouse et al., 2012; Hickie et al., 2013; Musiek et al., 2015; Blume et al., 2019; Bano-Otalora et al., 2021). In the design of our study, we considered these factors and ensured that appropriate precautions were taken to avoid disruption of circadian rhythms in all experimental animals. To achieve this, the experimental animals were exposed to 12 h light and 12 h dark phases. ECoG recording sessions were always performed in all rd10 mice at the same time period during the light phase and under ambient lighting conditions. Care was also taken to ensure that a healthy body weight of all mice was

maintained. No sudden weight loss was observed in all animals during the study period.

It is also important to note that brain oscillations recorded from EEG/ECoG have been well recognized as a basis for cognitive capacity, memory, and learning in animals and humans (Pietto et al., 2018; Buenrostro-Jáuregui et al., 2020; Šneider et al., 2020). Therefore, the simultaneous monitoring of behavioral changes and ECoG is particularly interesting in correlating data between brain activity and task-related behaviors (Miller, 2019). Apart from assuring proper sleep-wake cycle, maintenance of body weight and proper lighting conditions in experimental animals during our study; the behavior of the animals was carefully monitored during ECoG recording sessions. With regards to the animal behavior, all rd10 animals expressed active behaviors including manifesting free movement, coordinated exploration of their surrounding environment, reaching for food/water, paw licking and other grooming behaviors. No animal showed signs of distress or physical signs of depressive behavior during ECoG recording. All the aforementioned manifestations satisfied our criteria for an active awake rodent.

Prolonged Transcorneal Electrical Stimulation-Triggered Enhancement in Functional and Directional Connectivity Is Maintained in Visual and Non-visual Brain Regions

The data reported in the present study demonstrate that pTES triggers a long-lasting enhancement of coordinated theta, alpha and beta waves, which displays high levels of interregional coherence and connectivity as well as synchronized phase-amplitude coupling characteristics between theta and gamma oscillations in rd mice. This long-lasting enhancement in PAC, coherence and directional connectivity was observed not only in the visual region (primary visual cortex) of stimulated animals, but also featured in the non-visual region (prefrontal cortex). Invariably, this suggests that electrical stimulation of the retina does not only affect neurons of the primary visual cortex but also activates connectivity networks in the prefrontal cortex of rd animals.

In both primates and rodents, the prefrontal cortex has been reported to be involved in cognitive processes including working memory, attention, decision-making and cognitive flexibility. Arising from neuroanatomy, the prefrontal cortex has circuits that integrate diverse neural information from other cortical and subcortical regions including the basal ganglia, hippocampus and amygdala. The aforementioned design enables the prefrontal cortex exert highly coordinated cognitive functions that govern behavioral control. Working memory is defined as a system that enables short-term retainment (seconds to minutes time scale) of neural information for use in complex task completion (Funahashi, 2017; Jobson et al., 2021). The mPFC has been severally implicated in the working memory process. For example, early studies in rodents have demonstrated that mPFC lesions result in delayed response in task related behaviors and clear deficits for visual objects information

(Kesner et al., 1996; Kahn et al., 2012). Attention is a complex cognitive process that allows the brain to effectively assign sensory resources for instantaneous goals while disregarding other irrelevant sensory inputs. The crucial function of the prefrontal cortex has also been demonstrated in rodent-based attention tasks which resulted in choice accuracy reduction and slow responses for rats with lesioned mPFC (Chudasama et al., 2003). Decision-making is the executive capacity of an animal to choose an advantageous response from several possible choices. Evidence from neurophysiological recordings have proven that the orbitofrontal cortex (OFC) and the mPFC (specifically the anterior cingulate cortex) work together to update, evaluate and translate choice options into final decision actions in non-human primates (Hayden and Platt, 2010; Sul et al., 2010). Based on the aforementioned evidence of the crucial roles of the prefrontal cortex in cognition, we suggest that in our present study each of the properties of theta, alpha and beta oscillations observed in both prefrontal cortex and primary visual cortex indicate highly coordinated neural activities in the brain following retinal electrical stimulation. Indeed theta coherence and connectivity has been reported to be important in cognitive performance of task-related functions between the frontal regions, occipital, parietal, motor areas and sub-thalamic nucleus of the brain (Nurislamova et al., 2019). Alpha oscillations have been implicated in the directional coordination of control processes including task-related information. Specifically, these alpha waves have been severally associated with inhibitory functions where they have been shown to play crucial roles in reducing irrelevant neural connections thus enabling the brain to focus more on progressive connections (Wolff et al., 2017). Pre-clinical studies in retinal degeneration rodents have reported irrelevant spontaneous firing as neurophysiological-markers of the retinal degeneration pathology (Wang et al., 2016). Our present study showed an increased surge of alpha coherence and alpha directional connectivity between the prefrontal cortex and visual cortex which suppresses the interfering spontaneous firing in rd neurons and possibly establishes a more coordinated communication between neurons in the prefrontal cortex and visual cortex. Beta oscillations have previously been tagged to index changes in underlying neural activities in the sensorimotor cortex (Schmidt et al., 2019). In the present study, the increased surge of beta oscillations in coherence and connectivity measures may possibly be involved in global integration of newly established neural network connections that occurred in the rd brain during post-stimulation stage 1. Sham control group that did not received pTES displayed no change in the analyzed indices of brain coherence and connectivity which confirms that pTES is responsible for the observed alterations in brain coherence and connectivity of the stimulated test groups.

Based on the duration of the present study, the observed effects of pTES in both primary visual cortex and prefrontal cortex do not occur only 1-week after the start of pTES but appear to have maintained impacts for up to 2-weeks after the start of the 7-days pTES. This suggests that given the time period of the present study, pTES could possibly lead to the formation and strengthening of new pathways of synchronous neural connections in rd brain after electrical stimulation.

Although all stimulation currents enhanced and maintained theta-gamma modulation in one or more stimulation stages, 400 μ A showed the greatest maintenance effect followed by 500 μ A and lastly 600 μ A compared to the corresponding pre-stimulation PAC results. This phenomenon could possibly be explained by the higher tendency toward a saturated evoked response in the primary visual cortex neurons on application of 500 and 600 μ A stimulation current amplitudes, respectively, compared with 400 μ A (**Supplementary Figure 7**). Subsequently, due to coherence and connectivity between the primary visual cortex and prefrontal cortex, the high tendency toward a saturated evoked response in the primary visual cortex neurons with 500 and 600 μ A current stimulation extended to the prefrontal cortex and induced lower enhancement of brain coherence and connectivity on application of 500 and 600 μ A stimulations compared with 400 μ A (as already described in the “Result” section of the present study). Our data therefore indicates that the applied pTES facilitated specific cortical systems by progressive interactions with neuronal oscillators that are functionally coupled based on the applied current amplitude. As PAC has been reported to be critical in transfer of neural information across a wide range of spatio-temporal scales and integrates global communication among neural populations, it is speculated to have high relevance for cognitive processing (Lara et al., 2018; Munia and Aviyente, 2019). More compelling evidence recently supports the above report by highlighting the functional relevance of phase-amplitude coupling in visual perception (Zazio et al., 2020), visuomotor mapping (Tzvi et al., 2016), learning and memory consolidation (Cox et al., 2020).

Potential Involvement of the Pulvinar Nucleus in Prolonged Transcorneal Electrical Stimulation-Induced Enhancement of Functional and Directional Connectivity

Several studies that investigate the cellular basis of visual perception often consider direct corticocortical circuits as the predominant pathway for neuronal connectivity. Aside this corticocentric view of neural information transmission in the CNS, there is now emerging evidence for the crucial roles of indirect pathways that involve the pulvinar nucleus (Halassa and Kastner, 2017). In mammals, the pulvinar is the largest extrageniculate nucleus of the thalamus that provides an additional communication route between the visual regions of the cortex. Briefly, the pulvinar is bi-synaptically linked to the primary visual cortex and extrastriate visual cortical regions *via* cortico-thalamo-cortical projections (Arcaro et al., 2015; Bennett et al., 2019). This design strategically positions the pulvinar at the middle of several pathways between the thalamus and the cortex. Consequently, the pulvinar has been reported to play important roles in the contextual and multi-sensory processing (Ibrahim et al., 2016; Roth et al., 2016; Chou et al., 2020; Fang et al., 2020) and synchronization among cortical regions (Saalman et al., 2012; Schmid et al., 2012). Indeed, the pulvinar has previously been implicated in the control of neuronal oscillations particularly in the visual cortex. Recall

that synchronization of brain oscillations is a key marker for cortical processing. Accordingly, electrophysiological recordings from anesthetized cats have demonstrated that inactivation of the pulvinar induces desynchronization in areas 17 or 18 of the visual cortex (Wróbel et al., 2007; Cortes et al., 2020). The pulvinar contribution to corticocortical communication between higher visual areas (V4 and above) has also been investigated in recent studies (Saalman et al., 2012; Fiebelkorn et al., 2019). Results from these studies reveal the occurrence of alpha-driven pulvinar synchronized activity between interconnected cortical regions under attention-related tasks. In addition, the pulvinar has been reported to consist of two major cell types; the excitatory “relay” neurons which project to the cerebral cortex and the intrinsic inhibitory interneurons which are localized within the nucleus. Taking into consideration the aforementioned functional and anatomical characteristics of the pulvinar, we hypothesize that pTES produces the beneficial enhancement of brain connectivity by possible indirect activation of the pulvinar to establish a physiological balance in cortical excitation and inhibition. However, this hypothesis warrants further investigation for confirmation.

Implications for Retinitis Pigmentosa

In mammals, emotions have been described as canonical responses to situations that are linked to survival or well-being of the animal concerned. The neural circuits involved in emotional representation seems to functionally coordinate both visual and non-visual brain regions (Wyczesany et al., 2015; Kragel et al., 2019). For example, depression which has been found to originate from abnormal functioning of the medial prefrontal cortex has also been observed in visually impaired patients (Davey et al., 2017; Zheng et al., 2017). Specifically, retinitis pigmentosa has been reported to be emotionally devastating in affected individuals due to the anticipation of vision loss and the eventual blindness causes profound distress (Hahm et al., 2008). These factors alone increase retinitis pigmentosa patients’ vulnerability to depression. In fact, a higher prevalence of anxiety and depression has been reliably documented in retinitis pigmentosa patients compared with the general population without vision loss (Moschos et al., 2015). Consequently, clinical interventions that provide efficient therapies for depression treatment have become of core necessity in order to improve the overall quality of life in retinitis pigmentosa patients. In this regard, pTES has been found to attenuate depressive symptoms from rodents with visual deficit (Yu et al., 2019, 2021). This finding in addition to our present results is suggestive that pTES holds strong possibility of modulating higher cortical functions including pathways of cognition, emotion, awareness, and memory in retinitis pigmentosa patients. However, further experimental studies to confirm this possibility remains to be investigated.

In addition to the beneficial effect of pTES in depression, we believe that pTES can also be used to enhance visual-related behaviors specifically visual attention. Previous studies on visual detection tasks in healthy humans have applied tDCs to modulate spatial attention by enhancing the ratio of neural activity between the left and right hemispheres of the brain (Ni et al., 2019; Andres et al., 2020). In another study tDCs applied in the alpha

oscillatory spectrum was reported to facilitate cognitive control and improve performance in visual attention tasks (Clayton et al., 2019). Similar to the above studies, our present work shows clear evidence of pTES-induced enhancement in alpha oscillations and as previously stated, alpha oscillations have been shown to help the brain focus on relevant neuronal signals. Thus, like tDCs our present study suggests that pTES could possibly improve visual attention and thus may be applied for functional rehabilitation of visual neglect. However, the aforementioned claims can only be ascertained by more detailed experimentation.

Collectively, the data of the present study shows that pTES drastically improves network coherence and connectivity patterns both at the level of cross-oscillatory interaction and at the level of functional and directional inter-regional communication between the primary visual cortex and prefrontal cortex. To the best of our knowledge, this makes our study the first of its kind to demonstrate that pTES is able to alter coherence and connectivity measures of non-visual areas, in this case the prefrontal cortex. On this basis, a fundamental aspect of our study is that it provides an insight for which researchers in the field could apply pTES as a novel neuromodulatory approach to target both visual and non-visual regions of the brain directly from the mammalian eye. Thus, this serves as a simplistic strategy that is capable of opening new horizons for unlocking previously unexplored brain pathways with possible beneficial outcomes.

DATA AVAILABILITY STATEMENT

The original contributions presented in the study are included in the article/Supplementary Material, further inquiries can be directed to the corresponding author/s.

ETHICS STATEMENT

The animal study was reviewed and approved by the Animal Research Ethics Sub-Committee at City University of Hong Kong.

AUTHOR CONTRIBUTIONS

SA and LLHC designed the study and wrote the manuscript. SA performed the *in vivo* experiments. SA and AE analyzed the data. All authors contributed to the article and approved the submitted version.

FUNDING

This research was supported by the Research Grants Council of the Hong Kong Special Administrative Region (Grant Nos. CityU 11208218 and 11207419), the Innovation and Technology Fund Guangdong-Hong Kong Technology Cooperation Funding Scheme (GHP/078/18GD).

SUPPLEMENTARY MATERIAL

The Supplementary Material for this article can be found online at: <https://www.frontiersin.org/articles/10.3389/fncel.2022.785199/full#supplementary-material>

Supplementary Figure 1 | (A) Phase-amplitude comodulograms computed for ECoG signals obtained from the left primary visual cortex of sham control rd10 mice. (B) Mean M/I values for phases of slow theta waves (5.5–10 Hz) and amplitudes of fast medium-gamma oscillations (60–115 Hz) in the left primary visual cortex. (C) Phase-amplitude comodulograms computed for ECoG signals obtained from the left prefrontal cortex of sham control rd10 mice. (D) Mean M/I values for phases of slow theta waves (5.5–10 Hz) and amplitudes of both medium-gamma oscillations (60–115 Hz) and high-gamma oscillations (125–175 Hz) in the left prefrontal cortex. There was no significant change ($p > 0.025$) in theta medium-gamma phase amplitude coupling in the left primary visual cortex (A,B) of sham control rd10 mice ($n=6$) across all four stimulation stages. Similarly, in the left prefrontal cortex (C,D) there was no significant change in phase amplitude coupling between theta medium-gamma ($p > 0.025$) and theta high-gamma bands ($p > 0.025$), respectively, across all four stimulation stages. $\theta-\gamma_m$: Theta medium-gamma coupling; $\theta-\gamma_h$: Theta high-gamma coupling. NS, not significant; Error bar denotes SEM.

Supplementary Figure 2 | Delta and gamma coherence is unchanged between the left prefrontal cortex and left primary visual cortex after retinal electrical stimulation. Mean coherence values over two ECoG channels (left prefrontal cortex and primary visual cortex) from 400 μ A stimulation ($n=6$), 500 μ A stimulation ($n=6$), 600 μ A stimulation ($n=6$) during pre-stimulation (baseline), transient stimulation, post-stimulation stage 1 and post-stimulation stage 2. γ_l low-gamma; γ_m medium-gamma; γ_h high-gamma; γ_u ultra-gamma, NS, not significant ($P > 0.025$); Error bar denotes SEM.

Supplementary Figure 3 | Mean coherence between the left prefrontal cortex and left primary visual cortex is unchanged ($p > 0.025$) across all analyzed oscillatory bands in sham control rd10 mice. Mean coherence values over two ECoG channels (left prefrontal cortex and primary visual cortex) from sham control rd10 mice ($n=6$) during pre-stimulation (baseline), transient stimulation, post-stimulation stage 1 and post-stimulation stage 2. θ Theta; α alpha; β beta; γ_l low-gamma; γ_m medium-gamma; γ_h high-gamma; γ_u ultra-gamma, NS, not significant ($P > 0.025$); Error bar denotes SEM.

Supplementary Figure 4 | Delta and gamma corticocortical directional connectivity remains unchanged after retinal electrical stimulation. The average feedforward (upper) and feedback (lower) directional connectivity at three frequency bands from 400 μ A stimulation ($n=6$), 500 μ A stimulation ($n=6$), 600 μ A stimulation ($n=6$) was computed during pre-stimulation (baseline), transient stimulation, post-stimulation stage 1 and post-stimulation stage 2. γ_l low-gamma; γ_m medium-gamma; γ_h high-gamma; γ_u ultra-gamma. Feedforward (left primary visual cortex to left prefrontal cortex) and feedback (left prefrontal cortex to left primary visual cortex). NS, not significant ($P > 0.025$); Error bar denotes SEM.

Supplementary Figure 5 | Time course of feedforward (blue lines) and feedback (red lines) directional connectivity for theta, alpha and beta bands, respectively, from sham control rd10 mice ($n=6$) during pre-stimulation (10 min), transient stage (10 min), post-stimulation stage 1 (10 min) and post-stimulation stage 2 (10 min). Feedforward (left primary visual cortex to left prefrontal cortex) and feedback (left prefrontal cortex to left primary visual cortex).

Supplementary Figure 6 | Corticocortical directional connectivity across all analyzed bands remains unchanged in sham control rd10 mice ($n=6$). The average feedforward (upper) and feedback (lower) directional connectivity across all analyzed frequency bands from the sham control group was computed during pre-stimulation (baseline), transient stimulation, post-stimulation stage 1 and post-stimulation stage 2. θ Theta; α alpha; β beta; γ_l low-gamma; γ_m medium-gamma; γ_h high-gamma; γ_u ultra-gamma; Feedforward (left primary visual cortex to left prefrontal cortex) and feedback (left prefrontal cortex to left primary visual cortex). NS, not significant; Error bar denotes SEM.

Supplementary Figure 7 | Average dose response plot from the left primary visual cortex. The average response amplitudes were obtained from six rd10 mice.

Electrical evoked response across 19 current amplitudes and 10 Hz stimulation frequency, was fitted into sigmoid curves. The response amplitude was expressed as a percentage of the maximum EEP response. Effective concentration (EC) represents the effective response amplitude. Current amplitudes of 400, 500, and

600 μ A elicited an effective dose response amplitude of 50, 70, and 85%, respectively, across all applied stimulation frequencies. Beyond 500 and 600 μ A current stimulations, response amplitude only increases marginally as the curve approaches the saturation point.

REFERENCES

- Agadagba, S. K., and Chan, L. L. H. (2020). Spontaneous feedforward connectivity in electrically stimulated retinal degeneration mice(). *Annu. Int. Conf. IEEE Eng. Med. Biol. Soc.* 2020, 3513–3516. doi: 10.1109/embs44109.2020.9175231
- Agadagba, S. K., and Chan, L. L. H. (2021). Modulation of narrowband and broadband gamma connectivity in retinal degeneration mice according to electrical stimulation pulse width. *HKIE Trans.* 27, 148–155. doi: 10.33430/thie-2020-0006
- Agadagba, S. K., Li, X., and Chan, L. L. (2019). “Electroencephalogram power alterations in retinal degeneration mice after prolonged transcorneal electrical stimulation,” in *Proceedings of the 2019 9th International IEEE/EMBS Conference on Neural Engineering (NER)*, (Piscataway, NJ: IEEE), 219–222.
- Agadagba, S. K., Li, X., and Chan, L. L. H. (2020). Excitation of the pre-frontal and primary visual cortex in response to transcorneal electrical stimulation in retinal degeneration mice. *Front. Neurosci.* 14:572299. doi: 10.3389/fnins.2020.572299
- Andino-Pavlovsky, V., Souza, A. C., Scheffer-Teixeira, R., Tort, A. B., Etchenique, R., and Ribeiro, S. (2017). Dopamine modulates delta-gamma phase-amplitude coupling in the prefrontal cortex of behaving rats. *Front. Neural Circuits* 11:29. doi: 10.3389/fncir.2017.00029
- Andres, M., Masson, N., Larigaldie, N., Bonato, M., Vandermeeren, Y., and Dormal, V. (2020). Transcranial electric stimulation optimizes the balance of visual attention across space. *Clin. Neurophysiol.* 131, 912–920. doi: 10.1016/j.clinph.2019.12.415
- Arcaro, M. J., Pinsk, M. A., and Kastner, S. (2015). The anatomical and functional organization of the human visual pulvinar. *J. Neurosci.* 35, 9848–9871. doi: 10.1523/jneurosci.1575-14.2015
- Bano-Otolora, B., Martial, F., Harding, C., Bechtold, D. A., Allen, A. E., Brown, T. M., et al. (2021). Bright daytime light enhances circadian amplitude in a diurnal mammal. *Proc. Natl. Acad. Sci. U.S.A.* 118:e210094118. doi: 10.1073/pnas.2100941118
- Bazzigaluppi, P., Beckett, T. L., Koletar, M. M., Lai, A. Y., Joo, I. L., Brown, M. E., et al. (2018). Early-stage attenuation of phase-amplitude coupling in the hippocampus and medial prefrontal cortex in a transgenic rat model of Alzheimer's disease. *J. Neurochem.* 144, 669–679.
- Bennett, C., Gale, S. D., Garrett, M. E., Newton, M. L., Callaway, E. M., Murphy, G. J., et al. (2019). Higher-Order thalamic circuits channel parallel streams of visual information in mice. *Neuron* 102, 477–492. doi: 10.1016/j.neuron.2019.02.010
- Beyeler, M., Nanduri, D., Weiland, J. D., Rokem, A., Boynton, G. M., and Fine, I. (2019). A model of ganglion axon pathways accounts for percepts elicited by retinal implants. *Sci. Rep.* 9:9199. doi: 10.1038/s41598-019-45416-4
- Blatter, K., and Cajochen, C. (2007). Circadian rhythms in cognitive performance: methodological constraints, protocols, theoretical underpinnings. *Physiol. Behav.* 90, 196–208. doi: 10.1016/j.physbeh.2006.09.009
- Blume, C., Garbazza, C., and Spitschan, M. (2019). Effects of light on human circadian rhythms, sleep and mood. *Somnologie* 23, 147–156. doi: 10.1007/s11818-019-00215-x
- Buenrostro-Jáuregui, M., Rodríguez-Serrano, L. M., Chávez-Hernández, M. E., Tapia-de-Jesús, A., Mata-Luevanos, J., Mata, F., et al. (2020). Simultaneous monitoring of wireless electrophysiology and memory behavioral test as a tool to study hippocampal neurogenesis. *J. Vis. Exp.* 162:e61494. doi: 10.3791/61494
- Chellappa, S. L., Morris, C. J., and Scheer, F. A. J. L. (2018). Daily circadian misalignment impairs human cognitive performance task-dependently. *Sci. Rep.* 8:3041. doi: 10.1038/s41598-018-20707-4
- Chenais, N. A. L., Airaghi Leccardi, M. J. I., and Ghezzi, D. (2021). Photovoltaic retinal prosthesis restores high-resolution responses to single-pixel stimulation in blind retinas. *Commun. Mater.* 2:28. doi: 10.1038/s43246-021-00133-2
- Chou, X. L., Fang, Q., Yan, L., Zhong, W., Peng, B., Li, H., et al. (2020). Contextual and cross-modality modulation of auditory cortical processing through pulvinar mediated suppression. *Elife* 9:e54157. doi: 10.7554/eLife.54157
- Chow, A. Y. (2013). Retinal prostheses development in retinitis pigmentosa patients—progress and comparison. *Asia Pac. J. Ophthalmol.* 2, 253–268.
- Chudasama, Y., Pasetti, F., Rhodes, S. E., Lopian, D., Desai, A., and Robbins, T. W. (2003). Dissociable aspects of performance on the 5-choice serial reaction time task following lesions of the dorsal anterior cingulate, infralimbic and orbitofrontal cortex in the rat: differential effects on selectivity, impulsivity and compulsivity. *Behav. Brain Res.* 146, 105–119. doi: 10.1016/j.bbr.2003.09.020
- Clayton, M. S., Yeung, N., and Cohen Kadosh, R. (2019). Electrical stimulation of alpha oscillations stabilizes performance on visual attention tasks. *J. Exp. Psychol. Gen.* 148, 203–220. doi: 10.1037/xge0000502
- Cortes, N., de Souza, B. O. F., and Casanova, C. (2020). Pulvinar modulates synchrony across visual cortical areas. *Vision (Basel)* 4:22. doi: 10.3390/vision4020022
- Costumero, V., Bueichekú, E., Adrián-Ventura, J., and Ávila, C. (2020). Opening or closing eyes at rest modulates the functional connectivity of V1 with default and salience networks. *Sci. Rep.* 10:9137. doi: 10.1038/s41598-020-66100-y
- Cox, R., Rüber, T., Staresina, B. P., and Fell, J. (2020). Phase-based coordination of hippocampal and neocortical oscillations during human sleep. *Commun. Biol.* 3:176. doi: 10.1038/s42003-020-0913-5
- Davey, C. G., Breakspear, M., Pujol, J., and Harrison, B. J. (2017). A brain model of disturbed self-appraisal in depression. *Am. J. Psychiatry* 174, 895–903. doi: 10.1176/appi.ajp.2017.16080883
- De Hemptinne, C., Ryapolova-Webb, E. S., Air, E. L., Garcia, P. A., Miller, K. J., Ojemann, J. G., et al. (2013). Exaggerated phase-amplitude coupling in the primary motor cortex in Parkinson disease. *Proc. Natl. Acad. Sci. U.S.A.* 110, 4780–4785.
- Durand, S., Iyer, R., Mizuseki, K., de Vries, S., Mihalas, S., and Reid, R. C. (2016). A comparison of visual response properties in the lateral geniculate nucleus and primary visual cortex of awake and anesthetized mice. *J. Neurosci.* 36, 12144–12156.
- Facer-Childs, E. R., Boiling, S., and Balanos, G. M. (2018). The effects of time of day and chronotype on cognitive and physical performance in healthy volunteers. *Sports Med. Open* 4:47. doi: 10.1186/s40798-018-0162-z
- Fang, Q., Chou, X. L., Peng, B., Zhong, W., Zhang, L. I., and Tao, H. W. (2020). A differential circuit via retino-colliculo-pulvinar pathway enhances feature selectivity in visual cortex through surround suppression. *Neuron* 105, 355–369. doi: 10.1016/j.neuron.2019.10.027
- Fiebelkorn, I. C., Pinsk, M. A., and Kastner, S. (2019). The mediodorsal pulvinar coordinates the macaque fronto-parietal network during rhythmic spatial attention. *Nat. Commun.* 10:215. doi: 10.1038/s41467-018-08151-4
- Fisk, A. S., Tam, S. K. E., Brown, L. A., Vyazovskiy, V. V., Bannerman, D. M., and Peirson, S. N. (2018). Light and cognition: roles for circadian rhythms, sleep, and arousal. *Front. Neurol.* 9:56. doi: 10.3389/fneur.2018.00056
- Funahashi, S. (2017). Working memory in the prefrontal cortex. *Brain Sci.* 7:49. doi: 10.3390/brainsci7050049
- Garagnani, M., Lucchese, G., Tomasello, R., Wennekers, T., and Pulvermüller, F. (2017). A spiking neurocomputational model of high-frequency oscillatory brain responses to words and pseudowords. *Front. Comput. Neurosci.* 10:145. doi: 10.3389/fncom.2016.00145
- García, A., Ramírez, C., Martínez, B., and Valdez, P. (2012). Circadian rhythms in two components of executive functions: cognitive inhibition and flexibility. *Biol. Rhythm Res.* 43, 49–63. doi: 10.1080/09291016.2011.638137
- Hahn, B. J., Shin, Y. W., Shim, E. J., Jeon, H. J., Seo, J. M., Chung, H., et al. (2008). Depression and the vision-related quality of life in patients with retinitis pigmentosa. *Br. J. Ophthalmol.* 92, 650–654. doi: 10.1136/bjo.2007.127092
- Halassa, M. M., and Kastner, S. (2017). Thalamic functions in distributed cognitive control. *Nat. Neurosci.* 20, 1669–1679. doi: 10.1038/s41593-017-0020-1
- Hayden, B. Y., and Platt, M. L. (2010). Neurons in anterior cingulate cortex multiplex information about reward and action. *J. Neurosci.* 30, 3339–3346. doi: 10.1523/jneurosci.4874-09.2010

- Helfrich, R. F., Huang, M., Wilson, G., and Knight, R. T. (2017). Prefrontal cortex modulates posterior alpha oscillations during top-down guided visual perception. *Proc. Natl. Acad. Sci. U.S.A.* 114, 9457–9462.
- Hickie, I. B., Naismith, S. L., Robillard, R., Scott, E. M., and Hermens, D. F. (2013). Manipulating the sleep-wake cycle and circadian rhythms to improve clinical management of major depression. *BMC Med.* 11:79. doi: 10.1186/1741-7015-11-79
- Ibrahim, L. A., Mesik, L., Ji, X. Y., Fang, Q., Li, H. F., Li, Y. T., et al. (2016). Cross-modality sharpening of visual cortical processing through layer-1-mediated inhibition and disinhibition. *Neuron* 89, 1031–1045. doi: 10.1016/j.neuron.2016.01.027
- Jamil, A., Batsikadze, G., Kuo, H. I., Labruna, L., Hasan, A., Paulus, W., et al. (2017). Systematic evaluation of the impact of stimulation intensity on neuroplastic after-effects induced by transcranial direct current stimulation. *J. Physiol.* 595, 1273–1288.
- Jobson, D. D., Hase, Y., Clarkson, A. N., and Kalaria, R. N. (2021). The role of the medial prefrontal cortex in cognition, ageing and dementia. *Brain Commun.* 3:fcab125. doi: 10.1093/braincomms/fcab125
- Kahn, J. B., Ward, R. D., Kahn, L. W., Rudy, N. M., Kandel, E. R., Balsam, P. D., et al. (2012). Medial prefrontal lesions in mice impair sustained attention but spare maintenance of information in working memory. *Learn. Mem.* 19, 513–517. doi: 10.1101/lm.026302.112
- Keller, G. B., Bonhoeffer, T., and Hübener, M. (2012). Sensorimotor mismatch signals in primary visual cortex of the behaving mouse. *Neuron* 74, 809–815.
- Kesner, R. P., Hunt, M. E., Williams, J. M., and Long, J. M. (1996). Prefrontal cortex and working memory for spatial response, spatial location, and visual object information in the rat. *Cereb. Cortex* 6, 311–318. doi: 10.1093/cercor/6.2.311
- Kragel, P. A., Reddan, M. C., LaBar, K. S., and Wager, T. D. (2019). Emotion schemas are embedded in the human visual system. *Sci. Adv.* 5:eaaw4358. doi: 10.1126/sciadv.aaw4358
- Lara, G. A. d., Alekseichuk, I., Turi, Z., Lehr, A., Antal, A., and Paulus, W. (2018). Perturbation of theta-gamma coupling at the temporal lobe hinders verbal declarative memory. *Brain Stimul.* 11, 509–517. doi: 10.1016/j.brs.2017.12.007
- Lega, B., Burke, J., Jacobs, J., and Kahana, M. J. (2014). Slow-theta-to-gamma phase-amplitude coupling in human hippocampus supports the formation of new episodic memories. *Cereb. Cortex* 26, 268–278. doi: 10.1093/cercor/bhu232
- McFadyen, J., Mattingley, J. B., and Garrido, M. I. (2019). An afferent white matter pathway from the pulvinar to the amygdala facilitates fear recognition. *Elife* 8:e40766.
- McMackin, R., Muthuraman, M., Groppa, S., Babiloni, C., Taylor, J.-P., Kiernan, M. C., et al. (2019). Measuring network disruption in neurodegenerative diseases: new approaches using signal analysis. *J. Neurol. Neurosurg. Psychiatry* 90, 1011–1020.
- Michaels, T. I., Long, L. L., Stevenson, I. H., Chrobak, J. J., and Chen, C. M. A. (2018). Effects of chronic ketamine on hippocampal cross-frequency coupling: implications for schizophrenia pathophysiology. *Eur. J. Neurosci.* 48, 2903–2914.
- Michalareas, G., Vezoli, J., Van Pelt, S., Schoffelen, J.-M., Kennedy, H., and Fries, P. (2016). Alpha-beta and gamma rhythms subserve feedback and feedforward influences among human visual cortical areas. *Neuron* 89, 384–397.
- Miller, K. J. (2019). A library of human electrocorticographic data and analyses. *Nat. Hum. Behav.* 3, 1225–1235. doi: 10.1038/s41562-019-0678-3
- Moschos, M., Chatzirallis, A., and Chatziralli, I. (2015). Psychological aspects and depression in patients with retinitis pigmentosa. *Eur. J. Ophthalmol.* 25, 459–462. doi: 10.5301/ejo.5000590
- Mulckhuyse, M. (2018). The influence of emotional stimuli on the oculomotor system: A review of the literature. *Cogn. Affect. Behav. Neurosci.* 18, 411–425.
- Munia, T. T. K., and Aviyente, S. (2019). Time-frequency based phase-amplitude coupling measure for neuronal oscillations. *Sci. Rep.* 9:12441. doi: 10.1038/s41598-019-48870-2
- Murphy, M. C., Conner, I. P., Teng, C. Y., Lawrence, J. D., Safiullah, Z., Wang, B., et al. (2016). Retinal structures and visual cortex activity are impaired prior to clinical vision loss in glaucoma. *Sci. Rep.* 6:31464. doi: 10.1038/srep31464
- Musiek, E. S., Xiong, D. D., and Holtzman, D. M. (2015). Sleep, circadian rhythms, and the pathogenesis of Alzheimer disease. *Exp. Mol. Med.* 47:e148. doi: 10.1038/emmm.2014.121
- Nakamura, A., Cuesta, P., Kato, T., Arahata, Y., Iwata, K., Yamagishi, M., et al. (2017). Early functional network alterations in asymptomatic elders at risk for Alzheimer's disease. *Sci. Rep.* 7:6517. doi: 10.1038/s41598-017-06876-8
- Ni, A., Zhou, R., and Tian, F. (2019). Modulation of human visuospatial attention analysis by transcranial direct current stimulation (tDCS) in the line bisection performance. *Saudi J. Biol. Sci.* 26, 1956–1960. doi: 10.1016/j.sjbs.2019.06.007
- Nurislamova, Y. M., Novikov, N. A., Zhzhikashvili, N. A., and Chernyshev, B. V. (2019). Enhanced theta-band coherence between midfrontal and posterior parietal areas reflects post-feedback adjustments in the state of outcome uncertainty. *Front. Integr. Neurosci.* 13:14. doi: 10.3389/fnint.2019.00014
- Ohki, T., Matsuda, T., Gunji, A., Takei, Y., Sakuma, R., Kaneko, Y., et al. (2020). Timing of phase-amplitude coupling is essential for neuronal and functional maturation of audiovisual integration in adolescents. *Brain Behav.* 10:e01635.
- Pietto, M. L., Gatti, M., Raimondo, F., Lipina, S. J., and Kamienskowski, J. E. (2018). Electrophysiological approaches in the study of cognitive development outside the lab. *PLoS One* 13:e0206983. doi: 10.1371/journal.pone.0206983
- Preston, A. R., and Eichenbaum, H. (2013). Interplay of hippocampus and prefrontal cortex in memory. *Curr. Biol.* 23, R764–R773.
- Rahmatnejad, K., Ahmed, O. M., Waisbourd, M., and Katz, L. J. (2016). Non-invasive electrical stimulation for vision restoration: dream or reality? *Expert Rev. Ophthalmol.* 11, 325–327.
- Roth, M. M., Dahmen, J. C., Muir, D. R., Imhof, F., Martini, F. J., and Hofer, S. B. (2016). Thalamic nuclei convey diverse contextual information to layer 1 of visual cortex. *Nat. Neurosci.* 19, 299–307. doi: 10.1038/nn.4197
- Saalmann, Y. B., Pinsk, M. A., Wang, L., Li, X., and Kastner, S. (2012). The pulvinar regulates information transmission between cortical areas based on attention demands. *Science* 337, 753–756. doi: 10.1126/science.1223082
- Salimpour, Y., and Anderson, W. S. (2019). Cross-frequency coupling based neuromodulation for treating neurological disorders. *Front. Neurosci.* 13:125. doi: 10.3389/fnins.2019.00125
- Schmid, M. C., Singer, W., and Fries, P. (2012). Thalamic coordination of cortical communication. *Neuron* 75, 551–552. doi: 10.1016/j.neuron.2012.08.009
- Schmidt, R., Herrojo Ruiz, M., Kilavik, B. E., Lundqvist, M., Starr, P. A., and Aron, A. R. (2019). Beta oscillations in working memory, executive control of movement and thought, and sensorimotor function. *J. Neurosci.* 39:8231. doi: 10.1523/JNEUROSCI.1163-19.2019
- Šneidere, K. N., Mondini, S., and Stephens, A. (2020). Role of EEG in measuring cognitive reserve: a rapid review. *Front. Aging Neurosci.* 12:249. doi: 10.3389/fnagi.2020.00249
- Sokoliuk, R., and VanRullen, R. (2012). Cross frequency coupling during the resting state with and without visual input. *J. Vis.* 12, 131–131.
- Song, J., Wei, Y., and Ke, H. (2019). The effect of emotional information from eyes on empathy for pain: a subliminal ERP study. *PLoS One* 14:e0226211. doi: 10.1371/journal.pone.0226211
- Spaak, E., Bonnefond, M., Maier, A., Leopold, D. A., and Jensen, O. (2012). Layer-specific entrainment of gamma-band neural activity by the alpha rhythm in monkey visual cortex. *Curr. Biol.* 22, 2313–2318.
- Sul, J. H., Kim, H., Huh, N., Lee, D., and Jung, M. W. (2010). Distinct roles of rodent orbitofrontal and medial prefrontal cortex in decision making. *Neuron* 66, 449–460. doi: 10.1016/j.neuron.2010.03.033
- Suzuki, W. A., and Amaral, D. G. (1994). Topographic organization of the reciprocal connections between the monkey entorhinal cortex and the perirhinal and parahippocampal cortices. *J. Neurosci.* 14, 1856–1877.
- Tort, A. B., Komorowski, R., Eichenbaum, H., and Kopell, N. (2010). Measuring phase-amplitude coupling between neuronal oscillations of different frequencies. *J. Neurophysiol.* 104, 1195–1210.
- Türk-Browne, N. B. (2019). The hippocampus as a visual area organized by space and time: A spatiotemporal similarity hypothesis. *Vis. Res.* 165, 123–130.
- Tzvi, E., Verleger, R., Münte, T. F., and Krämer, U. M. (2016). Reduced alpha-gamma phase amplitude coupling over right parietal cortex is associated with implicit visuomotor sequence learning. *NeuroImage* 141, 60–70. doi: 10.1016/j.neuroimage.2016.07.019
- Varadarajan, S. G., and Huberman, A. D. (2018). Assembly and repair of eye-to-brain connections. *Curr. Opin Neurobiol.* 53, 198–209.
- Vossen, A., Gross, J., and Thut, G. (2015). Alpha power increase after transcranial alternating current stimulation at alpha frequency (α -tACS) reflects plastic changes rather than entrainment. *Brain Stimul.* 8, 499–508.

- Wang, Y., Chen, K., Xu, P., Ng, T. K., and Chan, L. L. H. (2016). Spontaneous neural activity in the primary visual cortex of retinal degenerated rats. *Neurosci. Lett.* 623, 42–46. doi: 10.1016/j.neulet.2016.04.062
- Waterhouse, J., Fukuda, Y., and Morita, T. (2012). Daily rhythms of the sleep-wake cycle. *J. Physiol. Anthropol.* 31:5. doi: 10.1186/1880-6805-31-5
- Wolff, N., Zink, N., Stock, A.-K., and Beste, C. (2017). On the relevance of the alpha frequency oscillation's small-world network architecture for cognitive flexibility. *Sci. Rep.* 7:13910.
- Wróbel, A., Ghazaryan, A., Bekisz, M., Bogdan, W., and Kamiński, J. (2007). Two streams of attention-dependent beta activity in the striate recipient zone of cat's lateral posterior-pulvinar complex. *J. Neurosci.* 27, 2230–2240. doi: 10.1523/jneurosci.4004-06.2007
- Wyczesany, M., Ligeza, T. S., and Grzybowski, S. J. (2015). Effective connectivity during visual processing is affected by emotional state. *Brain Imaging Behav.* 9, 717–728. doi: 10.1007/s11682-014-9326-8
- Xie, J., Wang, G.-J., Yow, L., Cela, C. J., Humayun, M. S., Weiland, J. D., et al. (2010). Modeling and percept of transcorneal electrical stimulation in humans. *IEEE Trans. Biomed. Eng.* 58, 1932–1939.
- Young, C. K., and Eggermont, J. J. (2009). Coupling of mesoscopic brain oscillations: recent advances in analytical and theoretical perspectives. *Prog. Neurobiol.* 89, 61–78.
- Yu, W. S., Chiu, J. L. Y., Muhammad Sharafuddin Bin, M. K., Tan, Z. K. S., Tse, C. K. A., Guan, L., et al. (2019). "Transcorneal electrical stimulation induced antidepressant-like effects in S334ter-line-3 rat model of retinal degeneration," in *Proceedings of the 6th Neurocon Meeting 2019*, Ambala.
- Yu, W. S., Kwon, S. H., Agadagba, S. K., Chan, L. L., Wong, K. H., and Lim, L. W. (2021). Neuroprotective effects and therapeutic potential of transcorneal electrical stimulation for depression. *Cells* 10:2492. doi: 10.3390/cells10092492
- Zazio, A., Schreiber, M., Miniussi, C., and Bortoletto, M. (2020). Modelling the effects of ongoing alpha activity on visual perception: The oscillation-based probability of response. *Neurosci. Biobehav. Rev.* 112, 242–253. doi: 10.1016/j.neubiorev.2020.01.037
- Zhang, L., Lee, J., Rozell, C., and Singer, A. C. (2019). Sub-second dynamics of theta-gamma coupling in hippocampal CA1. *Elife* 8:e44320.
- Zheng, J., Stevenson, R. F., Mander, B. A., Mnatsakanyan, L., Hsu, F. P., Vadera, S., et al. (2019). Multiplexing of theta and alpha rhythms in the amygdala-hippocampal circuit supports pattern separation of emotional information. *Neuron* 102, 887–898. e885.
- Zheng, Y., Wu, X., Lin, X., and Lin, H. (2017). The prevalence of depression and depressive symptoms among eye disease patients: a systematic review and meta-analysis. *Sci. Rep.* 7:46453. doi: 10.1038/srep46453

Author Disclaimer: Any opinions, findings, conclusions in this publication do not reflect the views of the Government of the Hong Kong Special Administrative Region, the Innovation and Technology Commission or the Innovation and Technology Fund Research Projects Assessment Panel.

Conflict of Interest: The authors declare that the research was conducted in the absence of any commercial or financial relationships that could be construed as a potential conflict of interest.

Publisher's Note: All claims expressed in this article are solely those of the authors and do not necessarily represent those of their affiliated organizations, or those of the publisher, the editors and the reviewers. Any product that may be evaluated in this article, or claim that may be made by its manufacturer, is not guaranteed or endorsed by the publisher.

Copyright © 2022 Agadagba, Eldaly and Chan. This is an open-access article distributed under the terms of the Creative Commons Attribution License (CC BY). The use, distribution or reproduction in other forums is permitted, provided the original author(s) and the copyright owner(s) are credited and that the original publication in this journal is cited, in accordance with accepted academic practice. No use, distribution or reproduction is permitted which does not comply with these terms.



Correlated Activity in the Degenerate Retina Inhibits Focal Response to Electrical Stimulation

Jungryl Ahn¹, Seongkwang Cha¹, Kwang-Eon Choi², Seong-Woo Kim^{2*}, Yongseok Yoo^{3*} and Yong Sook Goo^{1*}

¹ Department of Physiology, Chungbuk National University School of Medicine, Cheongju, South Korea, ² Department of Ophthalmology, Korea University College of Medicine, Seoul, South Korea, ³ Department of Electronics Engineering, Incheon National University, Incheon, South Korea

OPEN ACCESS

Edited by:

Günther Zeck,
Vienna University of Technology,
Austria

Reviewed by:

Michael Beyeler,
University of California,
Santa Barbara, United States
James Weiland,
University of Michigan, United States

*Correspondence:

Seong-Woo Kim
ksw64724@korea.ac.kr
Yongseok Yoo
yyoo@inu.ac.kr
Yong Sook Goo
ysgoo@chungbuk.ac.kr

Specialty section:

This article was submitted to
Cellular Neurophysiology,
a section of the journal
Frontiers in Cellular Neuroscience

Received: 04 March 2022

Accepted: 13 April 2022

Published: 04 May 2022

Citation:

Ahn J, Cha S, Choi K-E, Kim S-W,
Yoo Y and Goo YS (2022) Correlated
Activity in the Degenerate Retina
Inhibits Focal Response to Electrical
Stimulation.
Front. Cell. Neurosci. 16:889663.
doi: 10.3389/fncel.2022.889663

Retinal prostheses have shown some clinical success in patients with retinitis pigmentosa and age-related macular degeneration. However, even after the implantation of a retinal prosthesis, the patient's visual acuity is at best less than 20/420. Reduced visual acuity may be explained by a decrease in the signal-to-noise ratio due to the spontaneous hyperactivity of retinal ganglion cells (RGCs) found in degenerate retinas. Unfortunately, abnormal retinal rewiring, commonly observed in degenerate retinas, has rarely been considered for the development of retinal prostheses. The purpose of this study was to investigate the aberrant retinal network response to electrical stimulation in terms of the spatial distribution of the electrically evoked RGC population. An 8 × 8 multielectrode array was used to measure the spiking activity of the RGC population. RGC spikes were recorded in wild-type [C57BL/6J; P56 (postnatal day 56)], *rd1* (P56), *rd10* (P14 and P56) mice, and macaque [wild-type and drug-induced retinal degeneration (RD) model] retinas. First, we performed a spike correlation analysis between RGCs to determine RGC connectivity. No correlation was observed between RGCs in the control group, including wild-type mice, *rd10* P14 mice, and wild-type macaque retinas. In contrast, for the RD group, including *rd1*, *rd10* P56, and RD macaque retinas, RGCs, up to approximately 400–600 μm apart, were significantly correlated. Moreover, to investigate the RGC population response to electrical stimulation, the number of electrically evoked RGC spikes was measured as a function of the distance between the stimulation and recording electrodes. With an increase in the interelectrode distance, the number of electrically evoked RGC spikes decreased exponentially in the control group. In contrast, electrically evoked RGC spikes were observed throughout the retina in the RD group, regardless of the inter-electrode distance. Taken together, in the degenerate retina, a more strongly coupled retinal network resulted in the widespread distribution of electrically evoked RGC spikes. This finding could explain the low-resolution vision in prosthesis-implanted patients.

Keywords: retinal degeneration, electrical stimulation, *rd1* mice, *rd10* mice, non-human primate model, retinal ganglion cell, retinal network, correlation analysis

INTRODUCTION

Retinal prostheses aim to restore vision in the blind with retinal degeneration, such as retinitis pigmentosa (RP) and age-related macular degeneration (Weiland et al., 2011; Farvardin et al., 2018; Bloch et al., 2019; Palanker et al., 2020). The strategy of the retinal prosthesis is to activate intact retinal neurons, including bipolar cells or retinal ganglion cells (RGCs), bypassing degenerate photoreceptors.

Although retinal prostheses have shown some clinical success, a patient's visual acuity restored with electronic retinal devices is at best less than 20/420 (Stingl et al., 2013; Ayton et al., 2020). To improve visual acuity, many engineers have attempted to increase the spatial resolution of electrical devices by integrating a large number of smaller electrodes on an electronic chip (Zeng et al., 2019; Shire et al., 2020; Chenais et al., 2021b), optimizing electrode configurations (Wilke et al., 2011; Celik, 2017; Flores et al., 2018) or stacking more electrodes in a three-dimensional structure (Bendali et al., 2015; Davidsen et al., 2019; Seo et al., 2019). Physiologists have searched for optimal stimulation protocols, such as the minimum stimulation threshold required for local activation of target neurons to avoid axon bundle activation or non-specific activation of nearby RGCs (Sekirnjak et al., 2008; Jepson et al., 2013; Grosberg et al., 2017; Chang et al., 2019; Tandon et al., 2021).

As another physiological strategy for improving vision, the activation of surviving photoreceptors or bipolar cells has emerged as a novel approach that mimics the natural visual processing of the normal retina. Electrical activation of retinal neurons upstream of RGCs shows a burst-like physiological response similar to a light response, whereas direct RGC activation exhibits only a single spike. Thus, we call this response a network-mediated response originating from upstream neurons, such as bipolar cells and photoreceptors (Boinagrov et al., 2014; Im and Fried, 2015; Haq et al., 2018; Im et al., 2018).

Degenerate retina shows retinal remodeling and abnormal neural connections in the retinal network (Marc et al., 2003; Menzler and Zeck, 2011; Margolis et al., 2014; Jones et al., 2016). During photoreceptor degeneration, a significant rewiring process converts the retina into self-signaling neural networks, resulting in spontaneous hyperactivity. A possible physiological explanation of the low vision found in RP patients is a decrease in the signal-to-noise ratio (SNR) due to spontaneous hyperactivity of the RGCs (Goo et al., 2011b, 2016; Euler and Schubert, 2015; Ivanova et al., 2016; Haselier et al., 2017). This induces a less reliable RGC response to repetitive electrical stimulation (Ho et al., 2020; Yoon et al., 2020). Therefore, higher stimulation intensities may be required to electrically activate degenerate RGCs than that required for normal RGCs (Jensen and Rizzo, 2009; Goo et al., 2011b; Cha et al., 2021). However, all previous experiments have focused on the single RGC level response, not the population of RGC responses.

Therefore, in this study, we focused on the spatial distribution of electrically evoked RGC population responses. Through pharmacological experiments, we identified the neuronal mechanism underlying the aberrant spatial distribution of

RGC population responses in the degenerate retina. This may be considered a retinal origin of low-resolution vision even after retinal prosthesis implantation. Therefore, correction of abnormal rewiring could enable better visual acuity with retinal prostheses in the future.

MATERIALS AND METHODS

Animals

We used four types of mice: C57BL/6J strain (wild-type) at postnatal day 56 (P56) ($n = 14$), C3H/HeJ (*rd1*) at P56 ($n = 25$), B6CXB1-*Pde6b*^{*rd10*}/J (*rd10*) at P14 ($n = 5$), and *rd10* at P56 ($n = 6$). In this study, we compared the control and retinal degeneration (RD) mouse groups: wild-type (P56) vs. *rd1* (P56), and *rd10* (P14) vs. *rd10* (P56). At P56 in *rd1* mice, the retinas are no longer responsive to light, but the functional stability of the inner retinal neurons is well preserved (Margolis et al., 2008). At P14 in *rd10* mice, photoreceptors are almost conserved, similar to the wild-type (Chang et al., 2007; Gargini et al., 2007; Stasheff et al., 2011). In contrast, at P56 in *rd10* mice, retinal light responses were almost lost, but the functional stability of inner retinal neurons was well preserved. All mice were purchased from Jackson Laboratories (The Jackson Laboratory, Bar Harbor, ME, United States). Animal use protocols were approved by the Institutional Animal Care Committee of Chungbuk National University (approval number: CBNUA-1172-18-02). All the procedures followed the guidelines of the Association for Research in Vision and Ophthalmology Statement for the Use of Animals in Ophthalmic and Vision Research.

All *in vitro* macaque experiments were performed in accordance with ARRIVE guidelines [Institutional Animal Care Committee of the OSONG KBIO HEALTH (approval number: KBIO-IACUC-2020-054)]. We used three cynomolgus monkeys (*Macaca fascicularis*) as wild-type controls and two cynomolgus monkeys as the RD model induced by *N*-methyl-*N*-nitrosourea (MNU). Their average age was 49.8 ± 2.8 months, and their average body weight was 3.87 ± 0.65 kg. The detailed procedures for developing the RD macaque model are described in a previous study (Kim, 2021; Choi, 2022). Briefly, the RD model was induced in the right eye by intravitreal loading of MNU (concentration: >2 mg/mL, exposure time: 10 min), which selectively induces photoreceptor apoptosis. **Supplementary Figures 1, 2** showed the anatomical and electrophysiological retinal changes in the RD model 12 weeks after intravitreal MNU injection using *in vivo* assessments based on optical coherence tomography (OCT) and electroretinography (ERG). There was no significant change in retinal thickness before and after MNU injection in the foveal region with high cone cell density. However, in the periphery where the rod cell density is relatively high, the retinal thickness decreases from the retinal pigment epithelium (RPE) to the outer nuclear layer (ONL). Thus, the MNU-induced RD macaque model mimics RP in patients with peripheral visual field defects. For further *in vitro* macaque experiments, degenerate peripheral retinal regions were used.

The subjects were sacrificed approximately 3 months after MNU administration.

Retinal Preparation

Mice were anesthetized by intramuscular injection of 30 mg/kg tiletamine-zolazepam hydroxide (Zoletil 50; Virbac, São Paulo, Brazil), 10 mg/kg zylazine hydrochloride (Rumpun; Bayer Korea, Seoul, South Korea), and 5,000 IU heparin sodium (Heparin; JW Pharmaceutical Corp., Seoul, South Korea). Macaque monkeys were anesthetized with an intravenous injection of 1 mg/kg alfaxalone (Alfaxan; Vetoquinol United Kingdom, Towcester, United Kingdom) into the marginal auricular vein following premedication, which comprised a subcutaneous injection of 0.05 mg/kg atropine, intramuscular injection of 1 mg/kg xylazine (Rompun; Bayer Corp., Shawnee Mission, KA, United States), and 4 mg/kg azaperone (Stresnil; Mallinckrodt Veterinary Inc., Indianapolis, IN, United States). The subjects were euthanized immediately after the enucleation of the eyeball.

The detailed procedures for the preparation of *ex vivo* retinal patches have been described in previous studies (Stett et al., 2000; Ahn et al., 2015). Briefly, after eye enucleation, the retina was isolated from the sclera and RPE and cut into $2 \times 2 \text{ mm}^2$ patches. The retinal patch was prepared under the illumination of 4.3 nW/cm^2 in an artificial cerebrospinal fluid solution (124 mM NaCl, 10 mM glucose, 1.15 mM KH_2PO_4 , 25 mM NaHCO_3 , 1.15 mM MgSO_4 , 2.5 mM CaCl_2 , and 5 mM KCl) bubbled with 95% O_2 and 5% CO_2 to maintain a pH of 7.3–7.4 and a temperature of 32°C . The isolated retina was mounted on the RGC layer on a planar multi-electrode array (MEA) and continuously perfused with oxygenated solution (flow rate: 1–3 mL/min) during the experiment.

Multi-Electrode Recording System and Signal Processing

The data acquisition system (MEA60 system; Multichannel Systems GmbH, Reutlingen, Germany) included a planar 64-channel perforated MEA (60pMEA200/30iR), an amplifier (MEA1060), temperature control units (TC01), data acquisition hardware (Mc_Card), and software (Mc_Rack). The MEA contained 64 circular electrodes in an 8×8 grid layout with electrode diameters of $30 \mu\text{m}$ and inter-electrode distances of $200 \mu\text{m}$. The electrodes were coated with porous titanium nitride and embedded in a perforated polyimide foil that provided sufficient oxygen and nutrient supply to the retina. Multi-electrode recordings of retinal activity were obtained from 59 out of 64 electrodes, except for one reference electrode and four inactive electrodes with a bandwidth ranging from 1 to 3,000 Hz at a gain of 1,200. The data-sampling rate was 25 kHz for each electrode. From the raw waveform of the retinal recording, RGC spikes were isolated using a 100-Hz high-pass filter. Local field potential (LFP) traces were isolated from low-pass filtering using a 40-Hz cutoff frequency. The threshold for spike detection was set to four times the standard deviation of background noise. The recorded data were processed with spike sorting software (Offline Sorter; Plexon Inc., Dallas, TX, United States) for each MEA channel to separate multiunit activities containing different spike

waveforms into individual cell units using principal component analysis (Lewicki, 1998). Therefore, for a pair of RGCs, the interelectrode distance is the distance between the RGCs.

Cross-Correlation Analysis

The cross-correlation of two spike trains simultaneously recorded between the RGCs can be quantified using a cross-correlogram that displays the amount of synchronized firing between the two cells. First, we binned the spike trains in the RGC pairs to generate a binary number of spikes for each RGC, as a function of time. Next, we used the cross-correlation index (CCI) to quantify the strength of the correlation between the two RGCs. It is defined as the ratio between the probability of synchronized firing (i.e., two cells firing together during a time lag) and the expected probability of a statistically independent firing (Shlens et al., 2006). CCI was calculated using the following equation:

$$\text{CCI} = \log_2 \frac{P(A, B)}{P(A)P(B)} \quad (1)$$

where A and B denote events where RGC A and RGC B spike, respectively. Two independent spike trains had a CCI value of zero [$P(A)P(B) = P(A, B)$], with higher CCI values indicating higher synchrony.

In Equation 1, the time lag for probability calculation was chosen to be 0.2 s (200 ms), considering the fact that retinal remodeling occurs between inner retinal neurons through the gap junction relay between ON-cone bipolar cells and AII amacrine cells in the degenerate retina (Margolis et al., 2014; Trenholm and Awatramani, 2015). The time lag through indirect connections *via* the relays of inner retinal neurons, including bipolar or amacrine cells, which are upstream neurons of the RGC, is within approximately 200 ms (Brivanlou et al., 1998). The CCIs were calculated and plotted for interelectrode distances ranging from the nearest distance of 200–1,600 μm in steps of $200 \mu\text{m}$.

Electrical Stimulation

Using a stimulus generator (STG 1004, Multichannel Systems GmbH, Reutlingen, Germany), the current pulse train was delivered to the retinal preparation through one of the 60 channels (mostly channel 44 in the middle of the MEA), with the remaining channels serving as recording electrodes. The remaining channels of the MEA were binned into five groups (200–400, 400–600, 600–800, 800–1,000, and 1,000–1,200 μm) based on the distance between the stimulation and recording electrodes of the MEA. The stimulation consisted of symmetrical cathodic phase 1st biphasic pulses. The pulse duration was fixed at $500 \mu\text{s}$ /phase and pulse amplitudes of 5, 10, 20, 30, 40, and $50 \mu\text{A}$ /phase were applied. For each pulse amplitude, biphasic current pulses were applied 50 times once per second (1 Hz).

Pharmacological Treatment

The drug solution was applied *via* perfusion for at least 20 min before recording. A combination of $50 \mu\text{M}$ 6,7-dinitroquinoxaline-2,3-dione (DNQX, 0189, TOCRIS, Bristol, United Kingdom) and $50 \mu\text{M}$ DL-2-amino-5-phosphonopentanoic acid sodium salt (DL-AP5, 3693, TOCRIS,

Bristol, United Kingdom) was used to block the ionotropic glutamate AMPA/kainate receptors and NMDA receptors. Gap junction coupling was blocked using 100 μ M meclofenamic acid (MFA; M4531; Sigma-Aldrich, St. Louis, MO, United States).

Data Analysis

Data analysis was performed using commercial analysis software (NeuroExplorerTM; Plexon Inc., Dallas, TX, United States), commercial statistical software (IBM SPSS Statistics 24; IBM Corp., New York, NY, United States), and custom-made MATLAB (MathWorks, Natick, MA, United States) code.

The average spike frequency for the RGCs was calculated as the total number of spikes divided by the total recording time (3 min before electrical stimulation). Fast Fourier transform (FFT) was performed to detect the principal frequencies of LFPs commonly observed in degenerate retinas (Goo et al., 2011a; Yee et al., 2012; Biswas et al., 2014).

The temporal structure of the RGC response to electrical stimulation was investigated using a post-stimulus time histogram (PSTH). RGC response strength was quantified by counting the number of electrically evoked RGC spikes per pulse, which is the difference between the number of spikes during the 400 ms before and after stimulation. The purpose of this study is to identify the abnormal network response to electrical stimulation in the degenerate retina, so we focused on the network-mediated RGC response by activation of the inner nuclear layer rather than the direct RGC response. To consider only network-mediated RGC responses, we disregarded directly evoked RGC spikes within 10 ms after electrical stimulation. The stimulation threshold was defined as the current amplitude when the number of evoked RGC spikes per pulse was 0.5. Threshold charge density was calculated using the following equation:

$$\text{Threshold charge density} = \frac{I \times D}{\pi \times r^2} \quad (2)$$

where I is the threshold amplitude, D is the pulse duration, and r is the MEA electrode radius (15 μ m). The threshold charge and threshold charge density were always calculated from the 1st phase of the biphasic charge-balanced stimulus pulse. Electrical stimulation was applied to the retinal patches through one electrode of the MEA (mostly channel 44 in the middle of the MEA). The threshold charge density was measured for one stimulation electrode (Sekirnjak et al., 2006; Goo et al., 2011b; Abramian et al., 2014).

All results shown here, including spike frequency, inter-spike interval (ISI), LFP frequency, CCI, number of electrically evoked RGC spikes, threshold amplitude, threshold charge, and threshold charge density, were averaged for the analyzed neurons. Error bars indicate the mean \pm standard error of the mean. A paired t -test was performed for statistical analysis between the two groups ($*p < 0.05$, $**p < 0.01$, and $***p < 0.001$). Kruskal–Wallis test was performed with Tukey–Kramer, Bonferroni, and Scheffe *post hoc* tests ($p < 0.05$) to determine the statistical difference in CCI with inter-electrode distance and the number of evoked spikes with distance from the stimulation electrode.

RESULTS

Spontaneous Activity of Retinal Ganglion Cells in Normal and Degenerate Retinas

To compare the spontaneous activity of RGCs in normal and degenerate retinas, we analyzed 572 RGCs from 14 retinal patches from wild-type mice and 555 RGCs from 13 retinal patches from *rd1* mice. For the different aging of *rd10* mice, we analyzed 288 RGCs from five retinal patches (P14 mice) and 252 RGCs from six retinal patches (P56 mice). Furthermore, to test whether the physiological properties of the degenerate retina observed in *rd* mice are conserved in non-human primate RD retinas, we compared the spontaneous activity between wild-type macaque retinas (231 RGCs, three retinal patches) and RD macaque retinas (179 RGCs, two retinal patches).

Degenerate RGCs showed hyperactive and rhythmic spontaneous activities compared to wild-type RGCs in both mouse and macaque retinas. First, degenerate RGCs showed hyperactive spontaneous firing compared with wild-type RGCs (Figures 1A,B). In the RD group, including *rd1*, *rd10* (P56), and RD macaque retinas, the spike frequency of degenerate RGCs was significantly higher than that of other controls ($p < 0.001$). Second, degenerate RGCs showed rhythmic bursts, each with different interburst intervals within the degenerate group (Figure 1A). Each degenerate group showed a distinct peak in ISI histogram compared with the wild-type group (*rd1*: 124.84 ± 9.86 ms, *rd10* P56: 235.45 ± 16.89 ms, RD macaque: 68.38 ± 8.76 ms) (Figure 1C). Third, degenerate RGCs showed abnormal oscillations in LFPs that were not found in wild-type RGCs (Figure 1A). The main peaks in the LFP power spectrum were observed at approximately 10 Hz in *rd1* (11.95 ± 0.36), 5 Hz in *rd10* P56 (4.54 ± 0.57), and 20 Hz in RD macaque (19.14 ± 0.99) (Figure 1D).

These results are in line with those of previous reports (Borowska et al., 2011; Trenholm and Awatramani, 2015; Goo et al., 2016). Several physiological characteristics such as hyperactivity, rhythmic bursts, and LFP oscillations in degenerate RGCs have been observed in *rd1* and *rd10* mice with the complete photoreceptor loss. However, in this study, new observations were made in RD macaque retinas, with complete disappearance of the outer segment and outer nuclear layer induced by MNU injection (OCT-based histological findings in Supplementary Figure 1). It would be interesting to discover these physiological properties in non-human primate models. This suggests that several physiological properties, including hyperactivity, rhythmic bursts, and LFP oscillations, are generally observed in degenerate retinas across species.

Synchronized Firing Patterns Among Retinal Ganglion Cells in Degenerate Retinas

We investigated synchronized firing between RGC pairs in the control and RD groups. Figure 2A shows representative spike trains of two RGCs spaced 200 μ m apart in the wild-type and *rd1* mouse retinas. The *rd1* RGCs showed a strong spike correlation between the two RGCs, in contrast to wild-type RGCs.

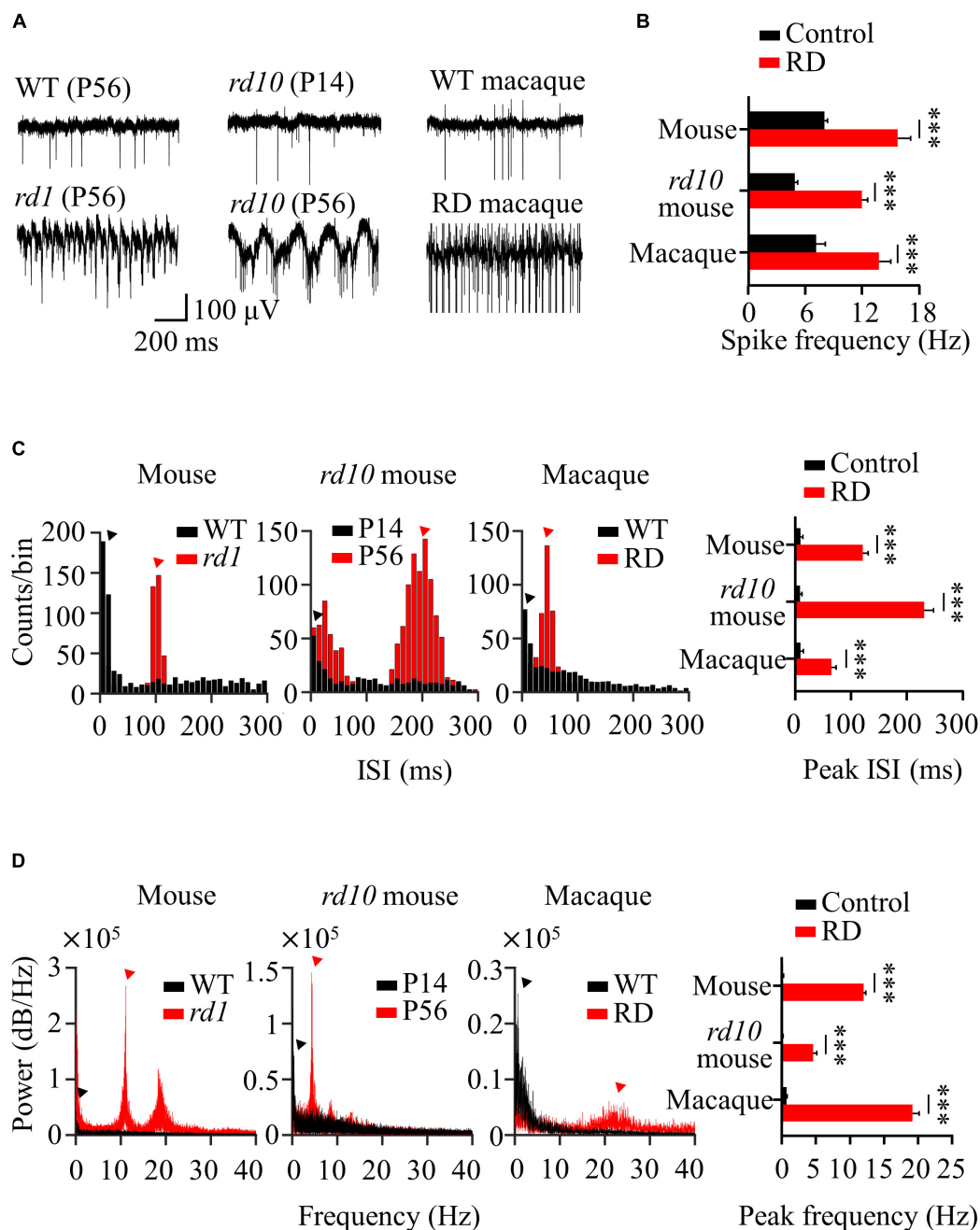


FIGURE 1 | Spontaneous activity of RGCs in normal and degenerate retinas. **(A)** Representative raw traces of RGCs observed in control (WT P56, *rd10* P14, WT macaque) and RD groups (*rd1* P56, *rd10* P56, RD macaque). **(B)** Spike frequency of RGCs for control and RD groups. **(C)** Inter-spike interval histogram. Red and black arrowheads indicate the main ISI peaks for each RD and control group. **(D)** Power spectral density using FFT for detection of the dominant LFP frequency. Statistically significant differences between each of the different groups are shown above (** $p < 0.001$).

In the raster plot, the spikes in *rd1* RGCs were relatively well synchronized over time. This synchronized pattern is represented by significant peaks in the cross-correlogram. In contrast, wild-type RGCs showed no correlated firing between the two RGCs, even at the nearest spacing of 200 μm . In the cross-correlogram, wild-type RGCs did not show significant peaks, indicating few synchronized firing events.

To evaluate the strength of the spike correlations between the RGC pairs, we calculated the CCIs for each RGC pair recorded in the individual channels of the MEA. The right panel of **Figure 2A** shows CCI as a function of the inter-RGC distance. The CCI of *rd1* RGCs decreased with increasing distance between RGC pairs, whereas wild-type RGCs showed almost zero CCIs, regardless of the distance between RGCs. Significant differences

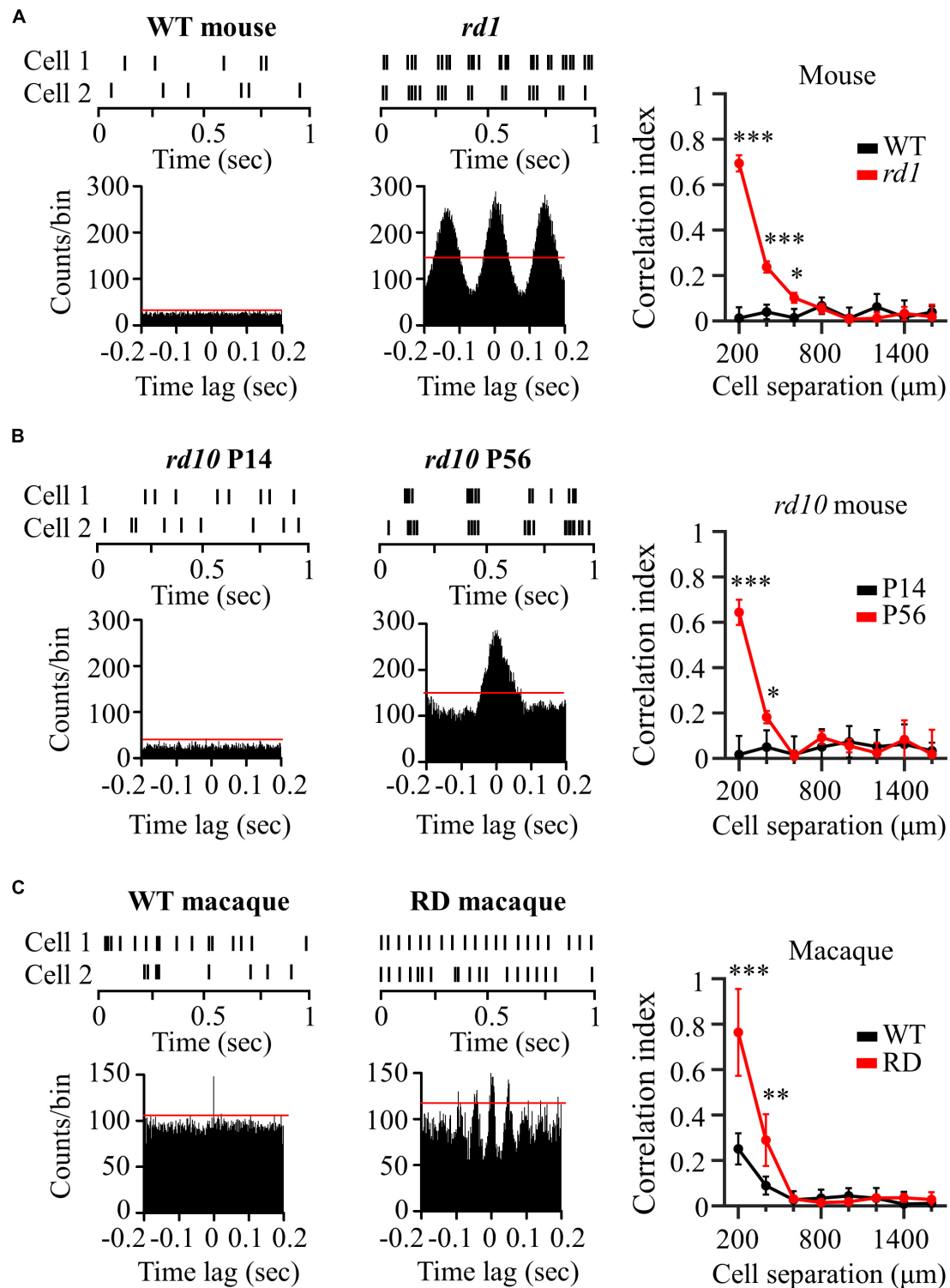


FIGURE 2 | Degenerate RGCs showed more synchronized firing patterns. **(A)** Cross-correlation between two RGCs in wild-type and *rd1* retinas. Top left panel: raster plot of wild-type RGCs with 200 μm spacing on the MEA. Lower left panel: cross-correlogram between RGC pairs. The time bin of the histogram is chosen to be 2 ms. The red line indicates the significance level, indicated by the 99% confidence limit of the time histogram. Top middle panel: raster plot of *rd1* RGCs. Lower middle panel: cross-correlogram for *rd1*. Right panel: Cross-correlation index (CCI) as a function of inter-RGC distance. The time lag is chosen to be 0.2 s. Statistical differences between wild-type and *rd1* mice are indicated by asterisks (** $p < 0.001$, ** $p < 0.01$, * $p < 0.05$). **(B)** Cross-correlation between two RGCs in *rd10* P14 and *rd10* P56. **(C)** Cross-correlation between two RGCs in wild-type and RD macaque.

in CCI between wild-type and *rd1* retinas were found for RGC pairs that were 200–600 μm apart. To determine the statistical difference in CCIs according to the inter-electrode distance, we performed Kruskal–Wallis test for wild-type and *rd1* retinas. Four statistically different groups (group 1, 200 μm ; group 2, 400 μm ; group 3, 600 μm ; and group 4, 800–1,600 μm , $p < 0.05$) were found in the *rd1* retina, whereas no significant differences were found in the wild-type retina ($p > 0.05$).

Figure 2B shows the representative spike trains of the two RGCs in the *rd10* P14 and *rd10* P56 retinas. Similar to the results shown in **Figure 2A**, for P56 at the more progressive degeneration stage, RGC pairs showed strong synchronization compared to RGCs for P14 before retinal degeneration. Significant differences in CCI between *rd10* P14 and *rd10* P56 retinas were observed between RGC pairs spaced 200–400 μm apart. For Kruskal–Wallis test of *rd10* P56, three statistically different groups (group 1: 200 μm ; group 2: 400 μm ; and group 3: 600–1,600 μm , $p < 0.05$) were shown with inter-electrode distances.

In macaque monkeys, in contrast to wild-type mice and *rd10* P14 mice, wild-type macaque RGCs showed temporally narrow correlated firing of 2 ms in the cross-correlogram (left panel of **Figure 2C**). The CCI of wild-type macaque retinas showed statistical differences according to inter-electrode distance (group 1, 200 μm ; group 2, 400 μm ; group 3: 600–1,600 μm , $p < 0.05$) (right panel of **Figure 2C**). This finding is compatible with those of previous macaque and marmoset studies (Shlens et al., 2006; Ahn et al., 2020). Narrow correlations arise from direct connections through gap junction channels between RGCs (Brivanlou et al., 1998).

Interestingly, RD macaque RGCs showed a wider temporal (~ 50 ms) correlation than did wild-type macaque RGCs (middle panel in **Figure 2C**). Previous studies have shown that broad correlations occur in indirect connections *via* the relays of inner retinal neurons, including bipolar or amacrine cells, which are upstream neurons of the RGC (Brivanlou et al., 1998). This suggests that connections between inner retinal neurons may be strengthened, indicating the potential for aberrant retinal remodeling in *rd* mice (Strettoi et al., 2003; Phillips et al., 2010; Choi et al., 2014). CCI in RD macaque retinas showed a statistically significant increase compared with wild-type macaque retinas for RGC pairs with 200–400 μm spacing (right panel in **Figure 2C**), consistent with those found in *rd* mice. Comprehensively, the degenerate retina has highly correlated RGCs compared to the wild-type retina in both mouse and macaque models.

Oscillatory Rhythm Leads to Multiple Peaks of Electrically Evoked Retinal Ganglion Cell Responses in Degenerate Retina

We compared electrically evoked RGC responses between the control and RD groups. For the control group, the left panels of **Figure 3** show representative RGC responses to electrical stimulation with a pulse amplitude of 50 μA and a pulse duration of 500 μs . Raster plots and PSTHs showed a single

burst and one PSTH peak within 100 ms of the stimulation onset. In contrast, RD RGCs showed rhythmic bursts and multiple PSTH peaks at ~ 10 Hz (*rd1*), ~ 5 Hz (*rd10* P56), and ~ 20 Hz (RD macaque) (middle panels in **Figure 3**), indicating that spontaneous oscillatory LFPs were also observed in the electrically evoked RGC responses.

The number of evoked RGC spikes was well modulated with increasing pulse amplitude in both the control and RD groups (right panels of **Figure 3**). At all pulse amplitudes, the number of evoked spikes was lower in the RD group than in the control group. Additionally, in terms of stimulation threshold parameters, including threshold amplitude, threshold charge, and threshold charge density, the RD group showed higher stimulation thresholds than did the control group (**Table 1**). Collectively, RD RGCs showed less response than control RGCs, suggesting that RD RGCs require higher stimulation charge injection to reach the levels of the wild-type RGC response in both mouse and macaque models.

Wide-Spreading Distribution of Electrically Evoked Retinal Ganglion Cell Population in Degenerate Retina

The spatial distribution of the evoked RGC population was characterized by response intensity as a function of the distance between the stimulation and recording electrodes. The number of electrically evoked RGC spikes was normalized to the range [0 1] using feature scaling based on min–max normalization. **Figure 4** compares the spatial changes in electrically evoked RGCs between the normal and degenerate retinas. Overall, RGCs in the control group showed a sharp decrease in response strength as they moved away from the stimulation electrode (left panels of **Figure 4**), suggesting that RGCs closer to the stimulation site were more effectively activated. Each spatial MEA color map for normalized RGC responses in one retinal patch showed a spatially confined RGC response to electrical stimulation (pulse amplitude: 50 μA , pulse duration: 500 μs). Contrastingly, RD RGCs showed a wide-spreading spatial distribution of electrically evoked RGC spikes, indicating a relatively gradual decreased pattern (right panels of **Figure 4**). Specifically, no change was noted in the response intensity of RD RGCs up to 800 μm (*rd1* and *rd10* P56) or 600 μm (RD macaques) to stimuli greater than 30 μA , except for a pulse amplitude of 10 μA . To quantify the spatial distribution of the RGC population in response to electrical stimulation, the distance from the normalized RGC response of 0.5 was used as the marginal distance for significant RGC activation. Normalized response stands for the normalized evoked spike number per pulse. Most RGCs in the control group had a distance of approximately 400 μm from the stimulation electrode (viewed at 30 μA , wild-type mice: 358 μm , *rd10* mice P14: 463 μm , wild-type macaque: 279 μm), whereas RD RGCs were more widely distributed (30 μA , *rd1* mice: 983 μm , *rd10* mice P56: 948 μm , RD macaque: 774 μm). Collectively, the normal retina showed a spatially confined RGC response to electrical stimulation, whereas the RD retina showed a spatially extended response to the same stimulus intensity.

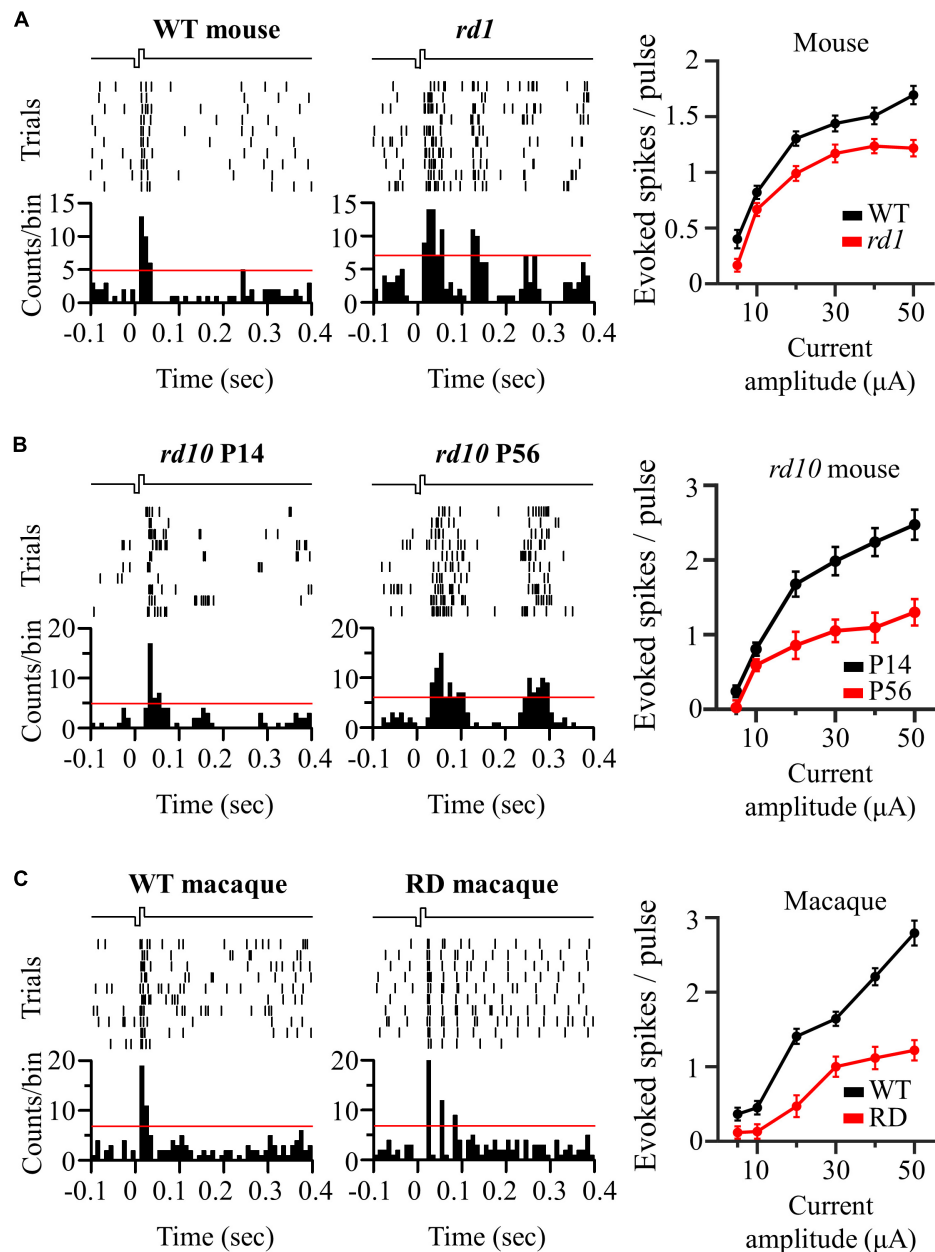


FIGURE 3 | Oscillatory rhythm leads to multiple peaks of electrically evoked RGC responses in degenerate retina. **(A)** The responses of wild-type and *rd1* RGCs that are located 200 μm away from the stimulation electrode upon electrical stimulation with a pulse amplitude of 50 μA and a pulse duration of 500 μs. Top left panel: raster plot of wild-type RGC (10 trials). Lower left panel: post-stimulus time histogram (PSTH) accumulated over 10 trials. The time bin for PSTH is chosen to be 10 ms. The red line indicates the significance level, expressed as the 99% confidence limit for PSTH. Top middle panel: raster plot of *rd1* RGC. Lower middle panel: PSTH on *rd1*. Right panel: RGC response curve with increasing pulse amplitude. **(B)** The same representative figures with *rd10* P14 and *rd10* P56. **(C)** The same representative figures with wild-type and RD macaque.

TABLE 1 | Comparison of threshold amplitude, threshold charge, and threshold charge density between control and RD groups.

	WT mouse	<i>rd1</i> mouse	<i>rd10</i> mouse (P14)	<i>rd10</i> mouse (P56)	WT macaque	RD macaque
Threshold amplitude (μA)	5.76 ± 0.64	10.47 ± 0.53 (***)	7.13 ± 0.45	9.68 ± 0.82 (**)	12.34 ± 0.91	25.75 ± 1.27 (***)
Threshold charge (nC/phase)	2.88 ± 0.32	5.24 ± 0.27 (***)	3.57 ± 0.23	4.84 ± 0.41 (**)	6.17 ± 0.46	12.88 ± 0.64 (***)
Threshold charge density (mC·cm ⁻² /phase)	0.41 ± 0.05	0.74 ± 0.04 (***)	0.51 ± 0.03	0.68 ± 0.06 (**)	0.87 ± 0.07	1.82 ± 0.09 (***)

Statistical differences between control and RD groups are indicated by asterisks (****p* < 0.001, ***p* < 0.01).

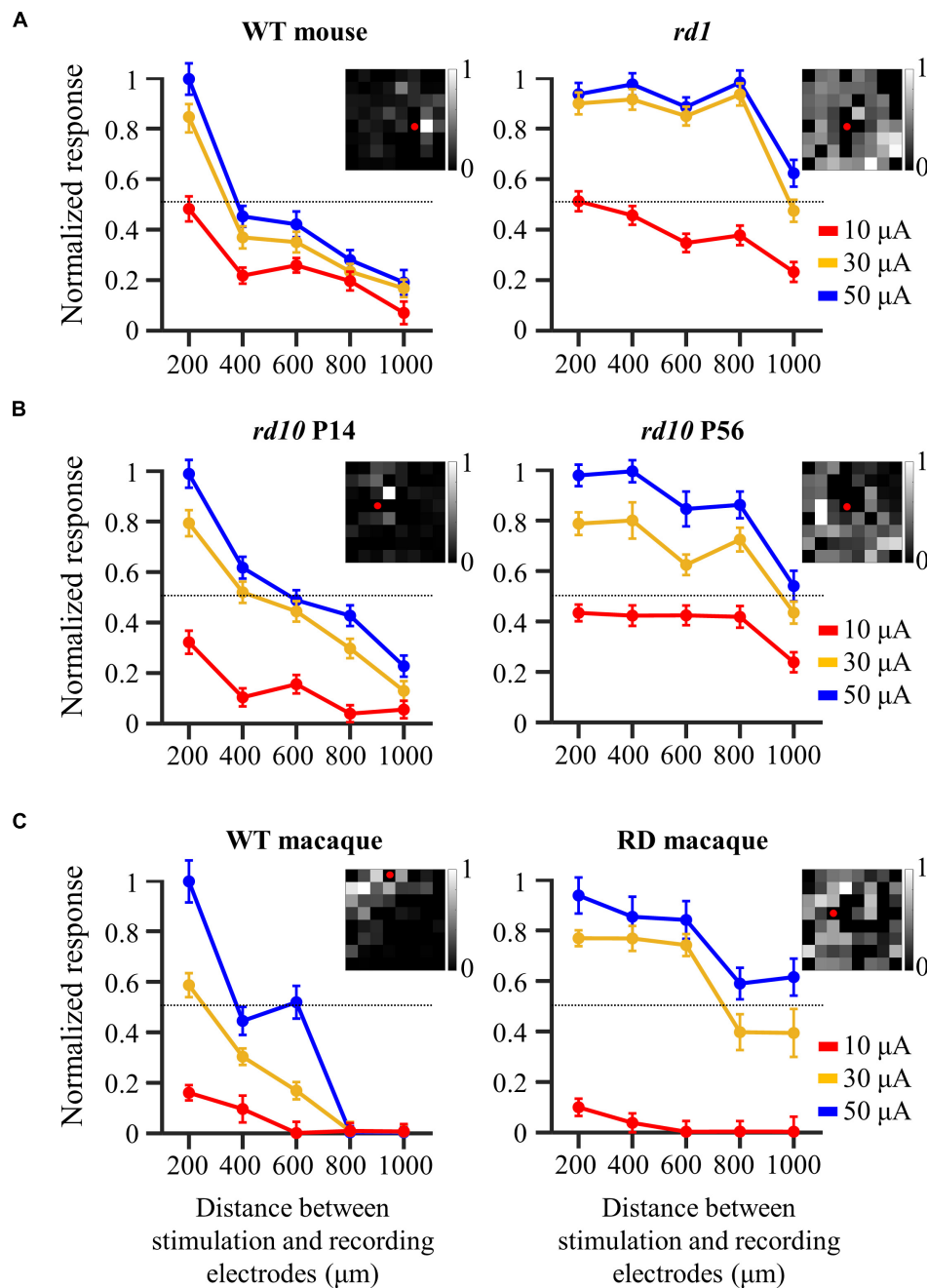


FIGURE 4 | Wide-spreading distribution of electrically evoked RGC population in the degenerate retina. **(A)** Changes in normalized RGC response with the distance between stimulation and recording electrodes in wild-type and *rd1* mice. **(B)** Changes in normalized RGC response with the distance between stimulation and recording electrodes in *rd10* P14 and *rd10* P56. **(C)** Changes in normalized RGC response with the distance between stimulation and recording electrodes in wild-type and RD macaque. Insets in A, B, and C represent the spatial MEA colormap (grayscale) for normalized RGC responses upon electrical stimulation with a pulse amplitude of 50 μA and a pulse duration of 500 μs in one representative retinal patch. Red dots represent the position of stimulation electrodes.

Origin of the Electrically Evoked Retinal Ganglion Cell Responses in the Degenerate Retina: Direct vs. Indirect

To investigate the origin of the electrical response shown in **Figure 4**, we performed a pharmaceutical experiment. Generally, there are two electrical responses. The first is the directly

evoked RGC response. The other is a network-mediated response through a synaptic relay after photoreceptor or bipolar cell activation. However, only bipolar cell activation owing to complete photoreceptor loss at *rd1* P56 can be considered here. To evaluate whether the electrically evoked RGC response was direct or indirect, blockers of excitatory input to the RGCs

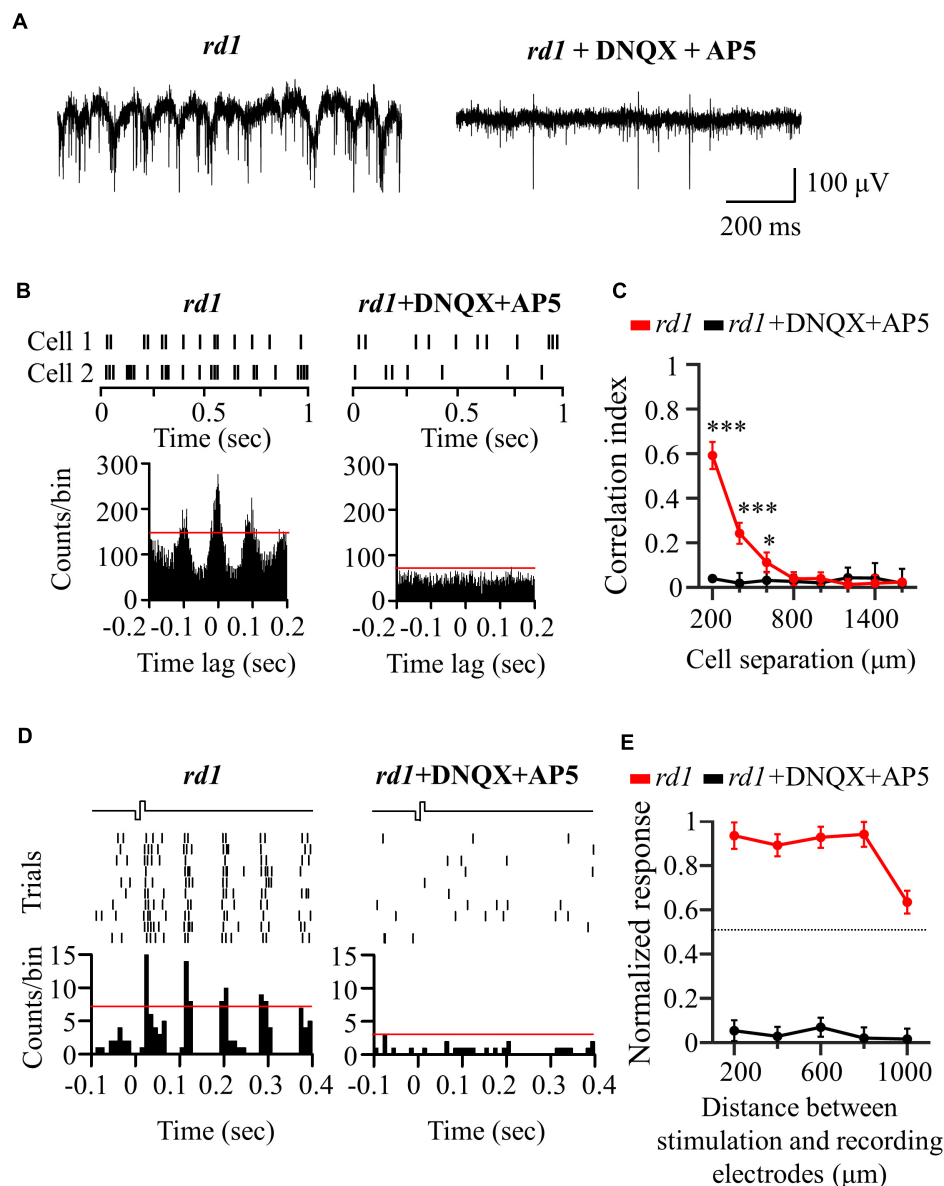


FIGURE 5 | Application of glutamatergic receptor blocker (DNQX and DL-AP5) completely blocked network-mediated RGC responses in the *rd1* retina.

(A) Representative raw traces of RGCs were shown for 1 s in *rd1* mice without and with glutamate receptor blockers. (B) Changes in synchronized firing between *rd1* RGCs after drug application. Top panels: raster plot of RGC with 200 μ m spacing on the MEA. Lower panel: cross-correlogram between RGCs. The time bin for correlograms is chosen to be 2 ms. The red line indicates the significance level represented by the 99% confidence limit of the correlogram. (C) CCI as a function of inter-RGC distance. The statistical differences before and after drug application are indicated by asterisks (***) and (*). (D) The responses of RGC that is 200 μ m away from the stimulation electrode to electrical stimulation with a pulse amplitude of 50 μ A and a pulse duration of 500 μ s. Top panels: raster plot of *rd1* RGC (10 trials). Lower panel: PSTHs. The time bin for PSTH is chosen to be 10 ms. The red line indicates the significance level, expressed as the 99% confidence limit for PSTH. (E) Normalized RGC response to electrical stimulation (pulse amplitude: 50 μ A, pulse duration: 500 μ s) with the distance between stimulation and recording electrodes without and with the presence of glutamate receptor blockers.

(ionotropic glutamate receptor blockers: 50 μ M DNQX and 50 μ M DL-AP5) were applied to the perfusion solution.

An additional six retinal patches and 343 RGCs were used in *rd1* mice for drug studies. First, Figure 5A shows the representative spontaneous activity of *rd1* RGCs recorded before and after the addition of blockers. The rhythmic bursts and LFPs disappeared within minutes after drug

application, confirming their identity as a network origin. Figure 5B shows exemplary responses from the two RGCs spaced 200 μ m apart. After drug application, synchronized firing between RGCs largely disappeared (Figure 5C). In addition, the electrically evoked RGC spikes completely disappeared when electrical stimulation was applied, suggesting that stimulation may involve presynaptic network activation

in RGCs (Figures 5D,E). These findings indicate that the electrically evoked RGC spikes recorded in the degenerate retina are network-mediated and are not generated by direct RGC activation.

Neuronal Mechanisms of Spatially Extended Retinal Ganglion Cell Responses in the Degenerate Retina

Our previous results showed that there were highly correlated RGCs in the degenerate retina (Figure 2). Furthermore, their synchronized firing and electrically evoked responses were network-mediated (Figure 5). Therefore, we hypothesized that the highly correlated retinal network caused spatial expansion of the RGC response to electrical stimulation, as shown in Figure 4. Previous studies on the degenerate retina have found that abnormal neural connections (retinal remodeling) occur specifically through the gap junction relay between ON-cone bipolar cells and AII amacrine cells (Menzler and Zeck, 2011; Margolis et al., 2014; Trenholm and Awatramani, 2015).

To test our hypothesis, we applied MFA (100 μ M) to block gap junction channels. An additional six retinal patches and 287 RGCs were used in the *rd1* mice. After MFA application, all rhythmic bursts, LFPs, and synchronized firing disappeared (Figures 6A–C). Moreover, multiple PSTH peaks observed during electrical stimulation disappeared, leaving only a single peak (Figure 6D). Concerning the spatial distribution of the electrically evoked RGC population, RGC activation became more localized after the application of gap junction blockers (Figure 6E), indicating that gap junctions indeed mediate spatially extended RGC responses in the degenerate retina.

DISCUSSION

Figure 7 shows a schematic representation of our findings. When the RD retina is electrically stimulated, the activated bipolar cells transmit an evoked potential to the downstream RGCs in the vertical pathway, whereas the evoked potential of bipolar cells is also transmitted to gap junction-coupled inner retinal neurons (AII amacrine cells or bipolar cells). Accordingly, the gap junction-coupled retinal network activated the RGC population globally (Figure 7A). With the application of glutamatergic synaptic blockers (DNQX and DL-AP5), synaptic input from the inner retinal neurons to RGCs was blocked, and no network-mediated RGC responses were observed (Figure 7B). However, after the gap junction blockade (MFA), the evoked potential to the bipolar cell is transmitted only to the downstream RGC through a direct synaptic connection (Figure 7C).

In conclusion, our results show that degenerate RGCs become more correlated as retinal degeneration progresses. A more strongly coupled retinal network leads to a wider spatial distribution of the electrically evoked RGC spikes. Therefore, focal RGC activation is implausible in the degenerate retina, which is a major cause of low visual acuity in patients after electronic retinal implantation.

Identification of Retinal Degeneration Stage Based on Abnormal Spontaneous Activity of Retinal Ganglion Cells

We found the abnormal spontaneous activity of RGCs in degenerate retinas from *rd1* P56, *rd10* P56, and RD macaque models (Figure 1). Degenerate RGCs showed higher spike firing rates and rhythmic bursts superimposed on oscillatory LFPs compared with controls, including wild-type mouse P56, *rd10* P14, and wild-type macaque models.

Our findings focus on the study of degenerate retinal networks in the intermediate RP stage. Many studies have noted abnormal spontaneous activity in the degenerate retina of *rd1* (Ye and Goo, 2007; Margolis et al., 2008; Stasheff, 2008; Menzler and Zeck, 2011; Trenholm et al., 2012; Yee et al., 2012) and *rd10* mice (Goo et al., 2011a; Stasheff et al., 2011; Biswas et al., 2014; Yoon et al., 2020). In particular, for *rd10* mice, the increase in spontaneous firing starts after \sim P20, when rod cells begin to die histologically, and remarkable hyperactivity was observed at \sim P45 when the rod cells almost disappeared (Gargini et al., 2007; Barhoum et al., 2008). However, a recent study following postnatal aging of *rd10* showed that spontaneous firing increased from P21 (Park et al., 2015), but there were no noticeable rhythmic bursts and oscillatory LFPs in most retinal patches until P30. A very small number of RGCs at P30 exhibited irregular LFP signals. LFP has been observed in *rd10* P45 (Goo et al., 2016). Therefore, we can infer rhythmic bursts and oscillatory LFPs as findings that indicate the onset of the intermediate RP phase when rod cells are almost lost. In this respect, our results focused on the intermediate RP stage (P56), when most photoreceptors have degenerated, but bipolar cells and RGCs remain intact.

Neural mechanisms underlying oscillatory LFPs have been studied in *rd1* and *rd10* mice. A well-known neural mechanism is that oscillations are an inherent physiological property of the electrically connected network between ON bipolar cells and AII amacrine cells (Borowska et al., 2011; Choi et al., 2014; Trenholm and Awatramani, 2015). This theory is understood by the fact that oscillatory LFP in the *rd* retina is inhibited by pharmacological blockade through the gap junction blocker, MFA. Thus, an electrically connected network between the ON bipolar cells and AII amacrine cells appears to be required to drive the LFP.

LFP was observed not only in transgenic *rd* mice but also in drug-induced rabbits (Ahn et al., 2019; Supplementary Figure 3) and macaque monkeys (Figure 1), in which rod cells were rapidly removed by MNU administration. The LFP was not observed in wild-type and drug-induced incomplete RD models (partial degeneration of the outer nuclear layer) but was found in the complete RD model (severe degeneration of the outer nuclear layer). Therefore, the LFP is not limited to a specific mouse model and can be a universal physiological marker for detecting changes in retinal networks that occur during the intermediate RP stage. However, this aberrant spontaneous RGC activity has not yet been studied *in vitro* and *in vivo* in human RP retinas. According to some studies, it has been reported that approximately 70% of patients with retinal

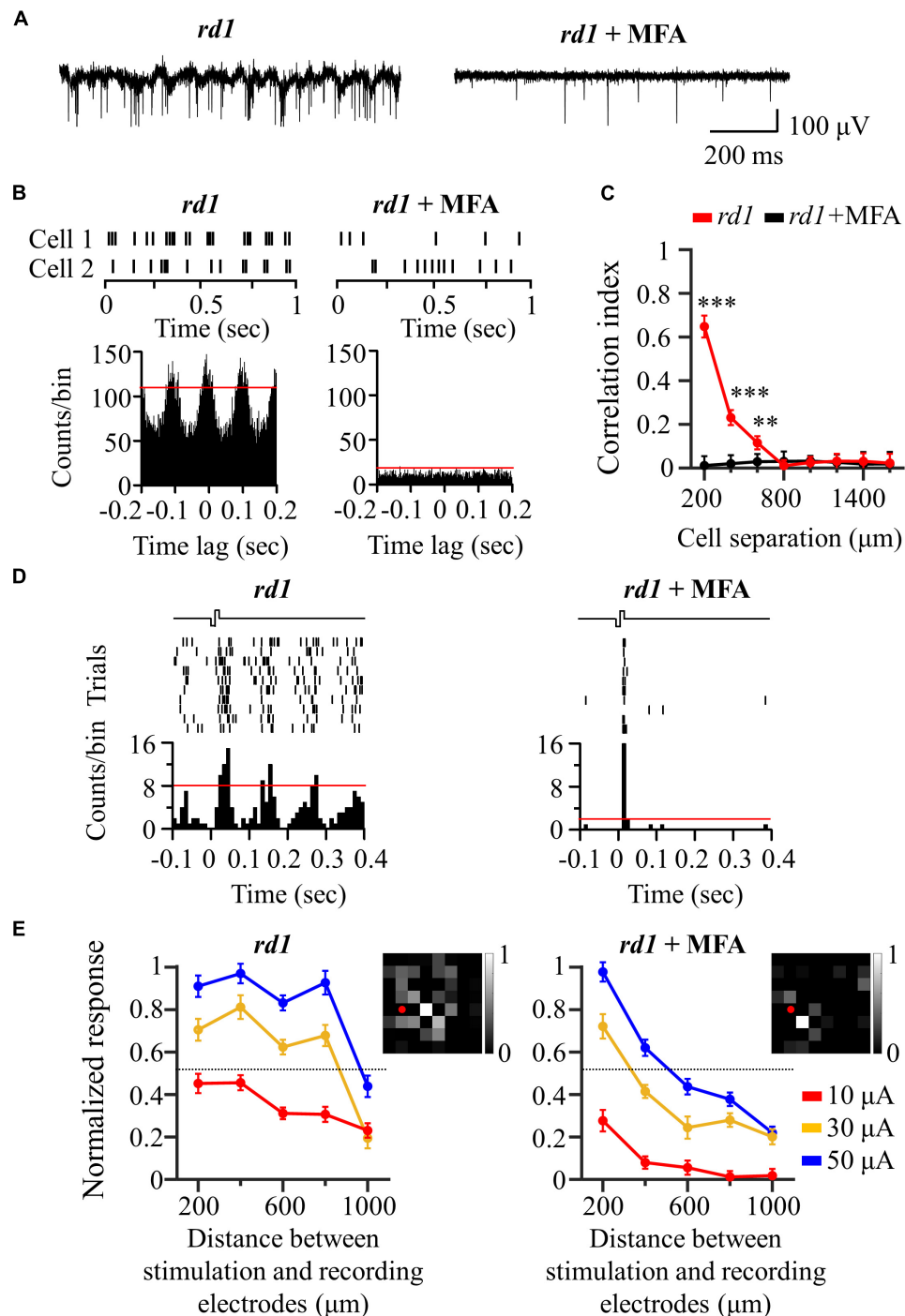


FIGURE 6 | Application of gap junction blocker (MFA) blocked inner-retinal neuron coupling. **(A)** Representative raw traces of RGCs were shown for 1 s in *rd1* mice without and with gap junction channel blockers. **(B)** Changes in synchronized firing between *rd1* RGCs after drug application. Top panels: raster plot of two RGCs with 200 μ m spacing on the MEA. Lower panels: cross-correlogram between RGCs. The time bin of correlograms is chosen to be 2 ms. The red line indicates the significance level represented by the 99% confidence limit of the correlogram. **(C)** CCI as a function of inter-RGC distance. Statistical differences before and after drug application are indicated by asterisks (** $p < 0.001$, ** $p < 0.01$). **(D)** The responses of RGC that is 200 μ m away from the stimulation electrode to electrical stimulation with a pulse amplitude of 50 μ A and a pulse duration of 500 μ s. Top panels: raster plot of *rd1* RGC (10 trials). Lower panel: PSTHs. The time bin for PSTH is chosen to be 10 ms. The red line indicates the significance level, expressed as the 99% confidence limit for PSTH. **(E)** Changes in normalized RGC response with the distance between stimulation and recording electrodes in the presence of gap junction channel blockers. Insets represent the spatial MEA colormaps (gray scale) for normalized RGC responses upon electrical stimulation with a pulse amplitude of 50 μ A and a pulse duration of 500 μ s in one representative retinal patch. Red dots indicate the position of stimulation electrodes.

degeneration see various visual symptoms, such as photopsia (brief flashes of light) and hallucinations of imaginary scenes (Heckenlively et al., 1988; Bittner et al., 2009; Brown et al., 2015). This abnormal visual perception may have been due to the appearance of spontaneously occurring RGC bursts superimposed on the LFP. Future studies in the retina of patients with RP are needed to elucidate the presence of abnormal spontaneous RGC activity, including hyperactive firing, rhythmic bursts, and LFP.

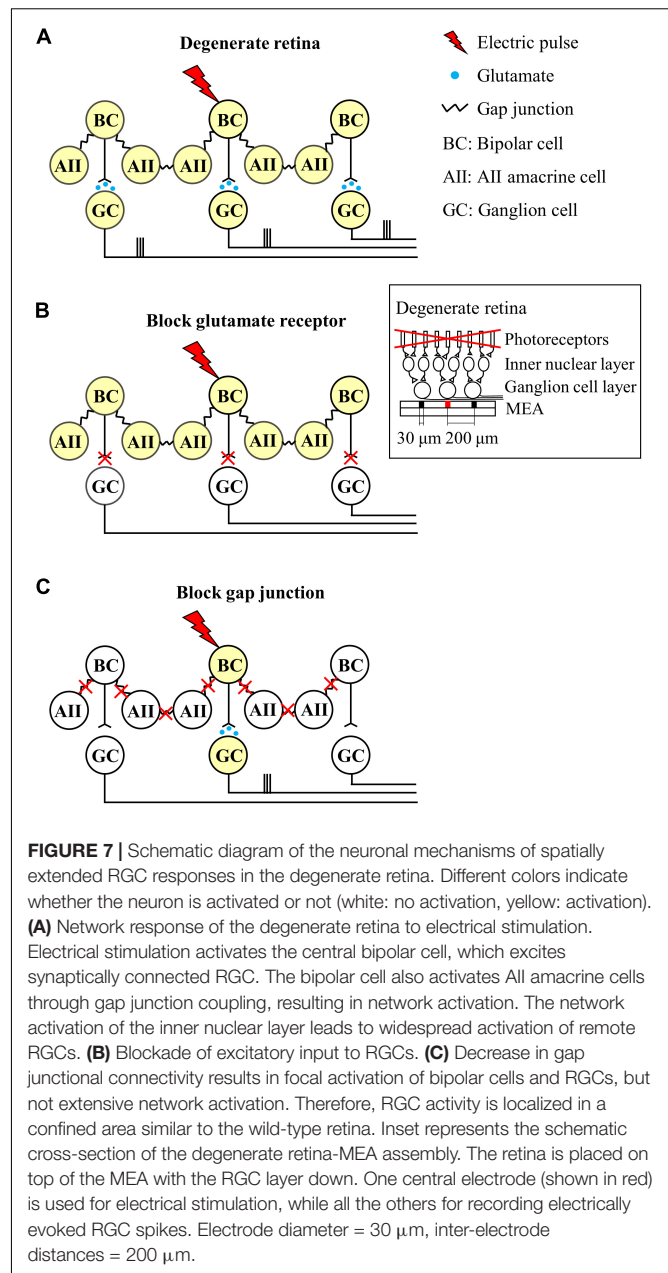
Synchronized Firing Patterns Among Retinal Ganglion Cells in Normal and Degenerate Retinas

Retinal neurons collectively fire spikes in response to the visual stimuli. For example, during retinal circuits development prior to eye-opening, RGCs exhibit strongly synchronized spontaneous activity in the retina (Wong, 1999; Demas et al., 2003). Their synchronized activity refines immature visual circuitry and retinal projections to higher-order cortical neurons (Wong, 1999; Demas et al., 2003).

In the mature visual system, nearby RGCs show synchronous activity that depends on stimulus parameters including spot size, luminance, and contrast (Mastrorade, 1989; Neuenschwander et al., 1999; Hu et al., 2010). Synchronized firing patterns also differ between species (Pryluk et al., 2019; Ahn et al., 2020). For instance, marmoset monkey RGCs show strong correlations between RGC pairs, whereas mouse RGCs show no synchrony. In particular, Shlens et al. found that macaque RGCs showed a narrow correlation of spike firing with a time lag of 2 ms and that there was little broad correlation between RGCs (Shlens et al., 2006, 2009), consistent with our findings (left panel in **Figure 2C**). For spontaneous firing, it is understandable that each pair of RGCs in the macaque retina is directly connected *via* gap junction channels (Brivanlou et al., 1998).

In addition to normal neural networks, abnormal neural connections have also been observed in retinal degeneration. In the case of retinal degeneration due to the loss of photoreceptor cells, *rd1* and *rd10* mouse RGCs showed abnormally correlated activity (Menzler and Zeck, 2011; Margolis et al., 2014). Therefore, abnormal intrinsic correlations can often be utilized as physiological indicators of retinal degeneration.

Our results also showed that *rd1* and *rd10* mouse RGCs exhibited strong synchronization compared to control RGCs (**Figures 2A,B**). Furthermore, RD RGCs showed highly correlated activity in macaque monkeys, a representative non-human primate model. Regarding why *rd1* retinas have significant correlations between RGCs up to 600 μm , whereas *rd10* P56 and RD macaques have correlations up to 400 μm (**Figure 2**), histologically, *rd1* almost loses its outer nuclear layer after P28 (Zhou et al., 2017). Conversely, *rd10* shows a remarkable decrease in rod cells at P45 (Gargini et al., 2007; Rosch et al., 2014); hence, *rd10* shows a slower degeneration than *rd1*. Therefore, it can be seen that, based on the same aging of P56, retinal degeneration and remodeling of *rd1* are more severe than that of *rd10*, and abnormal neural network



formation progresses further. However, for the RD macaque retina, unlike the RD mouse retina with genetic modification, drug administration may not allow the retinal network of RD macaques to have sufficient time for rewiring. In this study, we used RD macaque retinas 12 weeks after MNU administration for acute photoreceptor degeneration. Given the difference in lifespan between mice and primates, the time required for retinal network changes owing to retinal degeneration is longer in primates than in mice (Jones et al., 2016). More than 12 weeks after MNU administration, it is expected that retinal network changes in RD macaques will progress further.

Regarding the limitations of our study regarding synchronized firing patterns, we did not observe significant differences in

synchronized RGC firing in the control mouse group, even for the closest spacing of 200 μm . However, in previous studies, mouse RGCs have shown synchronized firing within $\sim 200\ \mu\text{m}$ (Volgyi et al., 2013; Roy et al., 2017; Zhang et al., 2020). When using high-density MEA with an inter-electrode spacing shorter than 200 μm (Miccoli et al., 2019), we would expect to observe correlated firing between a pair of RGCs within a distance of 200 μm . Nevertheless, the fact that RD RGCs have highly correlated networks compared to normal RGCs is uncontroversial.

Furthermore, we could not subdivide RGCs into ON and OFF types since there is no light-evoked RGC response due to complete photoreceptor loss by retinal degeneration. As discussed above, our results focused on the intermediate RP stage, when most photoreceptors have degenerated, but bipolar cells and RGCs remain intact. No light responses were observed in RGCs, including *rd1* and *rd10* genetic mice at P56, and drug-induced macaque RD models. Further histological studies are needed to differentiate between ON and OFF types. Some studies have demonstrated successful cell-type classification into ON and OFF RGCs based on soma size and depth of dendritic stratification within the inner plexiform layer (Margolis et al., 2008, 2014). In future studies, more detailed cross-correlation studies of RGC types with histological findings should be performed.

Spatially Extended Population Response to Electrical Stimulation in the Degenerate Retina

We observed a spatially extended response to electrical stimulation of the RD retina (**Figure 4**). As shown in **Figures 5, 6**, these RGC responses were transmitted through network activation, which was electrically connected to the inner retinal neurons. This phenomenon leads to the problem of unintentionally stimulating adjacent RGCs and consequently suppressing focal RGC activation.

Recently, simulation results were reported that compared the spatial resolution of reconstructed images between two groups by decoding electrically evoked RGC responses of healthy and RD retinas. The simulation showed that healthy retinas had good spatial resolution when reconstructing the RGC population response into visual scenes, whereas RD retinas had low spatial resolution (Golden et al., 2019). This is the first study to use computational modeling to explain the phenomenon of decreased visual acuity in patients with RP during electrical stimulation. In line with this, our results provide experimental evidence that explains the low spatial resolution of retinal coding for electrical stimulation. This RGC population response is transmitted to the visual cortex, a higher-order cortical nucleus, resulting in spatially low-resolution vision.

Relatively low stimulus intensity is required to avoid excessive activation of the retinal network. Based on the results of **Figures 4, 6** and Ryu et al. (2017), when a current of $\sim 10\ \mu\text{A}$ was stimulated to the retina, it was able to induce a relatively spatially localized RGC population response (Ryu et al., 2017). However, the problem is that stimulation of the retina with a

current intensity that is too low cannot guarantee a stable RGC response owing to the low SNR. This can be confirmed by the fact that the number of spikes evoked for a 10 μA stimulus was less than 1 (**Figure 3**).

Of course, the stimulation thresholds obtained in this study may be rather high, since the stimulation thresholds were derived from RGC responses that were at least 200 μm apart, in that stimulation and recording cannot be performed simultaneously from one electrode due to saturation of stimulation artifacts. Nevertheless, given the stimulus charge levels used in clinical trials for patients with RP (above the maximum charge of 25 nC used in this study) (Humayun et al., 2012; Chow, 2013; Fujikado et al., 2016), spatially extended population responses are expected to occur in the RD retina. This results in low visual acuity and low spatial resolution.

Furthermore, the stimulation pulse rate of 1 Hz used in this study is lower than clinically used pulse rates (at least 5 Hz or higher). Depending on which retinal neuron is stimulated, approximately 5 Hz is used for sub-retinal prosthesis, which stimulates the inner nuclear layer to induce network-mediated RGC responses (Zrenner et al., 2011; Chuang et al., 2014; Stingl et al., 2015).

The purpose of this study is to find the abnormal network response (wide-spreading spatial distribution of electrically-evoked RGC spikes) observed in the degenerate retina during electrical stimulation and to elucidate the neural mechanism of this phenomenon. Therefore, in this study, we tried to minimize the desensitization effect by choosing 1 Hz stimulation. In our previous publication, we applied electrical stimulation to *rd1* mouse retinas at P56 while increasing the pulse rate from 1 Hz to 10 Hz (Ryu et al., 2009). We observed a rapid decrease in electrically-evoked RGC spikes at a pulse rate of 5 Hz or higher even if the same pulse duration stimulation was applied to the degenerate retina. This desensitization of RGC responses to high-frequency stimuli has also been confirmed in other studies (Freeman and Fried, 2011; Im and Fried, 2016; Chenais et al., 2021a). Specifically, Chenais et al. (2021a) found that when the same pulse duration stimulation at high frequencies (1–20 Hz) was continuously applied to the *in-vitro rd10* mouse retinas at $\sim \text{P120}$, the network-mediated RGC responses became insensitive to stimuli above 5 Hz. Specifically, the number of electrically-evoked RGC spikes during high-frequency stimulation decreased rapidly after the first stimulation (**Figure 3** of Chenais et al., 2021a). In Chenais et al.'s study, a strategy to suppress RGC desensitization using time-varying, non-stationary stimulation (pulse duration modulation) was proposed.

Since the RD group showed spatially expanded responses of the RGC population compared with the control group at the same 1 Hz stimulation, there is a high possibility that the abnormal network responses are still maintained with higher pulse rates ($> 1\ \text{Hz}$). In future studies, we would like to observe if the spatially expanded RGC response still appears in the degenerate retina when applying a clinically used pulse rate with time-varying, non-stationary stimuli proposed by Chenais et al. (2021a). Whether the observed wide-spreading spatial distribution of electrically-evoked RGC spikes in RD retina is maintained, enhanced, or

suppressed during high frequency stimulation will be of great interest in the artificial vision community.

Clinical Implication for Retinal Prosthesis

The electrode location on the retinal layer determines one of two widely used stimulus configurations. One is epi-retinal and the other is a sub-retinal stimulus configuration. Epi-retinal stimulation directly activates RGCs, whereas sub-retinal stimulation primarily targets the surviving photoreceptors or intact bipolar cells. Epi-retinal stimulation has the advantage of enabling relatively simple RGC activation compared to complex network activation. However, the disadvantages are that RGCs fire only one spike regardless of stimulation intensity (non-naturalistic response) and non-selective activation of RGC axon bundles passing between the RGC layer and the stimulation electrode (Fried et al., 2009; Beyeler et al., 2019). In contrast, sub-retinal stimulation has the advantage of being suitable for mimicking natural retinal responses through network activation (Im and Fried, 2015). However, if retinal degeneration is severe and the inner nuclear layer containing bipolar cells is not preserved, sub-retinal stimulation is impractical.

Directly targeting RGCs can avoid problems associated with spatially extended RGC responses based on abnormal network activation. An *in vitro* study of *rd10* P130-260, mimicking the late RP stage, showed a spatially restricted RGC response through direct RGC activation (Corna et al., 2021). On the contrary, network activation targeting the inner nuclear layer appears to be problematic because of the highly correlated retinal networks after retinal degeneration has progressed severely. To avoid these issues, prosthetic implantation is recommended for patients in the early RP stage. Artificial retinal devices have been used in early-stage patients whose photoreceptors are not fully degenerated. Even in *in vitro* experiments, the activated RGC population showed spatially confined responses from *rd1* to P20 (Haq et al., 2018).

Nevertheless, solutions that suppress highly correlated RD networks should be considered if the scope of prosthetic coverage is not limited to the initial stage and needs to be expanded. The first step was to eliminate rhythmic bursts and local field potentials observed in the RD retina. Some studies have shown that the SNR of a single RGC response upon electrical stimulation improves after the application of drugs, such as MFA and benzodiazepines, with the disappearance of abnormal spontaneous activity (Toychiev et al., 2013; Eleftheriou et al., 2017; Gehlen et al., 2020). Our results, considering the response of the RGC population to electrical stimulation, demonstrated the effectiveness of drug treatment with MFA (Figure 6). However, in some clinical trials, drug treatment may be limited owing to unknown side effects, such as cytotoxicity.

Therefore, there is a need for a new electrical stimulation strategy that eliminates abnormal spontaneous activity with only an implanted electronic chip without the aid of drugs. It has been reported that high-amplitude electrical stimulation or asymmetric pulse stimulation targeting ON-bipolar cells (based on a simulation study) can suppress the aberrant

spontaneous activity of the RD retina at the single-cell level (Haselier et al., 2017; Loizos et al., 2018). Conversely, abnormal neural activity, including local field potential and synchronization between neurons, is commonly found in neurological diseases such as Parkinson's disease and epilepsy in addition to retinal degeneration (Lian et al., 2003; Rubchinsky et al., 2012; Wang et al., 2016). For therapeutic approaches, various types of electrical stimulation have been attempted, such as closed-loop systems for antiphase LFPs (Sanabria et al., 2020) and high-frequency stimulation above 100 Hz (Santaniello et al., 2015; Ma et al., 2019), to suppress aberrant activity in these neuropathological fields. As a breakthrough to overcome low-resolution vision in patients with RP, it may be promising to apply therapies developed in other neurological fields to retinal degeneration. Our results may serve as an initial database for further therapeutic studies.

CONCLUSION

We studied the aberrant network-mediated responses of RGCs to electrical stimulation using multielectrode arrays. First, no correlation was observed between RGCs in the control group, including wild-type mice, *rd10* P14 mice, and wild-type macaque retinas. Contrastingly, in the RD group, including *rd1*, *rd10* P56, and RD macaque retinas, RGCs were significantly correlated. Second, the number of electrically evoked RGC spikes decreased exponentially in the control group with the distance between the stimulation and recording electrodes, whereas electrically evoked RGC spikes were observed throughout the retina in the RD group regardless of the inter-electrode distance. Our results showed that degenerate RGCs were more correlated as retinal degeneration progressed. Highly correlated retinal networks lead to spatial expansion of RGC responses to electrical stimulation. It interferes with focal activation of RGCs in the degenerate retina, resulting in low-resolution vision in RP patients with retinal prostheses. This should be considered in the future to improve the visual acuity of prosthesis-implanted patients.

DATA AVAILABILITY STATEMENT

The raw data supporting the conclusions of this article will be made available by the authors, without undue reservation.

ETHICS STATEMENT

The animal study was reviewed and approved by Institutional Animal Care Committee of Chungbuk National University and Institutional Animal Care Committee of the OSONG KBIO HEALTH.

AUTHOR CONTRIBUTIONS

JA, YY, and YSG conceived the study. JA, SC, K-EC, and S-WK conducted the experiments. JA, SC, and K-EC analyzed the data.

JA, S-WK, YY, and YSG prepared the manuscript. All authors contributed to the article and approved the submitted version.

FUNDING

This research was supported in part by the Bio and Medical Technology Development Program (NRF-2017M3A9E2056460 and NRF-2017M3A9E2056458) and the Basic Science Research Program (NRF-2020R1A2C1005729, NRF-2021R1A6A3A01086439, and NRF-2022R1A2C2004793)

REFERENCES

- Abramian, M., Lovell, N. H., Habib, A., Morley, J. W., Suaning, G. J., and Dokos, S. (2014). Quasi-monopolar electrical stimulation of the retina: a computational modelling study. *J. Neural Eng.* 11:025002. doi: 10.1088/1741-2560/11/2/025002
- Ahn, J., Phan, H. L., Cha, S., Koo, K. I., Yoo, Y., and Goo, Y. S. (2020). Synchrony of spontaneous burst firing between retinal ganglion cells across species. *Exp. Neurobiol.* 29, 285–299. doi: 10.5607/en20025
- Ahn, K. N., Ahn, J. Y., Kim, J. H., Cho, K., Koo, K. I., Senok, S. S., et al. (2015). Effect of stimulus waveform of biphasic current pulse on retinal ganglion cell responses in retinal degeneration (rd1) mice. *Korean J. Physiol. Pharmacol.* 19, 167–175. doi: 10.4196/kjpp.2015.19.2.167
- Ahn, S. M., Ahn, J., Cha, S., Yun, C., Park, T. K., Goo, Y. S., et al. (2019). Development of a post-vitrectomy injection of N-methyl-N-nitrosourea as a localized retinal degeneration rabbit model. *Exp. Neurobiol.* 28, 62–73. doi: 10.5607/en.2019.28.1.62
- Ayton, L. N., Barnes, N., Dagnelie, G., Fujikado, T., Goetz, G., Hornig, R., et al. (2020). An update on retinal prostheses. *Clin. Neurophysiol.* 131, 1383–1398. doi: 10.1016/j.clinph.2019.11.029
- Barhoum, R., Martinez-Navarrete, G., Corrochano, S., Germain, F., Fernandez-Sanchez, L., de la Rosa, E. J., et al. (2008). Functional and structural modifications during retinal degeneration in the rd10 mouse. *Neuroscience* 155, 698–713. doi: 10.1016/j.neuroscience.2008.06.042
- Bendali, A., Rousseau, L., Lissorgues, G., Scorsone, E., Djilas, M., Degardin, J., et al. (2015). Synthetic 3D diamond-based electrodes for flexible retinal neuroprostheses: model, production and in vivo biocompatibility. *Biomaterials* 67, 73–83. doi: 10.1016/j.biomaterials.2015.07.018
- Beyeler, M., Nanduri, D., Weiland, J. D., Rokem, A., Boynton, G. M., and Fine, I. (2019). A model of ganglion axon pathways accounts for percepts elicited by retinal implants. *Sci. Rep.* 9:9199. doi: 10.1038/s41598-019-45416-4
- Biswas, S., Haselier, C., Mataruga, A., Thumann, G., Walter, P., and Muller, F. (2014). Pharmacological analysis of intrinsic neuronal oscillations in rd10 retina. *PLoS One* 9:e99075. doi: 10.1371/journal.pone.0099075
- Bittner, A. K., Diener-West, M., and Dagnelie, G. (2009). A survey of photopsias in self-reported retinitis pigmentosa: location of photopsias is related to disease severity. *Retina* 29, 1513–1521. doi: 10.1097/IAE.0b013e3181af0d57
- Bloch, E., Luo, Y., and da Cruz, L. (2019). Advances in retinal prosthesis systems. *Ther. Adv. Ophthalmol.* 11:2515841418817501. doi: 10.1177/2515841418817501
- Boinagrov, D., Pangratz-Fuehrer, S., Goetz, G., and Palanker, D. (2014). Selectivity of direct and network-mediated stimulation of the retinal ganglion cells with epi-, sub- and intraretinal electrodes. *J. Neural Eng.* 11:26008. doi: 10.1088/1741-2560/11/2/026008
- Borowska, J., Trenholm, S., and Awatramani, G. B. (2011). An intrinsic neural oscillator in the degenerating mouse retina. *J. Neurosci.* 31, 5000–5012. doi: 10.1523/JNEUROSCI.5800-10.2011
- Brivanlou, I. H., Warland, D. K., and Meister, M. (1998). Mechanisms of concerted firing among retinal ganglion cells. *Neuron* 20, 527–539. doi: 10.1016/s0896-6273(00)80992-7
- Brown, G. C., Brown, M. M., and Fischer, D. H. (2015). Photopsias: a key to diagnosis. *Ophthalmology* 122, 2084–2094. doi: 10.1016/j.ophtha.2015.06.025
- Celik, M. E. (2017). The effect of return electrode position on induced electric fields for electrical stimulation of retinal ganglion cells. *Acta Phys. Pol. A* 132, 493–495. doi: 10.12693/APhysPolA.132.493
- Cha, S., Choi, K. E., Ahn, J., Yoo, M., Jeong, Y., Kim, S. W., et al. (2021). Electrical response of retinal ganglion cells in an N-methyl-N-nitrosourea-induced retinal degeneration porcine model. *Sci. Rep.* 11:24135. doi: 10.1038/s41598-021-03439-w
- Chang, B., Hawes, N. L., Pardue, M. T., German, A. M., Hurd, R. E., Davisson, M. T., et al. (2007). Two mouse retinal degenerations caused by missense mutations in the beta-subunit of rod cGMP phosphodiesterase gene. *Vis. Res.* 47, 624–633. doi: 10.1016/j.visres.2006.11.020
- Chang, Y. C., Haji Ghaffari, D., Chow, R. H., and Weiland, J. D. (2019). Stimulation strategies for selective activation of retinal ganglion cell soma and threshold reduction. *J. Neural Eng.* 16:26017. doi: 10.1088/1741-2552/aaf92b
- Chenais, N. A. L., Leccardi, M. J. I. A., and Ghezzi, D. (2021b). Photovoltaic retinal prosthesis restores high-resolution responses to single-pixel stimulation in blind retinas. *Commun. Mater.* 2:28.
- Chenais, N. A. L., Airaghi Leccardi, M. J. I., and Ghezzi, D. (2021a). Naturalistic spatiotemporal modulation of epiretinal stimulation increases the response persistence of retinal ganglion cell. *J. Neural Eng.* 18:16016. doi: 10.1088/1741-2552/abc6df
- Choi, H., Zhang, L., Cembrowski, M. S., Sabottke, C. F., Markowitz, A. L., Butts, D. A., et al. (2014). Intrinsic bursting of AII amacrine cells underlies oscillations in the rd1 mouse retina. *J. Neurophysiol.* 112, 1491–1504. doi: 10.1152/jn.00437.2014
- Choi, K. E. (2022). *Outer Retinal Degeneration Nonhuman Primate Model by Temporal Tamponade of M-methyl-N-Nitrosourea in Cynomolgus Monkeys*. Ph.D. dissertation. Seoul: Korea University College of Medicine.
- Chow, A. Y. (2013). Retinal prostheses development in retinitis pigmentosa patients-progress and comparison. *Asia Pac. J. Ophthalmol.* 2, 253–268. doi: 10.1097/APO.0b013e3182a0b4fe
- Chuang, A. T., Margo, C. E., and Greenberg, P. B. (2014). Retinal implants: a systematic review. *Br. J. Ophthalmol.* 98, 852–856. doi: 10.1136/bjophthalmol-2013-303708
- Corna, A., Ramesh, P., Jetter, F., Lee, M. J., Macke, J. H., and Zeck, G. (2021). Discrimination of simple objects decoded from the output of retinal ganglion cells upon sinusoidal electrical stimulation. *J. Neural Eng.* 18:46086. doi: 10.1088/1741-2552/ac0679
- Davidson, R. S., Hemanth, S., Keller, S. S., Bek, T., and Hansen, O. (2019). Evaluation of the capacitive behavior of 3D carbon electrodes for sub-retinal photovoltaic prosthesis. *Micro Nano Eng.* 2, 110–116. doi: 10.1016/j.mne.2019.02.003
- Demas, J., Eglén, S. J., and Wong, R. O. (2003). Developmental loss of synchronous spontaneous activity in the mouse retina is independent of visual experience. *J. Neurosci.* 23, 2851–2860. doi: 10.1523/JNEUROSCI.23-07-02851.2003
- Eleftheriou, C. G., Cehajic-Kapetanovic, J., Martial, F. P., Milosavljevic, N., Bedford, R. A., and Lucas, R. J. (2017). Meclofenamic acid improves the signal to noise ratio for visual responses produced by ectopic expression of human rod opsin. *Mol. Vis.* 23, 334–345.
- Euler, T., and Schubert, T. (2015). Multiple independent oscillatory networks in the degenerating retina. *Front. Cell. Neurosci.* 9:444. doi: 10.3389/fncel.2015.00444
- Farvardin, M., Afarid, M., Attarzadeh, A., Johari, M. K., Mehryar, M., Nowroozzadeh, M. H., et al. (2018). The Argus-II retinal prosthesis implantation; from the global to local successful experience. *Front. Neurosci.* 12:584. doi: 10.3389/fnins.2018.00584

SUPPLEMENTARY MATERIAL

The Supplementary Material for this article can be found online at: <https://www.frontiersin.org/articles/10.3389/fncel.2022.889663/full#supplementary-material>

- Flores, T., Lei, X., Huang, T., Lorach, H., Dalal, R., Galambos, L., et al. (2018). Optimization of pillar electrodes in subretinal prosthesis for enhanced proximity to target neurons. *J. Neural Eng.* 15:36011. doi: 10.1088/1741-2552/aaac39
- Freeman, D. K., and Fried, S. I. (2011). Multiple components of ganglion cell desensitization in response to prosthetic stimulation. *J. Neural Eng.* 8:16008. doi: 10.1088/1741-2560/8/1/016008
- Fried, S. I., Lasker, A. C., Desai, N. J., Eddington, D. K., and Rizzo, J. F. III (2009). Axonal sodium-channel bands shape the response to electric stimulation in retinal ganglion cells. *J. Neurophysiol.* 101, 1972–1987. doi: 10.1152/jn.91081.2008
- Fujikado, T., Kamei, M., Sakaguchi, H., Kanda, H., Endo, T., Hirota, M., et al. (2016). One-year outcome of 49-channel suprachoroidal-transretinal stimulation prosthesis in patients with advanced retinitis pigmentosa. *Invest. Ophthalmol. Vis. Sci.* 57, 6147–6157. doi: 10.1167/iovs.16-20367
- Gargini, C., Terzibasi, E., Mazzoni, F., and Strettoi, E. (2007). Retinal organization in the retinal degeneration 10 (rd10) mutant mouse: a morphological and ERG study. *J. Comp. Neurol.* 500, 222–238. doi: 10.1002/cne.21144
- Gehlen, J., Esser, S., Schaffrath, K., Johnen, S., Walter, P., and Müller, F. (2020). Blockade of retinal oscillations by benzodiazepines improves efficiency of electrical stimulation in the mouse model of RP, rd10. *Invest. Ophthalmol. Vis. Sci.* 61:37. doi: 10.1167/iovs.61.13.37
- Golden, J. R., Erickson-Davis, C., Cottaris, N. P., Parthasarathy, N., Rieke, F., Brainard, D. H., et al. (2019). Simulation of visual perception and learning with a retinal prosthesis. *J. Neural Eng.* 16:25003. doi: 10.1088/1741-2552/aaf270
- Goo, Y. S., Park, D. J., Ahn, J. R., and Senok, S. S. (2016). Spontaneous oscillatory rhythms in the degenerating mouse retina modulate retinal ganglion cell responses to electrical stimulation. *Front. Cell. Neurosci.* 9:512. doi: 10.3389/fncel.2015.00512
- Goo, Y. S., Ye, J. H., Lee, S., Nam, Y., Ryu, S. B., and Kim, K. H. (2011b). Retinal ganglion cell responses to voltage and current stimulation in wild-type and rd1 mouse retinas. *J. Neural Eng.* 8:35003. doi: 10.1088/1741-2560/8/3/035003
- Goo, Y. S., Ahn, K. N., Song, Y. J., Ahn, S. H., Han, S. K., Ryu, S. B., et al. (2011a). Spontaneous oscillatory rhythm in retinal activities of two retinal degeneration (rd1 and rd10) mice. *Korean J. Physiol. Pharmacol.* 15, 415–422. doi: 10.4196/kjpp.2011.15.6.415
- Grosberg, L. E., Ganesan, K., Goetz, G. A., Madugula, S. S., Bhaskar, N., Fan, V., et al. (2017). Activation of ganglion cells and axon bundles using epiretinal electrical stimulation. *J. Neurophysiol.* 118, 1457–1471. doi: 10.1152/jn.00750.2016
- Haq, W., Dietter, J., and Zrenner, E. (2018). Electrical activation of degenerated photoreceptors in blind mouse retina elicited network-mediated responses in different types of ganglion cells. *Sci. Rep.* 8:16998. doi: 10.1038/s41598-018-35296-5
- Haselier, C., Biswas, S., Rosch, S., Thumann, G., Müller, F., and Walter, P. (2017). Correlations between specific patterns of spontaneous activity and stimulation efficiency in degenerated retina. *PLoS One* 12:e0190048. doi: 10.1371/journal.pone.0190048
- Heckenlively, J. R., Yoser, S. L., Friedman, L. H., and Oversier, J. J. (1988). Clinical findings and common symptoms in retinitis pigmentosa. *Am. J. Ophthalmol.* 105, 504–511. doi: 10.1016/0002-9394(88)90242-5
- Ho, E., Shmakov, A., and Palanker, D. (2020). Decoding network-mediated retinal response to electrical stimulation: implications for fidelity of prosthetic vision. *J. Neural Eng.* 17:66018. doi: 10.1088/1741-2552/abc535
- Hu, E. H., Pan, F., Volgyi, B., and Bloomfield, S. A. (2010). Light increases the gap junctional coupling of retinal ganglion cells. *J. Physiol.* 588(Pt 21), 4145–4163. doi: 10.1113/jphysiol.2010.193268
- Humayun, M. S., Dorn, J. D., da Cruz, L., Dagnelie, G., Sahel, J. A., Stanga, P. E., et al. (2012). Interim results from the international trial of Second Sight's visual prosthesis. *Ophthalmology* 119, 779–788. doi: 10.1016/j.optha.2011.09.028
- Im, M., and Fried, S. I. (2015). Indirect activation elicits strong correlations between light and electrical responses in ON but not OFF retinal ganglion cells. *J. Physiol.* 593, 3577–3596. doi: 10.1113/JP270606
- Im, M., and Fried, S. I. (2016). Temporal properties of network-mediated responses to repetitive stimuli are dependent upon retinal ganglion cell type. *J. Neural Eng.* 13:25002. doi: 10.1088/1741-2560/13/2/025002
- Im, M., Wergin, P., and Fried, S. I. (2018). Electric stimulus duration alters network-mediated responses depending on retinal ganglion cell type. *J. Neural Eng.* 15:36010. doi: 10.1088/1741-2552/aaadcl
- Ivanova, E., Yee, C. W., Baldoni, R., and Sagdullaev, B. T. (2016). Aberrant activity in retinal degeneration impairs central visual processing and relies on Cx36-containing gap junctions. *Exp. Eye Res.* 150, 81–89. doi: 10.1016/j.exer.2015.05.013
- Jensen, R. J., and Rizzo, J. F. III (2009). Activation of ganglion cells in wild-type and rd1 mouse retinas with monophasic and biphasic current pulses. *J. Neural Eng.* 6:35004. doi: 10.1088/1741-2560/6/3/035004
- Jepson, L. H., Hottowy, P., Mathieson, K., Gunning, D. E., Dabrowski, W., Litke, A. M., et al. (2013). Focal electrical stimulation of major ganglion cell types in the primate retina for the design of visual prostheses. *J. Neurosci.* 33, 7194–7205. doi: 10.1523/JNEUROSCI.4967-12.2013
- Jones, B. W., Pfeiffer, R. L., Ferrell, W. D., Watt, C. B., Marmor, M., and Marc, R. E. (2016). Retinal remodeling in human retinitis pigmentosa. *Exp. Eye Res.* 150, 149–165. doi: 10.1016/j.exer.2016.03.018
- Kim, S. W. (2021). “Effects of different subretinal implant designs on the retina in mini-pigs and drug induced incomplete outer retinal degeneration in cynomolgus monkey,” in *Proceedings of the 12th World Research Congress: The Eye and the Chip – Virtual Event* (Detroit, MI: HenryFord Health System). doi: 10.37783/crj-0025a
- Lewicki, M. S. (1998). A review of methods for spike sorting: the detection and classification of neural action potentials. *Network* 9, R53–R78.
- Lian, J., Bikson, M., Sciortino, C., Stacey, W. C., and Durand, D. M. (2003). Local suppression of epileptiform activity by electrical stimulation in rat hippocampus in vitro. *J. Physiol.* 547, 427–434. doi: 10.1113/jphysiol.2002.033209
- Loizos, K., Marc, R., Humayun, M., Anderson, J. R., Jones, B. W., and Lazzi, G. (2018). Increasing electrical stimulation efficacy in degenerated retina: stimulus waveform design in a multiscale computational model. *IEEE Trans. Neural Syst. Rehabil. Eng.* 26, 1111–1120. doi: 10.1109/TNSRE.2018.2832055
- Ma, W. J., Feng, Z. Y., Wang, Z. X., and Zhou, W. J. (2019). High-frequency stimulation of afferent axons alters firing rhythms of downstream neurons. *J. Integr. Neurosci.* 18, 33–41. doi: 10.31083/jjin.2019.01.18
- Marc, R. E., Jones, B. W., Watt, C. B., and Strettoi, E. (2003). Neural remodeling in retinal degeneration. *Prog. Retin. Eye Res.* 22, 607–655. doi: 10.1016/s1350-9462(03)00039-9
- Margolis, D. J., Gartland, A. J., Singer, J. H., and Detwiler, P. B. (2014). Network oscillations drive correlated spiking of ON and OFF ganglion cells in the rd1 mouse model of retinal degeneration. *PLoS One* 9:e86253. doi: 10.1371/journal.pone.0086253
- Margolis, D. J., Newkirk, G., Euler, T., and Detwiler, P. B. (2008). Functional stability of retinal ganglion cells after degeneration-induced changes in synaptic input. *J. Neurosci.* 28, 6526–6536. doi: 10.1523/JNEUROSCI.1533-08.2008
- Mastronarde, D. N. (1989). Correlated firing of retinal ganglion cells. *Trends Neurosci.* 12, 75–80. doi: 10.1016/0166-2236(89)90140-9
- Menzler, J., and Zeck, G. (2011). Network oscillations in rod-degenerated mouse retinas. *J. Neurosci.* 31, 2280–2291. doi: 10.1523/JNEUROSCI.4238-10.2011
- Miccoli, B., Lopez, C. M., Goikoetxea, E., Putzeys, J., Sekeri, M., Krylychkina, O., et al. (2019). High-density electrical recording and impedance imaging with a multi-modal CMOS multi-electrode array chip. *Front. Neurosci.* 13:641. doi: 10.3389/fnins.2019.00641
- Neuenschwander, S., Castelo-Branco, M., and Singer, W. (1999). Synchronous oscillations in the cat retina. *Vis. Res.* 39, 2485–2497. doi: 10.1016/s0042-6989(99)00042-5
- Palanker, D., Le Mer, Y., Mohand-Said, S., Muqit, M., and Sahel, J. A. (2020). Photovoltaic restoration of central vision in atrophic age-related macular degeneration. *Ophthalmology* 127, 1097–1104. doi: 10.1016/j.optha.2020.02.024
- Park, D., Senok, S., and Goo, Y. (2015). “Degeneration stage-specific response pattern of retinal ganglion cell spikes in rd10 mouse retina,” in *Proceedings of the 2015 37th Annual International Conference of the IEEE Engineering in Medicine and Biology Society (EMBC)*, Milan, 3351–3354. doi: 10.1109/EMBC.2015.7319110
- Phillips, M. J., Otteson, D. C., and Sherry, D. M. (2010). Progression of neuronal and synaptic remodeling in the rd10 mouse model of retinitis pigmentosa. *J. Comp. Neurol.* 518, 2071–2089. doi: 10.1002/cne.22322

- Pryluk, R., Kfir, Y., Gelbard-Sagiv, H., Fried, I., and Paz, R. (2019). A tradeoff in the neural code across regions and species. *Cell* 176, 597–609.e18. doi: 10.1016/j.cell.2018.12.032
- Rosch, S., Johnen, S., Muller, F., Pfarrer, C., and Walter, P. (2014). Correlations between ERG, OCT, and anatomical findings in the rd10 mouse. *J. Ophthalmol.* 2014:874751. doi: 10.1155/2014/874751
- Roy, K., Kumar, S., and Bloomfield, S. A. (2017). Gap junctional coupling between retinal amacrine and ganglion cells underlies coherent activity integral to global object perception. *Proc. Natl. Acad. Sci. U.S.A.* 114, E10484–E10493. doi: 10.1073/pnas.1708261114
- Rubchinsky, L. L., Park, C., and Worth, R. M. (2012). Intermittent neural synchronization in Parkinson's disease. *Nonlinear Dyn.* 68, 329–346. doi: 10.1007/s11071-011-0223-z
- Ryu, S. B., Choi, J. W., Ahn, K. N., Goo, Y. S., and Kim, K. H. (2017). Amplitude modulation-based electrical stimulation for encoding multipixel spatiotemporal visual information in retinal neural activities. *J. Korean Med. Sci.* 32, 900–907. doi: 10.3346/jkms.2017.32.6.900
- Ryu, S. B., Ye, J. H., Lee, J. S., Goo, Y. S., Kim, C. H., and Kim, K. H. (2009). Electrically-evoked neural activities of rd1 mice retinal ganglion cells by repetitive pulse stimulation. *Korean J. Physiol. Pharmacol.* 13, 443–448. doi: 10.4196/kjpp.2009.13.6.443
- Sanabria, D. E., Johnson, L. A., Yu, Y., Busby, Z., Nebeck, S., Zhang, J. Y., et al. (2020). Real-time suppression and amplification of frequency-specific neural activity using stimulation evoked oscillations. *Brain Stimul.* 13, 1732–1742. doi: 10.1016/j.brs.2020.09.017
- Santaniello, S., McCarthy, M. M., Montgomery, E. B., Gale, J. T., Kopell, N., and Sarma, S. V. (2015). Therapeutic mechanisms of high-frequency stimulation in Parkinson's disease and neural restoration via loop-based reinforcement. *Proc. Natl. Acad. Sci. U.S.A.* 112, E586–E595. doi: 10.1073/pnas.1406549111
- Sekirnjak, C., Hottoway, P., Sher, A., Dabrowski, W., Litke, A. M., and Chichilnisky, E. J. (2006). Electrical stimulation of mammalian retinal ganglion cells with multielectrode arrays. *J. Neurophysiol.* 95, 3311–3327. doi: 10.1152/jn.01168.2005
- Sekirnjak, C., Hottoway, P., Sher, A., Dabrowski, W., Litke, A. M., and Chichilnisky, E. J. (2008). High-resolution electrical stimulation of primate retina for epiretinal implant design. *J. Neurosci.* 28, 4446–4456. doi: 10.1523/JNEUROSCI.5138-07.2008
- Seo, H. W., Kim, N., Ahn, J., Cha, S., Goo, Y. S., and Kim, S. (2019). A 3D flexible microelectrode array for subretinal stimulation. *J. Neural Eng.* 16:56016. doi: 10.1088/1741-2552/ab36ab
- Shire, D. B., Gingerich, M. D., Wong, P. I., Skvarla, M., Cogan, S. F., Chen, J. H., et al. (2020). Micro-fabrication of components for a high-density sub-retinal visual prosthesis. *Micromachines* 11:944. doi: 10.3390/mi11100944
- Shlens, J., Field, G. D., Gauthier, J. L., Greschner, M., Sher, A., Litke, A. M., et al. (2009). The structure of large-scale synchronized firing in primate retina. *J. Neurosci.* 29, 5022–5031. doi: 10.1523/JNEUROSCI.5187-08.2009
- Shlens, J., Field, G. D., Gauthier, J. L., Grivich, M. I., Petrusca, D., Sher, A., et al. (2006). The structure of multi-neuron firing patterns in primate retina. *J. Neurosci.* 26, 8254–8266. doi: 10.1523/JNEUROSCI.1282-06.2006
- Stasheff, S. F. (2008). Emergence of sustained spontaneous hyperactivity and temporary preservation of OFF responses in ganglion cells of the retinal degeneration (rd1) mouse. *J. Neurophysiol.* 99, 1408–1421. doi: 10.1152/jn.00144.2007
- Stasheff, S. F., Shankar, M., and Andrews, M. P. (2011). Developmental time course distinguishes changes in spontaneous and light-evoked retinal ganglion cell activity in rd1 and rd10 mice. *J. Neurophysiol.* 105, 3002–3009. doi: 10.1152/jn.00704.2010
- Stett, A., Barth, W., Weiss, S., Haemmerle, H., and Zrenner, E. (2000). Electrical multisite stimulation of the isolated chicken retina. *Vis. Res.* 40, 1785–1795. doi: 10.1016/S0042-6989(00)00005-5
- Stingl, K., Bartz-Schmidt, K. U., Besch, D., Braun, A., Bruckmann, A., Gekeler, F., et al. (2013). Artificial vision with wirelessly powered subretinal electronic implant alpha-IMS. *Proc. Biol. Sci.* 280:20130077. doi: 10.1098/rspb.2013.0077
- Stingl, K., Bartz-Schmidt, K. U., Besch, D., Chee, C. K., Cottrill, C. L., Gekeler, F., et al. (2015). Subretinal visual implant alpha IMS—clinical trial interim report. *Vis. Res.* 111(Pt B), 149–160. doi: 10.1016/j.visres.2015.03.001
- Strettoi, E., Pignatelli, V., Rossi, C., Porciatti, V., and Falsini, B. (2003). Remodeling of second-order neurons in the retina of rd/rd mutant mice. *Vis. Res.* 43, 867–877. doi: 10.1016/S0042-6989(02)00594-1
- Tandon, P., Bhaskhar, N., Shah, N., Madugula, S., Grosberg, L., Fan, V. H., et al. (2021). Automatic identification of axon bundle activation for epiretinal prosthesis. *IEEE Trans. Neural Syst. Rehabil. Eng.* 29, 2496–2502. doi: 10.1109/TNSRE.2021.3128486
- Toychiev, A. H., Ivanova, E., Yee, C. W., and Sagdullaev, B. T. (2013). Block of gap junctions eliminates aberrant activity and restores light responses during retinal degeneration. *J. Neurosci.* 33, 13972–13977. doi: 10.1523/JNEUROSCI.2399-13.2013
- Trenholm, S., and Awatramani, G. B. (2015). Origins of spontaneous activity in the degenerating retina. *Front. Cell. Neurosci.* 9:277. doi: 10.3389/fncel.2015.00277
- Trenholm, S., Borowska, J., Zhang, J., Hoggarth, A., Johnson, K., Barnes, S., et al. (2012). Intrinsic oscillatory activity arising within the electrically coupled AII amacrine-ON cone bipolar cell network is driven by voltage-gated Na⁺ channels. *J. Physiol.* 590, 2501–2517. doi: 10.1113/jphysiol.2011.225060
- Volgyi, B., Pan, F., Paul, D. L., Wang, J. T., Huberman, A. D., and Bloomfield, S. A. (2013). Gap junctions are essential for generating the correlated spike activity of neighboring retinal ganglion cells. *PLoS One* 8:e69426. doi: 10.1371/journal.pone.0069426
- Wang, D. D., de Hemptinne, C., Miocinovic, S., Qasim, S. E., Miller, A. M., Ostrem, J. L., et al. (2016). Subthalamic local field potentials in Parkinson's disease and isolated dystonia: an evaluation of potential biomarkers. *Neurobiol. Dis.* 89, 213–222. doi: 10.1016/j.nbd.2016.02.015
- Weiland, J. D., Cho, A. K., and Humayun, M. S. (2011). Retinal prostheses: current clinical results and future needs. *Ophthalmology* 118, 2227–2237. doi: 10.1016/j.jophtha.2011.08.042
- Wilke, R. G., Moghadam, G. K., Lovell, N. H., Suaning, G. J., and Dokos, S. (2011). Electric crosstalk impairs spatial resolution of multi-electrode arrays in retinal implants. *J. Neural Eng.* 8:046016. doi: 10.1088/1741-2560/8/4/046016
- Wong, R. O. (1999). Retinal waves and visual system development. *Annu. Rev. Neurosci.* 22, 29–47. doi: 10.1146/annurev.neuro.22.1.29
- Ye, J. H., and Goo, Y. S. (2007). The slow wave component of retinal activity in rd/rd mice recorded with a multi-electrode array. *Physiol. Meas.* 28, 1079–1088. doi: 10.1088/0967-3334/28/9/009
- Yee, C. W., Toychiev, A. H., and Sagdullaev, B. T. (2012). Network deficiency exacerbates impairment in a mouse model of retinal degeneration. *Front. Syst. Neurosci.* 6:8. doi: 10.3389/fnsys.2012.00008
- Yoon, Y. J., Lee, J. I., Jang, Y. J., An, S., Kim, J. H., Fried, S. I., et al. (2020). Retinal degeneration reduces consistency of network-mediated responses arising in ganglion cells to electric stimulation. *IEEE Trans. Neural Syst. Rehabil. Eng.* 28, 1921–1930. doi: 10.1109/TNSRE.2020.3003345
- Zeng, Q., Zhao, S. S., Yang, H. G., Zhang, Y., and Wu, T. Z. (2019). Micro/nano technologies for high-density retinal implant. *Micromachines* 10:419. doi: 10.3390/mi10060419
- Zhang, L., Wu, Q. W., and Zhang, Y. F. (2020). Early visual motion experience shapes the gap junction connections among direction selective ganglion cells. *PLoS Biol.* 18:e3000692. doi: 10.1371/journal.pbio.3000692
- Zhou, T., Huang, Z., Sun, X., Zhu, X., Zhou, L., Li, M., et al. (2017). Microglia polarization with M1/M2 phenotype changes in rd1 mouse model of retinal degeneration. *Front. Neuroanat.* 11:77. doi: 10.3389/fnana.2017.00077
- Zrenner, E., Bartz-Schmidt, K. U., Benav, H., Besch, D., Bruckmann, A., Gabel, V. P., et al. (2011). Subretinal electronic chips allow blind patients to read letters and combine them to words. *Proc. Biol. Sci.* 278, 1489–1497. doi: 10.1098/rspb.2010.1747

Conflict of Interest: The authors declare that the research was conducted in the absence of any commercial or financial relationships that could be construed as a potential conflict of interest.

Publisher's Note: All claims expressed in this article are solely those of the authors and do not necessarily represent those of their affiliated organizations, or those of the publisher, the editors and the reviewers. Any product that may be evaluated in this article, or claim that may be made by its manufacturer, is not guaranteed or endorsed by the publisher.

Copyright © 2022 Ahn, Cha, Choi, Kim, Yoo and Goo. This is an open-access article distributed under the terms of the Creative Commons Attribution License (CC BY). The use, distribution or reproduction in other forums is permitted, provided the original author(s) and the copyright owner(s) are credited and that the original publication in this journal is cited, in accordance with accepted academic practice. No use, distribution or reproduction is permitted which does not comply with these terms.



Artificial Visual Information Produced by Retinal Prostheses

Sein Kim^{1†}, Hyeonhee Roh^{1,2†} and Maesoon Im^{1,3*}

¹ Brain Science Institute, Korea Institute of Science and Technology, Seoul, South Korea, ² School of Electrical Engineering, College of Engineering, Korea University, Seoul, South Korea, ³ Division of Bio-Medical Science & Technology, KIST School, University of Science and Technology, Seoul, South Korea

OPEN ACCESS

Edited by:

Stuart C. Mangel,
The Ohio State University,
United States

Reviewed by:

John Troy,
Northwestern University,
United States
Wei Tong,
The University of Melbourne, Australia

*Correspondence:

Maesoon Im
maesoon.im@kist.re.kr;
maesoon.im@gmail.com

[†]These authors have contributed
equally to this work

Specialty section:

This article was submitted to
Cellular Neurophysiology,
a section of the journal
Frontiers in Cellular Neuroscience

Received: 03 April 2022

Accepted: 18 May 2022

Published: 06 June 2022

Citation:

Kim S, Roh H and Im M (2022)
Artificial Visual Information Produced
by Retinal Prostheses.
Front. Cell. Neurosci. 16:911754.
doi: 10.3389/fncel.2022.911754

Numerous retinal prosthetic systems have demonstrated somewhat useful vision can be restored to individuals who had lost their sight due to outer retinal degenerative diseases. Earlier prosthetic studies have mostly focused on the confinement of electrical stimulation for improved spatial resolution and/or the biased stimulation of specific retinal ganglion cell (RGC) types for selective activation of retinal ON/OFF pathway for enhanced visual percepts. To better replicate normal vision, it would be also crucial to consider information transmission by spiking activities arising in the RGC population since an incredible amount of visual information is transferred from the eye to the brain. In previous studies, however, it has not been well explored how much artificial visual information is created in response to electrical stimuli delivered by microelectrodes. In the present work, we discuss the importance of the neural information for high-quality artificial vision. First, we summarize the previous literatures which have computed information transmission rates from spiking activities of RGCs in response to visual stimuli. Second, we exemplify a couple of studies which computed the neural information from electrically evoked responses. Third, we briefly introduce how information rates can be computed in the representative two ways – direct method and reconstruction method. Fourth, we introduce *in silico* approaches modeling artificial retinal neural networks to explore the relationship between amount of information and the spiking patterns. Lastly, we conclude our review with clinical implications to emphasize the necessity of considering visual information transmission for further improvement of retinal prosthetics.

Keywords: retinal prosthetics, visual information, neural computation, information theory, spike trains

INTRODUCTION

Vision is unarguably the most critical sensory modality (Hutmacher, 2019) among the five senses of humans. Diverse causes can result in low vision or blindness, and there have been numerous attempts to restore sight to blind individuals by electrically stimulating visual cortex (Dobelle et al., 1974, 1976), lateral geniculate nucleus (Pezaris and Reid, 2007), optic nerve (Gaillet et al., 2019), or retina (Humayun et al., 1996). In the case of retina, the electric stimulation is effective to elicit artificial visual percepts for outer retinal degenerative diseases such as retinitis pigmentosa and age-related macular degeneration, which primarily damage photoreceptors (Bunker et al., 1984; Curcio et al., 1996). Microelectronic retinal prostheses including commercialized ones

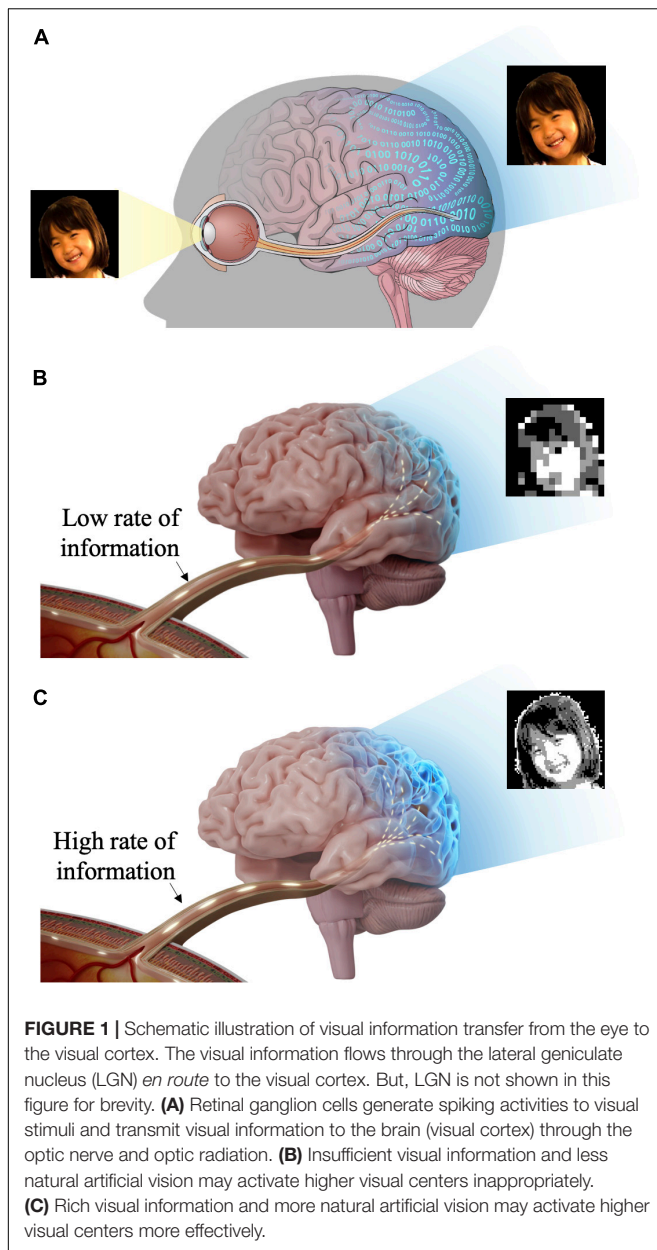
(e.g., Argus II, Alpha-IMS/AMS, and PRIMA) reported some promising clinical outcomes by electrically stimulating the remaining inner retinal neurons (Humayun et al., 1996; Rizzo et al., 2003; Fujikado et al., 2007; Zrenner et al., 2011; da Cruz et al., 2013; Dorn et al., 2013; Stingl et al., 2013; Shivdasani et al., 2017; Palanker et al., 2020). However, the best visual acuity of elicited artificial vision (20/460) (Palanker et al., 2020) is still far below the level of legal blindness (20/200) as well as normal vision (20/20). To achieve high-resolution visual prosthetics, various research groups have tried to electrically activate cells in only targeted small areas using hardware and software approaches. For example, several groups proposed novel designs of microelectrodes (Flores et al., 2018, 2019; Seo et al., 2020) or photovoltaic arrays (Ferlauto et al., 2018; Wang et al., 2021) to further localize electric current in a smaller region. Also, Jepson et al. (2014) used spatially patterned electric stimulation, and Weitz et al. (2015) demonstrated retinal activation in much smaller area with 25 ms-long pulses.

The other important research topic in retinal prosthetics has long been the cell-type specific stimulation. As the starting point of the most complex sensory system, and the mammalian retinas have numerous types of retinal ganglion cells (RGCs) which are the output spiking neurons sending neural signals to the downstream visual centers (Masland, 2001; Rockhill et al., 2004; Sanes and Masland, 2015; Baden et al., 2016). Among those types, ON and OFF RGCs are known to play a critical role in forming visual percepts (Schiller et al., 1986; Schiller, 1992). In addition to the asymmetries between light-evoked responses of the ON vs. the OFF pathways (Ölveczky et al., 2003; Margolis and Detwiler, 2007; Liang and Freed, 2012; Freed, 2017), retinal prosthetic studies reported contrasting differences between the two pathways (Freeman et al., 2010; Kameneva et al., 2010; Twyford et al., 2014; Im and Fried, 2015, 2016a; Lee and Im, 2019). However, given the unique mosaic arrangement of each type of RGCs (DeVries and Baylor, 1997; Masland, 2012), it seems almost inevitable to activate every type of RGCs located near a given electrode delivering electric stimulation. Nevertheless, it seems reasonable to aim more biased activation of the ON system because the earlier clinical trials reported dominantly bright sensation (Humayun et al., 1996, 2003; Fujikado et al., 2007; Naycheva et al., 2012). Recent studies demonstrated the ON/OFF response ratio can be increased by modulating several stimulus parameters such as stimulus durations (Im et al., 2018), repetition rates (Cai et al., 2011, 2013; Twyford et al., 2014; Im and Fried, 2016a), waveform shapes (Lee and Im, 2018), and current amplitudes (Lee and Im, 2019). The use of penetrating microelectrode to the specific stratification depth may enhance the cell-type specific activation of either ON or OFF RGCs (Roh et al., 2022). To date, however, it appears extremely challenging to achieve completely selective stimulation of targeted cell type(s) using electrical stimulation. In contrast, optogenetic approaches can selectively activate the ON pathway (Lagali et al., 2008; Gaub et al., 2014; Macé et al., 2015; Lu et al., 2016) but they need to address potential phototoxicity (Grimm et al., 2001; van Wyk et al., 2015; Simunovic et al., 2019) and/or low transfection efficiency of viral vectors (Lagali et al., 2008; Busskamp and Roska, 2011).

In addition to the aforementioned two important features (i.e., the spatial resolution and the cell type-specific stimulation), it may be critical to assess whether retinal prostheses restore ample enough information. It is because the remarkably complex retinal circuits compress the visual world in real-time (Kolb, 2003), making RGCs transmit an incredible amount of visual information to the brain (**Figure 1A**), which could be estimated as big as 875,000 bits/s (52.5 Mb/min) (Koch et al., 2006). Thus, less artificial information may confound the brain, resulting in unclear artificial visual percepts (**Figure 1B**), whereas more transferred information may help the brain more precisely recognize artificial visual images (**Figure 1C**). However, there has been a limited number of retinal prosthetic researches which had studied neural information aspects of electrically evoked spiking activities (Eger et al., 2005; Kang et al., 2021). Contrastingly, in the case of cochlear implants which show great clinical success, information transmission in the auditory system has been well studied (Mino, 2007; Zeng et al., 2008; Hannan et al., 2012; Moroz et al., 2012; Gao et al., 2013). Analyzing the RGC spiking activities using information theory is likely to help understanding how the brain deciphers artificial visual information (Quiñ Quiroga and Panzeri, 2009). In particular, it has been known that retinal spike trains are precisely structured to efficiently convey visual information (Berry et al., 1997). Therefore, other than simply re-activating RGCs to send spike trains to downstream neurons, it would be essential to understand how much information is encoded (Timme and Lapiš, 2018) by the ensemble of prosthetically evoked spikes arising in RGCs (Freeman et al., 2011) to estimate the quality of artificial vision. Also, information researches are likely to offer valuable insights for the improved performance of retinal implants.

NEURAL INFORMATION OF INTRINSIC VISUAL RESPONSES IN THE HEALTHY RETINA

The retina divides the complex visual world into several parallel pathways (Wässle, 2004; Roska et al., 2006; Nassi and Callaway, 2009) using the remarkable variety of RGC types (Baden et al., 2016). All RGCs in mammalian retinas encode visual information by spatiotemporal structure of spike trains but differently across the RGC types (Berry et al., 1997; Masland, 2001; Field and Chichilnisky, 2007; Zeck and Masland, 2007; Sanes and Masland, 2015). Much work has studied the relationship between spiking and information rates in RGC responses to light stimuli using several computational methods (Koch et al., 2004, 2006; Passaglia and Troy, 2004; Kang et al., 2021) (see a later section regarding how direct and reconstruction methods compute neural information). Particularly, it is notable that distinct RGC types showed different information rates (Koch et al., 2006). For example, in guinea pig retinas, two groups of RGCs with brisk or sluggish responses transmitted information of 21 ± 9 and 13 ± 7 bits/s ($n = 19$ and $n = 23$ cells), respectively (Koch et al., 2004). More recently, Kang et al. (2021) analyzed the amount of neural information conveyed through brisk transient (BT) and brisk sustained (BS) subtypes of ON and OFF pathways in rabbit



retinas. In responses to spot flashes, 1.83 ± 0.07 and 1.89 ± 0.04 bits/s of information were transmitted by ON BT and OFF BT cells, respectively; while 2.53 ± 0.08 and 3.00 ± 0.22 bits/s of information were transmitted by ON BS and OFF BS cells ($n = 15$ for each type), respectively.

Compared to laboratory stimuli such as stationary spot flashes, natural stimuli are known to evoke sparser spiking activities in RGCs (Kayser et al., 2003; David et al., 2004; Felsen et al., 2005; Puchalla et al., 2005; Touryan et al., 2005; Talebi and Baker, 2012; Im and Fried, 2016b). For example, about 65% of RGCs do not fire constantly in response to natural stimuli, and it has been argued that the sparse coding can reduce the number of activated neurons, thereby saving energy for information transmission (Wang et al., 2018). Given that natural stimuli

contain much bigger visual information than laboratory stimuli, it seems important to compare both amount and efficiency of information conveyed in responses arising from laboratory vs. natural stimuli.

ARTIFICIAL VISUAL INFORMATION OF ELECTRICALLY EVOKED RESPONSES IN THE DEGENERATE RETINA

Aforementioned examples suggest that, for high-quality artificial vision, it may be crucial to study whether electrically elicited spiking activities of RGCs in the degenerate retina convey visual information at a similar level of visually evoked responses arising in the normal retina (Fried et al., 2006; Freeman et al., 2011). Surprisingly, however, there are very few studies that have discussed the neural information produced by electric stimulation. For example, Eger et al. (2005) stimulated the cat retina electrically while recording neuronal activities at 15 sites in the visual cortex. They estimated 20–160 bits/s of information was transferred at a single recording site when a single electrode was activated (Eger et al., 2005). They also reported 500 bits/s of information was transmitted at 15 recording sites when seven electrodes were activated. However, the information rates varied noticeably between experiments depending on the positions of stimulation and recording sites since it was difficult to place electrodes accurately at corresponding retinotopic loci.

Another example investigated the amount of information elicited by both light and electric stimulation in more sophisticated ways (Kang et al., 2021). First, they classified RGCs into the four major types (i.e., BT and BS subtypes of ON and OFF pathways) in the healthy rabbit retina, and then analyzed spiking activities in each type to compare the neural information between light and electric responses of identical sets of RGCs. When the number of cells increased up to 15, electric responses of ON BT and BS RGCs displayed a similar level of neural information with their light responses, whereas electrically evoked responses of OFF BT and BS cells showed greatly reduced information than those of their light responses. Second, they tried to correlate the neural information and the cell-to-cell heterogeneity of spiking responses. Interestingly, the ON RGCs showed similarly heterogeneous responses regardless of light and electric stimuli. In contrast, the OFF RGCs showed much more homogeneous responses to electric than light stimuli. The reduced information by the homogeneous responses of OFF RGCs is consistent with previous studies which reported the amount of neural information increases with a higher cell-to-cell heterogeneity in naturally evoked neural activities (Chelaru and Dragoi, 2008; Padmanabhan and Urban, 2010). However, it is also noteworthy that there is an optimal level of population response heterogeneity which maximizes the transmission of neural information as well as minimizes the effect of external noises (Tkačik et al., 2010; Tripathy et al., 2013; Im and Kim, 2020). Kang et al. (2021) also demonstrated the ultimate heterogeneity (i.e., completely random spiking) of RGC responses is not ideal to transfer neural information because

they are less immune to noise: they showed the increased trial-to-trial variability (i.e., jitter) reduces the population neural information more substantially in random spiking responses than in physiological RGC responses which showed intermediate levels of the cell-to-cell heterogeneity. Given an earlier study that reported RGC spiking consistency is gradually reduced with advancing retinal degeneration (Yoon et al., 2020), the analyses of Kang et al. (2021) suggest that the amount of information transmitted to the brain decreases as the retina degenerates. For further improvement of retinal prosthetics, it may be critical to investigate how information rates can be enhanced in degenerate retinas by altering electric stimulation conditions.

TWO METHODS FOR NEURAL INFORMATION CALCULATION

Information theory can quantify how much information about a given external stimulus is conveyed by neural responses; and there are two representative ways to compute the information from neural spike trains (Borst and Theunissen, 1999; Passaglia and Troy, 2004). First, direct method can be applied to calculate average information transmitted by the difference between total entropy of the neural response and noise entropy (Figure 2A; Koch et al., 2004; Osborne et al., 2008; Stone, 2018; Kang et al., 2021). In this method, before calculating the entropy, spikes of each cell are allocated into time bins in a fixed duration which may differ depending on experimental methods (Koch et al., 2004). Then, if one or more spikes are present in a given time bin, 1 is assigned; while 0 is assigned if there are no spikes (Osborne et al., 2008; Kang et al., 2021). Before using this binary code array to calculate entropy, it is important to choose an appropriate length of binary code combinations depending on the particular context being experimented (Theunissen and Miller, 1995). Then, total entropy is calculated from the probability of particular binary code combinations in the entire recording. Similarly, noise entropy is also estimated but from the probability of particular binary code combinations at a specific given time relative to the identical stimuli (see Osborne et al., 2008; Stone, 2018 for more details).

Second, reconstruction method can be used which is a variant of the abovementioned direct method (Figure 2B; Borst and Theunissen, 1999). The reconstruction method can determine the neural responses based on the stimulus or predict what stimulus is given based on the response (Eger and Eckhorn, 2002; Victor, 2006). Unlike the direct method requiring no assumption, the reconstruction method estimates upper or lower bound of information depending on assumptions. When we assume neural responses have a Gaussian distribution over the frequency range then the upper bound is placed since Gaussian distribution has the maximum entropy (Borst and Theunissen, 1999; Passaglia and Troy, 2004). Alternatively, the lower bound is placed when we assume information can be decoded linearly to estimate the best possible stimulus from the neural responses (Borst and Theunissen, 1999). Because we cannot include all of the information with this assumption since neural responses are predominantly non-linear and Poisson process (Felsen and

Dan, 2005), it becomes the lower bound of the information. For the computation of information rates using the reconstruction method, the signal to noise ratio in the frequency domain must be calculated (see Passaglia and Troy, 2004 for more details).

In comparison between these two methods, the direct method needs a lot of experimental data to calculate since it has no assumptions with signals and it does not reveal which stimulus aspects are being encoded. In sharp contrast, the reconstruction method needs significantly less data than the direct method, making it useful for the field that has limited amount of available data.

RECENT *IN SILICO* COMPUTATIONAL NEUROSCIENCE APPROACHES FOR NEURAL INFORMATION ANALYSIS

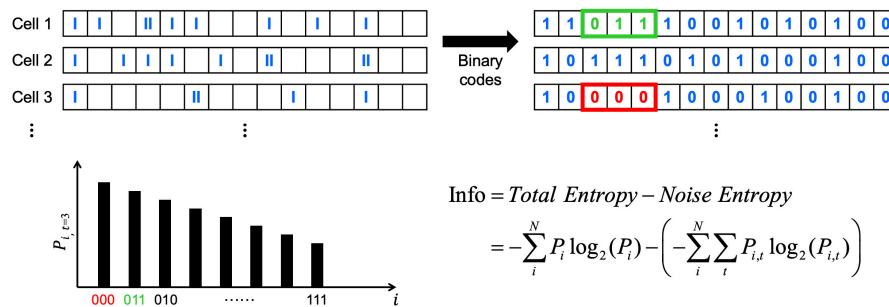
As an alternative to population responses recorded *in vivo* or *in vitro*, we can simulate population codes using computational tools. A few preceding studies suggest that the artificial retina model helps understand how the retina responds to stimuli and how the retina encodes visual information (Wohrer et al., 2006; Pei and Qiao, 2010). Also, Brette (2009) introduced an *in silico* approach to generate population codes based on the designed firing rate and pairwise correlation of spike trains. With the computational approaches using artificial spike trains, it is possible to more precisely analyze the relationship between the spiking elements and neural information.

Recently, Roh et al. (2021) used a modified version of “Brian 2” (Brette, 2009) to generate various sets of spike trains which have different levels of correlations; spike time tiling coefficients (STTCs) were calculated to quantify the correlations across spike trains (Cutts and Egle, 2014). Then, they analyzed neural information as a function of the correlation level for a wide range of average STTC values. According to the abovementioned study of Roh et al., the increased spiking heterogeneity across cells can enhance information transmission. Earlier, Hunsberger et al. (2014) reported the heterogeneity may better encode the stimulation by expressing complementary aspects of stimuli. In addition to the cell-to-cell spiking heterogeneity, other spiking features may be also crucial in better encoding visual information. For example, as a follow-up study of Roh et al. (2021) and Kim et al. (2022) further explored the relationship between information and other spiking elements such as mean firing rate and spiking duration. These *in silico* approaches may expedite future studies regarding how different stimulation parameters of retinal prostheses make RGCs transmit sufficient information to the brain.

CLINICAL IMPLICATIONS OF ARTIFICIALLY EVOKED VISUAL NEURAL INFORMATION

Other than the aforementioned studies (Eger et al., 2005; Kang et al., 2021; Roh et al., 2021; Kim et al., 2022), retinal prosthetics has not paid enough attention on how

A Direct Method



B Reconstruction Method

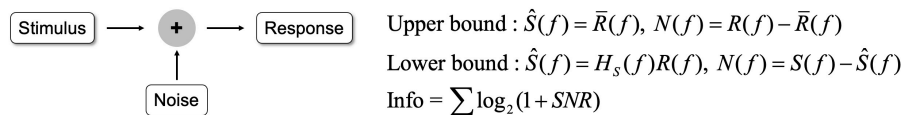


FIGURE 2 | The direct method and the reconstruction method can be applied to calculate information rates. **(A)** In the direct method, average information rates are the difference between total entropy and noise entropy. N represents the total number of possible binary code combinations, i represents binary code combination. P_i indicates probability of particular binary code combinations and similarly $P_{i,t}$ indicates the probability of particular binary code combinations at a specific time, t . **(B)** In the reconstruction method, average information rates are obtained from the signal to noise ratio (SNR). Signal and noise are calculated differently in each bound (see Passaglia and Troy, 2004 for how signal and noise are calculated). In here, $S(f)$ means signals which are the Fourier transforms of the stimulus, $R(f)$ means responses which are also the Fourier transforms of the response, respectively. $\hat{S}(f)$ means the best estimate of stimulus. In upper bound, $\hat{S}(f)$ is obtained by averaging $R(f)$ [i.e., $\bar{R}(f)$]. In lower bound, $\hat{S}(f)$ is obtained by the linear decoder filter, $H_s(f)$. $N(f)$ represents noise, and noise is also different in each bound. In upper bound, noise is the difference between response and average response, while noise is the difference between signals and estimated stimulus in lower bound.

their microelectronic devices and/or stimulation strategies improve electrically produced neural information. Although there is no direct clinical evidence supporting that prosthetic responses which transmit more information would be better perceived, it is important to note a recent sight restoration study demonstrated better animal behavior responses when the restored spiking activities were more heterogeneous across RGCs (Berry et al., 2017). Given the correlation between the cell-to-cell spiking heterogeneity and the transmitted neural information (Tripathy et al., 2013; Kang et al., 2021), the improved behavior of the animals is likely due to the enhanced visual information transmission. The optical stimulation using optogenetic approaches (Bi et al., 2006; Sahel et al., 2021), photoswitch compound (Tochitsky et al., 2016), and photoactivatable G protein-coupled receptor (Berry et al., 2017) must be promising vision restoration methods because they would not require any surgical implantation of microelectronic devices. However, in those fields as well, it is difficult to find analyses of artificially evoked neural information.

In the past clinical trials of microelectronic retinal prostheses, the most prosthetic users with retinitis pigmentosa were at the near-end stage of degeneration, who showed no light perception or hand motion (Humayun et al., 2003; Zrenner et al., 2011; Stingl et al., 2013; but, see Palanker et al., 2020, 2022 for prosthetic users with age-related macular degeneration who had still periphery vision). In such an advanced stage, their retinas were likely to send less neural information to the brain in response to electric stimulation.

It is because both direct and indirect activation of RGCs are likely to result in low information transmission rates as follow: (1) direct activation which can precisely elicit spike at intended timing may produce too homogeneous spiking across RGCs compared to natural spiking activity, and (2) indirect activation generates highly inconsistent (i.e., big trial-to-trial variability in each RGCs) network-mediated responses in severely degenerate retinas (Yoon et al., 2020), increasing noise which reduces information transmission (Kang et al., 2021). Numerous previous literatures have studied synchronous/correlated spiking activities of neighboring RGCs in responses to visual stimuli (Meister et al., 1995; DeVries, 1999; Puchalla et al., 2005; Shlens et al., 2008). Depending on the extent of response synchrony/correlation of neighboring RGCs, the brain might recognize different visual messages as argued earlier (Puchalla et al., 2005). However, systematic understanding is still lacking regarding electrically evoked responses, raising the need for such measurements.

CONCLUSION

The retina is remarkably complicated in both anatomic and functional aspects. Given the incredible complexity of the retina, it seems insufficient to simply make RGCs fire again for high-quality artificial vision. However, the field of retinal prosthetics has paid little attention on how much artificial visual information

could be created by implanted retinal prostheses and transmitted from the retina to the brain, compared to other aspects of electrically evoked retinal responses such as spike counts, firing rates, and so on. For the further improved quality of prosthetic vision, it may be critical to explore whether sufficient amount of visual information is transmitted from the retina to the brain. Probably, more information enhances the perception quality of artificial vision.

AUTHOR CONTRIBUTIONS

SK and HR contributed to drafting the manuscript and figures design. MI conceived the work and revised the manuscript. All authors read and approved the final manuscript.

REFERENCES

- Baden, T., Berens, P., Franke, K., Rosón, M. R., Bethge, M., and Euler, T. (2016). The functional diversity of retinal ganglion cells in the mouse. *Nature* 529, 345–350. doi: 10.1038/nature16468
- Berry, M. H., Holt, A., Levitz, J., Broichhagen, J., Gaub, B. M., Visel, M., et al. (2017). Restoration of patterned vision with an engineered photoactivatable G protein-coupled receptor. *Nat. Commun.* 8:1862. doi: 10.1038/s41467-017-01990-7
- Berry, M. J., Warland, D. K., and Meister, M. (1997). The structure and precision of retinal spike trains. *Proc. Natl. Acad. Sci. U.S.A.* 94, 5411–5416. doi: 10.1073/pnas.94.10.5411
- Bi, A., Cui, J., Ma, Y. P., Olshevskaya, E., Pu, M., Dizhoor, A. M., et al. (2006). Ectopic expression of a microbial-type rhodopsin restores visual responses in mice with photoreceptor degeneration. *Neuron* 50, 23–33. doi: 10.1016/j.neuron.2006.02.026
- Borst, A., and Theunissen, F. (1999). Information theory and neural coding. *Nat. Neurosci.* 2, 947–957. doi: 10.1038/14731
- Brette, R. (2009). Generation of correlated spike trains. *Neural Comput.* 21, 188–215. doi: 10.1162/neco.2008.12-07-657
- Bunker, C. H., Berson, E. L., Bromley, W. C., Hayes, R. P., and Roderick, T. H. (1984). Prevalence of retinitis pigmentosa in Maine. *Am. J. Ophthalmol.* 97, 357–365. doi: 10.1016/0002-9394(84)90636-6
- Busskamp, V., and Roska, B. (2011). Optogenetic approaches to restoring visual function in retinitis pigmentosa. *Curr. Opin. Neurobiol.* 21, 942–946. doi: 10.1016/j.conb.2011.06.001
- Cai, C., Ren, Q., Desai, N. J., Rizzo, J. F. 3rd., and Fried, S. I. (2011). Response variability to high rates of electric stimulation in retinal ganglion cells. *J. Neurophysiol.* 106, 153–162. doi: 10.1152/jn.00956.2010
- Cai, C., Twyford, P., and Fried, S. I. (2013). The response of retinal neurons to high-frequency stimulation. *J. Neural Eng.* 10:036009. doi: 10.1088/1741-2560/10/3/036009
- Chelaru, M. I., and Dragoi, V. (2008). Efficient coding in heterogeneous neuronal populations. *Proc. Natl. Acad. Sci. U.S.A.* 105, 16344–16349. doi: 10.1073/pnas.0807744105
- Curcio, C. A., Medeiros, N. E., and Millican, C. L. (1996). Photoreceptor loss in age-related macular degeneration. *Invest. Ophthalmol. Vis. Sci.* 37, 1236–1249.
- Cutts, C. S., and Eglén, S. J. (2014). Detecting pairwise correlations in spike trains: an objective comparison of methods and application to the study of retinal waves. *J. Neurosci.* 34, 14288–14303. doi: 10.1523/JNEUROSCI.2767-14.2014
- da Cruz, L., Coley, B. F., Dorn, J., Merlino, F., Filley, E., Christopher, P., et al. (2013). The Argus II epiretinal prosthesis system allows letter and word reading and long-term function in patients with profound vision loss. *Br. J. Ophthalmol.* 97, 632–636. doi: 10.1136/bjophthalmol-2012-301525
- David, S. V., Vinje, W. E., and Gallant, J. L. (2004). Natural stimulus statistics alter the receptive field structure of V1 neurons. *J. Neurosci.* 24, 6991–7006. doi: 10.1523/JNEUROSCI.1422-04.2004
- DeVries, S. H. (1999). Correlated firing in rabbit retinal ganglion cells. *J. Neurophysiol.* 81, 908–920. doi: 10.1152/jn.1999.81.2.908
- DeVries, S. H., and Baylor, D. A. (1997). Mosaic arrangement of ganglion cell receptive fields in rabbit retina. *J. Neurophysiol.* 78, 2048–2060. doi: 10.1152/jn.1997.78.4.2048
- Dobelle, W. H., Mladejovsky, M. G., Evans, J. R., Roberts, T. S., and Girvin, J. P. (1976). "Braille" reading by a blind volunteer by visual cortex stimulation. *Nature* 259, 111–112. doi: 10.1038/259111a0
- Dobelle, W. H., Mladejovsky, M. G., and Girvin, J. P. (1974). Artificial vision for the blind: electrical stimulation of visual cortex offers hope for a functional prosthesis. *Science* 183, 440–444. doi: 10.1126/science.183.4123.440
- Dorn, J. D., Ahuja, A. K., Caspi, A., da Cruz, L., Dagnelie, G., Sahel, J. A., et al. (2013). The detection of motion by blind subjects with the epiretinal 60-electrode (Argus II) retinal prosthesis. *JAMA Ophthalmol.* 131, 183–189. doi: 10.1001/2013.jamaophthalmol.221
- Eger, M., and Eckhorn, R. (2002). A model-based approach for the analysis of neuronal information transmission in multi-input and -output systems. *J. Comput. Neurosci.* 12, 175–200. doi: 10.1023/a:101658328930
- Eger, M., Wilms, M., Eckhorn, R., Schanze, T., and Hesse, L. (2005). Retino-cortical information transmission achievable with a retina implant. *Biosystems* 79, 133–142. doi: 10.1016/j.biosystems.2004.09.030
- Felsen, G., and Dan, Y. (2005). A natural approach to studying vision. *Nat. Neurosci.* 8, 1643–1646. doi: 10.1038/nn1608
- Felsen, G., Touryan, J., Han, F., and Dan, Y. (2005). Cortical sensitivity to visual features in natural scenes. *PLoS Biol.* 3:e342. doi: 10.1371/journal.pbio.0030342
- Ferlauto, L., Airaghi, Leccardi, M. J. I., Chenais, N. A. L., Gilliéron, S. C. A., Vagni, P., Bevilacqua, M., et al. (2018). Design and validation of a foldable and photovoltaic wide-field epiretinal prosthesis. *Nat. Commun.* 9:992. doi: 10.1038/s41467-018-03386-7
- Field, G. D., and Chichilnisky, E. J. (2007). Information processing in the primate retina: circuitry and coding. *Annu. Rev. Neurosci.* 30, 1–30. doi: 10.1146/annurev.neuro.30.051606.094252
- Flores, T., Huang, T., Bhuckory, M., Ho, E., Chen, Z., Dalal, R., et al. (2019). Honeycomb-shaped electro-neural interface enables cellular-scale pixels in subretinal prosthesis. *Sci. Rep.* 9:10657. doi: 10.1038/s41598-019-47082-y
- Flores, T., Lei, X., Huang, T., Lorach, H., Dalal, R., Galambos, L., et al. (2018). Optimization of pillar electrodes in subretinal prosthesis for enhanced proximity to target neurons. *J. Neural Eng.* 15:036011. doi: 10.1088/1741-2552/15/03/036011
- Freed, M. A. (2017). Asymmetry between ON and OFF α ganglion cells of mouse retina: integration of signal and noise from synaptic inputs. *J. Physiol.* 595, 6979–6991. doi: 10.1111/JP274736
- Freeman, D. K., Eddington, D. K., Rizzo, J. F. 3rd., and Fried, S. I. (2010). Selective activation of neuronal targets with sinusoidal electric stimulation. *J. Neurophysiol.* 104, 2778–2791. doi: 10.1152/jn.00551.2010
- Freeman, D. K., Rizzo, J. F. 3rd., and Fried, S. I. (2011). Encoding visual information in retinal ganglion cells with prosthetic stimulation. *J. Neural Eng.* 8:035005. doi: 10.1088/1741-2560/8/3/035005

FUNDING

This work was supported by the KIST (Korea Institute of Science and Technology) institutional grants (2E31821) and National R&D Program through the National Research Foundation of Korea (NRF) funded by the Ministry of Science and ICT (Nos. 2020R1C1C1006065, 2021M3F3A2A01037366, and 2022M3E5E8017395).

ACKNOWLEDGMENTS

We thank Joon Ho Kang and Taegon Kim for the helpful discussion on the neural information of retinal ganglion cell spiking activities.

- Fried, S. I., Hsueh, H. A., and Werblin, F. S. (2006). A method for generating precise temporal patterns of retinal spiking using prosthetic stimulation. *J. Neurophysiol.* 95, 970–978. doi: 10.1152/jn.00849.2005
- Fujikado, T., Morimoto, T., Kanda, H., Kusaka, S., Nakauchi, K., Ozawa, M., et al. (2007). Evaluation of phosphene elicited by extraocular stimulation in normals and by suprachoroidal-transretinal stimulation in patients with retinitis pigmentosa. *Graefes Arch. Clin. Exp. Ophthalmol.* 245, 1411–1419. doi: 10.1007/s00417-007-0563-z
- Gaillet, V., Cutrone, A., Artoni, F., Vagni, P., Mega Pratiwi, A., Romero, S. A., et al. (2019). Spatially selective activation of the visual cortex via intraneural stimulation of the optic nerve. *Nat. Biomed. Eng.* 4, 181–194. doi: 10.1038/s41551-019-0446-8
- Gao, X., Grayden, D. B., and McDonnell, M. D. (2013). Information theoretic optimization of cochlear implant electrode usage probabilities. *Annu. Int. Conf. IEEE Eng. Med. Biol. Soc.* 2013, 5974–5977. doi: 10.1109/EMBC.2013.6610913
- Gaub, B. M., Berry, M. H., Holt, A. E., Reiner, A., Kienzler, M. A., Dolgova, N., et al. (2014). Restoration of visual function by expression of a light-gated mammalian ion channel in retinal ganglion cells or ON-bipolar cells. *Proc. Natl. Acad. Sci. U.S.A.* 111, E5574–E5583. doi: 10.1073/pnas.1414162111
- Grimm, C., Wenzel, A., Williams, T., Rol, P., Hafezi, F., and Remé, C. (2001). Rhodopsin-mediated blue-light damage to the rat retina: effect of photoreversal of bleaching. *Invest. Ophthalmol. Vis. Sci.* 42, 497–505.
- Hannan, M. A., Abbas, S. M., Samad, S. A., and Hussain, A. (2012). Modulation techniques for biomedical implanted devices and their challenges. *Sensors (Basel)* 12, 297–319. doi: 10.3390/s120100297
- Humayun, M. S., De Juan, E., Dagnelie, G., Greenberg, R. J., Propst, R. H., and Phillips, D. H. (1996). Visual perception elicited by electrical stimulation of retina in blind humans. *Arch. Ophthalmol.* 114, 40–46. doi: 10.1001/archophth.1996.01100130038006
- Humayun, M. S., Weiland, J. D., Fujii, G. Y., Greenberg, R., Williamson, R., Little, J., et al. (2003). Visual perception in a blind subject with a chronic microelectronic retinal prosthesis. *Vision Res.* 43, 2573–2581. doi: 10.1016/s0042-6989(03)00457-7
- Hunsberger, E., Scott, M., and Eliasmith, C. (2014). The competing benefits of noise and heterogeneity in neural coding. *Neural Comput.* 26, 1600–1623. doi: 10.1162/NECO_a_00621
- Hutmacher, F. (2019). Why is there so much more research on vision than on any other sensory modality? *Front. Psychol.* 10:2246. doi: 10.3389/fpsyg.2019.02246
- Im, M., and Fried, S. I. (2015). Indirect activation elicits strong correlations between light and electrical responses in ON but not OFF retinal ganglion cells. *J. Physiol.* 593, 3577–3596. doi: 10.1113/JP270606
- Im, M., and Fried, S. I. (2016a). Temporal properties of network-mediated responses to repetitive stimuli are dependent upon retinal ganglion cell type. *J. Neural Eng.* 13:025002. doi: 10.1088/1741-2560/13/2/025002
- Im, M., and Fried, S. I. (2016b). Directionally selective retinal ganglion cells suppress luminance responses during natural viewing. *Sci. Rep.* 6:35708. doi: 10.1038/srep35708
- Im, M., and Kim, S. W. (2020). Neurophysiological and medical considerations for better-performing microelectronic retinal prostheses. *J. Neural Eng.* 17:033001. doi: 10.1088/1741-2552/ab8ca9
- Im, M., Werginz, P., and Fried, S. I. (2018). Electric stimulus duration alters network-mediated responses depending on retinal ganglion cell type. *J. Neural Eng.* 15:036010. doi: 10.1088/1741-2552/aaadcl
- Jepson, L. H., Hottowy, P., Mathieson, K., Gunning, D. E., Dąbrowski, W., Litke, A. M., et al. (2014). Spatially patterned electrical stimulation to enhance resolution of retinal prostheses. *J. Neurosci.* 34, 4871–4881. doi: 10.1523/JNEUROSCI.2882-13.2014
- Kameneva, T., Meffin, H., and Burkitt, A. N. (2010). Differential stimulation of ON and OFF retinal ganglion cells: a modeling study. *Conf. Proc. IEEE Eng. Med. Biol. Soc.* 2010, 4246–4249. doi: 10.1109/IEMBS.2010.5627176
- Kang, J. H., Jang, Y. J., Kim, T., Lee, B. C., Lee, S. H., and Im, M. (2021). Electric stimulation elicits heterogeneous responses in ON but not OFF retinal ganglion cells to transmit rich neural information. *IEEE Trans. Neural Syst. Rehabil. Eng.* 29, 300–309. doi: 10.1109/TNSRE.2020.3048973
- Kayser, C., Salazar, R. F., and König, P. (2003). Responses to natural scenes in cat V1. *J. Neurophysiol.* 90, 1910–1920. doi: 10.1152/jn.00195.2003
- Kim, S., Roh, H., and Im, M. (2022). *Neural Information of Artificial Vision Varies Depending on Mean Firing Rate and Spiking Duration. Accepted to be Presented at ARVO 2022.* Rockville, MD: Association for Research in Vision and Ophthalmology.
- Koch, K., McLean, J., Berry, M., Sterling, P., Balasubramanian, V., and Freed, M. A. (2004). Efficiency of information transmission by retinal ganglion cells. *Curr. Biol.* 14, 1523–1530. doi: 10.1016/j.cub.2004.08.060
- Koch, K., McLean, J., Segev, R., Freed, M. A., Berry, M. J. 2nd., Balasubramanian, V., et al. (2006). How much the eye tells the brain. *Curr. Biol.* 16, 1428–1434. doi: 10.1016/j.cub.2006.05.056
- Kolb, H. (2003). How the Retina Works: much of the construction of an image takes place in the retina itself through the use of specialized neural circuits. *Am. Sci.* 91, 28–35.
- Lagali, P. S., Balya, D., Awatramani, G. B., Münch, T. A., Kim, D. S., Busskamp, V., et al. (2008). Light-activated channels targeted to ON bipolar cells restore visual function in retinal degeneration. *Nat. Neurosci.* 11, 667–675. doi: 10.1038/nn.2117
- Lee, J.-I., and Im, M. (2018). Non-rectangular waveforms are more charge-efficient than rectangular one in eliciting network-mediated responses of ON type retinal ganglion cells. *J. Neural Eng.* 15:055004. doi: 10.1088/1741-2552/aad416
- Lee, J.-I., and Im, M. (2019). Optimal electric stimulus amplitude improves the selectivity between responses of ON versus OFF types of retinal ganglion cells. *IEEE Trans. Neural Syst. Rehabil. Eng.* 27, 2015–2024. doi: 10.1109/TNSRE.2019.2939012
- Liang, Z., and Freed, M. A. (2012). Cross inhibition from ON to OFF pathway improves the efficiency of contrast encoding in the mammalian retina. *J. Neurophysiol.* 108, 2679–2688. doi: 10.1152/jn.00589.2012
- Lu, Q., Ganjawala, T. H., Ivanova, E., Cheng, J. G., Troilo, D., and Pan, Z. H. (2016). AAV-mediated transduction and targeting of retinal bipolar cells with improved mGluR6 promoters in rodents and primates. *Gene Ther.* 23, 680–689. doi: 10.1038/gt.2016.42
- Macé, E., Caplette, R., Marre, O., Sengupta, A., Chaffiol, A., Barbe, P., et al. (2015). Targeting channelrhodopsin-2 to ON-bipolar cells with vitreally administered AAV Restores ON and OFF visual responses in blind mice. *Mol. Ther.* 23, 7–16. doi: 10.1038/mt.2014.154
- Margolis, D. J., and Detwiler, P. B. (2007). Different mechanisms generate maintained activity in ON and OFF retinal ganglion cells. *J. Neurosci.* 27, 5994–6005. doi: 10.1523/JNEUROSCI.0130-07.2007
- Masland, R. H. (2001). The fundamental plan of the retina. *Nat. Neurosci.* 4, 877–886. doi: 10.1038/nn0901-877
- Masland, R. H. (2012). The neuronal organization of the retina. *Neuron* 76, 266–280. doi: 10.1016/j.neuron.2012.10.002
- Meister, M., Lagnado, L., and Baylor, D. A. (1995). Concerted signaling by retinal ganglion cells. *Science* 270, 1207–1210. doi: 10.1126/science.270.5239.1207
- Mino, H. (2007). Encoding of information into neural spike trains in an auditory nerve fiber model with electric stimuli in the presence of a pseudospontaneous activity. *IEEE Trans. Biomed. Eng.* 54, 360–369. doi: 10.1109/TBME.2006.890486
- Moroz, A. S., McDonnell, M. D., Burkitt, A. N., Grayden, D. B., and Meffin, H. (2012). Information theoretic inference of the optimal number of electrodes for future cochlear implants using a spiral cochlea model. *Annu. Int. Conf. IEEE Eng. Med. Biol. Soc.* 2012, 2965–2968. doi: 10.1109/EMBC.2012.6346586
- Nassi, J., and Callaway, E. M. (2009). Parallel processing strategies of the primate visual system. *Nat. Rev. Neurosci.* 10, 360–372. doi: 10.1038/nrn2619
- Naycheva, L., Schatz, A., Röck, T., Willmann, G., Messias, A., Bartz-Schmidt, K. U., et al. (2012). Phosphene thresholds elicited by transcorneal electrical stimulation in healthy subjects and patients with retinal diseases. *Invest. Ophthalmol. Vis. Sci.* 53, 7440–7448. doi: 10.1167/iovs.12-9612
- Ölveczky, B. P., Baccus, S. A., and Meister, M. (2003). Segregation of object and background motion in the retina. *Nature* 423, 40140–40148. doi: 10.1038/nature01652
- Osborne, L. C., Palmer, S. E., Lisberger, S. G., and Bialek, W. (2008). The neural basis for combinatorial coding in a cortical population response. *J. Neurosci.* 28, 13522–13531. doi: 10.1523/JNEUROSCI.4390-08.2008
- Padmanabhan, K., and Urban, N. N. (2010). Intrinsic biophysical diversity decorrelates neuronal firing while increasing information content. *Nat. Neurosci.* 13, 1276–1282. doi: 10.1038/nn.2630
- Palanker, D., Le Mer, Y., Mohand-Said, S., Muqit, M., and Sahel, J. A. (2020). Photovoltaic restoration of central vision in atrophic age-related macular

- degeneration. *Ophthalmology* 127, 1097–1104. doi: 10.1016/j.ophtha.2020.02.024
- Palanker, D., Le Mer, Y., Mohand-Said, S., and Sahel, J. A. (2022). Simultaneous perception of prosthetic and natural vision in AMD patients. *Nat. Commun.* 13:513. doi: 10.1038/s41467-022-28125-x
- Passaglia, C. L., and Troy, J. B. (2004). Information transmission rates of cat retinal ganglion cells. *J. Neurophysiol.* 91, 1217–1229. doi: 10.1152/jn.00796.2003
- Pei, Z., and Qiao, Q. (2010). “An approximate retina model with cascade structures,” in *2010 Sixth International Conference on Natural Computation* 2009–2012, (Piscataway, NJ: IEEE).
- Pezaris, J. S., and Reid, R. C. (2007). Demonstration of artificial visual percepts generated through thalamic microstimulation. *Proc. Natl. Acad. Sci. U.S.A.* 104, 7670–7675. doi: 10.1073/pnas.0608563104
- Puchalla, J. L., Schneidman, E., Harris, R. A., and Berry, M. J. (2005). Redundancy in the population code of the retina. *Neuron* 46, 493–504. doi: 10.1016/j.neuron.2005.03.026
- Quian Quiroga, R., and Panzeri, S. (2009). Extracting information from neuronal populations: information theory and decoding approaches. *Nat. Rev. Neurosci.* 10, 173–185. doi: 10.1038/nrn2578
- Rizzo, J. F., Wyatt, J., Loewenstein, J., Kelly, S., and Shire, D. (2003). Perceptual efficacy of electrical stimulation of human retina with a microelectrode array during short-term surgical trials. *Invest. Ophthalmol. Vis. Sci.* 44, 5362–5369. doi: 10.1167/iops.02-0817
- Rockhill, R. L., Daly, F. J., MacNeil, M. A., Brown, S. P., and Masland, R. H. (2004). The diversity of ganglion cells in a mammalian retina. *J. Neurosci.* 22, 3831–3843. doi: 10.1523/JNEUROSCI.22-09-03831.2002
- Roh, H., Kim, E., Chung, S. M., Kang, J. H., Kim, T., and Im, M. (2021). Neural information of artificial vision varies depending on the level of spiking heterogeneity across retinal ganglion cells. *Invest. Ophthalmol. Vis. Sci.* 62:3228.
- Roh, H., Yoon, Y. J., Park, J. S., Kang, D. H., Kwak, S. M., Lee, B. C., et al. (2022). Fabrication of high-density out-of-plane microneedle arrays with various heights and diverse cross-sectional shapes. *Nano-Micro Lett.* 14:24. doi: 10.1007/s40820-021-00778-1
- Roska, B., Molnar, A., and Werblin, F. S. (2006). Parallel processing in retinal ganglion cells: how integration of space-time patterns of excitation and inhibition form the spiking output. *J. Neurophysiol.* 95, 3810–3822. doi: 10.1152/jn.00113.2006
- Sahel, J. A., Boulanger-Scemama, E., Pagot, C., Arleo, A., Galluppi, F., Martel, J. N., et al. (2021). Partial recovery of visual function in a blind patient after optogenetic therapy. *Nat. Med.* 27, 1223–1229. doi: 10.1038/s41591-021-01351-4
- Sanes, J. R., and Masland, R. H. (2015). The types of retinal ganglion cells: current status and implications for neuronal classification. *Annu. Rev. Neurosci.* 38, 221–246. doi: 10.1146/annurev-neuro-071714-034120
- Schiller, P. H. (1992). The ON and OFF channels of the visual system. *Trends Neurosci.* 15, 86–92. doi: 10.1016/0166-2236(92)90017-3
- Schiller, P. H., Sandell, J. H., and Maunsell, J. H. (1986). Functions of the ON and OFF channels of the visual system. *Nature* 322, 824–825. doi: 10.1038/322824a0
- Seo, H. W., Kim, N., and Kim, S. (2020). Fabrication of subretinal 3D microelectrodes with hexagonal arrangement. *Micromachines (Basel)* 11:467. doi: 10.3390/mi11050467
- Shivdasani, M. N., Sinclair, N. C., Gillespie, L. N., Petoe, M. A., Titchener, S. A., Fallon, J. B., et al. (2017). Identification of characters and localization of images using direct Multiple-electrode stimulation with a suprachoroidal retinal prosthesis. *Invest. Ophthalmol. Vis. Sci.* 58, 3962–3974. doi: 10.1167/iops.16-21311
- Shlens, J., Rieke, F., and Chichilnisky, E. (2008). Synchronized firing in the retina. *Curr. Opin. Neurobiol.* 18, 396–402. doi: 10.1016/j.conb.2008.09.010
- Simunovic, M. P., Shen, W., Lin, J. Y., Protti, D. A., Lisowski, L., and Gillies, M. C. (2019). Optogenetic approaches to vision restoration. *Exp. Eye Res.* 178, 15–26. doi: 10.1016/j.exer.2018.09.003
- Stingl, K., Bartz-Schmidt, K. U., Besch, D., Braun, A., Bruckmann, A., Gekeler, F., et al. (2013). Artificial vision with wirelessly powered subretinal electronic implant alpha-IMS. *Proc. Biol. Sci.* 280:20130077. doi: 10.1098/rspb.2013.0077
- Stone, J. V. (2018). *Principles of Neural Information Theory: Computational Neuroscience and Metabolic Efficiency*. Sheffield: Sebtel Press.
- Talebi, V., and Baker, C. L. Jr. (2012). Natural versus synthetic stimuli for estimating receptive field models: a comparison of predictive robustness. *J. Neurosci.* 32, 1560–1576. doi: 10.1523/JNEUROSCI.4661-12.2012
- Theunissen, F., and Miller, J. P. (1995). Temporal encoding in nervous systems: a rigorous definition. *J. Comput. Neurosci.* 2, 149–162. doi: 10.1007/BF00961885
- Timme, N. M., and Lapish, C. (2018). A tutorial for information theory in neuroscience. *eNeuro* 5, e52–e18. doi: 10.1523/ENEURO.0052-18.2018
- Tkačik, G., Prentice, J. S., Balasubramanian, V., and Schneidman, E. (2010). Optimal population coding by noisy spiking neurons. *Proc. Natl. Acad. Sci. U.S.A.* 107, 14419–14424. doi: 10.1073/pnas.1004906107
- Tochitsky, I., Helft, Z., Meseguer, V., Fletcher, R. B., Vessey, K. A., Telias, M., et al. (2016). How azobenzene photoswitches restore visual responses to the blind retina. *Neuron* 92, 100–113. doi: 10.1016/j.neuron.2016.08.038
- Touryan, J., Felsen, G., and Dan, Y. (2005). Spatial structure of complex cell receptive fields measured with natural images. *Neuron* 45, 781–791. doi: 10.1016/j.neuron.2005.01.029
- Tripathy, S. J., Padmanabhan, K., Gerkin, R. C., and Urban, N. N. (2013). Intermediate intrinsic diversity enhances neural population coding. *Proc. Natl. Acad. Sci. U.S.A.* 110, 8248–8253. doi: 10.1073/pnas.1221214110
- Twyford, P., Cai, C., and Fried, S. I. (2014). Differential responses to high-frequency electrical stimulation in ON and OFF retinal ganglion cells. *J. Neural Eng.* 11:025001. doi: 10.1088/1741-2560/11/2/025001
- van Wyk, M., Pielecka-Fortuna, J., Löwel, S., and Kleinlogel, S. (2015). Restoring the ON switch in blind retinas: opto-mGluR6, a next-generation, cell-tailored optogenetic tool. *PLoS Biol.* 13:e1002143. doi: 10.1371/journal.pbio.1002143
- Victor, J. D. (2006). Approaches to information-theoretic analysis of neural activity. *Biol. Theory* 1, 302–316. doi: 10.1162/biot.2006.1.3.302
- Wang, B. Y., Chen, Z. C., Bhuckory, M., Huang, T., Shin, A., Zuckerman, V., et al. (2021). Electronic “photoreceptors” enable prosthetic vision with acuity matching the natural resolution in rats. *bioRxiv [Preprint]* 452093. doi: 10.1101/2021.07.12.452093
- Wang, G., Wang, R., Kong, W., and Zhang, J. (2018). Simulation of retinal ganglion cell response using fast independent component analysis. *Cogn. Neurodyn.* 12, 615–624. doi: 10.1007/s11571-018-9490-4
- Wässle, H. (2004). Parallel processing in the mammalian retina. *Nat. Rev. Neurosci.* 5, 747–757. doi: 10.1038/nrn1497
- Weitz, A. C., Nanduri, D., Behrend, M. R., Gonzalez-Calle, A., Greenberg, R. J., Humayun, M. S., et al. (2015). Improving the spatial resolution of epiretinal implants by increasing stimulus pulse duration. *Sci. Transl. Med.* 7:318ra203. doi: 10.1126/scitranslmed.aac4877
- Wohrer, A., Kornprobst, P., and Viéville, T. (2006). “From light to spikes: a large-scale retina simulator,” in *The 2006 IEEE International Joint Conference on Neural Network Proceedings 4562–4570*, (Piscataway, NJ: IEEE).
- Yoon, Y. J., Lee, J. I., Jang, Y. J., An, S., Kim, J. H., Fried, S. I., et al. (2020). Retinal degeneration reduces consistency of network-mediated responses arising in ganglion cells to electric stimulation. *IEEE Trans. Neural Syst. Rehabil. Eng.* 28, 1921–1930. doi: 10.1109/TNSRE.2020.3003345
- Zeck, G. M., and Masland, R. H. (2007). Spike train signatures of retinal ganglion cell types. *Eur. J. Neurosci.* 26, 367–380. doi: 10.1111/j.1460-9568.2007.05670.x
- Zeng, F. G., Rebscher, S., Harrison, W., Sun, X., and Feng, H. (2008). Cochlear implants: system design, integration, and evaluation. *IEEE Rev. Biomed. Eng.* 1, 115–142. doi: 10.1109/RBME.2008.2008250
- Zrenner, E., Bartz-Schmidt, K. U., Benav, H., Besch, D., Bruckmann, A., Gabel, V. P., et al. (2011). Subretinal electronic chips allow blind patients to read letters and combine them to words. *Proc. Biol. Sci.* 278, 1489–1497.

Conflict of Interest: The authors declare that the research was conducted in the absence of any commercial or financial relationships that could be construed as a potential conflict of interest.

Publisher's Note: All claims expressed in this article are solely those of the authors and do not necessarily represent those of their affiliated organizations, or those of the publisher, the editors and the reviewers. Any product that may be evaluated in this article, or claim that may be made by its manufacturer, is not guaranteed or endorsed by the publisher.

Copyright © 2022 Kim, Roh and Im. This is an open-access article distributed under the terms of the Creative Commons Attribution License (CC BY). The use, distribution or reproduction in other forums is permitted, provided the original author(s) and the copyright owner(s) are credited and that the original publication in this journal is cited, in accordance with accepted academic practice. No use, distribution or reproduction is permitted which does not comply with these terms.



Progress on Designing a Chemical Retinal Prosthesis

Jiajia Wu¹, Corey M. Rountree², Sai-Siva Kare², Pradeep Kumar Ramkumar², John D. Finan² and John B. Troy^{1*}

¹ Department of Biomedical Engineering, Robert R. McCormick School of Engineering and Applied Science, Northwestern University, Evanston, IL, United States; ² Department of Mechanical and Industrial Engineering, College of Engineering, University of Illinois at Chicago, Chicago, IL, United States

The last major review of progress toward a chemical retinal prosthesis was a decade ago. Many important advancements have been made since then with the aim of producing an implantable device for animal testing. We review that work here discussing the potential advantages a chemical retinal prosthesis may possess, the spatial and temporal resolutions it might provide, the materials from which an implant might be constructed and its likely effectiveness in stimulating the retina in a natural fashion. Consideration is also given to implant biocompatibility, excitotoxicity of dispensed glutamate and known changes to photoreceptor degenerate retinas.

Keywords: retinal prosthesis, retinal degeneration, vision restoration, neurotransmitter-based prosthesis, glutamate stimulation, retinitis pigmentosa

OPEN ACCESS

Edited by:

Diego Ghezzi,
Swiss Federal Institute of Technology
Lausanne, Switzerland

Reviewed by:

Feng Pan,
Hong Kong Polytechnic University,
Hong Kong SAR, China

*Correspondence:

John B. Troy
j-troy@northwestern.edu

Specialty section:

This article was submitted to
Cellular Neurophysiology,
a section of the journal
Frontiers in Cellular Neuroscience

Received: 17 March 2022

Accepted: 17 May 2022

Published: 10 June 2022

Citation:

Wu J, Rountree CM, Kare S-S,
Ramkumar PK, Finan JD and Troy JB
(2022) Progress on Designing
a Chemical Retinal Prosthesis.
Front. Cell. Neurosci. 16:898865.
doi: 10.3389/fncel.2022.898865

INTRODUCTION

A decade has passed since the last review of chemical retinal prostheses (Iezzi and Finlayson, 2011), which focused on preliminary ideas and measurements critical to optimizing device design. Over the intervening period some of the ideas contained in that review article have been explored and it is now timely to examine progress made with an eye to the next stage of development. Recently, Strickland and Harris (2022) have drawn attention to some business and ethical challenges faced in bringing about the clinical application of retinal prostheses. Chemical retinal prostheses remain distant from clinical application at this time, so these broader societal questions are not considered here. For the reader interested in such questions, Troy (2015) might be a good starting point.

Like all retinal prostheses, those using chemical stimulation, target a patient population with a largely intact retinal output. Generally, the patient population will be those subject to diseases of photoreceptor loss, such as those with retinitis pigmentosa or those with age-related macular degeneration, although there are those with photoreceptor loss through injury who could also benefit from retinal prostheses.

ADVANTAGES OF A CHEMICAL PROSTHESIS

The key potential advantage chemical stimulation of the retina has over electrical stimulation is the fact that the natural activators of neurons are transmitter molecules; i.e., a chemical stimulus is more naturalistic. For both chemical and electrical stimulation, fine spatial vision requires close packing of stimulation sites. In the case of electrical stimulation, this necessitates small electrode tips with consequent high charge densities for neural stimulation resulting potentially in electrode tip erosion and the generation of chemical entities toxic to cells (Zheng et al., 2021). A chemical prosthesis with a high-density array of injection ports is itself challenging from an engineering perspective but, unlike with electrical prostheses, there does not seem to be a significant theoretical physical limit.

Another potential advantage of a chemical prosthesis might be its capacity to match itself to retinal circuitry. The most obvious example of this would be exploitation of the part played by glutamate release from photoreceptors in differentially activating OFF and ON bipolar cells (Whitaker et al., 2021), respectively, through their sign-conserving kainate or AMPA (DeVries, 2000) and sign-inverting mGluR6 (Pinto et al., 2007) receptors. But, additionally, the ability to release multiple chemicals (e.g., glutamate, GABA, glycine, acetylcholine, dopamine, kainate, AMPA) provides a wide set of neuromodulation possibilities. To date, effort has focused on injection of glutamate, the primary mechanism of excitatory neurotransmission from photoreceptors to bipolar cells to retinal ganglion cells. In this review article we consider only progress made toward a chemical prosthesis that dispenses glutamate.

COMPONENTS OF A CHEMICAL RETINAL PROSTHESIS

Figure 1 shows the components of a chemical retinal prosthesis. Two sites for implantation of retinal prostheses have been used for electrical stimulation and both have been investigated as potential sites for placement of chemical stimulation arrays. In one case, so-called epiretinal placement, a stimulation array is inserted into the vitreal chamber so that the points of stimulation lie adjacent to the retina's inner surface, close to the retinal ganglion cells (**Figure 1B**). The second potential site for array placement is in the space usually occupied by, now degenerated, photoreceptors. This is referred to as subretinal and results in the stimulation points adjacent to bipolar and horizontal cells (**Figure 1C**). The expected advantage of subretinal placement is that it would provide a naturalistic location from which glutamate could interact with OFF and ON bipolar cells, leading to natural modulation of the retina's OFF and ON pathways. The advantage of epiretinal placement would be that the vitreal space affords the possibility of a larger intraocular well for glutamate.

The surgical approaches taken for the implantation of electrical retinal prostheses are similar to those that would apply for the implantation of a chemical retinal prosthesis. For subretinal implantation, a temporary retinal detachment is involved, and methods are taken to secure the implant for both epiretinal and subretinal placements. For a fuller summary of surgical details for subretinal implants (see Besch et al., 2007; MacLaren, 2017) and for epiretinal implants see (Humayun et al., 2012).

All retinal prostheses require a camera system to capture an image and a means to translate that image into a pattern of retinal ganglion cell stimulation. Electrical prostheses accomplish this through pixelated electrical stimulation. Chemical retinal prostheses would use pixelated release of neurotransmitter. In this case, the spacing of pixels and its resultant spatial resolution are limited by the potential activation field of transmitter spread from an injection port (pixel). The potential for spatial resolution equivalent to or superior to that achieved for electrical stimulation has been demonstrated for

both epiretinal (Inayat et al., 2015) and subretinal chemical stimulation (Rountree et al., 2016, 2018). Nevertheless, further advance is needed to reach the visual acuity of a person defined sighted legally. A prototype of a chemical synapse chip was developed and shown to generate patterned retinal ganglion cell responses from *ex vivo* rat retina by Rountree et al. (2017a).

Higher spatial resolution is possible with less lateral spread of glutamate stimulation. The spread is dependent on the concentration and volume of glutamate injected. Finlayson and Iezzi (2010) investigated the concentration of glutamate needed to drive retinal responses in Sprague-Dawley and photoreceptor degenerate S334ter-4 rats when delivered to the epiretinal surface or 15–20 μm below that surface. Glutamate concentrations in the range 0.4–10 mM were effective for evoking responses from retinal ganglion cells. 0.25–10 mM glutamate injected 20 μm below the epiretinal surface has also been shown to be effective for stimulating-retinal ganglion cells of Hooded Long-Evans rats (Inayat et al., 2015). Inayat et al. (2015) also showed that the field of stimulation was reduced significantly when a small (< 10 μL) volume of glutamate was injected. Corresponding fields of glutamate stimulation have been reported for retinal ganglion cells of Hooded Long-Evans and photoreceptor degenerate S334ter-3 rat retinas for subretinal activation (Rountree et al., 2016, 2018, 2020). Hence, the potential for visual acuities in the legally sighted range seem attainable for a chemical retinal prosthesis with either epiretinal or subretinal placement.

No functioning chemical retinal prosthesis has been implanted in an animal model to date. But progress toward the fabrication of an implantable device has been made. **Figure 1A** shows what is envisaged. Rountree et al. (2020) showed that subretinal stimulation of retinal ganglion cells is improved substantially when injection ports penetrate some distance into the retina from the subretinal surface. The same is likely true for epiretinal stimulation, so a stimulation array with needle-like injection ports is envisaged. While most demonstrations of glutamate activation of retinal ganglion cells from the epiretinal (Finlayson and Iezzi, 2010; Inayat et al., 2015) or from the subretinal side (Rountree et al., 2016, 2018, 2020) have relied on pneumatic injection (Rountree et al., 2017b), it was recognized by Peterman et al. (2004) that electroosmotic flow might be better suited as a neurotransmitter release mechanism in a microfabricated device. Kare et al. (2021) have shown recently that electroosmosis can be used effectively to dispense glutamate to rat retinas and evoke responses from its ganglion cells with properties similar to those evoked through pneumatic actuation.

Silicon is not a suitable microfabrication material for an implantable retinal prosthesis because of its mechanical rigidity. Peterman et al. (2003) investigated the use of PDMS/SU-8, which, as a softer material, would more easily conform to the curvature of a retina. They showed its application as such for an epiretinal implant in a New Zealand White rabbit. SU-8 has been used widely as a structural material for applications such as complex microfluidic devices, lab-on-a-chip systems, and biomedical implants (Sato et al., 2006; Chaudhri et al., 2010; Altuna et al., 2013). Unique and novel fabrication techniques like grayscale lithography, e-beam lithography, X-ray lithography, and holographic lithography can

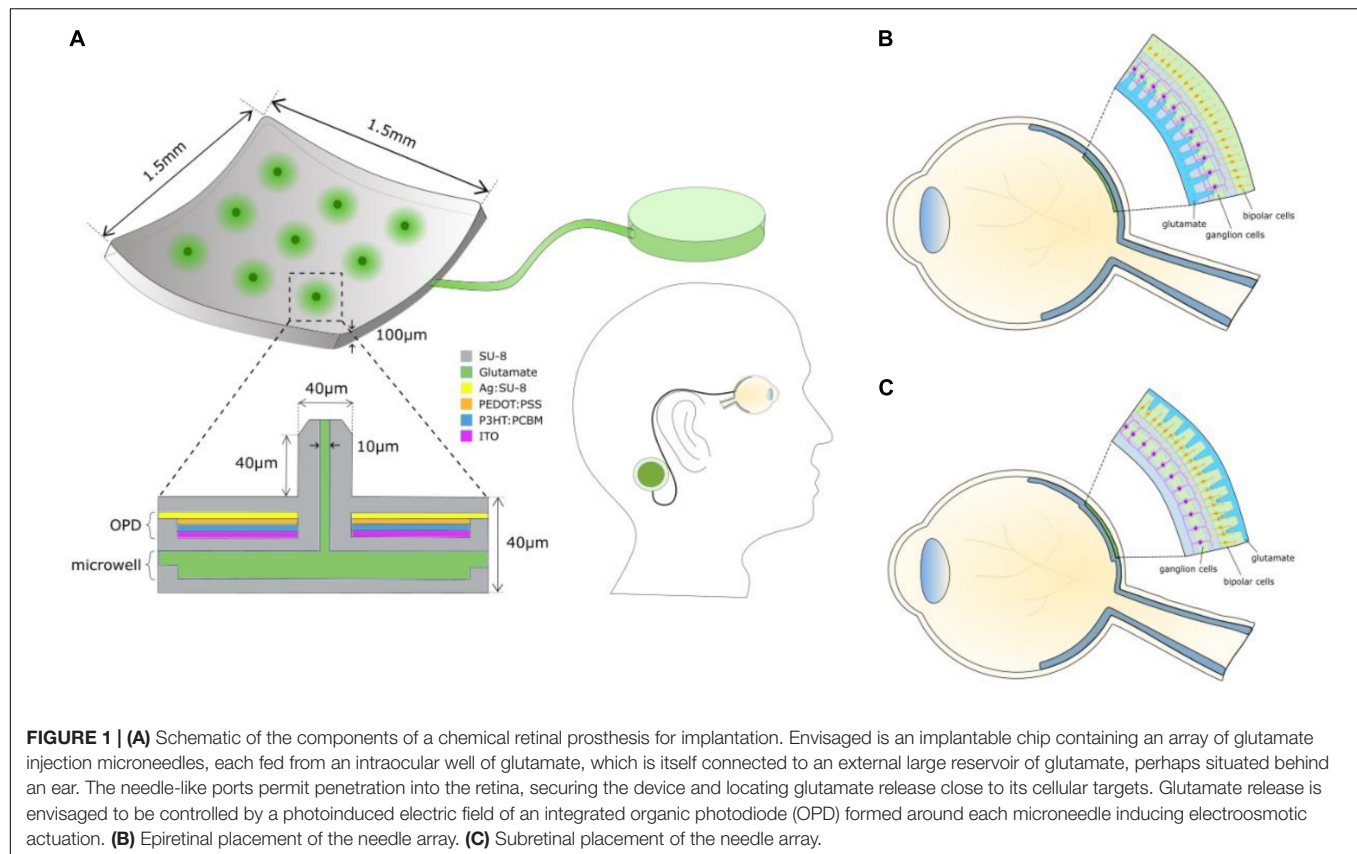


FIGURE 1 | (A) Schematic of the components of a chemical retinal prosthesis for implantation. Envisaged is an implantable chip containing an array of glutamate injection microneedles, each fed from an intraocular well of glutamate, which is itself connected to an external large reservoir of glutamate, perhaps situated behind an ear. The needle-like ports permit penetration into the retina, securing the device and locating glutamate release close to its cellular targets. Glutamate release is envisaged to be controlled by a photoinduced electric field of an integrated organic photodiode (OPD) formed around each microneedle inducing electroosmotic actuation. **(B)** Epiretinal placement of the needle array. **(C)** Subretinal placement of the needle array.

be used to generate sophisticated 3-D and ultra-high aspect ratio SU-8 microstructures with few processing steps (Bogdanov and Peredkov, 2000; Bilenberg et al., 2006; Rammohan et al., 2011; Lee et al., 2015). Bogdanov and Peredkov (2000) fabricated 100:1 aspect ratio SU-8 microstructures using X-ray lithography. Bilenberg et al. (2006) fabricated ~24 nm SU-8 nanochannels using e-beam lithography, and Rammohan et al. (2011) fabricated 3-D SU-8 microfluidic devices in a single step using grayscale lithography. So, the capacity to build small microfluidic systems with SU-8 has been well-established.

As demonstrated by Peterman et al. (2003), the mechanical flexibility of SU-8 is an advantage in fabricating biomedical implants. Tijero et al. (2009) developed flexible implantable SU-8 microprobes to monitor ischemia in rat kidneys. The development of flexible probes was necessary to minimize the loss of functionality due to micromotion between probe and tissue. The mechanical and electrical properties of SU-8 probes outperformed standard silicon and silicon carbide probes due to their flexibility. The processing costs and times were also lower for the development of SU-8 probes compared to silicon and silicon carbide probes. Huang et al. (2014) developed SU-8 neuroprobes for electrophysiological recordings and characterized the mechanical flexibility and biocompatibility both *in vitro* and *in vivo*. They concluded that the SU-8 neuroprobes not only withstood the resistance from brain tissue during surgical implantation but also possessed enough flexibility to prevent chronic tissue damage. Apart from SU-8 microprobes,

flexible 3-D SU-8 microfluidic devices have also been developed using lamination technology (Abgrall et al., 2006).

One potential area of concern for the design of a chemical retinal prosthesis is the space occupied by the reservoir for glutamate. However, preliminary calculations made by Inayat et al. (2015) suggest that an intraocular glutamate well (**Figure 1A**) with capacity for multi-day use would be possible, especially if located in the vitreal chamber. Moreover, whether glutamate is pooled for a subretinal or for an epiretinal prosthesis, replenishment of its well on a daily basis should work. **Figure 1A** envisages an external reservoir that would permit long-term glutamate dispensing and easy replenishment of the intraocular well.

BIOCOMPATIBILITY

The *in vitro* and *in vivo* biocompatibility of SU-8 have been thoroughly investigated. Kotzar et al. (2002) demonstrated the biocompatibility of SU-8 using cell culture models. Nemani et al. (2013) performed detailed *in vitro* and *in vivo* testing of the biocompatibility of SU-8 material. Cytotoxic tests, hemolytic assays, and agar diffusion assays have all demonstrated cell viability *in vitro*. SU-8 pads were implanted subcutaneously in mice for *in vivo* assessment of SU-8 biocompatibility. Based on these tests, the biocompatibility of SU-8 compares well to FDA approved implantable materials like silicone and medical steel.

Márton et al. (2020) assessed the biocompatibility of SU-8 devices implanted in the neocortex of rats. Based on their observations, SU-8 is a suitable implantable material for central nervous system tissue. Taken together, ease of fabrication, chemical stability, mechanical flexibility, and biocompatibility, SU-8 would appear to be a suitable material with which to fabricate a chemical retinal prosthesis.

STIMULATION OF RETINAL GANGLION CELLS WITH GLUTAMATE

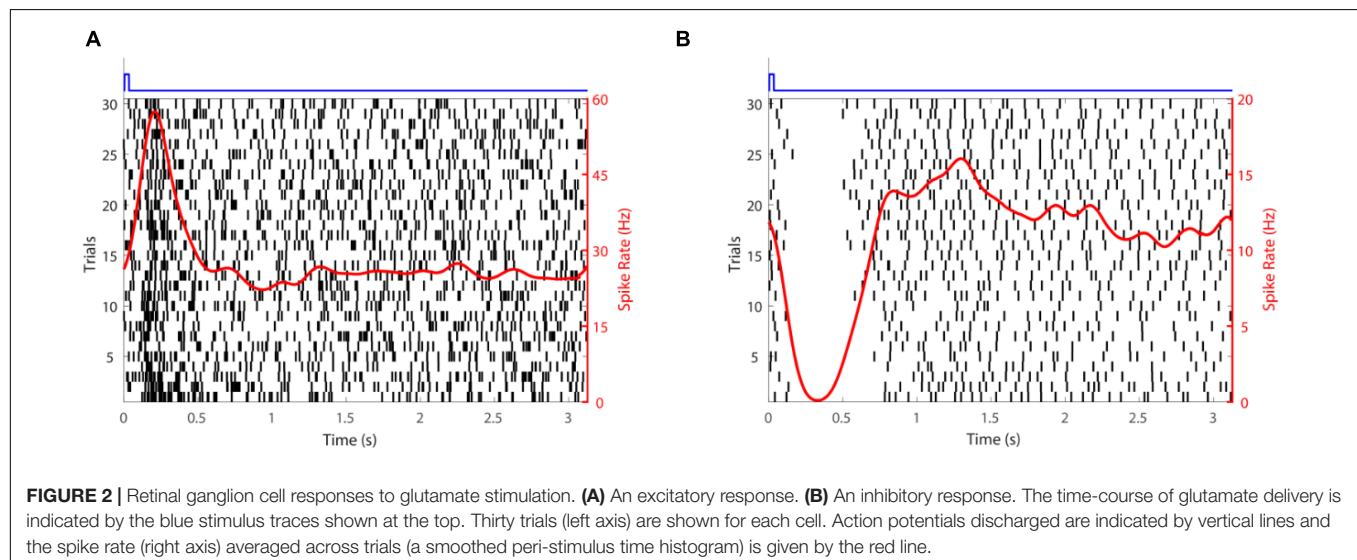
Glutamatergic stimulation of retinal ganglion cells has been accomplished to date through localized pulsatile dosing of the retina and this is how delivery of the neurotransmitter is envisaged for a chemical retinal prosthesis. This differs from the natural pattern of glutamate release by photoreceptors where the transmitter is released constantly in darkness and reduced by light. However, pulsatile release has been shown to evoke generally naturalistic spiking of retinal ganglion cells and has the benefit of limiting the quantity present in the retina of a potentially excitotoxic chemical.

The results of Finlayson and Iezzi (2010) indicated that epiretinal stimulation through glutamate often creates an initial suppression of retinal ganglion cell firing followed by excitation. However, for other retinal ganglion cells, glutamate stimulation was purely excitatory. Inayat et al. (2015) also report a complex mix of excitatory and inhibitory glutamate induced retinal ganglion cell responses with epiretinal stimulation. It seems likely that the inhibitory responses result from glutamate drive to amacrine cells which in turn provide GABAergic or glycinergic inhibitory drive to ganglion cells. The natural response of some retinal ganglion cells to visual stimulation is suppression of firing (Rodieck, 1967; Troy et al., 1989) so it would be incorrect to conclude that an inhibitory response from a ganglion cell to glutamate must imply inappropriate stimulation of the retinal output through glutamate. Nevertheless, the complex pattern of

responses of retinal ganglion cells to glutamate and the fact that, although less than the roughly forty types found in mouse (Baden et al., 2016; Rheaume et al., 2018), there are likely twenty or more types of ganglion cell in the human retina (Masri et al., 2019; Peng et al., 2019; Yan et al., 2020; Kim et al., 2022) throws into doubt the likelihood of evoking a fully naturalistic pattern of retinal ganglion cell activation from glutamate delivered through epiretinal placement.

NATURALISTIC STIMULATION

Subretinal placement would seem more likely to evoke a natural retinal response since the stimulation array seeks to replace photoreceptors and engage retinal circuits normally. **Figure 2** shows responses of two retinal ganglion cells to injection of glutamate subretinally. Given that glutamate excites OFF bipolar cells and inhibits ON bipolar cells (**Figure 3**), it was somewhat surprising that Rountree et al. (2016) found that the discharges of retinal ganglion cells in Hooded Sprague-Dawley rats showed an unexpected mix of excitatory and inhibitory responses to subretinal application of glutamate like that seen with epiretinal stimulation. The discharges of OFF retinal ganglion cells were depressed more often than those of ON or of ON-OFF retinal ganglion cells, so there was differential stimulation of the OFF and ON pathways but in a complex manner. It seems likely that the glutamate acted at its receptors on bipolar, amacrine and ganglion cells. Measurements of retinal local field potentials point to glutamate evoking responses in neurons of the inner nuclear layer (i.e., amacrine and bipolar cells). A similar pattern of subretinal differential (excitatory and inhibitory) stimulation of retinal ganglion cells has also been shown to occur in photoreceptor degenerate S334ter-3 rats. Preliminary investigation of subretinal stimulation with glutamate has also provided evidence of network-mediated responses in the photoreceptor degenerate rd1/rd1 mouse (Haq et al., 2018). Further investigation of how retinal circuits are



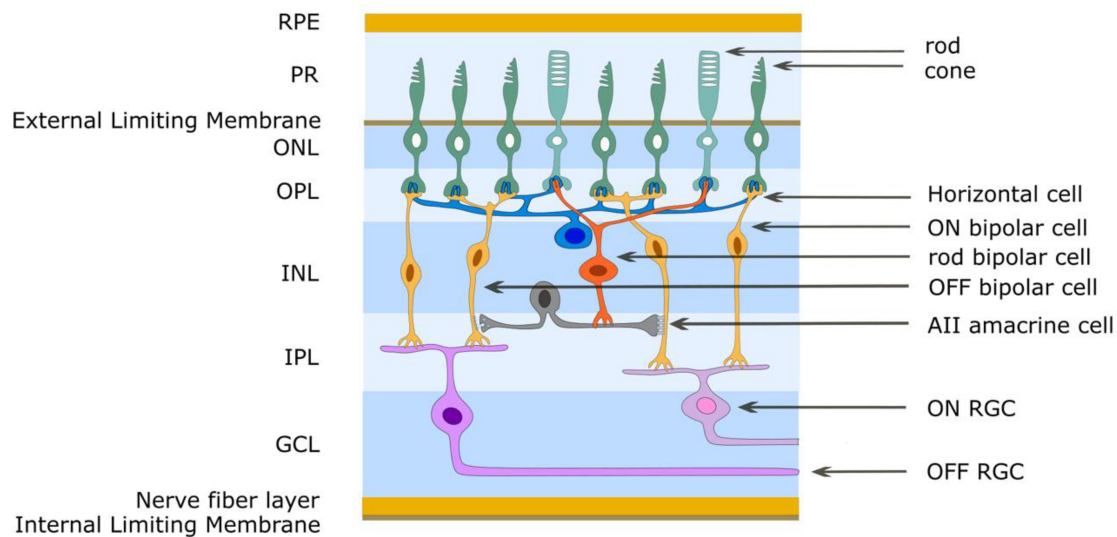


FIGURE 3 | Simplified schematic diagram of the OFF and ON retinal pathways. Glutamate is released from photoreceptor terminals in darkness in the outer plexiform layer and generates the OFF pathway by exciting OFF bipolar cells through ionotropic glutamate receptors. Glutamate acts on mGluR6 receptors of ON bipolar cells to create sign-inverting inhibitory responses, thus creating the ON pathway. Light reduces glutamate release from photoreceptors. The AII amacrine cell acts to create the OFF and ON pathways for rod-driven (scotopic) vision. The rod bipolar cell has mGluR6 receptors and gives an ON response to light. It also uses glutamate as its neurotransmitter and through ionotropic glutamate receptors depolarizes AII amacrine cells. This cell provides differential output to cone bipolar cells in the inner plexiform layer. ON cone bipolar cells are connected to the AII amacrine cell through gap junctions (excitatory) while OFF cone bipolar cells are connected to the AII amacrine cell by glycinergic (inhibitory) chemical synapses. RPE retinal pigment epithelium, PR photoreceptor outer segments, ONL outer nuclear layer, OPL outer plexiform layer, INL inner nuclear layer, IPL inner plexiform layer, GCL ganglion cell layer.

engaged both from epiretinal and subretinal sides is needed nevertheless for one to design a chemical prosthesis that could best mimic the retina's natural output.

The retina is known to reorganize its circuits after photoreceptor degeneration (**Figure 4**). Rodent models of retinal degeneration have been studied extensively (Strettoi and Pignatelli, 2000; Strettoi et al., 2002, 2003; Marc and Jones, 2003; Marc et al., 2007, 2008) and we also know something about how human retinas reform connections following photoreceptor loss. The animal models demonstrate that retinal degeneration passes through three stages: (1) neuronal death, (2) cell migration, and (3) circuit rewiring. Animals with cone-decimating degeneration lose their rods and cones during phase 1. In phase 2, the bipolar cells retract their dendrites and lose kainate (OFF bipolars) and mGluR6 (ON bipolars) responsivity; i.e., they become unresponsive to glutamate (but see Gayet-Primo and Puthussery, 2015). During phase 3, surviving bipolar, horizontal and amacrine cells generate anomalous sprouts which create novel synaptic connections with each other, thus rewiring retinal circuits. For animals with cone-sparing degeneration, cones outlive rods during phase 1. Some rod bipolar cells then create ectopic synapses with cones and transition from mGluR6 (ON) signaling to kainate/AMPA (OFF) signaling. As in cone-decimating degeneration, bipolar dendrites became atrophic during phase 2. But, sprouting from bipolar cells and synaptic rewiring in phase 3 is slowed because some rod bipolar cells remain in contact with cone pedicles. While studies of changes in photoreceptor degenerate human retina have been less extensive, the same general observations seem to hold

(Sullivan et al., 2007; Jones et al., 2012, 2016; Pfeiffer et al., 2020). While one might be inclined to believe that the inner retina is unaffected, cell migration of some retinal ganglion cells has been reported. One would be wise therefore to assume that post-photoreceptors retinal tissue has some significant differences from the physiological retina. Until a full characterization of the changes that occur for humans with photoreceptor degeneration and a means to define them for individual patients has been attained, it makes little sense to seek perfection in the design of a retinal prosthesis. The sound approach is to seek to drive retinal output as close to nature as possible and trust that higher levels of the visual system can learn to make sense of the signals generated. The fact that the patterns of glutamate activation in intact and photoreceptor degenerate rat models are seemingly similar offers hope that a chemical retinal prosthesis will function well for patients with photoreceptor loss.

One additional potential advantage of a chemical retinal prosthesis in the context of retinal remodeling following photoreceptor degeneration is that release of glutamate from the subretinal side might slow or counteract the processes driving remodeling. It would also be possible to corelease other chemical agents (e.g., trophic factors) that could guide the remodeling in a functional beneficent manner.

TEMPORAL RESOLUTION

Although this remains to be demonstrated with a retinal prosthesis, electrical stimulation of neurons is likely limited by

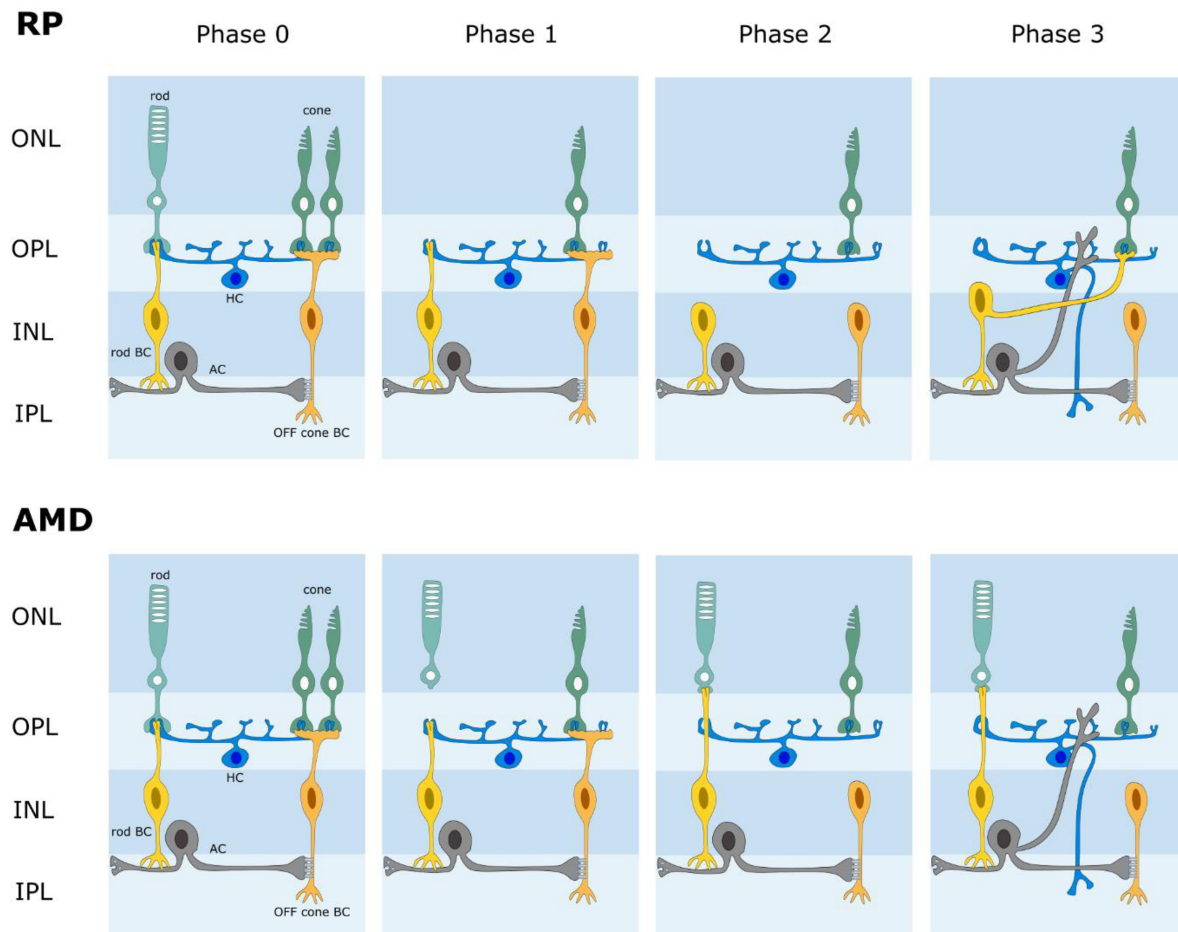


FIGURE 4 | Schematic diagram of retinal wiring stages following photoreceptor degeneration. AMD age-related macular degeneration. RP retinitis pigmentosa. In both AMD and RP, the retina undergoes a phased loss of cells and rewiring of its circuits. Phase 0 is normal retina. Phases 1–3 illustrate some changes that have been reported; i.e., photoreceptor loss, loss of connections between photoreceptors and bipolar cells, novel connections between rods and cone bipolar cells, retinal rewiring.

the refractoriness of their discharges. The ability to control the temporal frequency of chemical neural stimulation has more physical limitations. It takes time to dispense glutamate to its targets and time for those targets to respond. Early work by Finlayson and Iezzi (2010) suggested that activation rates with glutamate up to 3–5 Hz are possible. More recent work indicates that the range may be somewhat broader than this but still well below the critical flicker fusion frequency of photopic vision. Chemical retinal prostheses should have the temporal resolution to support visual tasks like reading but not those that require detection of rapid motion.

EXCITOTOXICITY

One of the main concerns for a prosthesis that dispenses glutamate to the retina is the known excitotoxicity of this chemical (Izumi et al., 1999; Delyfer et al., 2005; Kritsis et al., 2015). Excessive stimulation of glutamate receptors is known to cause cell death. The Müller cells of normal

retina uptake excess glutamate and convert it into non-toxic glutamine via glutamine synthetase (GS), then the glutamatergic neurons uptake the glutamine to synthesize glutamate (Riepe and Norenberg, 1978; Ishikawa, 2013; Liu et al., 2013). This glutamate-glutamine cycle allows neurons to avoid glutamate excitotoxicity. Inayat et al. (2015) estimated that the clearance rate for glutamate in a normal retina would be sufficient to avoid glutamate toxicity with a chemical retinal prosthesis. But, this estimate did not consider changes to the action of Müller cells in photoreceptor degenerate retina.

The normal retina expresses a low concentration of glutamate and high concentrations of glutamine and taurine in its Müller cells (Marc et al., 1995). At an early-stage of retinal degeneration, even before the initiation of photoreceptor loss, changes to this pattern of expression occur (Fletcher and Kalloniatis, 1996, 1997; Fletcher, 2000; Gibson et al., 2013; Pfeiffer et al., 2016). The immunoreactivities of glutamate and glutamine are both elevated in Müller cells, implying anomalous glutamate degradation. Hence, whether glutamate dispensed from a chemical retinal

prosthesis would be excitotoxic remains an open question needing further investigation.

NEXT STEPS

The next step in development of a chemical retinal prosthesis is to fabricate a microdevice that could be implanted in an animal model and test whether it can generate visual responses in cortical neurons (Frankowski et al., 2021) and behaviors indicative of visual perception (Feng et al., 2016). In this article, we have provided details of the materials that could be used for fabrication of such a device and a mechanism (electroosmosis) suitable for glutamate release. Additional investigation of how retinal neural circuits are modified in photoreceptor degeneration and how these modifications might affect glutamate driven retinal responses would help craft a prosthesis that maximizes the potential for visual restoration. *In vivo* testing of glutamate toxicity for an implanted device is needed too. We are entering an

exciting period for chemical retinal prosthesis development. After a long period of preliminary work, establishing feasibility and investigating the properties of retinal stimulation, the materials and mechanisms for microfabrication, the pieces seem now to be in place to build and test the first implantable device.

AUTHOR CONTRIBUTIONS

JW and JT conceived the idea and drafted the manuscript. PR, S-SK, CR, and JF made important contributions. JW and CR created the figures. JT led the overall work. All authors read and approved the submitted version.

FUNDING

This work was supported by NIH R21EB028069 to JF and JT.

REFERENCES

- Abgrall, P., Lattes, C., Conédéra, V., Dollat, X., Colin, S., and Gué, A. M. (2006). A novel fabrication method of flexible and monolithic 3D microfluidic structures using lamination of SU-8 films. *J. Micromech. Microeng.* 16:113.
- Altuna, A., Bellistri, E., Cid, E., Aivar, P., Gal, B., Berganzo, J., et al. (2013). SU-8 based microprobes for simultaneous neural depth recording and drug delivery in the brain. *Lab Chip* 13, 1422–1430. doi: 10.1039/c3lc41364k
- Baden, T., Berens, P., Franke, K., Rosón, M. R., Bethge, M., and Euler, T. (2016). The functional diversity of retinal ganglion cells in the mouse. *Nature* 529, 345–350. doi: 10.1038/nature16468
- Besch, D., Sachs, H., Szurman, P., Gülicher, D., Wilke, R., Reinert, S., et al. (2007). Extraocular surgery for implantation of an active subretinal visual prosthesis with external connections: feasibility and outcome in seven patients. *Br. J. Ophthalmol.* 92, 1361–1368. doi: 10.1136/bjo.2007.131961
- Bilenberg, B., Jacobsen, S., Schmidt, M. S., Skjolding, L. H., Shi, P., Bøggild, P., et al. (2006). High resolution 100 kV electron beam lithography in SU-8. *Microelectron. Eng.* 83, 1609–1612.
- Bogdanov, A. L., and Peredkov, S. S. (2000). Use of SU-8 photoresist for very high aspect ratio x-ray lithography. *Microelectron. Eng.* 53, 493–496.
- Chaudhri, B. P., Ceyssens, F., De Moor, P., Van Hoof, C., and Puers, R. (2010). A high aspect ratio SU-8 fabrication technique for hollow microneedles for transdermal drug delivery and blood extraction. *J. Micromech. Microeng.* 20:064006.
- Delyfer, V., Forster, M. N., Neveux, N., Picaud, S., Léveillard, T., and Sahel, J. A. (2005). Evidence for glutamate-mediated excitotoxic mechanisms during photoreceptor degeneration in the rd1 mouse retina. *Mol. Vision* 11, 688–696.
- DeVries, S. H. (2000). Bipolar cells use kainate and AMPA receptors to filter visual information into different channels. *Neuron* 28, 847–856. doi: 10.1016/s0896-6273(00)00158-6
- Feng, L., Chen, H., Yi, J., Troy, J. B., Zhang, H. F., and Liu, X. (2016). Long-term protection of retinal ganglion cells and visual function in mice with ocular hypertension. *Invest. Ophthalmol. Vis. Sci.* 57, 3793–3802.
- Finlayson, P. G., and Iezzi, R. (2010). Glutamate stimulation of retinal ganglion cells in normal and S334-ter3 rat retinas: a candidate for a neurotransmitter-based retinal prosthesis. *Invest. Ophthalmol. Vis. Sci.* 51, 3619–3628. doi: 10.1167/iovs.09-4877
- Fletcher, E. L. (2000). Alterations in neurochemistry during retinal degeneration. *Microsc. Res. Tech.* 50, 89–102. doi: 10.1002/1097-0029(20000715)50:2<89::AID-JEMT18>3.0.CO;2-9
- Fletcher, E. L., and Kalloniatis, M. (1996). Neurochemical architecture of the normal and degenerating rat retina. *J. Comp. Neurol.* 376, 343–360. doi: 10.1002/(SICI)1096-9861(19961216)376:3<343::AID-CNE18>3.0.CO;2-2
- Fletcher, E. L., and Kalloniatis, M. (1997). Neurochemical development of the degenerating rat retina. *J. Comp. Neurol.* 388, 1–22.
- Frankowski, J. C., Foik, A. T., Tierno, A., Machhor, J. R., Lyon, D. C., and Hunt, R. F. (2021). Traumatic brain injury to primary visual cortex causes long-lasting circuit dysfunction. *Commun. Biol.* 4:1297. doi: 10.1038/s42003-021-02808-5
- Gayet-Primo, J., and Puthussery, T. (2015). Alterations in kainate receptor and TRMP1 localization in bipolar cells after retinal photoreceptor degeneration. *Front. Cell. Neurosci.* 9:486. doi: 10.3389/fncel.2015.00486
- Gibson, R., Fletcher, E. L., Vingrys, A. J., Zhu, Y., Vessey, K. A., and Kalloniatis, M. (2013). Functional and neurochemical development in the normal and degenerating mouse retina. *J. Comp. Neurol.* 521, 1251–1267. doi: 10.1002/cne.23284
- Haq, W., Dietter, J., Bolz, S., and Zrenner, E. (2018). Feasibility study for a glutamate driven subretinal prosthesis: local subretinal application of glutamate on blind retina evoke network-mediated responses in different types of ganglion cells. *J. Neural Eng.* 15:045004. doi: 10.1088/1741-2552/aac811
- Huang, S. H., Lin, S. P., and Chen, J. J. (2014). In vitro and in vivo characterization of SU-8 flexible neuroprobe: from mechanical properties to electrophysiological recording. *Sens. Actuators A Phys.* 216, 257–265.
- Humayun, M. S., Dorn, J. D., da Cruz, L., Dagnelie, G., Sahel, J. A., Stanga, P. E., et al. (2012). Interim results from the international trial of second sight's visual prosthesis. *Ophthalmology* 119, 779–788. doi: 10.1016/j.ophtha.2011.09.028
- Iezzi, R., and Finlayson, P. G. (2011). “Neurotransmitter stimulation for retinal prosthesis: the artificial synapse chip,” in *Visual Prosthetics: Physiology, Bioengineering, Rehabilitation*, Chap. 9, ed. G. Dagnelie (Boston, MA: Springer), 173–191.
- Inayat, S., Rountree, C. M., Troy, J. B., and Saggere, L. (2015). Chemical stimulation of rat neurons: feasibility of an epiretinal neurotransmitter-based prosthesis. *J. Neural Eng.* 12:016010. doi: 10.1088/1741-2560/12/1/016010
- Ishikawa, M. (2013). Abnormalities in glutamate metabolism and excitotoxicity in the retinal diseases. *Scientifica* 2013:528940. doi: 10.1155/2013/528940
- Izumi, Y., Kirby, C. O., Benz, A. M., Olney, J. W., and Zorumski, C. F. (1999). Müller cell swelling, glutamate uptake, and excitotoxic neurodegeneration in the isolated rat retina. *Glia* 25, 379–389.
- Jones, B. W., Kondo, M., Terasaki, H., Lin, Y., McCall, M., and Marc, R. E. (2012). Retinal remodeling. *Jap. J. Ophthalmol.* 56, 289–306.
- Jones, B. W., Pfeiffer, R. L., Ferrell, W. D., Watt, C. B., Tucker, J., and Marc, R. E. (2016). Retinal remodeling and metabolic alterations in human AMD. *Front. Cell. Neurosci.* 10:103. doi: 10.3389/fncel.2016.00103
- Kare, S. S., Rountree, C. M., Troy, J. B., Finan, J. D., and Sagger, L. (2021). Neuromodulation using electroosmosis. *J. Neural Eng.* 18:046072. doi: 10.1088/1741-2552/ac00d3
- Kim, Y. J., Peterson, B. B., Crook, J. D., Joo, H. R., Wu, J., Puller, C., et al. (2022). Origins of directional selectivity in the primate retina. *Nat. Commun.* 13:2862. doi: 10.1038/s41467-022-30405-5

- Kotzar, G., Freas, M., Abel, P., Fleischman, A., Roy, S., Zorman, C., et al. (2002). Evaluation of MEMS materials of construction for implantable medical devices. *Biomaterials* 23, 2737–2750. doi: 10.1016/s0142-9612(02)00007-8
- Kritis, A. A., Stamoula, E. G., Paniskaki, K. A., and Vavilis, T. D. (2015). Researching glutamate – induced cytotoxicity in different cell lines: a comparative/collective analysis/study. *Front. Cell. Neurosci.* 9:91. doi: 10.3389/fncel.2015.00091
- Lee, J. B., Choi, K. H., and Yoo, K. (2015). Innovative SU-8 lithography techniques and their applications. *Micromachines* 6, 1–8.
- Liu, K., Wang, Y., Yin, Z., Weng, C., and Zeng, Y. (2013). Changes in glutamate homeostasis cause retinal degeneration in royal college of Surgeons rats. *Int. J. Mol. Med.* 31, 1075–1080. doi: 10.3892/ijmm.2013.1297
- MacLaren, R. E. (2017). Electronic retinal implant. *Eye* 31, 191–195.
- Marc, R. E., and Jones, B. W. (2003). Retinal remodeling in inherited photoreceptor degenerations. *Mol. Neurobiol.* 28, 139–148. doi: 10.1385/MN:28:2:139
- Marc, R. E., Jones, B. W., Anderson, J. R., Kinard, K., Marshak, D. W., Wilson, J. H., et al. (2007). Neural reprogramming in retinal degeneration. *Invest. Ophthalmol. Vis. Sci.* 48, 3364–3371. doi: 10.1167/iov.07-0032
- Marc, R. E., Jones, B. W., Watt, C. B., Vazquez-Chona, F., Vaughan, D. K., and Organisciak, D. T. (2008). Extreme retinal remodeling triggered by light damage: implications for age related macular degeneration. *Mol. Vision* 14, 782–806.
- Marc, R. E., Murry, R. F., and Basinger, S. F. (1995). Pattern recognition of amino acid signatures in retinal neurons. *J. Neurosci.* 15, 5106–5129. doi: 10.1523/JNEUROSCI.15-07-05106.1995
- Márton, G., Tóth, E. Z., Wittner, L., Fiáth, R., Pinke, D., Orbán, G., et al. (2020). The neural tissue around SU-8 implants: a quantitative in vivo biocompatibility study. *Mater. Sci. Eng. C* 112:110870. doi: 10.1016/j.msec.2020.110870
- Masri, R. A., Percival, K. A., Koizumi, A., Martin, P., and Grunert, U. (2019). Survey of retinal ganglion cell morphology in marmoset. *J. Comp. Neurol.* 527, 236–258. doi: 10.1002/cne.24157
- Nemani, K. V., Moodie, K. L., Brennick, J. B., Su, A., and Gimi, B. (2013). In vitro and in vivo evaluation of SU-8 biocompatibility. *Mater. Sci. Eng. C* 33, 4453–4459. doi: 10.1016/j.msec.2013.07.001
- Peng, Y. R., Shekhar, K., Yan, W., Herrmann, D., Sappington, A., Bryman, G. S., et al. (2019). Molecular classification and comparative taxonomies of foveal and peripheral cells in primate retina. *Cell* 176, 1222–1237. doi: 10.1016/j.cell.2019.01.004
- Peterman, M. C., Mehenti, M. Z., Bilbao, K. V., Lee, C. J., Leng, T., Noolandi, J., et al. (2003). The artificial synapse chip: a flexible retinal interface on directed retinal cell growth and neurotransmitter stimulation. *Artif. Organs* 27, 975–985. doi: 10.1046/j.1525-1594.2003.07307.x
- Peterman, M. C., Noolandi, J., Blumenkranz, M. S., and Fishman, H. A. (2004). Fluid flow past an aperture in a microfluidic channel. *Anal. Chem.* 76, 1850–1856. doi: 10.1021/ac035154m
- Pfeiffer, R. L., Marc, R. E., and Jones, B. W. (2020). Persistent remodeling and neurodegeneration in late-stage retinal degeneration. *Prog. Retin. Eye Res.* 74:100771. doi: 10.1016/j.preteyeres.2019.07.004
- Pfeiffer, R. L., Marc, R. E., Kondo, M., Terasaki, H., and Jones, B. W. (2016). Müller cell metabolic chaos during retinal degeneration. *Exp. Eye Res.* 150, 62–70. doi: 10.1016/j.exer.2016.04.022
- Pinto, L. H., Vitaterna, M. H., Shimomura, K., Siepka, S. M., McDermott, E. L., Balannik, V., et al. (2007). Generation, identification and functional characterization of the nob4 mutation of Grm6 in the mouse. *Vis. Neurosci.* 24, 111–123. doi: 10.1017/S0952523807070149
- Rammohan, A., Dwivedi, P. K., Martinez-Duarte, R., Katepalli, H., Madou, M. J., and Sharma, A. (2011). One-step maskless grayscale lithography for the fabrication of 3-dimensional structures in SU-8. *Sens. Actuators B Chem.* 153, 125–134.
- Rheume, B. A., Jereen, A., Bolisetty, M., Sajid, M. S., Yang, Y., Renna, K., et al. (2018). Single cell transcriptome profiling of retinal ganglion cells identifies cellular subtypes. *Nat. Commun.* 9:2759.
- Riepe, R. E., and Norenberg, M. D. (1978). Glutamine synthetase in the developing rat retina: an immunohistochemical study. *Exp. Eye Res.* 27, 435–444. doi: 10.1016/0014-4835(78)90022-2
- Rodieck, R. W. (1967). Receptive fields in the cat retina: a new type. *Science* 157, 90–92. doi: 10.1126/science.157.3784.90
- Rountree, C. M., Inayat, S., Troy, J. B., and Saggere, L. (2016). Differential stimulation of the retina with subretinally injected exogenous neurotransmitter: a biomimetic alternative to electrical stimulation. *Sci. Rep.* 6:38505. doi: 10.1038/srep38505
- Rountree, C. M., Raghunathan, A., Troy, J. B., and Saggere, L. (2017a). A prototype chemical synapse chip for spatially patterned neurotransmitter stimulation of the retina ex vivo. *Microsyst. Nanoeng.* 3:17052. doi: 10.1038/micronano.2017.52
- Rountree, C. M., Troy, J. B., and Saggere, L. (2017b). A methodology for in vitro biomimetic chemical neuromodulation of rat retinas with the neurotransmitter glutamate. *J. Vis. Exp.* 130:e56645.
- Rountree, C. M., Troy, J. B., and Saggere, L. (2018). Microfluidics-based subretinal chemical neuromodulation of photoreceptor degenerated retinas. *Invest. Ophthalmol. Vis. Sci.* 59, 418–430. doi: 10.1167/iov.17-23142
- Rountree, C. M., Troy, J. B., and Saggere, L. (2020). Investigation of injection depth for subretinal delivery of exogenous glutamate to restore vision via biomimetic chemical neuromodulation. *IEEE Trans. Biomed. Eng.* 67, 464–470. doi: 10.1109/TBME.2019.2915255
- Sato, H., Matsumura, H., Keino, S., and Shoji, S. (2006). An all SU-8 microfluidic chip with built-in 3D fine microstructures. *J. Micromech. Microeng.* 16:2318.
- Stretto, E., and Pignatelli, V. (2000). Modifications of retinal neurons in a mouse model of retinitis pigmentosa. *Proc. Natl. Acad. Sci. U.S.A.* 97, 11020–11025. doi: 10.1073/pnas.190291097
- Stretto, E., Pignatelli, V., Rossi, C., Porciatti, V., and Falsini, B. (2003). Remodeling of second-order neurons in the retina of rd/rd mutant mice. *Vision Res.* 43, 867–877. doi: 10.1016/s0042-6989(02)00594-1
- Stretto, E., Porciatti, V., Falsini, B., Pignatelli, V., and Rossi, C. (2002). Morphological and functional abnormalities in the inner retina of the rd/rd mouse. *J. Neurosci.* 22, 5492–5504. doi: 10.1523/JNEUROSCI.22-13-05492.2002
- Strickland, E., and Harris, M. (2022). *Their Bionic Eyes are now Obsolete and Unsupported*, 2nd Edn. New York, NY: IEEE Spectrum.
- Sullivan, R. K. P., Woldemussie, E., and Pow, D. V. (2007). Dendritic and synaptic plasticity of neurons in the human age-related macular degeneration retina. *Invest. Ophthalmol. Vis. Sci.* 48, 2782–2791. doi: 10.1167/iov.06-1283
- Tijero, M., Gabriel, G., Caro, J., Altuna, A., Hernández, R., Villa, R., et al. (2009). SU-8 microprobe with microelectrodes for monitoring electrical impedance in living tissues. *Biosens. Bioelectron.* 24, 2410–2416. doi: 10.1016/j.bios.2008.12.019
- Troy, J. B. (2015). Visual prostheses: technological and socioeconomic challenges. *Engineering* 1, 288–291.
- Troy, J. B., Einstein, G., Schuurmans, R. P., Robson, J. G., and Enroth-Cugell, C. (1989). Responses to sinusoidal gratings of two types of rarely encountered retinal ganglion cells of cat. *Vis. Neurosci.* 3, 213–223.
- Whitaker, C. M., Nobles, G., Ishibashi, M., and Massey, S. C. (2021). Rod and cone connections with bipolar cells in the rabbit retina. *Front. Cell. Neurosci.* 15:662329. doi: 10.3389/fncel.2021.662329
- Yan, W., Peng, Y. R., van Zyl, T., Regev, A., Shekhar, K., Juric, D., et al. (2020). Cell atlas of the human fovea and peripheral retina. *Sci. Rep.* 10:9802. doi: 10.1038/s41598-020-66092-9
- Zheng, X. S., Tan, C., Castagnola, E., and Cui, X. T. (2021). Electrode materials for chronic electrical microstimulation. *Adv. Healthcare Mater.* 10:2100119. doi: 10.1002/adhm.202100119

Conflict of Interest: The authors declare that the research was conducted in the absence of any commercial or financial relationships that could be construed as a potential conflict of interest.

Publisher's Note: All claims expressed in this article are solely those of the authors and do not necessarily represent those of their affiliated organizations, or those of the publisher, the editors and the reviewers. Any product that may be evaluated in this article, or claim that may be made by its manufacturer, is not guaranteed or endorsed by the publisher.

Copyright © 2022 Wu, Rountree, Kare, Ramkumar, Finan and Troy. This is an open-access article distributed under the terms of the Creative Commons Attribution License (CC BY). The use, distribution or reproduction in other forums is permitted, provided the original author(s) and the copyright owner(s) are credited and that the original publication in this journal is cited, in accordance with accepted academic practice. No use, distribution or reproduction is permitted which does not comply with these terms.



Stage-Dependent Changes of Visual Function and Electrical Response of the Retina in the *rd10* Mouse Model

Seongkwang Cha^{1†}, Jungryul Ahn^{1†}, Yurim Jeong¹, Yong Hee Lee², Hyong Kyu Kim³, Daekee Lee⁴, Yongseok Yoo^{5*} and Yong Sook Goo^{1*}

¹ Department of Physiology, Chungbuk National University School of Medicine, Cheongju, South Korea, ² Department of Biochemistry, Chungbuk National University School of Medicine, Cheongju, South Korea, ³ Department of Microbiology, Chungbuk National University School of Medicine, Cheongju, South Korea, ⁴ Department of Life Science, Ewha Womans University, Seoul, South Korea, ⁵ Department of Electronics Engineering, Incheon National University, Incheon, South Korea

OPEN ACCESS

Edited by:

Günther Zeck,
Vienna University of Technology,
Austria

Reviewed by:

Tamas Kovács-Öller,
University of Pécs, Hungary
William Grimes,
National Institutes of Health (NIH),
United States

*Correspondence:

Yongseok Yoo
yyoo@inu.ac.kr
Yong Sook Goo
ysgoo@chungbuk.ac.kr

[†] These authors have contributed
equally to this work and share first
authorship

Specialty section:

This article was submitted to
Cellular Neurophysiology,
a section of the journal
Frontiers in Cellular Neuroscience

Received: 22 April 2022

Accepted: 23 June 2022

Published: 19 July 2022

Citation:

Cha S, Ahn J, Jeong Y, Lee YH,
Kim HK, Lee D, Yoo Y and Goo YS
(2022) Stage-Dependent Changes
of Visual Function and Electrical
Response of the Retina in the *rd10*
Mouse Model.
Front. Cell. Neurosci. 16:926096.
doi: 10.3389/fncel.2022.926096

One of the critical prerequisites for the successful development of retinal prostheses is understanding the physiological features of retinal ganglion cells (RGCs) in the different stages of retinal degeneration (RD). This study used our custom-made *rd10* mice, C57BL/6-*Pde6b*^{em1(R560C)Dkl}/Korl mutated on the *Pde6b* gene in C57BL/6J mouse with the CRISPR/Cas9-based gene-editing method. We selected the postnatal day (P) 45, P70, P140, and P238 as representative ages for RD stages. The optomotor response measured the visual acuity across degeneration stages. At P45, the *rd10* mice exhibited lower visual acuity than wild-type (WT) mice. At P140 and older, no optomotor response was observed. We classified RGC responses to the flashed light into ON, OFF, and ON/OFF RGCs via *in vitro* multichannel recording. With degeneration, the number of RGCs responding to the light stimulation decreased in all three types of RGCs. The OFF response disappeared faster than the ON response with older postnatal ages. We elicited RGC spikes with electrical stimulation and analyzed the network-mediated RGC response in the *rd10* mice. Across all postnatal ages, the spikes of *rd10* RGCs were less elicited by pulse amplitude modulation than in WT RGCs. The ratio of RGCs showing multiple peaks of spike burst increased in older ages. The electrically evoked RGC spikes by the pulse amplitude modulation differ across postnatal ages. Therefore, degeneration stage-dependent stimulation strategies should be considered for developing retinal prosthesis and successful vision restoration.

Keywords: retinal ganglion cell, retinal degeneration, retinal prosthesis, optomotor response, multichannel recording

INTRODUCTION

Retinal prostheses for the blinds have received considerable attention. Patients with retinitis pigmentosa (RP) lose sight due to a gradual loss of photoreceptors in the outer nuclear layer (ONL) (Hartong et al., 2006). On the other hand, inner retinal neurons such as bipolar cells (BCs) or retinal ganglion cells (RGCs) remain preserved compared with photoreceptors (Stone et al., 1992;

Kim et al., 2002; Mazzoni et al., 2008). For patients with RP, retinal prostheses have successfully elicited phosphenes by electrically activating inner retinal neurons in the degenerate retina (Stingl et al., 2015; Luo and da Cruz, 2016). However, retinal prostheses have limited performance in clinical trials, resulting in poor visual acuity (less than 20/420) in device-implanted patients (Ayton et al., 2020; Im and Kim, 2020).

Among genetic models for human RP, the retinal degeneration (RD) 10 (*rd10*) mouse is a widely used animal model due to their delayed onset and slower progression of RD than *rd1* mice (Chang et al., 2002; Chang et al., 2007). Although the afferent nerve connection between the retina and the brain is maintained, histological and physiological changes appear in the remaining neurons with the progress of RD. The progress of RD distinguishes into three phases: Phase I: rod degeneration, Phase II: cone degeneration, and Phase III: remodeling of the remnant retinal network (Marc et al., 2003). Age-dependent histological changes were well investigated in the *rd10* mouse retinal neurons such as rods, cones, BCs, horizontal cells (HCs), amacrine cells (ACs), and RGCs (Chang et al., 2007; Gargini et al., 2007; Barhoum et al., 2008; Mazzoni et al., 2008; Phillips et al., 2010; Murakami et al., 2012; Pennesi et al., 2012; Li et al., 2019). In *rd10* mice, RD initiates around Postnatal day (P)18–20 due to the progressive death of rod photoreceptors, and the rod photoreceptor loss lasts until P45–70. Although the somas of cone photoreceptors preserve until P270–285, the degeneration of cone photoreceptors' outer and inner segments occurs before P70. Twenty percent of rod bipolar cells (RBCs) decrease between P45 and P105. Thirty-nine percent of HCs decrease between P45 and P270. Nevertheless, RGCs do not show significant changes until nine months of age.

In contrast to these histological studies, electrophysiological studies regarding electrically evoked RGC responses according to the degeneration stages are still insufficient. A few studies reported the light-driven RGC response or electrically evoked RGC response up to P60 in *rd10* mice (Stasheff et al., 2011; Yoon et al., 2020). These studies use limited postnatal days since they first classified the RGC types based on the light-driven response, then followed up on the RGC type-specific electrical response. However, our previous study using up to P238 *rd10* mice focused on the changes of a burst pattern of RGCs. From P14 to P30, electrically evoked RGC spikes show a single burst like WT, while multiple bursts appear around P45, and the frequency of multiple bursts slows down after P70 (P70 to P238) (Goo et al., 2011b, 2016; Park et al., 2015). Therefore, guided by histological and electrophysiological changes, we selected P30, P45, P70, P140, and P238 as representative ages for RD stages.

In this study, we observed the degeneration stage-dependent change of visual function and RGC responsiveness to light stimulation with our custom-made *rd10* mice, C57BL/6-*Pde6b*^{em1(R560C)Dkl}/Korl mutated on the *Pde6b* gene in C57BL/6J mouse with CRISPR/Cas9-based gene-editing method. In addition, we investigated the degeneration stage-dependent change of network-mediated responses of RGCs to electrical stimulation.

MATERIALS AND METHODS

Animals

This study was approved by the Institutional Animal Care and Use Committee of the Chungbuk National University (approval number: CBNUA-1520-21-01). All procedures followed the guidelines of the Association for Research in Vision and Ophthalmology Statement for the Use of Animals in Ophthalmic and Vision Research. In this study, we used newly established *rd10* mice (C57BL/6-*Pde6b*^{em1(R560C)Dkl}/Korl strain). The *rd10* mice in a genetically heterozygous state were obtained from the National Institute of Food and Drug Safety Evaluation (NIFDS, Cheongju, South Korea). The heterozygotes were bred to produce the homozygotes. Among the pups, we selected only homozygotes and used them for this study. Remained homozygotes were bred with C57BL/6J mice (Raonbio, Yongin, South Korea) to maintain heterozygotes. All mice were housed under a 12-h day/night cycle under standard conditions. The wild-type (WT) mice (C57BL/6J mice) were used as control. We used adult WT mice (around P70), considering the maturation of retinal tissue. Furthermore, we used *rd10* mice of P30, P45, P70, P140, and P238, considering their degeneration stages based on histological studies (Gargini et al., 2007; Pennesi et al., 2012) and our previous study (Park et al., 2015; Goo et al., 2016). For enucleation of the eye, mice were anesthetized with an intramuscular injection of 30 mg/kg of tiletamine-zolazepam hydroxide (Zoletil 50; Virbac, Sao Paulo, Brazil), 10 mg/kg of xylazine hydrochloride (Rumpun; Bayer Korea, Seoul, South Korea), and 5,000 IU of heparin sodium (heparin; JW Pharmaceutical Corp., Seoul, South Korea).

Generation and Genotyping of *rd10* Mouse

Using standard procedures, one-cell embryos were obtained from superovulated C57BL/6J (B6) female mice mated with B6 male mice. Cas9 mRNA and *Pde6b* sgRNA were prepared as described previously (Oh et al., 2021). The target sequence for *Pde6b* sgRNA is 5'-GCCGTGGCGCCAGTTGTGTTAGG-3' (underline indicates PAM sequence) (**Supplementary Figure 1A**). The oligodeoxynucleotides (ODNs, 5'-CTAGCCCATC CAATTTACATACGTACCATGAGTAGGGTAAACATGGTCTG GGCTACATTGAAGCCGTGGCACC AATTATGATACGTGAT TCTTCGATAGGCTTTGCTGACAGAGAA-TAGAAAGCGCA CCAAGACCTGGGGAGCAGAGTAC-3') contained codon 560 Arg (CGC) replaced by the Cys (TGC) sequence to introduce the desired knockin of mutation R560C with extra four silence mutations and overlapping the *Pde6b* exon 13 region for homologous recombination. We microinjected a mixture of 20 µg/ml sgRNA, 100 µg/ml ODNs, and 10 µg/ml Cas9 mRNA in 10 mM Tris-HCl, pH 7.4, and 0.1 mM EDTA into the pronucleus of one-cell eggs and transferred survived one-cell embryos into the pseudopregnant ICR females. Initial screening of F0 knockin mutants was analyzed by agarose gel electrophoresis of PCR product after restriction digestion with HhaI (**Supplementary Figure 1B**). Only mutant mice were

further crossed with B6 mice, and the exact sequence of knockin mutation was verified by sequencing after TA cloning of PCR product from F1 heterozygous mice (**Supplementary Figure 1C**). The heterozygotes mice were maintained by backcrossing with B6 mice for 2 to 3 more generations before interbreeding.

To routinely genotype the pups of *rd10* heterozygotes, we modified PCR primers as shown in **Figure 1A**. We extracted genomic DNA from the tail end of mice under P28. Briefly, 1 mm of the tail was incubated for 30 min at 95°C in an alkaline lysis buffer [25 mM NaOH (Sigma, Saint Louis, United States) and 0.2 mM EDTA (WELGENE, Gyeongsan, South Korea), pH 12]. After lysis, the samples were cooled at room temperature for 3 min and then a neutralization buffer [40 mM Tris-HCl (BioShop Canada Inc, Burlington, ON, Canada), pH 5.0] was added in a 1:1 ratio. The samples were centrifuged at 13,000 rpm for 2 min to separate only supernatants containing genomic DNA. After extracting genomic DNA, we amplified only 350 bp of PCR products, including the mutant point of exon 13 of the *Pde6b* gene (**Figure 1A**). The PCR was performed with 1 µg of the supernatant containing genomic DNA, and Maxime™ PCR PreMix (i-StarTaq, iNtRON Biotechnology, Seongnam, South Korea), primer mixture 10 pmol (Forward: 5'-AGCAGTATGAGAGGCTTGGA-3' and

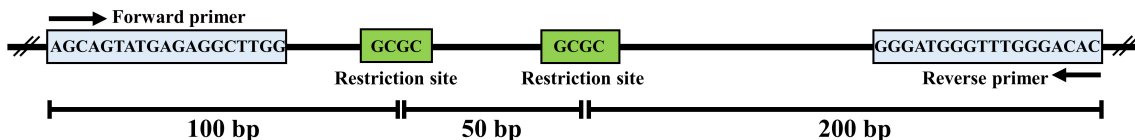
Reverse: 5'-GTGTCCCAAACCCATCCCTT-3') according to the following protocol: 1) initial denaturation at 95°C for 5 min, 2) 35 cycles of denaturation at 94°C for 30 s, annealing at 61°C for 30 s, and extension at 72°C for 1 min and final extension at 72°C for 5 min. PCR products were confirmed by electrophoresis in a 3% agarose gel (iNtRON Biotechnology, Seongnam, South Korea) (**Figure 1B**). Finally, to judge the allele, we digested the PCR products with 14 units of HhaI (New England Biolabs, Ipswich, MA, United States) restriction enzymes that recognize the sequence of 5'-GCGC-3'. The DNA fragments were confirmed by electrophoresis in a 3% agarose gel (**Figure 1C**).

Immunohistochemistry

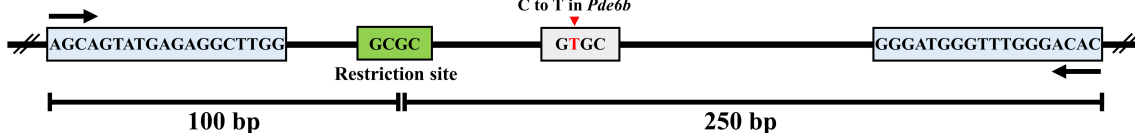
Four WT mice (at P70) and 20 *rd10* mice (at P30, P45, P70, P140, and P238) were used for immunohistochemistry. We took 30-µm retinal sections in the 4% agarose embedding (Sigma-Aldrich, Saint Louis, MO, United States) after fixation with ice-cold 4% paraformaldehyde (PFA) (Biosesang, Seongnam, South Korea). The retinal sections were blocked with 4% normal goat serum (NGS) (Vector Laboratories, Inc., Burlingame, CA, United States) in 0.5% Triton X-100 (Sigma-Aldrich, Saint Louis, MO, United States) solution for 12 h, followed by incubation with each primary antibody at 4°C overnight. The primary antibodies

A *Pde6b* (phosphodiesterase 6B) in Chromosome 5, missense mutation in exon 13

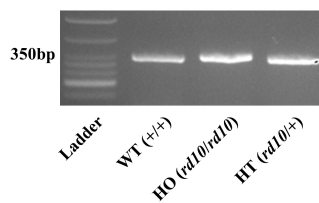
Pde6b-wild type



Pde6b-*rd10*



B



C

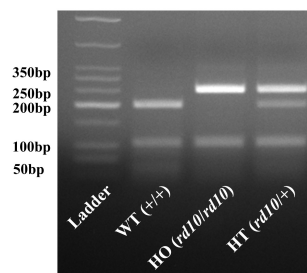


FIGURE 1 | Genotyping of C57BL/6-*Pde6b*^{em1(R560C)Dkl/Korl} knockin mice. **(A)** The structures of the *Pde6b*-wild type allele and *Pde6b*-*rd10* allele are shown. Mutation point exists in exon 13 of rod phosphodiesterase gene (*Pde6b*) located on chromosome five of wild-type (WT) mouse (C57BL/6J). The mutation point (C to T in *Pde6b*) is presented by the red arrow. The primer binding sites are represented by the blue box. The restriction sites of Hha I are represented by the green box. **(B)** All PCR products of *Pde6b* from three different mice, wild-type (WT) (+/+), HO (*rd10/rd10*), and HT (*rd10/+*), have the same size as 350bp. **(C)** Digestion of PCR products with Hha I yielded 3, 2, and 4 DNA fragments in WT (+/+), HO (*rd10/rd10*), and HT (*rd10/+*) samples, respectively.

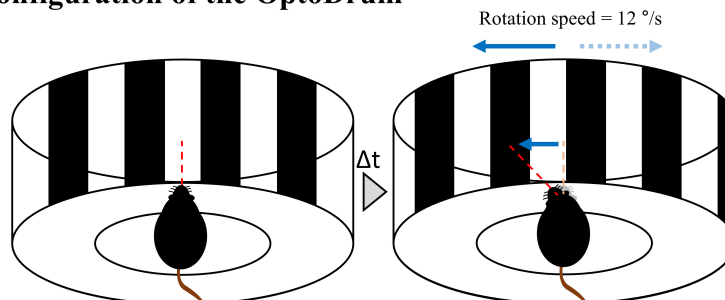
were anti-rabbit opsin antibody, Red/Green (1:200, #AB5405, Merck Millipore, Saint Louis, MO, United States), anti-mouse rhodopsin antibody (1:200, #O4886, Merck Millipore, Saint Louis, MO, United States), and anti-mouse glutamine synthetase (GS) antibody (1:200, #MAB302, Merck Millipore, Saint Louis, MO, United States). After incubation with primary antibodies, the secondary antibodies were treated in the retinal sections at 4°C for 2 h. The secondary antibodies were Alexa Fluor® 488 AffiniPure Goat Anti-Mouse IgG (1:500, #111-545-146, Jackson ImmunoResearch Inc., West Grove, PA, United States)

and Alexa Fluor® 647 AffiniPure Goat Anti-Rabbit IgG (1:500, #111-605-144, Jackson ImmunoResearch Inc., West Grove, PA, United States). The fluorescence image was captured using confocal microscopy (LSM800, Zeiss, Jena, Germany).

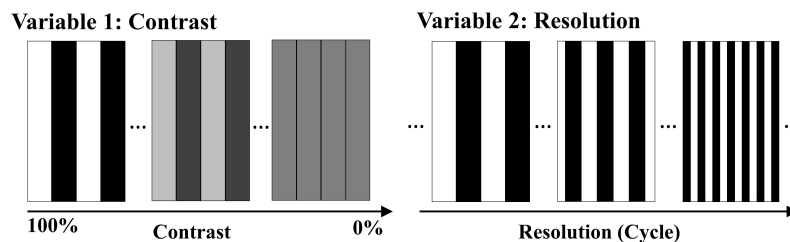
Optomotor Response

The optomotor response was evaluated using the Optodrum (Striatech GmbH, Tübingen, Germany). The mouse was positioned on an elevated stage at the height of 14.5 cm, which was placed in the center of the Optodrum (Figure 2).

A The configuration of the OptoDrum



B Protocols of light stimulation



C Success determination of optomotor response

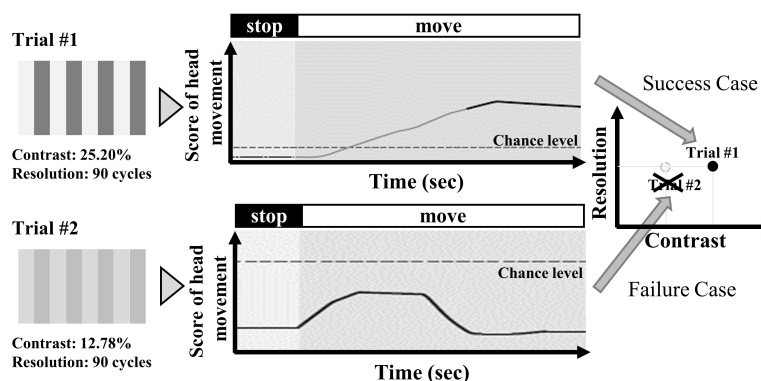
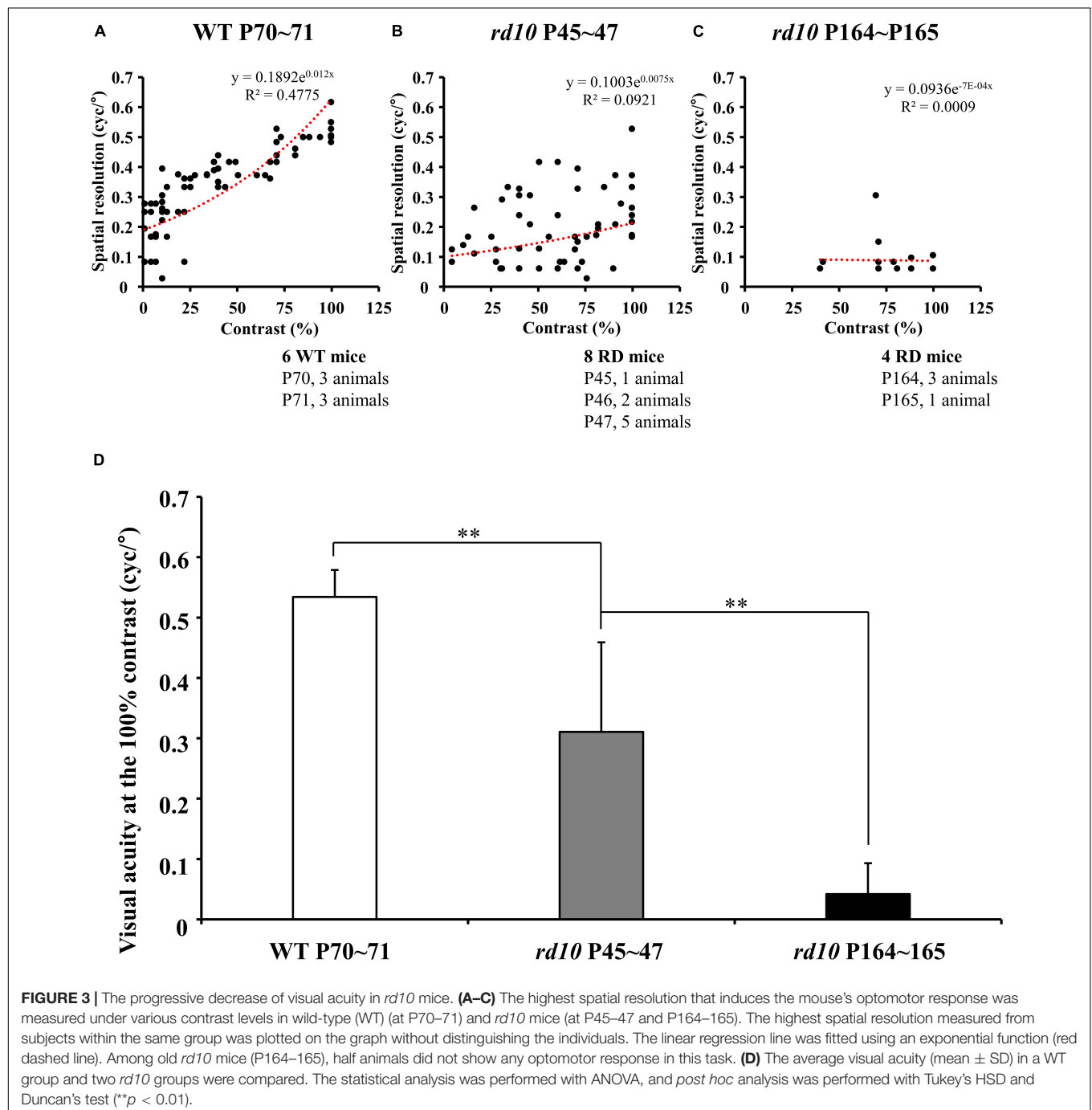


FIGURE 2 | Experimental setup for optomotor response. **(A)** The mouse is located in a virtual rotating drum center with a black and white stripe. The drum rotates clockwise or counterclockwise with 12°/s of velocity. **(B)** The stripe pattern of the virtual rotating drum can be modulated in terms of relative contrast between black and white bar and spatial resolution. The contrast changes from 100% (black = #000000 (Hex code color of RGB) and white = #FFFFFF) to 0% (black = #808080 and white = #808080). The spatial resolution changes from 0 cyc/° (cycles per degree) to 0.7 cyc/°. **(C)** Among experimental trials, the successful trial of optomotor response is determined if the head movement score exceeds the chance level of the stimulus-independent head motion.

The walls of the Optodrum consisted of four LCD monitors, and the ceiling and floor included mirrors. The stimulation presented on monitors formed a virtual rotating drum with the black-and-white stripe pattern (radiance = $2 \text{ W} \cdot \text{sr}^{-1} \cdot \text{m}^{-2}$). An automatically controlled tracking system centered the virtual rotating drum over the mouse's head. The virtual drum rotates clockwise or counterclockwise with $12^\circ/\text{s}$ of velocity. The stimulation was applied for at least 1 s and ended either after at most 7.5 s, or when the animal became restless and started walking around. Among experimental trials, the successful trial

of optomotor response was determined if the head movement score exceeded the chance level of the stimulus-independent head movement, which the algorithm of Optodrum provided (Benkner et al., 2013). Regarding the two parameters, contrast and spatial resolution, when we fix the contrast level, the spatial resolution (cycles per degree) was changed and vice versa. All the successful trials at either the lowest contrast level or highest spatial resolution were plotted on the graph of contrast versus spatial resolution (Figure 3). From this graph, we drew the linear regression curve, representing the visual acuity.



More details can be found in the manufacturer's publication (Benkner et al., 2013).

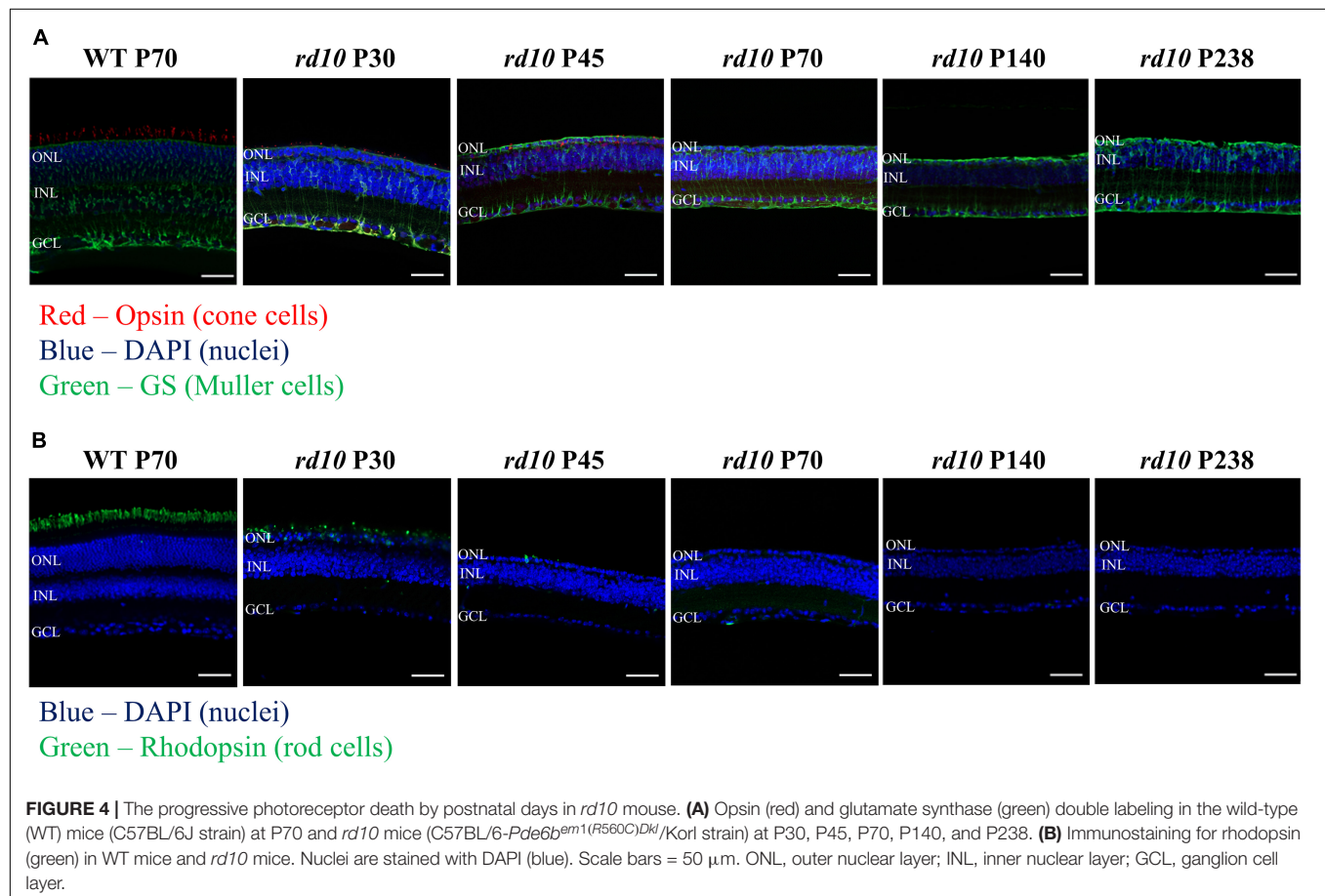
Electrophysiological Recording With Multi-Electrode Array

In vitro recording of RGC activities was performed as follows: The lens and vitreous body were removed from the extracted eyeball. The retina was isolated from the posterior structure of the eyeball and cut into approximately 5 mm × 5 mm, including the center of the retina. The flattened retinal patch was attached to the multi-electrode array (MEA) with the ganglion cell layer (GCL) facing down. Retinal preparation after removing the vitreous body was prepared under near-infrared illumination in an artificial cerebrospinal fluid (ACSF) solution (124 mM NaCl, 10 mM glucose, 1.15 mM KH₂PO₄, 25 mM NaHCO₃, 1.15 mM MgSO₄, 2.5 mM CaCl₂, and 5 mM KCl; all from Millipore, Burlington, ON, United States) bubbled with 95% O₂ and 5% CO₂ to maintain a pH of 7.3~7.4 at 25°C.

The retinal activities were extracellularly recorded using a 60-channel MEA recording system. Briefly, the MEA60 system (Multichannel Systems GmbH, Reutlingen, Germany) consists of an amplifier (MEA 1060-up), heating system (PH01 and TC01), peristaltic perfusion system (PPS2), data acquisition hardware (Mc_Card), plana perforated MEA (pMEA) (60pMEA200/30iR), and software (Mc_Rack). The retinal activities were recorded

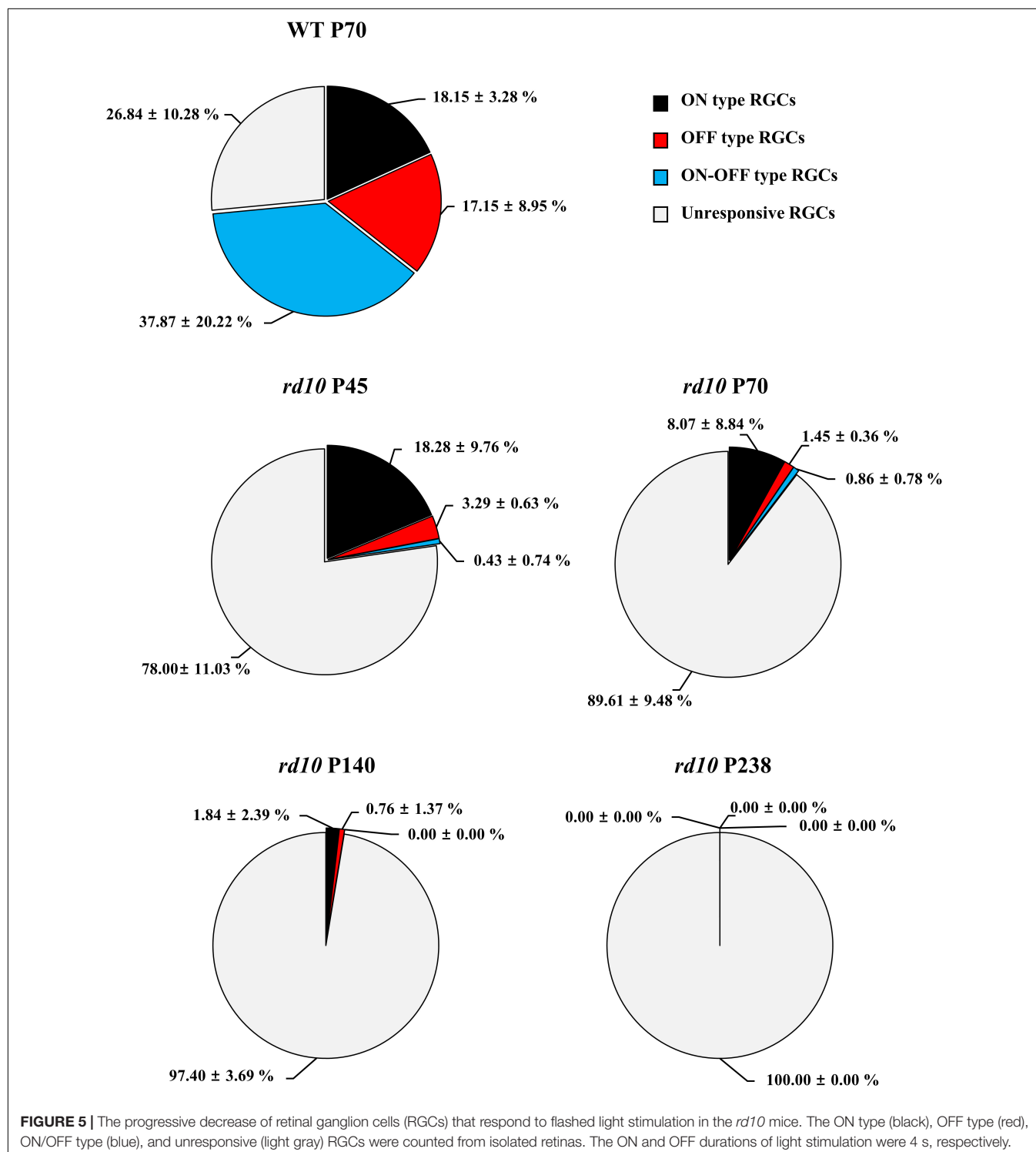
with a bandpass from 1 to 3,000 Hz, a gain of 1,200, and a sampling rate of 25 kHz. The pMEA has 59 titanium nitride (TiN) active electrodes in an 8 × 8 grid layout with an electrode diameter of 30 μm and inter-electrode distance of 200 μm on a porous polyimide foil isolator and a large internal reference electrode as channel 15. The four inactive channels are located at each corner of MEA to record an analog signal. Each active electrode has an impedance of 50 kΩ at 1 kHz. We continuously perfused with the oxygenated fresh ACSF to retinal tissue on the pMEA *via* small pores in the porous polyimide foil isolator using a peristaltic perfusion system (1–3 mL/min) during recording. The retinal activities were recorded after waiting 20 min for the stabilization of retinal tissue attached to pMEA.

Flashed white full-field illumination (ON 4 s, OFF 4 s, 50 times) was applied to confirm the retinal activities to light. Light stimulation was applied after dark adaptation for about 20 min. Light stimulation was implemented through software based on Psychtoolbox using Matlab (MathWorks, Natick, MA, United States). The light stimulation pattern was projected by a projector (ep7122; Hewlett-Packard, Palo Alto, CA, United States) and focused on a photoreceptor layer of retinal tissue by passing through multiple lenses and compressing the size to 5 mm × 5 mm. We controlled the intensity of applied light stimulation with 2.0ND filters (NE220B; Thorlabs Inc., NJ,



United States). The intensity of the full-field illumination was $40 \mu\text{W}/\text{cm}^2$ (light ON), and the intensity of the background illumination was $4.9 \mu\text{W}/\text{cm}^2$ due to the monitor's backlight (light OFF). The light condition was mesopic. In rodents, the mesopic light condition could activate rod photoreceptors like the scotopic condition (Kelber, 2018).

Using a stimulus generator (STG 1004, Multichannel systems GmbH, Reutlingen, Germany), the current pulse train was delivered to the retinal preparation through 1 of 60 channels (mostly channel 44 in the middle of the MEA), with the remaining channels serving as recording electrodes. Stimulation consisted of symmetrical cathodic phase-1st biphasic pulses.



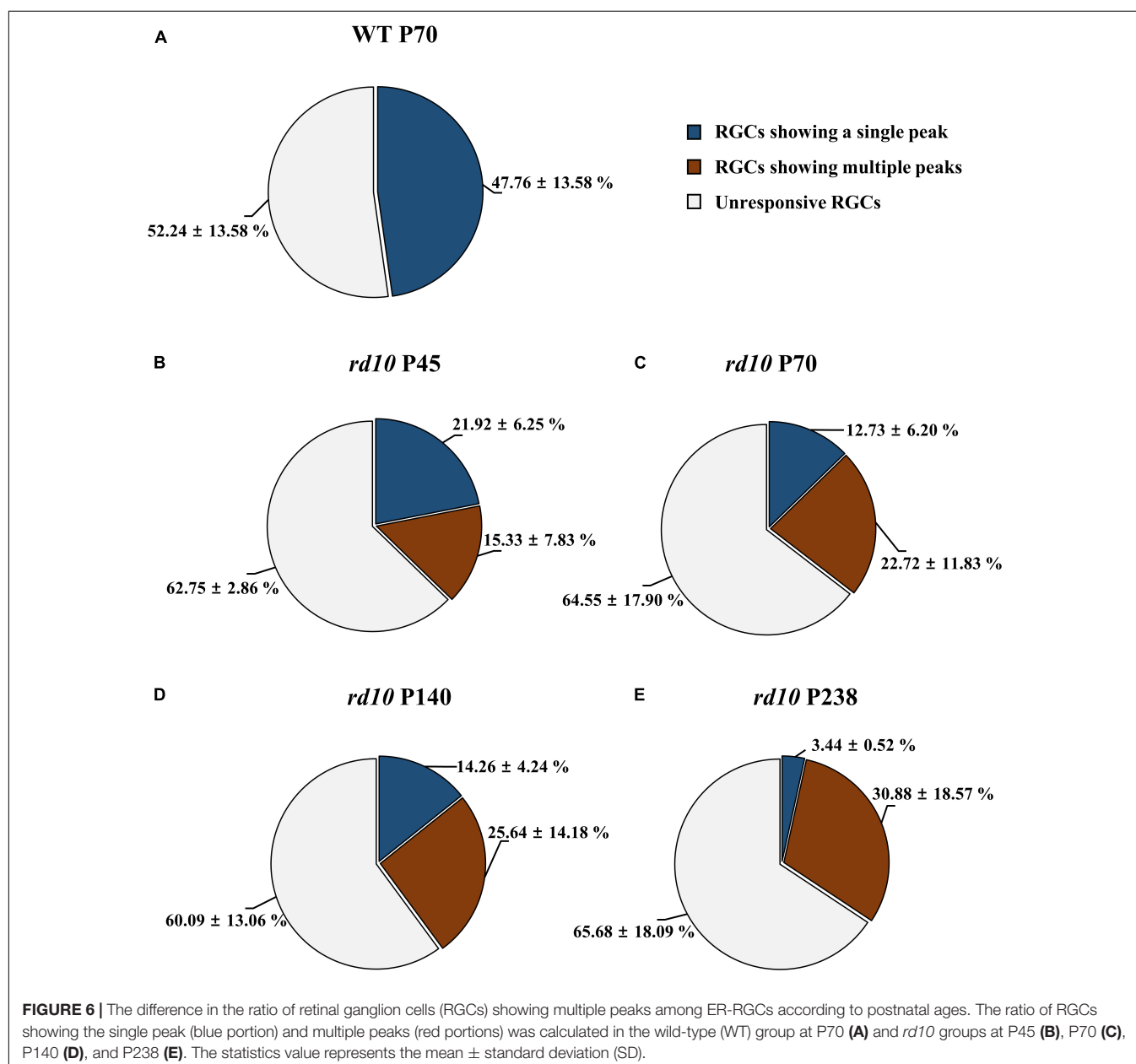
Pulse duration was fixed at 500 μ s/phase, and pulse amplitudes of 1, 5, 10, 20, 30, 40, and 50 μ A/phase were applied. Biphasic current pulses were applied 50 times once per second (1 Hz) for each pulse amplitude.

Data Analysis

Retinal ganglion cell spikes were processed as follows. We sorted the timestamp of RGC spikes from the raw signal trace recorded by MEA. First, the raw trace was processed with a 100 Hz cut-off high-pass filter to eliminate the low-frequency components such as hum noise or local field potential (LFP) oscillating rhythm (Goo et al., 2011a). Subsequently, the filtered signal was processed with a spike sorting software (Offline SorterTM; Plexon Inc., Dallas, TX, United States) to

separate multiunit activities containing different spike waveforms into individual cell units using principal component analysis (Lewicki, 1998). Finally, we isolated the timestamp of RGC spikes and analyzed them with commercial analysis software (NeuroExplorer[®]; Nex Technologies, Colorado Springs, CO, United States) and a custom-made MATLAB (MathWorks, Natick, MA, United States) codes.

The number of retinas used was three for WT and three for *rd10* per selected postnatal day (P45, P70, P140, and P238). With light stimulation, the number of RGCs harvested from WT was 322, and 310, 216, 315, and 310 at P45, P70, P140, and P238, respectively. Out of these RGCs, we classified the light-driven RGC responses as follows. The post-stimulus time histograms (PSTHs) with the light stimulus of 50 trials (recording time:



400 s, ON: 4 s, OFF: 4 s, 400 s/8 s = 50 trials) were obtained. When the RGC spike number within 100 ms after light stimulus onset, offset, and onset/offset in PSTH exceeds two times of spontaneous firing rates (marked by a red line), we classified the cell as ON, OFF, and ON/OFF type RGC, respectively (Masland, 2001; Stasheff, 2008; Stasheff et al., 2011; Baden et al., 2016) (**Supplementary Figure 2**).

With electrical stimulation, the number of RGCs harvested from WT was 198, and 298, 294, 229, and 205 at P45, P70, P140, and P238, respectively. Out of these RGCs, we defined the electrically evoked RGC responses as follows. First, we counted spontaneous RGC spikes, the average number of spikes in 25 s before the stimulation onset. Second, if RGC fires more than spontaneous spikes with electrical stimulation, the RGC was counted in the data pool. From the timestamp of RGC spikes, to consider only network-mediated RGC response, we eliminated spikes that appeared within 10 ms after stimulus onset to exclude the stimulus artifact or the direct response of RGC (Sekirnjak et al., 2006; Boinagrov et al., 2014; Ahn et al., 2017).

Then, we quantified electrically evoked RGC response for the time window of 100 ms and 500 ms and divided the responses into two groups based on the spike burst after stimulus onset in the PSTH or peri-stimulus raster plot. One group of RGCs showed a single peak of spike burst, while the other group of RGCs showed multiple peaks of spike burst.

For the group of RGCs showing multiple peaks of spike burst, the inter-peak frequency was estimated as follows: (1) The PSTH was calculated for each RGC using 50 electrical stimulations with the highest input current (50 μ A). (2) The power spectral density of the PSTH was calculated using the fast Fourier transform. (3) The frequency with the largest power was defined as the dominant frequency.

Statistical analysis was performed using commercial software (IBM SPSS Statistics 24; International Business Machines Corporation, IBM, New York, NY, United States). A paired Student's *t*-test was performed for statistical analysis between the two groups. An ANOVA analysis was performed with the *post-hoc* tests of Tukey's HSD and Duncan's test to determine the statistical difference among three and more groups.

RESULTS

Progressive Outer Retinal Degeneration by Postnatal Ages in *rd10* Mice (C57BL/6-*Pde6b*^{em1(R560C)}*Dkl*/Korl Strain)

First, we validated the alteration of histological phenotypes by postnatal days in our custom-made *rd10* mice (C57BL/6-*Pde6b*^{em1(R560C)}*Dkl*/Korl strain) to determine whether they are similar to the established *rd10* mice (B6.CXB1-*Pde6b*^{rd10}/J strain) or not. **Figure 4** shows visualized soma of retinal neurons, outer segments of photoreceptors, and cytosol of Müller cells. The ONL gradually decreases, leaving only a single layer of cell nucleus after P45 (**Figure 4B**). In addition, the fluorescence of outer segments of rod cells was not detected after P70, and the fluorescence of cone cells was not detected after P140 (**Figure 4A**). We also

confirmed the gliosis by Müller cells. After P45, the Müller cells grew and sealed the photoreceptor and RGC layers.

Progressive Decrease of Visual Acuity in *rd10* Mice by Postnatal Ages

The optomotor responses showed that the visual acuity of *rd10* mice was lower than that of WT mice although *rd10* mice were younger (at P45–47) than WT (at P70–71). For WT mice, the highest spatial resolution that induces the mouse's optomotor response linearly increased as the contrast of the stripes increased (**Figure 3A**). On the other hand, for *rd10* mice (P45–47), the highest spatial resolution was highly variable and lower than WT mice (**Figure 3B**). Older mice (P164–165) rarely showed an optomotor response at all contrast levels (**Figure 3C**). At the 100% contrast level, the mean visual acuity of *rd10* mice (0.31 ± 0.15 and 0.04 ± 0.05 cyc/° at P45 and P164, respectively) was significantly lower than that of WT mice (0.53 ± 0.04 cyc/°) (**Figure 3D**). Additionally, six *rd10* mice of older ages (three *rd10* mice at P174, one *rd10* mouse at P257, and two *rd10* mice at P259) were tested for visual acuity assessment. Still, no visual acuity was found at any contrast level (data not shown).

Progressive Decrease in the Ratio of Retinal Ganglion Cells Responding to Light Stimulation in *rd10* Mice

Next, we discovered that each RGC subtype divided by light response showed a different disappearance time course according to the postnatal ages. **Figure 5** shows the light stimulation-responsive RGCs (LR-RGCs) ratio in WT and *rd10*. We classified LR-RGCs into three groups (ON, OFF, and ON/OFF type) (Masland, 2001; Stasheff, 2008; Stasheff et al., 2011; Baden et al., 2016). Compared with the WT retina, the ratio of LR-RGCs in the P45 *rd10* retina decreased (73% vs. 22%), and with postnatal ages, the ratio of LR-RGCs decreased progressively (22, 10.4, 2.6, and 0%). At P45, the ON type response observed from RD retina was same with WT retina ($18.15 \pm 3.28\%$ and $18.28 \pm 3.28\%$, $p > 0.05$), while OFF type ($17.15 \pm 8.95\%$ and $3.29 \pm 0.63\%$, $p < 0.05$) and ON/OFF type ($37.87 \pm 20.22\%$ and $0.43 \pm 0.74\%$, $p < 0.05$) response significantly decreased. In P238 *rd10* retina, no LR-RGCs were found. The unresponsive RGCs to light stimulus may be due to some RGC subtypes not responding to full-field stimulation. Even in the WT retina, 27% of RGCs belong to this unresponsive group of RGCs.

Two Response Types of Retinal Ganglion Cells to Electrical Stimulation in *rd10* Mice

We discovered that the ratio of RGCs showing multiple peaks of spike burst in PSTH increased with postnatal ages in *rd10* mice. We elicited the RGC spikes with electrical stimulation and analyzed the network-mediated RGC response. Like the WT retina, the electrical stimulation-responsive RGCs (ER-RGCs) ratio was observed at ~40% regardless of the postnatal ages (**Figure 6**). **Figure 7** shows a typical RGC response pattern to amplitude-modulated electrical stimulation. In the WT group, only one response type was observed (**Figures 6A, 7A**). The

electrically evoked spikes formed a single peak within 100 ms from stimulus onset when the pulse amplitude exceeded a threshold level (Figure 7A). However, in the RD group, RGC responses were divided into two types (Figures 6B–E, 7B–E). One response type is a single peak like the WT group; the other response type is multiple peaks (Figures 7B–E).

The inter-peak frequency decreased from P45 to P140 and did not change from P140 to P238 (Figure 7F). At P45, the average dominant frequency was 8.7 Hz (SE = 0.7). At P70, the average dominant frequency was reduced to 6.8 Hz (SE = 0.4). This difference was statistically significant ($*p < 0.05$ with *t*-test). At P140, the average dominant frequency was further reduced to 4.6 Hz (SE = 0.2). The difference between the average dominant frequencies at P70 and P140 was statistically significant ($***p < 0.001$ with *t*-test). In contrast, the average dominant frequency at P238 was 4.4 Hz (SE = 0.4). The difference between the average dominant frequencies at P140 and P238 was not statistically significant (n.s., $p > 0.05$).

Multiple peaks occur within 500 ms after the onset of stimulation, but the temporal pattern of occurrence varies according to the postnatal ages. The number of peaks decreased, and the inter-peak intervals increased with older postnatal ages. Moreover, the ratio of RGCs showing multiple peaks among ER-RGCs gradually increased with the postnatal ages (Figures 6B–E). At P45, the number of RGCs showing multiple peaks was 0.70 times smaller than that of RGCs showing a single peak. The number of RGCs showing multiple peaks was 1.78 times, 1.80 times, and 8.98 times larger than that of RGCs showing a single peak, at P70, P140, and, P238, respectively.

Regardless of multiple peaks, the RGC spikes in *rd10* mice were less elicited by pulse amplitude modulation than in WT mice. Using the average number of spontaneous spikes as a reference, we calculated the relative ratio of the average number of spikes within the 100 or 500 ms from stimulus onset (Figure 8). First, for the group of RGCs showing a single peak, the RGC spikes increased with the increment of pulse amplitude from 10 to 50 μ A within 100 ms at P45. However, even if the pulse amplitude increased, the average number of RGC spikes after stimulus onset was similar to that of spontaneous spikes within 500 ms. Second, for the group of RGCs showing multiple peaks, except for the *rd10* P238 group, the response curves within 100 and 500 ms were similar to those of RGCs showing a single peak. However, in the *rd10* P238 group, the response curves within 100 ms as well as within 500 ms showed a linear relationship according to pulse amplitude increase.

DISCUSSION

Validation of Newly Established *rd10* Mice (C57BL/6-*Pde6b*^{em1(R560C)Dkl}/Korl)

The occurrence rate of RP is lower than that of other retinopathies (Cheung et al., 2010; Wong et al., 2014; Rim et al., 2017). In people aged 20–74 years, diabetic retinopathy (DR) prevalence is 8% in the United States and 10% in Southeast Asia (Cheung et al., 2010). The occurrence rate of RP is six cases/100,000 persons-year in the United States and 1.64

cases/100,000 persons-year in South Korea, regardless of age (Rim et al., 2017). However, RP is a monogenic disease, while DR and age-related macular degeneration (AMD) are chronic and polygenic diseases (Bowne et al., 2011; Ratnapriya and Chew, 2013; Cho and Sobrin, 2014). Therefore, in establishing an animal model, RP has advantages over DR or AMD since it requires an introduction of a single mutation into a single gene and the phenotype appears quickly at a younger age than DR or AMD.

The *rd1* and *rd10* mice are RP models with the *pde6b* gene mutations. The *rd1* mouse has a nonsense mutation, while the *rd10* mouse has a missense mutation (Chang et al., 2002, 2007). This difference causes delayed onset and slower progression of RD in the *rd10* mouse compared with the *rd1* mouse. The progressive death of rod photoreceptors appears from P16 to P60 in the *rd10* mouse, while it appears from P8 to P20 in the *rd1* mice (Pennesi et al., 2012). Thus, the *rd10* mouse can provide a wider therapeutic window than the *rd1* mouse.

In this study, we used the *rd10* mouse strain (C57BL/6-*Pde6b*^{em1(R560C)Dkl}/Korl) newly established by the National Institute of Food and Drug Safety Evaluation (NIFDS) of South Korea instead of the conventional *rd10* mouse strain (B6.CXB1-*Pde6b*^{rd10}/J) from Jackson Lab (Bar Harbor, ME, United States). We validated the histological and behavioral phenotype of the newly established *rd10* strain.

The histological findings in our study showed the progressive disappearance of the fluorescence signals of rhodopsin in rods and opsin in cones until P45 and P70, respectively. We also showed that a single row of nuclei was maintained in the ONL from P45 to P238 (Figure 4). In *rd10* mice, RD begins at P18–P20, and rod photoreceptor loss lasts until P45 (Chang et al., 2007; Gargini et al., 2007; Barhoum et al., 2008; Stasheff et al., 2011; Pennesi et al., 2012; Li et al., 2019). The cone photoreceptors disappear by 2 months after birth (~P60), but the single nuclear layer of the ONL persists until 9 months after birth (~P270) (Gargini et al., 2007). Our histological results are consistent with the literature.

Through behavioral experiments, we also show that the visual acuity of the newly established *rd10* strain is lower than that of WT mice. The measured visual acuity of WT mice at P70–P71 and *rd10* mice at P45–P47 and P164–P165 was 0.53 ± 0.04 cyc/°, 0.31 ± 0.15 cyc/°, and 0.04 ± 0.05 cyc/°, respectively (Figure 3). These behavioral phenotypes of our study and previous studies are compatible (Benkner et al., 2013; Vagni et al., 2019). In an earlier study using the Optodrum, for WT mice on P59–P63 and conventional *rd10* mice on P24–P32 and P86–91, the visual acuity of WT and *rd10* mice was 0.38 ± 0.005 cyc/°, 0.35 ± 0.009 cyc/°, and 0.2 cyc/°, respectively (Benkner et al., 2013). In a previous study using a different system for detecting an optomotor response from us, the visual acuity of WT and conventional *rd10* mice was 0.40 ± 0.01 cyc/° and 0.12 ± 0.01 cyc/°, respectively, at P30 (Vagni et al., 2019). In addition, they also showed that the visual acuity of conventional *rd10* mice strain declines with postnatal ages from P30 to P60 while WT mice maintain visual acuity until P60. Our results of the behavioral study are consistent with the literature.

In summary, the newly established *rd10* mice strain (C57BL/6-*Pde6b*^{em1(R560C)Dkl}/Korl) shows a histological and behavioral

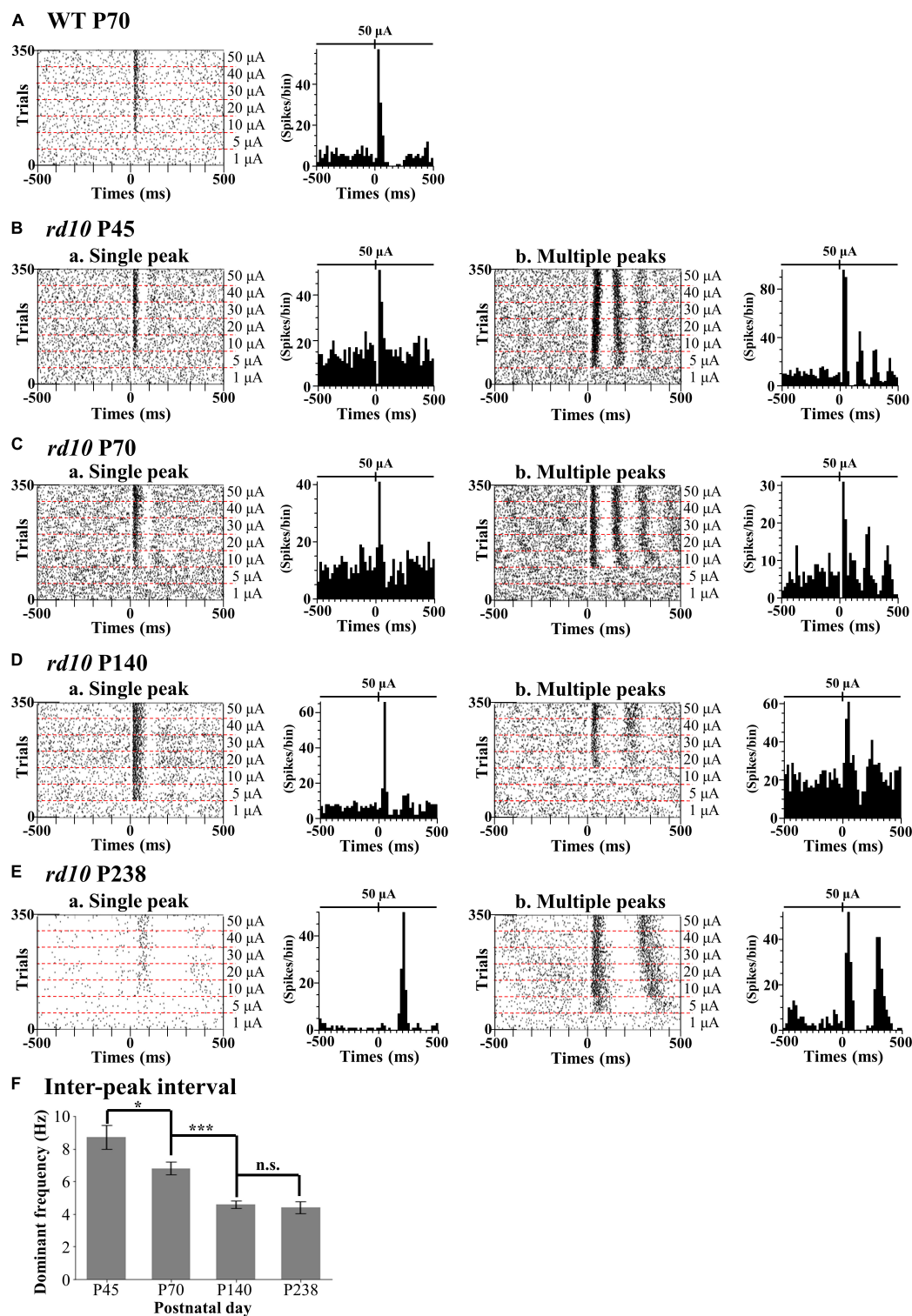


FIGURE 7 | Two different response patterns of the electrical stimulation-responsive retinal ganglion cells (ER-RGCs) according to postnatal ages. Typical response patterns to amplitude-modulated electrical stimulation in the wild-type (WT) group at P70 (**A**) and *rd10* groups at P45 (**B**), P70 (**C**), P140 (**D**), and P238 (**E**) are represented by a raster plot (left panel) and PSTH (right panel). We divided RGCs of *rd10* mice into two groups, single peak (a) and multiple peaks (b) based on the number of peaks in PSTH. The time window of the raster plot and PSTH is set for ± 500 ms. The 0 ms represents the time point of stimulus onset. In each raster plot, the stimulation amplitude increases from the bottom to the top row. PSTHs represent electrically evoked RGC response at the strongest pulse amplitude ($50 \mu\text{A}$). The y-axis of PSTH represents the spike number per bin (bin size is 20 ms). (**F**) The inter-peak frequency decreased from P45 to P140 and saturated. The average dominant frequency is shown for each degeneration stage, with error bars representing standard errors. Statistical significance between the average dominant frequencies was calculated for consecutive postnatal days using Student's *t*-test ($***p < 0.001$, $*p < 0.05$, and n.s., $p > 0.05$).

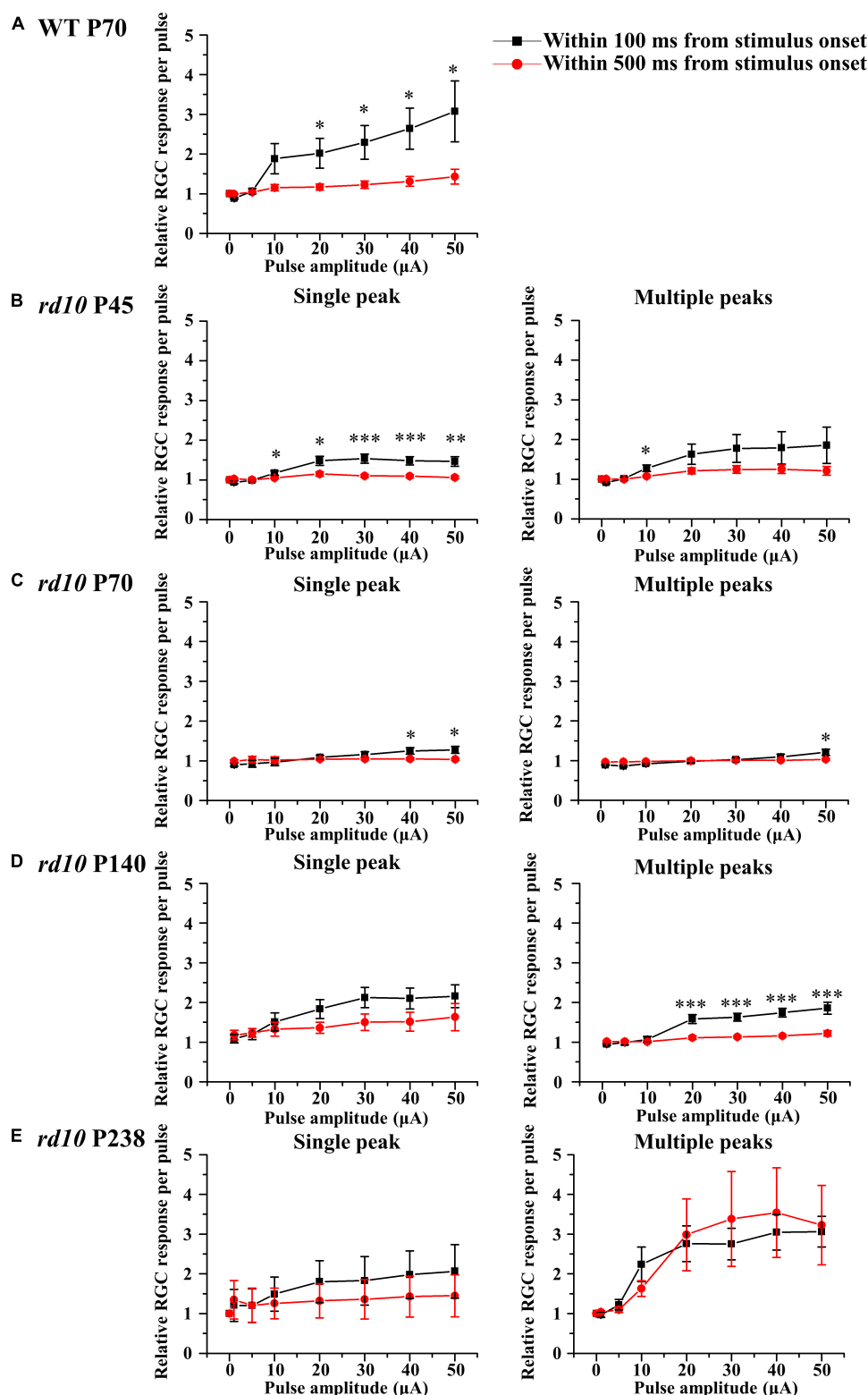


FIGURE 8 | The retinal ganglion cell (RGC) response curves to pulse amplitude modulation for a single peak (left column) or multiple peaks groups (right column). The RGC response curve plotted against pulse amplitude for the WT group at P70 (A) and *rd10* groups at P45 (B), P70 (C), P140 (D), and P238 (E) groups. Error bars represent the standard error of the mean (SEM). The curves drawn in black include the spikes within 100 ms after stimulus onset, and the curves drawn in red include the spikes within 500 ms after stimulus onset. Asterisks indicate statistical differences between 100 and 500 ms at each pulse amplitude (*** $p < 0.001$, ** $p < 0.01$, and * $p < 0.05$).

phenotype similar to that of the conventional *rd10* mice strain (B6.CXB1-*Pde6b*^{rd10}/J). Therefore, we believe that newly established *rd10* mice are as reliable as conventional *rd10* mice for RD animal models.

The ON Response Preserves Longer Than the OFF Response in *rd10* Mice With RD

We found the RGC type-dependent degeneration in *rd10* mice. The ON response sustained longer than the OFF response with RD. The OFF response quickly disappeared, while the ON response was preserved at P45. The ON response slowly disappeared until P140 (Figure 5). This study detected an average of 72% of LR-RGCs per patch from WT retinas with simple full-field illumination. Our experimental condition of light stimulation (OFF luminance ≈ 5.63 cd/m² and ON luminance ≈ 482.18 cd/m²) is mesopic, where both rod and cone photoreceptors respond to light stimulation (Tikidji-Hamburyan et al., 2017; Uchida et al., 2018).

We classified the LR-RGCs into three subtypes: ON, OFF, and ON/OFF (18, 17, and 38%, respectively). Even in the WT retina, 27% of RGCs belong to an unresponsive group of RGCs. The unresponsive RGCs to light stimulus may be due to some RGC subtypes not responding to full-field stimulation. As is well known, an RGC has a center-surround receptive field (Turner et al., 2018). If the center and surround of the receptive field are simultaneously stimulated, the RGC may not fire spikes due to center-surround antagonism. It was reported that full-field stimulation significantly reduced both the peak and the mean firing rates by 60% compared to an optimal spot stimulus (Sagdullaev and McCall, 2005). However, in our experimental setup with MEA, full-field stimulation still induced the light response in a substantial amount of RGCs ($\sim 73\%$) (Figure 5). In addition, there is a possibility that some unresponsive cells are displaced spiking-amacrine cells (ACs). In the mouse retina, around 37–59% of the displaced ACs exist in the GCL (Muller et al., 2010; Baden et al., 2016). The spiking ACs in the GCL are reported to respond to light stimulation because they are coupled with ipRGCs via gap junction (Reifler et al., 2015). However, to the authors' best knowledge, there is no report showing how many percentages of displaced ACs comprise the spiking ACs.

As the retina degenerates, the ratio of LR-RGCs progressively decreases until P140 and LR-RGCs completely disappear at P238 (Figure 5). One possible explanation for this reduced ratio of LR-RGCs between P70 and P140 is the second-stage degeneration of cone-cell death. The cone-cell death has been explained mainly through necroptosis and partly by receptor-interacting protein (RIP) kinase. The necroptosis occurs due to neurovascular remodeling. The neurovascular remodeling involves the blood-retina barrier (BRB) leak, the glial sealing in the choroid, and the displacement of the retinal pigment epithelium (RPE) cells (Murakami et al., 2012; Ivanova et al., 2019).

The cause of the distinct difference between ON and OFF RGC responses could be explained by the different electropharmacological properties between ON and OFF pathways. The preservation of the GCL even after RD (Figure 4B) implies that

the disappearance of OFF RGC response might be due to the reduced firing of OFF RGC, not due to the death of OFF RGCs. Therefore, we postulated the following hypothesis (Figure 9). The ON and OFF pathways in the normal retina consist of cone and rod pathways (Davanger et al., 1991; Wettschureck and Offermanns, 2005; Volgyi et al., 2013; Fain and Sampath, 2018). In the cone pathway, cone photoreceptors synapse with ON cone bipolar cells (ON CBCs) and OFF cone bipolar cells (OFF CBCs). ON CBCs and OFF CBCs directly synapse ON RGCs and OFF RGCs, respectively.

On the other hand, in the rod pathway, rod photoreceptors only synapse with RBCs. The RBCs indirectly connect with ON and OFF RGCs through AII ACs. In the *rd10* mice retina, the loss of rod photoreceptors (Figure 4) causes the subsequent decrease of glutamate concentration to RBCs. As a result, the membrane potential of RBCs and AII ACs will be depolarized and maintained regardless of ON and OFF stimulations. Consequently, the γ -aminobutyric acid (GABA) released from AII ACs to OFF CBC will inhibit the OFF response. On the contrary, the electrical synapse between AII AC and ON CBC might be enhanced, then ON RGCs are likely to fire spikes.

The Electrical Stimulation Hardly Elicits Retinal Ganglion Cells Spikes in Retinal Degeneration Compared With Wild-Type

Our results showed that RGCs in the RD retina produced fewer spikes than in the WT retina (Figure 8). *In vitro* studies using the mouse, rat, and pig models reported that fewer RGC spikes are evoked in the RD retina than in the WT retina with electrical stimulation (Goo et al., 2011b; Jensen, 2012; Cha et al., 2021). *In vivo* studies in human subjects also showed that higher stimulus intensity was required to induce phosphenes in patients with RP than in people with normal vision (Delbeke et al., 2001; Gekeler et al., 2006).

The difficulty in eliciting RGC spikes in the degenerate retina may be explained by spontaneous hyperactivity due to oscillations and multiple peaks of spike bursts of RGCs. As RD progresses, loss of photoreceptors leads to retinal remodeling in the INL (Jones et al., 2003; Marc et al., 2003; Jones et al., 2012), resulting in aberrant oscillation (frequency 5–10 Hz) through gap junction coupling between AII AC and ON CBC (Yee et al., 2012; Trenholm and Awatramani, 2015). Oscillations induce spontaneous hyperactivity with multiple bursts of RGCs, requiring a higher stimulation threshold for RGC activation (Margolis et al., 2008; Stasheff, 2008; Yee et al., 2012; Goo et al., 2016). Interestingly, the multiple bursts observed during electrical stimulation are also found in optogenetic stimulation (Reh et al., 2022). When Channelrhodopsin-2 expressed in RBCs of *rd10* mice (P182–215) was stimulated optogenetically, RGCs showed multiple bursts. No multiple bursts were found when local stimulation was applied to the retina, whereas multiple bursts were observed when larger retinal areas were stimulated. This finding suggests the possibility of large-scale network activation by gap junction coupling between AII AC and ON CBC. Recent studies support this hypothesis by showing that the stimulation efficiency is enhanced when oscillation and

multiple bursts are abolished by gap junction blockers such as meclofenamic acid (Eleftheriou et al., 2017; Ahn et al., 2022). This study and our previous report (Goo et al., 2016) showed that the number of *rd10* RGCs showing multiple bursts increased by the postnatal day (P45–P238) (Figure 6). Therefore, multiple bursts might be regarded as a physiological indicator in RD. In the future, instead of a conventional hardware-based approach such as increasing the number of electrodes in the prosthesis, the suppression of oscillation and multiple bursts could be an excellent strategy to improve the visual performance of retinal prosthesis.

Another possibility that RGC spikes are hardly elicited by electrical stimulation in the degenerated retina is shielding the electrical pulse to RGC by the Müller cell. As we showed in Figure 4A, as direct evidence of glia sealing in the degenerated retina after P45, Müller cell hypertrophy is detected through the glutamine synthetase (GS) signal. However, to show Müller cell hypertrophy, GFAP staining for Müller cell endfeet would be a better option than GS staining for Müller cell soma we used (Gargini et al., 2007). In future work, GFAP staining for Müller cell endfeet is planned. Several studies using various RD animals such as the mouse, rat, rabbit, pig, and human also reported the enclosure of RGCs by the Müller cell (Jones et al., 2003; Bringmann et al., 2006; Gargini et al., 2007; Wan et al., 2008; Ahn et al., 2019; Choi et al., 2021). The shielding by the Müller cell prevents BCs or RGCs from being stimulated by a 2D electrode (Aplin et al., 2016). By using 3D electrodes to get closer to BC or RGC (Airaghi Leccardi et al., 2019; Davidsen et al., 2019; Ho et al., 2019; Seo et al., 2019; Huang et al., 2021), we would expect to elicit more spikes under the same stimulus conditions with this study.

Progression of the Retinal Degeneration Causes the Increase in the Inter-peak Interval of Retinal Ganglion Cells to Electrical Stimulation

Our results showed that the inter-peak (inter-burst) interval of *rd10* RGCs increased with the postnatal ages (Figure 7F). The increase in the inter-peak interval with the progression of RD could be explained by a decrease in gap junction coupling between ACs and ON cone BCs. Gap junctions are essential for generating abnormal rhythmic bursts and oscillations in *rd10* RGCs (Toychiev et al., 2013; Menzler et al., 2014; Ivanova et al., 2016). In particular, it is well known that the gap junction coupling between AII ACs and ON-cone BCs is deeply involved in oscillation generation (Trenholm et al., 2012; Yee et al., 2012; Choi et al., 2014). Gap junction blocking with meclofenamic acid (MFA) induces a lower oscillation frequency (Choi et al., 2014). Therefore, the increase in the inter-peak interval (lower frequency of oscillation) of RGCs at P238 shown in Figure 7F may be associated with a decrease in gap junction coupling as RD progresses.

The other possibility is that the decrease in inhibitory input results in an increased inter-peak interval of RGCs observed in this study (Figure 7). Studies show that inhibitory input modulates the oscillation frequency (Ye and Goo, 2007; Biswas et al., 2014). The oscillations did not disappear when *rd10*

retinas were treated with GABA and glycine receptor inhibitors (bicuculine and strychnine, respectively), but the oscillation frequency decreased from ~6 to ~1 Hz. Indeed, previous histological findings seem to support this hypothesis. In *rd10* mice, the number of horizontal cells, one of the inhibitory retinal neurons, decreased significantly over time, approximately 19% between P42 and P98 and 29% at P252 (Gargini et al., 2007). Therefore, the gradual increase in the inter-peak interval of RGCs (lower frequency of oscillation) from P45 to P238 observed in this study may be closely related to the decrease in inhibitory input due to the reduction in the horizontal cell number during RD.

Efficiency of Electrical Stimulation Regarding the Presence of Multiple Peaks in Retinal Degeneration Retina

Unlike other age groups of *rd10* mice, RGCs showing multiple peaks of spike burst in the late stage of RD at P238 responded well to the electrical stimulation (Figure 8E). To quantify the electrically evoked RGC response, we calculated the mean firing rate within 100 or 500 ms from stimulus onset. The response profile of RGCs shows that a single peak appears within 100 ms from stimulus onset for both WT and RD. The first peak of multiple peaks also appears within 100 ms from stimulus onset in the RD. The other peaks of multiple peaks appear within 500 ms from stimulus onset. In RGCs showing a single peak from the WT and RD, due to spontaneously generated spikes within 100 to 500 ms, the mean firing rate within 500 ms is similar to the spontaneous firing rate (Figures 8A–E, left). The relative ratio of RGC response sticks to the value of 1.0 in the RD except for P238; the mean firing rate within 500 ms is similar to the spontaneous firing rate (Figures 8B–D, right). Our previous study reported that pulse amplitudes significantly modulate only the first and second peaks despite three and more multiple peaks appearing (Ryu et al., 2010). The group of RGCs in P238 has only two peaks within 500 ms from stimulus onset, while RGCs in the other age groups have third and more peaks within 500 ms from stimulus onset. The difference in time window showing first and second peaks at different degeneration stages could explain the flat RGC response curve with pulse amplitude modulation in the earlier stage of RD at P45 to P140 than P238. However, there are limited reports regarding the relationship between multiple peaks' presence and electrical stimulation's efficiency. Therefore, in the future, we are planning to explore this issue.

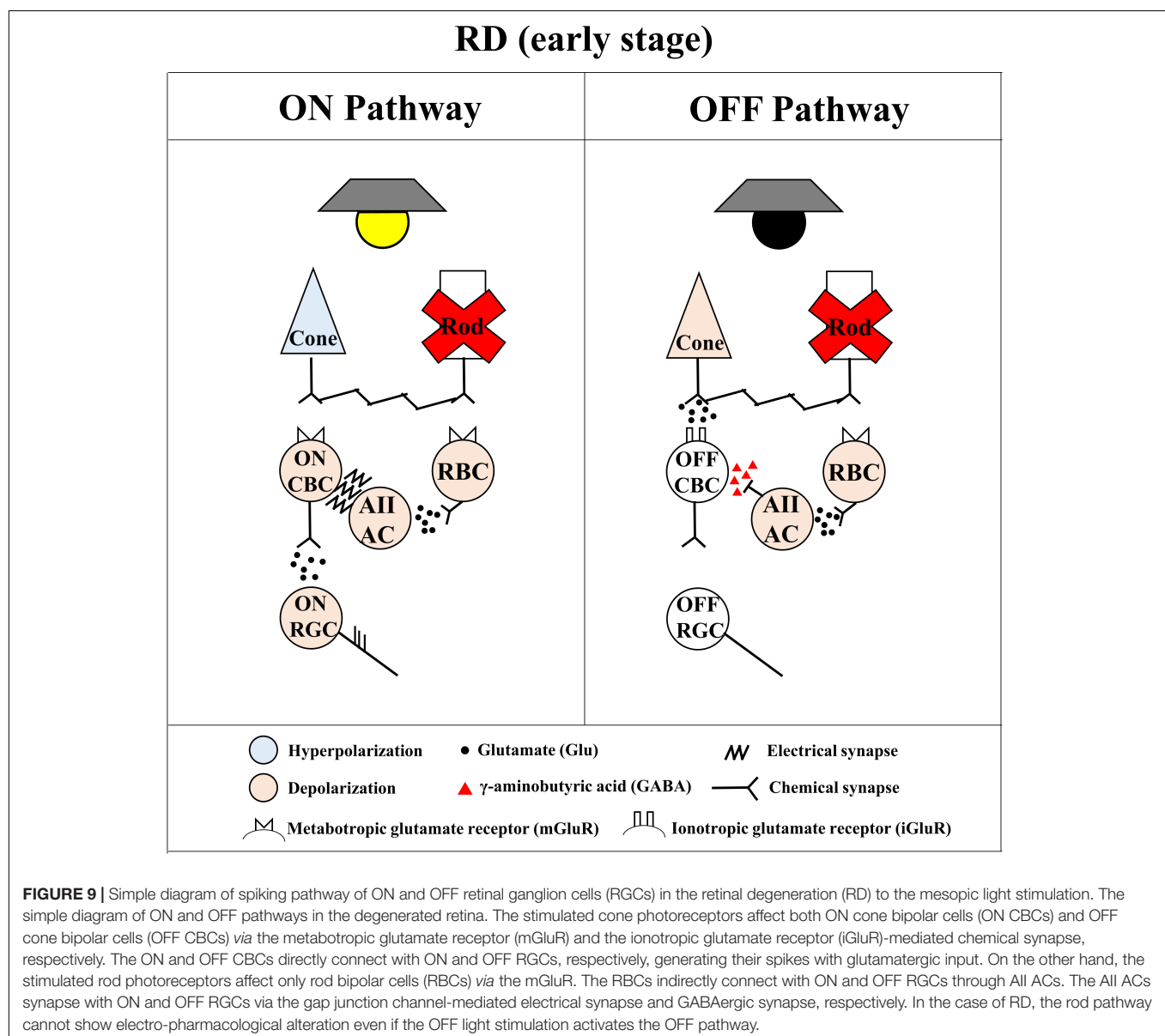
Clinical Implication and Future Work

To develop reliable retinal prostheses, we should find ways to effectively elicit RGC spikes with electrical stimulation (Stingl et al., 2017; Ayton et al., 2020; Delyfer et al., 2021; Yoon et al., 2021). The electrical stimulation elicits two different RGC spike responses according to the prosthesis location in the retina (Margalit et al., 2002; Zrenner, 2002; Ayton et al., 2020; Im and Kim, 2020). One is the direct response originating in RGCs by epi-retinal stimulation configuration. The other is the network-mediated response originating in BCs or photoreceptors by sub-retinal stimulation configuration (Boinagrov et al., 2014). While the direct response has the advantage of response modulation by

direct matching an RGC spike and a stimulus pulse, the network-mediated response has the advantage of mimicking the natural RGC response *via* the retinal network (Zrenner, 2002; Fried et al., 2006; Im and Fried, 2015; Im and Kim, 2020). Despite many efforts with retinal prostheses, regardless of their stimulus configuration, the artificial vision showed low spatial resolution performance below the 20/420 of visual acuity (Ayton et al., 2020; Im and Kim, 2020).

In the artificial vision research community, the main interests are how ON RGC and OFF RGC react to electrical stimulation and how efficiently and selectively ON or OFF RGC responses are activated. In literature, many efforts have been undertaken for this. As one of the stimulation strategies for improving the spatial resolution of retinal prostheses, selective activation of individual RGCs has been attempted (Tong et al., 2020). In direct response,

selective activation of ON or OFF RGCs *via* pulse amplitude modulation and frequency modulation is possible in the WT retina (Twyford et al., 2014; Guo et al., 2018; Kotsakidis et al., 2018). While OFF RGCs preferentially respond to the lower pulse amplitude ($<90 \mu\text{A}$) regardless of stimulus frequency, ON RGCs preferentially respond to the higher pulse amplitude ($>150 \mu\text{A}$) and stimulus frequency ($>2 \text{ kHz}$) (Tong et al., 2020). On the other hand, the electrically evoked network-mediated spikes are differently induced according to the RGC subtype *via* the pulse duration modulation in the WT retina (Im and Fried, 2015, 2016; Im et al., 2018). The ON RGC showed strong correlations between light-evoked spikes and electrically evoked network-mediated spikes but not the OFF RGC (Im and Fried, 2015). The repetitive stimulation leads to a reset of the ON RGC, but it leads to desensitization of the OFF RGC (Im and Fried, 2016). The



electrically evoked spikes of ON RGC were well-modulated to stimulus duration than the OFF RGC (Im et al., 2018). The ON RGC shows a gradual decline in peak firing rate and inter-trial correlation until P60 in *rd10* mice, but not the OFF RGC (Yoon et al., 2020). In addition, regarding the reliability of electrically evoked RGC response, ON RGC shows a gradual increment of fano factor until P60, but not the OFF RGC (Yoon et al., 2020). Our result with light stimulation shows that the ON response preserves longer than the OFF response in the early stage of RD (Figure 5). In our result with electrical stimulation, the network-mediated responses of OFF RGCs are likely to be elicited less than ON RGCs by the aberrant rod pathway in the RD (Figure 9). Like the previous reports, our result supports the electrically evoked network-mediated RGC responses favor ON RGCs. All these studies have been performed in explanted *in vitro* retinas. ON and OFF RGCs respond to opposite brightness polarities with natural light stimulation, but ON and OFF RGCs are stimulated simultaneously with electrical stimulation. To the best knowledge of the authors, there is no report for the selective activation of ON or OFF RGCs in retinal prosthesis implanted patients.

Electrical stimulation induces simultaneous excitation of ON and OFF RGC, which leads to the cancelation of signals in higher visual centers of the cortex (Kotsakidis et al., 2018). The optogenetic approach, a different approach for vision restoration, has been proposed to overcome this limitation of electrical stimulation. The optogenetic approach using channel rhodopsin has been proposed for the selective activation of ON or OFF RGCs (Provansal et al., 2022). Optogenetic therapy using ChrimsonR in the living primate (*Macaca fascicularis*) is reported to restore characteristic RGC responses to patterned stimuli (McGregor et al., 2020, 2022). In a clinical trial, an optogenetic approach using AAV2.7m8-CAG-ChrimsonR-tdTomato for one patient with RP showed an excellent success rate increment with objective visual detection task (before and after optogenetic approach: 5.8% vs. 41%, respectively) (Sahel et al., 2021). Even if this clinical success is from only one patient, this is a very promising result. The abovementioned ChrimsonR-mediated restoration is mediated by ON RGC response. However, in physiology, ON or OFF characteristics starts from ON BC or OFF BC not from ON RGC or OFF RGC. Therefore, selective activation of ON BC or OFF BC could be a good candidate for an optogenetic approach in the future.

In terms of using a natural visual pathway, the gene therapy that prevents the progression of RD or restores degenerated photoreceptors may also be an alternative to electrical stimulation. The gene therapy approach has been proposed to deliver WT copies of the defective gene into the photoreceptor of the RD. The CRISPR-Cas9 with adeno-associated viral (AAV) vector offers a viable strategy for restoring visual function in the RD mouse model (Pang et al., 2008; Moreno et al., 2018; Vagni et al., 2019; Nishiguchi et al., 2020). Supplementation of *Pde6b* (Pang et al., 2008; Vagni et al., 2019) or repression of *Nrl* (Moreno et al., 2018) in P7–14 *rd10* mice lead to delayed degeneration in comparison with untreated age-matched *rd10* mice. Supplementation of *Gnat1* also leads to delayed degeneration in *Pde6c^{cpfl1/cpfl1} Gnat1^{IRD2/IRD2}* mice (Nishiguchi et al., 2020).

CONCLUSION

This study observed the histological, behavioral, and electrophysiological phenotypes with degeneration stages in *rd10* mice. First, we validated age-dependent histological changes in the retina and behavioral changes in the optomotor response in the newly established *rd10* mice (C57BL/6-*Pde6b^{em1(R560C)Dkl}/Korl*). Therefore, the newly established *rd10* mice strain could be as reliably used as the conventional *rd10* mice strain (B6.CXB1-*Pde6b^{rd10}/J*) for the animal model for RP. Second, we investigated RGC response to light or electrical stimulations according to degeneration stages. By the light stimulus, the ON response sustains longer than the OFF response in the early stage of RD (P45). The *rd10* RGC generates fewer spikes than WT throughout the degeneration stages despite the same electrical stimulation parameters. With the progress of the degeneration stage, the number of RGCs which display PSTHs with multiple peaks increases. In addition, the electrically evoked RGC spikes by the pulse amplitude modulation differ across postnatal ages. Therefore, we suggest optimizing the stimulation protocol, such as nullifying multiple peaks, could benefit better clinical results.

DATA AVAILABILITY STATEMENT

The raw data supporting the conclusions of this article will be made available by the authors, without undue reservation.

ETHICS STATEMENT

The animal study was reviewed and approved by the Institutional Animal Care and Use Committee of the Chungbuk National University (approval number: CBNUA-1520-21-01).

AUTHOR CONTRIBUTIONS

SC, YHL, HKK, and YSG conceived the study. DL generated the newly established *rd10* mouse (C57BL/6-*Pde6b^{em1(R560C)Dkl}/Korl*) and interpreted data for the work. SC and YJ performed the experiments. SC, YJ, and JA analyzed the data. SC, JA, YY, and YSG wrote the manuscript. All authors contributed to the article and approved the submitted version.

FUNDING

This study was supported by a grant from the National Research Foundation (NRF) of Korea funded by the Korean government (NRF-2017M3A9E2056460 and NRF-2022R1A2C2004793).

ACKNOWLEDGMENTS

We thank NIFDS for providing C57BL/6-*Pde6b^{em1(R560)Dkl}/Korl* mice and their information. We also thank Striatech GmbH for letting us use the Optodrum.

SUPPLEMENTARY MATERIAL

The Supplementary Material for this article can be found online at: <https://www.frontiersin.org/articles/10.3389/fncel.2022.926096/full#supplementary-material>

Supplementary Figure 1 | Generation of *Pde6b* knockin mouse using CRISPR-Cas9. **(A)** A schematic illustration showing the location of the *Pde6b* target gRNA, HhaI restriction sites, and primer binding sites along with C to T mutation point. **(B)** Initial screening of F0 *Pde6b* knockin mutants with PCR genotyping. Digestion of PCR products with HhaI yielded 3, 4, and 2 DNA

fragments in wild type (+/+), heterozygote (+/M), and homozygote mutant (M/M) samples, respectively. **(C)** The exact sequence of knockin mutation was verified by sequencing after TA cloning of PCR product from F1 heterozygotes mice. The desired knockin of mutation R560C (red arrow) with extra 4 silence mutations (black arrows) are shown.

Supplementary Figure 2 | Example of the raster plot and the PSTH of light stimulus-responsive RGCs. The raster plot shows the time stamp of RGC spikes for each trial. The PSTH shows cumulated spike counts per bin for 50 trials of light stimulation (bin size is 20 ms). The bars above the raster plot represent the 4 s light onset and light offset. The ON and OFF RGCs shown include both the brisk transient (BT) and brisk sustained (BS) RGCs.

REFERENCES

- Ahn, J., Cha, S., Choi, K. E., Kim, S. W., Yoo, Y., and Goo, Y. S. S. (2022). Correlated activity in the degenerate retina inhibits focal response to electrical stimulation. *Front. Cell Neurosci.* 16:889663. doi: 10.3389/fncel.2022.889663
- Ahn, J., Choi, M. H., Kim, K., Senok, S. S., Cho, D. D., Koo, K. I., et al. (2017). The advantage of topographic prominence-adopted filter for the detection of short-latency spikes of retinal ganglion cells. *Korean J. Physiol. Pharmacol.* 21, 555–563. doi: 10.4196/kjpp.2017.21.5.555
- Ahn, S. M., Ahn, J., Cha, S., Yun, C., Park, T. K., Goo, Y. S., et al. (2019). Development of a post-vitreotomy injection of N-methyl-N-nitrosourea as a localized retinal degeneration rabbit model. *Exp. Neurobiol.* 28, 62–73. doi: 10.5607/en.2019.28.1.62
- Airaghi Leccardi, M. J. I., Vagni, P., and Ghezzi, D. (2019). Multilayer 3D electrodes for neural implants. *J. Neural Eng.* 16:026013. doi: 10.1088/1741-2552/aae191
- Aplin, F. P., Fletcher, E. L., Luu, C. D., Vessey, K. A., Allen, P. J., Guymer, R. H., et al. (2016). Stimulation of a suprachoroidal retinal prosthesis drives cortical responses in a feline model of retinal degeneration. *Invest. Ophthalmol. Vis. Sci.* 57, 5216–5229. doi: 10.1167/iov.16-19926
- Ayton, L. N., Barnes, N., Dagnelie, G., Fujikado, T., Goetz, G., Hornig, R., et al. (2020). An update on retinal prostheses. *Clin. Neurophysiol.* 131, 1383–1398. doi: 10.1016/j.clinph.2019.11.029
- Baden, T., Berens, P., Franke, K., Roman Roson, M., Bethge, M., and Euler, T. (2016). The functional diversity of retinal ganglion cells in the mouse. *Nature* 529, 345–350. doi: 10.1038/nature16468
- Barhoum, R., Martinez-Navarrete, G., Corrochano, S., Germain, F., Fernandez-Sanchez, L., de la Rosa, E. J., et al. (2008). Functional and structural modifications during retinal degeneration in the rd10 mouse. *Neuroscience* 155, 698–713. doi: 10.1016/j.neuroscience.2008.06.042
- Benkner, B., Mutter, M., Ecke, G., and Munch, T. A. (2013). Characterizing visual performance in mice: an objective and automated system based on the optokinetic reflex. *Behav. Neurosci.* 127, 788–796. doi: 10.1037/a0033944
- Biswas, S., Haselier, C., Mataruga, A., Thumann, G., Walter, P., and Muller, F. (2014). Pharmacological analysis of intrinsic neuronal oscillations in rd10 retina. *PLoS One* 9:e99075. doi: 10.1371/journal.pone.0099075
- Boinagrov, D., Pangratz-Fuehrer, S., Goetz, G., and Palanker, D. (2014). Selectivity of direct and network-mediated stimulation of the retinal ganglion cells with epi-, sub- and intraretinal electrodes. *J. Neural Eng.* 11:026008. doi: 10.1088/1741-2560/11/2/026008
- Bowne, S. J., Sullivan, L. S., Koboldt, D. C., Ding, L., Fulton, R., Abbott, R. M., et al. (2011). Identification of disease-causing mutations in autosomal dominant retinitis pigmentosa (adRP) using next-generation DNA sequencing. *Invest. Ophthalmol. Vis. Sci.* 52, 494–503. doi: 10.1167/iov.10-6180
- Bringmann, A., Pannicke, T., Grosche, J., Francke, M., Wiedemann, P., Skatchkov, S. N., et al. (2006). Muller cells in the healthy and diseased retina. *Prog. Retin. Eye Res.* 25, 397–424. doi: 10.1016/j.preteyeres.2006.05.003
- Cha, S., Choi, K. E., Ahn, J., Yoo, M., Jeong, Y., Kim, S. W., et al. (2021). Electrical response of retinal ganglion cells in an N-methyl-N-nitrosourea-induced retinal degeneration porcine model. *Sci. Rep.* 11:24135. doi: 10.1038/s41598-021-03439-w
- Chang, B., Hawes, N. L., Hurd, R. E., Davisson, M. T., Nusinowitz, S., and Heckenlively, J. R. (2002). Retinal degeneration mutants in the mouse. *Vision Res.* 42, 517–525.
- Chang, B., Hawes, N. L., Pardue, M. T., German, A. M., Hurd, R. E., Davisson, M. T., et al. (2007). Two mouse retinal degenerations caused by missense mutations in the beta-subunit of rod cGMP phosphodiesterase gene. *Vision Res.* 47, 624–633. doi: 10.1016/j.visres.2006.11.020
- Cheung, N., Mitchell, P., and Wong, T. Y. (2010). Diabetic retinopathy. *Lancet* 376, 124–136. doi: 10.1016/S0140-6736(09)62124-62123
- Cho, H., and Sobrin, L. (2014). Genetics of diabetic retinopathy. *Curr. Diab. Rep.* 14:515. doi: 10.1007/s11892-014-0515-z
- Choi, H., Zhang, L., Cembrowski, M. S., Sabottke, C. F., Markowitz, A. L., Butts, D. A., et al. (2014). Intrinsic bursting of AII amacrine cells underlies oscillations in the rd1 mouse retina. *J. Neurophysiol.* 112, 1491–1504. doi: 10.1152/jn.00437.2014
- Choi, K. E., Anh, V. T. Q., Kim, J. T., Yun, C., Cha, S., Ahn, J., et al. (2021). An experimental pig model with outer retinal degeneration induced by temporary intravitreal loading of N-methyl-N-nitrosourea during vitrectomy. *Sci. Rep.* 11:258. doi: 10.1038/s41598-020-79437-79431
- Davanger, S., Ottersen, O. P., and Storm-Mathisen, J. (1991). Glutamate, GABA, and glycine in the human retina: an immunocytochemical investigation. *J. Comp. Neurol.* 311, 483–494. doi: 10.1002/cne.903110404
- Davidson, R. S., Hemanth, S., Keller, S. S., Bek, T., and Hansen, O. (2019). Evaluation of the capacitive behavior of 3D carbon electrodes for sub-retinal photovoltaic prosthesis. *Micro Nano Eng.* 2, 110–116. doi: 10.1016/j.mne.2019.02.003
- Delbeke, J., Pins, D., Michaux, G., Wanet-Defalque, M. C., Parrini, S., and Veraart, C. (2001). Electrical stimulation of anterior visual pathways in retinitis pigmentosa. *Invest. Ophthalmol. Vis. Sci.* 42, 291–297.
- Delyfer, M. N., Gaucher, D., Mohand-Said, S., Barale, P. O., Rezaigui-Studer, F., Ayello-Scheer, S., et al. (2021). Improved performance and safety from Argus II retinal prosthesis post-approval study in France. *Acta Ophthalmol.* 99, e1212–e1221. doi: 10.1111/aos.14728
- Eleftheriou, C. G., Cehajic-Kapetanovic, J., Martial, F. P., Milosavljevic, N., Bedford, R. A., and Lucas, R. J. (2017). Meclofenamic acid improves the signal to noise ratio for visual responses produced by ectopic expression of human rod opsin. *Mol. Vis.* 23, 334–345.
- Fain, G., and Sampath, A. P. (2018). Rod and cone interactions in the retina. *F1000Res* 7:F1000 Faculty Rev-657.
- Fried, S. I., Hsueh, H. A., and Werblin, F. S. (2006). A method for generating precise temporal patterns of retinal spiking using prosthetic stimulation. *J. Neurophysiol.* 95, 970–978. doi: 10.1152/jn.00849.2005
- Gargini, C., Terzibasi, E., Mazzoni, F., and Strettoi, E. (2007). Retinal organization in the retinal degeneration 10 (rd10) mutant mouse: a morphological and ERG study. *J. Comp. Neurol.* 500, 222–238. doi: 10.1002/cne.21144
- Gekeler, F., Messias, A., Ottinger, M., Bartz-Schmidt, K. U., and Zrenner, E. (2006). Phosphenes electrically evoked with DTL electrodes: a study in patients with retinitis pigmentosa, glaucoma, and homonymous visual field loss and normal subjects. *Invest. Ophthalmol. Vis. Sci.* 47, 4966–4974. doi: 10.1167/iov.06-0459
- Goo, Y. S., Ahn, K. N., Song, Y. J., Ahn, S. H., Han, S. K., Ryu, S. B., et al. (2011a). Spontaneous oscillatory rhythm in retinal activities of two retinal degeneration (rd1 and rd10) mice. *Korean J. Physiol. Pharmacol.* 15, 415–422. doi: 10.4196/kjpp.2011.15.6.415
- Goo, Y. S., Ye, J. H., Lee, S., Nam, Y., Ryu, S. B., and Kim, K. H. (2011b). Retinal ganglion cell responses to voltage and current stimulation in wild-type and rd1 mouse retinas. *J. Neural Eng.* 8:035003. doi: 10.1088/1741-2560/8/3/035003

- Goo, Y. S., Park, D. J., Ahn, J. R., and Senok, S. S. (2016). Spontaneous oscillatory rhythms in the degenerating mouse retina modulate retinal ganglion cell responses to electrical stimulation. *Front. Cell Neurosci.* 9:512. doi: 10.3389/fncel.2015.00512
- Guo, T., Yang, C. Y., Tsai, D., Muralidharan, M., Suaning, G. J., Morley, J. W., et al. (2018). Closed-Loop efficient searching of optimal electrical stimulation parameters for preferential excitation of retinal ganglion cells. *Front. Neurosci.* 12:168. doi: 10.3389/fnins.2018.00168
- Hartong, D. T., Berson, E. L., and Dryja, T. P. (2006). Retinitis pigmentosa. *Lancet* 368, 1795–1809. doi: 10.1016/S0140-6736(06)69740-69747
- Ho, E., Lei, X., Flores, T., Lorach, H., Huang, T., Galambos, L., et al. (2019). Characteristics of prosthetic vision in rats with subretinal flat and pillar electrode arrays. *J. Neural Eng.* 16:066027. doi: 10.1088/1741-2552/ab34b3
- Huang, T. W., Kamins, T. I., Chen, Z. C., Wang, B. Y., Bhuckory, M., Galambos, L., et al. (2021). Vertical-junction photodiodes for smaller pixels in retinal prostheses. *J. Neural Eng.* 18:10.1088/1741-2552/abe6b8. doi: 10.1088/1741-2552/abe6b8
- Im, M., and Fried, S. I. (2015). Indirect activation elicits strong correlations between light and electrical responses in ON but not OFF retinal ganglion cells. *J. Physiol.* 593, 3577–3596. doi: 10.1113/JP270606
- Im, M., and Fried, S. I. (2016). Temporal properties of network-mediated responses to repetitive stimuli are dependent upon retinal ganglion cell type. *J. Neural Eng.* 13:025002. doi: 10.1088/1741-2560/13/2/025002
- Im, M., and Kim, S. W. (2020). Neurophysiological and medical considerations for better-performing microelectronic retinal prostheses. *J. Neural Eng.* 17:033001. doi: 10.1088/1741-2552/ab8ca9
- Im, M., Werginz, P., and Fried, S. I. (2018). Electric stimulus duration alters network-mediated responses depending on retinal ganglion cell type. *J. Neural Eng.* 15:036010. doi: 10.1088/1741-2552/aaadcl
- Ivanova, E., Alam, N. M., Prusky, G. T., and Sagdullaev, B. T. (2019). Blood-retina barrier failure and vision loss in neuron-specific degeneration. *JCI Insight* 5:e126747. doi: 10.1172/jci.insight.126747
- Ivanova, E., Yee, C. W., Baldoni, R. Jr., and Sagdullaev, B. T. (2016). Aberrant activity in retinal degeneration impairs central visual processing and relies on Cx36-containing gap junctions. *Exp. Eye Res.* 150, 81–89. doi: 10.1016/j.exer.2015.05.013
- Jensen, R. J. (2012). Activation of ganglion cells in wild-type and P23H rat retinas with a small subretinal electrode. *Exp. Eye Res.* 99, 71–77. doi: 10.1016/j.exer.2012.03.016
- Jones, B. W., Kondo, M., Terasaki, H., Lin, Y., McCall, M., and Marc, R. E. (2012). Retinal remodeling. *Jpn. J. Ophthalmol.* 56, 289–306. doi: 10.1007/s10384-012-0147-142
- Jones, B. W., Watt, C. B., Frederick, J. M., Baehr, W., Chen, C. K., Levine, E. M., et al. (2003). Retinal remodeling triggered by photoreceptor degenerations. *J. Comp. Neurol.* 464, 1–16. doi: 10.1002/cne.10703
- Kelber, A. (2018). Vision: rods see in bright light. *Curr. Biol.* 28, R364–R366. doi: 10.1016/j.cub.2018.02.062
- Kim, S. Y., Sada, S., Pearlman, J., Humayun, M. S., de Juan, E. Jr., et al. (2002). Morphometric analysis of the macula in eyes with disciform age-related macular degeneration. *Retina* 22, 471–477. doi: 10.1097/00006982-200208000-200208012
- Kotsakidis, R., Meffin, H., Ibbotson, M. R., and Kamenova, T. (2018). In vitro assessment of the differences in retinal ganglion cell responses to intra- and extracellular electrical stimulation. *J. Neural Eng.* 15:046022. doi: 10.1088/1741-2552/aac2f7
- Lewicki, M. S. (1998). A review of methods for spike sorting: the detection and classification of neural action potentials. *Network* 9, R53–R78.
- Li, B., Gografe, S., Munchow, A., Lopez-Toledano, M., Pan, Z. H., and Shen, W. (2019). Sex-related differences in the progressive retinal degeneration of the rd10 mouse. *Exp. Eye Res.* 187:107773. doi: 10.1016/j.exer.2019.107773
- Luo, Y. H., and da Cruz, L. (2016). The Argus(R) II retinal prosthesis system. *Prog. Retin. Eye Res.* 50, 89–107. doi: 10.1016/j.preteyres.2015.09.003
- Marc, R. E., Jones, B. W., Watt, C. B., and Strettoi, E. (2003). Neural remodeling in retinal degeneration. *Prog. Retin. Eye Res.* 22, 607–655.
- Margalit, E., Maia, M., Weiland, J. D., Greenberg, R. J., Fujii, G. Y., Torres, G., et al. (2002). Retinal prosthesis for the blind. *Surv. Ophthalmol.* 47, 335–356.
- Margolis, D. J., Newkirk, G., Euler, T., and Detwiler, P. B. (2008). Functional stability of retinal ganglion cells after degeneration-induced changes in synaptic input. *J. Neurosci.* 28, 6526–6536. doi: 10.1523/JNEUROSCI.1533-08.2008
- Masland, R. H. (2001). The fundamental plan of the retina. *Nat. Neurosci.* 4, 877–886. doi: 10.1038/nn0901-877
- Mazzoni, F., Novelli, E., and Strettoi, E. (2008). Retinal ganglion cells survive and maintain normal dendritic morphology in a mouse model of inherited photoreceptor degeneration. *J. Neurosci.* 28, 14282–14292. doi: 10.1523/JNEUROSCI.4968-08.2008
- McGregor, J. E., Godat, T., Dhakal, K. R., Parkins, K., Strazzeri, J. M., Bateman, B. A., et al. (2020). Optogenetic restoration of retinal ganglion cell activity in the living primate. *Nat. Commun.* 11:1703. doi: 10.1038/s41467-020-15317-15316
- McGregor, J. E., Kunala, K., Xu, Z., Murphy, P. J., Godat, T., Strazzeri, J. M., et al. (2022). Optogenetic therapy restores retinal activity in primate for at least a year following photoreceptor ablation. *Mol. Ther.* 30, 1315–1328. doi: 10.1016/j.ymthe.2021.09.014
- Menzler, J., Channappa, L., and Zeck, G. (2014). Rhythmic ganglion cell activity in bleached and blind adult mouse retinas. *PLoS One* 9:e106047. doi: 10.1371/journal.pone.0106047
- Moreno, A. M., Fu, X., Zhu, J., Katrekar, D., Shih, Y. V., Marlett, J., et al. (2018). In situ gene therapy via AAV-CRISPR-Cas9-Mediated targeted gene regulation. *Mol. Ther.* 26, 1818–1827. doi: 10.1016/j.ymthe.2018.04.017
- Muller, L. P., Do, M. T., Yau, K. W., He, S., and Baldrige, W. H. (2010). Tracer coupling of intrinsically photosensitive retinal ganglion cells to amacrine cells in the mouse retina. *J. Comp. Neurol.* 518, 4813–4824. doi: 10.1002/cne.22490
- Murakami, Y., Matsumoto, H., Roh, M., Suzuki, J., Hisatomi, T., Ikeda, Y., et al. (2012). Receptor interacting protein kinase mediates necrotic cone but not rod cell death in a mouse model of inherited degeneration. *Proc. Natl. Acad. Sci. U S A.* 109, 14598–14603. doi: 10.1073/pnas.1206937109
- Nishiguchi, K. M., Fujita, K., Miya, F., Katayama, S., and Nakazawa, T. (2020). Single AAV-mediated mutation replacement genome editing in limited number of photoreceptors restores vision in mice. *Nat. Commun.* 11:482. doi: 10.1038/s41467-019-14181-14183
- Oh, T. I., Lee, M., Lee, Y. M., Kim, G. H., Lee, D., You, J. S., et al. (2021). PGC1alpha loss promotes lung cancer metastasis through epithelial-mesenchymal transition. *Cancers (Basel)* 13:1772. doi: 10.3390/cancers13081772
- Pang, J. J., Boye, S. L., Kumar, A., Dinculescu, A., Deng, W., Li, J., et al. (2008). AAV-mediated gene therapy for retinal degeneration in the rd10 mouse containing a recessive PDEbeta mutation. *Invest. Ophthalmol. Vis. Sci.* 49, 4278–4283. doi: 10.1167/iovs.07-1622
- Park, D. J., Senok, S. S., and Goo, Y. S. (2015). Degeneration stage-specific response pattern of retinal ganglion cell spikes in rd10 mouse retina. *Conf. Proc. IEEE Eng. Med. Biol. Soc.* 2015, 3351–3354. doi: 10.1109/EMBC.2015.7319110
- Pennesi, M. E., Michaels, K. V., Magee, S. S., Maricle, A., Davin, S. P., Garg, A. K., et al. (2012). Long-term characterization of retinal degeneration in rd1 and rd10 mice using spectral domain optical coherence tomography. *Invest. Ophthalmol. Vis. Sci.* 53, 4644–4656. doi: 10.1167/iovs.12-9611
- Phillips, M. J., Otteson, D. C., and Sherry, D. M. (2010). Progression of neuronal and synaptic remodeling in the rd10 mouse model of retinitis pigmentosa. *J. Comp. Neurol.* 518, 2071–2089. doi: 10.1002/cne.22322
- Provansal, M., Marazova, K., Sahel, J. A., and Picaud, S. (2022). Vision restoration by optogenetic therapy and developments toward sonogenetic therapy. *Transl. Vis. Sci. Technol.* 11:18. doi: 10.1167/tvst.11.1.18
- Ratnapriya, R., and Chew, E. Y. (2013). Age-related macular degeneration-clinical review and genetics update. *Clin. Genet.* 84, 160–166. doi: 10.1111/cge.12206
- Reh, M., Lee, M. J., and Zeck, G. (2022). Expression of Channelrhodopsin-2 in rod bipolar cells restores ON and OFF responses at high spatial resolution in blind mouse retina. *Adv. Therapeut.* 5:2100164. doi: 10.1002/adtp.202100164
- Reifler, A. N., Chervenak, A. P., Dolikian, M. E., Benenati, B. A., Li, B. Y., Wachter, R. D., et al. (2015). All spiking, sustained ON displaced amacrine cells receive gap-junction input from melanopsin ganglion cells. *Curr. Biol.* 25, 2763–2773. doi: 10.1016/j.cub.2015.09.018
- Rim, T. H., Park, H. W., Kim, D. W., and Chung, E. J. (2017). Four-year nationwide incidence of retinitis pigmentosa in South Korea: a population-based retrospective study from 2011 to 2014. *BMJ Open* 7:e015531. doi: 10.1136/bmjopen-2016-015531

- Ryu, S. B., Ye, J. H., Goo, Y. S., Kim, C. H., and Kim, K. H. (2010). Temporal response properties of retinal ganglion cells in rd1 mice evoked by amplitude-modulated electrical pulse trains. *Invest. Ophthalmol. Vis. Sci.* 51, 6762–6769. doi: 10.1167/iov.10-5577
- Sagdullaev, B. T., and McCall, M. A. (2005). Stimulus size and intensity alter fundamental receptive-field properties of mouse retinal ganglion cells in vivo. *Vis. Neurosci.* 22, 649–659. doi: 10.1017/S0952523805225142
- Sahel, J. A., Boulanger-Scemama, E., Pagot, C., Arleo, A., Galluppi, F., Martel, J. N., et al. (2021). Partial recovery of visual function in a blind patient after optogenetic therapy. *Nat. Med.* 27, 1223–1229. doi: 10.1038/s41591-021-01351-1354
- Sekirnjak, C., Hottowy, P., Sher, A., Dabrowski, W., Litke, A. M., and Chichilnisky, E. J. (2006). Electrical stimulation of mammalian retinal ganglion cells with multi-electrode arrays. *J. Neurophysiol.* 95, 3311–3327. doi: 10.1152/jn.01168.2005
- Seo, H. W., Kim, N., Ahn, J., Cha, S., Goo, Y. S. S., and Kim, S. (2019). A 3D flexible microelectrode array for subretinal stimulation. *J. Neural Eng.* 16:056016. doi: 10.1088/1741-2552/ab36ab
- Stasheff, S. F. (2008). Emergence of sustained spontaneous hyperactivity and temporary preservation of OFF responses in ganglion cells of the retinal degeneration (rd1) mouse. *J. Neurophysiol.* 99, 1408–1421. doi: 10.1152/jn.00144.2007
- Stasheff, S. F., Shankar, M., and Andrews, M. P. (2011). Developmental time course distinguishes changes in spontaneous and light-evoked retinal ganglion cell activity in rd1 and rd10 mice. *J. Neurophysiol.* 105, 3002–3009. doi: 10.1152/jn.00704.2010
- Stingl, K., Bartz-Schmidt, K. U., Besch, D., Chee, C. K., Cottriall, C. L., Gekeler, F., et al. (2015). Subretinal visual implant alpha IMS—Clinical trial interim report. *Vision Res.* 111(Pt B), 149–160. doi: 10.1016/j.visres.2015.03.001
- Stingl, K., Schippert, R., Bartz-Schmidt, K. U., Besch, D., Cottriall, C. L., Edwards, T. L., et al. (2017). Interim results of a multicenter trial with the new electronic subretinal implant alpha AMS in 15 patients blind from inherited retinal degenerations. *Front. Neurosci.* 11:445. doi: 10.3389/fnins.2017.00445
- Stone, J. L., Barlow, W. E., Humayun, M. S., de Juan, E. Jr., and Milam, A. H. (1992). Morphometric analysis of macular photoreceptors and ganglion cells in retinas with retinitis pigmentosa. *Arch. Ophthalmol.* 110, 1634–1639. doi: 10.1001/archoph.1992.01080230134038
- Tikidji-Hamburyan, A., Reinhard, K., Storch, R., Dietter, J., Seitter, H., Davis, K. E., et al. (2017). Rods progressively escape saturation to drive visual responses in daylight conditions. *Nat. Commun.* 8:1813. doi: 10.1038/s41467-017-01816-1816
- Tong, W., Meffin, H., Garrett, D. J., and Ibbotson, M. R. (2020). Stimulation strategies for improving the resolution of retinal prostheses. *Front. Neurosci.* 14:262. doi: 10.3389/fnins.2020.00262
- Toychiev, A. H., Ivanova, E., Yee, C. W., and Sagdullaev, B. T. (2013). Block of gap junctions eliminates aberrant activity and restores light responses during retinal degeneration. *J. Neurosci.* 33, 13972–13977. doi: 10.1523/JNEUROSCI.2399-13.2013
- Trenholm, S., and Awatramani, G. B. (2015). Origins of spontaneous activity in the degenerating retina. *Front. Cell Neurosci.* 9:277. doi: 10.3389/fncel.2015.00277
- Trenholm, S., Borowska, J., Zhang, J. W., Hoggarth, A., Johnson, K., Barnes, S., et al. (2012). Intrinsic oscillatory activity arising within the electrically coupled AII amacrine-ON cone bipolar cell network is driven by voltage-gated Na⁺ plus channels. *J. Physiology-London* 590, 2501–2517. doi: 10.1113/jphysiol.2011.225060
- Turner, M. H., Schwartz, G. W., and Rieke, F. (2018). Receptive field center-surround interactions mediate context-dependent spatial contrast encoding in the retina. *eLife* 7:e38841. doi: 10.7554/eLife.38841
- Twyford, P., Cai, C., and Fried, S. (2014). Differential responses to high-frequency electrical stimulation in ON and OFF retinal ganglion cells. *J. Neural Eng.* 11:025001. doi: 10.1088/1741-2560/11/2/025001
- Uchida, M., Fitzgerald, M., Woodworth, H., Carrellas, N., Kelberman, C., and Biederman, J. (2018). Subsyndromal manifestations of depression in children predict the development of major depression. *J. Pediatr.* 201, 252–258.e1. doi: 10.1016/j.jpeds.2018.05.049
- Vagni, P., Perlini, L. E., Chenais, N. A. L., Marchetti, T., Parrini, M., Contestabile, A., et al. (2019). Gene editing preserves visual functions in a mouse model of retinal degeneration. *Front. Neurosci.* 13:945. doi: 10.3389/fnins.2019.00945
- Volgyi, B., Kovacs-Oller, T., Atlasz, T., Wilhelm, M., and Gabriel, R. (2013). Gap junctional coupling in the vertebrate retina: variations on one theme? *Prog. Retin. Eye Res.* 34, 1–18. doi: 10.1016/j.preteyeres.2012.12.002
- Wan, J., Zheng, H., Chen, Z. L., Xiao, H. L., Shen, Z. J., and Zhou, G. M. (2008). Preferential regeneration of photoreceptor from Muller glia after retinal degeneration in adult rat. *Vision Res.* 48, 223–234. doi: 10.1016/j.visres.2007.11.002
- Wettschureck, N., and Offermanns, S. (2005). Mammalian G proteins and their cell type specific functions. *Physiol. Rev.* 85, 1159–1204. doi: 10.1152/physrev.00003.2005
- Wong, W. L., Su, X., Li, X., Cheung, C. M., Klein, R., Cheng, C. Y., et al. (2014). Global prevalence of age-related macular degeneration and disease burden projection for 2020 and 2040: a systematic review and meta-analysis. *Lancet Glob. Health* 2, e106–e116. doi: 10.1016/S2214-109X(13)70145-70141
- Ye, J. H., and Goo, Y. S. S. (2007). The slow wave component of retinal activity in rd/rd mice recorded with a multi-electrode array. *Physiol. Meas.* 28, 1079–1088. doi: 10.1088/0967-3334/28/9/009
- Yee, C. W., Toychiev, A. H., and Sagdullaev, B. T. (2012). Network deficiency exacerbates impairment in a mouse model of retinal degeneration. *Front. Syst. Neurosci.* 6:8. doi: 10.3389/fnsys.2012.00008
- Yoon, Y. H., Humayun, M. S., and Kim, Y. J. (2021). One-Year anatomical and functional outcomes of the argus II implantation in korean patients with late-stage retinitis pigmentosa: a prospective case series study. *Ophthalmologica* 244, 291–300. doi: 10.1159/000513585
- Yoon, Y. J., Lee, J. I., Jang, Y. J., An, S., Kim, J. H., Fried, S. I., et al. (2020). Retinal degeneration reduces consistency of network-mediated responses arising in ganglion cells to electric stimulation. *IEEE Trans. Neural Syst. Rehabil. Eng.* 28, 1921–1930. doi: 10.1109/TNSRE.2020.3003345
- Zrenner, E. (2002). Will retinal implants restore vision? *Science* 295, 1022–1025. doi: 10.1126/science.1067996

Conflict of Interest: The authors declare that the research was conducted in the absence of any commercial or financial relationships that could be construed as a potential conflict of interest.

Publisher's Note: All claims expressed in this article are solely those of the authors and do not necessarily represent those of their affiliated organizations, or those of the publisher, the editors and the reviewers. Any product that may be evaluated in this article, or claim that may be made by its manufacturer, is not guaranteed or endorsed by the publisher.

Copyright © 2022 Cha, Ahn, Jeong, Lee, Kim, Lee, Yoo and Goo. This is an open-access article distributed under the terms of the Creative Commons Attribution License (CC BY). The use, distribution or reproduction in other forums is permitted, provided the original author(s) and the copyright owner(s) are credited and that the original publication in this journal is cited, in accordance with accepted academic practice. No use, distribution or reproduction is permitted which does not comply with these terms.



OPEN ACCESS

EDITED BY

Kwoon Y. Wong,
University of Michigan, United States

REVIEWED BY

James Weiland,
University of Michigan, United States
Cheri Deng,
University of Michigan, United States

*CORRESPONDENCE

Maesoon Im
maesoon.im@kist.re.kr;
maesoon.im@gmail.com

SPECIALTY SECTION

This article was submitted to
Cellular Neurophysiology,
a section of the journal
Frontiers in Cellular Neuroscience

RECEIVED 16 June 2022

ACCEPTED 18 July 2022

PUBLISHED 03 August 2022

CITATION

Badadhe JD, Roh H, Lee BC, Kim JH
and Im M (2022) Ultrasound
stimulation for non-invasive visual
prostheses.
Front. Cell. Neurosci. 16:971148.
doi: 10.3389/fncel.2022.971148

COPYRIGHT

© 2022 Badadhe, Roh, Lee, Kim and
Im. This is an open-access article
distributed under the terms of the
[Creative Commons Attribution License](#)
(CC BY). The use, distribution or
reproduction in other forums is
permitted, provided the original
author(s) and the copyright owner(s)
are credited and that the original
publication in this journal is cited, in
accordance with accepted academic
practice. No use, distribution or
reproduction is permitted which does
not comply with these terms.

Ultrasound stimulation for non-invasive visual prostheses

Jaya Dilip Badadhe^{1,2}, Hyeonhee Roh^{1,3}, Byung Chul Lee^{1,2,4},
Jae Hun Kim⁵ and Maesoon Im^{1,2*}

¹Brain Science Institute, Korea Institute of Science and Technology (KIST), Seoul, South Korea,

²Division of Bio-Medical Science & Technology, KIST School, University of Science and Technology (UST), Seoul, South Korea, ³School of Electrical Engineering, College of Engineering, Korea University, Seoul, South Korea, ⁴KHU-KIST Department of Converging Science and Technology, Kyung Hee University, Seoul, South Korea, ⁵Sensor System Research Center, Korea Institute of Science and Technology (KIST), Seoul, South Korea

Globally, it is estimated there are more than 2.2 billion visually impaired people. Visual diseases such as retinitis pigmentosa, age-related macular degeneration, glaucoma, and optic neuritis can cause irreversible profound vision loss. Many groups have investigated different approaches such as microelectronic prostheses, optogenetics, stem cell therapy, and gene therapy to restore vision. However, these methods have some limitations such as invasive implantation surgery and unknown long-term risk of genetic manipulation. In addition to the safety of ultrasound as a medical imaging modality, ultrasound stimulation can be a viable non-invasive alternative approach for the sight restoration because of its ability to non-invasively control neuronal activities. Indeed, recent studies have demonstrated ultrasound stimulation can successfully modulate retinal/brain neuronal activities without causing any damage to the nerve cells. Superior penetration depth and high spatial resolution of focused ultrasound can open a new avenue in neuromodulation researches. This review summarizes the latest research results about neural responses to ultrasound stimulation. Also, this work provides an overview of technical viewpoints in the future design of a miniaturized ultrasound transducer for a non-invasive acoustic visual prosthesis for non-surgical and painless restoration of vision.

KEYWORDS

ultrasound stimulation, neuromodulation, artificial vision, vision restoration, visual prosthesis

Introduction

Permanent blindness can be caused by diverse visual diseases such as retinitis pigmentosa (Yue et al., 2016), age-related macular degeneration (Jackson et al., 2002), and optic neuritis (Toosy et al., 2014). Although these diseases are incurable (Lo et al., 2020), the implantation of visual prostheses is one of the available options for vision restoration (Shepherd et al., 2013; Fernandez, 2018; Im and Kim, 2020;

Kim et al., 2022). Recently, electrical stimulation is used for the activation of neurons in the retina, optic nerve, lateral geniculate nucleus, and visual cortex. For example, Argus II (Humayun et al., 2009; Farvardin et al., 2018), Alpha IMA/AMS (Zrenner et al., 2011; Stingl et al., 2015), and Orion (Beauchamp et al., 2020) have been successfully implanted onto/underneath the human retina or at the visual cortex, respectively; and they have shown clinically promising results. However, there are still several challenges to be overcome for more useful visual prostheses. Those issues include slow perception of artificial vision, limited numbers of pixels (i.e., electrodes), invasiveness of microelectrodes, and so on.

Among those issues, the invasive implantation requires considerable surgical costs and may show surgical side effects. Many efforts have recently been made to implement non-invasive visual prostheses, including the investigation of optogenetics (Barrett et al., 2014), photoswitches (Tochitsky et al., 2016), and artificial opsins (Park et al., 2018; Berry et al., 2019). In the past decade, ultrasound-based neuromodulation in the brain and peripheral nervous system has gathered huge attention due to its non-invasiveness, deep penetration power through the skull with minimal neural tissue damage (Lee et al., 2016), and sub-mm focusing capability (Kim et al., 2021). Ultrasound has long been used for both diagnostic imaging (Wells, 2006) and therapeutic treatment (Steiss and McCauley, 2004) including cancer tissue destruction (Hsiao et al., 2016), proving its safety. In recent years, ultrasound stimulation technology (UST) has been used for neuromodulation of the nerve cells of the retina (Yue et al., 2016; Jiang et al., 2019; Lo et al., 2020) and of the visual cortex (Lee et al., 2016; Lu et al., 2021). The purpose of the present study is to overview recent studies regarding UST aiming for vision restoration as well as to discuss future perspectives on the development of acoustic visual prostheses.

Working principle of ultrasound stimulation

The application of ultrasound can make the following three physical events: (1) Increase in temperature, (2) Bubble formation and cavitation, and (3) Acoustic radiation force (Yoo et al., 2022). It has been known that neural activities can be induced by the aforementioned physical changes (O'Brien, 2007; Tyler et al., 2008; Plaksin et al., 2016). First, it had been demonstrated that high-intensity (>1 W/cm²) ultrasound can evoke action potentials in peripheral neuronal cells due to the increased excitability at higher temperature (Figure 1A1; Tsui et al., 2005; Yoo et al., 2022). Because too much heat damages tissue by protein denaturation and decreases synaptic transmission (Dalecki, 2004; O'Brien, 2007), low-intensity (<500 mW/cm²) ultrasound had been tested for neuromodulation without hyperthermia effect (Dalecki, 2004;

O'Brien, 2007). Interestingly, the neural activities were also modulated even with a minimal temperature rise, making the thermal mechanism less convincing.

Second, cavitation is a non-thermal effect caused by ultrasound (Figure 1A2), which directly modulates ion channels as well as the plasma membrane for neuromodulation (Fomenko et al., 2018). Cavitation makes gas bubbles forming, oscillating, and possibly collapsing within the tissue, resulting in stimulation of action potentials and synaptic transmission by deforming the bilayer lipid membrane (Krasovitski et al., 2011). The cavitation can happen by ultrasound waves at low frequency (1–3 MHz); however, acoustic pulses at higher frequencies (>4 MHz) are difficult to be used because oscillations in bubbles are difficult to be maintained during cavitation (Menz et al., 2019).

Lastly, acoustic radiation force is the most widely accepted potential physical mechanism of ultrasound-based neuromodulation (Figure 1A3). The mechanical force generated by steady acoustic pressure on the target neuron stretches the cell membrane and results in conformation and deformation of mechanosensitive ion channels in the cell membrane (Fomenko et al., 2018; Menz et al., 2019; Qian et al., 2022).

Mechanosensitive ion channels are transmembrane proteins that can detect and respond to mechanical stimuli; they can act as mechanosensitive nanosensor and provide a neuronal response to microbubbles generated by applied ultrasound (Figure 1B). Stretch-sensitive channels, displacement-sensitive channels, and shear stress-sensitive ion channels are commonly recognized as mechanosensitive ion channels (Morris, 1990). When the ultrasound is applied, mechanosensitive proteins undergo a conformational change that stimulates ion channels (Johns, 2002; Sukharev and Corey, 2004). Several earlier studies have focused on the significance of various mechanosensitive ion channels in various types of neurons (Menz et al., 2017; Ye et al., 2018; Wang et al., 2020; Yoo et al., 2022). Ultrasound has recently been used to trigger mechanosensitive K⁺, Ca²⁺, and Na⁺ channels that are found in the retina and brain (Maingret et al., 1999; Kubanek et al., 2016; Sorum et al., 2021). Those mechanosensitive proteins include MEC-4 (Kubanek et al., 2018), TRPP1/2 (Duque et al., 2022), TRPV1 (Yang et al., 2020), Piezo 1 (Qiu et al., 2019a), MscL (Ye et al., 2018), TRAAK (Sorum et al., 2021), and the K2p family (Zhao et al., 2017). Although it has not been fully understood, those mechanosensitive components are believed to play a critical role in neuromodulation using UST (Ye et al., 2018). To improve cell-type specificity, sonogenetics is also recently introduced (Ibsen et al., 2015; Qiu et al., 2019b; Yoo et al., 2022). The sonogenetics approach is a combination of ultrasound-based neuromodulation with mechanosensitive channel proteins, which can add cell type-specificity to conventional UST.

In addition to the direct activation of mechanosensitive ion channels, voltage-gated ion channels can be indirectly activated by ultrasound stimulation. For example, piezoelectric

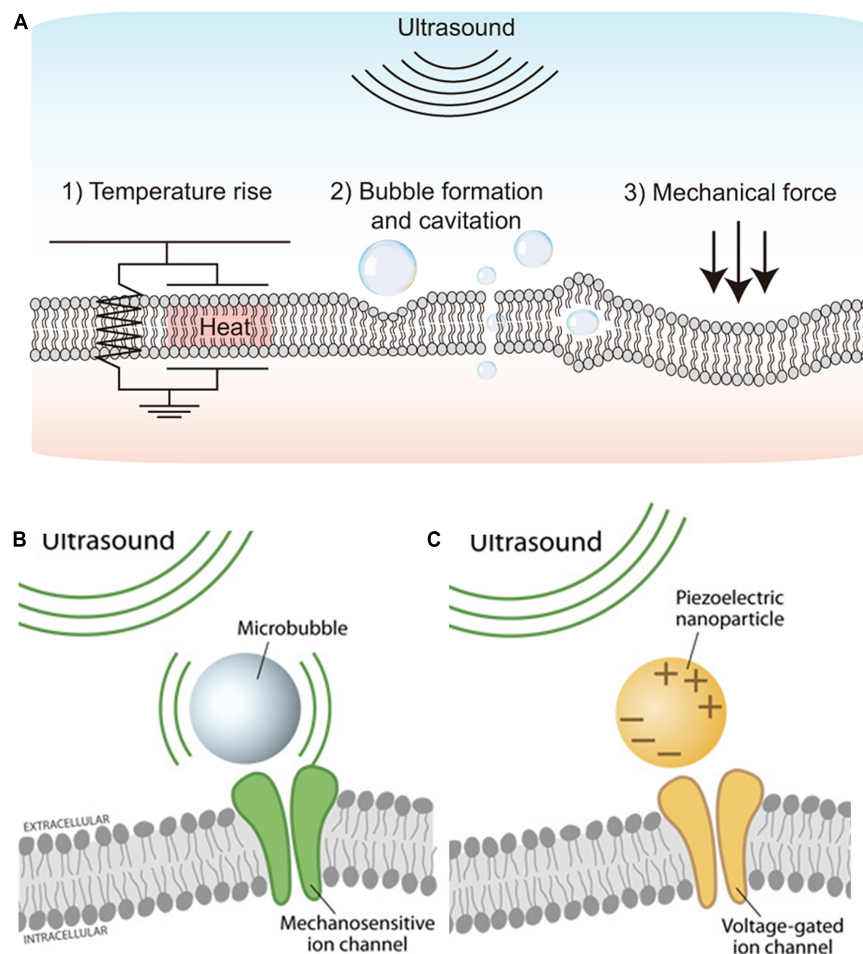


FIGURE 1

Schematics showing the ultrasound stimulation mechanism and ultrasound stimulation methods. (A) Physical mechanisms of ultrasound-based excitation on neurons. Biophysical effects of ultrasound such as (1) Temperature rise, (2) Bubble formation and cavitation, and (3) Mechanical force. Adapted from Yoo et al. (2022). (B) Microbubble-assisted ultrasound stimulation of mechanosensitive channels. Adapted from Rivnay et al. (2017). (C) Piezoelectric nanoparticle-assisted ultrasound stimulation of voltage-sensitive ion channel. Adapted from Rivnay et al. (2017).

nanoparticles stimulated by external ultrasound can generate electrical charges in the target tissues, activating voltage-gated ion channels for neuromodulation (Figure 1C). A previous study demonstrated piezoelectric stimulation induces Ca^{2+} influx that helps in neuronal stimulation (Marino et al., 2015). This indirect electrical stimulation assisted by piezoelectric nanoparticles can serve as nano-transducers at both tissue and cell levels (Marino et al., 2017; Rivnay et al., 2017; Cafarelli et al., 2021). Earlier studies have used boron nitride nanotubes (BNNTs), barium titanate nanoparticles (BTNPs), zinc oxide (ZnO) nanowires, and polyvinylidene fluoride-trifluoroethylene (PVDF-TrFE) as piezoelectric nanoparticles (Cafarelli et al., 2021). However, *in vivo* proof of the feasibility and efficacy of piezoelectric nanoparticles-based ultrasound therapy for vision restoration has yet to be demonstrated. Also, more in-depth studies may be required to explore any potential toxicity and long-term biocompatibilities of

piezoelectric nanoparticles (Cafarelli et al., 2021). For instance, piezoelectric nanoparticles such as lead zirconate titanate (PZT) are less biocompatible due to the lead element but further, PZT was made more biocompatible by treating its surface with titanium (Sakai et al., 2006).

Ultrasound stimulation of retina and visual cortex

Nowadays, low-intensity focused ultrasound (LIFUS) becomes widely used as a non-thermal, non-invasive approach for generating neuromodulation toward vision restoration (Baek et al., 2017; Fomenko et al., 2018; Jiang et al., 2018, 2019; Yuan et al., 2019). It has been repeatedly demonstrated that FUS can effectively stimulate the neurons *in vitro* (Menz et al., 2017; Cafarelli et al., 2021), *ex vivo* (Blackmore et al., 2019;

Menz et al., 2019; Sarica et al., 2022), and *in vivo* (Naor et al., 2012; Lee et al., 2015). For the vision restoration purpose, an acoustic retinal prosthesis (ARP) had been proposed for the first time by demonstrating a FUS neurostimulation of the retinal cells in anesthetized wild-type rats (Naor et al., 2012). The ARP consists of an ultrasound phased array and an external camera with an image processor, connected with the cornea via an acoustic coupling component, to transmit acoustic images onto the retina. Later, a high frequency (43 MHz) ultrasound was used for stimulation of the salamander retina which generates high spatiotemporal resolution and stable visual responses (Menz et al., 2013). The acoustic pulses focused on target cells produced spiking activities like both ON and OFF types of retinal ganglion cells (RGCs) with temporal precision similar to the visual responses. Their spatial resolution was $\sim 100\ \mu\text{m}$ but higher frequency ultrasound is expected to achieve smaller activation; however, it may damage lens tissues by generating heat. In another study, the responsiveness of RGCs in the rodent retinas to low frequency (2.25 MHz) FUS was systematically investigated (Jiang et al., 2018). Recently, RGC activities were modulated with even lower US frequency (1 MHz) at low-intensity ($0.5\ \text{W}/\text{cm}^2$) (Zhuo et al., 2022). The responses of RGCs greatly varied within each cell type as a function of different ultrasound intensities, suggesting neurophysiological properties of RGCs plays an important role in ultrasound responses. Also, the responses to ultrasound stimulation were not the same as those to light stimulation, implying some limitations for high-quality artificial vision. In the work of Jiang et al. (2018), double burst responses to ultrasound stimulation were observed; the latencies of second bursts were comparable to those of the delayed bursts that have been observed in electrical responses (Im and Fried, 2015; Im et al., 2018; Lee and Im, 2019; Kang et al., 2021). This similar temporal property suggests both ultrasound and electric stimulation may share common RGC activation mechanism(s). More recently, *in vivo* stimulation of blind rats' retina using a 3.1 MHz spherically focused single-element transducer was reported for the first time (Qian et al., 2022). The ultrasound stimulation of the retina in spatial resolution of $250\ \mu\text{m}$ evoked neural signals in the visual cortex (Figure 2A).

Different areas of retinal tissue can be simultaneously stimulated using a multiple-focus ultrasound transducer array (Li et al., 2018). For easy implementation of the ARP, another study proposed a flexible wearable contact lens transducer array that covers the entire pupil, enabling multi-depth stimulation (Gao et al., 2017). The multi-focused phased array transducers can be worn like a contact lens to the external surface of the eyeball. In the simulation study, it has been estimated that acoustic stimulation at 2.5 MHz can stimulate multiple points in the retina with $\sim 1.3\ \text{mm}$ lateral resolution (Gao et al., 2017). But, there was an issue limiting the application of this approach: the lens tissue in the eyeball absorbs ultrasound energy which further elevates the temperature at the treatment

site that can be harmful to the eye. To solve this issue, a racing array transducer similar to a contact lens was proposed for the development of ultrasound retinal stimulation (Yu et al., 2019). The racing array transducer was composed of an array of transducer elements aligned on a concave surface and the center part of the transducer was hollow. In the racing array transducer approach (Figure 2B), the ultrasound absorption in the lens was minimized by directly applying the ultrasound to retina tissue without passing through the lens tissue, thereby avoiding retinal damage due to the potential heating. For a wide coverage of the visual field, a large flexible 2D matrix form of a capacitive micromachined ultrasonic transducer (CMUT) array can be one of the promising candidate systems (Tyler et al., 2018). The CMUT also has advantages of high temporal resolution, reduced size of the focal spot sidelobes, as well as easy monolithic integration with microelectronics.

Ultrasound stimulation technology can be applied to not only the retina but also the visual cortex (Ghezzi, 2015; Kim et al., 2015; Naor et al., 2016; Lu et al., 2021). For instance, ultrasound was successfully applied transcranially to the primary visual cortex of sheep, generating electroencephalographic potentials associated with ultrasound stimulation (Lee et al., 2016). The transcranial focused ultrasound (tFUS) approach is known to be safe and effective for transient neuromodulation (Di Biase et al., 2019). Low-intensity tFUS has elicited blood-oxygen-level-dependent (BOLD) responses in the human primary visual cortex and associated visual areas in the visual cortex, which was correlated with the perception of phosphenes (Lee et al., 2016). The on-site acoustic intensity and spatial resolution of the ultrasonic treatment were estimated using a retrospective numerical simulation of acoustic wave propagation through the skull (Figure 2C). While ultrasound has to penetrate the porous skull in the case of the cortical stimulation, the ultrasound wave for the retinal stimulation passes through a clear homogenous soft medium such as aqueous humor. This technically means that the retinal stimulation has benefits to use the non-invasiveness because the ultrasound energy is less attenuated and the pathway of the ultrasound wave can be well predictable to make higher spatiotemporal focal spots. In contrast, the stimulation of intact visual cortex may have advantages over the stimulation of degenerate retina which is known to have significant remodeling (Jones et al., 2016).

In previous studies, only normal animals and humans with no vision impairment were evaluated (Legon et al., 2018; Di Biase et al., 2019). It was quite recent that tFUS stimulation was tested to evoke neuronal activities of the visual cortices of both normal and blind rats (Lu et al., 2021). Another study compared responses to ultrasound stimulation using both Long Evans (LE) and Royal College of Surgeon (RCS) rats (Qian et al., 2022). Intriguingly, RCS (blind) rats showed much bigger response onset latencies and considerably stronger responses than those

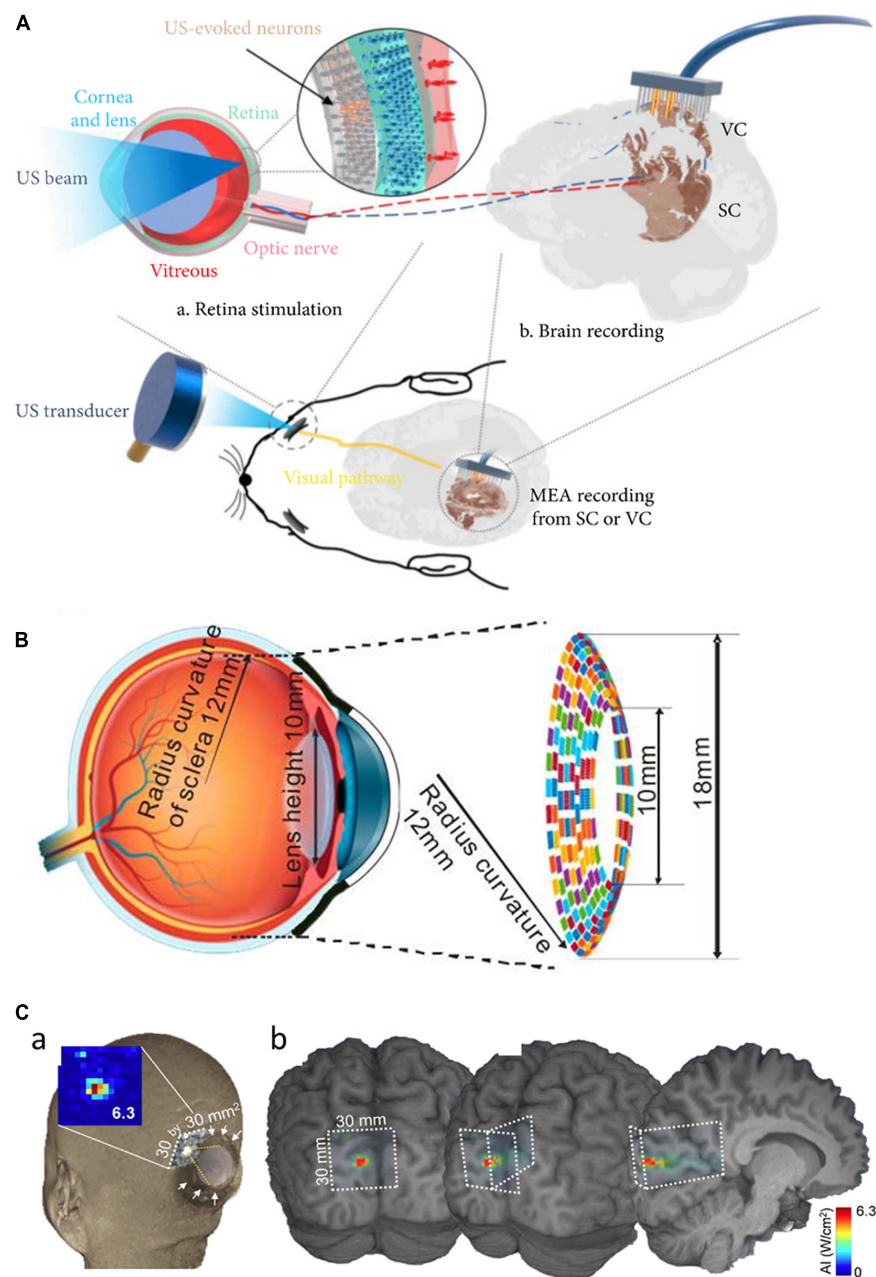


FIGURE 2

Focused ultrasound treatment for visual restoration. **(A)** Retinal neurons were excited by ultrasound waves which lead to the generation of the neural signal. These signals are transmitted to the brain via the optic nerve and the brain activity is recorded from the visual cortex or the superior colliculus. Adapted from Qian et al. (2022). **(B)** The circular racing array device for ultrasonic stimulation. Adapted from Yu et al. (2019). **(C)** In simulated acoustic intensity profiles, the acoustic focus was effectively projected to the targeted stimulatory site localized in the calcarine fissure (a), and acoustic energy was delivered to the visual cortex (b). Adapted from Lee et al. (2016).

of LE (normally sighted) rats, probably due to prolonged visual deprivation.

Although tFUS has been used to modulate neuronal activity deep in the brain (Tufail et al., 2011; Legon et al., 2014, 2018; Di Biase et al., 2019; Lu et al., 2021), these approaches have some limitations such as restricted to low-frequency stimulation, low

spatial resolution (>3 mm), and no cell-type selectivity. To overcome these issues, sonogenetics approach was explored (Ibsen et al., 2015). For example, a recent sonogenetics study expressed mechanosensitive ion channels (MscL) in the primary visual cortex of rodents; they achieved high spatial (~ 100 μ m) and temporal (<50 ms) resolution (Cadoni et al., 2021). It has

been known that the activation of 100 μm area in diameter would result in the restored visual acuity of 20/400 (Palanker et al., 2020). The increased sensitivity of neuronal cells to UST was observed by heterogeneously expressed MscL, which increases Ca^{2+} influx (Cadoni et al., 2021). Considering these results, the sonogenetic strategy may open a new door for the application of engineered mechanosensitive channels for vision restoration in blind patients.

Issues to be addressed for the development of successful acoustic visual prostheses

Retinal UST studies (Naor et al., 2012; Qian et al., 2022) showed a spatial resolution similar to that of the Argus II (electrical stimulation system), the first and only FDA approved retinal prostheses. Despite recent promising results of the ultrasound in vision restoration studies (Menz et al., 2017; Lu et al., 2021; Rousou et al., 2021), several issues need to be addressed further for the clinical success of acoustic visual prostheses. First, the mechanism of neuromodulation of ultrasound stimulation should be more comprehensively understood. In particular, it is unclear whether the neuromodulation effect of ultrasound is universal or limited to specific cell types as well as whether the cellular compartment responding to ultrasound is existing in the degenerate retinas (Lo et al., 2020). If the underlying mechanism is revealed, the ultrasound stimulation conditions (e.g., frequency, therapy duration, duty cycle, and intensity) can be further optimized to efficiently modulate neuronal activities and/or enhance spatiotemporal resolution. For example, it has been known that the physical effect varies with changes in acoustic frequency: cavitation decreases with increasing frequency, and acoustic radiation force increases with increasing frequency (Fan et al., 2021).

Second, additional studies are essential to determine the long-term reliability and/or safety of repetitive application of ultrasonic stimulation. To date, it has been reported that repeated application of ultrasound for 36–48 h did not alter fine membrane structures (Tyler et al., 2008). However, according to the FDA safety guidelines, the acoustic intensity on the eye should be less than 50 mW/cm^2 , which is substantially lower than the safety threshold for other organs (720 mW/cm^2) (Leary et al., 2008). Therefore, long-term mechanical damages due to continuous repetitive stimulation for dynamic artificial vision need to be additionally investigated. Also, the elevation of temperature can be unsafe for the eye. Typically, ultrasound transducers consume high power; therefore, future ultrasound-based visual prostheses must enable low-power neuromodulation not only for the light-weight batteries but also for less heat generation. Several recent

attempts have provided some solutions for the power issue with the wireless energy transfer such as ultrasonic power delivery (Jiang et al., 2022).

Third, although all the parts of the LIFUS system can be mountable on the eye with wireless power transfer, further miniaturization of the whole UST system would be necessary because the size of the external stimulator is highly dependent on the stimulating power. For example, in the case of the high intensity focused ultrasound (HIFUS) system, which needs a high voltage power supply to generate high pressure from an ultrasonic transducer, additional electronics such as power amplifiers may hinder the implementation of the wearable device size. However, technological advances for increased energy efficiency in transducers, wireless power transfer, and batteries are all expected to not only reduce the size of external stimulators but also lengthen operating hours. Indeed, recent publications have demonstrated a CMUT array with monolithically integrated circuits can be chronically implantable even on a rat (Seok et al., 2021a,b). A 2D ultrasonic transducer array system would be preferred to create multi-focused patterns of activities rather than a single transducer with a raster scanning (Lo et al., 2020), which requires lots of extra bulky moving components.

Conclusion

Thanks to the non-invasiveness, UST has a potential to be a burgeoning field in neural prosthetics. Ultrasound approaches are still in their early stages, and an understanding of interaction with cells/tissues will be important for its successful advancement in the future. Both animal and human studies affirm ultrasound neuromodulation can be helpful for simple and non-invasive interference of impaired visual functions (Lee et al., 2016; Qian et al., 2022). Despite the promising feasibility results, many questions regarding the technological framework of the UST are still unanswered. Most importantly, the working principle behind the biological transduction of ultrasound is yet to be completely understood whether related to particular cell types. There are not many reports about *in vivo* demonstration of vision restoration. However, due to its non-invasiveness and potential for high-resolution stimulation, UST can be widely preferred. It is further expected that the use of engineered neuronal cells with mechanosensitive ion channels would provide high spatiotemporal resolution. Future research work in the abovementioned areas is needed to make the UST to be clinically applicable in blind patients.

Author contributions

JB and HR contributed to drafting the manuscript. MI conceived the study and revised the manuscript. BL and JK

revised the manuscript. All authors read and approved the final manuscript.

Funding

This work was supported in part by the KIST (Korea Institute of Science and Technology) institutional grant (2E31821) and National R&D Program through the National Research Foundation of Korea (NRF) funded by the Ministry of Science and ICT (Nos. 2020R1C1C1006065, 2021M3F3A2A01037366, and 2022M3E5E8017395). Also, this work was supported in part by the Korea Medical Device Development Fund grant funded by the Korean government (Ministry of Science and ICT, Ministry of Trade, Industry and Energy, Ministry of Health and Welfare, Ministry of Food and Drug Safety) (Project Number: 202011D01).

References

- Baek, H., Pakk, K. J., and Kim, H. (2017). A review of low-intensity focused ultrasound for neuromodulation. *Biomed. Eng. Lett.* 7, 135–142. doi: 10.1007/s13534-016-0007-y
- Barrett, J. M., Berlinguer-Palmini, R., and Degenar, P. (2014). Optogenetic approaches to retinal prosthesis. *Vis. Neurosci.* 31, 345–354. doi: 10.1017/S0952523814000212
- Beauchamp, M. S., Oswalt, D., Pouratian, N., Bosking, W. H., Correspondence, D. Y., Sun, P., et al. (2020). Dynamic stimulation of visual cortex produces form vision in sighted and blind humans. *Cell* 181, 774–783. doi: 10.1016/j.cell.2020.04.033
- Berry, M. H., Holt, A., Salari, A., Veit, J., Visel, M., Levitz, J., et al. (2019). Restoration of high-sensitivity and adapting vision with a cone opsin. *Nat. Commun.* 10:1221. doi: 10.1038/s41467-019-09124-x
- Blackmore, J., Shrivastava, S., Sallet, J., Butler, C. R., and Cleveland, R. O. (2019). Ultrasound neuromodulation: A review of results, mechanisms and safety. *Ultrasound Med. Biol.* 45, 1509–1536. doi: 10.1016/j.ultrasmedbio.2018.12.015
- Cadoni, S., Demene, C., Provansal, M., Nguyen, D., Nelidova, D., Labernede, G., et al. (2021). Sonogenetic stimulation of the brain at a spatiotemporal resolution suitable for vision restoration. *bioRxiv* [Preprint]. doi: 10.1101/2021.11.07.467597
- Cafarelli, A., Marino, A., Vannozzi, L., Puigmarti-Luis, J., Pané, S., Ciofani, G., et al. (2021). Piezoelectric nanomaterials activated by ultrasound: The pathway from discovery to future clinical adoption. *ACS Nano* 15, 11066–11086. doi: 10.1021/acsnano.1c03087
- Dalecki, D. (2004). Mechanical bioeffects of ultrasound. *Annu. Rev. Biomed. Eng.* 6, 229–248. doi: 10.1146/annurev.bioeng.6.040803.140126
- Di Biase, L., Falato, E., and Di Lazzaro, V. (2019). Transcranial focused ultrasound (tFUS) and transcranial unfocused ultrasound (tUS) neuromodulation: From theoretical principles to stimulation practices. *Front. Neurol.* 10:549. doi: 10.3389/fneur.2019.00549
- Duque, M., Lee-Kubli, C. A., Tufail, Y., Magaram, U., Patel, J., Chakraborty, A., et al. (2022). Sonogenetic control of mammalian cells using exogenous transient receptor potential A1 channels. *Nat. Commun.* 13:600. doi: 10.1038/s41467-022-28205-y
- Fan, H., Shimba, K., Ishijima, A., Sasaoka, K., Takahashi, T., Chang, C.-H., et al. (2021). Acoustic frequency-dependent physical mechanism of sub-MHz ultrasound neurostimulation. *bioRxiv* [Preprint]. doi: 10.1101/2021.09.11.458049
- Farvardin, M., Afarid, M., Attarzadeh, A., Johari, M. K., Mehryar, M., Hossein Nowroozzadeh, M., et al. (2018). The Argus-II retinal prosthesis implantation: from the global to local successful experience. *Front. Neurosci.* 12:584. doi: 10.3389/fnins.2018.00584
- Fernandez, E. (2018). Development of visual neuroprostheses: Trends and challenges. *Bioelectron. Med.* 4:12. doi: 10.1186/s42234-018-0013-8
- Fomenko, A., Neudorfer, C., Dallapiazza, R. F., Kalia, S. K., and Lozano, A. M. (2018). Low-intensity ultrasound neuromodulation: An overview of mechanisms and emerging human applications. *Brain Stimul.* 11, 1209–1217. doi: 10.1016/j.brs.2018.08.013
- Gao, M., Yu, Y., Zhao, H., Li, G., Jiang, H., Wang, C., et al. (2017). Simulation study of an ultrasound retinal prosthesis with a novel contact-lens array for noninvasive retinal stimulation. *IEEE Trans. Neural Syst. Rehabil. Eng.* 25, 1605–1611. doi: 10.1109/tnsre.2017.2682923
- Ghezzi, D. (2015). Retinal prostheses: Progress towards the next generation implants. *Front. Neurosci.* 9:290. doi: 10.3389/fnins.2015.00290
- Hsiao, Y. H., Kuo, S. J., Tsai, H. D., Chou, M. C., and Yeh, G. P. (2016). Clinical application of high-intensity focused ultrasound in cancer therapy. *J. Cancer* 7, 225–231. doi: 10.7150/jca.13906
- Humayun, M. S., Dorn, J. D., Ahuja, A. K., Caspi, A., Filley, E., Dagnelie, G., et al. (2009). Preliminary 6 month results from the Argus II epiretinal prosthesis feasibility study. *Annu. Int. Conf. IEEE Eng. Med. Biol. Soc.* 2009, 4566–4568. doi: 10.1109/iembs.2009.5332695
- Ibsen, S., Tong, A., Schutt, C., Esener, S., and Chalasani, S. H. (2015). Sonogenetics is a non-invasive approach to activating neurons in *Caenorhabditis elegans*. *Nat. Commun.* 6:8264. doi: 10.1038/ncomms9264
- Im, M., and Fried, S. I. (2015). Indirect activation elicits strong correlations between light and electrical responses in ON but not OFF retinal ganglion cells. *J. Physiol.* 593, 3577–3596. doi: 10.1113/jp270606
- Im, M., and Kim, S. W. (2020). Neurophysiological and medical considerations for better-performing microelectronic retinal prostheses. *J. Neural Eng.* 17:033001. doi: 10.1088/1741-2552/ab8ca9
- Im, M., Werginz, P., and Fried, S. I. (2018). Electric stimulus duration alters network-mediated responses depending on retinal ganglion cell type. *J. Neural Eng.* 15:036010. doi: 10.1088/1741-2552/aaadc1
- Jackson, G. R., Owsley, C., and Curcio, C. A. (2002). Photoreceptor degeneration and dysfunction in aging and age-related maculopathy. *Ageing Res. Rev.* 1, 381–396. doi: 10.1016/S1568-1637(02)00007-7
- Jiang, L., Lu, G., Zeng, Y., Sun, Y., Kang, H., Burford, J., et al. (2022). Flexible ultrasound-induced retinal stimulating piezo-arrays for biomimetic visual prostheses. *Nat. Commun.* 13:3853. doi: 10.1038/s41467-022-31599-4
- Jiang, Q., Li, G., Zhao, H., Sheng, W., Yue, L., Su, M., et al. (2018). Temporal neuromodulation of retinal ganglion cells by low-frequency focused ultrasound stimulation. *IEEE Trans. Neural Syst. Rehabil. Eng.* 26, 969–976. doi: 10.1109/TNSRE.2018.2821194

Conflict of interest

The authors declare that the research was conducted in the absence of any commercial or financial relationships that could be construed as a potential conflict of interest.

Publisher's note

All claims expressed in this article are solely those of the authors and do not necessarily represent those of their affiliated organizations, or those of the publisher, the editors and the reviewers. Any product that may be evaluated in this article, or claim that may be made by its manufacturer, is not guaranteed or endorsed by the publisher.

- Jiang, X., Savchenko, O., Li, Y., Qi, S., Yang, T., Zhang, W., et al. (2019). A review of low-intensity pulsed ultrasound for therapeutic applications. *IEEE Trans. Biomed. Eng.* 66, 2704–2718. doi: 10.1109/TBME.2018.2889669
- Johns, L. D. (2002). Nonthermal effects of therapeutic ultrasound: The frequency resonance hypothesis. *J. Athl. Train.* 37, 293–299.
- Jones, B. W., Pfeiffer, R. L., Ferrell, W. D., Watt, C. B., Marmor, M., and Marc, R. E. (2016). Retinal remodeling in human retinitis pigmentosa. *Exp. Eye Res.* 150, 149–165. doi: 10.1016/j.exer.2016.03.018
- Kang, J. H., Jang, Y. J., Kim, T., Lee, B. C., Lee, S. H., and Im, M. (2021). Electric stimulation elicits heterogeneous responses in on but not off retinal ganglion cells to transmit rich neural information. *IEEE Trans. Neural Syst. Rehabil. Eng.* 29, 300–309. doi: 10.1109/tnsre.2020.3048973
- Kim, H., Park, M. Y., Lee, S. D., Lee, W., Chiu, A., and Yoo, S. S. (2015). Suppression of EEG visual-evoked potentials in rats through neuromodulatory focused ultrasound. *Neuroreport* 26, 211–215. doi: 10.1097/wnr.0000000000000330
- Kim, S., Jo, Y., Kook, G., Pasquinelli, C., Kim, H., Kim, K., et al. (2021). Transcranial focused ultrasound stimulation with high spatial resolution. *Brain Stimul.* 14, 290–300. doi: 10.1016/j.brs.2021.01.002
- Kim, S., Roh, H., and Im, M. (2022). Artificial visual information produced by retinal prostheses. *Front. Cell. Neurosci.* 16:911754. doi: 10.3389/fncel.2022.911754
- Krasovitski, B., Frenkel, V., Shoham, S., and Kimmel, E. (2011). Intramembrane cavitation as a unifying mechanism for ultrasound-induced bioeffects. *Proc. Natl. Acad. Sci. U.S.A.* 108, 3258–3263. doi: 10.1073/PNAS.1015771108
- Kubaneck, J., Shi, J., Marsh, J., Chen, D., Deng, C., and Cui, J. (2016). Ultrasound modulates ion channel currents. *Sci. Rep.* 6:24170. doi: 10.1038/srep24170
- Kubaneck, J., Shukla, P., Das, A., Baccus, S. A., and Goodman, M. B. (2018). Ultrasound elicits behavioral responses through mechanical effects on neurons and ion channels in a simple nervous system. *J. Neurosci.* 38, 3081–3091. doi: 10.1523/JNEUROSCI.1458-17.2018
- Leary, Brendan, Vaezy, and Shahram. (2008). *Marketing Clearance of Diagnostic Ultrasound Systems and Transducers Guidance for Industry and Food and Drug Administration Staff this Guidance Document Supersedes the Guidance Entitled "Information for Manufacturers Seeking Marketing Clearance of Diagnostic Ultrasound Systems and Transducers" dated Preface Public Comment*. Available online at: <https://www.regulations.gov> (accessed on May 9, 2022).
- Lee, J. I., and Im, M. (2019). Optimal electric stimulus amplitude improves the selectivity between responses of on versus off types of retinal ganglion cells. *IEEE Trans. Neural Syst. Rehabil. Eng.* 27, 2015–2024. doi: 10.1109/tnsre.2019.2939012
- Lee, W., Kim, H., Jung, Y., Song, I. U., Chung, Y. A., and Yoo, S. S. (2015). Image-guided transcranial focused ultrasound stimulates human primary somatosensory cortex. *Sci. Rep.* 5:8743. doi: 10.1038/srep08743
- Lee, W., Kim, H. C., Jung, Y., Chung, Y. A., Song, I. U., Lee, J. H., et al. (2016). Transcranial focused ultrasound stimulation of human primary visual cortex. *Sci. Rep.* 6:34020. doi: 10.1038/srep34026
- Ligon, W., Bansal, P., Tyshynsky, R., Ai, L., and Mueller, J. K. (2018). Transcranial focused ultrasound neuromodulation of the human primary motor cortex. *Sci. Rep.* 8:10007. doi: 10.1038/s41598-018-28320-1
- Ligon, W., Sato, T. F., Opitz, A., Mueller, J., Barbour, A., Williams, A., et al. (2014). Transcranial focused ultrasound modulates the activity of primary somatosensory cortex in humans. *Nat. Neurosci.* 17, 322–329. doi: 10.1038/nn.3620
- Li, G., Qiu, W., Hong, J., Jiang, Q., Su, M., Mu, P., et al. (2018). *Imaging-Guided Dual-Target Neuromodulation of the Mouse Brain Using Array Ultrasound*. New York, N.Y.: IEEE. doi: 10.1109/tuffc.2018.2847252
- Lo, P. A., Huang, K., Zhou, Q., Humayun, M. S., and Yue, L. (2020). Ultrasonic retinal neuromodulation and acoustic retinal prosthesis. *Micromachines* 11:929. doi: 10.3390/mi11100929
- Lu, G., Qian, X., Castillo, J., Li, R., Jiang, L., Lu, H., et al. (2021). Transcranial focused ultrasound for noninvasive neuromodulation of the visual cortex. *IEEE Trans. Ultrason. Ferroelectr. Freq. Control* 68, 21–28. doi: 10.1109/tuffc.2020.3005670
- Maingret, F., Fosset, M., Lesage, F., Lazdunski, M., and Honoré, E. (1999). TRAAK is a mammalian neuronal mechano-gated K⁺ channel. *J. Biol. Chem.* 274, 1381–1387. doi: 10.1074/JBC.274.3.1381
- Marino, A., Arai, S., Hou, Y., Sinibaldi, E., Pellegrino, M., Chang, Y. T., et al. (2015). Piezoelectric nanoparticle-assisted wireless neuronal stimulation. *ACS Nano* 9, 7678–7689. doi: 10.1021/acs.nano.5b03162
- Marino, A., Genchi, G. G., Mattoli, V., and Ciofani, G. (2017). Piezoelectric nanotransducers: The future of neural stimulation. *Nano Today* 14, 9–12. doi: 10.1016/j.nantod.2016.12.005
- Menz, M. D., Oralkan, Ö., Khuri-Yakub, P. T., and Baccus, S. A. (2013). Precise neural stimulation in the retina using focused ultrasound. *J. Neurosci.* 33, 4550–4560. doi: 10.1523/JNEUROSCI.3521-12.2013
- Menz, M. D., Ye, P., Firouzi, K., Nikoozadeh, A., Pauly, K. B., Khuri-Yakub, P., et al. (2019). Radiation force as a physical mechanism for ultrasonic neurostimulation of the ex vivo retina. *J. Neurosci.* 39, 6251–6264. doi: 10.1523/JNEUROSCI.2394-18.2019
- Menz, M. D., Ye, P., Firouzi, K., Pauly, K. B., Khuri-Yakub, B. T., and Baccus, S. A. (2017). Physical mechanisms of ultrasonic neurostimulation of the retina. *bioRxiv* [Preprint]. doi: 10.1101/231449
- Morris, C. E. (1990). Mechanosensitive ion channels. *J. Membr. Biol.* 113, 93–107. doi: 10.1007/BF01872883
- Naor, O., Hertzberg, Y., Zemel, E., Kimmel, E., and Shoham, S. (2012). Towards multifocal ultrasonic neural stimulation II: Design considerations for an acoustic retinal prosthesis. *J. Neural Eng.* 9:026006. doi: 10.1088/1741-2560/9/2/026006
- Naor, O., Krupa, S., and Shoham, S. (2016). Ultrasonic neuromodulation. *J. Neural Eng.* 13:031003. doi: 10.1088/1741-2560/13/3/031003
- O'Brien, W. D. (2007). Ultrasound-biophysics mechanisms. *Prog. Biophys. Mol. Biol.* 93, 212–255. doi: 10.1016/j.pbiomolbio.2006.07.010
- Palanker, D., Le Mer, Y., Mohand-Said, S., Muqit, M., and Sahel, J. A. (2020). Photovoltaic restoration of central vision in atrophic age-related macular degeneration. *Ophthalmol* 127, 1097–1104. doi: 10.1016/j.ophtha.2020.02.024
- Park, B., Yang, H., Ha, T. H., Park, H. S., Oh, S. J., Ryu, Y. S., et al. (2018). Artificial rod and cone photoreceptors with human-like spectral sensitivities. *Adv. Mater.* 30:e1706764. doi: 10.1002/adma.201706764
- Plaksin, M., Kimmel, E., and Shoham, S. (2016). Cell-type-selective effects of intramembrane cavitation as a unifying theoretical framework for ultrasonic neuromodulation. *eNeuro* 3, 229–244. doi: 10.1523/ENEURO.0136-15.2016
- Qian, X., Lu, G., Thomas, B. B., Li, R., Chen, X., Shung, K. K., et al. (2022). Noninvasive ultrasound retinal stimulation for vision restoration at high spatiotemporal resolution. *BME Front.* 2022:9829316. doi: 10.34133/2022/9829316
- Qiu, Z., Guo, J., Kala, S., Zhu, J., Xian, Q., Qiu, W., et al. (2019a). The mechanosensitive ion channel piezo1 significantly mediates in vitro ultrasonic stimulation of neurons. *iScience* 21, 448–457. doi: 10.1016/j.isci.2019.10.037
- Qiu, Z., Kala, S., Guo, J., Xian, Q., Zhu, J., and Sun, L. (2019b). Non-invasive and selective brain stimulation by ultrasound via activation of mechanosensitive ion channels. *Brain Stimul.* 12:475. doi: 10.1016/j.brs.2018.12.549
- Rivnay, J., Wang, H., Fenno, L., Deisseroth, K., and Malliaras, G. G. (2017). Next-generation probes, particles, and proteins for neural interfacing. *Sci. Adv.* 3:e1601649. doi: 10.1126/sciadv.1601649
- Rousou, C., Schuurmans, C. C. L., Urtti, A., Mastrobattista, E., Storm, G., Moonen, C., et al. (2021). Ultrasound and microbubbles for the treatment of ocular diseases: From preclinical research towards clinical application. *Pharmaceutics* 13:1782. doi: 10.3390/pharmaceutics13111782
- Sakai, T., Hoshiai, S., and Nakamachi, E. (2006). Biochemical compatibility of PZT piezoelectric ceramics covered with titanium thin film. *J. Optoelectron. Adv. Mater.* 8, 1435–1437.
- Sarica, C., Fomenko, A., Nankoo, J. F., Darmani, G., Vetkas, A., Yamamoto, K., et al. (2022). Toward focused ultrasound neuromodulation in deep brain stimulator implanted patients: Ex-vivo thermal, kinetic and targeting feasibility assessment. *Brain Stimul.* 15, 376–379. doi: 10.1016/j.brs.2021.12.012
- Seok, C., Yamaner, F. Y., Sahin, M., and Oralkan, Ö (2021a). A wearable ultrasonic neurostimulator - Part I: A 1D CMUT phased array system for chronic implantation in small animals. *IEEE Trans. Biomed. Circuits Syst.* 15, 692–704. doi: 10.1109/TBCAS.2021.3100458
- Seok, C., Adelegan, O. J., Biliroglu, A. Ö, Yamaner, F. Y., and Oralkan, Ö (2021b). A wearable ultrasonic neurostimulator - Part II: A 2D CMUT phased array system with a flip-chip bonded ASIC. *IEEE Trans. Biomed. Circuits Syst.* 15, 705–718. doi: 10.1109/TBCAS.2021.3105064
- Shepherd, R. K., Shivdasani, M. N., Nayagam, D. A. X., Williams, C. E., and Blamey, P. J. (2013). Visual prostheses for the blind. *Trends Biotechnol.* 31, 562–571. doi: 10.1016/j.tibtech.2013.07.001
- Sorum, B., Rietmeijer, R. A., Gopakumar, K., Adesnik, H., and Brohawn, S. G. (2021). Ultrasound activates mechanosensitive TRAAK K⁺ channels through the lipid membrane. *Proc. Natl. Acad. Sci. U.S.A.* 118:e2006980118. doi: 10.1073/pnas.2006980118
- Steiss, J. E., and McCauley, L. (2004). Therapeutic ultrasound. *Canine Rehabil. Phys. Ther.* 880, 324–336. doi: 10.1016/b978-0-7216-9555-6.50023-1
- Stingl, K., Bartz-Schmidt, K. U., Besch, D., Chee, C. K., Cotttriall, C. L., Gekeler, F., et al. (2015). Subretinal visual implant alpha ims-clinical trial interim report. *Vision Res.* 111, 149–160. doi: 10.1016/j.visres.2015.03.001

- Sukharev, S., and Corey, D. P. (2004). Mechanosensitive channels: Multiplicity of families and gating paradigms. *Sci. STKE* 2004:re4. doi: 10.1126/stke.2192004re4
- Tochitsky, I., Helft, Z., Meseguer, V., Fletcher, R. B., Vessey, K. A., Telias, M., et al. (2016). How azobenzene photoswitches restore visual responses to the blind retina. *Neuron* 92, 100–113. doi: 10.1016/j.neuron.2016.08.038
- Toosy, A. T., Mason, D. F., and Miller, D. H. (2014). Optic neuritis. *Lancet Neurol.* 13, 83–99. doi: 10.1016/s1474-4422(13)70259-x
- Tsui, P. H., Wang, S. H., and Huang, C. C. (2005). In vitro effects of ultrasound with different energies on the conduction properties of neural tissue. *Ultrasonics* 43, 560–565. doi: 10.1016/j.ultras.2004.12.003
- Tufail, Y., Yoshihiro, A., Pati, S., Li, M. M., and Tyler, W. J. (2011). Ultrasonic neuromodulation by brain stimulation with transcranial ultrasound. *Nat. Protoc.* 6, 1453–1470. doi: 10.1038/nprot.2011.371
- Tyler, W. J., Lani, S. W., and Hwang, G. M. (2018). Ultrasonic modulation of neural circuit activity. *Curr. Opin. Neurobiol.* 50, 222–231. doi: 10.1016/j.conb.2018.04.011
- Tyler, W. J., Tufail, Y., Finsterwald, M., Tauchmann, M. L., Olson, E. J., and Majestic, C. (2008). Remote excitation of neuronal circuits using low-intensity, low-frequency ultrasound. *PLoS One* 3:e3511. doi: 10.1371/journal.pone.0003511
- Wang, S., Meng, W., Ren, Z., Li, B., Zhu, T., Chen, H., et al. (2020). Ultrasonic neuromodulation and sonogenetics: A new era for neural modulation. *Front. Physiol.* 11:787. doi: 10.3389/fphys.2020.00787
- Wells, P. N. T. (2006). Ultrasound imaging. *Phys. Med. Biol.* 51, R83–R98. doi: 10.1088/0031-9155/51/13/r06
- Yang, Y., Pacia, C. P., Ye, D., Zhu, L., Baek, H., Yue, Y., et al. (2020). Sonogenetics for noninvasive and cellular-level neuromodulation in rodent brain. *bioRxiv* [Preprint]. doi: 10.1101/2020.01.28.919910
- Ye, J., Tang, S., Meng, L., Li, X., Wen, X., Chen, S., et al. (2018). Ultrasonic control of neural activity through activation of the mechanosensitive channel MscL. *Nano Lett.* 18, 4148–4155. doi: 10.1021/acs.nanolett.8b00935
- Yoo, S., Mittelstein, D. R., Hurt, R. C., Lacroix, J., and Shapiro, M. G. (2022). Focused ultrasound excites cortical neurons via mechanosensitive calcium accumulation and ion channel amplification. *Nat. Commun.* 13:493. doi: 10.1038/s41467-022-28040-1
- Yu, Y., Zhang, Z., Cai, F., Su, M., Jiang, Q., Zhou, Q., et al. (2019). A novel racing array transducer for noninvasive ultrasonic retinal stimulation: A simulation study. *Sensors* 19:1825. doi: 10.3390/s19081825
- Yuan, Y., Wang, Z., Wang, X., Yan, J., Liu, M., and Li, X. (2019). Low-intensity pulsed ultrasound stimulation induces coupling between ripple neural activity and hemodynamics in the mouse visual cortex. *Cereb. Cortex* 29, 3220–3223. doi: 10.1093/cercor/bhy187
- Yue, L., Weiland, J. D., Roska, B., and Humayun, M. S. (2016). Retinal stimulation strategies to restore vision: Fundamentals and systems. *Prog. Retin. Eye Res.* 53, 21–47. doi: 10.1016/j.preteyeres.2016.05.002
- Zhao, L., Feng, Y., Shi, A., Zhang, L., Guo, S., and Wan, M. (2017). Neuroprotective effect of low-intensity pulsed ultrasound against mpp+-induced neurotoxicity in pc12 cells: Involvement of k2p channels and stretch-activated ion channels. *Ultrasound Med. Biol.* 43, 1986–1999. doi: 10.1016/j.ultrasmedbio.2017.04.020
- Zhuo, S. Y., Li, G. F., Gong, H., Qiu, W. B., Zheng, H. R., and Liang, P. J. (2022). Low-frequency, low-intensity ultrasound modulates light responsiveness of mouse retinal ganglion cells. *J. Neural Eng.* 19:046012. doi: 10.1088/1741-2552/ac7d75
- Zrenner, E., Bartz-Schmidt, K. U., Benav, H., Besch, D., Bruckmann, A., Gabel, V. P., et al. (2011). Subretinal electronic chips allow blind patients to read letters and combine them to words. *Proc. Royal. Soc. B Biol. Sci.* 278, 1489–1497. doi: 10.1098/rspb.2010.1747



OPEN ACCESS

EDITED BY

Maesoon Im,
Korea Institute of Science and
Technology (KIST), South Korea

REVIEWED BY

Archana Jalligampala,
University of Louisville, United States
Jungryul Ahn,
Chungbuk National University,
South Korea

*CORRESPONDENCE

James D. Weiland
weiland@umich.edu

†These authors have contributed
equally to this work and share first
authorship

SPECIALTY SECTION

This article was submitted to
Cellular Neurophysiology,
a section of the journal
Frontiers in Cellular Neuroscience

RECEIVED 15 March 2022

ACCEPTED 15 July 2022

PUBLISHED 12 August 2022

CITATION

Li W, Haji Ghaffari D, Misra R and
Weiland JD (2022) Retinal ganglion cell
desensitization is mitigated by varying
parameter constant excitation pulse
trains.
Front. Cell. Neurosci. 16:897146.
doi: 10.3389/fncel.2022.897146

COPYRIGHT

© 2022 Li, Haji Ghaffari, Misra and
Weiland. This is an open-access article
distributed under the terms of the
Creative Commons Attribution License
(CC BY). The use, distribution or
reproduction in other forums is
permitted, provided the original
author(s) and the copyright owner(s)
are credited and that the original
publication in this journal is cited, in
accordance with accepted academic
practice. No use, distribution or
reproduction is permitted which does
not comply with these terms.

Retinal ganglion cell desensitization is mitigated by varying parameter constant excitation pulse trains

Wennan Li^{1†}, Dorsa Haji Ghaffari^{1†}, Rohit Misra¹ and
James D. Weiland^{1,2,3*}

¹Department of Biomedical Engineering, University of Michigan, Ann Arbor, MI, United States,

²Department of Ophthalmology and Visual Sciences, University of Michigan, Ann Arbor, MI, United

States, ³BioInterfaces Institute, University of Michigan, Ann Arbor, MI, United States

Retinal prostheses partially restore vision in patients blinded by retinitis pigmentosa (RP) and age-related macular degeneration (AMD). One issue that limits the effectiveness of retinal stimulation is the desensitization of the retina response to repeated pulses. Rapid fading of percepts is reported in clinical studies. We studied the retinal output evoked by fixed pulse trains vs. pulse trains that have variable parameters pulse-to-pulse. We used the current clamp to record RGC spiking in the isolated mouse retina. Trains of biphasic current pulses at different frequencies and amplitudes were applied. The main results we report are: (1) RGC desensitization was induced by increasing stimulus frequency, but was unrelated to stimulus amplitude. Desensitization persisted when the 20 Hz stimulation pulses were applied to the retinal ganglion cells at 65 μ A, 85 μ A, and 105 μ A. Subsequent pulses in the train evoked fewer spikes. There was no obvious desensitization when 2 Hz stimulation pulse trains were applied. (2) Blocking inhibitory GABA_A receptor increased spontaneous activity but did not reduce desensitization. (3) Pulse trains with constant charge or excitation (based on strength-duration curves) but varying pulse width, amplitude, and shape increased the number of evoked spikes/pulse throughout the pulse train. This suggests that retinal desensitization can be partially overcome by introducing variability into each pulse.

KEYWORDS

retinal ganglion cell (RGC), desensitization, electrical stimulation, retinal prosthesis, picrotoxin

Introduction

Retinal prostheses are implantable electronic devices designed to restore useful vision in blind patients through

electrical stimulation of the remaining inner retinal neurons (Bloch et al., 2019). From the first report of the implantation of a photovoltaic array in the suprachoroidal space of a blind volunteer (Tassicker, 1956), steady progress has yielded

several devices with market approval [Argus II (Second Sight, USA; Humayun et al., 2003), Alpha IMS (Retina Implant AG, Germany; Zrenner et al., 2011), IRIS II (Pixium, France), and Bionic Eye System (Bionic Vision Technologies, Australia; Ayton et al., 2014) or in clinical trials, including Prima (Pixium; Palanker et al., 2020)]. Retinal implants allow patients to recognize shapes, perceive the contrast between light and dark objects, and identify large letters (Zrenner et al., 2011; Humayun et al., 2012; Stingl et al., 2013; Ayton et al., 2014; Bloch et al., 2019). Although retinal prostheses improve the overall quality of life for patients (Humayun et al., 2012), the implants are not a replacement for normal vision due to the limitations (reproducibility of phosphenes, limited stimulation frequencies, low spatial resolution, etc.).

Several clinical studies have revealed that phosphenes become less bright with continuous stimulation in retinal prosthesis patients (Zrenner et al., 2011; Fornos et al., 2012; Stingl et al., 2017). In Argus II patients, the phosphene faded over several seconds, and some faded in less than 1 s (Fornos et al., 2012; Stronks et al., 2013; Stronks and Dagnelie, 2014; Weiland and Humayun, 2014). It has been reported that using relatively low stimulation rates can prevent fading, but this may result in “blinking” percepts, as noted in the Alpha-IMS patients when 5 Hz stimulation was used (Zrenner et al., 2011; Stingl et al., 2013, 2015). This significantly detracts from the usefulness of these systems.

The reduction of retinal ganglion cell (RGC) responses to repetitive electrical stimulation is referred to as desensitization (Jensen and Rizzo, 2007; Freeman and Fried, 2011; Im and Fried, 2016). This impedes high temporal resolution (Jensen and Rizzo, 2007; Fornos et al., 2012; Stingl et al., 2015; Höfling et al., 2020) and prevents the creation of continuous percepts. Studies have shown that the sensitivity of rabbit retinal ganglion cells to electrical stimulation progressively decreased with repeated stimulation at certain stimulation frequencies and this desensitization persisted in the presence of amacrine cell inhibition (Freeman and Fried, 2011). Other studies have also shown that the network mediated responses of ganglion cells to stimulation at 20 Hz would typically induce strong fading in mice (Sekhar et al., 2016) and rat retina (Sekirnjak et al., 2006). Although these findings suggest decreasing pulse frequency can eliminate perceptual fading, reducing frequency will lead to flickering and less effective artificial vision. Here, we replicate the findings showing desensitization and demonstrate a possible solution, which involves varying pulse parameters such as pulse width and amplitude, while maintaining the overall level of excitation provided by each pulse constant. This approach results in a more robust RGC response at frequencies that desensitize RGC output when constant pulse parameters are used.

Materials and methods

Preparation of the retina

All procedures were approved by the Institutional Animal Care and Use Committee at the University of Michigan. C57BL/6 mice aged 6–10 weeks were used in this study. Mice were anesthetized with an intraperitoneal (IP) injection of ketamine (100 mg/kg)/xylazine (10 mg/kg). Cornea, lens, and vitreous body were removed, and the retina was isolated from the pigment epithelium and cut into four pieces. Retina pieces were placed on filter article with ganglion cells layer up. The filter article with tissue was mounted in a chamber of an upright microscope (Olympus BX51WI) with 40× water immersion lenses. The chamber was continuously perfused with Ames solution (Sigma-Aldrich, St. Louis, MO USA; 4–6 ml/min) and equilibrated with 95% O₂ 5% CO₂ at 37°C.

Electrophysiological recordings

Current-clamp recording was used in this study using HEKA EPC10 (Warner Instrument) and was performed by making a hole in the inner limiting membrane with the glass pipette filled with an internal solution. Positive pressure was applied to expose RGCs. Cells 15–20 μm in diameter were selected for recording. The electrode internal solution contained (in mM): K-gluconate 111, NaCl 5, KCl 4, EGTA 2, HEPES 10, Mg-ATP4, Na-GTP 0.3, Tris2-phosphocreatine 7; (mOsm = 275, pH = 7.3). Pipette resistance at the beginning of the recordings was 3–6 MΩ.

Picrotoxin

Picrotoxin solution was prepared in normal Ames' solution containing DMSO to a maximal concentration of 0.1%. After testing thresholds of the cells, Picrotoxin (100 μM) was applied in the perfusion system to the bath by switching a three-way stopcock and 4–6 min was allowed for the drug to wash in and take effect. This is similar to the concentration used in other studies with isolated retina (Freeman and Fried, 2011).

Electrical stimulation

A single Pt-Ir disk electrode with a diameter of 75 μm was used for electrical stimulation, which was placed ~70 μm away and ~50 μm above the targeted retinal ganglion cell's soma before performing the current-clamp patching (Cho et al., 2011). The ground electrode was placed behind the retina on the photoreceptor side. Stimulus pulses were generated using Multi-

channel systems stimulus generator (STG 4008, Germany) in MC stimulus II software.

Threshold measurement

Amplitude for current stimuli was initially set to 25 μA and was increased in 20 μA steps until each pulse evoked at least one spike. Dose-response curves were created by fitting a logistic equation to the spike probability values vs. current amplitudes (1). The threshold was defined as the current value (in the equation below) when $p = 0.5$ (Cho et al., 2016).

$$p = \frac{a}{b + e^{-xc}} \quad (1)$$

Where p is the spike probability, x is the current amplitude, and a , b and c are constants.

Fixed parameter pulse trains characterize desensitization

We used pulses of fixed amplitude and duration to characterize desensitization. Pulse shape was cathodic-first, biphasic, with pulse width and interphase gap all set to 0.5 ms. Fixed pulse amplitudes of 65, 85, and 105 μA were used since these amplitudes were typically suprathreshold. Twenty pulses were delivered at 2 Hz and 20 Hz.

Varying parameter constant excitation (VPCE) pulse trains

We created four different sets of varying pulse trains, to compare fixed pulse trains. Pulse parameters, including pulse width, amplitude, polarity order, phase ratio (ratio of the anodic to cathodic phase duration), and interphase gap (IPG) were varied such that no two consecutive pulses were the same. We maintained constant excitation on each pulse in a train in two ways: (1) maintaining stimulus charge or (2) scaling charge according to a strength duration relationship (see details below). Pulse protocols are defined as follows: (1) Only pulse width is varied and charge per phase is kept constant. (2) Only pulse width is varied and charge per phase is calculated based on the strength-duration curve. (3) All parameters are varied and charge per phase is kept constant. (4) All parameters are varied and charge per phase is calculated based on the strength-duration curve. Because each cell can only be patched for a limited time, we tested VPCE trains with 105 μA , 0.5 ms biphasic, cathodic-first as the baseline. The pulse rate was maintained at 20 Hz. Using the baseline pulse and an RGC chronaxie of 0.33 ms (Sekirnjak et al., 2006; Chan et al., 2011), we calculated an asymptotic current (rheobase) of 83 μA ,

then used these values for rheobase and chronaxie to calculate pulse amplitude and duration, according to the relationship in equation (2).

$$a = \frac{irh}{1 - e^{-\frac{d}{\tau}}} \quad (2)$$

Where irh is the rheobase current, τ is the chronaxie, d is the pulse width, and a is pulse amplitude.

In protocols 1 and 2 (pulse width varied) there are six different pulse type that get repeated periodically. In protocols 3 and 4 (all parameters varied) there are five different combinations of pulse parameters that get repeated periodically. All VPCE pulse trains were delivered at 20 Hz. An example pulse train from protocol 3 is shown in Figure 1. Corresponding pulse parameters are shown in Table 1. Pulse parameters for protocols 1, 2, and 4 are provided as Supplementary Tables.

Data analysis and statistics

Action potential peaks within 5 ms of the pulse onset were counted as directly evoked spikes, originating in RGCs, and peaks within 50 ms of pulse onset were considered indirectly evoked spikes, originating in the inner nuclear layer (Boinagrov et al., 2014). The raw data were processed by using the analysis software Fitmaster (HEKA) and was exported to MATLAB for further analysis. Outliers were identified using the Z score for Outlier Detection: Z score = $(x - \text{mean})/\text{std. deviation}$. For studying the effect of VPCE pulse trains we used a linear mixed model (Harrison et al., 2018) with the total number of evoked spikes as the response variable, protocol number as a fixed effect variable and cell number (1–29) as a random effect variable. Intrinsic differences in RGC responses refer to RGC activation thresholds in response to electrical stimulation. This difference could be based on morphological and physiological variations between at least 20 types of RGCs in the retina (Fohlmeister and Miller, 1997; Masland, 2011). Different spontaneous firing rates and baseline membrane potentials of RGCs also contribute to variability in stimulation thresholds (Cho et al., 2016). This model was chosen to determine if the total spike number evoked by VPCE protocols is significantly different than the control pulse train considering the inherent variability in RGC responses. This analysis was done using the fitlme function in MATLAB and by incorporating the following equation:

$$y \sim p + (1|c) \quad (3)$$

Where y is the total number of spikes evoked by a VPCE pulse train, p is the protocol number (categorical variable) and c is the cell number.

We also used linear mixed models to evaluate the effect of amplitude and picrotoxin on the total number of evoked spikes

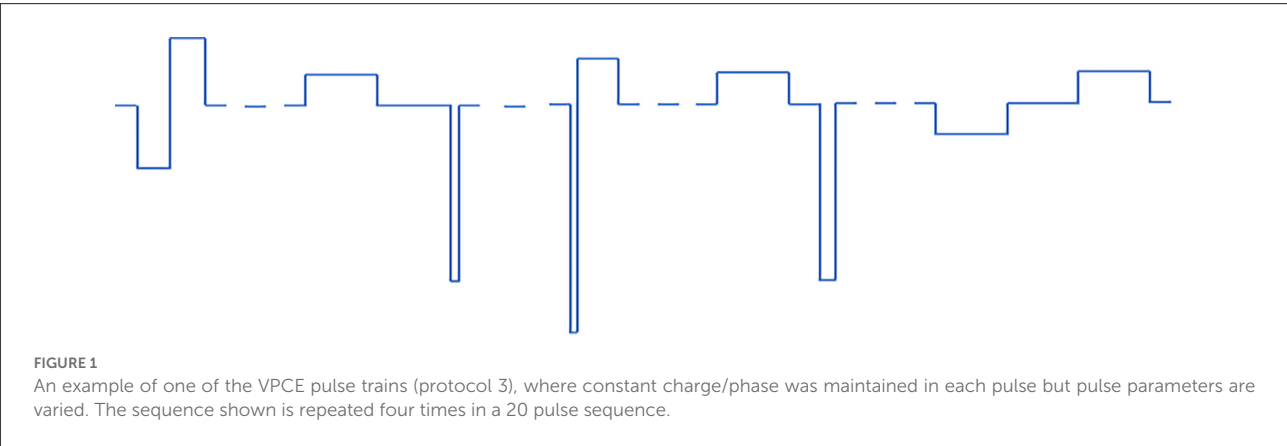


TABLE 1 Pulse parameters for protocol 3.

Pulse #	Phase 1 PW (ms)	Phase 1 amplitude (μA)	IPG (ms)	Phase 2 PW (ms)	Phase 2 amplitude (μA)	Charge density per phase (mC/cm ²)
1	0.5	−105	0	0.5	105	0.297
2	1	52.5	1	0.1	−525	0.297
3	0.06	−875	0	0.6	87.5	0.297
4	1	52.5	0.5	0.2	−262.5	0.297
5	1	−52.5	1	1	52.5	0.297

Pulses are repeated consecutively to create a train of 20 pulses.

with different stimulation frequencies. In this case, the total number of evoked spikes was the response variable, the variable under study (amplitude or picrotoxin) was the fixed effect variable and the cell number was the random effect variable. In all analyses, the response to the first three pulses (first 150 ms) was not included, since rapid desensitization occurs in that time window before RGC responses reach a steady state (Freeman and Fried, 2011).

Results

Effect of stimulation frequency and amplitude on RGC desensitization

Biphasic cathodic first pulses (0.5 ms/phase, 0.5 ms IPG) were applied at three current amplitudes (65 μA, 85 μA, and 105 μA) at pulse rates of 2 Hz and 20 Hz. Figures 2A,B show spike counts in 5 ms and 50 ms bins after the onset of each pulse ($n = 14$). For 20 Hz stimulation, the number of evoked spikes diminished with subsequent pulses relative to the first pulse at all stimulation amplitudes, while the number of evoked spikes was consistent for all pulses in the 2 Hz train. Result of the linear mixed model for spike count in 5 ms bins (Figure 2A) shows a significant increase in evoked spikes with 85 and 105 μA current amplitudes compared to 65 μA at 2 Hz ($p < 0.01^{**}$, $p < 0.001^{***}$). There was no significant change in the total number of evoked spikes with different amplitudes at 20 Hz. For

spike count in 50 ms bins (Figure 2B) there was a significant increase in evoked spikes with 85 and 105 μA current amplitudes compared to 65 μA at 2 Hz ($p < 0.01^{**}$, $p < 0.001^{***}$). At 20 Hz, there was a significant increase in evoked spikes with 105 μA compared to 65 μA ($p < 0.001^{***}$).

Effect of PTX on the RGC activity

Amacrine cells release inhibitory neuron transmitters including GABA. Prior work has shown that amacrine cells may inhibit RGC spiking during repetitive pulsing (Fried et al., 2006). Thus we examined the RGC excitability in the presence of picrotoxin (100 μM), the antagonist of the GABA_A receptor to partially reduce this inhibition. Figure 3 shows representative spikes trains before and after PTX was applied. RGC spontaneous spike rate increased after administration of PTX (Before PTX: 13.16 ± 3.85 spikes/s; After: 25.27 ± 4.65 spikes/s, $n = 24$, $p < 0.01^{**}$). RGC thresholds decreased after administration of PTX (Before PTX: 68.72 ± 10.33 μA; after PTX: 56.33 ± 8.68 μA, $n = 29$ $p < 0.01^{**}$). These implied that blocking amacrine cells' GABA_A receptor increased the excitability of RGCs as reflected by a decrease in activation thresholds.

With spike count in 5 ms bins (Figures 4A,B; $n = 14$) no significant change in total spike count was observed with PTX addition. With spike count in 50 ms bins for 2 Hz stimulation (Figure 5A), adding PTX resulted in a significant increase in total spike counts only for 85 and 105 μA stimulation

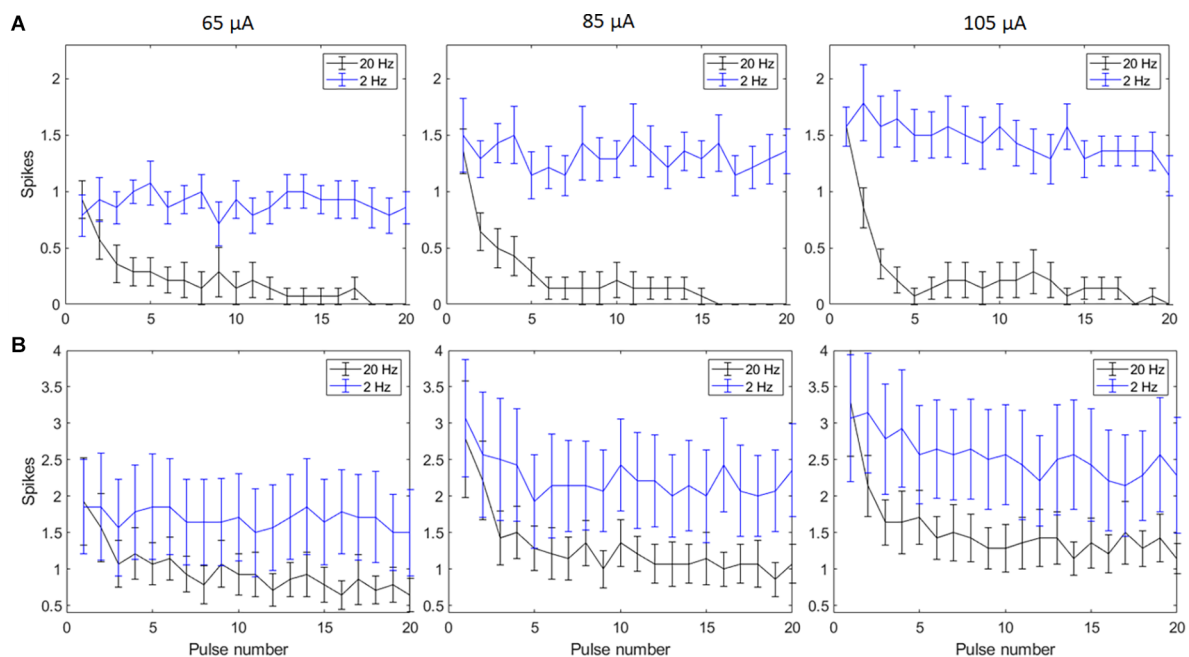


FIGURE 2

Spiking activity of RGCs in response to electrical stimulation ($n = 14$). The average number of RGC spikes counted in 5 ms (A) and 50 ms bins (B) in response to 20 pulses (0.5 ms/phase) delivered at three current amplitudes (65 μ A, 85 μ A, and 105 μ A) at pulse rates of 2 Hz and 20 Hz. Error bars show the standard error of the mean (SEM).

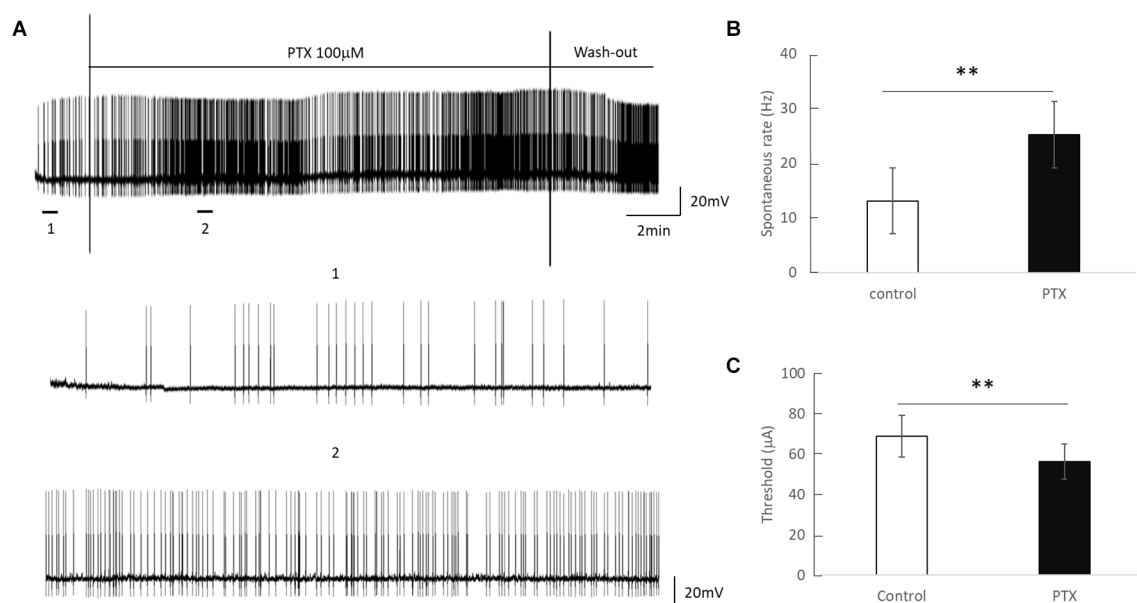


FIGURE 3

The effect of PTX (100 μ M) on the spontaneous spike rate of RGCs. (A) Spontaneous spikes of an RGC before and after application of PTX. One and two show zoomed-in traces for before and after application of PTX respectively. (B,C) PTX significantly increased spontaneous spike rate (** $p < 0.01$) and decreased the threshold (** $p < 0.01$) compared to control.

amplitudes. For 20 Hz stimulation (Figure 5B) no significant change in spike count was observed with PTX. These results indicate that PTX did not reduce desensitization. This is

consistent with results from Freeman 2011, who found that desensitization was not eliminated after blocking (Freeman and Fried, 2011).

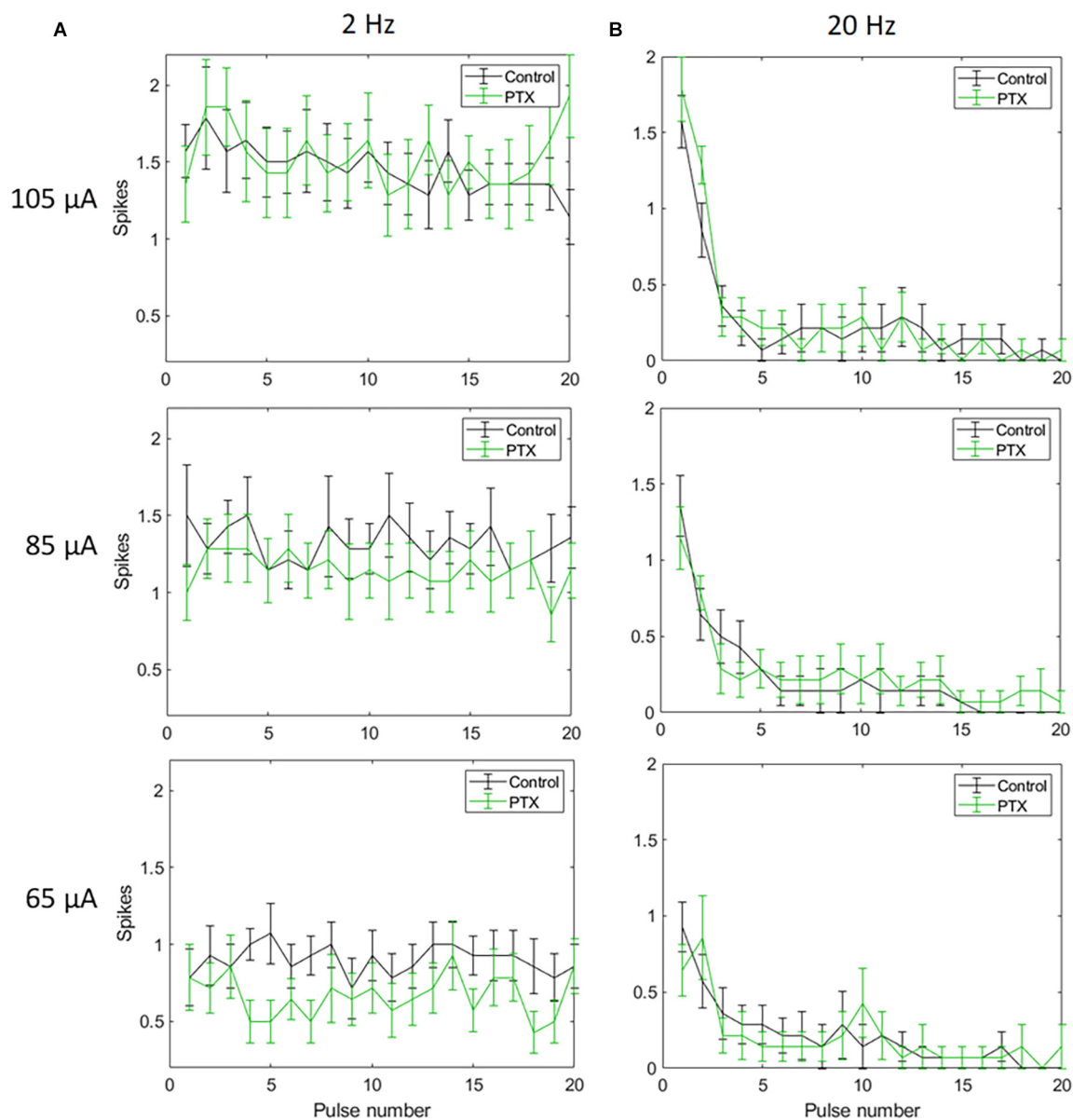


FIGURE 4

The effect of PTX on RGC spiking ($n = 14$) at different current amplitudes for stimulation delivered at 2 Hz (A) and 20 Hz (B). The average numbers of RGC spikes in response to 20 pulses delivered at three current amplitudes (65 μA , 85 μA , and 105 μA) are shown in each figure. Evoked spikes are counted in 5 ms bins after the onset of each pulse. Error bars show the standard error of the mean (SEM).

Effect of VPCE pulse trains on RGC desensitization

Applying VPCE pulse trains increased the RGC response rate during continuous pulsing at 20 Hz. RGC spike counts increased for all four VPCE protocols, but in a different way for each protocol ($n = 29$). Figures 6 and 7 show the effect of different protocols on spike numbers counted in 5 ms and 50 ms bins after the pulse onset with 20 consecutive pulses. The total number of evoked spikes was analyzed using

a linear mixed model. The protocol number was considered a fixed effect variable and the cell number (1–29) was considered a random effect variable. Results from this analysis show that all VPCE pulse protocols evoked a significantly higher number of spikes compared to the control pulse train. The rate of increase in total evoked spike counts in 5 ms bins (Figure 6) was 362%, 358%, 307%, and 299% for protocols 1, 2, 3, and 4 respectively. The rate of increase in total evoked spike counts in 50 ms bins (Figure 7) was 53.99%, 56.21%, 69.54%, and 67.97% for protocols 1,

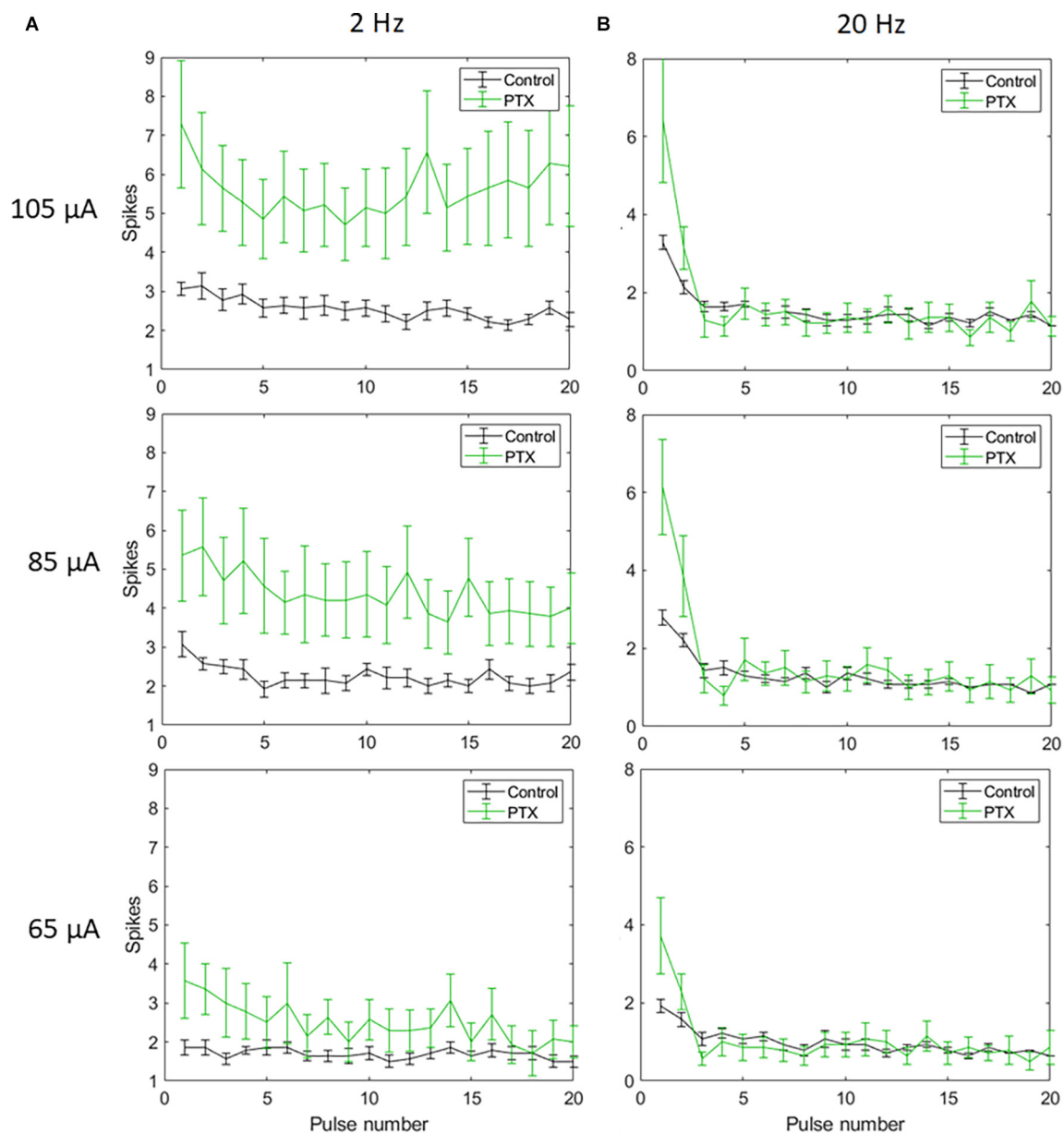


FIGURE 5

The effect of PTX on RGC spiking ($n = 14$) at different current amplitudes for stimulation delivered at 2 Hz (A) and 20 Hz (B). The average numbers of RGC spikes in response to 20 pulses delivered at three current amplitudes (65 μ A, 85 μ A, and 105 μ A) are shown in each figure. Evoked spikes are counted in 50 ms bins after the onset of each pulse. Error bars show the standard error of the mean (SEM).

2, 3, and 4 respectively. Observations for each protocol are given below.

Spike count in 5 ms bins after pulse onset

Average total spikes \pm SEM for the control pulse train = 3.75 ± 1.21 .

Protocol 1: Pulse width is varied; charge is kept constant (Figure 6A). No patterns were noted between

spike numbers evoked by consecutive pulses (average total spikes \pm SEM = 17.38 ± 2.51).

Protocol 2: Pulse width is varied; charge is calculated based on the SD curve (Figure 6B). No patterns were noted between spike numbers evoked by consecutive pulses (average total spikes \pm SEM = 17.24 ± 2.47).

Protocol 3: All pulse parameters are varied; charge is kept constant (Figure 6C). Pulses #5, 10, 15, and 20 generate a significantly lower number of spikes compared to other pulses. These pulses are symmetric cathodic-first with

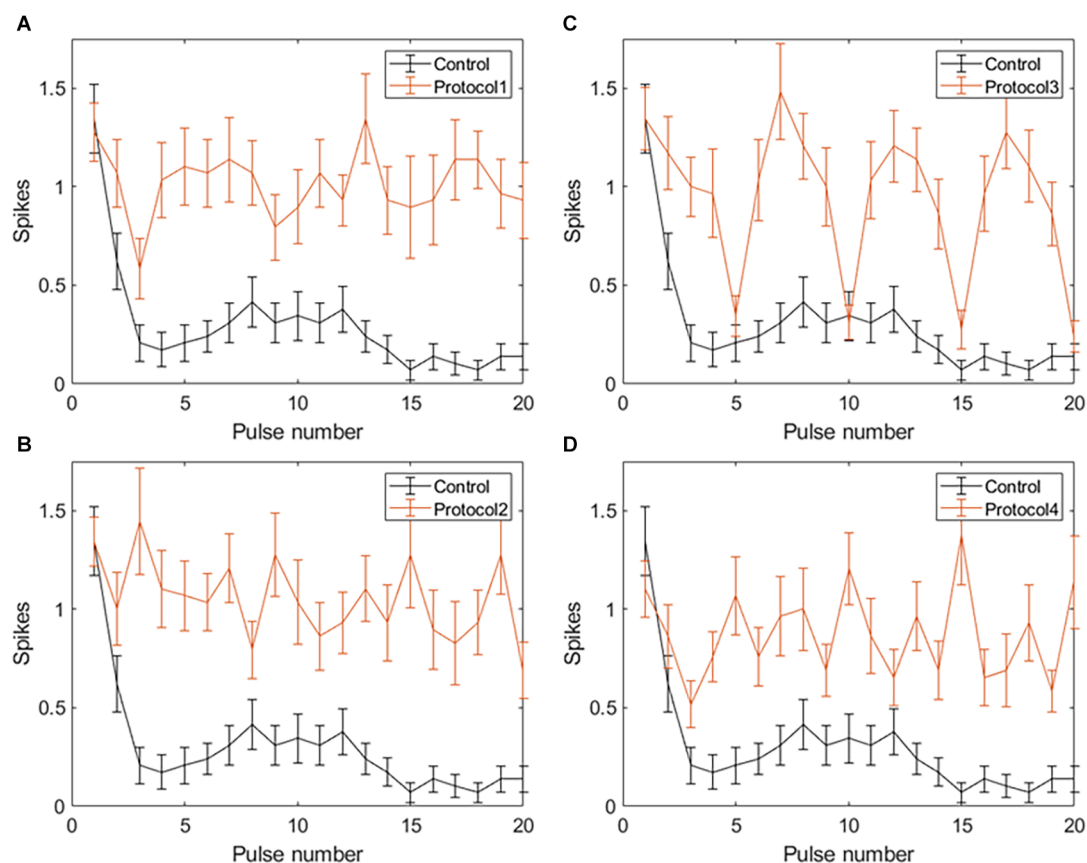


FIGURE 6

Spiking activity of RGCs in response to VPCE pulse trains and control pulse train at 20 Hz. Number of evoked spikes counted in 5 ms bins after the onset of each pulse is plotted against the pulse number ($n = 29$). The pulse sequences in [Table 1](#), [Supplementary Tables S1, S2, and S3](#) are repeated to create a train of 20 pulses. Spiking activity in response to (A) Protocol 1: pulse width varies and charge per phase is kept constant. (B) Protocol 2: pulse width varies and charge per phase is calculated based on strength-duration curve. (C) Protocol 3: all pulse parameters vary and the charge per phase is kept constant. (D) Protocol 4: all pulse parameters vary and charge per phase is calculated based on strength-duration curve.

1 ms pulse width and 1 ms IPG ([Table 1](#); average total spikes \pm SEM = 15.31 ± 2.58).

Protocol 4: All pulse parameters are varied; charge is calculated based on the SD curve ([Figure 6D](#)). No patterns were noted between spike numbers evoked by consecutive pulses (average total spikes \pm SEM = 15 ± 2.19).

Spike count in 50 ms bins after pulse onset

Average total spikes \pm SEM for the control pulse train = 26.38 ± 6.56 .

Protocol 1: Pulse width is varied; charge is kept constant ([Figure 7A](#)). No patterns were noted between spike numbers evoked by consecutive pulses (average total spikes \pm SEM = 40.62 ± 6.35).

Protocol 2: Pulse width is varied; charge is calculated based on SD curve ([Figure 7B](#)). Largest responses (more

spikes/pulse) were generated by a 1 ms, symmetric cathodic-first pulse (pulse #3, 9, 15 see [Supplementary Table S2](#)). These pulses were preceded by pulses of lower charge (average total spikes \pm SEM = 41.2 ± 5.89).

Protocol 3: All pulse parameters are varied; the charge is kept constant ([Figure 7C](#)). The largest responses were generated by pulse #2 ([Table 1](#)), asymmetric anodic-first with a short, high amplitude cathodic 2nd phase. Our prior work ([Chang et al., 2019](#); [Haji Ghaffari et al., 2020](#)) has shown that this type of pulse has a lower threshold compared to standard symmetric cathodic-first pulses (average total spikes \pm SEM = 44.72 ± 6.6).

Protocol 4: All pulse parameters are varied; charge is calculated based on the SD curve ([Figure 7D](#)). A significantly larger response was generated by pulse #5, symmetric cathodic-first with 1 ms pulse width, with the largest charge ([Supplementary Table S3](#)). Here, asymmetric anodic-first pulses are not as effective as in protocol 3, but due to the scaling of charge by the SD relationship, the asymmetric

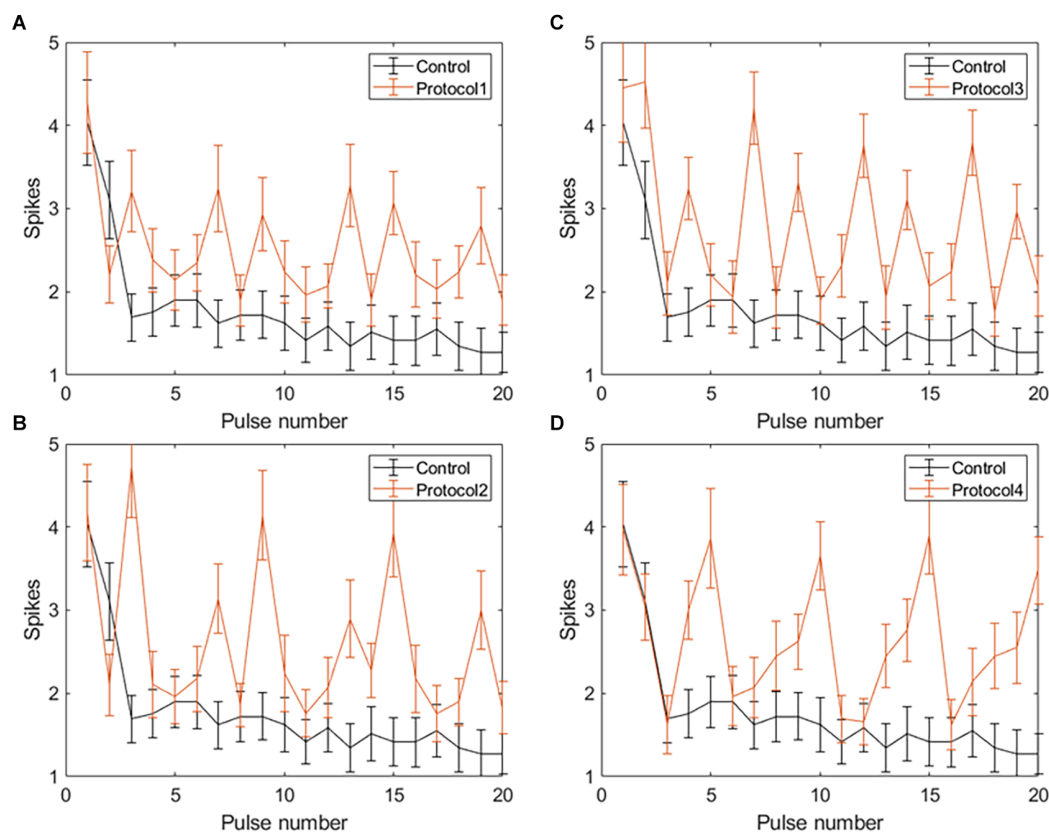


FIGURE 7

Spiking activity of RGCs in response to VPCE pulse trains and control pulse train at 20 Hz. The number of evoked spikes counted in 50 ms bins after the onset of each pulse is plotted against the pulse number ($n = 29$). The pulse sequences in [Table 1](#), [Supplementary Tables S1, S2, and S3](#) are repeated to create a train of 20 pulses. Spiking activity in response to (A) Protocol 1: pulse width varies and charge per phase is kept constant. (B) Protocol 2: pulse width varies and charge per phase is calculated based on strength-duration curve. (C) Protocol 3: all pulse parameters vary and the charge per phase is kept constant. (D) Protocol 4: all pulse parameters vary and charge per phase is calculated based on strength-duration curve.

anodic-first pulses in protocol 4 had less charge than those in protocol 3 (average total spikes \pm SEM = 44.31 ± 5.26 ; refer to [Supplementary Figure S2](#) for PSTH of all protocols).

Discussion

Prosthetic vision has helped improve light perception, motion detection, and performance in visually guided tasks for users blinded by retinal degenerative diseases ([Weiland et al., 2005](#); [Zrenner, 2013](#); [Edwards et al., 2018](#)). However, limitations such as the low resolution of stimulation, and fading of percepts make it challenging to perceive a continuous, high quality image ([Weiland and Humayun, 2014](#); [Erickson-Davis and Korzybska, 2021](#)). Retinal implant users are instructed to perform head movements to counteract fading of percepts that is due to neural adaptation in the retina and visual cortex ([Hsieh and Colas, 2012](#)). On the level of the retina, neural adaptation is thought to be caused by intrinsic desensitization

of bipolar cells, activation of presynaptic inhibitory networks, and desensitization of sodium channels in the RGC membrane ([Freeman and Fried, 2011](#); [Soto-Breceda et al., 2018](#); [Walston et al., 2018](#)).

We studied the retinal output evoked by fixed pulse trains vs. pulse trains that have variable parameters pulse-to-pulse, to test our hypothesis that VPCE trains will mitigate desensitization. Our main findings were as follows: (1) RGC desensitization was induced by increasing stimulus frequency but was unrelated to stimulus amplitude. There was no obvious desensitization when 2 Hz stimulation pulses were applied. (2) Blocking GABA_A receptor did not abolish the desensitization. (3) Applying a pulse train where pulse parameters varied (VPCE) resulted in less desensitization. The number of evoked spikes by electrical stimulation did not continuously decrease after the first pulse, but the spike/pulse rate was not stable as it was at 2 Hz.

A number of studies have demonstrated desensitization in RGCs. [Freeman and Fried \(2011\)](#) showed two time scales for desensitization in RGCs, rapid and slow, and that desensitization

is independent of amacrine cell inhibition. Fornos et al. (2012) showed that Argus II retinal prosthesis users report rapid fading of percepts and changing of percepts into dimmer and poorly localized percepts, which interrupts the perception of a meaningful image. Weitz et al. (2014) showed an increase in Argus II perception thresholds over time which indicated that the retina was getting desensitized. Several studies showed that inhibitory GABAergic and glycinergic feedback from amacrine cells truncates release from the bipolar cell terminals to generate phasic output signals (Awatramani and Slaughter, 2000). PTX may also combine GABA_A receptors on other retinal cells (e.g., bipolar cells) and decrease vesicle release to ganglion cells. And indirect stimulation of other retinal neurons causes feedback between them and RGCs, which modulates RGCs desensitization. However, inhibitory feedback is not the sole cause of desensitization, since Freeman and Fried (2011) found that desensitization remained after blocking amacrine cell input to bipolar cells. These studies demonstrated desensitization and possible mechanisms underlying it but did not propose stimulation strategies to minimize this effect.

Prior studies have assessed varying pulses to reduce desensitization. Our prior work on this topic looked over a longer time period (compared to the 20 pulses applied in the current study). During 1 h of epiretinal stimulation in the rat model, the evoked response strength (recorded at the superior colliculus) was measured every 5 min while applying either constant pulse trains or “time-varying” trains (Davuluri and Weiland, 2014). We noted that the evoked response strength decreased less during 1 h of stimulation when “time-varying” trains were used. Another study also showed that randomizing the inter-pulse interval can lower the response decay rate at 50 and 200 Hz but not with 10 Hz stimulation (Soto-Breceda et al., 2018). Chenais et al. (2021) demonstrated that a naturalistic stimulation strategy where electrical pulses are modulated spatiotemporally could mitigate the desensitization of RGCs in mouse retina. In this study, we varied pulse parameters so that no two consecutive pulses are the same, but we kept pulse frequency constant (20 Hz). Consistent with the prior work, our study found less sensitization when with time-varying pulse trains vs. constant pulse trains.

Electrical stimulation activates the retina in two ways: Direct stimulation which depolarizes RGCs and evokes action potentials (spikes), and network stimulation which depolarizes retinal cells presynaptic to RGCs, and evokes RGC spikes through synapses to RGCs. Prior work (Fried et al., 2006; Sekirnjak et al., 2006; Ahuja et al., 2008) has shown that network responses attenuate rapidly at about 10 pps and are completely absent at 20 pps. Inhibitory feedback from amacrine cells is one suspected mechanism (Fried et al., 2006), although attenuation of bipolar cell responses has been shown recently (Walston et al., 2018). Network responses are typified by a burst of RGC spikes after a single electrical pulse. In contrast,

direct stimulation typically evokes a single spike and that can be maintained at a frequency up to 100 Hz (Sekirnjak et al., 2006). A study of RGC responses at 2 and 16 pps found that the number of RGC spikes are decreased after the first pulse and blocking amacrine cells did not show a significant difference between the control and the blocker group at 2 and 16 Hz (Freeman and Fried, 2011), which matches our findings using 2 Hz and 20 Hz frequencies. In both the Freeman and our study, higher frequency pulse trains did evoke single spikes, which likely represent direct responses. We observed that an amplitude of 105 μ A caused a significant increase in the number of indirectly evoked spikes compared to a 65 μ A amplitude (Figure 2B). This is consistent with previous studies showing that synaptically evoked spikes (long latency) have higher current thresholds than directly evoked spikes (short latency) at a certain pulse width (Jensen et al., 2005). This suggests that higher current amplitudes are effective in increasing indirect RGC activation, but desensitization still persists with all amplitudes.

Applying VPCE pulse trains with 20 Hz frequency showed a significant increase in the total number of evoked spikes with all four protocols we tested. However, with all VPCE protocols, we observed variations in the evoked spike numbers with each consecutive pulse. RGCs show persistent desensitization in response to the control 20 Hz stimulation and this is evident in the persistently lowered number of spikes after the initial three pulses. This is in agreement with a previous research study showing a rapid desensitization mechanism for RGC spiking as well as a slow desensitization mechanism (Freeman and Fried, 2011). A similar pattern has been shown for the fading of percepts in retinal prosthesis users (Fornos et al., 2012), suggesting that the decline in RGC firing may be responsible for fading of percepts. Protocols 1, 2, and 4 provided a more stable spike count over time for directly evoked responses (Figure 6), which can be beneficial in providing a more stable image perception over time. The largest increases in the average spike numbers for indirectly evoked responses (Figure 7) were in response to longer pulse widths (1 ms), which may preferentially engage network stimulation. An exception to the general trend occurred with protocol 3, where pulse #5 (symmetric cathodic-first with 1 ms pulse width and 1 ms IPG) generates a significantly lower number of directly evoked spikes compared to other pulses (Figure 6C). This may be due to the constant charge approach used in protocol 3 and the known behavior that threshold charge increases with pulse width (Geddes and Bourland, 1985). In addition, longer pulses are known to preferentially evoke network activation (Fried et al., 2006). The same effect with the 1 ms pulse is observed with protocol 1, but not as pronounced as in protocol 3. It is unclear why these 1 ms pulses behave differently in protocols 1 and 3, but we speculate that the preceding pulse has some effect. Future studies of desensitization should

consider the order of delivered pulses. For example, a long anodic pulse (1st phase) may not evoke a spike but can increase the probability of a cell spiking if the cathodic 2nd phase is delivered subsequently (Chang et al., 2019; Haji Ghaffari et al., 2020). In this study, we focused on temporal aspects of RGC desensitization. Spatial desensitization of RGCs can occur with interpulse distances smaller than 800 μm (Jalligampala et al., 2016), and should be taken into account during multi-electrode stimulation. We did not study the effect of VPCE on different classes of RGCs (e.g., ON vs. OFF). Investigating VPCE on different morphological and physiological categories of RGCs will be an interesting future direction (Sanes and Masland, 2015). With photoreceptor degeneration, morphological changes can occur in the inner retina layers (Strettoi et al., 2003). It is shown that the spontaneous activity of RGCs increases with retinal degeneration (Stasheff, 2008). In addition, average RGC membrane potential is shown to be lower and activation thresholds in response to electrical stimulation are generally higher with retinal degeneration (Cho et al., 2016). Higher thresholds may affect how VPCE evokes RGC responses, for example, higher current amplitudes may be needed to stimulate RGCs. Results of this study can have implications for designing more effective stimulation protocols for retinal prostheses but will require more sophisticated stimulator chips to implement this technical solution.

Data availability statement

The raw data supporting the conclusions of this article will be made available by the authors, without undue reservation.

Ethics statement

The animal study was reviewed and approved by Institutional Animal Care and Use Committee at the University of Michigan.

References

- Ahuja, A. K., Behrend, M. R., Kuroda, M., Humayun, M. S., and Weiland, J. D. (2008). An *in vitro* model of a retinal prosthesis. *IEEE Trans. Biomed. Eng.* 55, 1744–1753. doi: 10.1109/tbme.2008.919126
- Awatramani, G. B., and Slaughter, M. M. (2000). Origin of transient and sustained responses in ganglion cells of the retina. *J. Neurosci.* 20, 7087–7095. doi: 10.1523/JNEUROSCI.20-18-07087.2000
- Ayton, L. N., Blamey, P. J., Guymer, R. H., Luu, C. D., Nayagam, D. A. X., Sinclair, N. C., et al. (2014). First-in-human trial of a novel suprachoroidal retinal prosthesis. *PLoS One* 9:e115239. doi: 10.1371/journal.pone.0115239
- Bloch, E., Luo, Y., and da Cruz, L. (2019). Advances in retinal prosthesis systems. *Ther. Adv. Ophthalmol.* 11:2515841418817501. doi: 10.1177/2515841418817501
- Boinagrov, D., Pangratz-Fuehrer, S., Goetz, G., and Palanker, D. (2014). Selectivity of direct and network-mediated stimulation of the retinal ganglion cells with epi-, sub- and intraretinal electrodes. *J. Neural Eng.* 11:026008. doi: 10.1088/1741-2560/11/2/026008
- Chan, L. L. H., Lee, E.-J., Humayun, M. S., and Weiland, J. D. (2011). Both electrical stimulation thresholds and SMI-32-immunoreactive retinal ganglion cell density correlate with age in S334ter line 3 rat retina. *J. Neurophysiol.* 105, 2687–2697. doi: 10.1152/jn.00619.2010
- Chang, Y. C., Ghaffari, D. H., Chow, R. H., and Weiland, J. D. (2019). Stimulation strategies for selective activation of retinal ganglion cell soma and threshold reduction. *J. Neural Eng.* 16:026017. doi: 10.1088/1741-2552/aaf92b

Author contributions

WL, DH, and JW designed the study and wrote the manuscript. WL performed the *in vitro* experiments. WL and DH analyzed the data. RM helped with design of pulse trains. All authors contributed to the article and approved the submitted version.

Funding

This research was supported by University of Michigan and National Eye Institute (#EY022931 and # EY013934).

Conflict of interest

The authors declare that the research was conducted in the absence of any commercial or financial relationships that could be construed as a potential conflict of interest.

Publisher's note

All claims expressed in this article are solely those of the authors and do not necessarily represent those of their affiliated organizations, or those of the publisher, the editors and the reviewers. Any product that may be evaluated in this article, or claim that may be made by its manufacturer, is not guaranteed or endorsed by the publisher.

Supplementary material

The Supplementary Material for this article can be found online at: <https://www.frontiersin.org/articles/10.3389/fncel.2022.897146/full#supplementary-material>.

- Chenais, N. A. L., Airaghi Leccardi, M. J. I., and Ghezzi, D. (2021). Naturalistic spatiotemporal modulation of epiretinal stimulation increases the response persistence of retinal ganglion cell. *J. Neural Eng.* 18:016016. doi: 10.1088/1741-2552/abed6f
- Cho, A., Ratliff, C., Sampath, A., and Weiland, J. (2016). Changes in ganglion cell physiology during retinal degeneration influence excitability by prosthetic electrodes. *J. Neural Eng.* 13:025001. doi: 10.1088/1741-2560/13/2/025001
- Cho, A. K., Sampath, A. P., and Weiland, J. D. (2011). Physiological response of mouse retinal ganglion cells to electrical stimulation: effect of soma size. *Annu. Int. Conf. IEEE Eng. Med. Biol. Soc.* 2011, 1081–1084. doi: 10.1109/IEMBS.2011.6090252
- Davuluri, N. S., and Weiland, J. D. (2014). “Time-varying pulse trains limit retinal desensitization caused by continuous electrical stimulation,” in *2014 36th Annual International Conference of the IEEE Engineering in Medicine and Biology Society* (Chicago, IL), 414–417. doi: 10.1109/EMBC.2014.6943616
- Edwards, T. L., Cottrill, C. L., Xue, K., Simunovic, M. P., Ramsden, J. D., Zrenner, E., et al. (2018). Assessment of the electronic retinal implant alpha AMS in restoring vision to blind patients with end-stage retinitis pigmentosa. *Ophthalmology* 125:432. doi: 10.1016/j.ophtha.2017.09.019
- Erickson-Davis, C., and Korzybska, H. (2021). What do blind people “see” with retinal prostheses? Observations and qualitative reports of epiretinal implant users. *PLoS One* 16:e0229189. doi: 10.1371/journal.pone.0229189
- Fohlmeister, J. F., and Miller, R. F. (1997). Mechanisms by which cell geometry controls repetitive impulse firing in retinal ganglion cells. *J. Neurophysiol.* 78, 1948–1964. doi: 10.1152/jn.1997.78.4.1948
- Fornos, A. P., Sommerhalder, J., da Cruz, L., Sahel, J. A., Mohand-Said, S., Hafezi, F., et al. (2012). Temporal properties of visual perception on electrical stimulation of the retina. *Invest. Ophthalmol. Vis. Sci.* 53, 2720–2731. doi: 10.1167/iov.11-9344
- Freeman, D. K., and Fried, S. I. (2011). Multiple components of ganglion cell desensitization in response to prosthetic stimulation. *J. Neural Eng.* 8:016008. doi: 10.1088/1741-2560/8/1/016008
- Fried, S. I., Hsueh, H. A., and Werblin, F. S. (2006). A method for generating precise temporal patterns of retinal spiking using prosthetic stimulation. *J. Neurophysiol.* 95, 970–978. doi: 10.1152/jn.00849.2005
- Geddes, L. A., and Bourland, J. D. (1985). The strength-duration curve. *IEEE Trans. Biomed. Eng.* 32, 458–459. doi: 10.1109/tbme.1985.325456
- Haji Ghaffari, D., Finn, K. E., Jegannathan, V. S. E., Patel, U., Wuyyuru, V., Roy, A., et al. (2020). The effect of waveform asymmetry on perception with epiretinal prostheses. *J. Neural Eng.* 17:045009. doi: 10.1088/1741-2552/aba07e
- Harrison, X. A., Donaldson, L., Correa-Cano, M. E., Evans, J., Fisher, D. N., Goodwin, C. E. D., et al. (2018). A brief introduction to mixed effects modelling and multi-model inference in ecology. *PeerJ* 6:e4794. doi: 10.7717/peerj.4794
- Höfling, L., Oesterle, J., Berens, P., and Zeck, G. (2020). Probing and predicting ganglion cell responses to smooth electrical stimulation in healthy and blind mouse retina. *Sci. Rep.* 10, 1–20. doi: 10.1038/s41598-020-61899-y
- Hsieh, P. J., and Colas, J. T. (2012). Perceptual fading without retinal adaptation. *J. Exp. Psychol. Hum. Percept. Perform.* 38, 267–271. doi: 10.1037/a0026963
- Humayun, M. S., Dorn, J. D., Da Cruz, L., Dagnelie, G., Sahel, J. A., Stanga, P. E., et al. (2012). Interim results from the international trial of second sight's visual prosthesis. *Ophthalmology* 119, 779–788. doi: 10.1016/j.ophtha.2011.09.028
- Humayun, M. S., Weiland, J. D., Fujii, G. Y., Greenberg, R., Williamson, R., Little, J., et al. (2003). Visual perception in a blind subject with a chronic microelectronic retinal prosthesis. *Vis. Res.* 43, 2573–2581. doi: 10.1016/s0042-6989(03)00457-7
- Im, M., and Fried, S. I. (2016). Temporal properties of network-mediated responses to repetitive stimuli are dependent upon retinal ganglion cell type. *J. Neural Eng.* 13:025002. doi: 10.1088/1741-2560/13/2/025002
- Jalligampala, A., Zrenner, E., and Rathbun, D. L. (2016). Spatial aspects of electrical desensitization in mouse retina. *IOVS ARVO J.* Available online at: <https://iovs.arvojournals.org/article.aspx?articleid=2561909>. Accessed April 22, 2022.
- Jensen, R. J., and Rizzo, J. F. (2007). Responses of ganglion cells to repetitive electrical stimulation of the retina. *J. Neural Eng.* 4, S1–S6. doi: 10.1088/1741-2560/4/1/S01
- Jensen, R. J., Ziv, O. R., and Rizzo, J. F. (2005). Thresholds for activation of rabbit retinal ganglion cells with relatively large, extracellular microelectrodes. *Invest. Ophthalmol. Vis. Sci.* 46, 1486–1496. doi: 10.1167/iov.04-1018
- Masland, R. H. (2011). Cell populations of the retina: the proctor lecture. *Invest. Ophthalmol. Vis. Sci.* 52, 4581–4591. doi: 10.1167/iov.10-7083
- Palanker, D., Le Mer, Y., Mohand-Said, S., Muqit, M., and Sahel, J. A. (2020). Photovoltaic restoration of central vision in atrophic age-related macular degeneration. *Ophthalmology* 127, 1097–1104. doi: 10.1016/j.ophtha.2020.02.024
- Sanes, J. R., and Masland, R. H. (2015). The types of retinal ganglion cells: current status and implications for neuronal classification. *Annu. Rev. Neurosci.* 38, 221–246. doi: 10.1146/annurev-neuro-071714-034120
- Sekhar, S., Jalligampala, A., Zrenner, E., and Rathbun, D. L. (2016). Tickling the retina: integration of subthreshold electrical pulses can activate retinal neurons. *J. Neural Eng.* 13:046004. doi: 10.1088/1741-2560/13/4/046004
- Sekirnjak, C., Hottoway, P., Sher, A., Dabrowski, W., Litke, M., Chichilnisky, E. J., et al. (2006). Electrical stimulation of mammalian retinal ganglion cells with multielectrode arrays. *J. Neurophysiol.* 95, 3311–3327. doi: 10.1152/jn.01168.2005
- Soto-Breceda, A., Kamenewa, T., Meffin, H., Maturana, M., and Ibbotson, M. R. (2018). Irregularly timed electrical pulses reduce adaptation of retinal ganglion cells. *J. Neural Eng.* 15:056017. doi: 10.1088/1741-2552/aad46e
- Stasheff, S. F. (2008). Emergence of sustained spontaneous hyperactivity and temporary preservation of OFF responses in ganglion cells of the retinal degeneration (rd1) mouse. *J. Neurophysiol.* 99, 1408–1421. doi: 10.1152/jn.00144.2007
- Stingl, K., Bartz-Schmidt, K. U., Besch, D., Braun, A., Bruckmann, A., Gekeler, F., et al. (2013). Artificial vision with wirelessly powered subretinal electronic implant alpha-IMS. *Proc. R. Soc. B Biol. Sci.* 280:20130077. doi: 10.1098/rspb.2013.0077
- Stingl, K., Bartz-Schmidt, K. U., Besch, D., Chee, C. K., Cottrill, C. L., Gekeler, F., et al. (2015). Subretinal visual implant α IMS—Clinical trial interim report. *Vis. Res.* 111, 149–160. doi: 10.1016/j.visres.2015.03.001
- Stingl, K., Schippert, R., Bartz-Schmidt, K. U., Besch, D., Cottrill, C. L., Edwards, T. L., et al. (2017). Interim results of a multicenter trial with the new electronic subretinal implant alpha AMS in 15 patients blind from inherited retinal degenerations. *Front. Neurosci.* 11:445. doi: 10.3389/fnins.2017.00445
- Strettoi, E., Pignatelli, V., Rossi, C., Porciatti, V., and Falsini, B. (2003). Remodeling of second-order neurons in the retina of rd/rd mutant mice. *Vis. Res.* 43, 867–877. doi: 10.1016/s0042-6989(02)00594-1
- Stronks, C. H., Barry, M. P., and Dagnelie, G. (2013). Electrically elicited visual evoked potentials in argus II retinal implant wearers. *Invest. Ophthalmol. Vis. Sci.* 54, 3891–3901. doi: 10.1167/iov.13-11594
- Stronks, C. H., and Dagnelie, G. (2014). The functional performance of the argus II retinal prosthesis. *Expert Rev. Med. Devices* 11, 23–30. doi: 10.1586/17434440.2014.862494
- Tassicker, G. E. (1956). Preliminary report on a retinal stimulator. *Br. J. Physiol. Opt.* 13, 102–105.
- Walston, S. T., Chow, R. H., and Weiland, J. D. (2018). Direct measurement of bipolar cell responses to electrical stimulation in wholemount mouse retina. *J. Neural Eng.* 15:046003. doi: 10.1088/1741-2552/aab4ed
- Weiland, J. D., and Humayun, M. S. (2014). Retinal prosthesis. *IEEE Trans. Biomed. Eng.* 61, 1412–1424. doi: 10.1109/TBME.2014.2314733
- Weiland, J. D., Liu, W., and Humayun, M. S. (2005). Retinal prosthesis. *Annu. Rev. Biomed. Eng.* 7, 361–401. doi: 10.1146/annurev.bioeng.7.060804.100435
- Weitz, A. C., Behrend, M. R., Ahuja, A. K., Christopher, P., Wei, J., Wuyyuru, V., et al. (2014). Interphase gap as a means to reduce electrical stimulation thresholds for epiretinal prostheses. *J. Neural Eng.* 11:016007. doi: 10.1088/1741-2560/11/1/016007
- Zrenner, E. (2013). Fighting blindness with microelectronics. *Sci. Transl. Med.* 5:210ps16. doi: 10.1126/scitranslmed.3007399
- Zrenner, E., Bartz-Schmidt, K. U., Benav, H., Besch, D., Bruckmann, A., Gabel, V. P., et al. (2011). Subretinal electronic chips allow blind patients to read letters and combine them to words. *Proc. R. Soc. B Biol. Sci.* 78, 1489–1497. doi: 10.1098/rspb.2010.1747



OPEN ACCESS

EDITED BY

Shelley Fried,
Massachusetts General Hospital
and Harvard Medical School,
United States

REVIEWED BY

Biju B. Thomas,
University of Southern California,
United States
Mohit Naresh Shivdasani,
University of New South Wales,
Australia

*CORRESPONDENCE

Ione Fine
ione.fine@uw.edu

SPECIALTY SECTION

This article was submitted to
Neuroprosthetics,
a section of the journal
Frontiers in Neuroscience

RECEIVED 21 March 2022

ACCEPTED 11 July 2022

PUBLISHED 24 August 2022

CITATION

Yücel EI, Sadeghi R, Kartha A,
Montezuma SR, Dagnelie G, Rokem A,
Boynton GM, Fine I and Beyeler M
(2022) Factors affecting two-point
discrimination in Argus II patients.
Front. Neurosci. 16:901337.
doi: 10.3389/fnins.2022.901337

COPYRIGHT

© 2022 Yücel, Sadeghi, Kartha,
Montezuma, Dagnelie, Rokem,
Boynton, Fine and Beyeler. This is an
open-access article distributed under
the terms of the [Creative Commons
Attribution License \(CC BY\)](#). The use,
distribution or reproduction in other
forums is permitted, provided the
original author(s) and the copyright
owner(s) are credited and that the
original publication in this journal is
cited, in accordance with accepted
academic practice. No use, distribution
or reproduction is permitted which
does not comply with these terms.

Factors affecting two-point discrimination in Argus II patients

Ezgi I. Yücel¹, Roksana Sadeghi², Arathy Kartha³,
Sandra Rocio Montezuma⁴, Gislin Dagnelie³, Ariel Rokem^{1,5},
Geoffrey M. Boynton¹, Ione Fine^{1*} and Michael Beyeler^{6,7}

¹Department of Psychology, University of Washington, Seattle, WA, United States, ²Department of Biomedical Engineering, Johns Hopkins School of Medicine, Baltimore, MD, United States, ³Department of Ophthalmology, Johns Hopkins School of Medicine, Baltimore, MD, United States, ⁴Department of Ophthalmology and Visual Neurosciences, University of Minnesota, Minneapolis, MN, United States, ⁵eScience Institute, University of Washington, Seattle, WA, United States, ⁶Department of Computer Science, University of California, Santa Barbara, Santa Barbara, CA, United States, ⁷Department of Psychological and Brain Sciences, University of California, Santa Barbara, Santa Barbara, CA, United States

Two of the main obstacles to the development of epiretinal prosthesis technology are electrodes that require current amplitudes above safety limits to reliably elicit percepts, and a failure to consistently elicit pattern vision. Here, we explored the causes of high current amplitude thresholds and poor spatial resolution within the Argus II epiretinal implant. We measured current amplitude thresholds and two-point discrimination (the ability to determine whether one or two electrodes had been stimulated) in 3 blind participants implanted with Argus II devices. Our data and simulations show that axonal stimulation, lift and retinal damage all play a role in reducing performance in the Argus 2, by either limiting sensitivity and/or reducing spatial resolution. Understanding the relative role of these various factors will be critical for developing and surgically implanting devices that can successfully subserve pattern vision.

KEYWORDS

sight restoration, retinal prosthesis, retina, current spread, modeling, psychophysics

Introduction

Diseases such as Retinitis Pigmentosa (RP) and Age-Related Macular Degeneration (AMD) cause photoreceptor degeneration that results in severe loss of vision at later stages (Pfeiffer et al., 2020). RP affects approximately 1/4,000 (Ayuso and Millan, 2010) and late AMD affects 1/300 adults globally (Wong et al., 2014). While some of these diseases have treatments that slow progression (Mitchell et al., 2018), none are curable. Once the disease has progressed to severe vision loss, one of the few potential treatments is implantation with a retinal or cortical prosthesis. Based on a principle similar to cochlear implants, retinal implants use an array of electrodes to stimulate

remaining (non-photoreceptor) neurons in the retina to evoke phosphenes. The Argus II (Second Sight Medical Products, Inc.) is one of two FDA-approved devices, with the other being a suprachoroidal device (Ayton et al., 2014). Currently, there are more than 350 individuals worldwide using Argus II devices (Ayton et al., 2020a). Although the production and implantation of the Argus II ended in 2019, there is ongoing research to develop other epiretinal devices (Ferlauto et al., 2018; Nano Retina, 2020).

The perceptual experience of clinically implanted Argus II patients has been variable (Erickson-Davis and Korzybska, 2021). In many patients a significant proportion of electrodes cannot elicit percepts within safe current density limits (Ahuja et al., 2013), and only limited pattern vision is generated by the device (Stronks and Dagnelie, 2014; da Cruz et al., 2016; Arevalo et al., 2021).

A variety of factors are likely responsible for the limited pattern vision found in Argus II devices (Caspi and Zivotofsky, 2015). These include the decoupling of retinotopic stimulation from eye-position (Caspi et al., 2017), the fact that the percepts produced by the electrodes are not well formed “pixels” (Nanduri et al., 2012; Luo et al., 2016; Beyeler et al., 2019), and an inability to resolve individual electrodes.

Two-point discrimination (the ability to determine whether one or two percepts are seen when a pair of electrodes are stimulated) is thought to be a particularly useful measure for characterizing the ability to resolve individual electrodes within an array (Ayton et al., 2020b). Unlike other spatial acuity tasks, such as grating acuity or square localization, two-point acuity is not susceptible to blurring by eye-movements. Thus, two-point discrimination is useful for characterizing losses in spatial resolution at a retinal level. An ability to resolve whether one or two electrodes have been stimulated is *necessary* but not *sufficient* for good visual performance with a prosthetic device; however, one previous study does suggest a correlation between two-point discrimination and grating spatial acuity in Argus II patients (Lauritzen et al., 2011).

Here we measured both current amplitude thresholds and two-point discrimination performance in three participants diagnosed with severe retinitis pigmentosa and chronically implanted with the Argus II epiretinal prosthesis (Table 1). Electrical stimulation was delivered directly to single or pre-selected pairs of electrodes (Figure 1). We measured single electrode thresholds using a yes-no procedure, and measured two-point discrimination thresholds by stimulating a pair of electrodes and asking participants both to report the number of phosphenes and draw the phosphene shape(s) on a tablet touch screen.

Having measured current amplitude and two-point discrimination thresholds, we used a combination of regression analyses and simulations to examine the role of physical distance between electrodes, current amplitude, axonal stimulation, height of the electrode above the retinal surface (lift), and retinal

damage, with the goal of examining how these various factors affect both sensitivity and two-point discrimination.

Our modeling section has three stages:

Stage I: Estimating electrode-electrode distance to and along axonal bundles

We began by using the *pulse2percept* model (Beyeler et al., 2019) to estimate the position of the array on the retinal surface, the distance between electrodes, and the distance to a shared axonal bundle for each pair of electrodes. These estimates were then used as predictive factors in our regression models (Stage II).

Stage II: Regression modeling: The effects of physical and axonal distance on two-point discrimination thresholds

Next, we fit nested linear logistic models to determine which factors—physical distance between electrodes, mean current amplitude of the two electrodes, and distance to axon (as estimated in Stage I), best predicted our psychophysical data.

Stage III: Current spread modeling: The effects of retinal damage and electrode lift on thresholds and two-point discrimination thresholds

Finally, we used a simple version of a “scoreboard” model to estimate the relative contributions of electrode lift from the retinal surface and retinal damage on both current amplitude thresholds and two-point discrimination performance. The scoreboard model assumes that each electrode generates a unitary, circular percept in the region of visual space that corresponds to the retinal position of that electrode, as would be predicted if electrical stimulation only elicited firing in ganglion cell bodies close to the electrode (Fine and Boynton, 2015).

Psychophysics

Methods

Participants

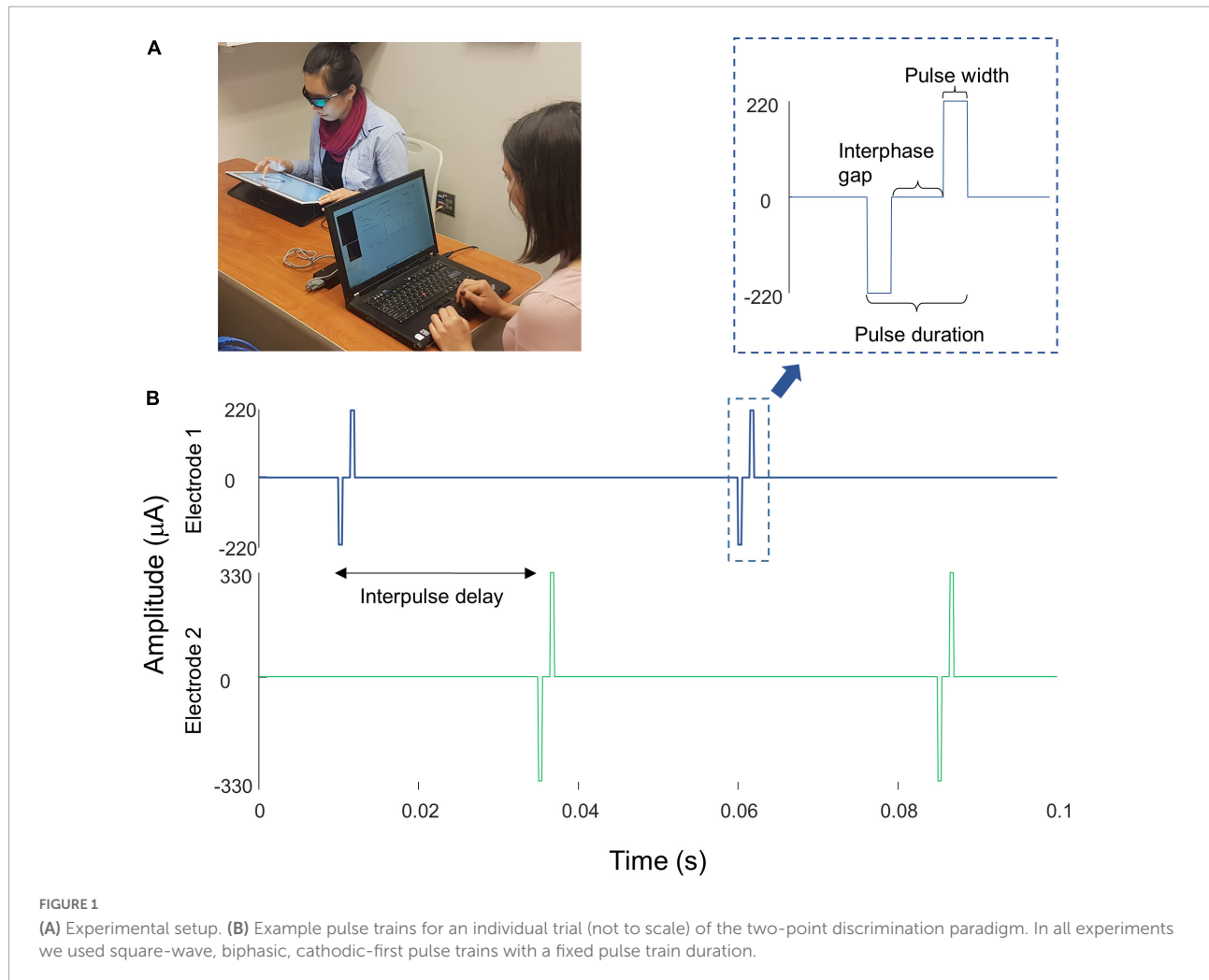
Our initial participant pool consisted of nine participants with Argus II retinal prostheses (Second Sight Medical Products, Inc.): six participants implanted and tested at the Retina Service at the University of Minnesota, and three tested at the Lions Vision Research and Rehabilitation Center at Johns Hopkins University; one of these patients was implanted at Wills Eye Hospital in Philadelphia, the other two at the Johns Hopkins Wilmer Eye Institute.

Unfortunately, five of the six University of Minnesota participants almost never reported seeing two percepts when stimulated with a pair of electrodes, and the one participant

TABLE 1 Patient demographics.

Participant ID	Second sight participant ID	Implant	Eye	Age at testing	Date of implantation	Date of testing
S1	12-005	Argus II	Right Eye	83	2009	2019
S2	12-104	Argus II	Right Eye	61	2015	2019
S3	13-101	Argus II	Right Eye	74	2014	2019

All data reported in this paper were collected at Johns Hopkins University Wilmer Eye Institute.



who did report seeing two percepts on a reasonable proportion of trials (7/49 in session 1; 35/90 in session 2) also reported seeing two percepts on 6/7 (no stimulation) catch trials. Consequently, we excluded the Minnesota participant data from further analysis.

Of the patients tested at Johns Hopkins, S1 was implanted as part of the Argus II Feasibility Study ([clinicaltrials.gov](https://clinicaltrials.gov/ct2/show/study/NCT00407602) trial NCT00407602), whereas S2 and S3 were implanted after Argus II became commercially available in 2013, see [Table 1](#). The data described in this paper (Johns Hopkins participants) were collected in two sessions, with each session taking roughly 3 h, including frequent breaks.

Data were collected at the Retina Service at the University of Minnesota and the Lions Vision Research and Rehabilitation Center at Johns Hopkins University, and were provided to UW researchers in a de-identified format. The study was approved by IRBs of the University of Washington and Johns Hopkins University.

Stimuli

The Argus II retinal prosthesis consists of an epiretinal electrode array implanted in the macular region of the retina, an ASIC chip, RF transmitter and receiver coil, as well as glasses containing a mini camera (not used in our experiment)

and a video processing unit (VPU), see [Ahuja et al. \(2011\)](#), for more detail. The signal from the VPU is received by the internal receiver coil, and the ASIC chip generates the electrical pulses that are then sent to the electrode array, a grid of 6×10 platinum disk electrodes in a rectangular grid arrangement with 225 μm diameter and 575 μm center-to-center separation.

We stimulated electrodes directly by connecting the VPU of each participant's device to a psychophysical testing computer provided by Second Sight Medical Products, Inc., see [Figure 1A](#). Electrode stimulation was controlled by in-house software programmed in MATLAB by Second Sight Medical Products, Inc. (Mathworks, MATLAB Version: 7.1, R14SP3), that sent current waveforms directly to the electrodes (by-passing the camera). Stimuli consisted of biphasic, cathodic-first, charge-balanced, square-wave pulse trains with frequency, interphase gap, interpulse delay (the offset between pulses on different electrodes) and pulse train duration parameters as shown in [Figure 1B](#) and [Table 2](#). Stimulation current amplitudes were kept below a charge density limit of $1 \text{ mC}/\text{cm}^2/\text{phase}$.

Identifying electrodes with lower perceptual thresholds

A proprietary fast threshold estimation procedure, SwiftPA ([Second Sight Medical Products Inc, 2013](#)) was used to determine which electrodes had electrical thresholds below the safety limit. Stimulation consisted of 0.46 ms, cathodic-first pulse trains of 1 s duration. Starting from the top left electrode, a yes-no procedure was used to determine whether stimulation produced a detectable phosphene. If participants failed to detect a phosphene the amplitude of the electrical stimulation was increased. If participants reported a phosphene the amplitude was held constant. After 3 consecutive correct detections, testing moved to the next electrode. We limited further testing to a subset of the electrodes which produced 3 consecutive correct detections at a current amplitude below the safety limit (10 electrodes in S1, 7 electrodes in S2, and 10 electrodes in S3). These electrodes were selected to have low thresholds, and to be spread as widely apart as possible on the array.

Current amplitude detection threshold measurements

We then used proprietary software (Argus II-Hybrid Threshold) provided by Second Medical Products Inc. to carry out an adaptive, single interval yes-no procedure to measure detection thresholds (50% detection performance) within electrodes pre-selected by the SwiftPA procedure, methodological details are explained more fully in [Ahuja et al. \(2013\)](#).

To avoid adaptation effects ([Horsager et al., 2009](#); [Pérez Fornos et al., 2012](#)) we interleaved threshold measurements across electrodes within each run. Up to six electrodes were

tested within a single run. Each trial started with an audio prompt. Then one of the six selected electrodes (selected pseudorandomly) was stimulated at either 20 or 6 Hz, with a pulse train duration of either 250 or 500 ms (depending on what the participants used in their daily life, see [Table 2](#)), square-wave pulse width of 0.46 ms, and interphase gap of 0 or 1 ms. The amplitude of stimulation was adapted through a staircase procedure. The participant was asked to report whether or not they had seen a phosphene on that trial using a game controller and feedback was given on each trial. Each run consisted of a maximum of 60 trials per electrode (5 blocks of 12 trials), for a maximum of 360 trials, and 4 catch trials per block ([Second Sight Medical Products Inc, 2013](#)). Each run was followed by a brief rest, which ended based on participant feedback.

Perceptual thresholds for detection at a given electrode were calculated by pooling data across all trials. The probability of reporting a percept as a function of stimulus intensity was fit with a psychometric function using maximum likelihood estimation, and the current amplitude detection threshold was defined as the stimulus amplitude at which the participant reported a percept 50% of the time ([Watson and Robson, 1981](#); [Wichmann and Hill, 2001](#); [Ahuja et al., 2013](#)).

Two-point discrimination measurements

For each participant, we selected electrodes with the lowest detection thresholds and paired them in all possible combinations. Stimulation was carried out at an amplitude twice the detection threshold, or at a maximum of 660 μA (the charge density limit of $1 \text{ mC}/\text{cm}^2/\text{phase}$ for a 0.46 ms pulse). On each trial, we asked “how many shapes did you see” and asked them to draw the phosphene shape(s) on a tablet touch screen.

Parameters used for each participant are shown in [Table 2](#). The pulse width was always 0.46 ms, with an interphase gap of 1 ms for S2 and 3, and no interphase gap for S1, based on the stimulation parameters each individual was accustomed to through daily use. Stimulation was interleaved, with either a 25 ms (20 Hz) or 83 ms (6 Hz) interpulse delay between the beginning of each pulse on one electrode and the beginning of the corresponding pulse on the second electrode, [Figure 1B](#).

In each experimental run, every possible pair of electrodes was tested 3 times. On each trial, participants verbally reported the number of shapes they were seeing, gave a qualitative description (e.g., “the one on the bottom is smaller,” “left one is twice as big as right one—they are side by side”) and traced the perceived phosphene shape(s) on a tablet (drawing data not reported here). Although the “correct” answer was always two percepts, participants were never given feedback as to how many electrodes had been stimulated. Importantly, the number of shapes drawn by the participant was almost always consistent with the number of shapes they verbally reported, suggesting that they were not reporting whether they saw one or two shapes on the basis of the overall brightness or size of the percept.

TABLE 2 Stimulation protocol and parameters for all experiments.

	Patient ID	Experiment	Frequency (Hz)	Interphase gap (ms)	Interpulse delay (ms)	Duration (ms)
1 st Session	S1	Perceptual Threshold	20	0	N/A	250
	S2	Perceptual Threshold	6	1	N/A	250
	S3	Perceptual Threshold	6	1	N/A	250
	S1	Two-point Discrimination	20	0	25	250
	S2	Two-point Discrimination	20	0	25	250
	S2	Two-point Discrimination	6	0	83	500
	S3	Two-point Discrimination	6	1	83	500
	S3	Two-point Discrimination	6	1	83	500
2 st Session	S1	Perceptual Threshold	20	0	N/A	250
	S2	Perceptual Threshold	6	1	N/A	500
	S3	Perceptual Threshold	6	1	N/A	500
	S1	Two-point Discrimination	6	1	83	500
	S2	Two-point Discrimination	6	1	83	500
	S3	Two-point Discrimination	6	1	83	500
	S3	Two-point Discrimination	6	1	83	500

TABLE 3 Current amplitude detection thresholds (50% detection performance) and reports of daily usage.

	Median threshold (μ A)	Interquartile range (μ A)	Minimum threshold (μ A)	Maximum threshold (μ A)	Daily use
S1	274	218–331	153	484	3–4 days a week, 3–5 h a day, for an average of 20 h a week
S2	476	355–621	217	645	Approximately once a month
S3	210	177–280	89	323	Used the device almost every day outdoors, for a limited amount of time, averaging about 2 h a day.

We included $\sim 25\%$ of catch trials, randomly interspersed, in which neither of the electrodes was stimulated. We deliberately used no stimulation as compared to single electrode stimulation during catch trials, because we were concerned that differences in brightness or size might allow participants to differentiate between single and paired stimulation in the absence of genuine pattern vision (see section “Discussion”).

The order of the trials was pseudorandomized. We asked participants to avoid head and eye movements to maximize stability of the perceived phosphene locations, but to maximize participant comfort we did not use a chin rest.

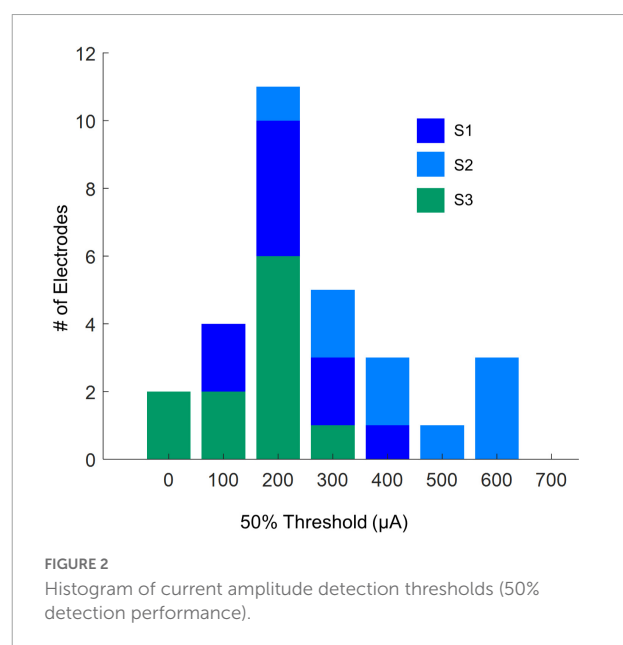
Results

Current amplitude detection thresholds

Table 3 shows 50% current amplitude detection thresholds and self-reported daily usage for all three participants, and Figure 2 shows a histogram of current amplitude thresholds for all participants.

Two-point discrimination thresholds

In the paired electrode stimulation experiment, we asked the question “How many shapes did you see?” Participants could potentially report any value, and they were then asked to draw



what they saw. Table 4 shows the reported number of percepts and the probabilities of each verbal response.

Trials where participants did not report seeing a percept were discarded (0–4%). The few trials where participants

TABLE 4 Reported number of percepts and their frequency and probability in the two-point discrimination experiment.

	Reported number of percepts	Frequency	Probability $P("X" 2)$
S1	"0"	0	0.00
	"1"	66	0.31
	"2"	114	0.69
	"3"	0	0.00
S2	"0"	2	0.04
	"1"	29	0.54
	"2"	20	0.37
	"3"	3	0.06
S3	"0"	0	0.00
	"1"	38	0.36
	"2"	67	0.64
	"3"	0	0.00

reported 3 percepts (0–6%) or more percepts were collapsed with trials where participants reported 2 percepts for the remainder of the analyses.

Given that we always used paired electrode stimulation, we were concerned that participants might shift their criterion for reporting two percepts over the course of the experiment. However, there was little evidence that the probability of participants reporting two (or more) percepts changed substantially either within or across sessions (although it should be noted that electrode pairs varied between sessions, [Table 5](#), which may have masked some experience driven effects). For S3 there was a significant increase in the probability of reporting two percepts between the first and second $\frac{1}{2}$ of trials in session 2. The reason for this is not clear, but might possibly be due to an improved ability to recognize two percepts with experience. Since there was little effect of time on our two-point discrimination data we did not use time as a factor in our further analyses. The number of shapes participants drew consistently matched their verbal report, throughout every session.

The probability of reporting 1 or 2 (or more) percepts during catch trials (with no stimulation) also remained reliably low throughout the experiment (S1:0/15 trials, S2:2/12 trials, S3: 0/16 trials).

Optical coherence tomography data

Unfortunately, it was impossible to collect useable optical coherence tomography (OCT) images for the region of the retina including the array in S2 and S3. OCT data from S1, 2 years after implantation (2011), are shown in [Figure 3](#). In this patient the array appears to be flush to the retinal surface, but there is some thickening (evidence of potential damage) of the retina underneath the array.

Relationship with device use

In a separate questionnaire, participants were asked how often they used their device. Participants varied widely in device use, see [Table 3](#). S1, who had a median amplitude threshold of 274 μA and saw 2 percepts 69% of the time with paired stimulation, used the device most consistently, reporting using the device 3–4 days a week, 3–5 h a day, for an average of 20 h a week. S3, who had a median amplitude threshold of 210 μA and saw 2 percepts 64% of the time with paired stimulation, used the device almost every day when outdoors, but for a limited amount of time, averaging about 2 h a day. S2, who had a median amplitude threshold of 476 μA and saw 2 percepts only 37% of the time with paired stimulation, reported using the device once a month.

Modeling

Pulse2percept analyses and current amplitude threshold estimates were carried out in Python using pulse2percept ([Beyeler et al., 2017](#)) and in-house code. The remaining analyses were carried out in MATLAB (Mathworks, MATLAB Version: 9.10.0, R2021a) using in-house code. All in-house code can be found at https://github.com/VisCog/Argus_current_spread.

Stage I: Estimating electrode-electrode distance to and along axonal bundles

As an initial step we estimated distance to and along axonal bundles for each pair of electrodes.

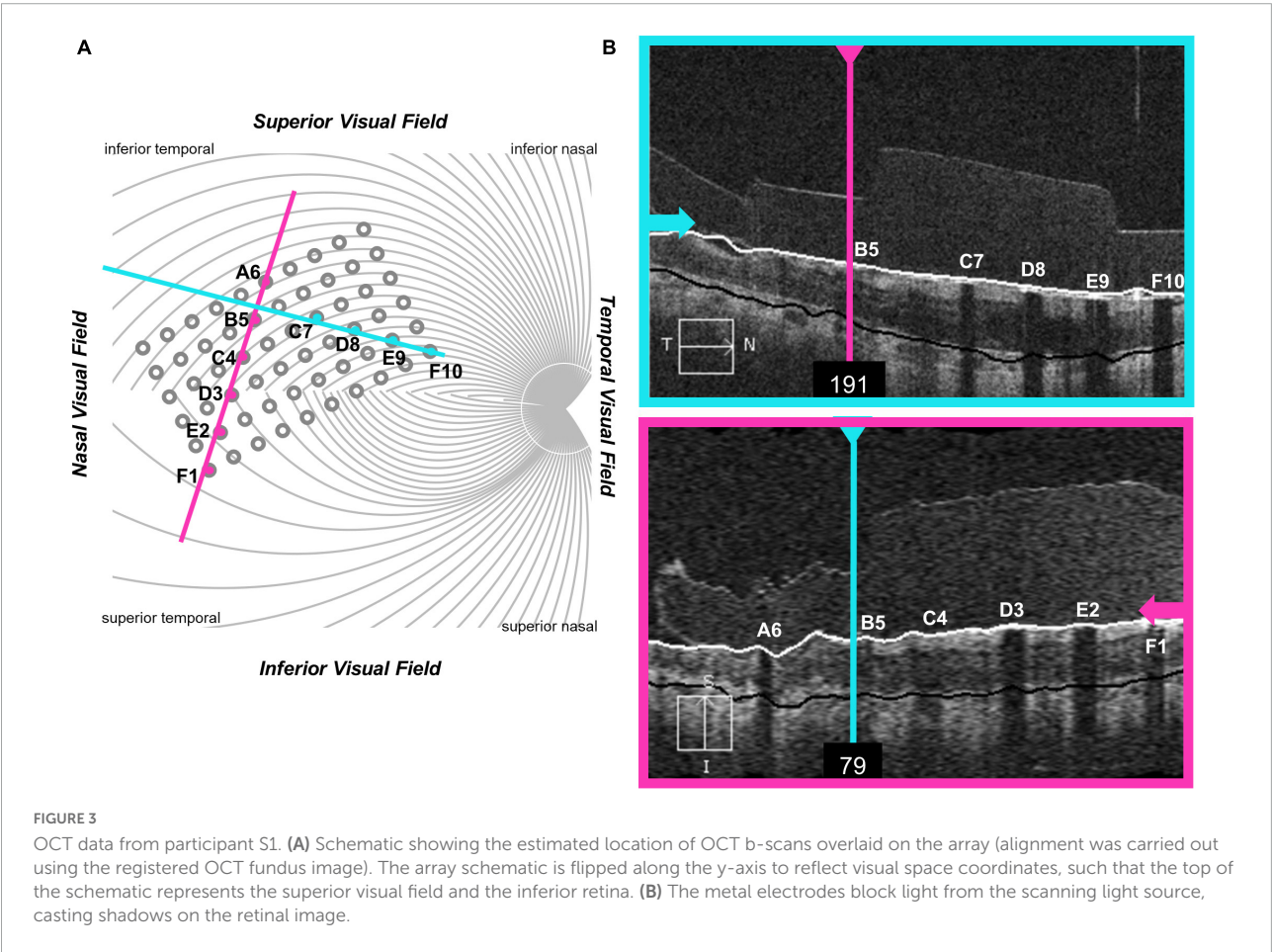
Both electrophysiological ([Fried et al., 2009](#)) and psychophysical data ([Beyeler et al., 2019](#)) suggest that axonal stimulation may contribute significantly to the poor resolution of retinal prostheses. Axonal stimulation is a particular concern for epiretinal prostheses, such as the Argus II which are placed on the nerve fiber layer, adjacent to the axon fiber bundles of retinal ganglion cells. Depending on stimulus conditions, participants implanted with the Argus II describe the phosphenes generated by single electrodes as elongated, due to activation of passing axon fibers, resulting in perceptual distortions (individual electrodes producing “streaks” instead of punctate spots) that vary in their length and orientation across the retinal surface in a way that can be predicted based on the known axon fiber trajectories ([Nanduri et al., 2012](#); [Beyeler et al., 2019](#)).

It is not yet entirely clear how sensitivity to electrical stimulation falls off as a function of distance from the initial segment ([Fried et al., 2009](#)), with psychophysically estimated decay constants ranging widely from 500–1,420 μm

TABLE 5 Probability of reporting two percepts, within and across sessions.

Participant	Session	1st half of trials in session	2nd half of trials in session	Unique electrodes tested
S1	Session 1	0.73 [0.48,0.89]	0.93 [0.7, 0.99]	A4, A8, D1, E10, F2
	Session 2	0.68 [0.57, 0.77]	0.50 [0.4, 0.62]	A2, A4, A8, B3, B6, D1, D8, E10, E3, F2, F7
S2	Session 1	0.33 [0.12, 0.65]	0.56 [0.27, 0.81]	B6, B9, F7, F9
	Session 2	0.39 [0.2, 0.61]	0.44 [0.25, 0.66]	A10, B10, B5, B6, B9, F7, F9
S3	Session 1	0.71 [0.25, 0.66]	0.59 [0.41, 0.74]	A8, B10, B4, C6, C8, C9, D6, E9, F10
	Session 2	0.35 [0.19, 0.55]	0.91 [0.72, 0.97]	A6, A8, B10, B9, D6, F10

Values in the bracket are 95% confidence intervals calculated by Wilson method.



(Beyeler et al., 2019). Nonetheless, if axonal stimulation plays a significant role in reducing resolution, then distance, both to and along a shared axon bundle should predict how many distinct percepts are seen when two electrodes are stimulated.

Methods

To provide a measure of the distance to and along axon bundles we used an existing computational model developed by Beyeler et al. (2019). This model begins by using ophthalmic fundus photographs in which an eye care provider marked the optic nerve, fovea, and the center of the implant on the fundus, using photos taken pre- and post-surgery. These landmarks

were then used to estimate the array center with respect to the fovea, the array rotation with respect to the horizontal raphe, and the retinal distance between the fovea and the optic nerve head for each participant. In the human retina, the extended raphe is typically located $15^{\circ} \pm 2^{\circ}$ inferiorly to a horizontal line at the latitude of the fovea through the center of the optic disk. We approximated this by fitting a parabola centered on the optic nerve and approximating the horizontal raphe as parallel to the axis of symmetry on the abscissa (Jansonius and Schiefer, 2020).

The spatial layout of axonal pathways was calculated using *pulse2percept* software (Beyeler et al., 2017), that simulates

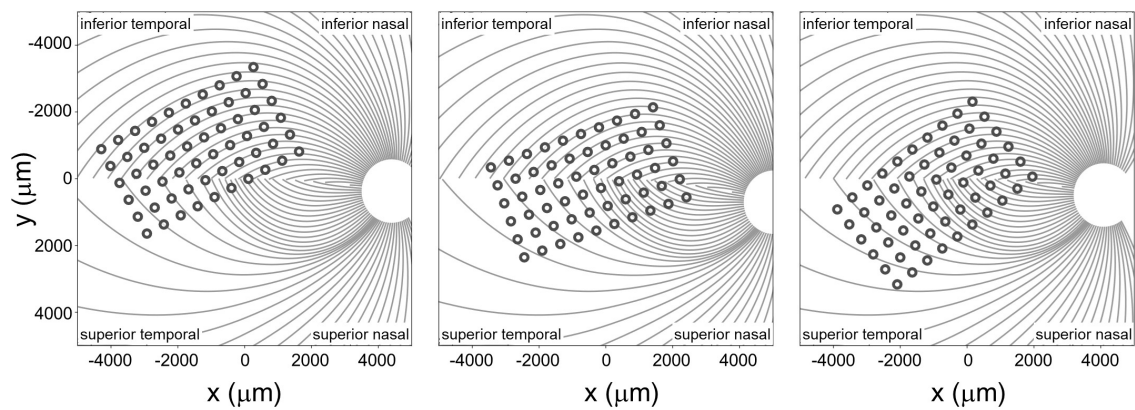


FIGURE 4

Estimated position of the electrode array on the retinal surface for all three participants (see Beyeler et al., 2019 for estimation methods) overlaid on estimates of the axon fiber pathways for that participant. Note that all panels are in visual space coordinates, with the upper visual field at the top of the figure.

pathways using a model (Jansonius et al., 2009) that assumes that the trajectories of the optic nerve fibers can be described in a modified polar coordinate system (r, ϕ) with its origin located in the center of the optic disk. Each nerve fiber is modeled as a spiral defined by the angular position of the trajectory at its starting point at a circle around the center of the optic disk, with a second parameter describing the curvature of the spiral, see Figure 4.

Given that the size of the Argus II electrodes is large compared to the density of the underlying axon pathways, it was assumed that an electrode always sits on top of a ganglion axon fiber bundle. We simulated 400 axonal bundles, which provided sufficient resolution to ensure that there was an axonal bundle underneath every electrode.

We defined three inter-electrode distance values, Figure 5:

1. **Physical distance** was defined as the Euclidean center-to-center distance between two electrodes on the retinal surface.
2. **Distance to axon** (d_{axon12}) was defined as the minimum distance between two electrodes (e_1, e_2) and the axons closest to them. This was calculated by:
 - a. Selecting the axonal bundles a_1 and a_2 that fell beneath each of the two electrodes.
 - b. Determining the closest Euclidean distance from the center of each electrode to the fellow axon bundle: $d_{e_1 a_2} = \min[d(e_1, a_2)]$ and $d_{e_2 a_1} = \min[d(e_2, a_1)]$
 - c. Choosing the minimum distance of the pair, $d_{axon12} = \min[d_{e_1 a_2}, d_{e_2 a_1}]$.
 (An alternative would have been to calculate the distance to the axon bundle midway between the two electrodes, but this would have essentially resulted in the same values, halved).

3. **Distance along axon** was defined as the distance between an electrode and the point on its axon that is closest to the axon of the other electrode.

Results

These three measures of distance on the retina were strongly correlated with each other. The Pearson correlation coefficient between physical distance and distance to axon was $r(337) = 0.58$, $p < 0.0001$, between physical distance and distance along axon was $r(337) = 0.84$, $p < 0.0001$, and between distance to axon and distance along axon was $r(337) = 0.28$, $p < 0.0001$.

Intuitively, the reason for this is that (except when electrodes are on the opposite side of the Raphe) the shortest distance to the axon (orange line in Figure 5B) tended to fall along a line that was close to orthogonal to the distance along the axon (purple line), since axonal bundle curvature (purple line) tended to be relatively small. As a result, these three distances form the edges of an approximate right triangle, with the hypotenuse as the Euclidean distance between two electrodes (green line) and distance to and along the axon (with a slight curvature) forming the other two sides. Because these three co-varying distance variables essentially contain 2 degrees of freedom, we only included physical distance and distance to axon as predictive factors in our modeling.

Stage II: Regression modeling: The effects of spatial and axonal distance on two-point discrimination thresholds

Next, we fit nested linear logistic models to determine which factors—physical distance between electrodes, mean

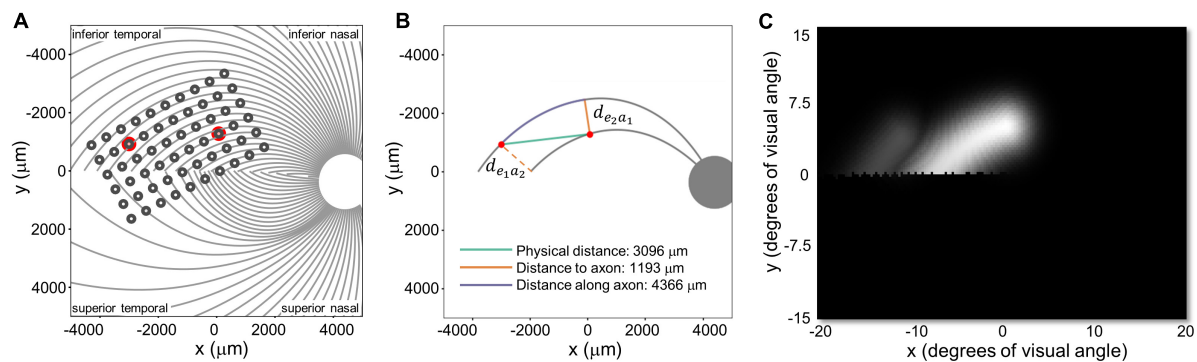


FIGURE 5

(A) Estimated position of the electrode array on the retinal surface for S1 (replotted from Figure 4A). (B) Examples of distance to and along axon fibers, $d_{e_1a_2}$ and $d_{e_2a_1}$ refer to the shortest distance from an electrode to the axonal bundle closest to fellow electrode. (C) Predicted percept for the two electrodes shown in panels (A,B). Note that all panels are in visual space coordinates, with the upper visual field at the top of the figure.

amplitude of the currents of both electrodes, and distance to axon (as estimated in modeling stage I), best predicted our psychophysical data.

Methods

The probability of participants reporting 2 (or more) shapes when 2 electrodes were stimulated, $P('2'|2)$, was modeled using logistic regression. We used a maximum likelihood chi-squared test to determine whether adding parameters improved model fits. Across all analyses that included current amplitude as a factor, subject identity had little additional predictive value and so it was not included as a factor.

Regression was done both using a two-factor model with inter-electrode physical distance and mean stimulation amplitude of the two electrodes as predictors, and with a three factor model that included distance to axon across the pair of electrodes as a third predictor.

Results – two factor model

We began with a two factor model that included (1) physical distance and (2) the mean stimulation amplitude of the two electrodes as predictors.

A maximum likelihood chi-squared test shows that both factors statistically improved the fit to the data, Table 6.

The best-fitting two-factor model predicts the probability of seeing two percepts as:

$$P('2'|2) = \exp(-0.0599 - 0.00314 (\text{Mean Amplitude}) + 0.000829 (\text{Physical Distance})) \quad (1)$$

Figure 6A shows the binned participant performance values and the surface predicting the probability of reporting 2 percepts based on the logistic regression model. Figure 6B shows predicted 65%, 75% and 85% two-point discrimination iso-performance curves based on the surface of Figure 6A.

As expected, the probability of seeing two percepts increased as a function of physical distance and decreased as a function of mean amplitude. We used this two-factor logistic regression model fit, whose surface is shown in Figure 6A, to define the two-point discrimination threshold as the inter-electrode distance for which participants should report two percepts on 75% of trials at each participant's median current amplitude detection threshold ($S1 = 2,394 \mu\text{m}/8.3^\circ$, $S2 = 3,127 \mu\text{m}/10.9^\circ$, $S3 = 2,161 \mu\text{m}/7.5^\circ$; reported in microns on the retina and degrees of visual angle, assuming a conversion of $288 \mu\text{m} = 1^\circ$ (Drasdo and Fowler, 1974), shown with black bars in Figure 7A. For comparison, the approximate size of the Argus II prosthetic array was $3,675 \times 5,975 \mu\text{m}/12.8 \times 21^\circ$, with a distance between neighboring electrodes of $575 \mu\text{m}/2^\circ$. Thus, a spacing of about four electrodes is needed to report two percepts on 75% of trials.

Results – three factor model

Distance to axon also had significant predictive value, as shown in Table 5. Within this 3-factor model, the ability to predict whether one or two percepts were reported was best modeled as:

$$P('2'|2) = \exp(-0.1839 - 0.0030 (\text{Mean Amplitude}) + 0.000602 (\text{Distance}) + 0.000502581 (\text{Distance to axon})) \quad (2)$$

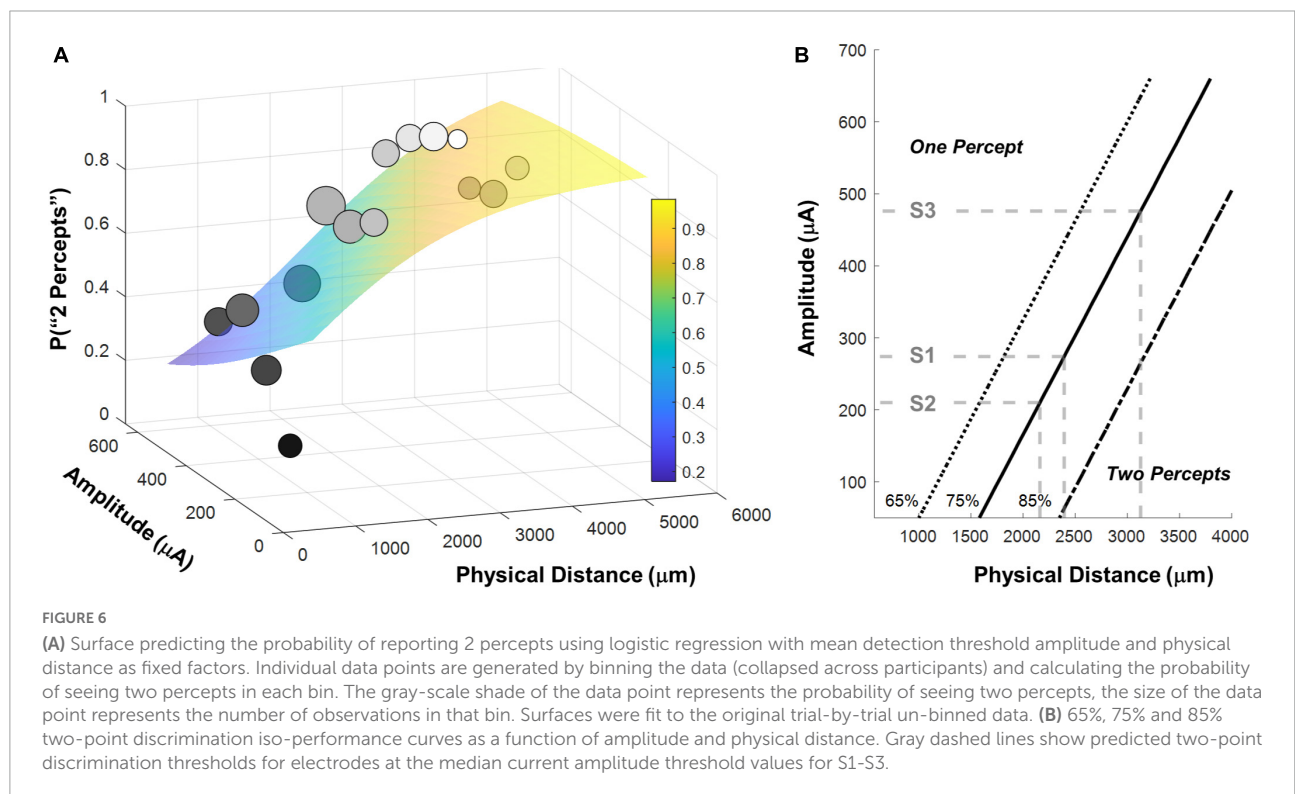
As noted above, physical distance and distance to axon were strongly correlated. Correlations between independent variables do not reduce the predictive power of a model but it becomes difficult to disentangle the separate effects of each explanatory variable on the explained variable (Kutner et al., 2004). Thus, the beta weights of regression Equation 2 should be interpreted with caution.

Therefore, to estimate the size of the effect of axonal stimulation on two-point discrimination thresholds we began with the 2-factor regression model described in Equation 1

TABLE 6 Logistic regression model parameters and statistical significance.

		Estimate	95% CI		$\chi^2(1)$	Pr($> \chi^2$)
			Lower	Upper		
2-factor model	Amplitude	−0.003014	−0.005144	−0.000883	7.87	0.005022
	Physical Distance	0.000829	0.000575	0.001084	50.64	< 0.0001
3-factor model	Amplitude	−0.003	−0.005145	−0.000840	7.61	0.005802
	Physical Distance	0.000602	0.000309	0.000895	18.40	< 0.0001
	Distance to Axon	0.000503	−0.000876	−0.000129	7.20	0.007279

The intercepts are not included in the table, but are included in Equations 1, 2.



and Figure 6, fixed the best-fitting factor weights for these two factors, then added distance to axon as an additional factor. This allowed us to calculate the probability of reporting two percepts when the distance to axon was zero (i.e., the two electrodes fell on the same axon bundle, shown in the lower surface of Figure 8A) vs. when the distance to axon was equal to the physical distance (i.e., axonal stimulation was minimized, upper surface of Figure 8A).

Figure 8 shows 75% iso-performance contours for these upper and lower surfaces. As expected, the effects of axonal stimulation are smaller when the physical distance between the two electrodes is small. According to the model, if axonal stimulation were minimized, the physical distance between the electrodes that would result in a 75% two-point discrimination threshold for each participant's median current amplitude threshold would be S1 = 2,151 $\mu\text{m}/7.5^\circ$, S2 = 2,812 $\mu\text{m}/9.8^\circ$,

S3 = 1,942 $\mu\text{m}/6.7^\circ$, respectively, shown by the dark gray bars in Figure 7. This corresponds to a reduction in the two-point distance threshold of $\sim 0.8^\circ$ for S1 and S3, and $\sim 1.1^\circ$ for S2.

Stage III: Current spread modeling: The effects of retinal damage and electrode lift on thresholds and two-point discrimination thresholds

Having estimated the effect of axonal stimulation on two-point discrimination performance, we simulated a simplified “scoreboard” model to identify how retinal damage and lift might influence amplitude and two-point discrimination thresholds. According to the scoreboard model, the main determinant of whether one or two percepts are seen will be the

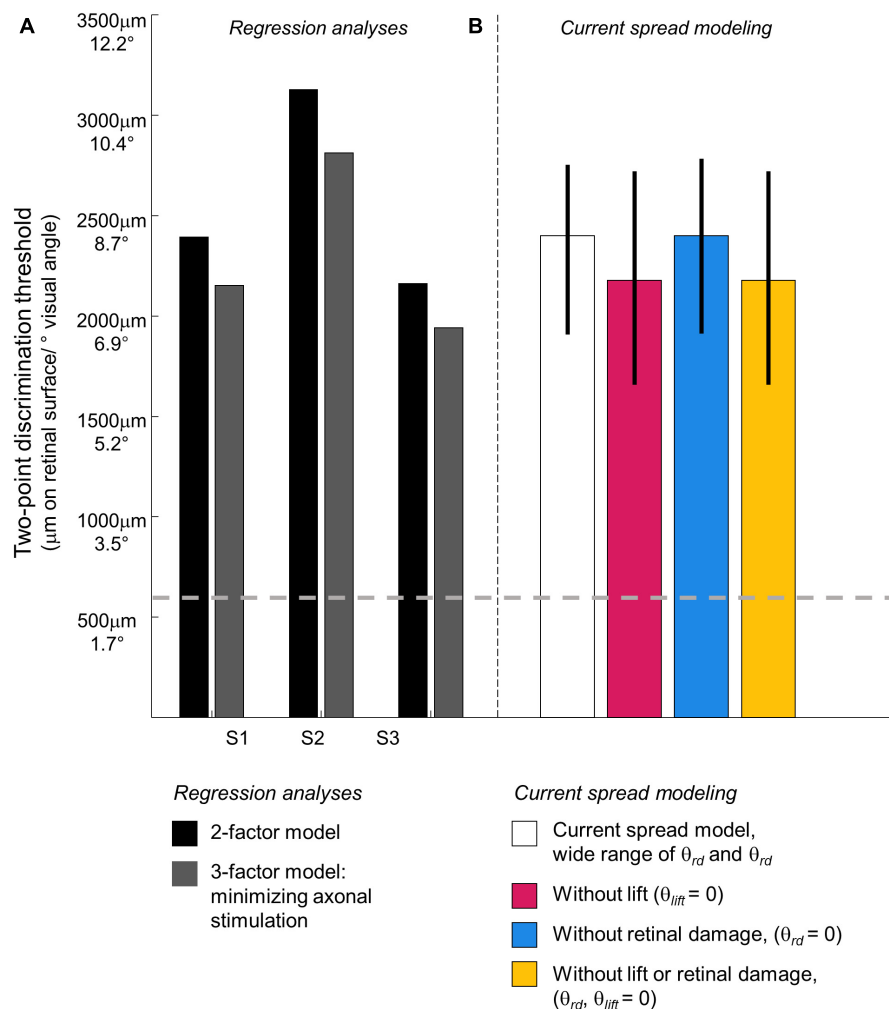


FIGURE 7

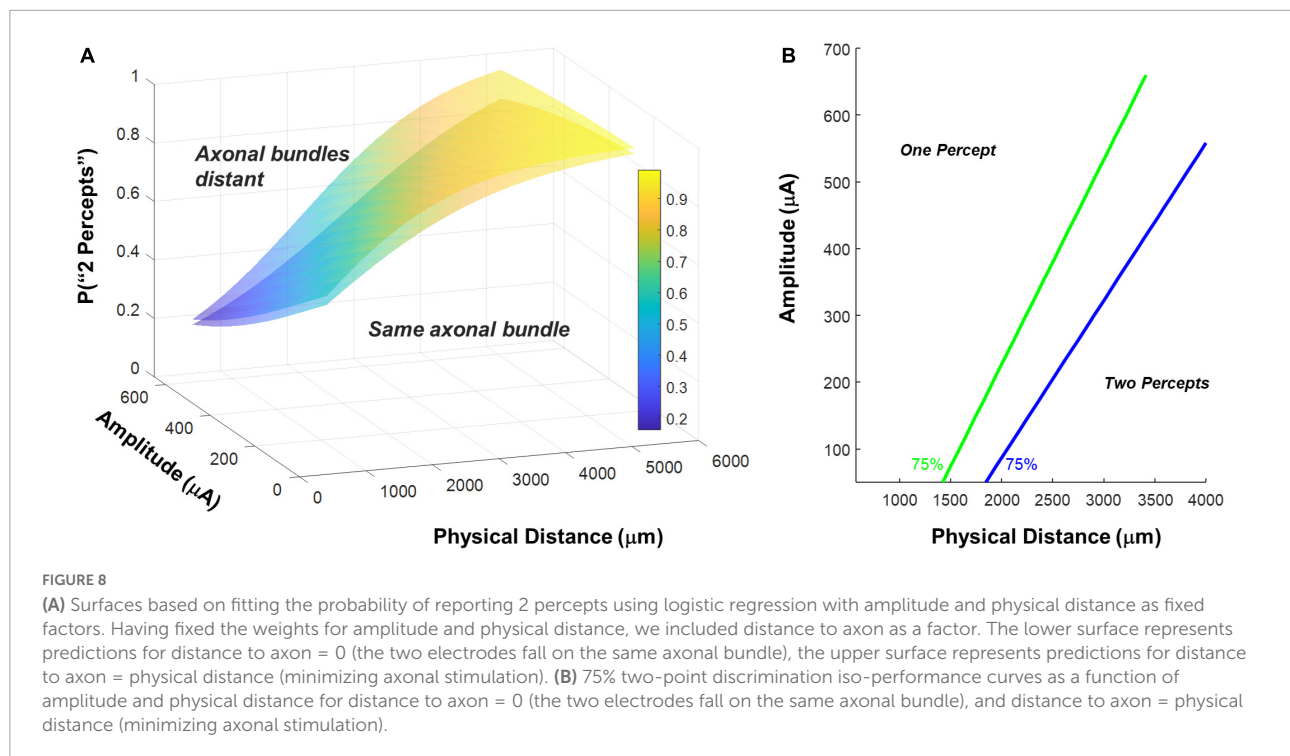
Predicted two-point discrimination thresholds. The gray dashed line shows the resolution limit (2°) that would be obtained if individuals saw two-points when neighboring electrodes were stimulated (Stronks and Dagnelie, 2014). (A) Stage II. Regression analyses. Black bars: The predicted 75% two-point discrimination thresholds with current amplitudes set to each participant's median current amplitude detection threshold; Gray bars: The predicted 75% two-point detection thresholds if axonal stimulation is minimized. (B) Stage III. Current spread modeling. Empty bar: Predicted 75% two-point discrimination thresholds across the full range of simulation parameterizations that could predict the iso-performance contour predicted by regression analyses; Blue bar: Predicted 75% two-point discrimination thresholds with no retinal damage ($\theta_{rd} = 0$); Pink bar: Predicted 75% two-point discrimination thresholds with the electrode flush to the retinal surface ($\theta_{lift} = 0$); Yellow bar: Predicted 75% two-point discrimination thresholds with no retinal damage and the electrode flush to the retinal surface ($\theta_{rd}, \theta_{lift} = 0$). Error bars represent the 5–95% confidence range of simulation outcomes.

overlap of the current fields generated by the electrodes on the retinal surface. This overlap is affected by the physical distance between the electrodes along the retinal plane, “lift” of the electrodes from the retinal surface, and the current amplitude on the electrodes.

As lift increases, so does the current amplitude required to elicit a percept. A larger current amplitude at a greater distance from the retina results in a broad current spread on the retinal surface. Extensive psychophysical work with early participants implanted with the Argus I and II devices has shown that, for individual electrodes, it is possible to predict the size, threshold and brightness of suprathreshold phosphenes as a function of

frequency and amplitude, with reasonable accuracy, once the height of the electrode off the retinal surface is included as a factor (de Balthasar et al., 2008; Horsager et al., 2009; Nanduri et al., 2012; Ahuja et al., 2013).

Various types of retinal damage may also increase the current needed to generate a percept and thereby affect amplitude thresholds and possibly two-point discrimination. Possible causes of retinal damage include severe disease-related degeneration, damage to the retina as a result of surgical implantation, or damage caused by the presence of the array. A variety of studies have found evidence suggestive of retinal damage in retinal prosthesis patients (Gregori et al.,



2018; Lin et al., 2019; Rizzo et al., 2019; Patelli et al., 2020). This damage seems to have a variety of causes including inflammation, “boggy” (sic) thickening, schisis and fibrosis, intraretinal fluid (IRF) cysts, as well as a “snowplow” effect of the electrode array pressing against the retina and causing adjacent thickening (Gregori et al., 2018; Patelli et al., 2020). While many of these conditions are common in late stage RP patients, they seem to be exacerbated in the implanted eye (Lin et al., 2019). In addition, over time many patients also develop membranes (both adherent to and separated from the retina) between the retina and the array. For example, Patelli et al. (2020) observed in one patient the formation of retinal fibrosis and schisis within 2 years of implantation which resulted in higher thresholds in 34 out of 60 electrodes. After the removal of retinal fibrosis, 20 out of 60 electrodes were reactivated; suggesting this fibrosis was responsible for reducing electrode sensitivity.

Methods

We simulated current spread as a function of 3D distance from the edge of the electrode as follows:

$$I_{xyz} = \frac{I_0}{1 + (kr)^a} \quad (3)$$

Where I_0 is the stimulating current and r is the 3D distance from the edge of the electrode (Ahuja et al., 2008). Parameters k and a describe current spread. The range of k and a values were chosen to approximate previous psychophysical data describing threshold as a function of lift (de Balthasar et al., 2008; Ahuja et al., 2013), and be consistent with more elaborate

neurophysiological models (Esler et al., 2018). The parameter a varied between 1–3, and k varied between 6–20, providing a parameterization of current spread that widely spanned the neurophysiologically plausible range. For both a and k , larger values represent higher amounts of tissue electrical resistance, so current amplitudes drop more quickly as a function of r .

Figure 9 shows two example simulations for a pair of electrodes, separated by $d = 1,400 \mu\text{m}$, $a = 1.5$, $k = 15$, lifted by $150 \mu\text{m}$ and $750 \mu\text{m}$ above the retinal surface. The higher an electrode is lifted off the retinal surface, the greater the electrode current required to produce an electric field gradient sufficient to elicit spikes in the axons passing through the retinal surface. The bottom panels represent a top view, showing current at the retinal plane. Both simulations of Figure 9 have a maximum current value of $100 \mu\text{A}$ at the retinal surface, however, the region of high current is much broader for the electrode pair that are lifted $750 \mu\text{m}$ above the retinal surface.

Thus, for electrodes that are lifted off the surface, the increased overlap between the current fields is likely to reduce the ability to differentiate two distinct phosphenes. We represented this overlap by calculating the decrease in current amplitude at the point intermediate between the electrodes (I_{mid} , cyan stars) compared to the point of maximum current (I_{max} , blue stars), on the retinal surface. This “dip” in current was calculated as:

$$\text{dip} = 100 \left(\frac{I_{\text{max}} - I_{\text{mid}}}{I_{\text{max}}} \right) \quad (4)$$

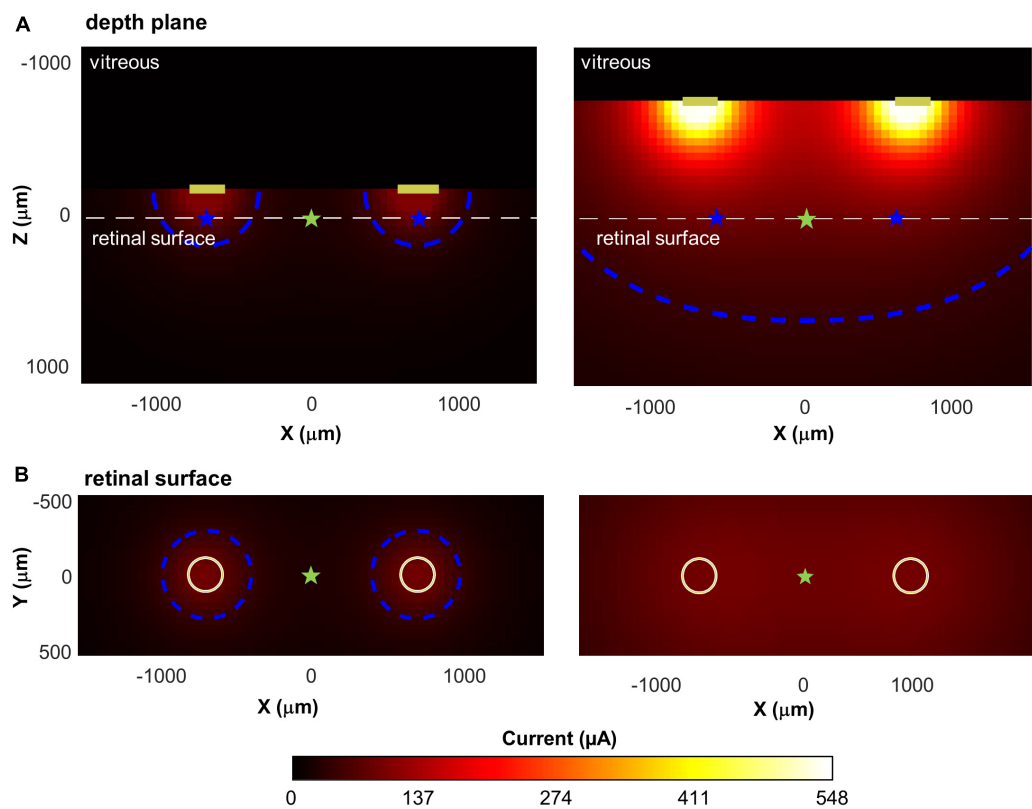


FIGURE 9

Illustration of current spread for two pairs of disk electrodes, separated by 1,400 μm , with different lifts from the retinal surface. Top: Cross-sectional view through the retina; Bottom: View of the retina from above. Current amplitude at the electrode was fixed to produce a maximum of 100 μA of current on the retina. (A) Lifted 150 microns above the retinal surface. (B) Lifted 750 microns above the surface. The white dashed line in the upper panels shows the location of the retinal surface. Blue contour lines in each panel represent 50 μA ; cyan star: the intermediate point between the electrodes; blue star: the point of maximum current on the retinal surface.

In Figure 9, when electrodes are lifted 150 μm above the retinal surface (Panel A), $I_{\text{max}} = 100 \mu\text{A}$, $I_{\text{mid}} = 26 \mu\text{A}$, $\text{dip} = 74\%$, whereas when electrodes are lifted 750 μm above the retinal surface (Panel B), $I_{\text{max}} = 100 \mu\text{A}$, $I_{\text{mid}} = 93 \mu\text{A}$, $\text{dip} = 7\%$.

We assumed that the measured threshold current for seeing a percept at an electrode (I_0) could be described as a multiplicative combination of three factors:

$$I_0 = \theta_{\text{lift}} \cdot \theta_{\text{rd}} \cdot \theta_{\text{baseline}} \quad (5)$$

θ_{baseline} is the current required to elicit enough spikes to reach psychophysical threshold for an electrode flush to the retinal surface in an RP patient whose retina is undamaged. We fixed $\theta_{\text{baseline}} = 50 \mu\text{A}$, based on the maximum sensitivity observed in previous psychophysical data (de Balthasar et al., 2008; Horsager et al., 2009; Ahuja et al., 2013).

θ_{lift} represents a multiplicative increase in electrode current required as a result of the electrode being lifted above the retinal surface. The value of θ_{lift} monotonically increases as a function of lift, with a non-linear curve that depends on a and k , as described by Equation 3.

θ_{rd} represents an additional multiplicative increase in the current amplitude required to reach threshold, which we propose is likely due to various types of retinal damage.

We simulated a wide range of k , a , θ_{rd} , and θ_{lift} (corresponding to lifts of 0–1,000 μm) for single electrodes. For each combination of parameters, we used least squares function minimization to find the electrode current, I_0 , required to reach threshold for that parameterization.

We then simulated pairs of electrodes across a wide range of physical distances ($d = 250$ –8,000 μm). Stimulation amplitude was fixed at twice threshold for that parameterization (or 660 μA , whichever was smallest). For each parameterization we calculated dip . A final parameter, dip criterion , is the dip value that results in a 75% two-point discrimination performance. We assumed that a 75% probability of seeing two percepts required a dip criterion $> 20\%$.

Results

Across each simulated value of a , k , θ_{rd} , θ_{lift} , and dip criterion we calculated both the predicted detection threshold amplitude and the physical distance that produced $\text{dip} = \text{dip}$

criterion. From these simulations we created iso-dip contours as a function of physical distance and I_0 . We sub-selected those simulated iso-dip contours that were reasonably close (mean squared error < 20 μA) to the predicted 75% iso-performance contour for minimal axonal stimulation and whose parameterizations resulted in single electrode thresholds between 177 and 660 μA . These successful parameterizations are shown in **Figure 10A**, with the green line representing the estimated 75% iso-performance curve for minimal axonal stimulation from the regression analyses described earlier, replotted from **Figure 8B**.

Current amplitude thresholds in our patients were consistently higher (by a factor of 4–12x) than 50 μA (see **Table 3**), suggesting that θ_{rd} and/or θ_{lift} , play an important role in determining threshold. This is confirmed by the scatter plots of θ_{rd} vs. θ_{lift} for successful simulations, **Figure 10B**, where there is an absence of scatter points with both low θ_{rd} and θ_{lift} . Although the broad range of plausible outcomes generated by our simulations makes it difficult to definitively attribute the degree to which elevated thresholds and an inability to resolve individual electrodes can be attributed to retinal damage vs. lift; our simulations suggest that both damage and/or lift may play a role.

Next, using the parameterizations that successfully predicted two-point discrimination performance, we examined how retinal damage (θ_{rd}) and lift from the retinal surface (θ_{lift}) affected spatial two-point discrimination thresholds. We calculated predicted two-point discrimination thresholds across all values of a , k , θ_{rd} , θ_{lift} , and *dip criterion*. The probability distributions of the predicted two-point discrimination thresholds of our current spread model, which spanned a 95% confidence interval of 1,908–2,750 μm , was consistent with predicted thresholds for each participant when axonal stimulation was minimized, ($S1 = 2,151$, $S2 = 2,812$, $S3 = 1,942 \mu\text{m}$).

Figure 10C also shows the predicted probability distribution of the two-point discrimination thresholds after having either set $\theta_{rd} = 0$ (blue curves), $\theta_{lift} = 0$ (pink curves), or both $\theta_{lift} = 0$ and $\theta_{rd} = 0$ (yellow curves). Median values across successful parameterizations are shown with error bars representing the interquartile range of simulation outcomes in **Figure 7B**.

According to our model, when $\theta_{lift} = 0$, the median two-point discrimination limit fell from 2,399 $\mu\text{m}/8.3^\circ$ to 2,176 $\mu\text{m}/7.6^\circ$, pink bar and curve in **Figures 7B**, **10C** respectively. Thus, lift might have limited the ability to spatially resolve individual electrodes in our participants.

In contrast, the effect of retinal damage ($\theta_{rd} = 0$, blue bar and curves in **Figures 7B**, **10C**) on two-point discrimination thresholds was very small. Although our model includes the effect that retinal damage requires higher current amplitudes to reach threshold in our model dip is calculated based on current amplitude on the retina. It is assumed, based on previous data

(Greenwald et al., 2009; Nanduri et al., 2012), that brightness is linearly related to current. Since the effects of increasing current amplitude is simply to multiplicatively scale current on the retina, increases in current amplitude have no effect on *dip*. Thus, our simulations suggest that the correlation between low thresholds and better two-point discrimination found in our participants is likely “driven” by lift rather than retinal damage.

The yellow curve of $\theta_{lift} = 0$ and $\theta_{rd} = 0$, overlapping with the pink curve, can be thought of as a theoretical two-point resolution limit for the Argus II array if axonal stimulation, retinal damage and lift were not a factor: corresponding to an improvement of $\sim 0.8^\circ$.

Discussion

As described in the Introduction, one of the main obstacles to the development of retinal prosthesis technology is that for many participants current amplitude thresholds tend to be relatively high across many or all electrodes, and only a minority of participants implanted with the Argus II clearly demonstrate pattern vision. Our aim was to understand what limits both sensitivity (perceptual thresholds) and the ability to spatially resolve two electrodes (two-point discrimination) in patients implanted with Argus II prostheses.

We measured perceptual detection thresholds, two-point discrimination thresholds, and collected self-reported daily use data. S1, who had a median amplitude threshold of 274 μA and two-point discrimination threshold of 2,394 μm , used the device most consistently. S3, who had a median amplitude threshold of 210 μA and two-point discrimination threshold of 2,161 μm , used the device averaging about 2 h a day. S2, who had a median amplitude threshold of 476 μA and two-point discrimination threshold of 3,136 μm , reported using the device once a month. While we cannot draw conclusions generalizable to larger population from a three-participant study, it is intriguing that patients S1 and S3, who had lower amplitude and two-point discrimination thresholds, used their devices far more often than S2, suggesting that two-point discrimination thresholds and or current amplitude thresholds are related to the functional utility of the device. Further research using two-point discrimination thresholds in larger cohort studies would be needed to establish the importance of this measure as a predictor of device usability in daily life functions.

Ultimately, according to our modeling, without axonal stimulation or lift our participants’ spatial resolution performance would likely have improved by ~ 1.6 – 1.8° , or approximately 20%. Our simulated lower limit was approximately 2,176 $\mu\text{m}/7.6^\circ$, (interquartile range 1,937–2,718 μm), equal to a spacing of almost 4 electrodes, corresponding to a logMAR acuity of roughly 2.7. This theoretical limit based

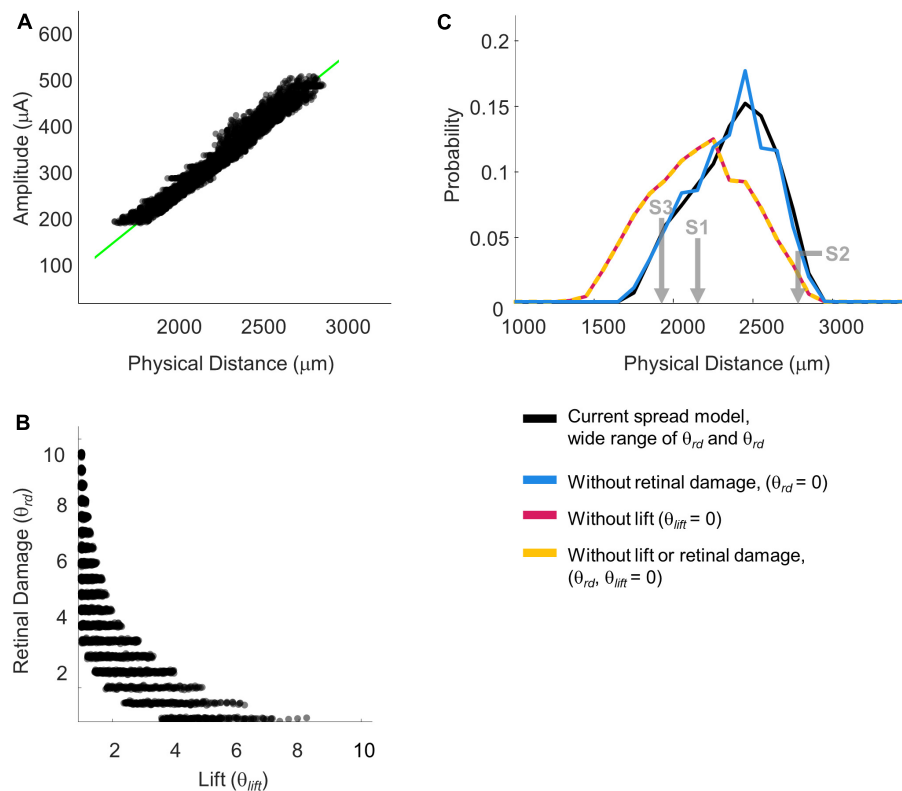


FIGURE 10

Simulation parameterizations that match participant performance. (A) The green line representing 75% iso-performance without axonal stimulation is replotted from Figure 6. Multiple overlapping black lines show simulated iso-dip contours sub-selected from parameterizations that matched the 75% two-point discrimination iso-performance curve. (B) Scatter plot of θ_{rd} vs. θ_{lift} for parameterizations which resulted in iso-dip contours [the black lines in panel (A)] that closely resembled the predicted 75% iso-performance contour with minimal axonal stimulation [the green line in panel (A)]. (C) Probability distributions of predicted two-point discrimination thresholds.

on our simulations, is very similar to those observed in the better performing Argus II participants (Humayun et al., 2012; da Cruz et al., 2016).

There are a variety of reasons why a pair of electrodes might merge into a single percept.

Current field overlap and lift

One obvious reason is overlap in electrode current fields, as demonstrated in Figure 9. This overlap is primarily driven by the physical distance between electrodes on the retinal surface and the lift of the array from the retinal surface.

Threshold amplitude has previously been shown to be correlated with electrode-retina distance (de Balthasar et al., 2008; Ahuja et al., 2013; Shivdasani et al., 2014; Xu et al., 2021). However, our simulations suggest that current threshold should not be considered a simple proxy for electrode-retina distance, since retinal damage may also play a significant role in elevating thresholds.

Receptive field overlap

A second way percepts can overlap (also consistent with the “scoreboard model”) is when the phosphenes elicited by individual ganglion cells overlap. For the Argus II, receptive field sizes are small relative to the resolution of the array. The edge-to-edge separation of electrodes in the Argus II is approximately 1.3 degrees of visual angle. The Argus II is typically implanted over the fovea, and subtends 20° of visual angle along its longer side. At 7 degrees eccentricity (2,000 µm from the fovea), most receptive field sizes are less than 1/3°, while at 15 degrees eccentricity (~4,300 µm from the fovea) most receptive field sizes are less than 1° (Dacey and Petersen, 1992). Thus, the loss of resolution caused by ganglion receptive field sizes was likely negligible, compared to the resolution of the array, and was not examined in our analysis. Theoretically, retinal degeneration might lead to an increase in receptive field sizes: either due to some sort of perceptual adaption, or due to a sampling bias if ganglion cells with small receptive fields were differentially affected by disease. However, this effect would have to be

unrealistically massive to have any effect on spatial resolution in our participants.

Axonal stimulation

Percepts can also overlap as a consequence of axonal stimulation, when overlapping axon fiber bundles pass under, or close to, both electrodes in a pair. We found that a “scoreboard + axon map” regression model, that included a factor based on axonal stimulation, outperformed the simple “scoreboard” (limited to amplitude and Euclidean distance) model, suggesting that axonal stimulation did play a role in reducing the ability to resolve individual electrodes. However, as shown in **Figures 7, 8**, the effects of axonal stimulation on two-point discrimination performance were not particularly large: a regression analysis suggested that minimizing axonal stimulation would reduce the two-point discrimination threshold by approximately 1 degree.

We did not model the effects of axonal stimulation on amplitude thresholds. However, axonal stimulation is unlikely to affect current amplitude thresholds significantly—under most stimulation protocols axonal thresholds are very similar to thresholds near the ganglion soma (Jensen et al., 2005; Vilkhukh et al., 2021).

Retinal damage

As described in the Stage III modeling section, various types of retinal damage have been observed in Argus II patients (Gregori et al., 2018; Lin et al., 2019; Rizzo et al., 2019; Patelli et al., 2020). It has been previously noted that some forms of damage such as inflammation reduces the separation between the electrodes and the retina; leading the researchers to hypothesize that this effect might serve to reduce perceptual thresholds (Gregori et al., 2018; Rizzo et al., 2019). However, this has never been confirmed with behavioral sensitivity data.

Electrical resistance is likely to be influenced by electrode-retina distance and retinal damage in complex ways. Histopathological assessments of one post-mortem implanted eye suggests the formation of fibrosis and schisis consisting of compact collagen-rich membrane with macrophages (Rizzo et al., 2019; Patelli et al., 2020). On the one hand, the vitreous fluid has low resistance, and inflammation and IRF cysts are also likely to lower resistance; on the other, membranes and fibrosis are likely to increase resistance. We did not explicitly model these interactive effects, choosing instead to simulate a wide range of a and k values.

Our simulations suggest that retinal damage may well play a significant role in elevating thresholds. However, according to our simulations (if we are correct in our assumption that

brightness scales roughly linearly with amplitude) the main impact of retinal damage is high thresholds, rather than a loss of the ability to resolve individual electrodes, since our dip calculation is unaffected by a linear scaling of retinal current amplitudes.

Strengths and limitations of our two-point discrimination paradigm

Although stimulating electrodes at double threshold amplitude was used to roughly match the percept brightness across electrodes, there likely remained significant differences in the brightness across electrodes (Greenwald et al., 2009; Nanduri et al., 2012). The percepts elicited by individual electrodes also likely differed dramatically in their shapes across the array (Luo et al., 2016; Beyeler et al., 2019). Percepts elicited by two-electrode stimulation were also likely to have been consistently brighter than single-electrode stimulation. Because many electrodes had stimulation levels near the safety limit during the experiment, it was impossible to increase stimulation amplitude on single electrodes as a means of preventing patients from using brightness as a cue (Ayton et al., 2020a). Nor was there any way of minimizing differences in percept size between single and paired stimulation.

As a result, it is likely that stimulation from single vs. paired electrodes would have produced distinguishable percepts. Our goal was to prevent participants from using brightness, shape or size information when making their “one vs. two percept” judgments.

Participants were explicitly asked to report, “How many percepts did you see?” and were told that brightness and the size of percepts would not provide a reliable cue. Participants reported one vs. two percepts with roughly equal frequency throughout the experiment. Importantly, their drawings (whether they drew one or two shapes) matched these verbal responses on a trial-by-trial basis. We also chose not to use single-electrode stimulation as catch trials, and gave no feedback.

However, results from this protocol should be interpreted very differently from those using a more traditional two-point discrimination methodology with single electrode catch trials and feedback (Ayton et al., 2020a). With feedback our participants would likely have quickly learned to discriminate single and dual electrode stimulation simply based on the shape and/or brightness of percepts.

Comparison with previous studies – amplitude thresholds

Although we did not formally measure thresholds on all electrodes due to time constraints, we found that a significant

TABLE 7 Comparison of tasks used to measure spatial acuity.

Task	Within-array resolution required	Affected by eye- and head movements	Literature
Two-point resolution	Yes*	No	Lauritzen et al., 2011
Grating acuity	Yes*, at frequencies above 2.9 logMAR in the Argus II (Stronks and Dagnelie, 2014)	Yes	Better than 2.9 logMAR Humayun et al., 2012: 21.88% Ho et al., 2015: 48.2–33.3% da Cruz et al., 2016: 38% Schaffrath et al., 2019: 10% Arevalo et al., 2021: 40%
Square localization / Direction of motion	Within array localization is not required for square localization or direction of motion (with feedback). For square localization (and possibly direction of motion) it is likely that many participants rely on scanning head-movements and use the percepts generated by the array as a merged single “phosphene” (Peli, 2020).	Yes	Ahuja et al., 2011; Humayun et al., 2012; Rizzo et al., 2014; Ho et al., 2015; da Cruz et al., 2016; Schaffrath et al., 2019; Naidu et al., 2020; Arevalo et al., 2021

*As described above, cues such as brightness and shape distortions are extremely difficult to entirely eliminate in Argus II participants.

proportion of individual electrodes did not elicit phosphenes using the SwiftPA procedure.

On the whole, the electrode sensitivity of our subject group seems comparable to that reported in other studies. In a previous study by Ahuja et al. (2013), detection thresholds could not be estimated within the range of amplitudes permitted by charge density safety limits in a significant proportion of electrodes (0–83% depending on participant). In a study by Naidu et al. (2020), thresholds could only be measured in 60% of electrodes. Xu et al. (2021) similarly could not measure individual thresholds in a significant proportion of electrodes.

Comparison with previous studies – spatial vision

As shown in Table 7, grating acuity, direction of motion discrimination, and square localization are the most commonly used measures of the spatial resolution of the Argus II implant. While these tasks provide a good assessment of real-world spatial acuity, they are influenced by both eye and head-movements, and therefore cannot be used to measure losses in spatial resolution at the retinal level, which is best assessed by two-point discrimination task. A previous study has found a correlation between two-point discrimination and grating spatial acuity in Argus II patients (Lauritzen et al., 2011), suggesting that resolution at the retinal level does influence visual performance on other tasks that are more closely related to “real world” vision.

Table 7 summarizes previous studies that assessed spatial vision with the Argus II across a range of tasks.

Out of our nine original participants only three showed evidence of within array resolution and were selected for further testing. Although other studies have not examined two-point discrimination, the grating acuity task at spatial frequencies higher than 2.9 logMAR also requires within-array resolution (though this task may be more difficult, due to blurring due to eye-movement/head motion). In previous studies only 10–40% of Argus II patients performed better with the device on vs. off in a grating acuity task at frequencies higher than 2.9 logMAR, Table 7.

In previous studies it has been difficult to find a clear link between either height from the retinal surface or retinal damage as measured using OCT and spatial performance (Rizzo et al., 2019). One reason for this may be that many tasks used for functional assessment (e.g., square localization) are not specifically designed to test within-array resolution while excluding the effects of eye-movements.

Limitations

One important limitation of our study is that we collected two-point discrimination data in just three participants, those tested at Johns Hopkins Eye Center. Moreover, as noted in the Methods, these three were selected as the best of 9 participants across two centers. Such a small participant group cannot support population level inferences; our data are best considered as three “case studies” illustrating a range of outcomes. In addition, because our data were collected over a relatively small number of sessions we do not have longitudinal data that might provide insight into the effects of the array shifting/lifting or continued retinal degeneration.

Our simulations also include significant uncertainty. First, our estimates of the distance to axon certainly includes variability due to errors in our estimation of axon bundle trajectories. Second, our estimates of current spread include a broad range of possible values, making our estimates of the relative importance of electrode lift and retinal damage quite broad. Finally, the θ_{rd} parameter that we interpret as retinal damage, simply reflects an increase in threshold unexplained by θ_{lift} , which potentially could be explained by other factors.

Future directions

Placing an electrode array close to the surface without causing retinal damage is extremely difficult (Gregori et al., 2018). This makes it important to know whether successful outcomes depend on placing an array proximal to the retinal surface, avoiding retinal damage or (more likely) both. Unfortunately, we could not obtain high quality OCT images that would allow us to directly estimate the height of electrodes from the retinal surface, so our simulations can only indirectly infer the relative importance of retinal lift vs. retinal damage. However, our simulations do suggest, somewhat unsurprisingly, that avoiding both lift and significant retinal damage are likely to be critical for a successful retinal implant.

Future work relating two-point discrimination to imaging data that includes array-retina positioning, structural measures of retinal integrity and more detailed computational modeling, based on data from a larger number of participants will likely be needed to fully understand the relative importance of these various factors in reducing the ability to resolve the percepts elicited by individual electrodes, and thereby develop implants which can successfully subserve pattern vision.

Data availability statement

The datasets presented in this study can be found in online repositories. The names of the repository/repositories and accession number(s) can be found below: https://github.com/VisCog/Argus_current_spread.

Ethics statement

The studies involving human participants were reviewed and approved by University of Washington and Johns Hopkins University, Institutional Review Boards. The patients/participants provided their written informed consent

to participate in this study. Written informed consent was obtained from the individual(s) for the publication of any potentially identifiable images or data included in this article.

Author contributions

EY, MB, IF, and AR contributed to the conception and design of the study. EY, MB, AK, RS, SM, GB, and GD collected the data. EY, AR, GB, and IF performed the modeling and statistical analysis. EY and IF wrote the first draft of the manuscript. All authors contributed to the data and modeling interpretation, manuscript revision, read, and approved the submitted version.

Funding

EY was funded through a University of Washington Institute for Neuroengineering and University of Washington eScience Institute Washington Research Foundation Innovation Graduate Fellowship in Neuroengineering Fellowship; NIH-NEI R01-62-5032 (IF and GB) and NIH R00 EY029329 (MB).

Acknowledgments

We thank the scientists in Second Sight Medical Products Inc., for technical support and assistance, with particular thank to Arup Roy and Jessy Dorn.

Conflict of interest

The authors declare that the research was conducted in the absence of any commercial or financial relationships that could be construed as a potential conflict of interest.

Publisher's note

All claims expressed in this article are solely those of the authors and do not necessarily represent those of their affiliated organizations, or those of the publisher, the editors and the reviewers. Any product that may be evaluated in this article, or claim that may be made by its manufacturer, is not guaranteed or endorsed by the publisher.

References

- Ahuja, A., Behrend, M., Kuroda, M., Humayun, M., and Weiland, J. (2008). An *In Vitro* Model of a Retinal Prosthesis. *IEEE Trans. Biomed. Eng.* 55, 1744–1753. doi: 10.1109/tbme.2008.919126
- Ahuja, A., Dorn, J., Caspi, A., McMahon, M., Dagnelie, G., daCruz, L., et al. (2011). Blind subjects implanted with the Argus II retinal prosthesis are able to improve performance in a spatial-motor task. *Bri. J. Ophthalmol.* 95, 539–543. doi: 10.1136/bjo.2010.179622
- Ahuja, A., Yeoh, J., Dorn, J., Caspi, A., Wuyyuru, V., McMahon, M., et al. (2013). Factors Affecting Perceptual Threshold in Argus II Retinal Prosthesis Subjects. *Transl. Vis. Sci. Technol.* 2:1. doi: 10.1167/tvst.2.4.1
- Arevalo, J., Al Rashaed, S., Alhamad, T., Al Kahtani, E., Al-Dhibi, H., et al. (2021). Argus II retinal prosthesis for retinitis pigmentosa in the Middle East: The 2015 Pan-American Association of Ophthalmology Gradle Lecture. *Int. J. Retin. Vitro.* 7:65. doi: 10.1186/s40942-021-00324-6
- Ayton, L., Barnes, N., Dagnelie, G., Fujikado, T., Goetz, G., Hornig, R., et al. (2020a). An update on retinal prostheses. *Clin. Neurophysiol.* 131, 1383–1398. doi: 10.1016/j.clinph.2019.11.029
- Ayton, L., Rizzo, J., Bailey, I., Colenbrander, A., Dagnelie, G., Gerschhat, D., et al. (2020b). Harmonization of Outcomes and Vision Endpoints in Vision Restoration Trials: Recommendations from the International HOVER Taskforce. *Transl. Vis. Sci. Technol.* 9:25. doi: 10.1167/tvst.9.8.25
- Ayton, L., Blamey, P., Guymier, R., Luu, C., Nayagam, D., Sinclair, N., et al. (2014). First-in-Human Trial of a Novel Suprachoroidal Retinal Prosthesis. *PLoS One* 9:e115239. doi: 10.1371/journal.pone.0115239
- Ayuso, C., and Millan, J. (2010). Retinitis pigmentosa and allied conditions today: A paradigm of translational research. *Genome Med.* 2:34. doi: 10.1186/gm155
- Balthasar, C., Patel, S., Roy, A., Freda, R., Greenwald, S., Horsager, A., et al. (2008). Factors Affecting Perceptual Thresholds in Epiretinal Prostheses. *Invest. Ophthalmol. Vis. Sci.* 49, 2303–2314. doi: 10.1167/iovs.07-0696
- Beyeler, M., Boynton, G., Fine, I., and Rokem, A. (2017). pulse2percept: A Python-based simulation framework for bionic vision. *bioRxiv* [Preprint]. doi: 10.1101/148015
- Beyeler, M., Nanduri, D., Weiland, J., Rokem, A., Boynton, G., and Fine, I. (2019). A model of ganglion axon pathways accounts for percepts elicited by retinal implants. *Sci. Rep.* 9:9199. doi: 10.1038/s41598-019-45416-4
- Caspi, A., and Zivotofsky, A. (2015). Assessing the utility of visual acuity measures in visual prostheses. *Vis. Res.* 108, 77–84. doi: 10.1016/j.visres.2015.01.006
- Caspi, A., Roy, A., Dorn, J., and Greenberg, R. (2017). Retinotopic to Spatiotopic Mapping in Blind Patients Implanted With the Argus II Retinal Prosthesis. *Invest. Ophthalmol. Vis. Sci.* 58:119. doi: 10.1167/iovs.16-20398
- da Cruz, L., Dorn, J., Humayun, M., Dagnelie, G., Handa, J., Barale, P. O., et al. (2016). Five-Year Safety and Performance Results from the Argus II Retinal Prosthesis System Clinical Trial. *Ophthalmology* 123, 2248–2254. doi: 10.1016/j.optha.2016.06.049
- Dacey, D., and Petersen, M. (1992). Dendritic field size and morphology of midganglion and parasol ganglion cells of the human retina. *Proc. Natl. Acad. Sci. U.S.A.* 89, 9666–9670. doi: 10.1073/pnas.89.20.9666
- Drasdo, N., and Fowler, C. (1974). Non-linear projection of the retinal image in a wide-angle schematic eye. *Br. J. Ophthalmol.* 58, 709–714. doi: 10.1136/bjo.58.8.709
- Erickson-Davis, C., and Korzybska, H. (2021). What do blind people “see” with retinal prostheses? Observations and qualitative reports of epiretinal implant users. *PLoS One* 16:e0229189. doi: 10.1371/journal.pone.0229189
- Esler, T., Kerr, R., Tahayori, B., Grayden, D., Meffin, H., and Burkitt, A. (2018). Minimizing activation of overlying axons with epiretinal stimulation: The role of fiber orientation and electrode configuration. *PLoS One* 13:e0193598. doi: 10.1371/journal.pone.0193598
- Ferlauto, L., Airaghi Leccardi, M., Chenais, N., Gilliéron, S., Vagni, P., Bevilacqua, M., et al. (2018). Design and validation of a foldable and photovoltaic wide-field epiretinal prosthesis. *Nat. Commun.* 9:992. doi: 10.1038/s41467-018-03386-7
- Fine, I., and Boynton, G. (2015). Pulse trains to percepts: The challenge of creating a perceptually intelligible world with sight recovery technologies. *Philos. Trans. R. Soc. B Biol. Sci.* 370:20140208. doi: 10.1098/rstb.2014.0208
- Fried, S., Lasker, A., Desai, N., Eddington, D., and Rizzo, J. (2009). Axonal Sodium-Channel Bands Shape the Response to Electric Stimulation in Retinal Ganglion Cells. *J. Neurophysiol.* 101, 1972–1987. doi: 10.1152/jn.91081.2008
- Greenwald, S., Horsager, A., Humayun, M., Greenberg, R., McMahon, M., and Fine, I. (2009). Brightness as a Function of Current Amplitude in Human Retinal Electrical Stimulation. *Invest. Ophthalmol. Vis. Sci.* 50:5017. doi: 10.1167/iovs.08-2897
- Gregori, N., Callaway, N., Hoepfner, C., Yuan, A., Rachitskaya, A., and Feuer, W. (2018). Retinal Anatomy and Electrode Array Position in Retinitis Pigmentosa Patients After Argus II Implantation: An International Study. *Am. J. Ophthalmol.* 193, 87–99. doi: 10.1016/j.ajo.2018.06.012
- Ho, A., Humayun, M., Dorn, J., Cruz, L., Dagnelie, G., Handa, J., et al. (2015). Long-Term Results from an Epiretinal Prosthesis to Restore Sight to the Blind. *Ophthalmology* 122, 1547–1554. doi: 10.1016/j.optha.2015.04.032
- Horsager, A., Greenwald, S., Weiland, J., Humayun, M., Greenberg, R., McMahon, M., et al. (2009). Predicting visual sensitivity in retinal prosthesis patients. *Invest. Ophthalmol. Vis. Sci.* 50, 1483–1491. doi: 10.1167/iovs.08-2595
- Humayun, M., Dorn, J., Cruz, L., Dagnelie, G., Sahel, J. A., Stanga, P., et al. (2012). Interim Results from the International Trial of Second Sight's Visual Prosthesis. *Ophthalmology* 119, 779–788. doi: 10.1016/j.optha.2011.09.028
- Jansonius, N., and Schiefer, U. (2020). Anatomical Location of the Raphe and Extended Raphe in the Human Retina: Implications for Assessment of the Optic Nerve with OCT. *Transl. Vis. Sci. Technol.* 9:3. doi: 10.1167/tvst.9.11.3
- Jansonius, N., Nevalainen, J., Selig, B., Zangwill, L., Sample, P., Budde, W., et al. (2009). A mathematical description of nerve fiber bundle trajectories and their variability in the human retina. *Vis. Res.* 49, 2157–2163. doi: 10.1016/j.visres.2009.04.029
- Jensen, R., Ziv, O., and Rizzo, J. (2005). Thresholds for Activation of Rabbit Retinal Ganglion Cells with Relatively Large, Extracellular Microelectrodes. *Invest. Ophthalmol. Vis. Sci.* 46:1486. doi: 10.1167/iovs.04-1018
- Kutner, M., Nachtsheim, C., Neter, J., and Li, W. (2004). *Applied Linear Statistical Models*. New York, NY: McGraw-Hill/Irwin.
- Lauritzen, T., Nanduri, D., Weiland, J., Dorn, J., McClure, K., Greenberg, R., et al. (2011). Inter-electrode Discriminability Correlates With Spatial Visual Performance In ArgusTM II Subjects. *Invest. Ophthalmol. Vis. Sci.* 52:4927.
- Lin, T. C., Wang, L. C., Yue, L., Zhang, Y., Falabella, P., Zhu, D., et al. (2019). Histopathologic Assessment of Optic Nerves and Retina From a Patient With Chronically Implanted Argus II Retinal Prosthesis System. *Transl. Vis. Sci. Technol.* 8:31. doi: 10.1167/tvst.8.3.31
- Luo, Y. L., Zhong, J., Clemon, M., and Cruz, L. (2016). Long-term Repeatability and Reproducibility of Phosphene Characteristics in Chronically Implanted Argus II Retinal Prosthesis Subjects. *Am. J. Ophthalmol.* 170, 100–109. doi: 10.1016/j.ajo.2016.07.021
- Mitchell, P., Liew, G., Gopinath, B., and Wong, T. (2018). Age-related macular degeneration. *Lancet* 392, 1147–1159. doi: 10.1016/S0140-6736(18)31550-2
- Naidu, A., Ghani, N., Yazdanie, M., and Chaudhary, K. (2020). Effect of the electrode array-retina gap distance on visual function in patients with the Argus II retinal prosthesis. *BMC Ophthalmol.* 20:366. doi: 10.1186/s12886-020-01631-6
- Nanduri, D., Fine, I., Horsager, A., Boynton, G., Humayun, M., Greenberg, R., et al. (2012). Frequency and Amplitude Modulation Have Different Effects on the Percepts Elicited by Retinal Stimulation. *Invest. Ophthalmol. Vis. Sci.* 53, 205–214. doi: 10.1167/iovs.11-8401
- Nano Retina (2020). *Safety and Performance Evaluation of the NR600 System in Subjects With End-stage Inherited Outer Retinal Degenerative Diseases [White paper]*. Herzliya: Nano Retina.
- Patelli, F., Falleni, M., Colombo, L., Martinelli, C., Tosi, D., Bulfamante, G., et al. (2020). EPIRETINAL FIBROSIS REMOVAL IN AN ARGUS II-IMPLANTED EYE: Histological Characteristics and Functional Results. *Retina* 40, 2403–2409. doi: 10.1097/IAE.0000000000002780
- Peli, E. (2020). Testing Vision Is Not Testing For Vision. *Transl. Vis. Sci. Technol.* 9:32. doi: 10.1167/tvst.9.13.32
- Pérez Fornos, A., Sommerhalder, J., Cruz, L., Sahel, J., Mohand-Said, S., Hafezi, F., et al. (2012). Temporal properties of visual perception on electrical stimulation of the retina. *Invest. Ophthalmol. Vis. Sci.* 53, 2720–2731. doi: 10.1167/iovs.11-9344
- Pfeiffer, R., Marc, R., and Jones, B. (2020). Persistent remodeling and neurodegeneration in late-stage retinal degeneration. *Prog. Retin. Eye Res.* 74:100771. doi: 10.1016/j.preteyeres.2019.07.004

- Rizzo, S., Belting, C., Cinelli, L., Allegrini, L., Genovesi-Ebert, F., Barca, F., et al. (2014). The Argus II Retinal Prosthesis: 12-Month Outcomes from a Single-Study Center. *Am. J. Ophthalmol.* 157, 1282–1290. doi: 10.1016/j.ajo.2014.02.039
- Rizzo, S., Cinelli, L., Finocchio, L., Tartaro, R., Santoro, F., and Gregori, N. (2019). Assessment of Postoperative Morphologic Retinal Changes by Optical Coherence Tomography in Recipients of an Electronic Retinal Prosthesis Implant. *JAMA Ophthalmol.* 137, 272–278. doi: 10.1001/jamaophthalmol.2018.6375
- Schaffrath, K., Schellhase, H., Walter, P., Augustin, A., Chizzolini, M., Kirchhof, B., et al. (2019). One-Year Safety and Performance Assessment of the Argus II Retinal Prosthesis: A Postapproval Study. *JAMA Ophthalmol.* 137:896. doi: 10.1001/jamaophthalmol.2019.1476
- Second Sight Medical Products Inc (2013). *Argus® II Retinal Prosthesis System Surgeon Manual*. Los Angeles, CA: Second Sight Medical Products Inc.
- Shivdasani, M., Sinclair, N., Dimitrov, P., Varsamidis, M., Ayton, L., Luu, C., et al. (2014). Factors Affecting Perceptual Thresholds in a Suprachoroidal Retinal Prosthesis. *Invest. Ophthalmol. Vis. Sci.* 55, 6467–6481. doi: 10.1167/iovs.14-14396
- Stronks, H., and Dagnelie, G. (2014). The functional performance of the Argus II retinal prosthesis. *Expert Rev. Med. Devices* 11, 23–30. doi: 10.1586/17434440.2014.862494
- Vilkhu, R., Madugula, S., Grosberg, L., Gogliettino, A., Hottowy, P., Dabrowski, W., et al. (2021). Spatially patterned bi-electrode epiretinal stimulation for axon avoidance at cellular resolution. *J. Neural Eng.* 18:066007. doi: 10.1088/1741-2552/ac3450
- Watson, A., and Robson, J. (1981). Discrimination at threshold: Labelled detectors in human vision. *Vis. Res.* 21, 1115–1122. doi: 10.1016/0042-6989(81)90014-6
- Wichmann, F., and Hill, N. (2001). The psychometric function: I. Fitting, sampling, and goodness of fit. *Percept. Psychophys.* 63, 1293–1313. doi: 10.3758/BF03194544
- Wong, W., Su, X., Li, X., Cheung, C., Klein, R., Cheng, C. Y., et al. (2014). Global prevalence of age-related macular degeneration and disease burden projection for 2020 and 2040: A systematic review and meta-analysis. *Lancet Glob Health* 2, e106–e116. doi: 10.1016/S2214-109X(13)70145-1
- Xu, L., Rachitskaya, A., DeBenedictis, M., Bena, J., Morrison, S., and Yuan, A. (2021). Correlation between Argus II array–retina distance and electrical thresholds of stimulation is improved by measuring the entire array. *Eur. J. Ophthalmol.* 31, 194–203. doi: 10.1177/1120672119885799



OPEN ACCESS

EDITED BY

Leanne Chan,
City University of Hong Kong, Hong
Kong SAR, China

REVIEWED BY

Hsin Chen,
National Tsing Hua University, Taiwan
Yan Liu,
Shanghai Jiao Tong University, China

*CORRESPONDENCE

Yuki Hayashida
hayashida@info.mie-u.ac.jp

SPECIALTY SECTION

This article was submitted to
Diagnostic and Therapeutic Devices,
a section of the journal
Frontiers in Medical Technology

RECEIVED 24 April 2022

ACCEPTED 08 August 2022

PUBLISHED 13 September 2022

CITATION

Hayashida Y, Kameda S, Umehira Y,
Ishikawa S and Yagi T (2022)
Multichannel stimulation module as a
tool for animal studies on cortical
neural prostheses.
Front. Med. Technol. 4:927581.
doi: 10.3389/fmedt.2022.927581

COPYRIGHT

© 2022 Hayashida, Kameda, Umehira,
Ishikawa and Yagi. This is an
open-access article distributed under
the terms of the [Creative Commons
Attribution License \(CC BY\)](https://creativecommons.org/licenses/by/4.0/). The use,
distribution or reproduction in other
forums is permitted, provided the
original author(s) and the copyright
owner(s) are credited and that the
original publication in this journal is
cited, in accordance with accepted
academic practice. No use, distribution
or reproduction is permitted which
does not comply with these terms.

Multichannel stimulation module as a tool for animal studies on cortical neural prostheses

Yuki Hayashida^{1,2*}, Seiji Kameda¹, Yuichi Umehira¹,
Shinnosuke Ishikawa¹ and Tetsuya Yagi^{1,3}

¹Division of Electrical, Electronic and Information Engineering, Graduate School of Engineering, Osaka University, Suita, Japan, ²Department of Information Engineering, Graduate School of Engineering, Mie University, Tsu, Japan, ³Department of Electrical and Electronic Engineering, School of Engineering, Fukui University of Technology, Fukui, Japan

Intracortical microstimulation to the visual cortex is thought to be a feasible technique for inducing localized phosphenes in patients with acquired blindness, and thereby for visual prosthesis. In order to design effective stimuli for the prosthesis, it is important to elucidate relationships between the spatio-temporal patterns of stimuli and the resulting neural responses and phosphenes through pre-clinical animal studies. However, the physiological basis of effective spatial patterns of the stimuli for the prosthesis has been little investigated in the literature, at least partly because that the previously developed multi-channel stimulation systems were designed specifically for the clinical use. In the present, a 64-channel stimulation module was developed as a scalable tool for animal experiments. The operations of the module were verified by not only dry-bench tests but also physiological animal experiments *in vivo*. The results demonstrated its usefulness for examining the stimulus-response relationships in a quantitative manner, and for inducing the multi-site neural excitations with a multi-electrode array. In addition, this stimulation module could be used to generate spatially patterned stimuli with up to 4,096 channels in a dynamic way, in which the stimulus patterns can be updated at a certain frame rate in accordance with the incoming visual scene. The present study demonstrated that our stimulation module is applicable to the physiological and other future studies in animals on the cortical prostheses.

KEYWORDS

animal experiment, multichannel microstimulation, neural prosthesis, neural excitation, neuromorphic device, optical imaging, preclinical study, stimulator device

Introduction

In previous chronic and acute studies on patients with acquired blindness or those undergoing brain surgeries, conscious perception of small spots of light, commonly known as phosphenes, was artificially elicited by electrical stimulation applied to the surface of the visual cortex (1–8). Since some of these patients could perceive multiple distinct phosphenes in response to the stimuli delivered from spatially separated multiple

electrodes, phosphene-based visual prosthesis was expected to be realized (9, 10). However, a critical drawback of this type of stimulation was that the threshold current required to induce the phosphene was in the range of milli-amperes, and that the stimulating electrodes were of relatively large size (i.e., milli-meters in diameter) for reducing the risk of water electrolysis at the electrode-electrolyte interface during the stimulus current injection (11, 12). These challenges in the cortical-based prosthesis should be overcome, at least partially, by applying intracortical microstimulation because phosphenes were able to be elicited by stimulus current of a few tens of micro-amperes or less using micron-sized electrodes inserted in the visual cortices of humans (13, 14) [see also Button and Putnam (15)] or non-human primates (16). Therefore, the intracortical visual prosthesis has been considered promising (17–19) and thought to be applicable to a broad range of acquired blindness conditions (e.g., blindness due to glaucoma, diabetic retinopathy, or dysfunctions in the subcortical visual pathway). In addition, compared with other visual prostheses, it is expected that the largest number of phosphenes may be supplied because of the relatively large tissue area available for the electrode implantation (17, 20). After decades from the detailed clinical experiments on the intracortical visual prosthesis (21), a recent clinical trial verified the feasibility of this type of visual prosthesis (22, 23).

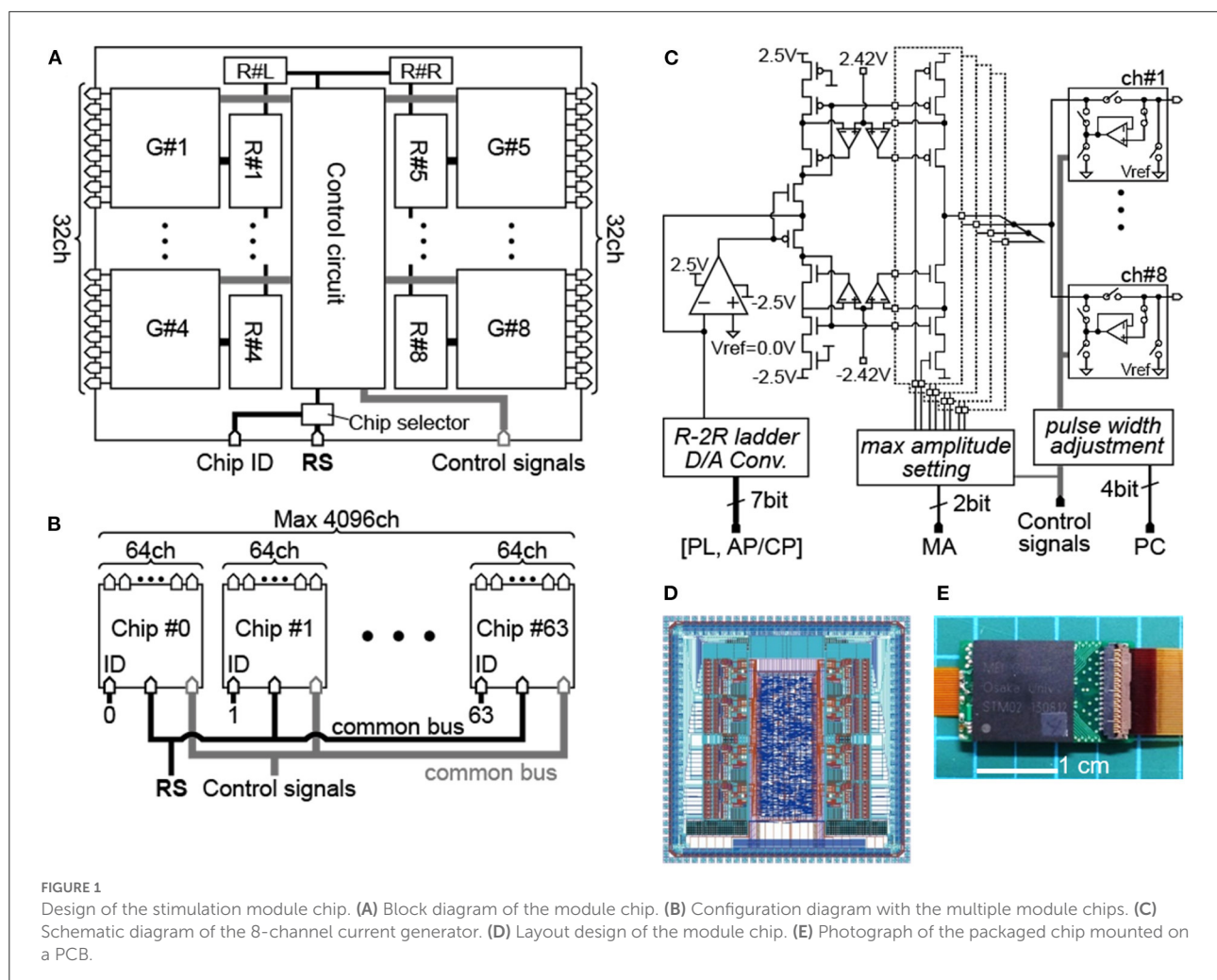
In order to design effective stimuli for the prosthesis, it is thought to be important to elucidate relationships between stimulus parameters and the corresponding properties of neural responses through animal studies. According to previous experiments on the chronaxie estimated for the direct excitation of cortical neurons in cats, the stimulus pulse duration of a few hundred microseconds per phase is considered favorable (1, 24, 25). And, with using such a pulse duration (e.g., 200 μ sec/phase), the threshold current required for the cortical neural excitation was in the range of several to a few tens of microamperes in rodents with progressive vision loss (26) as well as normal sight (27, 28). These parameter ranges of the stimulus (i.e., pulse duration and current amplitude) used in the animal studies are in agreement with those for inducing phosphenes by microstimulation in either blind or normal sighted human patients (13, 14, 23) and non-human primates (16, 29). Also, it was reported that the stimulus-induced neural excitations gradually decreased in response to the repetitive pulse stimulation with the frequency of 100–200 Hz in the rodent visual cortex (28). This could explain the clinical and psychophysical observations (30, 31), in which the consciously perceivable phosphenes induced by such a high-frequency stimulation gradually faded in appearance during its relatively long stimulus duration (0.5–1 sec). Based on these lines of results, it is expected that physiological studies in experimental animals provide the basis of effective stimulus parameters applicable to the prostheses.

Previous psychophysical studies with using simulated phosphenes in normal sighted humans suggested that 325–650 dots of phosphenes distributed two-dimensionally in the visual field might be a minimum requirement for achievement of some visually guided tasks (e.g., reading text, eye-hand coordination, and walking in a simplified or virtual maze) (32–35). Accordingly, the electronic device systems that are capable of generating stimuli with spatial patterns from a few tens to several hundred output channels have been developed in previous studies (36–40). Since those systems were specifically designed to be suitable for the clinical purpose, their usability in physiological animal experiments were least demonstrated. Hence, cortical neural responses to spatial patterns of the stimuli with multiple electrodes have been little investigated in the literature. In order to reveal the physiological basis of effective patterns of the stimuli for the prosthesis, a multi-channel stimulation module usable for the animal studies in various scales is required. The objective of the present study is to develop such a stimulation module, and to examine its usability through not only dry-bench tests but also physiological experiments. In addition, we preliminarily demonstrate that this module can be integrated into a prototype prosthesis system for future animal studies.

Multichannel stimulation module Design

First, we defined the following as variable parameters of the biphasic current pulse stimulus: the amplitude and duration of each of the cathodic and anodic phases, the temporal order of the phases (i.e., cathodic-first or anodic-first), the inter-phase interval, and the inter-pulse interval. Based on previous studies on the chronaxie (1, 29–31) and the charge threshold for inducing phosphenes (13, 14, 16, 29) or neural excitations (27, 28), the temporal accuracy and the amplitude resolution for controlling those variable parameters of stimulus were roughly determined to be less than several micro-seconds and a few micro-amperes, respectively. Also, we assumed that the pulse repetition frequency of stimulation (i.e., the inverse of the inter-pulse interval) was less than 300 Hz (30, 41). Therefore, if a single pulse of the biphasic current stimulus has the duration of around 0.4 msec, for instance (30), then eight stimulus pulses can be accommodated within such an inter-pulse interval. In addition, the spatial pattern of stimuli should better be updated at 30–50 frames per second (42, 43). These numerical conditions were considered for designing the stimulation module, as described below.

Figure 1A shows the main block diagram of our stimulation module as an ASIC chip. Given the chip die size of about 4-by-4 mm, we arranged eight current generators (“G#1” to “G#8” in the figure) together with other circuit blocks in the chip.



Based on the above-mentioned consideration of the inter-pulse interval, each of those current generators has eight channels for the stimulus output. Thus, stimulus current pulses can be generated from 8 channels in parallel, or 64 channels at maximum in time-division semi-parallel mode. For use of the time division multiplexing with the 1:8 configuration (i.e., 8 output channels per current generator), the maximum rate of the stimulus pulse repetition in a given output channel is limited by the total length of time required for completing all stimulus outputs from the 8 output channels in a given current generator. The shortest time required for multiplex switching from one to the next output channel is $\sim 7.8 \mu\text{s}$ in the present design. Thus, if the time length of every biphasic stimulus pulse is 0.4 msec for instance, then the maximum pulse repetition rate in a given output channel to be $\sim 306 \text{ Hz}$. For controlling the stimulus outputs from the 64 channels, on-chip register memories are implemented (44). Namely, each of the current generators contains a set of data registers (“R#1” to “R#8” in the figure) that stores the stimulation parameters

for every output channel, including the current amplitude, the sequential order of output from the channels, and the stimulus on/off switching. In addition, a pair of data registers (“R#L” and “R#R” in the figure) sets the circuit operation parameters, such as maximum current output range, use of the inrush current suppression (described later), and bias voltages in the current generator circuits. Detailed information on these registers, such as hardware locations, register names, data contents, and data sizes, is listed in Table 1. To reduce the overhead time for storing the data into these registers, they are divided into three groups depending on the frequency of data update (see the leftmost column in Table 1). Register group #1 (“Reg1,” 64 bits) manages the stimulus on/off switching and is updated synchronously with the spatial pattern of stimuli. Register group #2 (“Reg2,” 192 bits) is used to set the stimulation sequence and is updated at a moderate frequency. Register group #3 (“Reg3,” 1160 bits) consists of registers for the other stimulus and circuit parameters and is updated infrequently.

TABLE 1 Setting parameters stored to the built-in registers.

Register	Location	Name	Contents	Size
Reg.1	R#1~#8	STP (G, Ch)	Stimulation position	8 G × 8 Ch × 1 bit (on/off) = 64 bits
Reg.2	R#1~#8	STS (G, Ch)	Stimulation sequence	8 G × 8 Ch × 3 bits (8 time slots) = 192 bits
Reg.3	R#1~#8	AP (G, Ch)	Anodic phase amplitude	8 G × 8 Ch × 6 bits (0~63) = 384 bits
		CP (G, Ch)	Cathodic phase amplitude	8 G × 8 Ch × 6 bits (-63~0) = 384 bits
		RP (G, Ch)	Reference channel position	8 G × 8 Ch × 1 bits (on/off) = 64 bits
		PA (G, Ch)	Pulse width adjustment	8 G × 8 Ch × 4 bits (-7~+8) = 256 bits
		MA (S)	Max amplitude	2 S (left/right) × 2 bits (4 steps) = 4 bits
		ICS (S)	In-rush current suppression	2 S × 2 bits = 4 bits
		OTR (S)	Others	2 S × 32 bits = 64 bits

G denotes current generator. Ch denotes output channel. S denotes the side, left or right.

In addition to the register setting (“RS”) signals mentioned above, the digital control signals are also provided from an external device to the module chip *via* bus input ports (“RS” and “Control signals” in Figures 1A,B). Besides, an individual module chip is pre-assigned with an identification (ID) number using a 6-bit digital code set *via* another input port (“Chip ID” in Figure 1A). As illustrated in Figure 1B, multiple module chips (up to $2^6 = 64$) can be connected to the two common buses for the RS and Control signals. The 6-bit ID code is used as the header of the RS signal, and a chip selector circuit in each of the module chip enables updating of the registers when the header is matched with the pre-assigned ID number. After completing the register updates for all of the module chips, the stimulus outputs from all the module chips (up to 64 chips) are driven by the Control signals on the common bus. In other words, the control of a single chip or multiple chips is divided into two phases: initialization and stimulation. In the initialization phase, the data sets in the Reg2 and Reg3 are updated on a chip-by-chip basis. The time required for this phase is 136.2 μ sec per chip and thus 8.717 msec for 64 chips at 10 Mbps (17, 45, 46). In the stimulation phase, the data sets in the Reg1 are also updated on a chip-by-chip basis, and then all of the module chips are operated to output the stimulus current pulses by the Control signals in a time-division semi-parallel mode with eight timeslots. The time durations required for updating the Reg1 are 7.3 μ sec per chip and 467.2 μ sec for 64 chips at 10 Mbps for instance (17, 45, 46). This overhead time is thought to be short enough to control the 64 chips and thus 4,096 stimulating electrodes while updating the stimulation position in the data in the Reg1 (i.e., the spatial patterns of stimuli) every 20 msec (i.e., 50 frame-per-second) for instance (42, 43).

Figure 1C shows the circuit diagram of the current generator, which is composed of an R-2R ladder-type current-mode D/A converter, a differential amplifier, pMOS and nMOS current mirrors, and output circuits (47). In addition, in each of the current mirrors, the gain boosting circuitry with a pair of auxiliary amplifiers is incorporated to realize high output

impedance in the voltage range below ± 2.42 V. The stimulus current amplitude can be set with a 6-bit code and the maximum output range of the current mirror output is selectable from approximately ± 100 to ± 400 μ A by a $\sim \pm 100$ - μ A step (“max amplitude setting” in the figure). For instance, considering the threshold stimulus charge for inducing phosphenes or neural excitations (21, 30), the maximum output range of $\sim \pm 100$ μ A would be selected as a default. In this range, the amplitude resolution is approximately 1.56 μ A (i.e., 100 μ A divided by 2^6). In an actual fabricated chip of the module, however, the amplitude resolution varies between anodic and cathodic currents in a given current generator, and varies also among different current generators (but not among 8 output channels of the same current generator), mostly because of the difference in property of the current mirrors.

The output current flows into or out of either one of eight output circuit blocks (boxes in the rightmost of Figure 1C), each of which is connected to a stimulating electrode at its output port (from “ch#1” to “ch#8”). Thus, by controlling these output circuits, current stimulation is realized by time division with the eight stimulating electrodes. In general, when the surface potential of the electrode in contact with the tissue differs from the potential of the current mirror output, and if the output circuit is a simple analog switch, then an inrush current accompanying the potential difference occurs at the moment when the switch is connected. Therefore, as illustrated in the boxes in Figure 1C, a feedback buffer circuit is added to connect the circuit output and the current mirror output, and the potentials of the current mirror output and the electrode can be rendered equal until the instant before stimulation to suppress the inrush current.

We implemented also a circuit that enables fine adjustment to the pulse width of the second phase in a biphasic stimulus pulse (“pulse-width adjustment” in Figure 1C) for reducing the charge imbalance due to the nMOS/pMOS mismatch. The second phase duration can be either increased or decreased at ~ 1.95 μ sec/step with a 4-bit code in every current

generator. In addition, as shown in the boxes in Figure 1C, a switch for shorting of each output channel to a reference electrode/potential (“Vref” in the figure) in the tissue is also built into the output circuit such that charges accumulated at the electrode surface and in the tissue, as well as the residual DC current (48), can be further reduced through such a shorted connection. In practice, the amplitudes and the durations of both anodic and cathodic phases are first set, and then the pulse width adjustment would be used to minimize the charge imbalance for every current generator, while measuring the output current in a dry-bench test and/or a wet-bench test prior to an animal experiment. For certain animal experiments, this procedure can be enough for determining the stimulus charge with the best possible accuracy. However, the balancing of charge only with this procedure may not be perfect, and gradual charge accumulation might occur due to unpredictable factors in biological tissues and the electrode-tissue interface during a long-term stimulation in animals *in vivo*. In such a case, the shorting to Vref can reduce the charge accumulation to compensate for the imperfectness of the above-mentioned procedure. At least in some animal experiments, these two approaches, i.e., fine pulse-width adjustment and output shorting, suffice for suppression of the voltage accumulation during repetitive pulsing of the stimulus current (12), and may offer an alternative to attaining a perfect charge balance of every single stimulus pulse (49–54). Besides, these circuit operations are optional, allowing the user to intentionally test the possible effects of charge imbalance on neural responses or electrode/tissue damages in experimental animals.

Figure 1D shows the layout design of the module chip with a die size of 3.64 mm by 3.64 mm, in which the control circuit at the center and the eight current generators at the right and left sides are recognizable. This chip was fabricated *via* the 0.25- μ m CMOS process (Taiwan Semiconductor Manufacturing Co., Ltd), packaged and mounted on a printed circuit board (PCB) (Figure 1E).

Dry-bench test

Basic operations of the module were bench tested. In those tests, the 6-bit high/low voltage code for the “Chip ID” was supplied from the power line on the PCB. The RS and Control signals fed to the chip were generated by either one of a portable pattern generator (UPG-2116, Japan Data Systems Inc., Hyogo, Japan), an FPGA integration module (Spartan-6, Xilinx, CA, U.S.A.; XEM6010-LX150, Opal Kelly Inc., OR, USA), or a prototype wireless module system (55). Some examples of the results of dry-bench tests are described below.

First, the power consumption of the module chip was measured. The SPICE simulation with the present chip design produced an estimated power consumption of ~ 2.54 mW without stimulus output, and an actual power consumption

measured in the dry-bench test was ~ 2.27 mW. When the number of the output channel in use was increased under the condition that the biphasic current pulses (~ 40 μ A/phase in amplitude, 0.1 msec/phase in duration, 200 Hz in frequency) were passed for every output channel to a ~ 10 -k Ω resistor, the actual power consumption increased by ~ 21 μ W per channel. These actual power consumptions changed little ($<0.5\%$) when the clock frequency for generating the digital RS and Control signals was varied in the range of 1–12 MHz.

Second, the output DC impedance of the current generator in the module was examined. An Ampere meter (ammeter) and a voltage source (34405A and E3631A, Agilent Technologies Inc., CA, USA.) were connected in series to one of the output channels of the module. The voltage at the channel output was varied from zero to either $+2.5$ or -2.5 V by the voltage source while the command current amplitude of the current generator in the stimulation module was set to a constant value of either one of approximately ± 10 , ± 20 , ± 40 , and ± 80 μ A, and the actual output current was measured by the ammeter. Figures 2A,B plots the measured output current against the voltage at the channel output. In either the anodic (A) or the cathodic (B) direction, the output current level remains constant when the output voltage is less than approximately ± 2.4 volts, which is the limit voltage determined by the gain boosting circuitry in the current generator (see Figure 1C). The output current level varies less than 0.1 μ A (the resolution of the ammeter used) in total when the output voltage level varies from 0 to $\sim \pm 2.4$ volts, indicating that the output DC impedance is higher than 24 M Ω . This was the case in all the 8 current generators, and hence all the 64 output channels.

Third, the pulse output from the current generator in the module was examined with using practical impedance loads. The parallel circuit of a resistor and a capacitor was used as a model of the electrode-electrolyte interface (11), and was connected in series with a ~ 1 -k Ω resistor (“Rs”) to one of the output channels of the module (Figure 2C). Two model circuits were used in this test example; one mimicked a metal-based electrode usable for intracortical stimulation (16) (~ 33.7 k Ω at 1 kHz), and another mimicked a similar electrode but with much smaller surface area (~ 325 k Ω at 1 kHz). Figure 2D shows the current traces recorded as voltage drops across the resistor Rs (“Iout” in Figure 2C) and Figure 2E shows the resulting voltages recorded with respect to the voltage reference (“Vout” in Figure 2C). The waveforms of the current pulses are nearly the same (red and green traces in D) regardless of the difference in voltage drop (red and green traces in E) between the two model circuits. As expected, when the output voltage exceeds the limit voltage of $\sim \pm 2.4$ V, the current output from the generator is limited (Figures 2F,G). Namely, at the amplitude setting of $\sim \pm 80$ μ A, the current amplitude during the cathodic phase was first kept near the command value, but subsequently decreased to a smaller value as the output voltage reached the limit voltage. The similar tests were conducted with using other

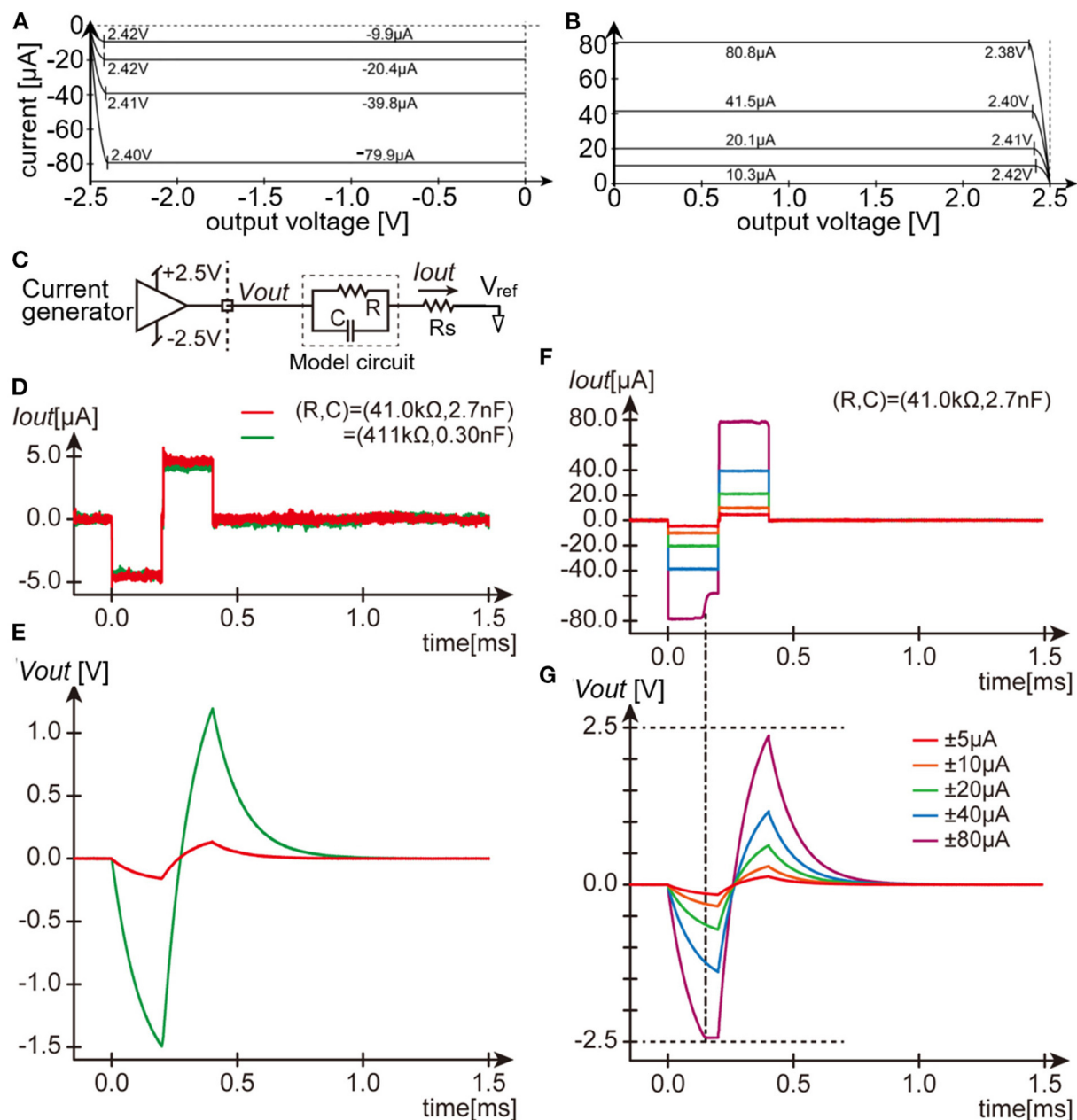


FIGURE 2

Dry-bench tests of the stimulation module. (A,B) Measurements of the output DC impedance of the current generator for the negative current (A) and positive current (B). (C) Schematic circuit diagram testing the current pulse output. (D,E) Recorded traces of the output current pulses (D) and the resulting output voltage (E) with the same amplitude setting but with two different parameters of the model circuit. (F,G) Recorded traces of the output current pulses (F) and the resulting output voltage (G) with different amplitude settings and with the same model circuit parameters. Note the voltage drop across R_s ($\sim 80\text{mV}$ in the largest case) is hardly visible in the traces in (E,G).

output load impedance ranging from ~ 8 to $\sim 513\text{ k}\Omega$ at 1 kHz . The 10–90% rise time was equal to or shorter than $5\text{ }\mu\text{sec}$, and the current amplitude during the cathodic and anodic phases were fluctuated by less than 10 %, as far as the output voltage were below the limit value and as the output impedance was lower than around $\sim 150\text{ k}\Omega$ at 1 kHz (not shown). We also

verified that the current outputs greater than $\pm 100\text{ }\mu\text{A/phase}$ in amplitude were able to be generated when a $1\text{-k}\Omega$ resistor was connected as the output load (Supplementary Figure 1).

Fourth, we verified that the current pulse outputs from all the 64 output channels of the module can be operated in a time-division semi-parallel manner. A $\sim 10\text{-k}\Omega$ resistor was

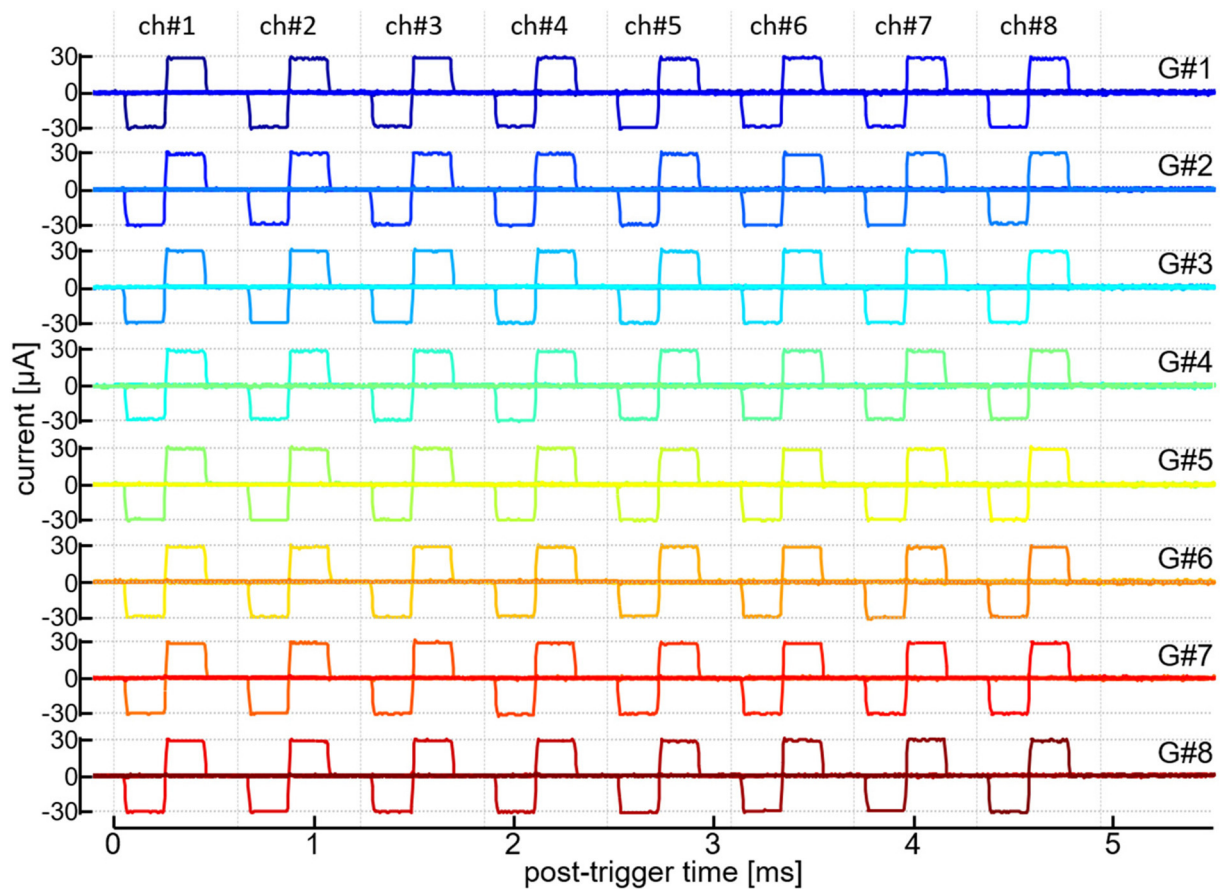


FIGURE 3
Time-division semi-parallel mode of stimulus outputs. Recorded traces of the output current pulses from 64 output channels are shown on the same timeline axis. Labels in the rightmost, “G#1” to “G#8,” indicate the current generators in operation. Labels in the uppermost, “ch#1” to “ch#8,” indicate the output channels of every current generator.

connected to every output channel and the current output was recorded as voltage drop across the resistor. **Figure 3** shows the traces of those current outputs from all the 64 channels. In this recording, a time window of $\sim 4,936 \mu\text{sec}$ was divided into 8 timeslots and, in each of those time slots, every current generator (from “G#1” to “G#8”) generated the biphasic current pulse with one out of the 8 output channels (from “ch#1” to “ch#8”). The register setting values for the anodic and cathodic amplitudes (i.e., AP and CP in **Table 1**) of every current generator were selected so that the actual amplitudes in all the 64 output channels were approximately $\pm 30 \mu\text{A}$. In the figure, each row overlays 8 traces of the current outputs from the 8 output channels of a particular current generator, and the 64 traces on the same timeline are shown. The onset and offset timings as well as the amplitudes of these current pulses little fluctuated when the same pattern of the outputs were repeated, showing the reliable operation of the time-division semi-parallel mode. Also, the time precision as well as the current amplitude accuracy were little affected by

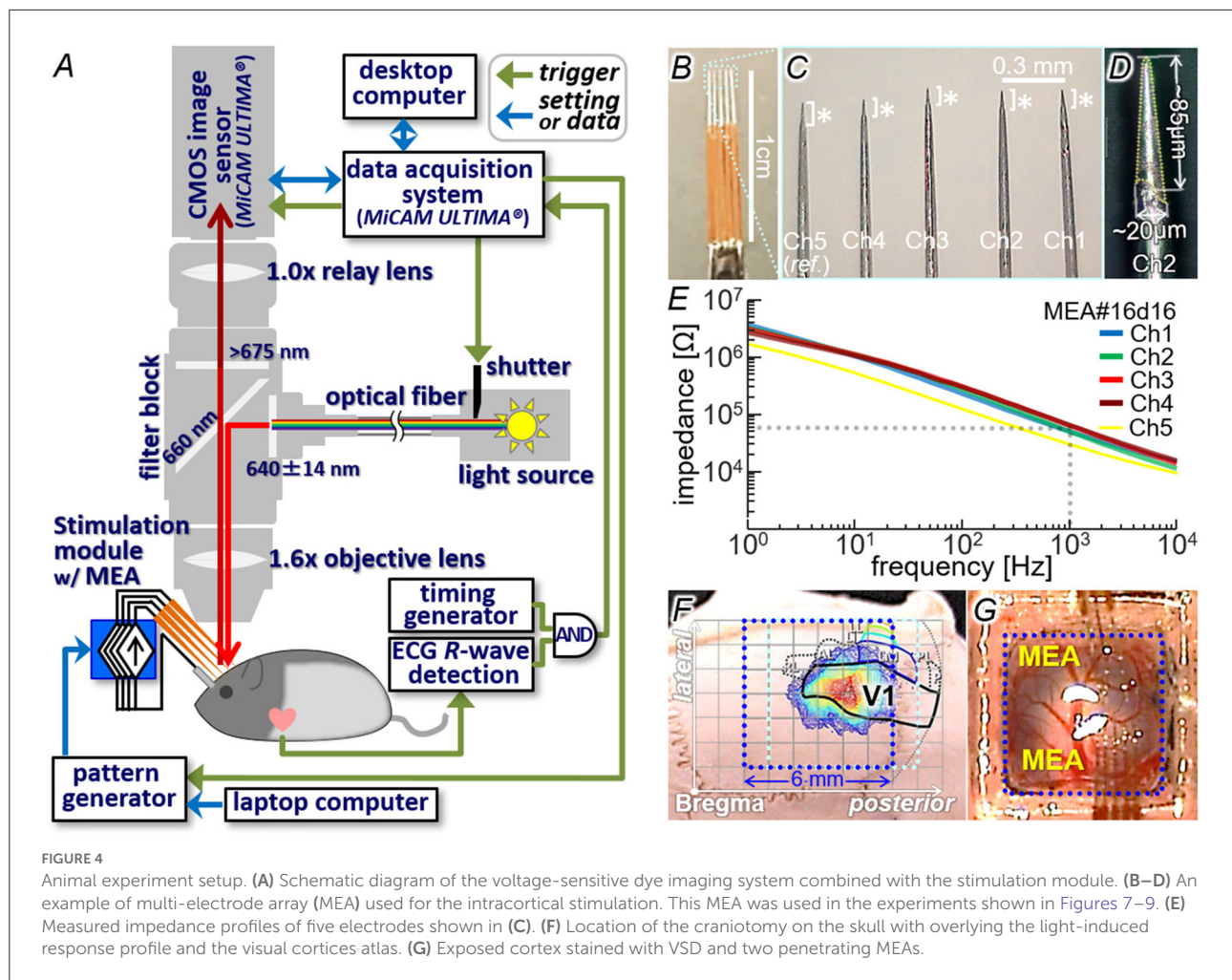
varying the number of the generators/output channels in use (not shown).

Physiological experiments

Our previous studies demonstrated the usefulness of the voltage-sensitive dye (VSD) imaging technique for measurements of the spatio-temporal neural responses to single-site microstimulation in the visual cortex of rodents *in vivo* (26–28, 56). We utilized this technique to examine the practical usability of the stimulation module for multi-site neural excitations in the cortex.

Methods

All animal care and experimental procedures in the present study were approved by the Animal Experiments Committee



of Osaka University and conducted in conformity with the ‘Guidelines for Proper Conduct of Animal Experiments’ by the Science Council of Japan. The Long-Evans rats (24 rats, 6 to 16 weeks old, male and female; Japan SLC Inc., Shizuoka, Japan) were used because of their enough area of the visual cortex for insertion of a multi-electrode array (MEA) (Figure 4G). During the surgery and the imaging experiment, the animal’s rectal temperature was feedback-controlled at $\sim 37^{\circ}\text{C}$ and electrocardiogram (ECG) was monitored. The surgical procedures and the dye staining were almost the same as those in the previous experiments in rats *in vivo* (26, 55). In brief, following administration of atropine (10 μg) and dexamethasone (20 μg), anesthesia was made with either (1) intraperitoneal (IP) injection of a mixture of medetomidine (0.15 mg/kg-b.w.), midazolam (2 mg/kg-b.w.) and butorphanol tartrate (2.5 mg/kg-b.w.), (2) IP injection of urethane (5 ml/kg-b.w. with 25 wt-% soln.), or (3) isoflurane inhalation (0.5–4 % at ~ 0.5 –2 l/min). Craniotomy was performed on the right posterior parietal bone (2–8 or 3–9 mm posterior and 1–7 mm lateral from the Bregma; blue

and light blue dotted boxes in Figure 4F) and a custom-made chamber was attached on the bone around the craniotomy. The exposed cortex with the dura intact or removed partially was stained with VSD (RH1691 or RH2080; Optical Imaging, Ltd, Rehovot, Israel). The dye staining of layer II/III (57) was confirmed in a coronal section of the cerebrum after the imaging experiment.

Figure 4A illustrates the imaging setup (26, 55) combined with the stimulation module. Similar to the dry-bench test, the RS and Control signals fed to the stimulation module were generated by either the portable pattern generator or the prototype wireless system (see Section Dry-bench test). A custom-designed MEA (MicroProbes, Inc., MD, USA; Figures 4B–D), in which three to five needle-shaped iridium electrodes were aligned in line, was connected to the output channels of the stimulation module. In the example shown in the figure, the inter-tip distances were ~ 0.29 – 0.36 mm (C) and the electrically-exposed tips (asterisks in C and area with dotted outline in D) had conical shapes with base diameters of $\sim 20\mu\text{m}$ and lengths of roughly $100\mu\text{m}$ (D). Before the

experiment, the exposed tip of each electrode was activated so that the impedance was reduced to $\sim 10\text{--}65\text{ k}\Omega$ at 1 kHz as measured in an artificial cerebrospinal fluid (Figure 4E). The operations of the stimulation module and the imaging system were controlled with using a common trigger signal generated with reference to the ECG R-wave (arrows of “trigger” in Figure 4A). In some experiments, a commercially available desktop stimulator (STG2008 with the $\pm 1.6\text{-mA}$ current range, MultiChannel Systems, GmbH, Germany) was also used for comparison. The imaging method was the same as that in the previous experiments (26, 55). In brief, the VSD fluorescence emitted from a $6.25 \times 6.25\text{-mm}$ area on the cortex under the excitation illumination was captured at 1000 frames/s with a $100 \times 100\text{-pixel}$ CMOS sensor (MiCAM-Ultima, BrainVision, Inc., Tokyo, Japan). The captured image stream was processed as described previously (26, 27) so that the pixel values of an image represent the fractional fluorescence changes induced by the stimulus (referred to as $\Delta F/F$ in the following text). In the $\Delta F/F$ image stream, the increase and decrease of pixel value correspond to relative depolarization and hyperpolarization, respectively, of the cytoplasmic membrane.

In order to identify the area of the primary visual cortex (V1), diffuse light stimulation ($\sim 13\text{--}16\text{ photon}/\mu\text{m}^2/\text{msec}$ in intensity and 20–500 msec in duration; 525-nm LED as the source) was applied to the left eye *via* a light guide. At 20–40 msec after the stimulus onset, an increase in $\Delta F/F$ was initiated in a certain cortical area (color contour plot in Figure 4; also Figures 6B, 7B), the location of which agreed with the V1 location on the rat brain atlas (58, 59) (black outline in Figure 4F). Through the craniotomy window, the electrode tip was inserted in the V1 area to reach a depth of 300–600 μm from the surface (Figure 4G). The insertion angle was approximately 40° to the cortical surface plane. With this configuration, the cortical surface was only slightly obscured from sight by the electrode shafts of MEA under the epifluorescence microscope (see Figures 6A, 7A, 9A). A pellet or winding wire of Ag/AgCl was placed as the return electrode for stimulation in the head chamber, or in the mouth in a few experiments. The return electrode was connected the voltage reference port of the stimulation module or of the desk-top stimulator. The current pulse stimuli were delivered at inter-stimulus intervals of more than 10 sec to avoid any irreversible effects on the tissue and/or the response.

Results

Although proper operations of the stimulation module as an electronic device were verified in the dry-bench test (Section Dry-bench test), yet the tests in animals *in vivo* were considered essential since the electrode-electrolyte interface as well as other current-passing pathway in the biological tissues could exhibit non-linear electro-chemical properties (60). Therefore,

the current pulse outputs through the MEA inserted in the cortex *in vivo* was first examined. In addition to the stimulation module, the desktop stimulator was used as a reference in the same animals and MEAs. Figures 5A,B shows an example of the current pluses recorded as voltage drops across a 1-k Ω resistor between one of the stimulating electrodes and an output channel of the desktop stimulator (A) or the stimulation module (B). The command amplitude of the current pulse was varied in the range from approximately ± 5 to $\pm 30\text{ }\mu\text{A}$ by a $\sim 5\text{-}\mu\text{A}$ step. With a given amplitude setting, the current traces were averaged across sixteen recordings to reduce noise. As shown in Figure 5A, the onset of the cathodic pulse with relatively small amplitude settings was delayed, and the rise and fall time at the onset and offset of the current pulses was 20 μsec or longer. These characteristics of the current outputs were within the specifications of the stimulator used here, thereby ensuring the practically adequate configuration of the electrode placement and the current-passing pathway in the animal. When the stimulator was replaced with the stimulation module (Figure 5B), the rise and fall time at the current pulse onset and offset was nearly equal to or shorter than 5 μsec , and the amplitude was kept stable in either the cathodic or anodic phase with every amplitude setting. This was similar also in other animals and electrodes (see Figure 5E and Supplementary Figures 2A,C), indicating the reliable control of stimuli by the module.

Figure 5C shows a plot of the charges delivered by the stimulus pulses in either the cathodic or the anodic phase. The measured values (i.e., the time-integral of the current trace) deviated slightly from the command values when the stimulation module was used (red dots in the plot). These deviations were similar between the negative and positive charges. Figure 5D shows the difference between the positive and negative charges (i.e., the imbalanced charge) plotted against the charge delivered by the cathodic pulse. Since the maximum output range of the module was set to be $\sim \pm 100\text{ }\mu\text{A}$ and in turn the amplitude resolution was approximately $1.56\text{ }\mu\text{A}$ (see Section Design), the theoretical upper limit of the charge imbalance between the cathodic and anodic phases was $\pm 156\text{ pC}$. Consistently, the imbalanced charges (red dots in the plot) were smaller than this limit (indicated by hatching in the figure). Such a measurable amount of the charge imbalance could be reduced by utilizing the pulse-width adjustment in the stimulation module (see Section Design), as shown in Figures 5E,F. The current amplitude and the pulse duration were set to be $\sim \pm 30\text{ }\mu\text{A}/\text{phase}$ and $0.2\text{ msec}/\text{phase}$, respectively, as the command values. With these settings, the offset timing of the anodic phase was shifted from one to the next by using the pulse-width adjustment function, and the corresponding current traces were recorded, as shown in Figure 5E. In the figure, eleven traces are superimposed, and each of these traces represents a single recording sweep. The inset shows an expanded view of the current traces near the offset of the anodic phase.

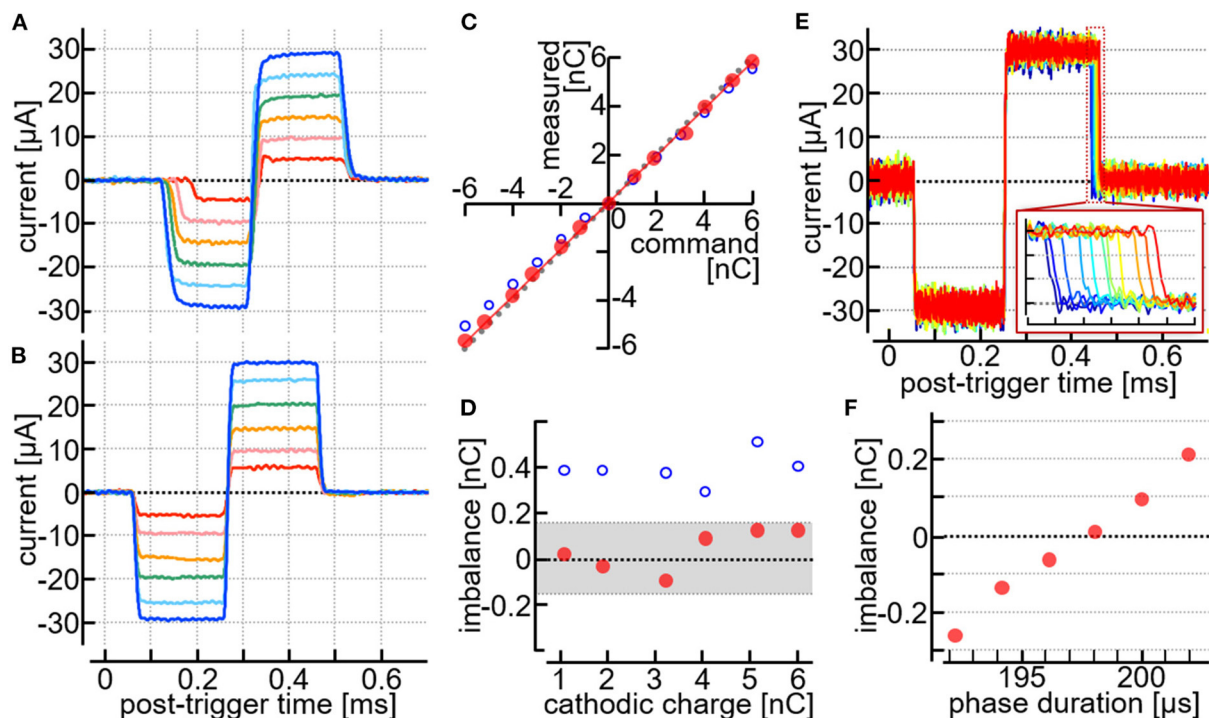


FIGURE 5

Stimulus current pulses recorded in animals *in vivo*. (A,B) Recorded traces of the current pulses generated by a desktop stimulator (A) and the stimulation module (B) with the same MEA in the same rat. (C,D) Measured current amplitudes plotted against the command amplitudes (C), and the imbalance charges plotted against the charges delivered by the cathodic pulses (D). Data taken from the results in (A,B). (E,F) Testing the pulse width adjustments of the anodic phase. The animal was different from one used in (A–D). (E) Current traces with different settings of the anodic pulse width. Inset in (E), Expanded view of the offset of the anodic phase. (F) Imbalanced charges plotted against the command duration of the anodic phase. The imbalanced charges were calculated as the time integral of the recorded current trace from time zero to 0.5 ms.

Figure 5F plots the imbalanced charge against the adjusted pulse width of the anodic phase. At the best setting in this example, namely a pulse width shorter than 200 μsec by $\sim 1.95 \mu\text{sec}$, the imbalanced charge was reduced marginally below $+6 \text{ pC}$.

Finally, the usability of the stimulation module for the physiological experiments *in vivo* was examined. The same set of the current pulses shown in Figure 5 was used as the stimuli. Figure 6C shows an example of pseudo-color time-lapse images of the $\Delta F/F$ signal in response to the stimuli delivered *via* one of the electrodes in MEA. As compared in the top two rows of the figure, when the current amplitude was greater than $\sim 5 \mu\text{A}/\text{phase}$, the increase in $\Delta F/F$ corresponding to neural excitations appeared significant. The increase in $\Delta F/F$ was initially induced near the tip of the stimulating electrode (red line in the figure shows the outline of shadow of the electrode), and then propagated to its surrounding area in the next several milliseconds. The spatial extent of this propagation was larger as the current amplitude was increased from ~ 10 to $\sim 20 \mu\text{A}/\text{phase}$ (the third and fourth rows from the top in the figure) and nearly saturated when the current amplitude was greater than $\sim 20 \mu\text{A}/\text{phase}$ (two rows at the bottom in the figure). The saturation

of the response was not due to a saturation of the output voltage in the stimulation module (Supplementary Figures 2A,B), and was similar when the desktop stimulator instead of the stimulation module was used in this particular animal and the electrode (Supplementary Figures 2C–F). Figure 6D shows the time courses of the changes in $\Delta F/F$ near the tip of the electrode. In response to the stimuli, the $\Delta F/F$ signal increased to reach the positive peak at 11–15 msec post-stimulus time, and then returned to the original level after a few to several hundred milliseconds. In the case that the current amplitude was greater than $\sim 10 \mu\text{A}/\text{phase}$, the $\Delta F/F$ signal decreased below the original level to reach the negative peak at around 100 msec post-stimulus time. These were consistent with those observed in the previous experiments (26, 27). Figure 6E plots the positive peak amplitudes of the $\Delta F/F$ responses against the stimulus charges. For this figure, the data sets obtained from multiple samples were averaged ($n = 8$ electrodes in 6 rats) and fitted with a modified Hill function (dotted blue line), providing approximate values of $\sim 0.9 \text{ nC}/\text{phase}$ for the threshold charge (I_{th}), $\sim 2.4 \text{ nC}/\text{phase}$ for the charge that induced the half-maximum response amplitude (I_{50}), and ~ 2.5 for the Hill coefficient (N).

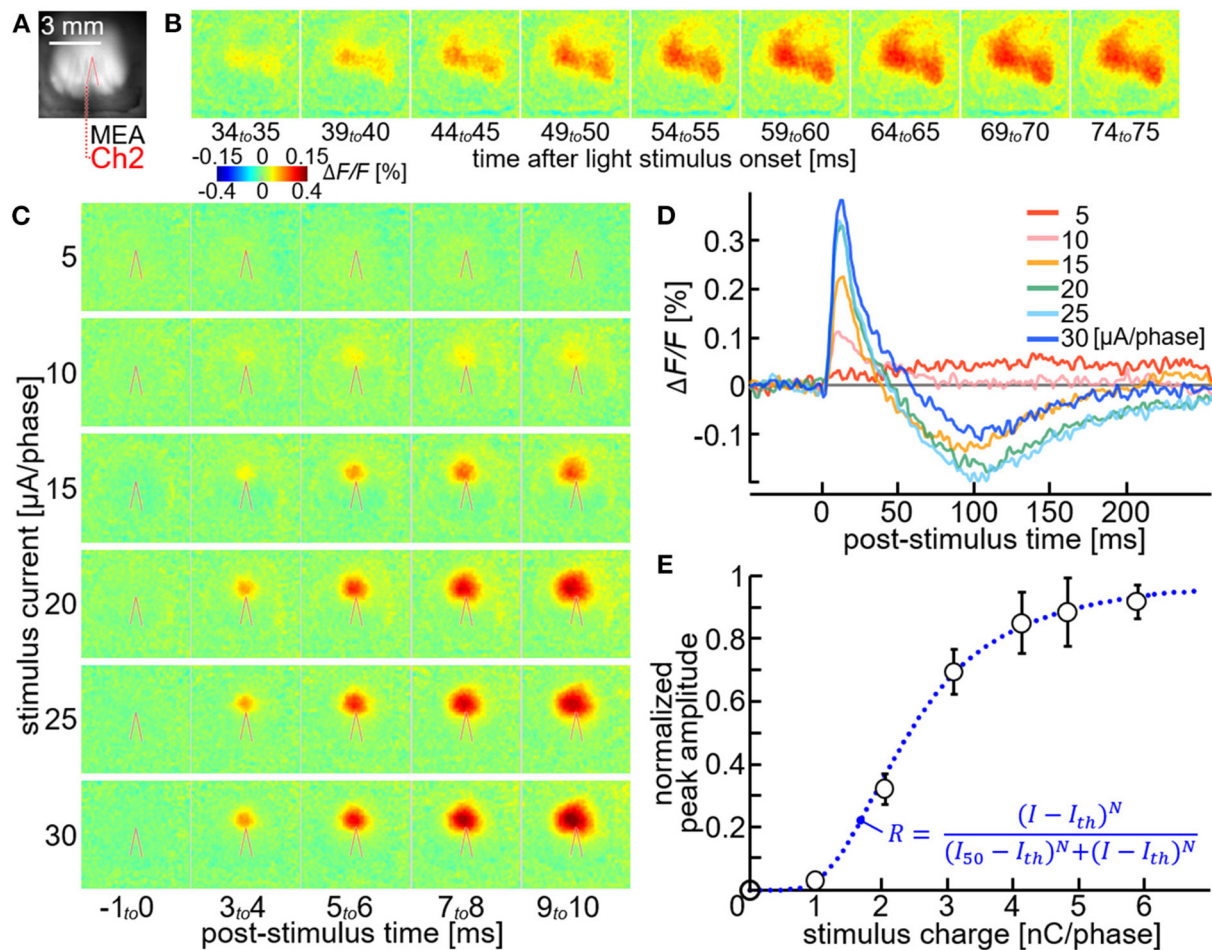


FIGURE 6
Neural excitations with using the stimulation module. (A) VSD fluorescence image of the cortex. Red line indicates the outline of shadow of the stimulating electrode shaft. (B,C) Pseudo-color time-lapse images of the rational VSD fluorescence change ($\Delta F/F$) induced by the light stimulus (B) or the microstimulation with different current amplitudes (C). (D) Time courses of the $\Delta F/F$ measured near the stimulating electrode tip. Different colors represent different stimulus amplitudes. (E) Normalized peak response amplitude plotted against the stimulus charge. The data were obtained with a total of 8 electrodes in 6 rats. The plot and error bars indicate the mean \pm s.e.m. for the 8 data sets. The smooth line indicates the fitted curve of a modified Hill function (inset).

Figure 7 shows an example of the multi-site neural excitations with using the stimulation module. Figure 7A shows the VSD fluorescence image of the exposed cortex superimposed with the locations of four electrodes of the MEA (colored outlines of shadows of the electrodes; Ch1, Ch2, Ch3, and Ch4). The current pulse with the amplitude of $\sim 30 \mu\text{A/phase}$ was delivered from either one of those four electrodes (four rows from the top in Figures 7C,D). In each of the four cases, the increase in $\Delta F/F$ was initiated at around a few milliseconds post-stimulus time, as shown in Figure 7C. The center peak positions of these initial responses shifted from one another by around 0.3–0.4 mm within the V1, consistent with the tip positions of the four electrodes (outlines of shadows of the electrodes). In each of the four cases, the increase in $\Delta F/F$ propagated to its surrounding area in V1 in the next

several milliseconds, and then further circuit activations were induced in V1 as well as extra-V1 areas in the next tens of milliseconds, as shown in Figure 7D. The spatiotemporal patterns of those cortical activations differed from each other among the four cases. In the experiment shown in the bottom row in Figures 7C,D, the current pulses with the amplitude of $\sim 10 \mu\text{A/phase}$ were delivered simultaneously from three of those electrodes (Ch1 to 3). As shown in the image frames at 3–4 and 5–6 msec post-stimulus time (Figure 7C), the spatial profile of the initial increase in $\Delta F/F$ was slightly more elongated in the anterior-posterior direction than those induced by the single-site stimulation. The spatiotemporal pattern of the cortical activation induced after this initial excitation appeared somehow similar to that induced by the stimulus with the electrode Ch2 (Figure 7D).

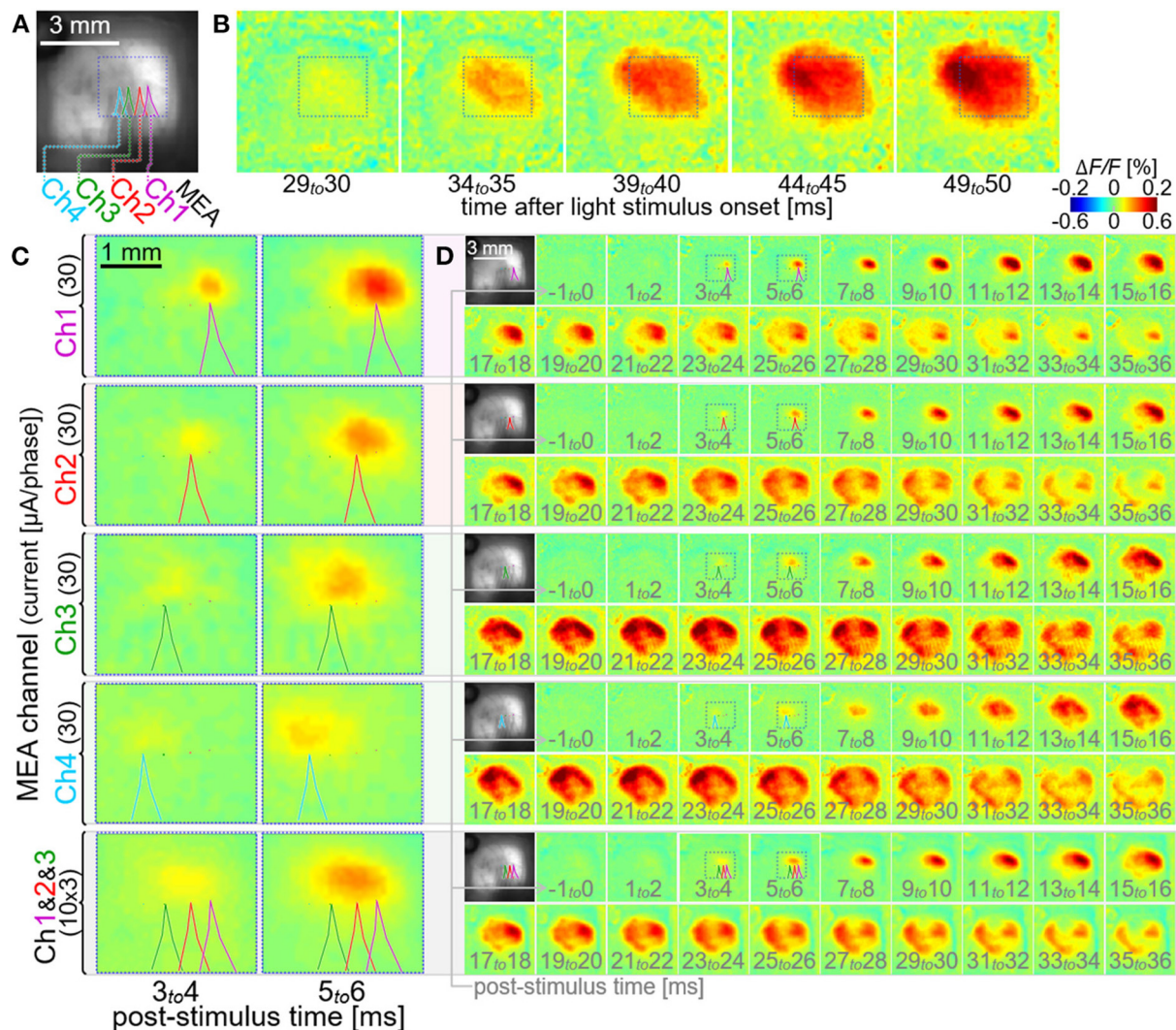


FIGURE 7

Multi-site neural excitations with using the stimulation module. (A) VSD fluorescence image of the cortex. Colored lines indicate the outlines of shadows of four stimulating electrode shafts, Ch1, Ch2, Ch3, and Ch4. (B–D) Pseudo-color time-lapse $\Delta F/F$ images induced by the light stimulus (B) or the current stimuli delivered individually via either one of the four electrodes [upper four rows in (C,D)] and simultaneously via three electrodes [bottom row in (C,D)]. The images in C show expanded views of the VSD images in the dotted boxes in (D). All the dotted boxes in (A–D) represent the same region on the cortex in the animal.

Figure 8 shows an example of the sequential multi-site neural excitations with the stimulation module. The current pulse with the amplitude of $\sim 30 \mu A/\text{phase}$ was sequentially delivered from the electrode Ch1 to Ch3. The time interval between the two pulses was set to be 20 msec (Figure 8A), since the previous physiological study showed that the inhibitory circuit is recruited in this time range after the preceding stimulus pulse (27, 61). As expected, the circuit activation seen after the second stimulus pulse decayed more rapidly (VSD images and spatial line profiles from 29 to 38 msec in Figures 8B,D, respectively) than that seen after the first stimulus pulse (VSD images and spatial line profiles from 9 to 18 msec in Figures 8B,D, respectively), and the neural excitation induced

by the third stimulus pulse (bottom row in Figure 8C; green traces in Figures 8D,E) was significantly smaller in amplitude than those induced by the first and second stimulus pulses (top and middle rows in Figure 8C; purple and red traces in Figures 8D,E).

To our best knowledge, this is the first time that the spatio-temporal patterns of cortical neural responses to multi-channel stimulation at a millisecond time resolution was examined. The results demonstrated that the stimulation module can be used to induce the neural excitations in different spatial locations within V1, and to examine the non-linear interaction of those neural excitations and the subsequent circuit activations in the visual cortices. Further experiments are necessary to investigate

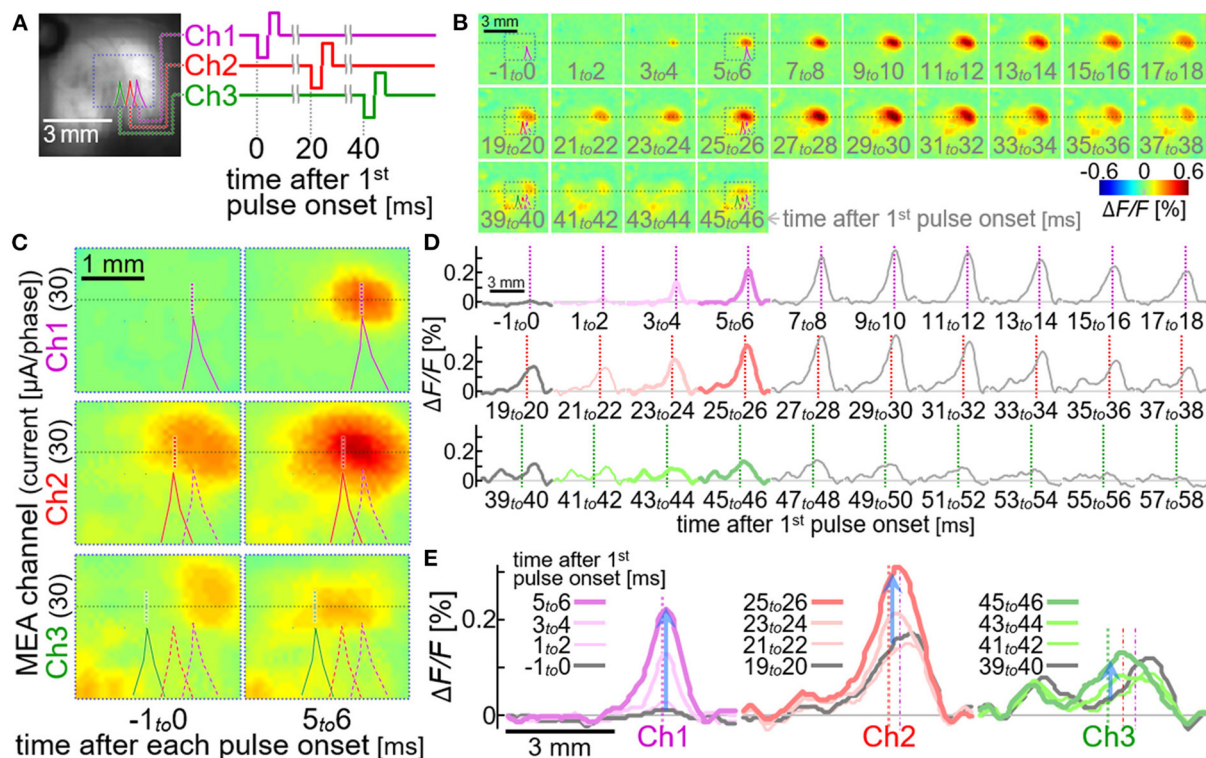


FIGURE 8

Sequential multi-site neural excitations with using the stimulation module. (A) VSD fluorescence image of the cortex. Colored lines indicate the outlines of shadows of three stimulating electrode shafts, Ch1, Ch2 and Ch3. The diagram on the right shows timing of the stimulus pulses delivered from the three electrodes. (B,C) Pseudo-color time-lapse $\Delta F/F$ images induced by the sequential stimulation. The images in (C) show expanded views of the VSD images in the dotted boxes in (B). All the dotted boxes in (A–C) represent the same region on the cortex in the animal. (D,E) Spatial line profiles of the VSD signal along the line in (B). Colored profiles in (D) are expanded and superimposed in (E). Upward blue arrows represent the positions and the amplitudes of the maximum increases in VSD signal induced in 5–6 msec after the stimulus pulses.

quantitative relationships between the spatiotemporal patterns of the stimulation and the corresponding neural responses. Nevertheless, these results suggested that the stimulation module is useful for such physiological investigations.

We also examined the neural excitations induced by the bipolar stimulation (Figure 9). One of five MEA channels (Ch5) was electrically shorted to the Ag/AgCl reference electrode by the switch in the output circuit (see boxes in the rightmost of Figure 1C) to act as a return electrode for stimulation. Either one of the remaining four MEA channels (from Ch1 to Ch4) were paired with this return electrode to act as a working electrode for stimulation. The current pulse with the amplitude of $\sim 30 \mu\text{A}/\text{phase}$ was delivered from either of those four pairs of electrodes. The same current pulse was also delivered either of the four working electrodes in the monopolar configuration. Figure 9B shows the VSD images in response to the bipolar stimulation, and Figure 9C compares the spatial line profiles of VSD signals in response to the bipolar stimulation (red traces) and the monopolar stimulation (blue dotted traces). When the inter-tip distance of the MEA pair was $\sim 0.6 \text{ mm}$ or longer (i.e., when either of Ch1, Ch2 and Ch3 was used

as the working electrode), the neural excitations were initiated in two discernible locations (3–4 msec post-stimulus time in Figure 9B), and those were larger in amplitude and wider in spatial extent (red traces in Figure 9C) than those induced by the monopolar stimulation (blue traces in Figure 9C). When the inter-tip distance of the MEA pair was $\sim 0.3 \text{ mm}$ (i.e., when Ch4 was used as the working electrode), the spatial profile of the neural excitation was similar to that induced by the monopolar stimulation (the rightmost plots in Figure 9C).

This result demonstrated that the ability of the stimulation module to arrange the working-returning electrode combination by electronic means can be beneficial in modifying the spatial pattern of neural excitation while keeping the stimuli the same.

Dynamic operation test

For future behavioral assessment of the phosphene-based vision in animals, a system capable of generating spatially patterned stimuli in accordance with the visual scene would be required (62). The present stimulation module was designed

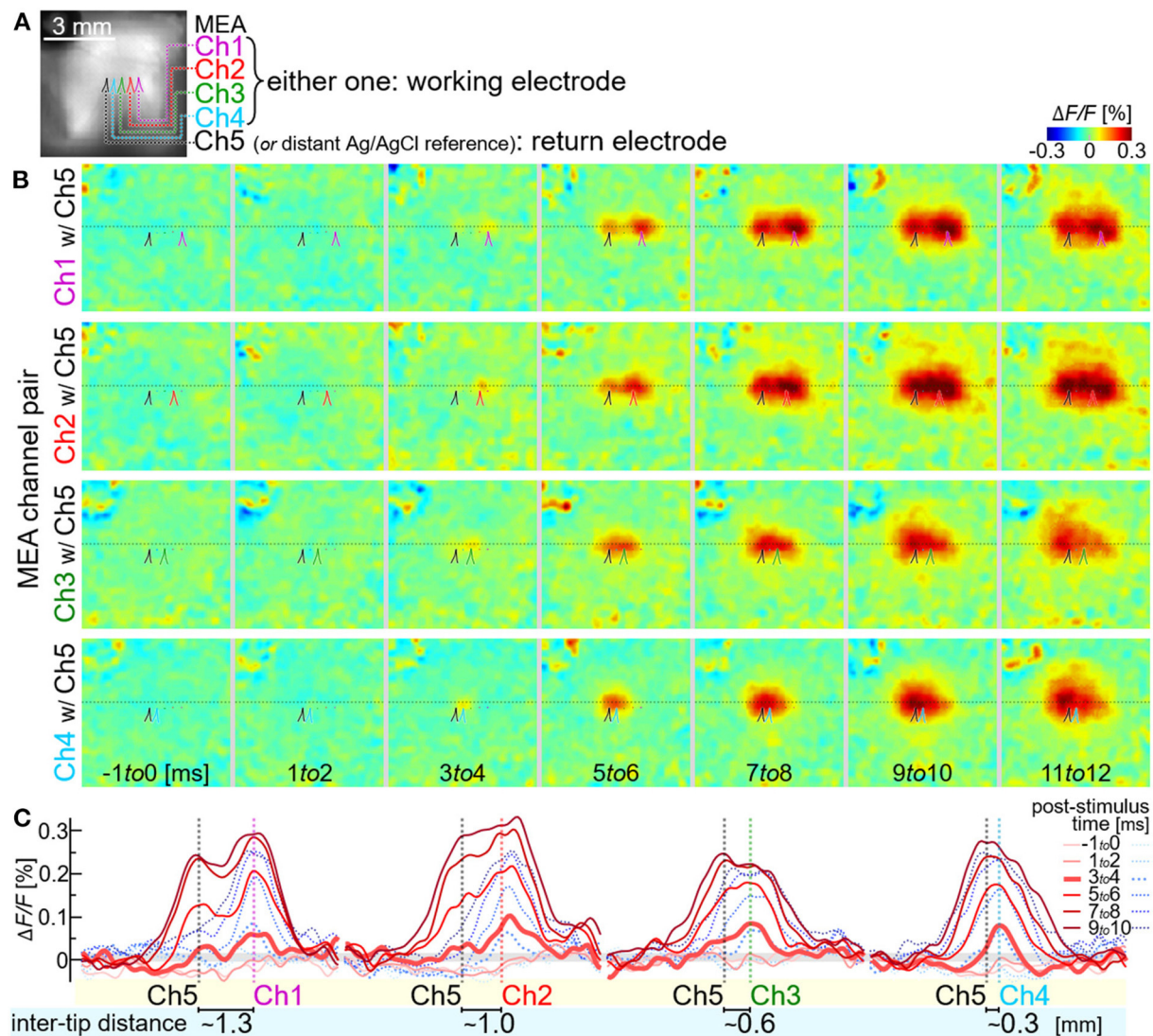


FIGURE 9

Neural excitations by the bipolar stimulation with using the stimulation module. **(A)** VSD fluorescence image of the cortex. Colored lines indicate the outlines of shadows of five stimulating electrode shafts, Ch1–Ch5. **(B)** Pseudo-color time-lapse $\Delta F/F$ images induced by the stimuli with different pairs of the electrodes. **(C)** Spatial line profiles of the VSD signal along the line in **(B)**. Red and blue traces indicate the responses to the bipolar and the monopolar stimulations, respectively. Either of the working electrodes, Ch1 to Ch4, and the distant Ag/AgCl reference electrode were used for the monopolar stimulation.

to generate a spatial pattern of stimuli with the 64 output channels based on the stimulation position data stored in the register, Reg. 1 in Table 1 (Section Design). Thus, by updating these data at a certain temporal rate, various stimulus patterns can be generated from moment to moment. In this section, such a dynamic operation with the stimulation module was tested by employing the previously developed retinal circuit emulator (63) as a data generator of the stimulation position. Figure 10 illustrates a block diagram of the testing system. First, the emulator (Figure 10, leftmost) captures and processes the incoming images to send out an image stream of the point-process spike signals, as describe previously (63). For the present

system, the spike signal image is reformatted into 64-by-64 pixels at a time step of 5 msec [cf. 128-by-128 pixels, 0.5-msec resolution in the original format (63)]. Each pixel in the image takes a value of 0 or 1 and represents the all-or-none spike. Second, every frame in the image stream is sectioned into 64 blocks of 8-by-8 pixel by using a single-board computer (Raspberry Pi 4 Model B, Raspberry Pi Foundation, Cambridge, U.K.), and is sent block by block to the FPGA module. Third, each of those blocks is tagged with a particular Chip ID code by the FPGA, and is used as the stimulation position data for the particular stimulation module. The RS signal other than the stimulation position data (i.e., data for Reg. 2 and Reg. 3

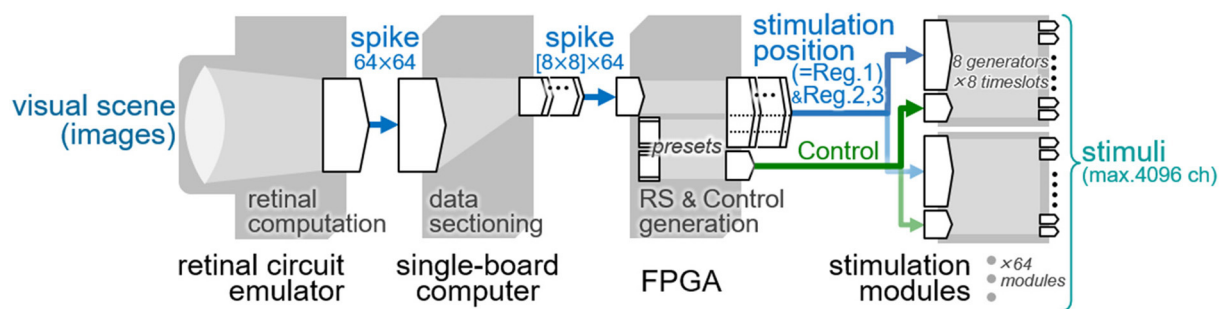


FIGURE 10
Block diagram of the testing system of the dynamic operation. The data flow from the left to right.

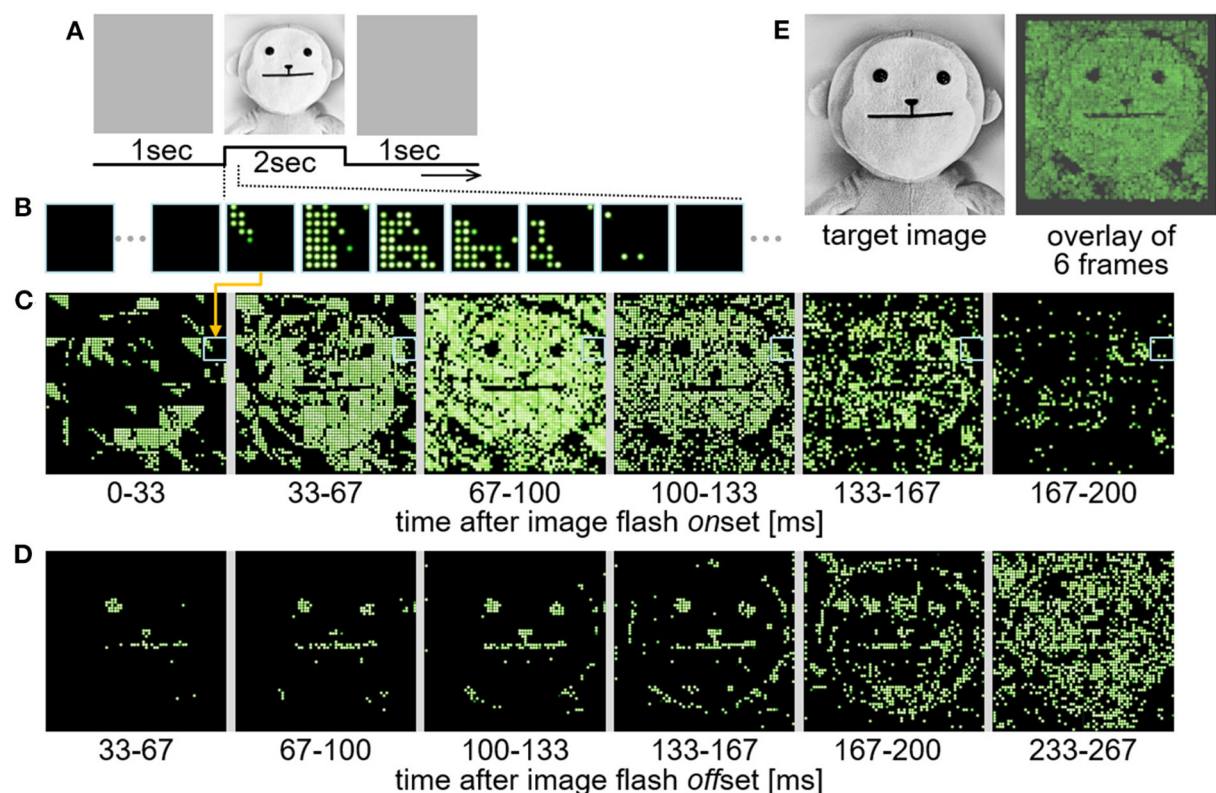


FIGURE 11
Demonstration test of the real time dynamic operation. (A) Image flash stimulation applied to the retinal circuit emulator. An image of a doll was displayed for 2 seconds after a full-field gray image. (B) An example of time-lapse images of the 8-by-8 LED lighting patterns generated by the current outputs from the stimulation module. Each of these images are digital photographs captured at ~ 30 fps by a camcorder. (C,D) Combined time-lapse images of 64 of the 8-by-8 LED lighting patterns generated by the stimulation module after the onset (C) and the offset (D) of the image flash stimulation. (E) Comparison between the target image (left) and the resulting LED lighting pattern (right) in which 6 image frames shown in (C) are overlaid.

in Table 1) as well as the Control signal are also generated by the FPGA. Fourth, all the settings (i.e., Reg. 1, 2 and 3) are stored in the built-in registers of the stimulation modules, and then the stimuli were output from those modules based on the Control signals. In the present, an 8-by-8 light-emitting diode

(LED) array instead of stimulating electrodes is connected to the output channels of the stimulation module for a demonstration purpose. Each of the current generators in the stimulation module injects a monophasic current pulse ($50 \mu\text{A}$ in amplitude, 1.8 msec in duration) into a driver circuit of each LED. Thus,

the light of each LED is turned on or off depending on the 0 or 1 in the stimulation position data, and in turn, spatial stimulus patterns generated by the stimulation module are visualized as LED lighting patterns.

In the test using this system, the input images (Figure 11A) were displayed on a computer monitor in front of the retinal circuit emulator and the resulting LED lighting patterns (Figure 11B) were captured by a camcorder (EX-ZR1800, Casio Computer Co., Ltd., Tokyo, Japan). The frame rates of the monitor and the camcorder were 144 and 30 frame-per-second, respectively. In the present, one pair of the stimulation module and the LED array was used to save hardware resources and avoid any complications in the test. Although the FPGA in the system was capable of feeding all the stimulation position data to the 64 stimulation modules at a certain frame rate, only one of those data blocks was actually used for the current outputs from the stimulation module (the other data blocks were discarded). Therefore, a total of 64 trials were performed while changing the block used for the current outputs, and in each of those trials, the LED lighting patterns were captured as an image stream by the camcorder. The 64 image streams were combined offline. Figures 11C,D shows an example of the time-lapse images taken from the combined image stream. In this test, the output response type emulated in the retinal circuit emulator was a transient ON type, which generates spikes in response to positive contrast steps in an image stream (63). Hence, the LEDs were turned on by the positive contrast steps appeared at the onset and offset (Figures 11C,D, respectively) of the image flash stimulation shown in Figure 11A. For a better comparison with the image flash stimulation, the 6 image frames shown in Figure 11C are overlaid in Figure 11E (right panel), showing a reasonable correspondence between the target image (left panel) and the resulting LED lighting pattern. Here, the rate of updating the spatial stimulus pattern with the 4,096 channels was around 30 frame-per-second. This limit of the data transmission was due to the transmission rate from the single-board computer to the FPGA. Nevertheless, this result showed that the present stimulation module is applicable to a dynamic pattern stimulation in accordance with the visual scene.

The hardware volume of the 64-channel system used in this test was about $22.5 \times 7 \times 11.5$ (w×h×d) cm without the retinal circuit emulator (Supplementary Figure 3). To extend this to a 4,096-channel system, 64 boards of the stimulation module (“d” in Supplementary Figure 3) and 8 printed-circuit boards that connect the interface circuit board (“c” in Supplementary Figure 3) to the stimulation module boards are needed. These components are estimated to consume a volume of about $10 \times 4 \times 4.5$ (w×h×d) cm. Therefore, the total hardware volume of the 4,096-channel system is estimated to be $22.5 \times 7 \times 14$ (w×h×d) cm or smaller. The power consumption of the 64-channel system without the emulator was around 9.6 W or lower in total, including ~4–7 W for

the single board computer, ~2.0–2.5 W for the FPGA module, ~3.6 mW for the stimulation module (see Section Dry-bench test), and others. Although the exact amount of the power consumption varies with time and depends on the state, the total power consumption of the 4,096-channel system is estimated to be around 9.83 W or lower. Based on these estimates, the 4,096-channel system is considered to be practically usable for experimental studies in restrained animals, but difficult in freely-moving animals. In order to use the 4,096-channel system in freely-moving animals, wireless data and power transmission devices together with data compression/expansion processors are thought to be required.

Discussion

In this study, we developed the multichannel stimulation module for pre-clinical animal experiments (Figure 1). The proper operations of this module were verified in the dry-bench tests (Figures 2, 3) and with the intracortical electrodes in experimental animals *in vivo* (Figures 4, 5). Practical usefulness of this module for the physiological investigations in experimental animals *in vivo* was demonstrated (Figures 6–9). Also, we showed that the dynamic operation of our stimulation module enables the spatial patterns of stimuli can be updated at a certain frame rate in synchronization with the visual scene (Figures 10, 11). For induction of spatially discernible multiple phosphenes in the visual field, the electrodes delivering the stimuli in the cortex should be separated from each other at certain distances. In clinical trials on intracortical stimulation of the visual cortex in humans (14, 21) and in psychophysical studies in non-human primates (8, 31), the shortest distance between a pair of adjacent electrodes delivering the threshold stimuli to induce two distinct phosphenes was estimated to be around 0.5 mm (64). Assuming that the exposed surface area of the hemispheric V1 (not including the area in the calcarine fissure) is around 689 mm² (65), the total number of the electrodes implantable in this area is approximately 2,700 if they are placed at the shortest inter-electrode distance (i.e., 0.5 mm). Such high-density electrode implantation might be infeasible considering the difficulties of the surgery of the electrode insertion (66). A possible alternative strategy is to implant the electrodes at relatively longer inter-electrode distances (e.g., 1–2 mm) in the area of not only V1 but also the secondary visual cortex (2) in both hemispheres such that phosphenes might be induced in a relatively large portion of the visual field (34, 35). With either possibility, the number of the electrodes achievable in the future is thought to be in the range of a few to several thousand channels. The recent experiments in non-human primates have suggested the feasibility of a high-channel-count stimulation to achieve the phosphene-based shape perception (62). For designing the effective stimuli with using such a large number of stimulation

channels, unraveling the physiological basis of the phosphene induction through preclinical animal experiments is thought to be inevitable.

A microstimulation system with the fully distributed architecture (41) and monolithic architecture (67) capable of driving nearly or more than a thousand intracortical electrodes have been previously proposed. With such a large number of the channels, the spatial pattern of stimulus should be updated dynamically in response to the visual scene of the outside world, although the transcutaneous wireless data transmission for the implant are limited (45, 46). Therefore, in order to achieve a certain frame rate for updating the stimulus pattern, a data compression/expansion function implemented in micro-processors would be required for future prosthetic systems (68, 69). In envisioning such a system with embedded micro-processors (68), the modular architecture is thought to be preferable for control of the stimuli with a large number of the electrodes in a unified manner. In previous, a modular architecture system capable of supporting nearly one thousand stimulating electrodes has been developed (36). Since this system was designed specifically for clinical application purpose, the microstimulation module chip included in the system had the output pads that could be directly attached to a multielectrode array of a specific design (a 4-by-4 array of electrodes with inter-electrode distance of 0.4 mm). Also, in other multi-channel stimulation devices designed for the clinical application of the cortical visual prostheses, the stimulation device and the multi-electrode array are designed to be packaged together (40, 70). Therefore, with either of those devices, the spatial arrangement of the electrodes is fixed, and not adjustable to various experiments in animals. The difference in design between the devices for the clinical application and the animal experiment is thought to be based on a priority trade-off between the safeness and the multi-functionality (flexibility) since the floor space and affordable energy consumption in a device chip is limited. One of the most important concerns in clinical use of a multi-channel stimulator may be the safeness of stimulation in long-term use. For this objective, the on-chip wireless communication function, which eliminates the need for the troublesome (possibly unsafe) hardwiring from a stimulator device to the electrodes, would be feasible (40) [see also Wong et al. (70)]. However, implementing this function in a chip may not allow many output channels and/or other (possibly redundant) functions to be implemented in the same chip to save the floor space and energy consumption. On the other hand, the stimulator device that is usable for animal experiments may require multiple functions and scalability, with which physiological/behavioral effects of a variety of stimulus parameters can be examined in different animal models with different cortical sizes. In the present stimulator module, one of the key features that differentiate it from the previously proposed stimulators is the combination of various electronic functions. Those include the on-chip register memory, the

pulse width adjustment, the output circuit in every channel, and the chip ID elements for the common-bus digital control. By using these functions, not only the shape of each biphasic current pulse (i.e., the cathodic/anodic polarity order, the amplitudes and durations in cathodic and anodic phases, and the inter-phase intervals) but also other parameters (e.g., the degree of charge imbalance, the combination of working-returning electrodes, the temporal order of pulse deliveries among multiple channels), as well as the number of stimulating electrodes in operation can be digitally controlled in a dynamic way. Besides, different from the previous devices, the accurate controls of stimuli by the present module have been proven under the practical conditions of animal experiments. We would not claim that the present stimulation module is state-of-the-art in terms of electronic design, but we do believe that our module is a proven electronic device useful in animal experiments.

During injection of the stimulus current *via* the electrode, the voltage drop at the electrode-electrolyte interface must be maintained within the water potential window in order to prevent the water electrolysis and irreversible reactions of the electrode material (11, 12). Previous studies suggested that some types of the metal-surface electrodes meet such a requirement (71–73) and are considered to be usable for intracortical stimulation (14, 37, 38, 74). The potential window with those electrodes is roughly from -1 to $+1$ V (11). Thus, although the limit voltage of $\sim \pm 2.4$ V in the present stimulation module can be a limiting factor of the stimulus current amplitude (Figures 2A,B,F,G), the water potential window is more critical than this limit voltage in the intracortical stimulation. We used the electrodes with activated iridium-oxide surface in our experiments (Figures 4B–D) and verified that the interface voltage drop could be maintained below the safe limit (11, 12) while the neural excitations were induced (Supplementary Figure 2). We also observed that the interface voltage was asymmetry in waveform between the cathodic and anodic phases (Supplementary Figures 2B,D), consistent with the asymmetric nature of the chemical reactions underlying the charge deliveries between these opposite phases, and with previous observations made in saline *in vitro* (11). Considering the non-linearities of both charge injection and neuronal excitability, it would be interesting to examine the effects of asymmetric current pulses on the electrode-electrolyte interface voltage and the neuronal membrane voltage at high temporal resolution. For such electrochemical and physiological experiments, the present stimulation module can offer reliable control of the stimulus waveform (Figure 5). In addition, the stimulation module can generate the stimulus current greater than ± 100 μ A/phase in amplitude (Supplementary Figure 1). It is estimated that the impedance of an Ir-Ox-surface electrode with a conical tip of ~ 64 μ m in base diameter and ~ 320 μ m in length should suffice for delivering the stimulus current of 100–400 μ A/phase in amplitude while keeping the voltage

within the water potential window. However, the insertion of such a large electrode in the cortex should induce the serious foreign-body tissue response in a few tens of minutes (75). In addition, the stimulation with such a large current may not be suitable for inducing a spatially localized neural excitation. Therefore, it is practically infeasible for one to deliver the large current to the neurons with an intracortical electrode in the acute physiological experiment. Another option is to use a planar electrode with a large diameter (e.g., $\sim 200\ \mu\text{m}$, resulting an interface area similar to the above-mentioned large conical-tip electrode) placed on the cortical surface. The present stimulation module should be usable for such a cortical surface stimulation with the large current, although in this case, a different recording technique rather than the VSD imaging is needed for testing the effects of stimuli on neural responses.

Since we employed rats as the experimental animal and the optical imaging as the measurement method, the number of stimulating electrodes inserted in their V1 without significantly obscuring the cortical surface from sight under the microscope optics was limited to several, at least in the present experimental setup. Therefore, the stimulation patterns we examined were relatively simple, but not very elaborated in terms of electronics. Such simplicity, however, allowed us to analyze the correspondence between the stimuli and the resulting neural responses at fine spatiotemporal scales. In the present study, this is considered essential in confirming the physiological effects of microstimulation generated by the present stimulation module. Previously, the current steering/focusing technique was applied in cochlear implants (76) [also Constandinou et al. (77) for the vestibular prosthesis] and retinal prostheses (78). On the other hand, it is uncertain whether or how such a stimulation strategy is beneficial for the intracortical neural prostheses. This is in part since the neural responses to multi-site microstimulation in the cortex have not been revealed quantitatively through physiological experiments in previous studies. Based on the present experiments in the rat visual cortex *in vivo*, the spatial profile of the neural excitation appeared to be modifiable by the spatial arrangement of the stimulus current delivery *via* multiple intracortical electrodes (Figures 7, 9). A recent study proposed a novel type of multielectrode lead in which logically configurable 216 microelectrode pads are implemented (79). The ability of dynamically combining the microelectrode pads into several groups of the stimulus bus line in this state-of-the-art electrode device seems to be compatible with the time-division multiplexing current outputs in our stimulation device. Such a combination might open a new possibility of highly flexible neural stimulation in not only the deep brain stimulation, but also cortical prostheses.

Since the action potentials are initiated in a neuron population within a millisecond after the stimulus pulse onset (61), the VSD imaging at a millisecond resolution is considered to be suited for revealing dynamic interactions

among stimuli and neural responses across multiple sites with the current steering/focusing stimuli in the visual cortices (27, 28, 56) as well as the somatosensory cortex (80). The multi-site intracortical stimulation generated by using our stimulation module and the VSD imaging may serve as a useful platform for examining the effects of different strategies of multi-site stimulation on the spatiotemporal neural responses. Although the VSD imaging can supply a foundation for testing the spatio-temporal neural responses to multi-site microstimulation, we also need to test/evaluate the perceptual consequences of the stimulations (81). Therefore, as a next step, the *in-vivo* physiological experiments should be combined with psychophysical/behavioral experiments in the same animal models for further understanding and development of cortical prostheses. As we showed in the demonstration test (Figure 11), multiple number of the stimulation module can be used in a unified manner for the dynamic pattern stimulation. Since the number of the module used is scalable for different animals with different cortical area where the electrodes are implanted, the different levels of the phosphene perceptions (e.g., from brightness localization to shape perception, or from static phosphene to moving phosphene) would be tested in those different animal models.

Data availability statement

The original contributions presented in the study are included in the article/Supplementary material, further inquiries can be directed to the corresponding author.

Ethics statement

The animal study was reviewed and approved by Animal Experiments Committee of Osaka University.

Author contributions

TY and YH designed the study. YH, SK, and TY designed the specifications of stimulation module. SK designed the circuits of stimulation module. SK and YH conducted the dry-bench tests. YU and YH designed and conducted the animal experiments and analyzed the animal experimental data. SI and YH developed and tested the dynamic operation testing system. YH wrote the manuscript. All authors contributed to the article and approved the submitted version.

Funding

This work was supported partly by the MEXT project, Creating Hybrid Organs of the future at Osaka University,

and Grant-in-Aid for Scientific Research from MEXT, Japan (18K12059 and 22K12781 to YH and 20H00606 to TY).

Acknowledgments

We are thankful to A-R-Tec Corp. for supporting with designing, fabrication, and packaging of the stimulation module chip, to Mr. Naoki Satoshiro and Mr. Kosuke Takayama for assisting with some dry-bench tests, to Mr. Tetsushi Tasaki and Mr. Kosuke Takayama for assisting with development of the dynamic operation testing system, to Mr. Ryosuke Okada for assisting with some dynamic operation tests. A-R-Tec Corp. was not involved in the study design, collection, analysis, interpretation of data, the writing of this article or the decision to submit it for publication.

Conflict of interest

The authors declare that the research was conducted in the absence of any commercial or financial relationships that could be construed as a potential conflict of interest.

Publisher's note

All claims expressed in this article are solely those of the authors and do not necessarily represent those of their affiliated

organizations, or those of the publisher, the editors and the reviewers. Any product that may be evaluated in this article, or claim that may be made by its manufacturer, is not guaranteed or endorsed by the publisher.

Supplementary material

The Supplementary Material for this article can be found online at: <https://www.frontiersin.org/articles/10.3389/fmedt.2022.927581/full#supplementary-material>

SUPPLEMENTARY FIGURE 1

Example of the current outputs with different maximum amplitude settings in an output channel of the stimulation module. Panels from top to bottom rows show the recorded current traces as the 2-bit code of Max amplitude (see Table 1) was varied from 3 to 0 (in decimal number). In each panel, the 6-bit codes of Cathodic and Anodic phase amplitudes (see Table 1) were changed from 63 to 0 (in decimal number) along the time axis.

SUPPLEMENTARY FIGURE 2

Recorded traces of the stimulus current pulse (A,C) and the resulting output voltage (B,D) in the stimulation module (A,B) and the desktop stimulator (C,D). (E) Pseudo-color time-lapse $\Delta F/F$ images induced by the stimuli with the desktop stimulator. (F) Time courses of the $\Delta F/F$ measured near the stimulating electrode tip. Different colors represent different stimulus amplitudes. The experiments here were made with the same electrode in the same animal as those in Figures 6A–D.

SUPPLEMENTARY FIGURE 3

A photograph of the 64-channel system used in the test shown in Figure 11.

References

- Brindley GS, Lewin W. The sensations produced by electrical stimulation of the visual cortex. *J Physiol.* (1968) 196:479–93. doi: 10.1113/jphysiol.1968.sp008519
- Brindley GS, Donaldson PE, Falconer MA, Rushton DN. The extent of the region of occipital cortex that when stimulated gives phosphenes fixed in the visual field. *J Physiol.* (1972) 225:57P–8P.
- Dobelle WH, Mladejovsky MG, Girvin JP. Artificial vision for the blind: electrical stimulation of visual cortex offers hope for a prosthesis. *Science.* (1974) 183:440–4. doi: 10.1126/science.183.4123.440
- Dobelle WH, Mladejovsky MG. Phosphenes produced by electrical stimulation of human occipital cortex, and their application to the development of a prosthesis for the blind. *J Physiol.* (1974) 243:553–76. doi: 10.1113/jphysiol.1974.sp010766
- Foerster O. Beiträge zur Pathophysiologie der Sehbahn und der Sehsphäre. *J Psychol Neurol Lpz.* (1929) 39:463–85.
- Krause F. Die Sehbahnen in chirurgischer Beziehung und die faradische Reizung des Sehzentrums. *Klin Wochenschr.* (1924) 3:1260–5. doi: 10.1007/BF01735820
- Pollen DA. Some perceptual effects of electrical stimulation of the visual cortex in man. In: *The Nervous System 2, The Clinical Neurosciences* (ed, DB Tower). New York: Raven Press, p. 519–528. (1975).
- Talalla A, Bullara L, Pudenz R. Electrical stimulation of the human visual cortex; preliminary report. *Canad J Neurol Sci.* (1974) 1:236–8. doi: 10.1017/S031716710001982X
- Dobelle WH, Mladejovsky MG, Evans JR, Roberts TS, Girvin JP. Braille reading by a blind volunteer by visual cortex stimulation. *Nature.* (1976) 259:111–2. doi: 10.1038/259111a0
- Lewis PM, Rosenfeld JV. Electrical stimulation of the brain and the development of cortical visual prostheses: An historical perspective. *Brain Res.* (2016) 1630:208–24. doi: 10.1016/j.brainres.2015.08.038
- Cogan SF. Neural stimulation and recording electrodes. *Annu Rev Biomed Eng.* (2008) 10:275–309. doi: 10.1146/annurev.bioeng.10.061807.160518
- Merrill DR, Bikson M, Jefferys JG. Electrical stimulation of excitable tissue: design of efficacious and safe protocols. *J Neurosci Methods.* (2005) 141:171–98. doi: 10.1016/j.jneumeth.2004.10.020
- Bak M, Girvin JP, Hambrecht FT, Loeb GE, Schmid EM. Visual sensations produced by intracortical microstimulation of the human occipital cortex. *Med Biol Eng Comput.* (1990) 28:257–9. doi: 10.1007/BF02442682
- Schmidt EM, Bak MJ, Hambrecht FT, Kufta CV, O'Rourke DK, Vallabhanath P. Feasibility of a visual prosthesis for the blind based on intracortical microstimulation of the visual cortex. *Brain.* (1996) 119:507–22. doi: 10.1093/brain/119.2.507
- Button J, Putnam T. Visual response to cortical stimulation in the blind. *J Iowa Med Soc.* (1962) 52:17–21.
- Bartlett JR, Doty RW. An exploration of the ability of macaques to detect microstimulation of striate cortex. *Acta Neurobiol Exp.* (1980) 40:713–27. doi: 10.1007/978-94-009-8225-3_4
- Lewis PM, Ackland HM, Lowery AJ, Rosenfeld JV. Restoration of vision in blind individuals using bionic devices: a review with a focus on cortical visual prostheses. *Brain Res.* (2015) 1595:51–73. doi: 10.1016/j.brainres.2014.11.020
- Normann RA, Maynard EM, Guillory KS, Warren DJ. Cortical implants for the blind. *IEEE Spectrum.* (1996) 33:54–9. doi: 10.1109/6.490057
- Tehovnik EJ, Slocum WM, Smirnakis SM, Tolia AS. Microstimulation of visual cortex to restore vision. *Prog Brain Res.* (2009) 175:347–74. doi: 10.1016/S0079-6123(09)17524-6
- Pezaris JS, Eskandar EN. Getting signals into the brain: visual prosthetics through thalamic microstimulation. *Neurosurg Focus.* (2009) 27:E6. doi: 10.3171/2009.4.FOCUS0986

21. Schmidt EM. Finding from chronic optic nerve and cortical stimulation. In: Dagnelie G, editor. *Visual Prosthetics: Physiology, Bioengineering, Rehabilitation*. New York, NY: Springer. p. 301–315. (2011). doi: 10.1007/978-1-4419-0754-7_15
22. Fernández E, Alfaro A, Toledano R, Albisua J, García A. Perceptions elicited by electrical stimulation of human visual cortex. *Invest Ophthalmol Vis Sci*. (2015) 56:777. doi: 10.1172/JCI151331
23. Fernández E, Alfaro A, Soto-Sánchez C, Gonzalez-Lopez P, Lozano AM, Peña S, et al. Visual percepts evoked with an intracortical 96-channel microelectrode array inserted in human occipital cortex. *J Clin Invest*. (2021) 131:e151331. doi: 10.1172/JCI151331
24. Stoney SD, Thompson WD, Asanuma H. Excitation of pyramidal tract cells by intracortical microstimulation: effective extent of stimulating current. *J Neurophysiol*. (1968) 31:659–69. doi: 10.1152/jn.1968.31.5.659
25. Asanuma H, Arnold A, Zarzecki P. Further study on the excitation of pyramidal tract cells by intracortical microstimulation. *Exp Brain Res*. (1976) 26:443–61. doi: 10.1007/BF00238820
26. Miyamoto S, Suematsu N, Umehira Y, Hayashida Y, Yagi T. Age-related changes in the spatiotemporal responses to electrical stimulation in the visual cortex of rats with progressive vision loss. *Scientific Rep*. (2017) 7:14165. doi: 10.1038/s41598-017-14303-1
27. Fehérvári TD, Okazaki Y, Sawai H, Yagi T. In vivo voltage-sensitive dye study of lateral spreading of cortical activity in mouse primary visual cortex induced by a current impulse. *PLoS ONE*. (2015) 10:e0133853. doi: 10.1371/journal.pone.0133853
28. Hayashida Y, Takeuchi K, Ishikawa N, Okazaki Y, Fehérvári TD, Tanaka H, et al. Voltage-sensitive dye imaging of the visual cortices responding to electrical pulses at different intervals in mice in vivo. In: *36th Annual International Conference of the IEEE Engineering in Medicine and Biology Society 2014*. p. 402–405. (2014). doi: 10.1109/EMBC.2014.6943613
29. Bartlett JR, DeYoe EA, Doty RW, Lee BB, Lewine JD, Negrão N, et al. Psychophysics of electrical stimulation of striate cortex in macaques. *J Neurophysiol*. (2005) 94:3430–42. doi: 10.1152/jn.00406.2005
30. Cicmil N, Krug K. Playing the electric light orchestra—how electrical stimulation of visual cortex elucidates the neural basis of perception. *Phil Trans R Soc B*. (2015) 370:20140206. doi: 10.1098/rstb.2014.0206
31. Tehovnik EJ, Tolia AS, Sultan F, Slocum WM, Logothetis NK. Direct and indirect activation of cortical neurons by electrical microstimulation. *J Neurophysiol*. (2006) 96:512–21. doi: 10.1152/jn.00126.2006
32. Cha K, Horch KW, Normann RA. Simulation of a phosphene-based visual field: visual acuity in a pixelized vision system. *Annu Biomed Eng*. (1992) 20:439–49. doi: 10.1007/BF02368135
33. Cha K, Horch KW, Normann RA. Mobility performance with a pixelized vision system. *Vis Res*. (1992) 32:1367–72. doi: 10.1016/0042-6989(92)90229-C
34. Srivastava NR, Troyk PR, Towle VL, Curry D, Schmidt E, Kufta C, et al. Estimating Phosphene Maps for Psychophysical Experiments used in Testing a Cortical Visual Prosthesis Device. In: *3rd International IEEE/EMBS Conference on Neural Engineering 2007*. p. 130–133. (2007). doi: 10.1109/CNE.2007.369629
35. Srivastava NR, Troyk PR, Dagnelie G. Detection, eye-hand coordination and virtual mobility performance in simulated vision for a cortical visual prosthesis device. *J Neural Eng*. (2009) 6:035008. doi: 10.1088/1741-2560/6/3/035008
36. Coulombe J, Sawan M, Gervais JF. A highly flexible system for microstimulation of the visual cortex: design and implementation. *IEEE Trans Biomed Circuits Syst*. (2007) 1:258–69. doi: 10.1109/TBCAS.2007.916026
37. Fernández E, Normann RA, CORTIVIS. approach for an intracortical visual prostheses. In: *Artificial Vision-A Clinical Guide (ed, VP Gabel)*. Switzerland: Springer. p. 191–201. (2017). doi: 10.1007/978-3-319-41876-6_15
38. Lowery AJ, Rosenfeld JV, Rosa MGP, Brunton E, Rajan R, Mann C, et al. Monash Vision Group's Gennaris Cortical Implant for Vision Restoration. In: *Artificial Vision-A Clinical Guide (ed, VP Gabel)*, Switzerland: Springer, p. 215–225. (2017). doi: 10.1007/978-3-319-41876-6_17
39. Normann RA, Greger BA, House P, Romero SF, Pelayo F, Fernandez E. Toward the development of a cortically based visual neuroprosthesis. *J Neural Eng*. (2009) 6:035001. doi: 10.1088/1741-2560/6/3/035001
40. Troyk PR. The intracortical visual prosthesis project. In: *Artificial Vision-A Clinical Guide (ed, VP Gabel)*, Switzerland: Springer, p. 203–214. (2017). doi: 10.1007/978-3-319-41876-6_16
41. Ghovanloo M, Najafi K, A. modular 32-site wireless neural stimulation microsystem. *IEEE J Solid-State Circ*. (2004) 39:2457–66. doi: 10.1109/JSSC.2004.837026
42. Lange Dzn H. Research into the Dynamic Nature of the Human Fovea→ Cortex Systems with Intermittent and Modulated Light. I Attenuation Characteristics with White and Colored Light. *J Opt Soc Am*. (1958) 48:784–9. doi: 10.1364/JOSA.48.000784
43. Kelley DH. Spatio-temporal frequency characteristics of color-vision mechanisms. *J Opt Soc Am*. (1974) 64:983–90. doi: 10.1364/JOSA.64.000983
44. Jones KE, Normann RA. An advanced demultiplexing system for physiological stimulation. *IEEE Trans Biomed Eng*. (1997) 44:1210–20. doi: 10.1109/10.649992
45. Bocan KN, Sejdíć E. Adaptive Transcutaneous Power Transfer to Implantable Devices: A State of the Art Review. *Sensors (Basel)*. (2016) 16:E393. doi: 10.3390/s16030393
46. Lee HM, Kiani M, Ghovanloo M. Advanced wireless power and data transmission techniques for implantable medical devices. In: *IEEE Custom Integrated Circuits Conference (CICC) 2015*. p. 1–8. (2015). doi: 10.1109/CICC.2015.7338412
47. Kameda, S., Hayashida, Y., Tanaka, Y., Akita, D., and Yagi, T. A multichannel current stimulator chip for spatiotemporal pattern stimulation of neural tissues. In: *36th Annual International Conference of the IEEE Engineering in Medicine and Biology Society 2014*. p. 5011–5015. (2014). doi: 10.1109/EMBC.2014.6944750
48. Shepherd RK, Linahan N, Xu J, Clark GM, Araki S. Chronic electrical stimulation of the auditory nerve using noncharge-balanced stimuli. *Acta Otolaryngologica*. (1999) 119:674–84. doi: 10.1080/00016489950180621
49. Donaldson ND, Donaldson PE. When are actively balanced biphasic ('Lilly') stimulating pulses necessary in a neurological prosthesis? I historical background; Pt resting potential; Q studies. *Med Biol Eng Comput*. (1986) 24:41–49. doi: 10.1007/BF02441604
50. Lilly JC, Hughes JR, Alvord EC, Galkin TW. Brief noninjurious waveforms for stimulation of the brain. *Science*. (1955) 121:468–9. doi: 10.1126/science.121.3144.468
51. Ortmanns M, Unger N, Rocke A, Gehrke M, Tietdke HJ. A 0.1 mm², digitally programmable nerve stimulation pad cell with high voltage capability for a retinal implant. In: *IEEE International Solid State Circuits Conference-Digest of Technical Papers 2006*. p. 89–98. (2006). doi: 10.1109/ISSCC.2006.1696037
52. Sit JJ, Sarpeshkar R. A low-power blocking-capacitor-free charge-balanced electrode-stimulator chip with less than 6 nA DC error for 1-mA full-scale stimulation. *IEEE Trans Biomed Circuits Syst*. (2007) 1:172–83. doi: 10.1109/TBCAS.2007.911631
53. Sooksood K, Stieglitz T, Ortmanns M. An active approach for charge balancing in functional electrical stimulation. *IEEE Trans Biomed Circuits Syst*. (2010) 4:162–70. doi: 10.1109/TBCAS.2010.2040277
54. Suanning GJ, Lovell NH. CMOS neurostimulation ASIC with 100 channels scaleable output and bidirectional radio-frequency telemetry. *IEEE Trans Biomed Eng*. (2001) 48:248–60. doi: 10.1109/10.909646
55. Hayashida Y, Umehira Y, Takatani K, Futami S, Kameda S, Kamata T, et al. Cortical neural excitations in rats in vivo with using a prototype of a wireless multi-channel microstimulation system. In: *37th Annual International Conference of the IEEE Engineering in Medicine and Biology Society (EMBC) 2015*. p. 1642–1645. (2015). doi: 10.1109/EMBC.2015.7318690
56. Fehérvári TD, Yagi T. Population response propagation to extrastriate areas evoked by intracortical electrical stimulation in V1. *Front Neural Circuit*. (2016) 10:6. doi: 10.3389/fncir.2016.00006
57. Lippert MT, Takagaki K, Xu W, Huang X, Wu J-Y. Methods for voltage-sensitive dye imaging of rat cortical activity with high signal-to-noise ratio. *J Neurophysiol*. (2007) 98:502–12. doi: 10.1152/jn.01169.2006
58. Paxinos G, Watson C. *The Rat Brain in Stereotaxic Coordinates—7th Ed*. London: Academic Press. (2013).
59. Sefton AJ, Dreher B, Harvey AR, Martin PR. Chapter 30 - Visual System. In: Paxinos G, editor. *The Rat Nervous System*. 4th Ed. Amsterdam: Elsevier (2015). p. 947–983. doi: 10.1016/B978-0-12-374245-2.00030-9
60. McAdams ET, Lackermeier A, McLaughlin JA, Macken D. The linear and non-linear electrical properties of the electrode-electrolyte interface. *Biosensors Bioelectron*. (1995) 10:67–74. doi: 10.1016/0956-5663(95)96795-Z
61. Tanaka Y, Nomoto T, Shiki T, Sakata Y, Shimada Y, Hayashida Y, et al. Focal activation of neuronal circuits induced by microstimulation in the visual cortex. *J Neural Eng*. (2019) 16:036007. doi: 10.1088/1741-2552/ab0b80
62. Chen X, Wang F, Fernandez E, Roelfsema PR. Shape perception via a high-channel-count neuroprosthesis in monkey visual cortex. *Science*. (2020) 370:1191–6. doi: 10.1126/science.abd7435

63. Hayashida Y, Kudo Y, Ishida R, Okuno H, Yagi T. Retinal Circuit Emulator With Spatiotemporal Spike Outputs at Millisecond Resolution in Response to Visual Events. *IEEE Trans Biomed Circ Syst.* (2017) 11:597–611. doi: 10.1109/TBCAS.2017.2662659
64. Tehovnik EJ, Slocum WM. Two-photon imaging and the activation of cortical neurons. *Neurosci.* (2013) 245:12–25. doi: 10.1016/j.neuroscience.2013.04.022
65. Stensaas SS, Eddington DK, Dobelle WH. The topography and variability of the primary visual cortex in man. *J Neurosurg.* (1974) 40:747–55. doi: 10.3171/jns.1974.40.6.0747
66. Rousche PJ, Normann RA. A method for pneumatically inserting an array of penetrating electrodes into cortical tissue. *Ann Biomed Eng.* (1992) 20:413–22. doi: 10.1007/BF02368133
67. Piedade M, Gerald J, Sousa LA, Tavares G, Tomas P. Visual neuroprosthesis: A non invasive system for stimulating the cortex. *IEEE Trans Circuits Syst / Fundam Theory Appl.* (2005) 52:2648–62. doi: 10.1109/TCSI.2005.857923
68. Sugiura T, Khan AU, Yu J, Takeuchi Y, Kameda S, Kamata T, et al. A programmable controller for spatio-temporal pattern stimulation of cortical visual prosthesis. In: *IEEE Biomedical Circuits and Systems Conference (BioCAS).* p. 432–435. (2016). doi: 10.1109/BioCAS.2016.7833824
69. Sugiura T, Imai M, Yu J, Takeuchi Y. A low-energy application specific instruction-set processor towards a low-computational lossless compression method for stimuli position data of artificial vision systems. *J Inform Process.* (2017) 25:210–9. doi: 10.2197/ipsjip.25.210
70. Wong YT, Feleppa T, Mohan A, Browne D, Szlawski J, Rosenfeld JV, et al. CMOS stimulating chips capable of wirelessly driving 473 electrodes for a cortical vision prosthesis. *J Neural Eng.* (2019) 16:026025. doi: 10.1088/1741-2552/ab021b
71. Janders M, Egert U, Stelzle M, Nisch W. Novel thin-film titanium nitride micro-electrodes with excellent charge transfer capability for cell stimulation and sensing applications. In: *Proceedings of 18th Annual International Conference of the IEEE Engineering in Medicine and Biology Society.* p. 1191–1193, (1996).
72. Robblee LS, Lefko JL, Brummer SB. Activated Ir: An electrode suitable for reversible charge injection in saline. *J Electrochem Soc.* (1983) 130:731–2. doi: 10.1149/1.2119793
73. Weiland JD, Anderson DJ, Humayun MS. In vitro electrical properties for iridium oxide versus titanium nitride stimulating electrodes. *IEEE Trans Biomed Eng.* (2002) 49:1574–9. doi: 10.1109/TBME.2002.805487
74. Troyk PR, Bradley D, Bak M, Cogan S, Erickson R, Hu Z, et al. Intracortical visual prosthesis research – Approach and progress. In: *2005 IEEE Engineering in Medicine and Biology 27th Annual Conference.* (2005) p. 1–5. doi: 10.1109/IEMBS.2005.1616216
75. Kozai TDY, Jaquins-Gerstl AS, Vazquez AL, Michael AC, Cui XT. Brain tissue responses to neural implants impact signal sensitivity and intervention strategies. *ACS Chem Neurosci.* (2015) 6:48–67. doi: 10.1021/cn500256e
76. Berenstein CK, Mens LH, Mulder JJ, Vanpoucke FJ. Current steering and current focusing in cochlear implants: comparison of monopolar, tripolar, and virtual channel electrode configurations. *Ear Hear.* (2008) 29:250–60. doi: 10.1097/AUD.0b013e3181645336
77. Constandinou TG, Georgiou J, Toumazou C. A partial-current steering biphasic stimulation driver for vestibular prostheses. *IEEE Trans Biomed Circuits Syst.* (2008) 2:106–13. doi: 10.1109/TBCAS.2008.927238
78. Bareket L, Barriga-Rivera A, Zapf MP, Lovell NH, Suanning GJ. Progress in artificial vision through suprachoroidal retinal implants. *J Neural Eng.* (2017) 14:045002. doi: 10.1088/1741-2552/aa6cbb
79. Anderson DN, Anderson C, Lanka N, Sharma R, Butson CR, Baker BW, et al. The μ DBS: multiresolution, directional deep brain stimulation for improved targeting of small diameter fibers. *Front Neurosci.* (2019) 13:1152. doi: 10.3389/fnins.2019.01152
80. Butovas S, Schwarz C. Spatiotemporal effects of microstimulation in rat neocortex: a parametric study using multielectrode recordings. *J Neurophysiol.* (2003) 90:3024–39. doi: 10.1152/jn.00245.2003
81. Tehovnik EJ, Slocum WM. Electrical induction of vision. *Neurosci Biobehavior Rev.* (2013) 37:803–18. doi: 10.1016/j.neubiorev.2013.03.012



OPEN ACCESS

EDITED BY

Yael Hanein,
Tel Aviv University, Israel

REVIEWED BY

Jae-Ik Lee,
Massachusetts General Hospital and
Harvard Medical School, United States
James Weiland,
University of Michigan, United States

*CORRESPONDENCE

Andreea Elena Cojocaru
andreea-elena.cojocaru@tuwien.ac.at
Günther Zeck
guenther.zeck@tuwien.ac.at

SPECIALTY SECTION

This article was submitted to
Cellular Neurophysiology,
a section of the journal
Frontiers in Cellular Neuroscience

RECEIVED 31 August 2022

ACCEPTED 10 November 2022

PUBLISHED 09 December 2022

CITATION

Cojocaru AE, Corna A, Reh M and
Zeck G (2022) High spatial resolution
artificial vision inferred from the spiking
output of retinal ganglion cells
stimulated by optogenetic and
electrical means.
Front. Cell. Neurosci. 16:1033738.
doi: 10.3389/fncel.2022.1033738

COPYRIGHT

© 2022 Cojocaru, Corna, Reh and
Zeck. This is an open-access article
distributed under the terms of the
Creative Commons Attribution License
(CC BY). The use, distribution or
reproduction in other forums is
permitted, provided the original
author(s) and the copyright owner(s)
are credited and that the original
publication in this journal is cited, in
accordance with accepted academic
practice. No use, distribution or
reproduction is permitted which does
not comply with these terms.

High spatial resolution artificial vision inferred from the spiking output of retinal ganglion cells stimulated by optogenetic and electrical means

Andreea Elena Cojocaru^{1*}, Andrea Corna¹, Miriam Reh² and
Günther Zeck^{1*}

¹Institute of Biomedical Electronics, TU Wien, Vienna, Austria, ²Institute for Ophthalmic Research at the University of Tübingen, Tübingen, Germany

With vision impairment affecting millions of people world-wide, various strategies aiming at vision restoration are being undertaken. Thanks to decades of extensive research, electrical stimulation approaches to vision restoration began to undergo clinical trials. Quite recently, another technique employing optogenetic therapy emerged as a possible alternative. Both artificial vision restoration strategies reported poor spatial resolution so far. In this article, we compared the spatial resolution inferred *ex vivo* under ideal conditions using a computational model analysis of the retinal ganglion cell (RGC) spiking activity. The RGC spiking was stimulated in epiretinal configuration by either optogenetic or electrical means. RGCs activity was recorded from the *ex vivo* retina of transgenic late-stage photoreceptor-degenerated mice (rd10) using a high-density Complementary Metal Oxide Semiconductor (CMOS) based microelectrode array. The majority of retinal samples were stimulated by both, optogenetic and electrical stimuli using a spatial grating stimulus. A population-level analysis of the spiking activity of identified RGCs was performed and the spatial resolution achieved through electrical and optogenetic photo-stimulation was inferred using a support vector machine classifier. The best f_1 score of the classifier for the electrical stimulation in epiretinal configuration was 86% for 32 micron wide gratings and increased to 100% for 128 microns. For optogenetically activated cells, we obtained high f_1 scores of 82% for 10 microns grid width for a photo-stimulation frequency of 2.5 Hz and 73% for a photo-stimulation frequency of 10 Hz. A subsequent analysis, considering only the RGCs modulated in both electrical and optogenetic stimulation protocols revealed no significant difference in the prediction accuracy between the two stimulation modalities. The results presented here indicate that a high spatial resolution can be achieved for electrical or optogenetic artificial stimulation using the activated retinal ganglion cell output.

KEYWORDS

retinal ganglion cell, optogenetics, epiretinal electrical stimulation, channelrhodopsin-2, CMOS-based microelectrode array

Introduction

Optogenetic therapy emerged as a method in modern neuroscience at the beginning of the 2000s, when several research groups showed the use of the technique for the light-induced control of the excitable cells' activity (Bi et al., 2006; Ivanova et al., 2010). As of last year, we witnessed the results of the first patient in the clinical trial NCT03326336 to report a partial recovery of vision after undergoing optogenetic therapy (Sahel et al., 2021). Various approaches have been taken in the search for the most suitable cell type target for photo-stimulation: focusing on the bipolar cells (BC; Lagali et al., 2008; Doroudchi et al., 2011; Cehajic-Kapetanovic et al., 2015; Macé et al., 2015; van Wyk et al., 2015; Kralik et al., 2022; Reh et al., 2022), the remaining photoreceptors (Busskamp et al., 2010; Khabou et al., 2018) or the retinal ganglion cells (RGC; Jacobson et al., 2005; Bi et al., 2006; Ivanova et al., 2010; Gauvain et al., 2021; Reh et al., 2021). In the case of retinitis pigmentosa or age-related macular degeneration (AMD), the photoreceptor cell layers degrade progressively, leaving the RGC layer largely intact. In turn, this makes the RGCs a potentially attractive target. Recent evidence (Lu et al., 2020; Reh et al., 2022) compared the efficacy of targeting rodBCs or RGCs for optogenetic vision restoration and found that, despite the higher cell density and the ability of the BCs to preserve the inner information processing mechanism of the retina, RGCs are a potentially better target. This result is puzzling and may be attributed either to the strong spontaneous activity in the mouse line with targeted rod BCs (Reh et al., 2022) or to differences in the stimulation protocols.

In contrast, the activation of retinal cells through electrical stimulation has been studied for several decades now (Palanker and Goetz, 2018; Ayton et al., 2020), leading to market-approved electronic implants such as Argus II (Humayun et al., 2012; da Cruz et al., 2016; Second Sight, USA), Alpha AMS (Stingl et al., 2017; Zrenner et al., 2017; Palanker and Goetz, 2018; Ayton et al., 2020; Retina Implant, Germany) and IRIS II (Muqit et al., 2019; Pixium Vision, France). Implant prototypes include PRIMA (Palanker and Goetz, 2018; Palanker et al., 2020; Pixium Vision, France), which uses a subretinal configuration and infrared light stimulation on honeycomb structured photodiodes or POLYRETINA (Ferlauto et al., 2018; Chenais et al., 2021), aiming at a significant sight restoration. Despite the initial success, currently, there is no retinal prosthesis with CE or FDA approval on the market. One of the shortcomings of electrical stimulation is the relatively poor spatial resolution, which did not overcome legal blindness. This had been attributed to either axonal activation for epiretinal stimulation (Beyeler et al., 2019, but see the alternative proposal in Weitz et al., 2015) or the spread of the stimulating unconfined electric field for subretinal stimulation (Palanker et al., 2005; Loudin et al., 2007; Wilke et al., 2011).

An open scientific question remained, if artificial stimulation applied directly to the retinal ganglion cells achieves a higher

resolution as expected from the RGC's morphology, which includes the soma but also the much larger dendritic tree and the elongated axons. Cell soma, dendrites, and axons are often transduced in optogenetic therapy (Shemesh et al., 2017; Forli et al., 2021; but see Greenberg et al., 2011) or may be activated by electrical stimulation (Beyeler et al., 2019; Tandon et al., 2021). To answer this question, we applied a stimulus protocol, where elongated grating patterns were reversed at a defined temporal frequency. This protocol has been previously reported for subretinal electrical (Lorach et al., 2015; Chenais et al., 2021) and for optogenetic stimulation (Cideciyan et al., 2016; Reh et al., 2021). The highest grating frequency which differentially activates RGCs determines the highest spatial resolution. Although previous reports from our lab (Corna et al., 2021; Reh et al., 2021) indicate that a high spatial resolution may be achieved by direct artificial stimulation of RGCs, the results were not conclusive for two reasons. Previous experiments were performed on different retinæ, while the degree of retinal degeneration and remodeling had been reported to show a center-to-periphery gradient (Gargini et al., 2007). Secondly, the stimulation protocol used previously for electrical stimulation (Corna et al., 2021) was less suited to estimate spatial selectivity. To overcome these limitations we performed here artificial stimulations on the very same retinal portion in the same experimental condition and compared the inferred spatial resolution from the recorded RGC activity using the same computational analysis method.

The RGC neural activity was recorded using a Complementary Metal-Oxide-Semiconductor microelectrode array (CMOS-MEA) while stimulating the *ex vivo* retina of adult *rd10* transgenic mice. We employed a support vector machine classifier to infer the spatial resolution achievable through either one of the two stimulation methods from the RGC spiking recorded in the same retinæ to optogenetic and electrical stimuli.

Materials and methods

Retinal preparation

Ex vivo retinæ of adult, photoreceptor-degenerated *rd10* transgenic mice expressing the light sensitive opsin channel rhodopsin-2 (ChR2) in retinal neurons were used in this study. All experimental procedures were reported and approved by the Center for Biomedical Research, Medical University Vienna, Austria. In the current work, ChR2 was expressed in either rod-bipolar cells ($n = 3$ retinal samples, two female mice and one male, aged between 208 and 281 days post-natal) as described in Reh et al. (2022) or in the parvalbumin-positive retinal ganglion cells ($n = 6$ retinal samples from mice of either sex aged between

214 and 358 days post-natal) as described in Reh et al. (2021). At this age, all photoreceptors are fully degenerated (Chang et al., 2002; Gargini et al., 2007). Parvalbumin-positive RGCs represent approximately 30% of the total RGC population, comprising ON as well as OFF RGC classes (Yi et al., 2012). We could not identify ON or OFF RGC types here, since all photoreceptors degenerated at the age studies here (Cha et al., 2022).

The *ex vivo* retinal samples were prepared in carbogenated (95% O₂, 5% CO₂) Ames' medium (Ames A1420, NaHCO₃, Sigma Aldrich GmbH, Vienna, Austria), using dim red light under a dissection microscope (Leica Mikrosysteme G.m.b.H., Vienna, Austria). After mice were euthanized by cervical dislocation and after enucleation, a small incision was performed above the ora serrata to release the pressure inside the eye and ensure sample oxygenation. Next, a circular cut was made around the eyeball, the lens was removed and, by gentle movements of the forceps, the sclera and retinal pigment epithelium (RPE) were separated from the retina. Following the removal of the vitreous, a retinal portion was cut and placed on the sensor array of a CMOS-based MEA chip, with the RGC layer facing the recording sites (Figure 1A).

Prior to the sample preparation, the surface of the recording chip (CMOS MEA, see below) was cleaned with Tickopur (R60, 5%, 80°C, Dr. H. Stamm GmbH Chemische Fabrik, Berlin, Germany) and rinsed with distilled water. The active area was covered with a few microliters of poly-L-lysine (1 mg/ml, Sigma Aldrich GmbH, Vienna, Austria) in order to ensure tight tissue adhesion. The coating process proved to not affect the electrical stimulation, as shown in previous work (Eickenscheidt and Zeck, 2014; Stutzki et al., 2016).

The chip's chamber, containing the retinal sample was filled with Ames' medium and perfused constantly with the same carbonated solution to ensure the cells' viability. The temperature in the recording chamber was kept between 34 and 36°C. All recordings were conducted in the dark.

Electrical stimulation

In the current study, we used a commercial CMOS-MEA5000 system (Multi Channel Systems MCS GmbH, Reutlingen, Germany) for simultaneous stimulation and recording and CMOS-MEA chips as described previously (Bertotti et al., 2014; Corna et al., 2021). The chips comprise a recording array with 65 by 65 recording sites each of them separated by 16 µm and a second stimulation array comprising 32 by 32 stimulation sites with a center-to-center distance of 32 µm. The array of recording sites is interspersed with stimulation electrodes. To increase the stimulation strength (i.e., capacitive stimulation current), the top oxide was omitted leaving the chip surface with a native oxide only (Corna et al., 2021).

We applied cosine stimuli, as described in Corna et al. (2021), delivered at 40 Hz and a peak-to-peak amplitude of 2.5 V applied between the capacitive electrode and the ground electrode (Ag/AgCl) submerged in the recording solution. The selected stimulation charge density was 15 µC/cm² and it was determined as described in Corna et al. (2018). The stimuli were presented as alternating gratings with a phase reversal. In the following, we will refer to the two spatial patterns per stimulation as “phase 1” and “phase 2”. The electrical stimuli were detected by the neighboring sensors as sinusoidal stimulus artifacts.

Photo-stimulation

Intense light stimulation was delivered by a CoolLED pE-4000 system (CoolLED Ltd., Andover, UK) projecting onto a digital mirror device (Rapp Optoelectronic GmbH, Wedel, Germany). The patterned light stimuli (460 nm) were focused onto the retina through a microscope (Olympus) equipped with a 5× objective (Olympus MPlanFL N). This combination of systems allows for a patterned stimulation with micrometer range precision (Figure 1C). We projected the grating stimuli at two frequencies, 2.5 Hz, as previously used in Reh et al. (2022) and at 10 Hz (Reh et al., 2021).

Data processing

Prior to the statistical analyses, the raw extracellular voltages recorded during optogenetic stimulation were filtered with a second order high pass Bessel filter at 200 Hz and a second order low pass Bessel filter at 5,000 Hz (Figure 1G), while the raw data from the electrical stimulation was high pass filtered with a fourth order Butterworth function at 1,000 Hz and low pass filtered with a second order Bessel function at 3,000 Hz (Figures 1D,E). Due to the sensor drift (Figure 1F) introduced by the blue light used for optogenetic stimulation, a sensor reset (duration 200 µs) was applied every 400 ms. This method, however, comes with the cost of introducing an additional artifact. In order to remove it, we used a method described in Reh et al. (2021) in which the raw data is divided in time intervals according to the times of the sensor reset. From these sequences of data, a “drift curve”, the result of a 2nd order Savitzky-Golay filter with an 800 µs windows, was subtracted from the raw data and this new dataset was filtered with a high-pass, 2nd order Butterworth filter of 100 Hz. Following this procedure, the signal data corresponding to the timestamps in which the sensor reset occurred was replaced by noise taken from the same recorded data. The last step in the preprocessing stage was further filtering the data, as described previously.

Spike sorting for the identification of single RGC units was performed using the CMOS-MEA-Tools software (Multi

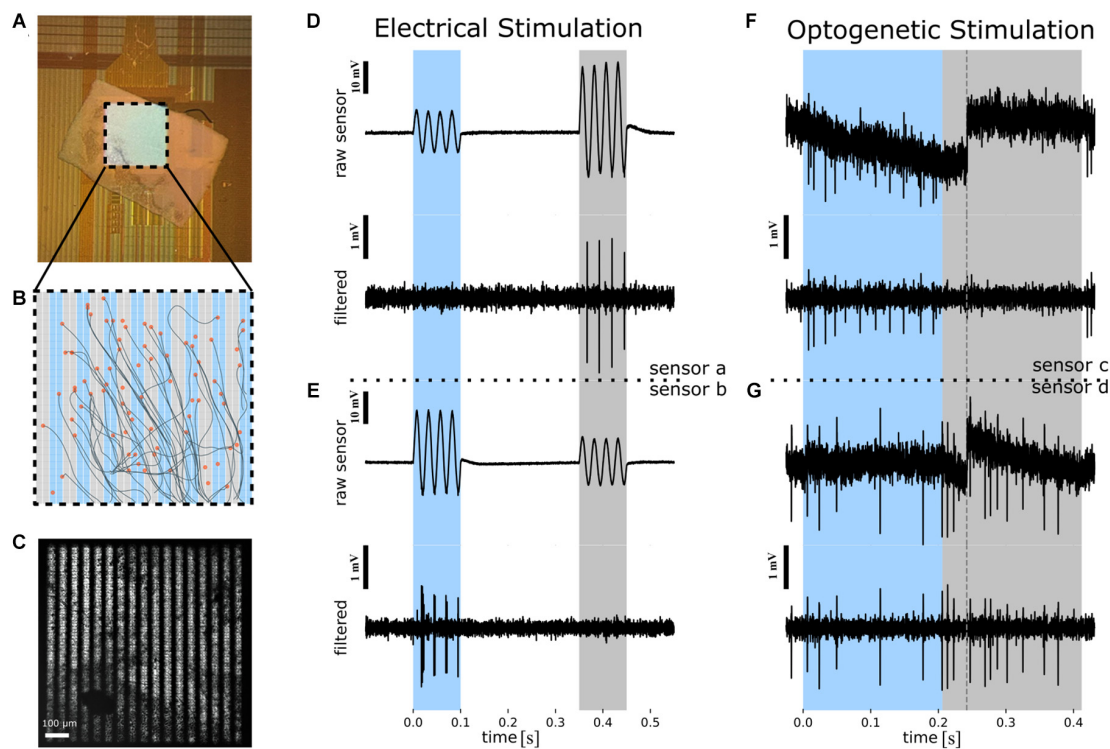


FIGURE 1

Overview of the experimental protocol used to infer the spatial resolution of the stimulus based on the RGC spiking. **(A)** Photograph of *ex vivo* rd10 retina interfaced to a CMOS-MEA. The central square ($1 \times 1 \text{ mm}^2$) comprises 1,024 capacitive stimulation electrodes and 4,225 recording sites. **(B)** Schematic of the stimulation array with 1,024 stimulation electrodes. The recording sites are in the same area, with each stimulation electrode being enclosed by four recording sites (not shown here). Cell positions (orange circles) and inferred axon pathways are shown. In the background (blue and gray) the two phases of the reversed grating stimulus are shown. **(C)** Microscopic image of the retina on the CMOS MEA with the optogenetic photo-stimulation pattern superimposed. Scale bar: $100 \mu\text{m}$. **(D)** The electrical stimulation protocol exemplified using the raw voltage of one recording sensor (recording site a). *Upper panel*: Four sinusoidal stimulation waveforms were applied to “blue” stimulation electrodes (panel B) between 0 and 100 ms, followed by four stimulation waveforms applied to the “gray” electrodes (panel B) between 350 and 450 ms. The selected recording sensor records a higher extracellular voltage artifact for stimulation with gray stimulation electrode as compared to stimulation with blue electrodes. Note that the same stimulus amplitude was applied to “blue” and “gray” electrodes. Scale bar: 10 mV. *Lower panel*: High-pass filtered extracellular voltage of the signal shown in the upper panel reveals spiking in each cycle of the four sinusoidal waveforms for stimulation with the gray electrodes only. Scale bar: 1 mV. **(E)** Detection of selective electrical activation revealed by a second sensor (“recording site b”). Description of the traces as in **(D)**. **(F)** The optogenetic stimulation protocol exemplified using the raw voltage of one recording sensor (recording site c). *Upper panel*: Spatially patterned photo-stimuli with fine gratings were projected onto selected regions of the CMOS sensor array (see panel C) between 0 and 200 ms, followed by a reverse grating between 200 and 400 ms. Dashed line in the raw extracellular voltage trace marks a sensor reset. Scale bar: 10 mV. *Lower panel*: High-pass filtered extracellular voltage of the signal shown in the upper panel reveals spiking during one of the stimulation phases (marked with “blue”). **(G)** Detection of selective optogenetic activation revealed by another sensor (“recording site d”). Description of the traces as in **(F)**. RGC, retinal ganglion cell; CMOS MEA, Complementary Metal-Oxide-Semiconductor microelectrode array.

Channel Systems MCS GmbH, Reutlingen, Germany), which applies a sorting algorithm based on independent component analysis (Leibig et al., 2016).

A manual curation was applied to the sorted datasets to ensure that the cells were properly identified. The measures of interest for this post-processing step were IsoIBG, separability, and Signal-to-Noise-Ratio (SNR). IsoIBG (Neymotin et al., 2011) is a measure of the separation, in feature space, between the neural signal amplitudes and the other peak amplitudes, considered as background noise. When the sorter identifies only a single waveform cluster, the IsoIBG gets assigned a not a number value (NaN). Therefore, we chose to keep

only the units (cells) which had numerical values. Separability measures the separation between different units' clusters and the dimensions dominated by noise. A higher value of the separability ensures a clearer neural spike-noise distinction, hence the choice of imposing a 2.5 threshold on this metric. As the IsoIBG alone is not always a very informative metric (Neymotin et al., 2011), we considered also the SNR as being within the range of 3.3 and 14 for the case of electrical stimulation recordings.

For a qualitative estimation of how well RGCs are activated by artificial stimuli we calculated the relative change in firing rate as follows:

$$\text{RFR} = \frac{FR_{\text{phase1}} - FR_{\text{phase2}}}{FR_{\text{phase1}} + FR_{\text{phase2}}}$$

Equation 1. The formula for the relative change in firing rate (RFR) of the RGCs identified. FR_{phase1} and FR_{phase2} stand for firing rate values in phase 1 and firing rate values in phase 2, respectively.

Pattern classification using support vector machines

The statistical analysis of the data was performed using a classification method, the support vector machines¹ (Drucker et al., 1997; Pisner and Schnyer, 2019). Due to its relative ease on the resources during the training phase and its performance, it began to gain popularity in the bioengineering field (Pisner and Schnyer, 2019).

In brief, this method uses a way of finding a hyperplane in an n -dimensional space, where n is the number of features, that distinctly classifies data points. The hyperplanes are, in fact, the decision boundaries of the classifier and the data points falling on either side of the hyperplane will be assigned to one class or the other. To maximize the margin of the classifier, the algorithm makes use of the so-called “support vectors”, which are data points that are found closer to the hyperplane and influence its position and orientation. The main goal of the classifier is to minimize the errors. To do so, it uses a cost function to perform the learning and the optimizations; in this case, the cost function is the hinge loss.

In our current approach, we calculated the number of spikes per stimulus duration in each of the repetitions for every cell in a recording and constructed an input variable (x), a vector of a length n equal to the number of cells in a given recording. The total dataset thus constructed consisted of m such vectors, with m being the number of repetitions for a recording. Ultimately, the task was a binary classification problem of assigning the vector of firing rates in one repetition and phase to one of the two phases. Out of the classifier's results, we could then infer the spatial resolution achieved by the stimulation protocols.

Specifically, for our case, we used the SVM () class of scikit-learn's module, with a radial basis function kernel (rbf) and we imposed a regularization by a C constant of 1. The goal of such a kernel transformation is to project the original data point into a new dimensionality such that it becomes easier to separate the data belonging to each class using simple linear methods. Since scaling is a sensitive matter in the training of such a classifier, we investigated multiple scaling methods, concluding that the best performance for the given datasets is achieved by standardizing

the values using the Standard Scaler () method, which follows a formula as in Eq. 2.

$$z = \frac{(x - \mu)}{\sigma}$$

Equation 2. The standard score formula as calculated for a sample x . μ denotes the mean of the training samples, while σ denotes the standard deviation of the training samples.

To ensure the reproducibility of our experiment, the randomness was controlled by setting a seed to a constant. The datasets were split into train and test sample sizes in a ratio of 80/20. The ability of the model to generalize was evaluated through cross-validation. We made use of the StratifiedKFold() class of scikit-learn, with a 10-fold split. Using this method, random parts of the dataset are selected and the results of the classifier's performance are returned in the form of an average value.

One way to visualize the outcomes of the classification task is to use a confusion matrix (Tharwat, 2018), such as in Table 1. Different metrics typically used to assess the quality of the results, such as accuracy, precision, or recall are further extracted from this matrix.

To evaluate the classifier's performance, we referred to the f_1 score, a metric which can be calculated as the harmonic mean of the precision and recall, as in Eq. 3.

$$f_1 = 2 \frac{P \cdot R}{P + R} \equiv \frac{TP}{TP + \frac{1}{2}(FP + FN)}$$

Equation 3. f_1 score formula. Here, P denotes the value of the precision and R the value of the recall, respectively. TP refers to the number of true positives, FP the value of the false positives, and FN the value of the false negatives. For the definition of TP , FP , and FN see Table 1.

Results

In this study, we investigated the spatial resolution achieved through electrical or optogenetic stimulation of RGCs in adult transgenic rod degenerated mice (rd10-ChR2). The retina was interfaced with the RGC layer facing the recording and

TABLE 1 Confusion matrix table.

	Predicted	
	True positive (TP)	False positive (FP)
Actual	False negative (FN) Type II error	Type I error True negative (TN)

The values computed are typically given in percentages and correspond to the percentage of either correctly or wrongly classified data points. The confusion matrix is used to calculate the f_1 score (Eq. 3).

¹ Support Vector Machines. <https://scikit-learn.org/stable/modules/svm.html>

stimulation sites of CMOS MEA chips (Figure 1A). This high density of the recording sites allows electrical imaging of somatic and axonal activity in a large RGC population (Figure 1B) as well as the option to electrically stimulate the retinal neurons. Within the 10 different retinal portions stimulated and analyzed in the following we identified artificial activation in over 800 RGCs.

Patterned photo-stimulation of optogenetically transduced retinal neurons with fine gratings evokes spatially confined RGC activation

In the first experiment we investigated the response of RGCs upon photo-stimulation of optogenetically transduced retinal neurons. Patterned photo-stimulation *in vitro* was applied at high precision using a focused stimulus projection through a microscope objective (Figure 1C). We, therefore, investigated protocols using alternating gratings with a bar width ranging between 5 and 128 μm . The RGC spiking activity during stimulus presentation was recorded and assigned to individual RGCs (see “Materials and methods” section, Figure 1B).

As a qualitative presentation of the stimulated cells’ spiking activity, raster plots of selected RGCs obtained after repetitive stimulation with grating pattern reversals of one spatial frequency are shown in Figures 2A,B. The raster plots show the spiking activity recorded from two cells to a spatial grating comprising 50 μm wide bars and reversed with a frequency of either 2.5 Hz or 10 Hz. For both frequencies, a robust spiking was recorded without any sign of fading, i.e., decrease of the spiking with an increasing repetition rate. The peri-stimulus histograms in Figures 2A,B qualitatively show the preference of each of the two selected cells for one grating phase. This result is surprising, given that the dendritic tree of RGCs spans about 200 μm in diameter and thus each phase of the grating covers part of the dendrites. In Supplementary Figure 1 we present the raster plots and PSTH of two RGCs to optogenetic stimulation with very fine gratings (10 μm).

To quantify the activation of RGCs by photo-stimulation we calculated the relative change in firing rate (RFR, defined in the “Materials and methods” section) for the two phases of the grating. An RFR value of 1 implies activity exclusively in phase 1, a value of -1 exclusive activation in phase 2. The RFR for the cell population stimulated with the 50 and 500 μm grating is shown in Figures 2C,D (for 2.5 Hz), and Figures 2E,F (for

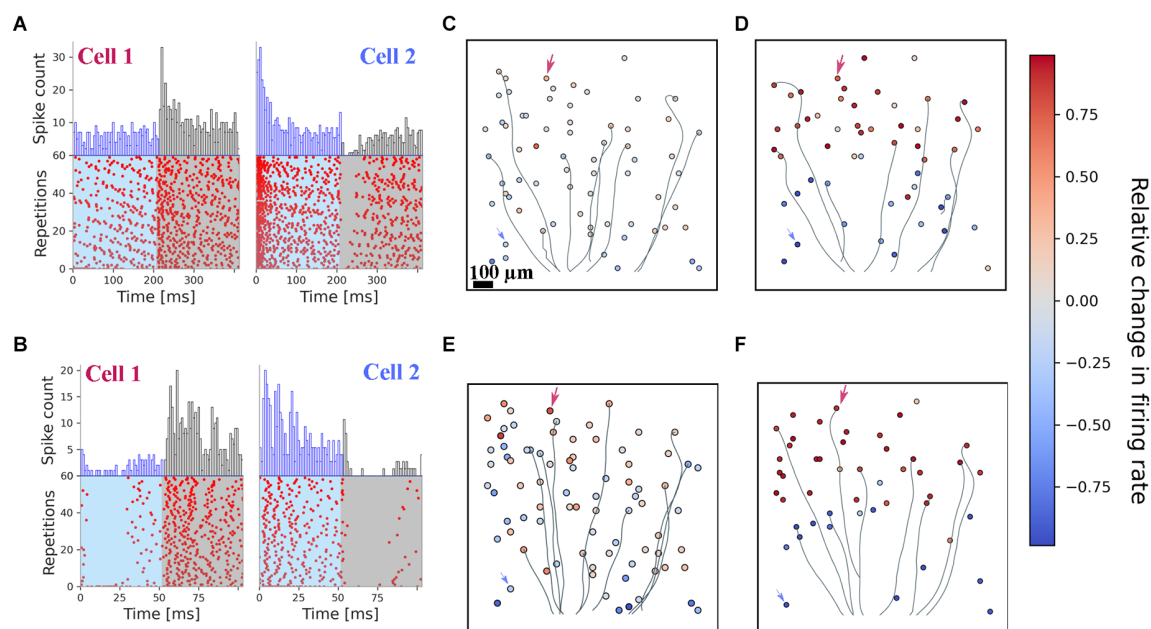


FIGURE 2

Optogenetic stimulation with fine gratings evokes spatially restricted RGC spiking. All results presented here originate from one retina. (A) Raster plots of two exemplary RGCs stimulated for 24 s with an alternating stimulus at a spatial frequency of 50 μm . Every 200 ms, the spatial pattern was switched. A preferential activation is detected for both cells. (B) Raster plots of the very same RGCs, for a stimulus presented at 10 Hz temporal switching and a 50 μm grating width. Both RGCs cells show a preferential response to one of the two stimulation phases. (C,D) Spatial mapping of identified RGCs for the 2.5 Hz pattern switching with a 50 μm (C) and 500 μm (D) grating width. Color coded is the relative change in firing rate between the two stimulation phases. Arrows indicate the two selected cells’ positions depicted in panel (A). RGC axons are inferred from the spike-triggered averaging; only a few of them are shown here for visualization purposes. (E,F) Spatial mapping of identified RGCs for the 10 Hz pattern reversal with a spatial frequency of 50 μm (E) and 500 μm (F). Color coded is the relative change in firing rate between the two stimulation phases. Arrows indicate the two selected cells’ positions depicted in panel (B).

10 Hz), respectively. Electrical imaging of the interfaced retina allows identification of the RGC position and for most cells of the corresponding axon. Axons of a few selected RGCs are included here as well. Although the photostimulus was presented across the axon in each phase, we did not detect axonal activation. This is most obvious for large gratings (500 μm ; **Figures 2D,F**), where the stimulus can be easily detected by the eye from the relative change in firing rate for both frequencies (2.5 Hz and 10 Hz). For this example, phase 1 stimulated the upper part of the RGCs on the array.

We investigated gratings ranging between 5 and 100 μm (with 500 μm serving as a control). The distribution of RFR values obtained for the individual grid width is shown in **Supplementary Figure 2**. We note that for each grating the distribution is different from a unimodal distribution (Hartigan dip test). These RFRs different from zero suggests that a computational model, which uses a large RGC population (>30 cells) and thereby “considers” cells with non-zero RFRs may

succeed to infer the correct stimulus (i.e., grating pattern). In the next step we analyzed the effect of electrical stimulation and return to the discrimination task using a computational model.

Electrical stimulation with fine gratings evokes spatially confined RGC activation

We next analyzed the RGC spiking upon electrical stimulation using a grating stimulus (**Figure 1B**) analogous to the optogenetic photostimulation. The grating comprised a set of electrodes arranged in rectangular shapes ($1 \times 1 \text{ mm}^2$) with a grid width of either 32, 64 or 128 μm (see “Materials and methods” Section). During one stimulus period, which we referred to as “phase 1” (100 ms long), every second column (32 \times 1 electrodes) stimulated the retina while for the alternating columns the electrode voltage was left floating. After a break of 250 ms, the electrodes in the spatial “phase 2” were stimulated.

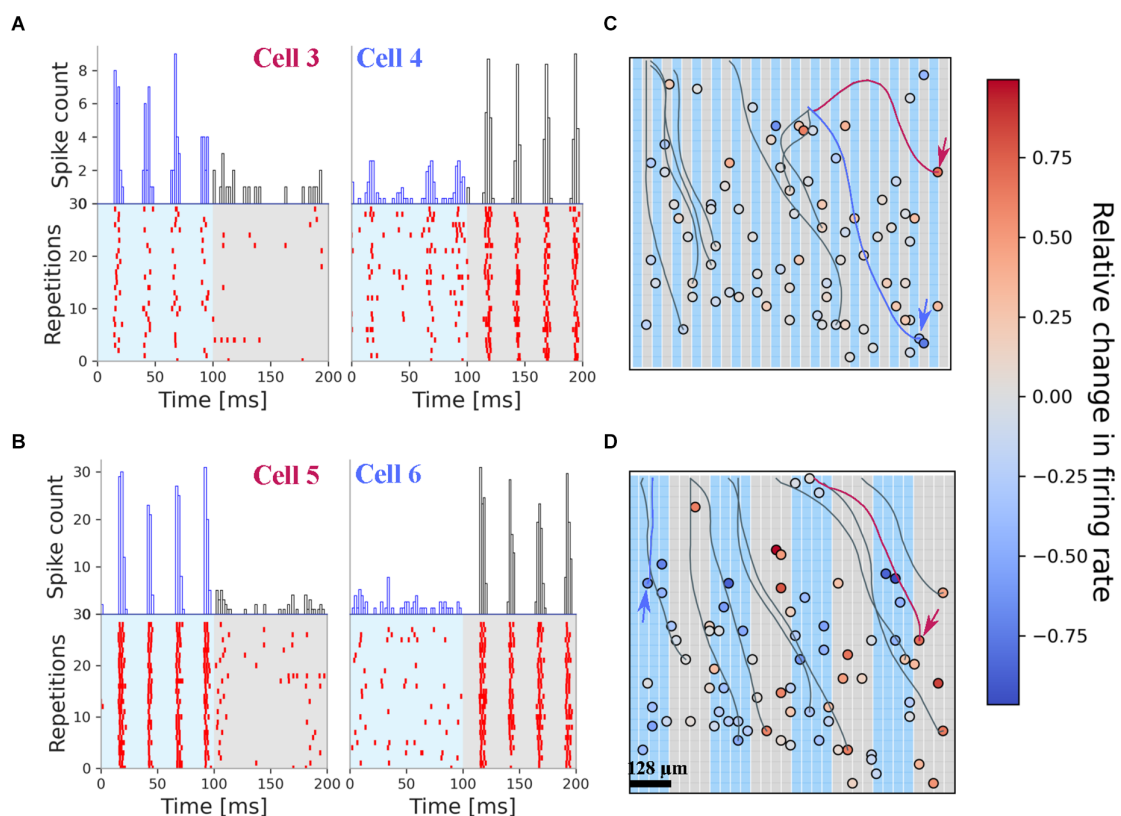


FIGURE 3

Electrical stimulation with fine gratings evokes spatially restricted RGC spiking. All results presented here originate from one retina. **(A)** Rasterplot of two selected RGCs upon stimulation with fine grating stimuli (bar width: 32 μm). Cell 3 is stimulated only in phase 1 (0–100 ms) while cell 4 is stimulated in phase 2 (100–200 ms). The cell positions are marked with arrows in panel **(C)**. **(B)** Rasterplot of two selected RGCs upon stimulation with grating stimuli (bar width: 128 μm). The spiking pattern for each cell is confined to one phase. The cell positions are marked with arrows in panel **(D)**. **(C)** Positions of the RGC on the stimulation array. Color-coded is the relative change in firing rate. The background colors of the grating mark the electrodes used in phase 1 and phase 2. The results presented here were obtained after stimulation with 32 μm narrow gratings (panel **A**). For visualization purposes, only a few axons are shown. **(D)** Positions of the RGC on the stimulation array, with the corresponding color coding of the relative change in firing rate. Note the dominant red colors on top of the gray stimulation electrodes indicating selective activation by this stimulus.

The spatial resolution of the grating stimulus is limited by the size of stimulation electrode (32 μm).

The spiking activity of two exemplary RGCs to 30 repetitions of the same stimulus pattern (32 μm grid width) is shown in **Figure 3A**. The spiking in the interstimulus interval is not shown. The two cells were selected to demonstrate their selective activation by one single phase but not the second. Note, that the two cells are activated within each phase of the four sinusoidal stimuli without fading (i.e., decrease in firing rate). A second example (**Figure 3B**) from the same retina shows an even stronger firing and selective activation of the RGC in only one of the grating phases, i.e., grating reversals. The stronger response is probably caused by the extended stimulation area, now covering 4×32 single electrodes (i.e., $128 \times 1,024 \mu\text{m}^2$). For these RGCs, no weak activation in the non-preferred phase was detected.

The relative change in firing rate (RFR) of 80 RGCs in one retina sample for the 32 microns grating stimulus is shown in **Figure 3C**, while the RFR of these RGCs responding to the 128 microns grating stimulus is shown in **Figure 3D**. We note, that most RGCs are activated by both stimuli—however, for the narrow gratings the number dropped slightly. No effort was undertaken here to clarify the difference in identified RGCs. There are 45% of the RGCs where the RFR is higher than 0.01. Thus, as a first qualitative result, we report that electrical stimuli with spatial gratings as small as 32 μm evoke different spiking activity in the stimulated RGCs. This qualitative result was found in all investigated retinas. In a control experiment, we investigated an rd10 retina, which did not express ChR2. Here again, we found the same high discrimination result.

In addition to the RGC soma our algorithm identifies the corresponding axon. Exemplary axons are shown in **Figures 3C,D**. We note that these axons cross the stimulation electrodes and may potentially be activated. However, the selective stimulation shown in **Figures 3A,B** for four RGCs demonstrate that axons are not activated here. The avoidance of axonal stimulation in epiretinal configuration for low-frequency (40 Hz) stimuli strengthens the result of previous reports, where the stimulus shape was a small square (Corna et al., 2021) or a single circular electrode (Weitz et al., 2015).

Discrimination of fine spatial grating stimuli using computational modeling of the stimulated RGC spiking

In the next step we employed a support vector machine (SVM) classifier to infer the presented stimulus (“phase 1” or “phase 2”) from the firing rates of the RGCs. Given the values of the firing rate of the recorded cells in each of the stimulation phases in a training set, the classifier was asked to assign the correct stimulation phase for a test set. The training comprised 80% of the stimulus repetitions,

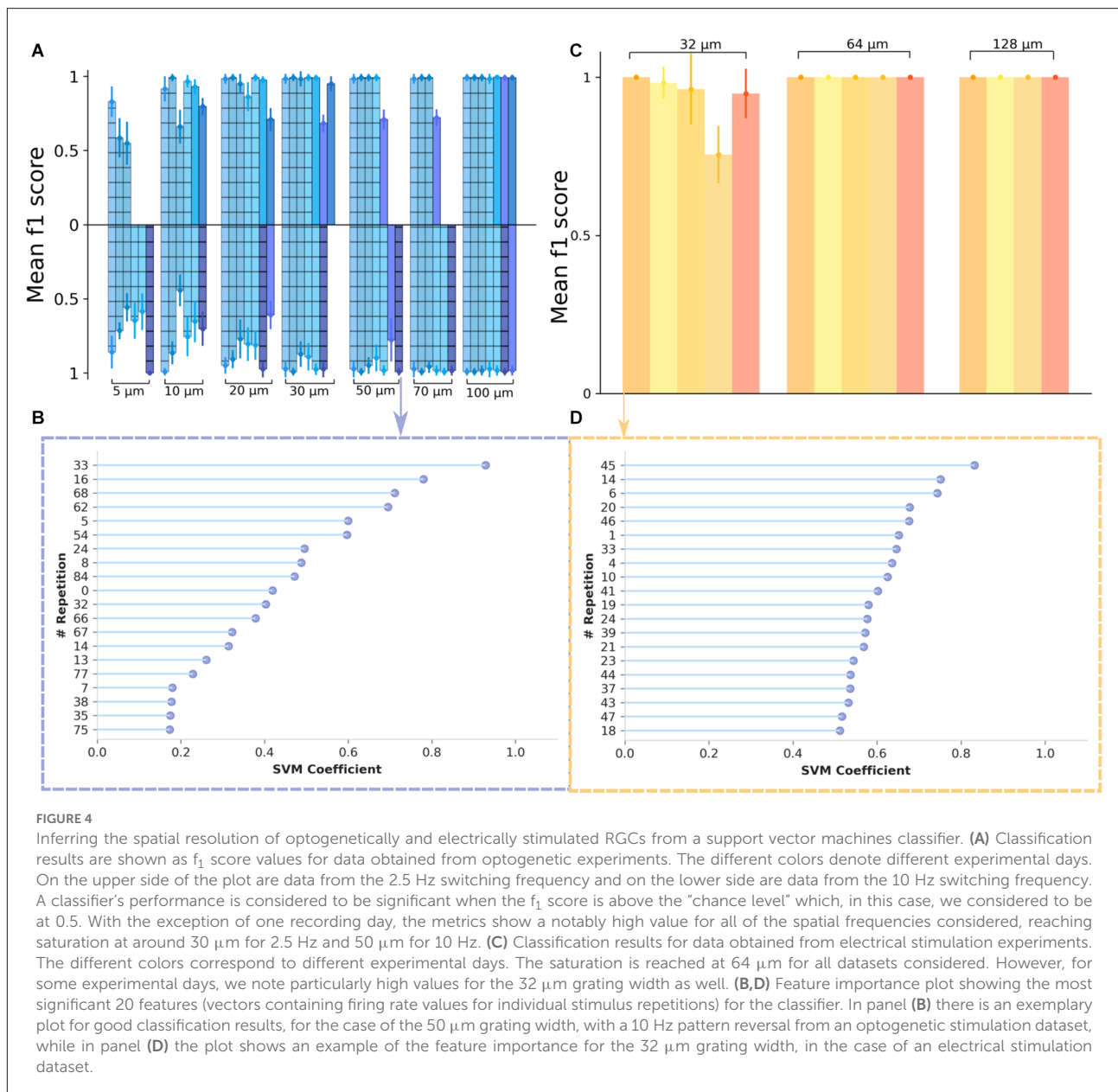
while the remaining repetitions were used to test the discrimination performance.

We chose to refer to the f_1 score as a metric and, to test the robustness of the model, we used a 10 fold cross-validation (see “Materials and methods” Section), while also shuffling the data to ensure a random selection. In the first analysis, we investigated the cell responses to different switching frequencies: at 10 Hz and 2.5 Hz, respectively. The predictions (f_1 -score) for optogenetic stimulation and various spatial frequencies are shown in **Figure 4A** (frequency 2.5 Hz—upper bar plots; 10 Hz—lower bar plots). The results are presented separately for recordings made on retinas where ChR2 was expressed in RGCs (hashed bars) and for recordings where ChR2 was expressed in rod BCs (filled bars). We obtained remarkably high metrics in the case of optogenetic stimulation. The results indicate that the classifier performs well, with only small standard deviation values, ranging between 1% and 12%, and f_1 scores above 73% for all experiments with gratings at least 10 μm wide. Individual values varied between preparations. Without differentiating between the two strains, the average f_1 -score for the grating of 30 μm was 93.7% for 2.5 Hz ($n = 8$ experiments), 94.3% for 10 Hz ($n = 6$ experiments), 83% for the grating of 10 μm at 2.5 Hz frequency switch ($n = 6$ experiments), and 73.1% for 10 Hz ($n = 6$ experiments). Considering the difference between the strains we noted, for the 20 μm grating and a 2.5 Hz stimulation a score of 95.5% for the samples where ChR2 was expressed in the RGCs ($n = 5$ experiments) and 84.1% for the other mouse strain ($n = 2$ experiments), while for 30 μm , delivered at 2.5 Hz, a score of 98.3% was obtained for samples with transduced RGCs ($n = 5$ experiments) and 87.48% for the samples with transduced rod BCs ($n = 3$ experiments). Although the number of recordings prevents a rigorous test for statistical significance, we identify a high prediction accuracy for narrow gratings in both mouse strains.

The high prediction accuracy is quite remarkable, provided that both gratings with narrow stripes stimulate the RGCs. We asked, if the high prediction value is mainly determined by one or a few stimulated RGCs. The percentage of contributing cells was above 20% of the whole population irrespective of the stimulation frequencies (2.5 and 10 Hz).

These values are in agreement with a previous study on optogenetic stimulation of RGCs (Reh et al., 2021). However, we also had recordings where the classifier showed poor performance. To identify a potential source, we plotted the most informative features, the ones with the highest coefficients of the SVM, considering data from optogenetic stimulation with a phase reversal at 10 Hz and a spatial frequency of 50 μm (**Figure 4B**). From **Figure 4B**, we see that the coefficients are not uniformly distributed, the classifier assigns weights to the incorrectly classified data.

Next, we asked how well the two grating stimuli are discriminated upon electrical epiretinal stimulation. After initial processing of the recordings, we employed the support vector



machines (SVM) classifier to infer the stimulation phase from the firing rates of the RGC. The firing rates of all identified RGCs (irrespective if they were stimulated or not) were used as input values of the SVM (see "Materials and methods" Section).

To test the robustness of the model, we used the StratifiedKFold() method, with 10 folds, while also shuffling the data to ensure a random selection. The results (**Figures 4C,D**) indicate that the classifier performs well, with only small standard deviation values, ranging between 5% and 13%. The mean f_1 -score for electrical stimulation with a 32 μm wide grating stimulus was 86.4% ($n = 5$ experiments) and higher for larger gratings.

Finally, we evaluated four recordings were for both, optogenetic and electrical stimulation a sufficiently large number of retinal ganglion cells (>30 RGCs) was responsive to both stimulation modalities. Recordings where either modality activated too few cells were not compared as this biased the evaluation. We first restricted the evaluation to the subset of RGCs activated by electrical and optogenetic stimuli (**Figure 5A**). The average prediction accuracy (f_1 score) based on this subset was: 87.7% for electrical stimulation with 32 μm gratings and 89.8% for optogenetic stimulation with 30 μm gratings. These average values are not statistically different (Wilcoxon-Rank-Sum test); however, the low number

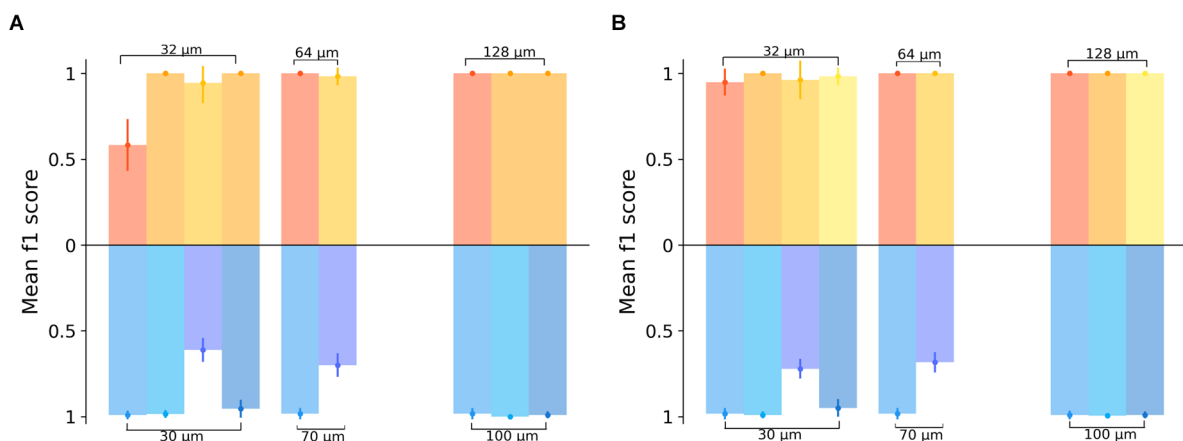


FIGURE 5

Comparing the spatial resolution of electrically or optogenetically stimulated RGCs in the same retinal sample. **(A)** Classification results of the grating pattern reversal stimuli inferred from a subset of RGCs responding to both stimulation types, electrical (yellow) and optogenetic (blue). In the upper part of the graph, the yellow color-coded bars show the results obtained from four different electrically stimulated retinæ. The blue scheme shows the results for the same responsive RGCs in the same four retinæ upon optogenetic stimulation. Each bar for the electrical stimulation corresponds to a bar on the optogenetic stimulation at the same x-position on the graph, indicating that the same experimental day and the same sample was used in the analysis. We note that for gratings wider 32 μm not all protocols were applied or activated sufficient RGCs. **(B)** Classification results for the full datasets in the four retinæ stimulated by electrical and optogenetic means, i.e., with RGCs responding to either electrical or optogenetic stimulation. In the upper part of the graph, the yellow color-coded bars show the results from the RGC datasets upon electrical stimulation, while in the lower part the prediction results inferred from the optogenetic stimulation are shown. Each bar for the electrical stimulation corresponds to a bar on the optogenetic stimulation at the same x-position on the graph, indicating that the same sample was considered in both cases.

of retinal samples compared here ($n = 4$) prevents a rigorous interpretation. The number of RGCs identified upon electrical or optogenetic stimulation in one single retina is not identical. We, therefore, compared the prediction for the four retina using for each retinae the entire responsive RGC population (Figure 5B). The prediction results increased only slightly for both electrical and optogenetic stimulation when considering the full RGC population activated by each modality (average f_1 score = 97.8% for electrical stimuli with 32 μm gratings vs. average f_1 score = 90.1% for optogenetic stimulation with 30 μm gratings). On average, high discrimination f_1 scores were detected irrespective of the stimulation method, when considering retinae stimulated by both modalities.

Discussion

In this study, we estimated the spatial resolution achieved by electrical or optogenetic artificial stimulation using the spiking output of the activated retinal ganglion cells. The artificial stimuli were applied in epiretinal configuration to late-stage photoreceptor degenerated retina. The spatial resolution was inferred from the discrimination of grating pattern reversal stimuli based on a computational model using the activity of retinal ganglion cells. The model provided a high degree of discriminability for optogenetic stimuli with very fine gratings (f_1 score > 73%, 10 μm bar width) and a similarly high degree

of discrimination for electrical stimuli (>86%, 32 μm bar width). These results are remarkable given that the retinal ganglion cell's morphology extends over a much larger diameter.

In the following we relate our results to previous work, discuss them from a biophysical perspective and conclude with suggestions how these results may be used for the development of further retinal implants.

The results presented here aimed to clarify the question, how the two investigated artificial stimulation strategies (optogenetic or electrical) compare when applied to the *ex vivo* retina. To eliminate variability across preparations we investigated the very same *ex vivo* retina subjected to both stimulus modalities, which had not been the case in previous studies (Corna et al., 2021; Reh et al., 2021, 2022). Our results indicate that high and very similar discrimination scores are obtained for the two stimulus modalities using the same computational model. The discriminability of electrical grating stimuli (32 μm –0.54 cpd) and of optogenetic stimuli (10 μm –1.75 cpd) can only be explained by a local stimulation of cell somata and/or axon initial segment while avoiding dendrites and distal axonal compartments. The stimulation of the axon initial segment, the most excitable cellular compartment (Fried et al., 2009; Werginz et al., 2014) cannot be identified or distinguished in this study from the stimulation of the cell body.

For optogenetic stimulation we observed two spiking patterns in the stimulated RGCs: if ChR2 was expressed in rod bipolar cells, we detected RGC spiking always in

both phases of the grating stimulus. This result indicates qualitatively that even at the late retinal degeneration stage the synaptic connectivity between bipolar cells and retinal ganglion cells is preserved. In contrast, when ChR2 was expressed in PV-positive RGCs we detected often increased spiking in one of the two stimulus phases only (Figure 2A). This result indicates that for optogenetic stimulation at either 10 or 2.5 Hz only the cell soma and/or the axon initial segment is activated. The results for optogenetic stimulation extend those presented earlier by our lab (Reh et al., 2021, 2022). For stimulation of optogenetically transduced rod bipolar cells, the discrimination reported previously (Reh et al., 2022) was not as high as reported here. Possible reasons might be the different computational algorithm as well as variability in the recordings.

The estimation of spatial resolution for electrical stimuli followed the approach used by Lorach et al. (2015) and by Chenais et al. (2021) and is spatially equivalent to the optogenetic stimulus. However, in contrast to, the pulsatile stimuli used in previous work (Lorach et al., 2015) we did not encounter fading of the induced RGC spiking activity, but a reliable response (Figures 3A,B) to all sinusoidal stimuli. More interestingly, we did not detect spiking activity caused by the grating stimulus for one of the reversals. This is in contrast to the results obtained for short pulsatile waveforms (Lorach et al., 2015; Chenais et al., 2021) and may help to solve the open question of avoidance of axonal stimulation (Beyeler et al., 2019; Tandon et al., 2021; Vilku et al., 2021) in epiretinal configuration. The grating stimulus used here isolates the source of activation, i.e., helps separate between activation of the soma and distal axons. If distal axons would be activated the RGC spike pattern should be identical for every stimulus phase. Our results of phase-specific RGC activation (Figures 3A,B) indicate direct somatic stimulation. For narrow grids (bar width: 32 μm), we detected for some cells a stimulation in both stimulus phases. This suggests that for the monopolar configuration used here the electric field is not confined to the 32 μm above the electrodes but spreads laterally. A better discrimination and refinement may be obtained if the return electrode is close to the stimulation electrode (Ho et al., 2018) or by three-dimensional structures (Flores et al., 2019). Note, that for grids with a high spatial resolution we detected few cells with a relative firing rate exceeding 0.1. Therefore, the statement of high spatial resolution in artificial vision should be carefully distinguished from the statement of identifying small objects, which had been addressed i.e., by Chenais et al. (2021). The latter appears more difficult and potentially conflicting with electrode safety issues (Corna et al., 2018).

In laboratory conditions, we and others have reported high spatial and temporal resolution of stimulated RGC activity both for epiretinal electrical (Weitz et al., 2015; Corna et al., 2021) and optogenetic stimulation (Ferrari et al., 2020; Gauvain et al., 2021; Reh et al., 2021; Chaffiol et al., 2022; Khabou

et al., 2022). This represents an encouraging result for future vision restoration. However, it also contrasts with many *in vivo* studies (Tomita et al., 2010; Ganjawala et al., 2019; McGregor et al., 2020), including the reports from human patients (Humayun et al., 2012; Stingl et al., 2017; Palanker et al., 2020; Sahel et al., 2021). We speculate that in laboratory conditions precise optical focus is easily achieved but may represent a challenge for most *in vivo* optogenetic conditions (Ronzitti et al., 2017). Similarly, for *ex vivo* electrical stimulation the interfacing between stimulation electrodes and RGCs within the recording time of a few hours is very tight (Zeitler et al., 2011) in contrast to the $\sim 20\mu\text{m}$ assumed *in vivo* (Ayton et al., 2020). Furthermore, the poor resolution achieved by electrical epiretinal implants had been attributed to axonal activation leading to elongated percepts (Beyeler et al., 2019). Sinusoidal stimuli likely improve the resolution (Weitz et al., 2015; Corna et al., 2021), but this had not been tested in clinical trials. Finally, we have implicitly assumed here that the differential response of RGCs to different artificial grating stimuli can be transferred to visual acuity. This needs to be confirmed in future studies using healthy retina and physiological light stimuli.

One of the future goals may therefore be to consider the lessons learned in recent years for future implants. Several promising developments are underway, including the optimization of electrical stimulation waveforms (Schütz et al., 2020; Löhler et al., 2022), optimization of optogenetic transduction using novel AAV viruses (Gauvain et al., 2021), and focused photo-stimulation (Ronzitti et al., 2017; Emiliani et al., 2022).

Data availability statement

The datasets presented in this study can be found in online repositories. The names of the repository/repositories and accession number(s) can be found below: https://gitlab.com/CAE157/frontiers_in_neuroscience_code_base.

Author contributions

ACoj performed the data analysis, part of the experiments, and wrote the manuscript. ACor and MR gathered experimental data. GZ contributed to the experimental planning and manuscript writing. All authors contributed to the article and approved the submitted version.

Funding

This work has received funding from the European Union's Horizon 2020 research and innovation program under

the Marie Skłodowska-Curie grant agreement No. 861423 (enTRAIN Vision).

Acknowledgments

We would like to thank enTRAIN Vision project for financial support.

Conflict of interest

The authors declare that the research was conducted in the absence of any commercial or financial relationships that could be construed as a potential conflict of interest.

References

- Ayton, L. N., Barnes, N., Dagnelie, G., Fujikado, T., Goetz, G., Hornig, R., et al. (2020). An update on retinal prostheses. *Clin. Neurophysiol.* 131, 1383–1398. doi: 10.1016/j.clinph.2019.11.029
- Bertotti, G., Barnes, N., Dagnelie, G., Fujikado, T., Goetz, G., Hornig, R., et al. (2014). “A CMOS-based sensor array for in-vitro neural tissue interfacing with 4225 recording sites and 1024 stimulation sites,” in *IEEE 2014 Biomedical Circuits and Systems Conference, BioCAS 2014—Proceedings*, (Lausanne, Switzerland: Institute of Electrical and Electronics Engineers Inc.), 131, 304–307. doi: 10.1109/BioCAS.2014.6981723
- Beyeler, M., Nanduri, D., Weiland, J. D., Rokem, A., Boynton, G. M., and Fine, I. (2019). A model of ganglion axon pathways accounts for percepts elicited by retinal implants. *Sci. Rep.* 9:9199. doi: 10.1038/s41598-019-45416-4
- Bi, A., Cui, J., Ma, Y.-P., Olshevskaya, E., Pu, M., Dizhoor, A. M., et al. (2006). Ectopic expression of a microbial-type rhodopsin restores visual responses in mice with photoreceptor degeneration. *Neuron* 50, 23–33. doi: 10.1016/j.neuron.2006.02.026
- Busskamp, V., Duebel, J., Balya, D., Fradot, M., Viney, T. J., Siebert, S., et al. (2010). Genetic reactivation of cone photoreceptors restores visual responses in retinitis pigmentosa. *Science* 329, 413–417. doi: 10.1126/science.1190897
- Cehajic-Kapetanovic, J., Eleftheriou, C., Allen, A. E., Milosavljevic, N., Pienaar, A., Bedford, R., et al. (2015). Restoration of vision with ectopic expression of human rod opsin. *Curr. Biol.* 25, 2111–2122. doi: 10.1016/j.cub.2015.07.029
- Cha, S., Ahn, J., Jeong, Y., Lee, Y. H., Kim, H. K., Lee, D., et al. (2022). Stage-dependent changes of visual function and electrical response of the retina in the rd10 mouse model. *Front. Cell. Neurosci.* 16:926096. doi: 10.3389/fncel.2022.926096
- Chaffiol, A., Provansal, M., Joffrois, C., Blaize, K., Labernede, G., Goulet, R., et al. (2022). *In vivo* optogenetic stimulation of the primate retina activates the visual cortex after long-term transduction. *Mol. Ther. Methods Clin. Dev.* 24, 1–10. doi: 10.1016/j.omtm.2021.11.009
- Chang, B., Hawes, N. L., Hurd, R. E., Davisson, M. T., Nusinowitz, S., and Heckenlively, J. R. (2002). Retinal degeneration mutants in the mouse. *Vis. Res.* 42, 517–525. doi: 10.1016/s0042-6989(01)00146-8
- Chenais, N. A. L., Airaghi Leccardi, M. J. I., and Ghezzi, D. (2021). Photovoltaic retinal prosthesis restores high-resolution responses to single-pixel stimulation in blind retinas. *Commun. Mater.* 2:28. doi: 10.1038/s43246-021-00133-2
- Cideciyan, A. V., Roman, A. J., Jacobson, S. G., Yan, B., Pascolini, M., Chang, J., et al. (2016). Developing an outcome measure with high luminance for optogenetics treatment of severe retinal degenerations and for gene therapy of cone diseases. *Invest. Ophthalmol. Vis. Sci.* 57, 3211–3221. doi: 10.1167/iovs.16-19586
- Corna, A., Herrmann, T., and Zeck, G. (2018). Electrode-size dependent thresholds in subretinal neuroprosthetic stimulation. *J. Neural Eng.* 15:045003. doi: 10.1088/1741-2552/aac1c8
- Corna, A., Ramesh, P., Jetter, F., Lee, M.-J., Macke, J. H., and Zeck, G. (2021). Discrimination of simple objects decoded from the output of retinal ganglion cells upon sinusoidal electrical stimulation. *J. Neural Eng.* 18:46086. doi: 10.1088/1741-2552/ac0679
- da Cruz, L., Dorn, J. D., Humayun, M. S., Dagnelie, G., Handa, J., Barale, P. O., et al. (2016). Five-year safety and performance results from the argus II retinal prosthesis system clinical trial. *Ophthalmology* 123, 2248–2254. doi: 10.1016/j.optha.2016.06.049
- Doroudchi, M. M., Greenberg, K. P., Liu, J., Silka, K. A., Boyden, E. S., Lockridge, J. A., et al. (2011). Virally delivered channelrhodopsin-2 safely and effectively restores visual function in multiple mouse models of blindness. *Mol. Ther.* 19, 1220–1229. doi: 10.1038/mt.2011.69
- Drucker, H., Greenberg, K. P., Liu, J., Silka, K. A., Boyden, E. S., Lockridge, J. A., et al. (1997). Support vector regression machines. *Adv. Neural Inform. Process. Sys.* 19, 155–161.
- Eickenscheidt, M., and Zeck, G. (2014). Action potentials in retinal ganglion cells are initiated at the site of maximal curvature of the extracellular potential. *J. Neural Eng.* 11:036006. doi: 10.1088/1741-2560/11/3/036006
- Emiliani, V., Entcheva, E., Hedrich, R., Hegemann, P., Lüscher, C., Mahn, M., et al. (2022). Optogenetics for light control of biological systems. *Nat. Rev. Methods Primers* 2:55. doi: 10.1038/s43586-022-00136-4
- Ferlauto, L., Leccardi, M. J. I. A., Chenais, N. A. L., Gilliéron, S. C. A., Vagni, P., Bevilacqua, M., et al. (2018). Design and validation of a foldable and photovoltaic wide-field epiretinal prosthesis. *Nat. Commun.* 9:992. doi: 10.1038/s41467-018-03386-7
- Ferrari, U., Deny, S., Sengupta, A., Caplette, R., Trapani, E., Sahel, J. A., et al. (2020). Towards optogenetic vision restoration with high resolution. *PLoS Comput. Biol.* 16:e1007857. doi: 10.1371/journal.pcbi.1007857
- Flores, T., Huang, T., Bhuckory, M., Ho, E., Chen, Z., Dalal, R., et al. (2019). Honeycomb-shaped electro-neural interface enables cellular-scale pixels in subretinal prosthesis. *Sci. Rep.* 9:10657. doi: 10.1038/s41598-019-47082-y
- Forli, A., Pisoni, M., Printz, Y., Yizhar, O., and Fellin, T. (2021). Optogenetic strategies for high-efficiency all-optical interrogation using blue-light-sensitive opsins. *eLife* 10:e63359. doi: 10.7554/eLife.63359
- Fried, S. I., Lasker, A. C. W., Desai, N. J., Eddington, D. K., and Rizzo, J. F., 3rd (2009). Axonal sodium-channel bands shape the response to electric stimulation in retinal ganglion cells. *J. Neurophysiol.* 101, 1972–1987. doi: 10.1152/jn.91081.2008
- Ganjawala, T. H., Lu, Q., Fennner, G. W., Abrams, T. H., and Pan, Z.-H. (2019). Improved CoChR variants restore visual acuity and contrast sensitivity in a mouse model of blindness under ambient light conditions. *Mol. Ther.* 27, 1195–1205. doi: 10.1016/j.yimthe.2019.04.002
- Gargini, C., Terzibasi, E., Mazzoni, F., and Strettoi, E. (2007). Retinal organization in the retinal degeneration 10 (rd10) mutant mouse: a morphological and ERG study. *J. Comp. Neurol.* 500, 222–238. doi: 10.1002/cne.21144
- Gauvain, G., Akolkar, H., Chaffiol, A., Arcizet, F., Khoei, M. A., Desrosiers, M., et al. (2021). Optogenetic therapy: high spatiotemporal resolution and pattern

Publisher's note

All claims expressed in this article are solely those of the authors and do not necessarily represent those of their affiliated organizations, or those of the publisher, the editors and the reviewers. Any product that may be evaluated in this article, or claim that may be made by its manufacturer, is not guaranteed or endorsed by the publisher.

Supplementary material

The Supplementary Material for this article can be found online at: <https://www.frontiersin.org/articles/10.3389/fncel.2022.1033738/full#supplementary-material>.

discrimination compatible with vision restoration in non-human primates. *Commun. Biol.* 4:125. doi: 10.1038/s42003-020-01594-w

Greenberg, K. P., Pham, A., and Werblin, F. S. (2011). Differential targeting of optical neuromodulators to ganglion cell soma and dendrites allows dynamic control of center-surround antagonism. *Neuron* 69, 713–720. doi: 10.1016/j.neuron.2011.01.024

Ho, E., Smith, R., Goetz, G., Lei, X., Galambos, L., Kamins, T. I., et al. (2018). Spatiotemporal characteristics of retinal response to network-mediated photovoltaic stimulation. *J. Neurophysiol.* 119, 389–400. doi: 10.1152/jn.00872.2016

Humayun, M. S., Dorn, J. D., Dagnelie, G., Sahel, J. A., and Stanga, P. E. (2012). Interim results from the international trial of second sight's visual prosthesis. *Ophthalmology* 119, 779–788. doi: 10.1016/j.ophtha.2011.09.028

Ivanova, E., Hwang, G. S., Pan, Z.-H., and Troilo, D. (2010). Evaluation of AAV-mediated expression of Chop2-GFP in the marmoset retina. *Invest. Ophthalmol. Visual Sci.* 51, 5288–5296. doi: 10.1167/iiov.10-5389

Jacobson, S. G., Aleman, T. S., Cideciyan, A. V., Sumaroka, A., Schwartz, S. B., Windors, E. A., et al. (2018). Identifying photoreceptors in blind eyes caused by RPE65 mutations: prerequisite for human gene therapy success. *Proc. Natl. Acad. Sci. U S A* 102, 6177–6182. doi: 10.1073/pnas.0500646102

Khabou, H., Garita-Hernandez, M., Chaffiol, A., Reichman, S., Jaillard, C., Brazhnikova, E., et al. (2018). Noninvasive gene delivery to foveal cones for vision restoration. *JCI Insight* 3:e96029. doi: 10.1172/jci.insight.96029

Khabou, H., Garita-Hernandez, M., Chaffiol, A., Reichman, S., Jaillard, C., Brazhnikova, E., et al. (2022). Optogenetic targeting of AII amacrine cells restores retinal computations performed by the inner retina. *bioRxiv* [Preprint]. doi: 10.1101/2022.07.28.501925

Kralik, J., Stocker, N., and Kleinlogel, S. (2022). Bipolar cell targeted optogenetic gene therapy restores parallel retinal signaling and high-level vision in the degenerated retina. *Commun. Biol.* 5:116. doi: 10.1038/s42003-022-04016-1

Lagali, P. S., Balya, D., Awatramani, G. B., Münch, T. A., Kim, D. S., Busskamp, V., et al. (2008). Light-activated channels targeted to ON bipolar cells restore visual function in retinal degeneration. *Nat. Neurosci.* 11, 667–675. doi: 10.1038/nm.2117

Leibig, C., Wachtler, T., and Zeck, G. (2016). Unsupervised neural spike sorting for high-density microelectrode arrays with convolutive independent component analysis. *J. Neurosci. Methods* 271, 1–13. doi: 10.1016/j.jneumeth.2016.06.006

Löhler, P., Pickhinke, A., Erbslöh, A., Kokozinski, R., Seidl, K. (2022). "SoC for retinal ganglion cell stimulation with integrated sinusoidal kilohertz frequency waveform generation," in *2022 17th Conference on Ph.D. Research in Microelectronics and Electronics (PRIME)*, (Villasimius, SU, Italy: IEEE), 271, 341–344. doi: 10.1109/PRIME55000.2022.9816766

Lorach, H., Goetz, G., Smith, R., Lei, X., Mandel, Y., Kamins, T., et al. (2015). Photovoltaic restoration of sight with high visual acuity. *Nat. Med.* 21, 476–482. doi: 10.1038/nm.3851

Loudin, J. D., Simanovskii, D. M., Vijayraghavan, K., Sramek, C. K., Butterwick, A. F., Huie, P., et al. (2007). Optoelectronic retinal prosthesis: system design and performance. *J. Neural Eng.* 4, S72–S84. doi: 10.1088/1741-2560/4/1/S09

Lu, Q., Ganjawala, T. H., Krstevski, A., Abrams, G. W., and Pan, Z. H. (2020). Comparison of AAV-mediated optogenetic vision restoration between retinal ganglion cell expression and ON bipolar cell targeting. *Mol. Ther. Methods Clin. Dev.* 18, 15–23. doi: 10.1016/j.omtm.2020.05.009

Macé, E., Lu, Q., Ganjawala, T. H., Krstevski, A., Abrams, G. W., Pan, Z. H., et al. (2015). Targeting channelrhodopsin-2 to ON-bipolar cells with vitreally administered AAV restores ON and OFF visual responses in blind mice. *Mol. Ther.* 23, 7–16. doi: 10.1038/mt.2014.154

McGregor, J. E., Godat, T., Dhakal, K. R., Parkins, K., Strazzeri, J. M., Bateman, B. A., et al. (2020). Optogenetic restoration of retinal ganglion cell activity in the living primate. *Nat. Commun.* 11:1703. doi: 10.1038/s41467-020-15317-6

Muqit, M. M. K., Velikay-Parel, M., Weber, M., Dupeyron, G., Audemard, D., Corcostegui, B., et al. (2019). Six-month safety and efficacy of the intelligent retinal implant system II device in retinitis pigmentosa. *Ophthalmology* 126, 637–639. doi: 10.1016/j.ophtha.2018.11.010

Neymotin, A. S., Lytton, W. W., Olypher, A. V., and Fenton, A. A. (2011). Measuring the quality of neuronal identification in ensemble recordings. *J. Neurosci.* 31, 16398–16409. doi: 10.1523/JNEUROSCI.4053-11.2011

Palanker, D., and Goetz, G. (2018). Restoring sight with retinal prostheses. *Physics Today* 71, 26–32. doi: 10.1063/PT.3.3970

Palanker, D., Vankov, A., and Huie, P. (2005). Design of a high-resolution optoelectronic retinal prosthesis. *J. Neural Eng.* 2, S105–S120. doi: 10.1088/1741-2560/2/1/012

Palanker, D., Le Mer, Y., Mohand-Said, S., Muqit, M., and Sahel, S. A. (2020). Photovoltaic restoration of central vision in atrophic age-related macular degeneration. *Ophthalmology* 127, 1097–1104. doi: 10.1016/j.ophtha.2020.02.024

Pisner, D. A., and Schnyer, D. M. (2019). "Support vector machine," in *Machine Learning: Methods and Applications to Brain Disorders*, 31, (Cambridge, Massachusetts, USA: Academic Press), 101–121. doi: 10.1016/B978-0-12-815739-8.00006-7

Reh, M., Lee, M. J., Schmierer, J., and Zeck, G. (2021). Spatial and temporal resolution of optogenetically recovered vision in ChR2-transduced mouse retina. *J. Neural Eng.* 18:056013. doi: 10.1088/1741-2552/abe39a

Reh, M., Lee, M.-J., and Zeck, G. (2022). Expression of channelrhodopsin-2 in rod bipolar cells restores ON and OFF responses at high spatial resolution in blind mouse retina. *Adv. Ther.* 5:2100164. doi: 10.1002/adtp.202100164

Ronzitti, E., Ventalon, C., Canepari, M., Forget, B. C., Papagiakoumou, E., and Emiliani, V. (2017). Recent advances in patterned photostimulation for optogenetics. *J. Opt.* 19:113001. doi: 10.1088/2040-8986/aa8299

Sahel, J.-A., Boulanger-Scemama, E., Pagot, C., Arleo, A., Galluppi, F., Martel, J. N., et al. (2021). Partial recovery of visual function in a blind patient after optogenetic therapy. *Nat. Med.* 27, 1223–1229. doi: 10.1038/s41591-021-01351-4

Schütz, H., Boulanger-Scemama, E., Pagot, C., Arleo, A., Galluppi, F., Martel, J. N., et al. (2020). "Pseudo-recovery of visual function as an efficient electrode driver for sinusoidal stimulation of retinas," in *Proceedings - IEEE International Symposium on Circuits and Systems*, (Seville, Spain: Institute of Electrical and Electronics Engineers Inc.), 1–5. doi: 10.1109/ISCAS45731.2020.9180425

Shemesh, O. A., Tanese, D., Zampini, V., Linghu, C., Piatkevich, K., Ronzitti, E., et al. (2017). Temporally precise single-cell-resolution optogenetics. *Nat. Neurosci.* 20, 1796–1806. doi: 10.1038/s41593-017-0018-8

Stingl, K., Schippert, R., Bartz-Schmidt, K. U., Besch, D., Cottrill, C. L., Edwards, T. L., et al. (2017). Interim results of a multicenter trial with the new electronic subretinal implant alpha AMS in 15 patients blind from inherited retinal degenerations. *Front. Neurosci.* 11:445. doi: 10.3389/fnins.2017.00445

Stutzki, H., Helmhold, F., Eickenscheidt, M., and Zeck, G. (2016). Subretinal electrical stimulation reveals intact network activity in the blind mouse retina. *J. Neurophysiol.* 116, 1684–1693. doi: 10.1152/jn.01095.2015

Tandon, P., Bhaskhar, N., Shah, N., Madugula, S., Grosberg, L., Fan, V. H., et al. (2021). Automatic identification of axon bundle activation for epiretinal prosthesis. *IEEE Trans. Neural Syst. Rehabil. Eng.* 29, 2496–2502. doi: 10.1109/TNSRE.2021.3128486

Tharwat, A. (2018). Classification assessment methods. *Appl. Comput. Informatics* 17, 168–192. doi: 10.1016/j.aci.2018.08.003

Tomita, H., Sugano, E., Isago, H., Hiroi, T., Wang, Z., Ohta, E., et al. (2010). Channelrhodopsin-2 gene transduced into retinal ganglion cells restores functional vision in genetically blind rats. *Exp. Eye Res.* 90, 429–436. doi: 10.1016/j.exer.2009.12.006

van Wyk, M., Pielecka-Fortuna, J., Löwel, S., and Kleinlogel, S. (2015). Restoring the ON switch in blind retinas: opto-mGluR6, a next-generation, cell-tailored optogenetic tool. *PLoS Biol.* 13:e1002143. doi: 10.1371/journal.pbio.1002143

Vilkhu, R. S., Madugula, S. S., Grosberg, L. E., Gogliettino, A. R., Hottowy, P., Dabrowski, W., et al. (2021). Spatially patterned bi-electrode epiretinal stimulation for axon avoidance at cellular resolution. *bioRxiv* [Preprint]. doi: 10.1088/1741-2552/ac3450

Weitz, A. C., Nanduri, D., Behrend, M. R., Gonzalez-Calle, A., Greenberg, R. J., Humayun, M. S., et al. (2015). Improving the spatial resolution of epiretinal implants by increasing stimulus pulse duration. *Sci. Transl. Med.* 7:318ra203. doi: 10.1126/scitranslmed.aac4877

Werginz, P., Fried, S. I., and Rattay, F. (2014). Influence of the sodium channel band on retinal ganglion cell excitation during electric stimulation - a modeling study. *Neuroscience* 266, 162–177. doi: 10.1016/j.neuroscience.2014.01.067

Wilke, R. G. H., Moghadam, G. K., Lovell, N. H., Suaning, G. J., and Dokos, S. (2011). Electric crosstalk impairs spatial resolution of multi-electrode arrays in retinal implants. *J. Neural Eng.* 8:046016. doi: 10.1088/1741-2560/8/4/046016

Yi, C.-W., Yu, S.-H., Lee, E.-S., Lee, J.-G., and Jeon, C.-J. (2012). Types of parvalbumin-containing retinotectal ganglion cells in mouse. *Acta Histochem. Cytochem.* 45, 201–210. doi: 10.1267/ahc.11061

Zeidler, R., Fromherz, P., and Zeck, G. (2011). Extracellular voltage noise probes the interface between retina and silicon chip. *Appl. Phys. Lett.* 99:263702. doi: 10.1063/1.3672224

Zrenner, E., Yi, C. W., Yu, S. H., Lee, E. S., Lee, J. G., Jeon, C. J., et al. (2017). "The subretinal implant ALPHA: implantation and functional results," in *Artificial Vision*, eds V. Gabel (Cham: Springer), 65–83. doi: 10.1007/978-3-319-41876-6_6



OPEN ACCESS

EDITED BY

Maesoon Im,
Korea Institute of Science
and Technology (KIST), South Korea

REVIEWED BY

Mohit Naresh Shivdasani,
University of New South Wales,
Australia

*CORRESPONDENCE

Eduardo Fernández
e.fernandez@umh.es

SPECIALTY SECTION

This article was submitted to
Cellular Neurophysiology,
a section of the journal
Frontiers in Cellular Neuroscience

RECEIVED 01 September 2022

ACCEPTED 24 November 2022

PUBLISHED 13 December 2022

CITATION

Grani F, Soto-Sánchez C, Fimia A and
Fernández E (2022) Toward
a personalized closed-loop
stimulation of the visual cortex:
Advances and challenges.
Front. Cell. Neurosci. 16:1034270.
doi: 10.3389/fncel.2022.1034270

COPYRIGHT

© 2022 Grani, Soto-Sánchez, Fimia
and Fernández. This is an open-access
article distributed under the terms of
the [Creative Commons Attribution
License \(CC BY\)](#). The use, distribution
or reproduction in other forums is
permitted, provided the original
author(s) and the copyright owner(s)
are credited and that the original
publication in this journal is cited, in
accordance with accepted academic
practice. No use, distribution or
reproduction is permitted which does
not comply with these terms.

Toward a personalized closed-loop stimulation of the visual cortex: Advances and challenges

Fabrizio Grani¹, Cristina Soto-Sánchez^{1,2}, Antonio Fimia ³
and Eduardo Fernández^{1,2*}

¹Institute of Bioengineering, Universidad Miguel Hernández de Elche, Elche, Spain, ²Biomedical Research Networking Center in Bioengineering, Biomaterials and Nanomedicine (CIBER-BBN), Madrid, Spain, ³Departamento de Ciencia de Materiales, Óptica y Tecnología Electrónica, Universidad Miguel Hernández de Elche, Elche, Spain

Current cortical visual prosthesis approaches are primarily unidirectional and do not consider the feed-back circuits that exist in just about every part of the nervous system. Herein, we provide a brief overview of some recent developments for better controlling brain stimulation and present preliminary human data indicating that closed-loop strategies could considerably enhance the effectiveness, safety, and long-term stability of visual cortex stimulation. We propose that the development of improved closed-loop strategies may help to enhance our capacity to communicate with the brain.

KEYWORDS

closed-loop stimulation, visual prostheses, neural interfaces, brain stimulation, local field potentials

Introduction

Visual impairment has a profound impact on the lives of those who experience it (Bourne et al., 2017). Although some novel clinical approaches are becoming available (Higuchi et al., 2017; De Silva and Moore, 2022; Panikker et al., 2022; Van Gelder et al., 2022), unfortunately, there is no treatment for all causes of blindness (Fernandez, 2018; Fernandez et al., 2020). Thus, there are many blind patients for whom there is still no medical treatment. As a consequence of this growing and clearly unmet need, numerous groups worldwide are pursuing other approaches to provide at least a rudimentary sense of vision to the blind.

Visual prostheses are promising solutions to restore functional vision (i.e., visual percepts that could help blind people to recognize objects or to navigate in complex environments). Retinal prostheses are the most successful approach in this field to date

(Nowik et al., 2020; Picaud and Sahel, 2020; Nanegrungsunk et al., 2022), but patients with severe retinal degeneration, glaucoma, or optic atrophy cannot get benefit from a retinal prosthesis. Therefore, there are compelling reasons for the development of alternative approaches that can bypass the retina to restore a functional sense of vision.

In this framework, although the optic nerve or lateral geniculate nucleus could be good targets (Nguyen et al., 2016; Gaillet et al., 2020; Borda et al., 2022; Rassia et al., 2022), several groups are trying to develop visual prostheses designed to directly stimulate the visual cortex (Lee et al., 2016; Beauchamp et al., 2020; Fernandez et al., 2021; Bosking et al., 2022). However, the biological and engineering problems for the success of cortical implants are much more complex than originally believed and involve, for example, long-term biocompatibility issues and challenges related to the encoding of visual information and the delivery of information to implants (Fernandez et al., 2020). In addition, we should be aware that the human brain is arguably one of the most complex systems in nature and that cortical stimulation should be safe, precise, and effective.

To achieve the ambitious objectives envisioned by cortical visual prostheses, we should be able to stimulate the occipital cortex in a way as similar as possible to the physiological response to visual stimuli, mimicking the human visual pathway (Nirenberg and Pandarinath, 2012; Qiao et al., 2019; Brackbill et al., 2020; Li et al., 2022; Price and Gavornik, 2022). In this framework, we should consider that closed-loop circuits exist in just about every part of the nervous system (Farkhondeh Tale Navi et al., 2022; Khodagholy et al., 2022). However, current cortical visual prosthesis approaches are primarily unidirectional and do not incorporate any adaptive system for the modulation of the electrical stimulation used to induce visual perception. Herein, we briefly introduce some recent advances for better control of brain stimulation and present preliminary human data suggesting that a closed-loop approach could significantly improve the performance, safety, and long-term stability of the stimulation of visual cortex neurons.

Learning to control brain electrical stimulation

Electrical stimulation of the brain is the basis of many technologies for the restoration of sensory and motor functions. Brain stimulation has been used for reducing tremors in Parkinson's patients, controlling epileptiform activity, and improving mood in patients with severe depression (Lozano et al., 2019). Additionally, it is now possible to create artificial sensations, with unprecedented resolution, *via* delivery of intracortical microstimulation (Fernandez et al., 2021; Fernandez, 2022; Fifer et al., 2022). However, most current brain stimulation approaches cannot flexibly control the patterns of

activity because, for it to work, we need to know the activity of the neurons surrounding the electrodes and modulate the electrical stimulation in function of this neural activity.

Although stimulating electrodes allow control of the dynamics of populations of neurons, they do not provide insights into the electrophysiological activity of the neurons surrounding the electrodes. Thus, a critical step in the development of closed-loop approaches is the creation of microelectrodes and technologies capable of performing simultaneous stimulation and recording of neural activity.

Currently, bidirectional electrodes that allow stimulation and recording of neural activity at the same time exist, but are limited by the artifacts generated in the recordings by the stimulation (Xu et al., 2018). The detailed description of techniques and materials that allow for the recording of neural activity has been described elsewhere (Stevenson and Kording, 2011; Chen et al., 2017; Hong et al., 2021), but extracellular recordings are the more common type associated with *in vivo* brain recordings. Briefly, electrodes of the order of microns are implanted into the brain and positioned close enough to the neurons of interest to detect the fluctuations in voltage across their membranes. To record from several neurons, a series of microelectrodes can be organized to form a microelectrode array. The main advantage of these microelectrode arrays is that by recording from a number of neurons simultaneously, we can extract more accurately the complex patterns of neuronal activity and get some insights into the information flow (Hong et al., 2021).

Some recent works have led to the development of novel forms of neuromodulation, which are facilitating the ability to manipulate populations of neurons in near real-time. These techniques are based on recording the neural activity around the electrodes and adjusting the electrical stimulation in function of the observed neural activity (closed-loop stimulation). According to the use of the closed-loop approach, these techniques can be divided in device fitting techniques and therapy/efficacy techniques (Table 1).

This procedures allow an improved control of some neurological conditions such as epilepsy (Ranjandish and Schmid, 2020; Farkhondeh Tale Navi et al., 2022), and can also be used for better control of obsessive-compulsive disorders and depression (Figue et al., 2022; Visser-Vandewalle et al., 2022). Furthermore, it has been shown that the outcome of brain stimulation to treat Parkinson's disease can be improved by recording brain activity and stimulating only when the local field potentials collected by electrodes inserted in the subthalamic nucleus exceed a certain threshold (Little et al., 2013), or by associating the brain stimulation to specific phases of patients' tremor activity (Cagnan et al., 2017). Also, the electrical stimulation of the spinal cord for pain therapy can be adjusted based on the evoked compound action potential (ECAP) (Mekhail et al., 2020), while the movement output in spinal cord stimulation for motor recovery can be controlled in

TABLE 1 Examples of closed-loop strategies for neural prostheses.

Aim	Description	Utility	Research/Clinical	References
Epilepsy treatment	Electrical stimulation only when epileptic seizures are detected	Therapy	Clinical	Ranjandish and Schmid, 2020; Farkhondeh Tale Navi et al., 2022
Obsessive-compulsive disorder control	Biomarker-based deep brain stimulation	Therapy	Research	Vissani et al., 2022
Depression control	Biomarker-based deep brain stimulation	Therapy	Research	Scangos et al., 2021
Parkinson's disease control	Electrical stimulation based on local field potentials (LFP) power	Therapy	Clinical	Little et al., 2013
Parkinson's disease control	Electrical stimulation based on the phase of hands tremor	Therapy	Research	Cagnan et al., 2017
Fitting of cochlear implants	Fitting of stimulation threshold based on the contraction of stapedius muscle	Fitting	Research	Weiss et al., 2021
Fitting of cochlear implants	Fitting of stimulation threshold based on evoked compound action potential (ECAP)	Fitting	Research	McKay et al., 2013
Fitting of cochlear implants	Fitting of stimulation threshold based on electrically evoked auditory brainstem response (EABR)	Fitting	Research	Guenser et al., 2015
Fitting of cochlear implants	Fitting of stimulation threshold based on cortical auditory evoked potentials (CAEPs)	Fitting	Research	Visram et al., 2015
Spinal cord stimulation for pain therapy	Adjusting stimulation current based on the measured ECAP	Therapy	Clinical	Mekhail et al., 2020
Spinal cord stimulation for motor control	Modulation of gait features through stimulation parameters	Therapy	Research	Wenger et al., 2014
Retinal electrical stimulation for visual restoration	Modulation of electrical stimulation based on retinal ganglion cells response	Therapy	Research	Guo et al., 2018; Spencer et al., 2019; Shah and Chichilnisky, 2020
Fitting of intracortical visual prostheses	Measure the response of V4 neurons to V1 stimulation	Fitting	Research	Chen et al., 2020
Increase efficacy of stimulation in intracortical visual prostheses	Increase efficacy of electrical stimulation in the visual cortex by LFP phase-locked stimulation	Therapy	Research	Allison-Walker et al., 2020
Brain state dependent stimulation in cortical visual prostheses	Look for a brain state in which stimulating is easier to induce visual perception	Therapy	Research	van Vugt et al., 2018

closed-loop changing the stimulation parameters (Wenger et al., 2014).

The above-mentioned approaches can also be applied to the field of sensory prostheses. Thus, the automatic tuning of stimulation thresholds in cochlear implants can be done by measuring the contraction of the stapedius muscle. This muscle contracts to protect the inner ear from very loud sounds (Borg and Zakrisson, 1973) and measuring its contraction provides objective feedback on the loudness of the sound induced by the electrical stimulation (Weiss et al., 2021). Other measures like ECAP (McKay et al., 2013), electrically evoked auditory brainstem response (EABR) (Guenser et al., 2015), cortical auditory evoked potentials (CAEPs) (Visram et al., 2015) have been studied to automatically fit cochlear implants, but none of them reached a clinical application.

In retinal prosthesis, research on closed-loop stimulation have been done to optimize the stimulation parameters to obtain the desired retinal ganglion cells output in response to a given visual input (Guo et al., 2018; Spencer et al., 2019; Shah and Chichilnisky, 2020). The same approach could be applied in

cortical visual prosthesis using the activity of cortical neurons instead of retinal ganglion cells. For this to be optimal, a larger part of the visual field should be covered by the electrodes in cortical visual prostheses with respect to the current research devices.

However, even with a smaller covering of the visual field it should be feasible to design and develop similar approaches in the field of cortical visual prosthesis for controlling the timing of stimulation, reducing charge requirements, and fitting the device faster. In this framework, a recent study in monkey visual cortex shows that the activity of neurons in V4 provides direct insight into the efficacy of the stimulation in V1 (Chen et al., 2020). This suggests that neurons in higher visual areas could be used, for example, to estimate and adjust V1 thresholds on hundreds of electrodes. Furthermore, besides adjusting the thresholds, the brain signals collected by the electrodes in the visual cortex could reveal a brain state in which it is easier to induce perception. Some preliminary studies in rats support this point of view and show that it is possible to use the information from the local field potentials (LFPs) as

control signals to specify the precise timing of stimulation to reduce charge requirements (Allison-Walker et al., 2020). Moreover, it has been shown in humans that there is a causal relationship between cortical excitation and phosphene perception so that the phase of pre-stimulus oscillatory activity seems linked to visual perception (Dugue et al., 2011), and other studies suggest that the power spectral density at low frequency ($f < 30$ Hz) contains information about visual perception (Gail et al., 2004). Hence, we can hypothesize that the incorporation of measures of neural activity around stimulating electrodes could be helpful to enhance the effectiveness and safety of any cortical visual prostheses. In addition, we could also incorporate other measures such as linear combinations of brain signals in different bandwidths and even information about the pupil size and eye movements to improve the safety, robustness, and reliability of conscious visual perceptions (van Vugt et al., 2018). Table 1 presents some closed-loop neural stimulation approaches currently used, specifying if they are in clinical or research status.

Toward personalized closed-loop stimulation in cortical visual prostheses

Currently, most cortical visual prostheses are primarily unidirectional or open-loop, passing the visual information from the outside world captured by the image acquisition sensors to the implanted microelectrode arrays. In the future, it is expected that a high number of microelectrodes can be implanted into the brain to provide a functional vision, and such a large number of implanted electrodes may pose several stimulation problems (Fernandez, 2018; Rotermund et al., 2019). Therefore, we have to start reconsidering and improving our methods of cortical stimulation for example with closed-loop approaches (Figure 1A; Rotermund et al., 2019).

It has been estimated that we need at least 625 electrodes implanted in visual areas for reading (although at lower speeds) and navigating through complex visual environments (Chen et al., 1992). However, finding the lowest current thresholds able to induce visual perceptions from each single electrode is a time-consuming procedure that requires the user's feedback. Moreover, perception thresholds could vary over time, requiring the users to calibrate each electrode many times. As the brain signals surrounding the electrodes contain information about the spread of currents and brain dynamics, we could determine if the currents used are enough to induce perception simply by measuring the brain response to electrical stimulation. For this to be possible, the brain signals during (or after) stimulation should have distinguishable features in case of perception or no perception. Figure 1B shows an example from our ongoing experiments with intracortical microelectrodes

in blind volunteers in which the neuronal activity after stimulation increases when the stimulation intensity is enough to induce perception (40 μ A in this case). This approach can also be used to construct psychometric curves (relation between stimulus intensity and perception probability) that are practically indistinguishable of the standard psychometric curves using users' feed-back. Figure 1C shows an example for a single electrode using current intensities from 0 to 140 μ A. However, the most robust and reliable features to automatically find perception thresholds still need to be investigated.

On the other hand, there is a need to reduce power consumption and the charge required to elicit reliable phosphene. In this context, brain activity and other physiological signals could be used to find a brain state in which inducing visual perception is easier, thus decreasing the currents needed to induce the visual perceptions. Using the same stimulation parameters, a given pulse train might produce a visual perception or not according to the LFP phase at which the stimulation is sent (Figures 1D,E). This has been reported in experiments in rats (Allison-Walker et al., 2020) and using non-invasive transcranial magnetic stimulation (TMS) in sighted humans (Dugue et al., 2011), but the feasibility of LFP phase-locked stimulation with intracortical electrodes in humans still remains unexplored. Nevertheless, targeting the right LFP phase before stimulation could allow to reduce charge requirements. Figure 1F shows an example.

Algorithms for closed-loop stimulation

Figure 2 introduces some possible algorithms for closed-loop stimulation in the framework of a cortical visual prosthesis. Briefly, to search for perception thresholds (Figure 2A), a stimulation with an initial current level I_0 is sent from one electrode or a group of electrodes. Then, the brain signals during and after the stimulation (up to 1 s) are recorded and used to extract perception-related features. If perception is detected, the current I used to stimulate is set as the perception threshold for that electrode or group of electrodes. If perception is not detected from the extracted features, a new stimulation train is sent with a higher current intensity $I = I_{-1} + \Delta I$, where I_{-1} is the previous current intensity and ΔI is the increment of current intensity for each step. The velocity of this algorithm to find perception thresholds depends on the initial current intensity I_0 and on ΔI size. Bigger ΔI values will speed up the threshold finding at the cost of reducing the precision of the threshold. Furthermore, we can start with I_0 values close to the last perception thresholds to improve processing speed.

To stimulate the desired LFP phase in real time, we can use the approach proposed by Blackwood et al. (2018). First, we have to record 1-second windows of the raw signal and then filter this

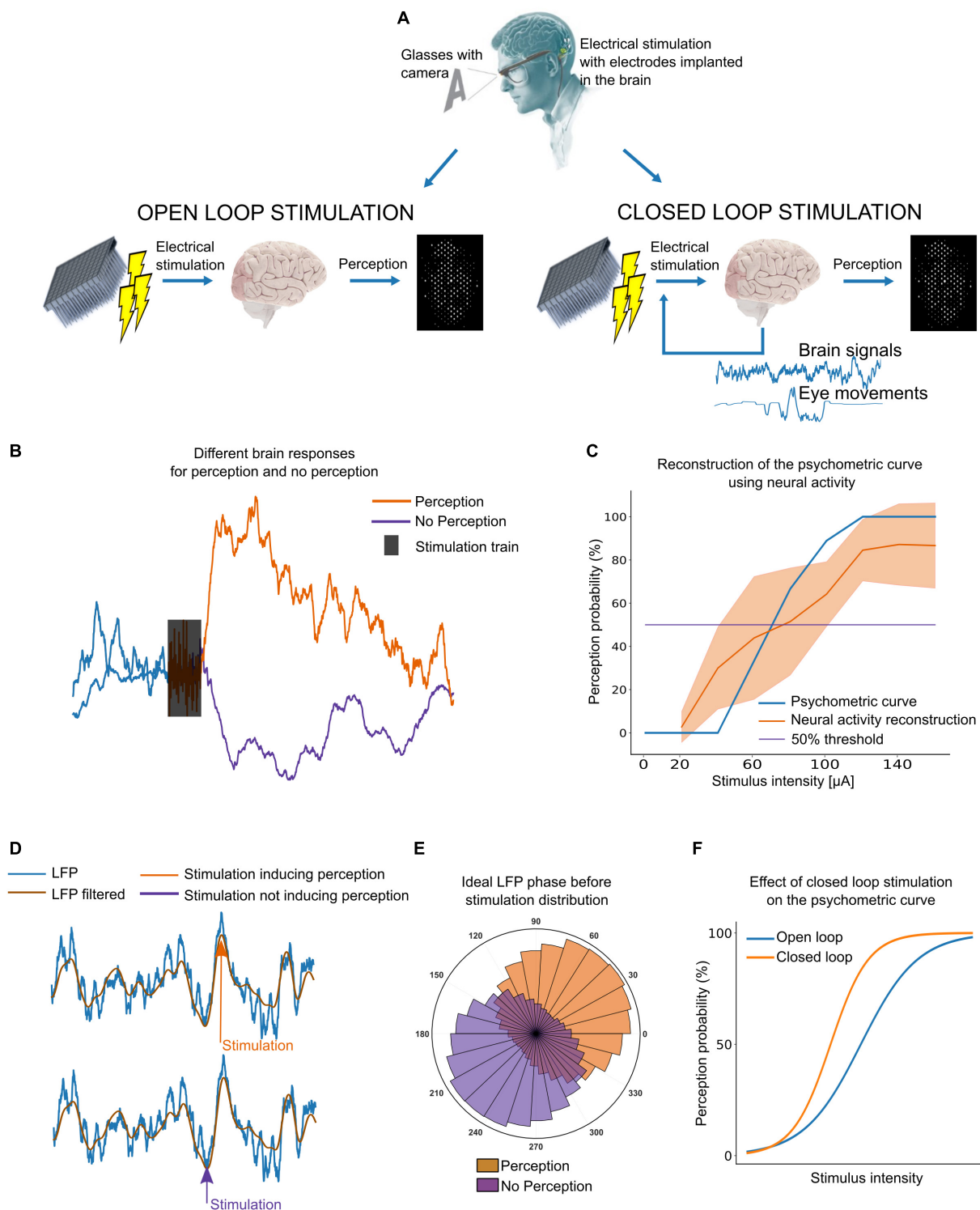


FIGURE 1

Closed-loop stimulation of the visual cortex. **(A)** Diagram of open-loop versus closed-loop stimulation approaches. **(B)** Example of intracortical brain signals. A clear difference between perception and no perception is needed to adjust the current to induce perception without the user's feedback. **(C)** Example of a psychometric curve obtained with user's feedback (blue) and neural signals (orange). **(D)** Local field potentials (LFP) phase dependent response to stimulation. Inducing perception might be easier by stimulating the right LFP phase. **(E)** Ideally, the distribution of LFP phase should be different for perception and no perception. **(F)** Stimulating at the right LFP phase, we could decrease the charge required to reliably evoke phosphenes.

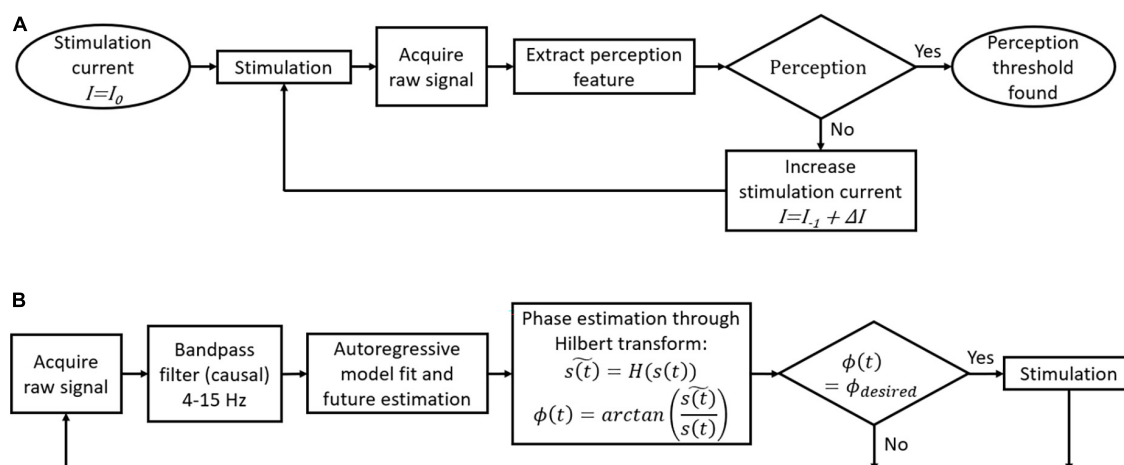


FIGURE 2

Flowcharts of possible closed-loop algorithms for a cortical visual prosthesis. (A) Automatic threshold adjustment for perception. (B) Local field potentials (LFP)-phase locked stimulation.

signal between 4 and 15 Hz. As the phase estimation of the last point in the window data is not accurate without knowing the future behavior of the signal, an autoregressive model is fitted to estimate the future trend. The Hilbert transform is then used to estimate the current phase, and a stimulation train is sent only if the current phase is the desired one (Figure 2B). We have recently tested this algorithm using intracortical signals from the visual cortex of a human blind volunteer at a sampling rate of 30 kHz and we obtained an error of $\pm 20^\circ$ in the LFP phase estimation (Grani et al., 2022b).

Discussion

Research on real-time closed-loop neural systems has built upon contributions from neuroscientists, engineers and clinicians, and may prove essential for future cortical visual prostheses, especially when high-number microelectrodes are used. As a result, the next frontier in cortical visual prosthesis may be the development of bidirectional implantable systems with enhanced abilities to modulate and manipulate populations of neurons in real-time. These closed-loop approaches could be able to use information from neural recordings to adjust the optimal stimulation, reduce charge requirements, and improve stimulation performance. However, there are still a number of important issues and challenges to overcome. For example, the stability of signals over time, the influence of movements on signal quality, and the higher energy consumption needed to perform closed-loop stimulation.

Although closed-loop stimulation might increase the safety, performance and usability of cortical visual prostheses, many questions need to be solved before it can be implemented in clinical devices able to continuously record and stimulate from

hundreds of electrodes. For instance, the battery of the system needs to last at least for an entire day but adding a real-time brain signal analysis processor to the device would increase the energy consumption. This represents a significant challenge as the sampling frequency often used to get reliable neural signals is 30 kHz. Moreover, in order not to add complexity to the whole device, many signals should be excluded from the closed-loop approach. For example, perception could be inferred from EEG signals in the occipital cortex (Gail et al., 2004), but adding a standard EEG cap to the prosthesis will decrease the overall wearability, and the users might not want to use it on a daily basis.

Intracortical signals captured from the same electrodes used to stimulate cortical areas are the best candidates to build these closed-loop stimulation approaches. However, the signals collected during electrical stimulation are usually corrupted by the stimulation artifacts. Different signal processing techniques and electronic front-end designs can be used to retrieve the signals from stimulation artifacts (Wagenaar and Potter, 2002; Zhou et al., 2018) but these techniques do not work when the amplifiers are saturated. If this is the case, the blanking or exclusion of data during stimulation could be a good option. In addition, a discrimination between perception features and artifacts could be possible assuming that the artifact features increase linearly with the current intensity, while features linked to perception should have a different behavior, starting to increase only after the perception threshold.

On the other hand, as the microelectrodes have to be permanently implanted in the user's brain, it is important that the signals on which closed-loop stimulation is based are stable over time. Some studies show that the number of reliable spikes captured by intracortical electrodes decreases with time (Sharma et al., 2015), while LFPs are more stable (Grani et al., 2022a).

Therefore, closed-loop approaches based on LFP recordings could be more stable over time than approaches based on single neuron spikes and become the basis for future closed-loop approaches.

Datasets using current intensities able to induce perception 50% of the time, could be of great help to get better insight into these issues and help to investigate in which brain state it is easier to induce visual perceptions. Ideally, the LFP phase before stimulation could be significantly different in case of perception and no perception as it is shown in **Figure 1E**. However, we do not yet know if the same phase of the LFP is valid for all the electrodes. Thus, the neural population around each electrode could determine the preferred LFP phase, which means that to modulate the neural response to stimulation, perhaps we should consider the specific dynamics of every single electrode. In addition, the real-time detection of this parameter can also be associated with uncertainties that reduce the accuracy of phase estimation. Further, although different algorithms have been proposed for continuous phase estimation in real-time (Kim et al., 2016; Blackwood et al., 2018), this locked phase stimulation can also limit the time resolution of the stimulation. Thus, it seems that the frequency of ongoing oscillations is around 10 Hz (Dugue et al., 2011), which means that the preferred phase should appear approximately every 100 ms, limiting to this time the refresh rate of the visual prosthesis. Therefore, all these results must be confirmed in real-life environments, and there is still not enough information about the period of the local field potential that corresponds to maximum excitability nor about how many feedback channels can be reliably provided in parallel.

Another complementary and not mutually exclusive approach could be to reproduce the responses of cortical neurons to different visual stimuli (Guo et al., 2018; Spencer et al., 2019; Shah and Chichilnisky, 2020). Sighted animal models with intracortical electrodes in the visual cortex could be used to obtain visual cortex responses to different visual patterns. Then, knowing the neural activity elicited by a visual stimulus and the neural activity elicited by each electrical stimulation parameter, the stimulation parameters could be shaped to obtain the desired neural activity for a certain visual perception. However, there is no guarantee that eliciting with electrical stimulation the same activity of a natural image in V1 creates the same image perception. In addition, we have to consider that the perception experience is modulated by higher cortical areas (van Vugt et al., 2018) and could also be different in a brain deprived of visual information (Merabet et al., 2007; Fernandez, 2018).

All the progress in neural technologies, neuroscience, electronics, and bioengineering together with increased intelligence in neural systems can help to foster the development of improved custom-tailored devices, which will incorporate advanced closed-loop algorithms for restoring some functional sight to blind people. Therefore, we expect that in the future,

closed-loop stimulation will offer more safety, precision, and personalization of cortical visual neuroprostheses approaches.

Data availability statement

The original contributions presented in this study are included in the article/supplementary material, further inquiries can be directed to the corresponding author.

Ethics statement

The studies involving human participants were reviewed and approved by Hospital General Universitario de Elche Clinical Research Committee. The patients/participants provided their written informed consent to participate in this study.

Author contributions

FG, CS-S, AF, and EF contributed to the design, implementation of the research, and writing of the manuscript. All authors contributed to the article and approved the submitted version.

Funding

Funding was provided by grant PROMETEO/2019/119 from the Generalitat Valenciana (Spain), by the European Union's Horizon 2020 Research and Innovation Programme under grant agreement No. 899287 (project NeuraViPer) and under the Marie Skłodowska-Curie grant agreement No. 861423 (enTRAIN Vision), and by Ministerio de Ciencia e Innovación (Spain) by grant PDC2022-133952-I00.

Conflict of interest

The authors declare that the research was conducted in the absence of any commercial or financial relationships that could be construed as a potential conflict of interest.

Publisher's note

All claims expressed in this article are solely those of the authors and do not necessarily represent those of their affiliated organizations, or those of the publisher, the editors and the reviewers. Any product that may be evaluated in this article, or claim that may be made by its manufacturer, is not guaranteed or endorsed by the publisher.

References

- Allison-Walker, T. J., Ann Hagan, M., Chiang Price, N. S., and Tat Wong, Y. (2020). Local field potential phase modulates neural responses to intracortical electrical stimulation. *Annu. Int. Conf. IEEE Eng. Med. Biol. Soc.* 2020, 3521–3524. doi: 10.1109/EMBC44109.2020.9176186
- Beauchamp, M. S., Oswald, D., Sun, P., Foster, B. L., Magnotti, J. F., Niketghad, S., et al. (2020). Dynamic stimulation of visual cortex produces form vision in sighted and blind humans. *Cell* 181, 774.e5–783.e5. doi: 10.1016/j.cell.2020.04.033
- Blackwood, E., Lo, M. C., and Alik Widge, S. (2018). Continuous phase estimation for phase-locked neural stimulation using an autoregressive model for signal prediction. *Annu. Int. Conf. IEEE Eng. Med. Biol. Soc.* 2018, 4736–4739. doi: 10.1109/EMBC.2018.8513232
- Borda, E., Gaillet, V., Airaghi Leccardi, M. J. I., Zollinger, E. G., Moreira, R. C., and Ghezzi, D. (2022). Three-dimensional multilayer concentric bipolar electrodes restrict spatial activation in optic nerve stimulation. *J. Neural Eng.* 19:036016. doi: 10.1088/1741-2552/ac6d7e
- Borg, E., and Zakrisson, J. E. (1973). Letter: stapedius reflex and speech features. *J. Acoust. Soc. Am.* 54, 525–527. doi: 10.1121/1.1913610
- Bosking, W. H., Oswald, D. N., Foster, B. L., Sun, P., Beauchamp, M. S., and Yoshor, D. (2022). Percepts evoked by multi-electrode stimulation of human visual cortex. *Brain Stimul.* 15, 1163–1177. doi: 10.1016/j.brs.2022.08.007
- Bourne, R. R. A., Flaxman, S. R., Braithwaite, T., Cicinelli, M. V., Das, A., Jonas, J. B., et al. (2017). Magnitude, temporal trends, and projections of the global prevalence of blindness and distance and near vision impairment: a systematic review and meta-analysis. *Lancet Glob. Health* 5, e888–e897. doi: 10.1016/S2214-109X(17)30293-0
- Brackbill, N., Rhoades, C., Kling, A., Shah, N. P., Sher, A., Litke, A. M., et al. (2020). Reconstruction of natural images from responses of primate retinal ganglion cells. *eLife* 9:e58516. doi: 10.7554/eLife.58516
- Cagnan, H., Pedrosa, D., Little, S., Pogossyan, A., Cheeran, B., Aziz, T., et al. (2017). Stimulating at the right time: phase-specific deep brain stimulation. *Brain* 140, 132–145. doi: 10.1093/brain/aww286
- Cha, K., Horch, K. W., and Normann, R. A. (1992). Mobility performance with a pixelized vision system. *Vision Res.* 32, 1367–1372.
- Chen, R., Canales, A., and Anikeeva, P. (2017). Neural recording and modulation technologies. *Nat. Rev. Mater.* 2:16093. doi: 10.1038/natrevmats.2016.93
- Chen, X., Wang, F., Fernandez, E., and Roelfsema, P. R. (2020). Shape perception via a high-channel-count neuroprosthesis in monkey visual cortex. *Science* 370, 1191–1196. doi: 10.1126/science.abd7435
- De Silva, S. R., and Moore, A. T. (2022). Optogenetic approaches to therapy for inherited retinal degenerations. *J. Physiol.* 600, 4623–4632. doi: 10.1113/JP282076
- Dugue, L., Marque, P., and VanRullen, R. (2011). The phase of ongoing oscillations mediates the causal relation between brain excitation and visual perception. *J. Neurosci.* 31, 11889–11893. doi: 10.1523/JNEUROSCI.1161-11.2011
- Farkhondeh Tale Navi, F., Heysieattalab, S., Ramanathan, D. S., Raoofy, M. R., and Nazari, M. A. (2022). Closed-loop modulation of the self-regulating brain: a review on approaches, emerging paradigms, and experimental designs. *Neuroscience* 483, 104–126. doi: 10.1016/j.neuroscience.2021.12.004
- Fernandez, E. (2018). Development of visual Neuroprostheses: trends and challenges. *Bioelectron. Med.* 4:12. doi: 10.1186/s42234-018-0013-8
- Fernandez, E. (2022). Selective induction of fingertip sensations for better neuroprosthetic control. *Neurology* 98, 261–262. doi: 10.1212/WNL.00000000000013177
- Fernandez, E., Alfaro, A., Soto-Sanchez, C., Gonzalez-Lopez, P., Lozano, A. M., Pena, S., et al. (2021). Visual percepts evoked with an intracortical 96-channel microelectrode array inserted in human occipital cortex. *J. Clin. Invest.* 131:e151331. doi: 10.1172/JCI151331
- Fernandez, E., Alfaro-Saez, A., and Gonzalez-Lopez, P. (2020). Toward long-term communication with the brain in the blind by intracortical stimulation: challenges and future prospects. *Front. Neurosci.* 11:681. doi: 10.3389/fnins.2020.00681
- Fifer, M. S., McMullen, D. P., Osborn, L. E., Thomas, T. M., Christie, B., Nickl, R. W., et al. (2022). Intracortical somatosensory stimulation to elicit fingertip sensations in an individual with spinal cord injury. *Neurology* 98, e679–e687. doi: 10.1212/WNL.00000000000013173
- Figee, M., Riva-Posse, P., Choi, K. S., Bederson, L., Mayberg, H. S., and Kopell, B. H. (2022). Deep brain stimulation for depression. *Neurotherapeutics* 19, 1229–1245. doi: 10.1007/s13311-022-01270-3
- Gail, A., Brinksmeier, H. J., and Eckhorn, R. (2004). Perception-related modulations of local field potential power and coherence in primary visual cortex of awake monkey during binocular rivalry. *Cereb. Cortex* 14, 300–313. doi: 10.1093/cercor/bhg129
- Gaillet, V., Cutrone, A., Artoni, F., Vagni, P., Mega Pratiwi, A., Romero, S. A., et al. (2020). Spatially selective activation of the visual cortex via intraneural stimulation of the optic nerve. *Nat. Biomed. Eng.* 4, 181–194. doi: 10.1038/s41551-019-0446-8
- Grani, F., Soto-Sanchez, C., Farfan, F. D., Alfaro, A., Grima, M. D., Rodil Doblado, A., et al. (2022a). Time stability and connectivity analysis with an intracortical 96-channel microelectrode array inserted in human visual cortex. *J. Neural Eng.* 19:045001. doi: 10.1088/1741-2552/ac801d
- Grani, F., Soto-Sanchez, C., Rodil, A., Grima, M. D., Farfan, F., Calvo, M., et al. (2022b). "Performance evaluation of a real-time phase estimation algorithm applied to intracortical signals from human visual cortex," in *Artificial Intelligence in Neuroscience: Affective Analysis and Health Applications*, eds J. M. Ferrández Vicente, J. R. Álvarez-Sánchez, F. de la Paz López, and H. Adeli (Cham: Springer), 516–525.
- Guenser, G., Laudanski, J., Phillipon, B., Backus, B. C., Bordure, P., Romanet, P., et al. (2015). The relationship between electrical auditory brainstem responses and perceptual thresholds in Digisonic(R) SP cochlear implant users. *Cochlear Implants Int.* 16, 32–38. doi: 10.1179/1754762814Y.00000000082
- Guo, T., Yang, C. Y., Tsai, D., Muralidharan, M., Suaning, G. J., Morley, J. W., et al. (2018). Closed-loop efficient searching of optimal electrical stimulation parameters for preferential excitation of retinal ganglion cells. *Front. Neurosci.* 12:168. doi: 10.3389/fnins.2018.00168
- Higuchi, A., Kumar, S. S., Benelli, G., Alarfaj, A. A., Munusamy, M. A., Umezawa, A., et al. (2017). Stem cell therapies for reversing vision loss. *Trends Biotechnol.* 35, 1102–1117. doi: 10.1016/j.tibtech.2017.06.016
- Hong, J. W., Yoon, C., Jo, K., Won, J. H., and Park, S. (2021). Recent advances in recording and modulation technologies for next-generation neural interfaces. *iScience* 24:103550. doi: 10.1016/j.isci.2021.103550
- Khodagholy, D., Ferrero, J. J., Park, J., Zhao, Z., and Gelinis, J. N. (2022). Large-scale, closed-loop interrogation of neural circuits underlying cognition. *Trends Neurosci.* 45, 968–983. doi: 10.1016/j.tins.2022.10.003
- Kim, L., Harer, J., Rangamani, A., Moran, J., Parks, P. D., Widge, A., et al. (2016). Predicting local field potentials with recurrent neural networks. *Annu. Int. Conf. IEEE Eng. Med. Biol. Soc.* 2016, 808–811. doi: 10.1109/EMBC.2016.7590824
- Lee, S. W., Fallegger, F., Casse, B. D., and Fried, S. I. (2016). Implantable microcoils for intracortical magnetic stimulation. *Sci. Adv.* 2:e1600889. doi: 10.1126/sciadv.1600889
- Li, Y., Tan, Z., Wang, J., Wang, M., and Wang, L. (2022). Neural substrates of external and internal visual sensations induced by human intracranial electrical stimulation. *Front. Neurosci.* 16:918767. doi: 10.3389/fnins.2022.918767
- Little, S., Pogossyan, A., Neal, S., Zavala, B., Zrinzo, L., Hariz, M., et al. (2013). Adaptive deep brain stimulation in advanced Parkinson disease. *Ann. Neurol.* 74, 449–457. doi: 10.1002/ana.23951
- Lozano, A. M., Lipsman, N., Bergman, H., Brown, P., Chabardes, S., Chang, J. W., et al. (2019). Deep brain stimulation: current challenges and future directions. *Nat. Rev. Neurol.* 15, 148–160. doi: 10.1038/s41582-018-0128-2
- McKay, C. M., Chandan, K., Akhoun, I., Siciliano, C., and Kluk, K. (2013). Can ECAP measures be used for totally objective programming of cochlear implants? *J. Assoc. Res. Otolaryngol.* 14, 879–890. doi: 10.1007/s10162-013-0417-9
- Mekhail, N., Levy, R. M., Deer, T. R., Kapural, L., Li, S., Amirdelfan, K., et al. (2020). Long-term safety and efficacy of closed-loop spinal cord stimulation to treat chronic back and leg pain (Evoke): a double-blind, randomised, controlled trial. *Lancet Neurol.* 19, 123–134. doi: 10.1016/S1474-4422(19)30414-4
- Merabet, L. B., Rizzo, J. F. III, Pascual-Leone, A., and Fernandez, E. (2007). 'Who is the ideal candidate?': decisions and issues relating to visual neuroprosthesis development, patient testing and neuroplasticity. *J. Neural Eng.* 4, S130–S135. doi: 10.1088/1741-2560/4/1/S15
- Nanengrungsunk, O., Au, A., Sarraf, D., and Sadda, S. R. (2022). New frontiers of retinal therapeutic intervention: a critical analysis of novel approaches. *Ann. Med.* 54, 1067–1080. doi: 10.1080/07853890.2022.2066169
- Nguyen, H. T., Tangutooru, S. M., Rountree, C. M., Kantzos, A. J., Tarlochan, F., Yoon, W. J., et al. (2016). Thalamic visual prosthesis. *IEEE Trans. Biomed. Eng.* 63, 1573–1580. doi: 10.1109/TBME.2016.2567300

- Nirenberg, S., and Pandarinath, C. (2012). Retinal prosthetic strategy with the capacity to restore normal vision. *Proc. Natl. Acad. Sci. U.S.A.* 109, 15012–15017. doi: 10.1073/pnas.1207035109
- Nowik, K., Langwinska-Wosko, E., Skopinski, P., Nowik, K. E., and Szaflik, J. P. (2020). Bionic eye review - An update. *J. Clin. Neurosci.* 78, 8–19. doi: 10.1016/j.jocn.2020.05.041
- Panikker, P., Roy, S., Ghosh, A., Poornachandra, B., and Ghosh, A. (2022). Advancing precision medicines for ocular disorders: diagnostic genomics to tailored therapies. *Front. Med.* 9:906482. doi: 10.3389/fmed.2022.906482
- Picaud, S., and Sahel, J. A. (2020). [Vision restoration: science fiction or reality?]. *Med. Sci.* 36, 1038–1044. doi: 10.1051/medsci/2020213
- Price, B. H., and Gavornik, J. P. (2022). Efficient temporal coding in the early visual system: existing evidence and future directions. *Front. Comput. Neurosci.* 16:929348. doi: 10.3389/fncom.2022.929348
- Qiao, K., Chen, J., Wang, L., Zhang, C., Zeng, L., Tong, L., et al. (2019). Category decoding of visual stimuli from human brain activity using a bidirectional recurrent neural network to simulate bidirectional information flows in human visual cortices. *Front. Neurosci.* 13:692. doi: 10.3389/fnins.2019.00692
- Ranjandish, R., and Schmid, A. (2020). A review of microelectronic systems and circuit techniques for electrical neural recording aimed at closed-loop epilepsy control. *Sensors* 20:5716. doi: 10.3390/s20195716
- Rassia, K. E. K., Moutoussis, K., and Pezaris, J. S. (2022). Reading text works better than watching videos to improve acuity in a simulation of artificial vision. *Sci. Rep.* 12:12953. doi: 10.1038/s41598-022-10719-6
- Rotermund, D., Ernst, U. A., and Pawelzik, K. R. (2019). Open Hardware for neuro-prosthesis research: a study about a closed-loop multi-channel system for electrical surface stimulations and measurements. *HardwareX* 6:e00078. doi: 10.1016/j.ohx.2019.e00078
- Scangos, K. W., Khambhati, A. N., Daly, P. M., Makhoul, G. S., Sugrue, L. P., Zamanian, H., et al. (2021). Closed-loop neuromodulation in an individual with treatment-resistant depression. *Nat. Med.* 27, 1696–1700. doi: 10.1038/s41591-021-01480-w
- Shah, N. P., and Chichilnisky, E. J. (2020). Computational challenges and opportunities for a bi-directional artificial retina. *J. Neural Eng.* 17:055002. doi: 10.1088/1741-2552/aba8b1
- Sharma, G., Annetta, N., Fridenberg, D., Blanco, T., Vasconcelos, D., Shaikhouni, A., et al. (2015). Time stability and coherence analysis of multiunit, single-unit and local field potential neuronal signals in chronically implanted brain electrodes. *Bioelectron. Med.* 2, 63–71. doi: 10.15424/bioelectronmed.2015.00010
- Spencer, M. J., Kameneva, T., Grayden, D. B., Meffin, H., and Burkitt, A. N. (2019). Global activity shaping strategies for a retinal implant. *J. Neural Eng.* 16:026008. doi: 10.1088/1741-2552/aa071
- Stevenson, I. H., and Kording, K. P. (2011). How advances in neural recording affect data analysis. *Nat. Neurosci.* 14, 139–142. doi: 10.1038/nn.2731
- Van Gelder, R. N., Chiang, M. F., Dyer, M. A., Greenwell, T. N., Levin, L. A., Wong, R. O., et al. (2022). Regenerative and restorative medicine for eye disease. *Nat. Med.* 28, 1149–1156. doi: 10.1038/s41591-022-01862-8
- van Vugt, B., Dagnino, B., Vartak, D., Safaai, H., Panzeri, S., Dehaene, S., et al. (2018). The threshold for conscious report: signal loss and response bias in visual and frontal cortex. *Science* 360, 537–542. doi: 10.1126/science.aar7186
- Visram, A. S., Innes-Brown, H., El-Deredy, W., and McKay, C. M. (2015). Cortical auditory evoked potentials as an objective measure of behavioral thresholds in cochlear implant users. *Hear. Res.* 327, 35–42.
- Vissani, M., Nanda, P., Bush, A., Neudorfer, C., Dougherty, D., and Richardson, R. M. (2022). Toward closed-loop intracranial neurostimulation in obsessive-compulsive disorder: a crisis of access. *Nat. Med.* 28, 1529–1532. doi: 10.1038/s41591-022-01879-z
- Wagenaar, D. A., and Potter, S. M. (2002). Real-time multi-channel stimulus artifact suppression by local curve fitting. *J. Neurosci. Methods* 120, 113–120. doi: 10.1016/s0165-0270(02)00149-8
- Weiss, N. M., Ovari, A., Oberhoffner, T., Demaret, L., Bicer, A., Schraven, S., et al. (2021). Automated detection of electrically evoked stapedius reflexes (eSR) during cochlear implantation. *Eur. Arch. Otorhinolaryngol.* 278, 1773–1779. doi: 10.1007/s00405-020-06226-x
- Wenger, N., Moraud, E. M., Raspopovic, S., Bonizzato, M., DiGiovanna, J., Musienko, P., et al. (2014). Closed-loop neuromodulation of spinal sensorimotor circuits controls refined locomotion after complete spinal cord injury. *Sci. Transl. Med.* 6:255ra133. doi: 10.1126/scitranslmed.3008325
- Xu, J., Guo, H., Nguyen, A. T., Lim, H., and Yang, Z. (2018). A bidirectional neuromodulation technology for nerve recording and stimulation. *Micromachines* 9:538. doi: 10.3390/mi9110538
- Zhou, A., Johnson, B. C., and Muller, R. (2018). Toward true closed-loop neuromodulation: artifact-free recording during stimulation. *Curr. Opin. Neurobiol.* 50, 119–127. doi: 10.1016/j.conb.2018.01.012



OPEN ACCESS

EDITED BY
Dao-Qi Zhang,
Oakland University, United States

REVIEWED BY
Feng Pan,
Hong Kong Polytechnic University,
Hong Kong SAR, China
Ning Tian,
The University of Utah, United States

*CORRESPONDENCE
Maesoon Im
✉ maesoon.im@kist.re.kr;
✉ maesoon.im@gmail.com

SPECIALTY SECTION
This article was submitted to
Cellular Neurophysiology,
a section of the journal
Frontiers in Cellular Neuroscience

RECEIVED 04 December 2022

ACCEPTED 19 January 2023

PUBLISHED 06 February 2023

CITATION

Roh H, Otgondemberel Y, Eom J, Kim D and
Im M (2023) Electrically-evoked responses
for retinal prostheses are differentially altered
depending on ganglion cell types in outer
retinal neurodegeneration caused by *Crb1*
gene mutation.
Front. Cell. Neurosci. 17:1115703.
doi: 10.3389/fncel.2023.1115703

COPYRIGHT

© 2023 Roh, Otgondemberel, Eom, Kim and Im.
This is an open-access article distributed under
the terms of the [Creative Commons Attribution
License \(CC BY\)](#). The use, distribution or
reproduction in other forums is permitted,
provided the original author(s) and the
copyright owner(s) are credited and that the
original publication in this journal is cited, in
accordance with accepted academic practice.
No use, distribution or reproduction is
permitted which does not comply with
these terms.

Electrically-evoked responses for retinal prostheses are differentially altered depending on ganglion cell types in outer retinal neurodegeneration caused by *Crb1* gene mutation

Hyeonhee Roh^{1,2}, Yanjinsuren Otgondemberel¹,
Jeonghyeon Eom^{1,3}, Daniel Kim^{1,4} and Maesoon Im^{1,5*}

¹Brain Science Institute, Korea Institute of Science and Technology, Seoul, Republic of Korea, ²School of Electrical Engineering, Korea University, Seoul, Republic of Korea, ³School of Electrical Engineering, Kookmin University, Seoul, Republic of Korea, ⁴Department of Biomedical Sciences, Seoul National University College of Medicine, Seoul, Republic of Korea, ⁵Division of Bio-Medical Science & Technology, KIST School, University of Science and Technology, Seoul, Republic of Korea

Background: Microelectronic prostheses for artificial vision stimulate neurons surviving outer retinal neurodegeneration such as retinitis pigmentosa (RP). Yet, the quality of prosthetic vision substantially varies across subjects, maybe due to different levels of retinal degeneration and/or distinct genotypes. Although the RP genotypes are remarkably diverse, prosthetic studies have primarily used retinal degeneration (*rd*) 1 and 10 mice, which both have *Pde6b* gene mutation. Here, we report the electric responses arising in retinal ganglion cells (RGCs) of the *rd8* mouse model which has *Crb1* mutation.

Methods: We first investigated age-dependent histological changes of wild-type (*wt*), *rd8*, and *rd10* mice retinas by H&E staining. Then, we used cell-attached patch clamping to record spiking responses of ON, OFF and direction selective (DS) types of RGCs to a 4-ms-long electric pulse. The electric responses of *rd8* RGCs were analyzed in comparison with those of *wt* RGCs in terms of individual RGC spiking patterns, populational characteristics, and spiking consistency across trials.

Results: In the histological examination, the *rd8* mice showed partial retinal foldings, but the outer nuclear layer thicknesses remained comparable to those of the *wt* mice, indicating the early-stage of RP. Although spiking patterns of each RGC type seemed similar to those of the *wt* retinas, correlation levels between electric vs. light response features were different across the two mouse models. For example, in comparisons between light vs. electric response magnitudes, ON/OFF RGCs of the *rd8* mice showed the same/opposite correlation polarity with those of *wt* mice, respectively. Also, the electric response spike counts of DS RGCs in the *rd8* retinas showed a positive correlation with their direction selectivity indices ($r = 0.40$), while those of the *wt* retinas were negatively correlated ($r = -0.90$). Lastly, the spiking timing consistencies of late responses were largely decreased in both ON and OFF RGCs in the *rd8* than the *wt* retinas, whereas no significant difference was found across DS RGCs of the two models.

Conclusion: Our results indicate the electric response features are altered depending on RGC types even from the early-stage RP caused by *Crb1* mutation. Given the

various degeneration patterns depending on mutation genes, our study suggests the importance of both genotype- and RGC type-dependent analyses for retinal prosthetic research.

KEYWORDS

retinitis pigmentosa, retinal degeneration, artificial vision, retinal prosthesis, electrical stimulation

1. Introduction

Outer retinal degenerative diseases such as age-related macular degeneration (AMD) and retinitis pigmentosa (RP) cause loss of photoreceptors (Figure 1A), subsequent remodeling of retinal neural circuits, and profound visual impairment (Marc and Jones, 2003; Marc et al., 2003; Hartong et al., 2006; Jager et al., 2008). In the past two decades, various microelectronic prosthetic systems have demonstrated electrical stimulation of surviving neurons can elicit spiking activities in retinal ganglion cells (RGCs), offering artificial visual percepts in blind individuals (Humayun et al., 1996; Rizzo et al., 2003; Zrenner et al., 2011). Also, several clinical trials showed quite promising outcomes of Argus II (Second Sight), Alpha IMS/AMS (Retina Implant AG), and PRIMA (Pixium Vision), making those retinal prostheses commercialized in the past or near commercialization (Humayun et al., 1996; Ahuja et al., 2011; Zrenner et al., 2011; da Cruz et al., 2013; Stingl et al., 2015; Palanker et al., 2020, 2022). However, the best quality of electrically-evoked prosthetic vision (20/460) (Palanker et al., 2020) has reached yet to neither the level of independent walks without guide dog/cane nor the level of legal blindness (20/200). Moreover, prosthetic users who suffered from RP showed considerably different levels of restored vision (Stingl et al., 2015), hindering the wide use of retinal prostheses. For instance, some retinal prosthetic users were able to recognize/localize testing objects while others were unable to perceive any artificial visual sensation (Stingl et al., 2015).

The remarkable variety of disease genotypes can be one of the critical factors that may have caused the substantial performance variation. For example, inheritance of RP can be classified into three major groups (second row of Figure 1B): autosomal recessive (50–60%), autosomal dominant (30–40%), and X-linked (5–15%) RPs (Hartong et al., 2006). In addition to the highest proportion, the autosomal recessive RP (ARRP) has remarkably heterogeneous genotypes (bottom row of Figure 1B), which are known to, along with other factors (e.g., environment, gender, and epigenetics), result in the different levels/patterns of retinal degeneration in each individual (Chang et al., 2011). Similar with RP, AMD genotypes are also variegated, which include single nucleotide polymorphisms (SNPs) in vascular endothelial growth factor (*VEGF*), and pigment epithelium-derived factor (*PEDF*), complement factor H (*CFH*), and high-temperature requirement factor A1 (*HTRA1*) genes (Mori et al., 2010; Black and Clark, 2016; Battu et al., 2022). Each genotype disrupts distinct pathways and/or functions of the retina and expresses unique phenotypes (Berger et al., 2010; Verbakel et al., 2018), raising a possibility that electrically-evoked spiking responses (hereafter referred to as electric responses) of RGCs are significantly different depending on the genotype. Therefore, comprehensive neurophysiological understandings of electric responses arising in each genotype are necessary for advanced vision restoration for both RP and AMD patients.

In previous retinal prosthetic researches using RP animal models, retinal degeneration 1 (*rd1*) and 10 (*rd10*) mice have been widely

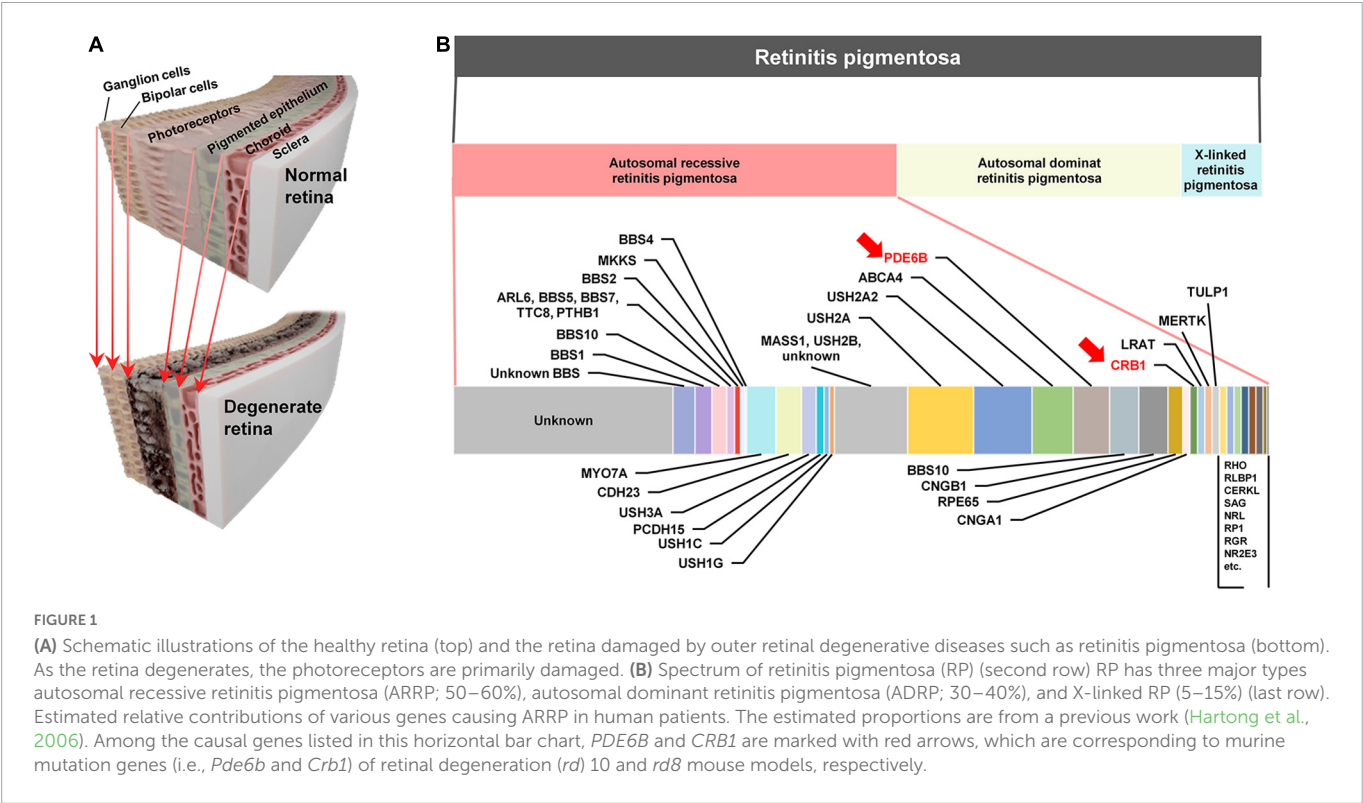
used, which are the well-established mouse models of the ARRP (Chang et al., 2002; Gargini et al., 2007). Those two models have a *Pde6b* genetic mutation in common, which is responsible for encoding β -subunit of cyclic guanosine monophosphate (cGMP)-specific phosphodiesterase (PDE). It has been known that cGMP PDE plays a crucial role in the phototransduction of photoreceptors as an important enzyme for regulating the level of cGMP, which is an intracellular signaling molecule known as a second messenger (Chang et al., 2002). The difference between the two models is that the *rd10* model mimics human RP better in terms of its slower disease progression than the *rd1* model (Gargini et al., 2007). However, given the fact that the ARRP has numerous different genotypes (Figure 1B; Chang et al., 2002; Hartong et al., 2006; Bravo-Gil et al., 2017; Verbakel et al., 2018), it is essential to examine other genotypes for successful clinical outcomes of retinal prostheses. For example, the mutation of *Crb1* gene is another genotype of the ARRP, which is currently available as *rd8* mouse model (see Table 1 for comparisons across *rd1*, *rd10*, and *rd8* mice) (Mehalow et al., 2003). The *Crb1* gene is strongly associated with epithelial polarity by its emplacement proximal to the adhesion junction in the outer limiting membrane (OLM) (Mehalow et al., 2003; Aredo et al., 2015). Accordingly, retinal foldings and/or disassembled retinal layers were observed in the mouse models carrying *Crb1* mutation (Mehalow et al., 2003; van de Pavert et al., 2004; van de Pavert et al., 2007). Similarly, patients with *CRB1* mutations also showed abnormal laminar structures or retinal telangiectasia with exudation (Jacobson et al., 2003; Bujakowska et al., 2015). Despite of its availability and clinical importance, *rd8* mice have not been well studied in both visual neuroscience and retinal prosthetics.

In the present work, we characterized electric responses arising in three distinct physiological types of RGCs in the *rd8* mouse model (e.g., ON, OFF, and ON-OFF direction-selective RGCs). We also correlated electric responses of RGCs with their own visually-evoked responses and compared the correlations with those of wild-type (*wt*) RGCs. Lastly, we examined the spiking consistencies across repeats of electric stimuli in each type. By comparing the response features of those three RGC types across diverse genotypes and healthy animals (e.g., *rd8* and *wt* mice in the present work, *rd1/10* and *wt* mice in the earlier studies) translational differences of microelectronic prostheses may be estimated, which would be applicable to patient selection.

2. Materials and methods

2.1. Animals

The animal experiment protocols were approved by the Institutional Animal Care and Use Committee of the KIST (KIST-2020-156, KIST-2021-09-105, KIST-5088-2022-05-076). Wild-type (*wt*; C57BL/6J strain) and retinal degeneration 8 (*rd8*; C57BL/6N strain) mice were purchased from Daehan BioLink (Eumseong,



South Korea) and Young Bio (Seongnam, South Korea), respectively. These two strains were used for electrophysiological recordings and histological analyses. For histological comparison only, *rd10* (B6.CXB1-*Pde6b*^{rd10}/J) mice were also used. The first breeding pairs of *rd10* mice were purchased from Jackson Lab (Bar Harbor, ME, USA), and then its colony has been maintained in the KIST animal

facility. All mice were anesthetized via inhalation of vaporizing isoflurane and euthanized by cervical dislocation.

2.2. Histological analysis

After euthanasia, a mouse eyeball was fixed in David's fixative and 10% neutral buffered formalin (NBF) solution (GD Chem, Eumseong, South Korea). The eyeball was washed with tap water and embedded in paraffin. The prepared sample was sectioned to be 4 μ m in thickness using a rotary microtome (Shandon Finesse ME, Thermo Fisher Scientific, Waltham, MA, USA). The sectioned samples were mounted on each slide glass and dried on a slide warmer (C-SL, Changshin Science, Seoul, South Korea). After that, the slide glass with the retinal tissue was placed into an oven at 58–60°C to increase attachment between the tissue and the slide glass. Lastly, the prepared samples were stained with hematoxylin and eosin (H&E). Then, the H&E-stained retina samples were imaged using a microscope (BX50, Olympus, Tokyo, Japan).

In this study, to compare histological changes in the three different mouse models (i.e., *wt*, *rd8*, and *rd10* mice; Figures 2, 3) as a function of the aging/degeneration level, animals were sacrificed at various ages ranging from 3 to 25 weeks old. In the case of *rd10* mice, it has been known that almost no visual responses are recordable after postnatal days (PD) 60, indicating the advanced stage of retinal degeneration (Gargini et al., 2007). According to previous literature (Aredo et al., 2015), *rd8* animals at postnatal weeks (PW) 3–25 were thought to be at the early stage of retinal degeneration based on their phenotypes such as yellow fundus spots caused by subretinal microglia/macrophages. Also, in the aspects of retinal outer nuclear layer (ONL) thickness (Figure 3) and electroretinogram (ERG) signal loss (Table 1), the *rd8* mice used in this work can be considered at the

TABLE 1 Qualitative comparisons of major characteristics across *rd1*, *rd10* and *rd8* mouse RP models (Hawes et al., 2000; Chang et al., 2002; Mehalow et al., 2003; Hartong et al., 2006).

	<i>rd1</i>	<i>rd10</i>	<i>rd8</i>
Mutation	<i>Pde6b</i> (Nonsense)	<i>Pde6b</i> (Missense)	<i>Crb1</i>
Phenotype	Vessel attenuation Pigment patch in the fundus	Sclerotic retinal vessels	Large white deposits Retinal folding corresponds to white spot
Chromosome (mouse)	Chr.5	Chr.5	Chr.1
Chromosome (human)	Chr.4p16	Chr.4p16	Chr.1q25
Retinal ONL loss by (month)	1	2	30
Recordable ERG responses	PD14–PD16	PD14–PD28	PD14–PD365
Prevalence (in autosomal recessive population)	4–5%		1%

Ages of animals showing recordable electroretinogram (ERG) responses are in postnatal days (PD). ONL: Outer Nuclear Layer.

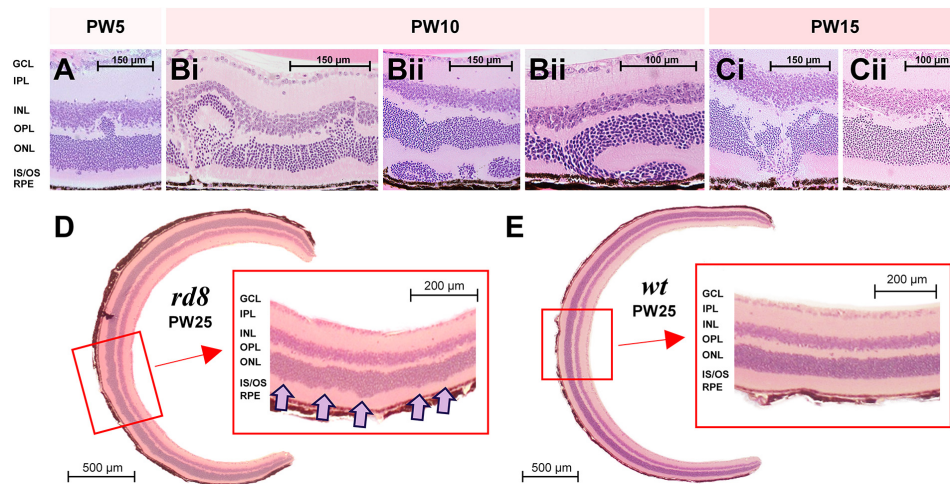


FIGURE 2

Diverse shapes of retinal folds were found in H&E staining images of *rd8* retinas at various ages. (A) A retinal fold was observed from a retina of a *rd8* mouse sacrificed in postnatal weeks (PW) 5. Scale bar is displayed on each panel. GCL, ganglion cell layer; IPL, inner plexiform layer; INL, inner nuclear layer; OPL, outer plexiform layer; ONL, outer nuclear layer; IS/OS, inner segment/outer segment of photoreceptor; RPE, retinal pigment epithelium. (B) Same as panel (A) but from *rd8* animals sacrificed in PW10. Retinas shown in panels (Bi,Bii) are from two different animals. Two panels marked as (Bii) show different areas of the same retina. (C) Same as panel (A) but from an *rd8* animal sacrificed in PW15. Retinas shown in panels (Ci,Cii) are from the same animal but two different retinas. (D) Cross-sectional image of the whole retina of a PW25 *rd8* mouse. (inset) A magnified view showing a wiggly borderline between ONL and IS/OS layer. Wiggly spots are marked with pink arrows. (E) Same as D but from an age-matched wild-type (*wt*) mouse (PW25). Inset shows a clear borderline between ONL and IS/OS layer.

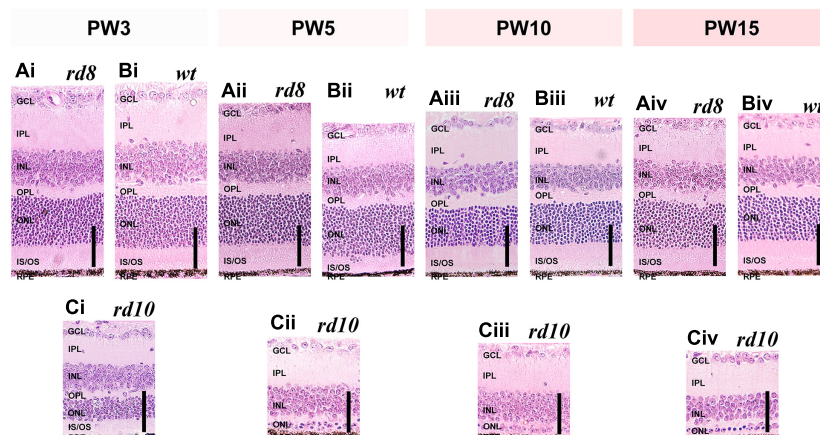


FIGURE 3

Histological analyses show similar thickness changes of retinal layers as a function of ages in *rd8* and wild-type (*wt*) retinas while *rd10* retinas show remarkably thickness decrement. (Ai–Aiv) H&E staining images of *rd8* retinas of mice at four age groups: postnatal weeks (PW) 3, 5, 10, and 15, respectively. (Bi–Biv) Same as panel (A) but for age-matched *wt* mouse retinas. (Ci–Civ) Same as panel (A) but for age-matched *rd10* mouse retinas. Profound thinning is observed in both ONL and IS/OS layer. Each vertical scale bar at bottom right of every panel indicates 50 μ m. GCL: ganglion cell layer, IPL: inner plexiform layer, INL: inner nuclear layer, OPL: outer plexiform layer, ONL: outer nuclear layer, IS/OS: inner segment/outer segment of photoreceptor, RPE: retinal pigment epithelium.

early degeneration stage because they were similar to the early stage of *rd10* animals (Hawes et al., 2000; Chang et al., 2002).

2.3. Preparation of retina and electrophysiology

For electrophysiological recordings, all retina tissues of *rd8* (PW8–18) and *wt* (PW8–10) were isolated from an eyeball after the euthanasia and flat-mounted on a filter paper with the photoreceptor layer facing down. The prepared sample was immersed in a

customized chamber attached on a slide glass. Cell-attached patch clamping method was used to record spiking activities of alpha retinal ganglion cells (RGCs) in both *wt* and *rd8* mice. Alpha RGCs were identified by their large (> 20 μ m) somata (Pang et al., 2003; Murphy and Rieke, 2006). Preparation of retinal sample and physiological/electrophysiology recording were conducted under the red illumination.

Glass pipettes were tailored using a micropipette puller (Model P-97, Sutter Instrument, Novato, CA, USA) and used as patch electrodes (8–12 M Ω). Two chloride-coated silver wires shaped in balls were placed at the two opposite edges of the recording chamber

to serve as ground electrodes. Data were recorded and low-pass filtered at 2 kHz using an amplifier (MultiClamp 700B, Molecular Devices, Sunnyvale, CA, USA). Acquired data were digitized by a data acquisition card (PCI-MIO-16E-4, National Instruments, Austin, TX, USA). During the recordings, oxygenated Ames' medium (Sigma-Aldrich, St. Louis, MO, USA) was continuously perfused at ~4 ml/min and the temperature was maintained at 34–36°C. There was a small hole (~2 mm in diameter) at the center of the filter paper that allowed light stimulation from the bottom of the microscope stage.

2.4. Light stimulation for RGC type classification

Physiological types of RGCs were identified by following two steps: First, a white spot on a gray background was projected onto the photoreceptor layer of target cells. Depending on their responses to the 1-s-long stationary spot flashes (diameter ranged from 100 to 1,000 μm and the biggest responses were used for later correlation analyses), RGCs were classified into either ON, OFF, or ON-OFF types (Figure 4). Second, we additionally identified whether the recorded cells were direction-selective (DS): a long white rectangular bar (300 μm \times 1,800 μm) on a gray background was moved in 12 different directions (0–330° in 30° steps) at 600 $\mu\text{m/s}$. ON-OFF DS RGCs showed consistent spiking responses to both leading and trailing edges of the bright moving bar, which were ON and OFF responses, respectively. Throughout the present study, DS RGCs exclusively mean ON-OFF DS RGCs because we excluded ON type of DS cells in our analyses (Im and Fried, 2016a).

In summary, this work analyzed responses of the non-DS ON, non-DS OFF (hereafter referred to simply as ON and OFF, respectively), and ON-OFF DS RGCs in *rd8* and *wt* retinas ($n = 14, 15$, and 6 for ON, OFF, and DS cells from 19 different *rd8* retinas; $n = 10$ and 11 for ON and OFF cells from 14 *wt* retinas). The light stimuli were delivered to the retina sample using an LCD projector (PH550, LG, Seoul, South Korea) and every light stimulus was repeated at least three times for a given cell.

2.5. Electric stimulation

Electrical stimuli were delivered by a 10 k Ω platinum-iridium electrode (MicroProbes, Gaithersburg, MD, USA); its conical tip had a height of ~125 μm and a base diameter of ~30 μm . The top portion of the electrode was exposed with no insulation layer, which had a surface area of ~5,900 μm^2 . After touching the inner limiting membrane (ILM), the tip of the stimulating electrode was positioned ~25 μm above the ILM surface and ~50 μm laterally away from the target cell body using a micromanipulator (MPC-200, Sutter Instrument, Novato, CA, USA). The electric stimuli were generated by a stimulus generator (STG2004, Multi-Channel Systems GmbH, Reutlingen, Germany). A monophasic cathodal current of 100 μA in amplitude (i.e., –100 μA) was delivered for 4 ms. An identical electric stimulus was repeated typically seven times (at least six times) to a given cell. Data acquisition and electric stimuli were controlled by custom software written in LabVIEW (National Instruments, Austin, TX, USA) and MATLAB (MathWorks, Natick, MA, USA).

2.6. Analyses of RGC spiking responses

Timings of stimulus-evoked spikes were detected by custom MATLAB code. In the case of electrically-evoked spikes, additional code was used before the spike detection to remove electric artifacts from raw recordings. Also, the spiking activities of electric responses were divided into early, late, and total responses in the same way of previous studies (Tsai et al., 2009; Im and Fried, 2015; Im et al., 2018; Lee and Im, 2018, 2019; Yoon et al., 2020; Ogtongdemberel et al., 2021). In other words, to divide direct and indirect responses, we separate the spiking activities of each type RGC into early and late responses based on the end of first burst (Figures 4A–C). The range of early response was displayed on raster plots (Figures 4A–C) of each RGC type with yellow bands (i.e., spikes elicited within 50, 6, and 55 ms from the stimulus onset for ON, OFF, and DS RGCs, respectively) (Yoon et al., 2020; Ogtongdemberel et al., 2021). The rest of the spiking activities was referred to as late responses. These ranges for early and late responses were largely similar in responses to electric pulses ranging from several hundred microseconds to Roh et al. (2022) and several milliseconds (Im et al., 2018). To investigate correlations between response magnitudes of light- and electrically-evoked spiking activities, we created scatter plots for peak firing rate (PFR) or spike count for each component of electric responses (i.e., early, late, and total response) (Figures 5, 6). We computed firing rates in each 20-ms-long bin with a rolling step of 5 ms (Figure 5).

To further characterize the DS cell responses, we calculated direction selectivity indices (DSIs) from the light responses arising from the moving bars as outlined in our previous work (Im and Fried, 2016a; Ogtongdemberel et al., 2021) by using the following equation:

$$\text{DSI} = 1 - \frac{\text{Area}_{\text{Preferred}}}{\text{Area}_{\text{Null}}}$$

where $\text{Area}_{\text{Preferred}}$ and $\text{Area}_{\text{Null}}$ are the areas of the preferred- and the null-side halves in the polar plots of their moving bar responses (Im and Fried, 2016a). The preferred direction was first determined as the vector sum of spiking responses arising from the white bars moved in all 12 directions, and then the null direction was assigned to be the opposite to the preferred direction. The DSI_{ON} and DSI_{OFF} were computed from polar plots of ON and OFF responses, then averaged for DSI_{AVG} which was used in the scatter plot (Figure 6). We excluded RGCs which had $\text{DSI}_{\text{AVG}} < 0.5$ to limit our study for highly directional cells.

We also examined the spike timing consistency of electric responses across repeated stimulation (typically 7 trials and at least 6 trials) by computing the spike time tiling coefficient (STTC) which is defined by the following equation (Cutts and Egle, 2014):

$$\text{STTC} = \frac{1}{2} \left(\frac{P_A - T_B}{1 - P_A T_B} + \frac{P_B - T_A}{1 - P_B T_A} \right)$$

where P_A is the proportion of spikes from spike train A that lie within time window ($\pm \Delta t$) of each spike from spike train B, T_A is the proportion of the total recording period which contains any spikes within $\pm \Delta t$ from spike train A. P_B and T_B are similarly calculated. In the present work, we used Δt of 10 ms for the STTC computation. Inter-trial pair-wise STTC values were visualized as heatmaps for early and late responses (Figures 7A, 8A, for non-DS and DS RGCs respectively). Every STTC values were also shown as violin plots (Figures 7B, 8B).

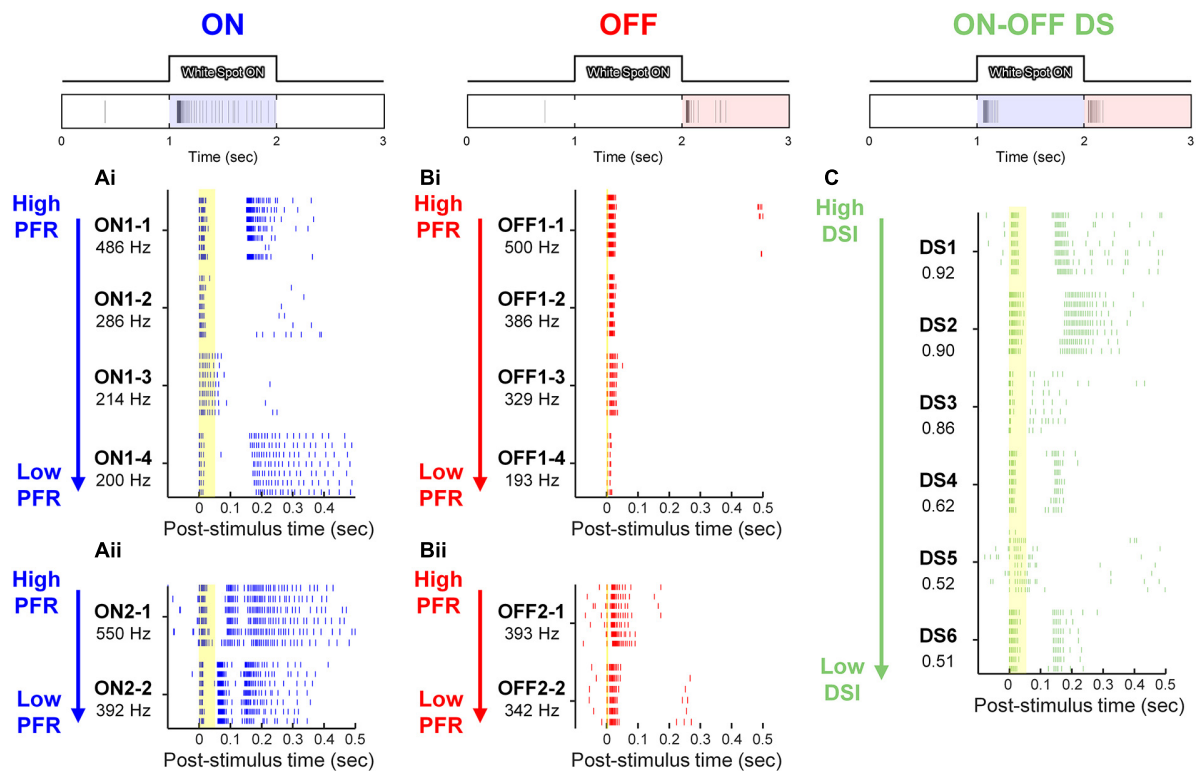


FIGURE 4

Electrically-evoked responses from 6 representative RGCs in the three physiological types of *rd8* retinas. At top of each panel, representative light-evoked responses of ON, OFF, and ON-OFF DS RGC to 1-s-long white spot flash are shown. (A*i*,A*ii*) Raster plots of ON RGCs are shown in the order of peak firing rate (PFR), which is shown below each cell ID. Each vertical tick of raster plots indicates a single spike. Each cell contains responses to stimuli repeated for 6 or 7 times. Spiking patterns of ON RGCs were divided into either two (A*i*) or three (A*ii*) bursts. (B*i*,B*ii*) Same as panel (A) but for OFF RGCs. The responses of OFF cells were also divided into two types: abrupt spiking ending (B*i*), and gradual tapering off of spiking activity (B*ii*). (C) Raster plots of ON-OFF DS RGCs are displayed in the descending order of direction selectivity index (DSI). Yellow vertical bands in raster plots indicate the range of early response of each cell type (i.e., 0–50, 0–6, and 0–55 ms for ON, OFF, and DS RGCs, respectively).

2.7. Statistical analysis

To evaluate the correlation level between light and electric responses (Im and Fried, 2015), we computed Pearson's product-moment coefficient (hereafter referred to as Pearson's r or r -value) from data points shown in each scatter plot (e.g., PFRs and spike counts of electric vs. light responses). Statistical comparisons were performed using one-way ANOVA with Holm-Sidak post-hoc analyses to examine the statistical significance.

3. Results

3.1. Retinal degeneration pattern of *rd8* mice is distinct

It has been well known that phenotypes such as the speed and the pattern of retinal degeneration are substantially different depending on the mutation genes (Chang et al., 2002). For instance, although *rd1/rd10* and *rd8* mice are all RP mouse models, they showed significant distinctions in their phenotypes due to genetic differences as summarized in Table 1. The distinctive phenotypic features of the *rd8* model include large white retinal deposits and idiosyncratic retinal foldings (Chang et al., 2002; Mehalow et al., 2003). Indeed, our own H&E staining images showed retinal foldings

of the *rd8* mice at various ages (Figures 2A–C). To longitudinally study morphological changes as a function of the degree of retinal degeneration, we sacrificed *rd8* mice at postnatal weeks (PW) 3, 5, 10, 15, and 25. Both size and shape of retinal foldings varied depending on neither age (at least in the age range we tested) nor locations (e.g., central vs. peripheral retinas) (Figures 2A–C). For example, older animals did not necessarily show bigger retinal foldings, consistent with a previous report (Mehalow et al., 2003). Also, even in the oldest animal we tested (PW25), there were retinal slices that had no retinal foldings observed in the whole eyeball cross-sections (Figure 2D). There was no bias of the retinal folding spots to either central or peripheral retinas. Intriguingly however, its outer retinal border of the outer nuclear layer (ONL; photoreceptor cell body layer) was wiggly as clearly shown in the inset (see pink arrows of Figure 2D). This wiggly borderline was found in most slices at various portions throughout all age ranges (i.e., PW3–25) of *rd8* mice we used for H&E staining, which was also reported in the previous work (Mehalow et al., 2003). Probably, the severely wiggling spots at the early onset of degeneration may further develop to be retinal foldings in *rd8* mice. In contrast, the PW25 *wt* retina showed the straight border of the ONL (Figure 2E).

We also compared histological changes of non-folding/-wiggly areas of the *rd8* retinas with age-matched *wt* and *rd10* samples. The ONL thickness change with aging of the *rd8* mice was similar to that of *wt* mice until PW15 (compare Figures 3A vs. 3B), suggesting

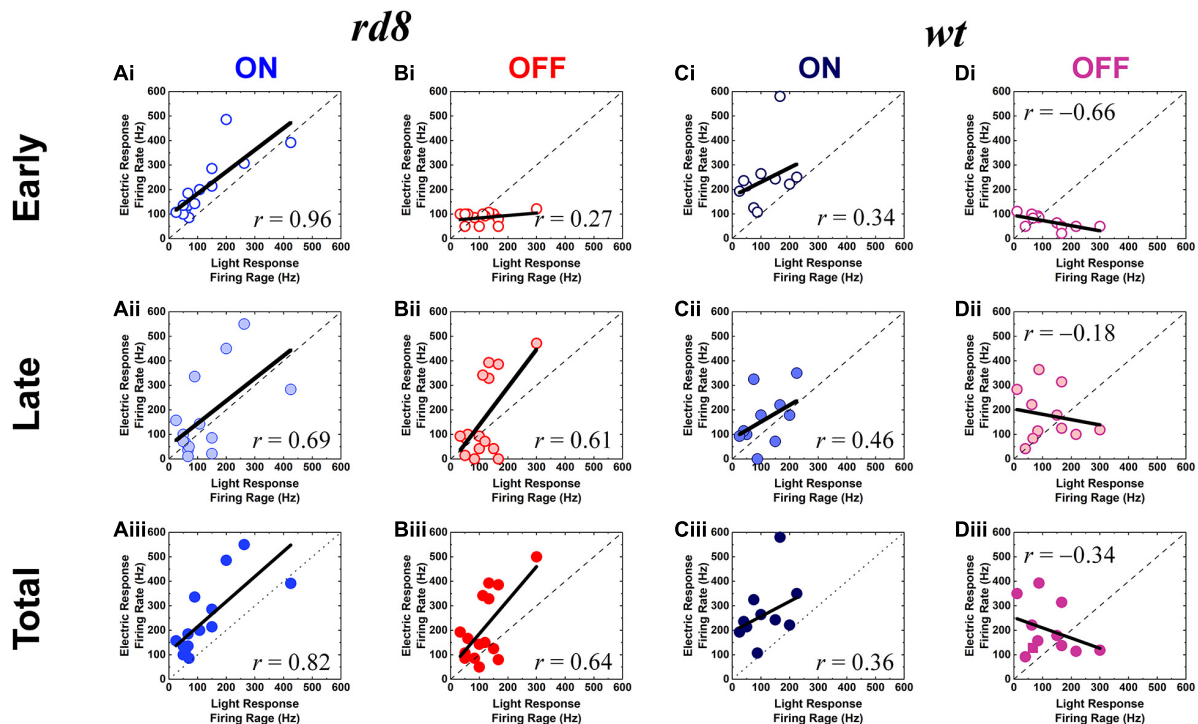


FIGURE 5

Electric responses are well correlated with light responses in both ON and OFF RGCs of the *rd8* retinas, and ON but not OFF RGCs of the *wt* retinas. (Ai–Aiii) Scatter plots of peak firing rate (PFR) for electric response vs. PFR for light response of the ON RGCs in the *rd8* retinas. Scatter plots are shown for (Ai) early, (Aii) late, and (Aiii) total response, respectively. Each data point is from a different cell. Dashed line indicates linear fitting curve of all data points, and the level of correlation (r -value) is shown in each plot. (Bi–Biii) Same as panels (Ai–Aiii) but for the OFF RGCs in the *rd8* retinas. (Ci–Ciii) Same as panels (Ai–Aiii) but for the wild-type (*wt*) mouse retinas. (Di–Diii) Same as panels (Bi–Biii) but for the *wt* mouse retinas.

the photoreceptor degeneration was minimal in the non-folding/-wiggly areas. In detail, the ONL thicknesses of the *rd8* and *wt* retinas at PW3 were ~ 57 and ~ 62 μm , respectively (Figures 3Ai, 3Bi), which were at the time point where retinal development was just completed. Then, the ONL thicknesses remained quite similar until PW5 (Figures 3Aii, 3Bii). The ONLs were shown to be thinning down from PW10 (Figures 3Aiii, 3Biii), and the thicknesses reached down to ~ 55 and ~ 51 μm at the age of PW15 (Figures 3Aiv, 3Biv). In contrast, the ONL thickness in *rd10* mice at PW3 was only ~ 28 μm (Figure 3Ci), which is about half of the thickness of *wt* and *rd8* mice at the same age. The *rd10* ONL became only 2–3 rows of nuclei at PW5 (Figure 3Cii) and finally showed a single row of nuclei in the thickness of ~ 8 μm at PW15 (Figure 3Civ). Taken together, these results clearly show much slower degeneration speed of the *rd8* mice than the *rd10* counterpart. Therefore, the *rd8* model offers possibilities of not only studying the other genotype but also carefully exploring the early stage of retinal degeneration.

3.2. Electrically-evoked response patterns of individual *rd8* RGCs seem largely similar to those of *wt* RGCs but their populational characteristics differ

Although *rd8* mice have been used for some histological studies (Chang et al., 2002; Mehalow et al., 2003; Hippert et al., 2015), it has not been explored how their RGCs respond to electric stimulation. Given the minimal retinal thinning (Figure 3) and the sporadic

retinal foldings (Figure 2), there is a likelihood that electrically-evoked responses of *rd8* RGCs may have similar spiking features with those of *wt* RGCs. On the other hand, the retinal degeneration may differentially alter complex retinal circuitries of distinct physiological types of RGCs. Accordingly, we questioned how similar spiking activities arise in each RGC type between the *rd8* and *wt* retinas. To compare with our previous results recorded from *wt* and *rd10* mice (Yoon et al., 2020; Otgondemberel et al., 2021), the *rd8* retinas were electrically stimulated with a 4-ms-long monophasic cathodal current (-100 μA). We recorded spiking responses from 14 ON, 15 OFF, and 6 DS RGCs of *rd8* animals at PW8–18, and analyzed the RGCs as a whole regardless of the ages because the retinal foldings did not show dependence on age (Figure 2) and the histological changes (i.e., thickness of ONL) of the *rd8* retinas were minimal during that time period (Figure 3). A previous work also indicated the relatively steady state in ONL thickness of the *rd8* retinas between PW3 and PW12 as compared to other mouse models including *rd1* mouse (Hippert et al., 2015).

In the early degeneration state, the light-evoked spiking activities of the *rd8* retina were still strong enough to distinguish the RGC type (top row of Figure 4). Among all RGCs classified by their light responses, the electrically-evoked responses of representative 6 cells of each RGC type were shown (Figures 4A–C), which showed the highest peak firing rate (PFR) in ON and OFF types (Figures 4A, B). The spiking patterns of those RGCs seemed largely similar to those reported earlier by our group from the healthy retinas (Tsai et al., 2009; Im and Fried, 2015, 2016b; Im et al., 2018; Lee and Im, 2019; Otgondemberel et al., 2021), but minor deviations were observed in

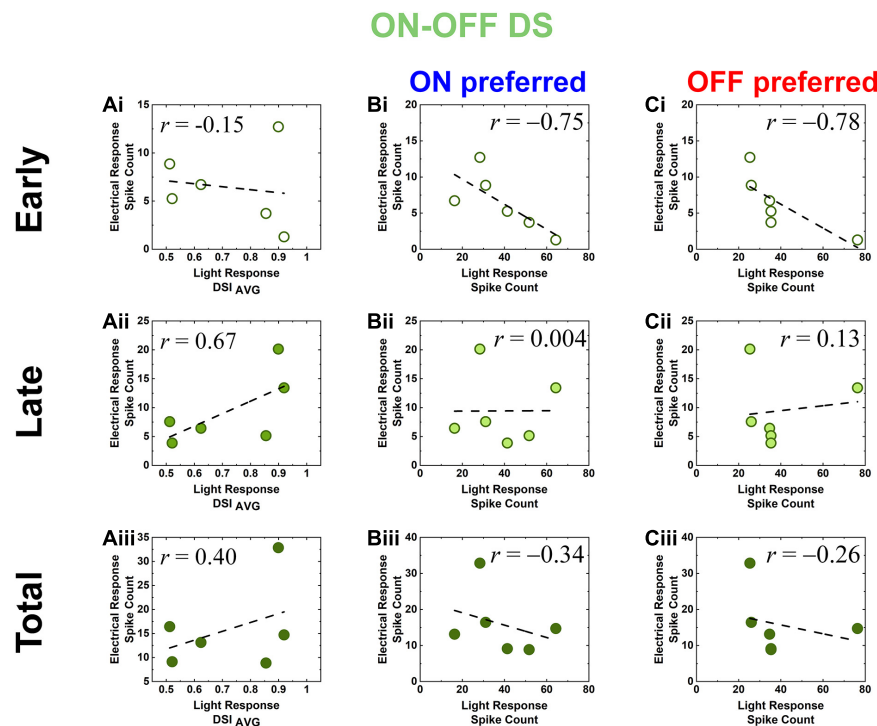


FIGURE 6

Electric response magnitudes (spike count) of DS RGCs in *rd8* and *wt* retinas show opposite correlations with their direction selectivity indices and light response spike count. **(Ai–Aiii)** Scatter plots of electric response [early, late, and total responses in panels **(Ai–Aiii)**, respectively] spike count vs. light response DSI_{AVG} in the same cell for all DS RGCs recorded from *rd8* retinas. Each data point is from a different cell. Level of correlation (r -value) is shown in each plot. Dashed line indicates linear fitting curve in each panel. **(Bi–Biii)** Scatter plots of electric response (spike count) vs. leading edge (ON) of moving bar light response (spike count) in the same cell for all DS RGCs recorded from the *rd8* retinas. Scatter plots are shown for **(Bi)** early, **(Bii)** late, and **(Biii)** total responses, respectively. **(Ci–Ciii)** Same as panels **(Ai–Aiii)** but for trailing edge (OFF) of moving bar light response.

responses of ON and DS RGCs. For example, most ON RGCs showed two bursts of spikes which were separated by silent periods ($n = 12/14$; **Figure 4Ai**), while some ON RGCs showed three bursts ($n = 2/14$; **Figure 4Aii**). These results were similar to the spiking patterns of the ON brisk sustained (BS) and brisk transient (BT) sub-types of the rabbit retinas, respectively; however, the mouse alpha RGCs we targeted are known to have sustained type only in the ON pathway. In our previous recordings from the *wt* mouse retinas, all ON alpha RGCs generated two bursts of spikes (Lee and Im, 2018, 2019). Thus, the occurrence of the ON RGCs responding with the three bursts seems to be resulted from retinal degeneration.

In contrast to the responses of ON cells, responses of OFF RGCs displayed much shorter or almost no spike-free intervals between bursts of spikes (**Figure 4B**), which is consistent with our earlier reports (Im and Fried, 2015, 2016b). Spiking activities of some OFF cells ended their spiking rather abruptly ($n = 10/15$; **Figure 4Bi**) while other OFF cells were gradually tapered off with increasing inter-spike intervals ($n = 5/15$; the first row of **Figure 4Bii**). These results are consistent with those observed from responses of OFF BT and BS subtypes, respectively (Im and Fried, 2015). Taken together with the emergence of the three-burst spiking ON cells, our results suggest that the early-stage degeneration of *rd8* mice may minimally affect the ON system only and more than the OFF counterpart at the individual RGC level.

The raster plots of *rd8* DS RGCs were listed in the descending order of their direction selectivity indices (DSIs) (**Figure 4C**) because our previous research that used *wt* mouse retinas found electrically-evoked late responses lasted longer when DSI was smaller

(Otgondemberel et al., 2021). However, the DS RGCs of *rd8* animals showed the opposite trend: the late responses (i.e., spiking activities outside of the yellow band indicating early responses in **Figure 4C**) were usually longer lasting with bigger DSI (except DS3 and DS5). This contrast was another minor deviation between the *rd8* and *wt* retinas, raising a possibility that populational response characteristics of DS RGCs may be different between the two groups.

3.3. Correlations between response magnitudes to electric vs. light stimuli were differently altered depending on pathways in *rd8* mice

To quantitatively analyze populational response difference between the *rd8* and *wt* retinas in non-DS RGCs, we plotted the PFR of electric vs. light responses of ON and OFF RGCs (**Figure 5**). In those scatter plots, the correlation levels between the two responses were characterized to see if how similar spiking response magnitudes can arise from electric stimulation, which seems critical for high-quality prosthetic vision that can be better perceived (Im and Fried, 2015). Interestingly, for all three components (e.g., early, late, and total responses) of electric responses in comparison with their own light responses, the ON/OFF RGCs of the *rd8* retinas showed similar/opposite correlation levels with those of *wt* retinas, respectively (compare **Figures 5A** vs. **5C** for similar correlation

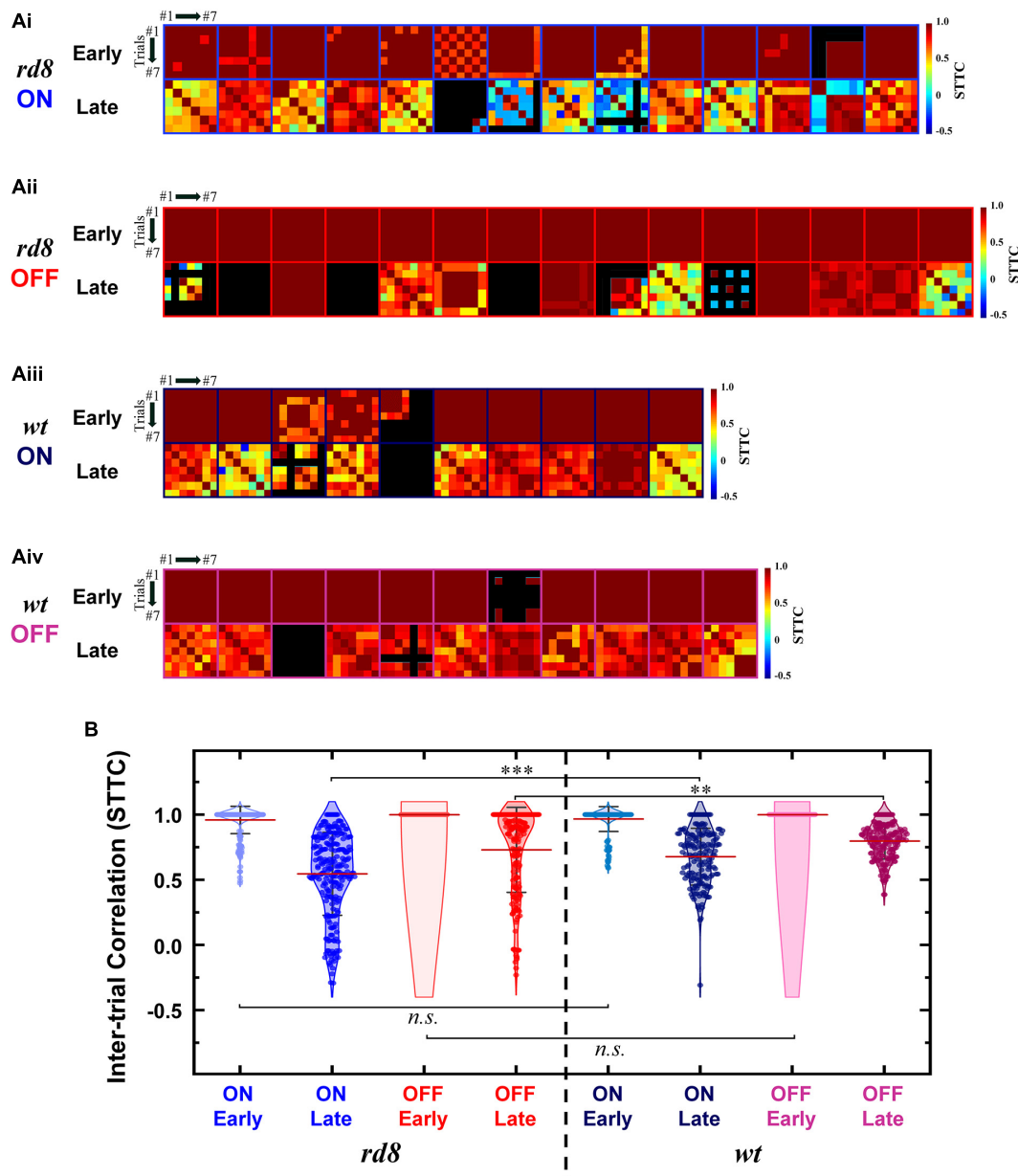


FIGURE 7

Spike timing of late response becomes less consistent in both ON and OFF RGCs of *rd8* than wild-type (*wt*) retinas. (Ai) Color-coded heatmaps of the spike time tiling coefficients (STTCs) of early and late responses for each ON RGC from the *rd8* retinas. (Aii) Same as panel (Ai) but for OFF RGCs in the *rd8* retinas. (Aiii,Aiv) Same as panels (Ai,Aii) but for the *wt* mouse retinas. An identical stimulus repeated typically for 7 times (at least 6 times). Black color in matrices indicates no response was elicited in those trials. (B) Violin plots of all STTCs computed from all *rd8* and wt RGCs. Red horizontal line indicates average STTC value of each group. Four violin plots on the left side of the *rd8* retinas and the other four violin plots on the right side are from the *wt* retinas. Statistical significance was assessed using the one-way ANOVA with Holm-Sidak post-hoc comparisons; *** $p < 0.001$, ** $p < 0.01$, and *n.s.* means not significant.

levels in ON RGCs, and Figures 5B vs. 5D for opposite correlation levels in OFF RGCs).

From the prosthetic perspective, it is particularly notable that both ON and OFF RGCs in the *rd8* retinas generated electric responses which were positively proportional to light responses in terms of spiking magnitudes (Figures 5A, B). For example, the PFRs of the total responses of the *rd8* retinas had fairly high *r*-values for both ON and OFF RGCs (0.82 and 0.64 in Figures 5Aiii, Biii, respectively). Although the positive correlation between the two responses seems to be preferred for appropriate perception of electrically-evoked artificial neural signals, the correlation difference

between the ON and OFF pathways may be essential for prosthetic users to discern luminance increment/decrement at a given location of the visual space (Im and Fried, 2015). Because the indiscriminate activations of ON and OFF RGCs which tile the retina at different stratification depths are inevitable with currently available electric stimulation methods, it may induce difficulties in determining whether the stimulation spot is bright or dark if electric responses of both ON and OFF channels are well-correlated (i.e., similar) with their light responses (see section “Discussion”). In contrast to the *rd8* cells, the RGCs of *wt* retinas demonstrated contrary correlation levels between electric vs. light responses in the ON vs. the OFF systems: the

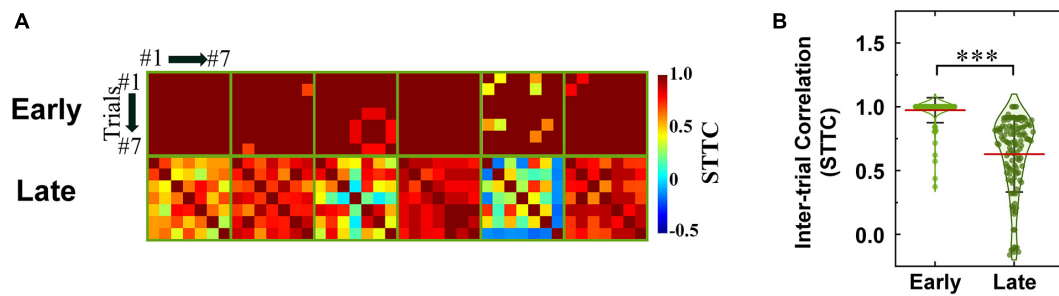


FIGURE 8

Spike timing consistencies of DS RGCs in *rd8* retinas are comparable to those of DS RGCs in *wt* retinas. (A) Color-coded heatmaps of the spike time tiling coefficients (STTCs) of early and late responses in the *rd8* DS RGCs. An identical stimulus repeated typically for seven times (at least six times). Black color in matrices indicates no response was elicited in those trials. (B) Violin plots of all STTCs computed from *rd8* RGCs. Red horizontal line indicates average STTC value of each group. Statistical significance test was performed using the one-way ANOVA with Holm–Sidak *post-hoc* comparisons; *** $p < 0.001$. Statistical significance comparisons between *rd8* and *wt* RGCs are shown in Table 2.

ON RGCs showed the positive correlations ($r = 0.34, 0.46$, and 0.36 in early, late, and total response; Figures 5Ci–Ciii) while the OFF cells exhibited negative correlations ($r = -0.66, -0.18$, and -0.34 in early, late, and total response, respectively; Figures 5Di–Diii). These contrasting correlation levels between ON and OFF pathways in the *wt* mouse retinas are consistent with those reported from the healthy rabbit retinas (Im and Fried, 2015). Also, this contrast is expected to make electric responses of ON cells better perceivable than those of OFF cells (Im and Fried, 2015), probably eliciting “bright” phosphenes in prosthetic users. It is noteworthy again, however, that the *rd8* RGCs did not generate the opposite correlation levels between the ON and the OFF types (compare Figures 5A, B).

Another distinct populational features of the *rd8* RGCs was also observed in DS RGCs: since the responses of *wt* DS RGC were already investigated by creating scatter plots of spike counts in our earlier work (Otgondemberel et al., 2021), we similarly plotted spike counts as a function of average DSI (DSI_{AVG}) (Figure 6A). Spike counts of the early responses in the *rd8* DS RGCs yielded a weak negative correlation with the DSI_{AVG} , which was somewhat analogous to *wt* ones ($r = -0.15$ vs. -0.57 for *rd8* vs. *wt*; see Otgondemberel et al., 2021 for *wt* data). However, spike counts of the late and the total responses showed sharp contrasts between the *rd8* and *wt* retinas, having positive correlations in the *rd8* DS RGCs ($r = 0.67$ and 0.40 for the late and the total responses, respectively; Figures 6Aii, Aiii) but negative correlations in the *wt* DS RGCs ($r = -0.98$ and -0.90 for the late and the total responses, respectively; see Otgondemberel et al., 2021 for *wt* data). These contrasting results suggest that the activation of inhibitory presynaptic neurons of the retinal circuit might be fairly decreased even from the early stage of degeneration (see section “Discussion”). Taken all together, although it was hard to notice any substantial difference in spiking patterns of individual RGCs in the *rd8* retinas (minimal difference in ON RGCs and almost no difference in OFF and DS RGCs; see Figures 4B, C) compared to those of the *wt* retinas (Lee and Im, 2018, 2019; Yoon et al., 2020; Otgondemberel et al., 2021), their populational characteristics appeared to be markedly altered in OFF and DS pathways (Figures 5, 6A) even with the early progression of retinal degeneration caused by *Crb1* mutation.

Since the generation of robust spiking responses to both increment and decrement of luminance is another hallmark of DS RGCs, it is important to know, for retinal prosthetic application, if one component of light responses (i.e., ON or OFF) correlates

better with its electric response over one another. In scatter plots of the DS RGCs (Figures 6B, C), the light and electric responses generally showed negative correlations in the *rd8* retinas (early and total electric responses with ON and OFF preferred light responses; Figures 6Bi, Biii, Ci, Ciii). Meanwhile, the late electric response of the *rd8* DS cells showed little or almost no correlation with either ON or OFF light responses ($r = 0.004$ and 0.13 for ON and OFF preferred, respectively; Figures 6Bii, Cii). In the case of *wt* retinas (Otgondemberel et al., 2021), however, the spike count correlation between light and the electric responses showed positive correlations in all response components (i.e., early, late, and total responses). It is noteworthy that the overall tendencies in the correlations between electric vs. light responses were opposite between the *rd8* vs. *wt* DS cells. Given the young ages (PW8–18) of the *rd8* animals, our results suggest that the complex retinal circuit of DS cells may be affected even from the early-stage retinal degeneration. Accordingly, it would be intriguing to study how the complicatedly-functioning RGC types respond differently to electric stimulation at the early stage of RPs and how they lead to different clinical outcomes of retinal prostheses.

3.4. Trial-to-trial spiking consistency in response to electric stimulation was affected only in non-DS RGCs of *rd8* mice

Healthy neural systems decrease their spiking variability across trials in response to external stimulus (Churchland et al., 2010). However, neurodegeneration seems to increase spiking variabilities in neural responses to stimuli: we recently reported that the variabilities of *rd10* RGC spiking activities arising from electric stimulation increased with the advancing level of the retinal degeneration (Yoon et al., 2020). This increased inconsistency is likely to prevent electrically-evoked spiking activities from being accurately perceived by the higher visual centers (Yoon et al., 2020). In the case of RGCs in the *rd8* retinas, the reduced consistency was not readily notable from the raster plots shown earlier (Figures 4A, B). However, a couple of *rd8* DS cells (i.e., DS3 and DS5) showed relatively higher variability across repeats of an identical stimulus than other DS RGCs which demonstrated consistent spiking patterns across trials ($n = 4/6$; Figure 4C).

To more systematically investigate the level of inter-trial variabilities of the *rd8* responses to electric stimulation, we calculated

the spike time tiling coefficients (STTCs) and compared them with those from the *wt* mice (Figures 7, 8 for non-DS and DS RGCs, respectively). All STTC values of early and late responses across 6–7 repeated stimuli were plotted as color-coded heat matrices for individual cells (Figures 7A, 8A) and violin plots for each type (Figures 7B, 8B). Commonly, regardless of the cell type and the strain, the STTC values of the early responses were markedly high (see first rows of Figures 7Ai–Aiv, 8A). Also, no statistical significance was found between the early responses of the *rd8* and *wt* RGCs (Figures 7B for non-DS cell; *rd8* DS RGC data were compared with *wt* DS RGC data reported in Otgondemberel et al. (2021)). However, the spike timing variabilities of the late responses were significantly increased in the *rd8* RGCs compared to the *wt* RGCs but only in non-DS types (Figures 7B). Also, the difference in the average STTCs ($STTC_{AVG}$) between the *rd8* and *wt* late responses was larger in the ON RGCs (0.55 and 0.68 from the *rd8* and *wt* retinas, respectively; $p < 0.001$; Figure 7B) than in the OFF RGCs (0.73 and 0.80 from the *rd8* and *wt* retinas, respectively; $p < 0.01$; Figure 7B). In our previous study (Yoon et al., 2020), the inter-trial consistency of late response in the *rd10* ON RGCs decreased progressively from postnatal days (PD) 15–60, whereas the STTCs of the *rd10* OFF RGCs remained unchanged until PD19 and then decreased drastically from PD31. Therefore, the response consistency-wise, the degeneration level of the *rd8* mice (PW8–18) used in this study seems to be similar to that of the *rd10* mouse at the age between PD19 and 31. Although the histological analyses showed too different retinal thicknesses (Figure 3), it is likely that the neuronal component which is critical for the spiking response consistency may undergo similar level of degeneration in those two age groups in the two strains (i.e., PW8–18 of *rd8* mice and PD19–31 of *rd10* mice).

Similarly, the spiking consistency of DS RGC was also investigated (Figure 8). Interestingly, even though the correlation levels between electric and light responses of the *rd8* DS RGCs were quite different from those of *wt* ones (Figure 6), the variabilities of spike timing were well maintained in the *rd8* retinas (Figure 8) compared to the *wt* retinas (Otgondemberel et al., 2021). Because of DS3 and DS5, the $STTC_{AVG}$ of the *rd8* DS cells was slightly

decreased, but it was not significantly different from that of the *wt* DS cells. Taken all together, the early-stage retinal degeneration in the *rd8* model seems to differentially affect RGC response consistencies to electric stimulation depending on the pathway (i.e., the ON pathway most and the DS pathway least). It has been well known that non-DS and DS RGCs have distinct types of presynaptic inhibitory neurons such as AII vs. starburst types of amacrine cells for non-DS and DS RGCs, respectively (Figure 9). Perhaps, those inhibitory neurons might have been affected in different degrees by retinal degeneration of the *rd8* mice, and probably causing the difference in the electrically-evoked spiking consistency changes (see DISCUSSION).

4. Discussion

4.1. Early retinal degeneration alters electrically-evoked response features of RGCs depending on physiological types

We first expected RGCs in the *rd8* mice would generate spiking patterns of electric responses which are similar to those of *wt* RGCs due to the following two reasons: First, the ages of the *rd8* mice used in our experiments were ranging from PW8 to 18, which can be considered to be at very early degeneration stage (Hawes et al., 2000; Chang et al., 2002; Aleman et al., 2011; Arede et al., 2015; Hippert et al., 2015). Also, our previous report using *rd10* mice (Yoon et al., 2020) also demonstrated that electric responses of ON and OFF RGCs at early degeneration stage are not that altered in comparison with those of *wt* mice. Second, the areas affected by retinal degeneration were small as shown in a little portion of retinal slices of the *rd8* mice (Figure 2) although we were not able to quantify the exact ratio of retinal foldings or wiggly borderline because we did not investigate every single slice of the whole retina. Consistent with our initial expectation, the spiking patterns arising in the *rd8* RGCs looked quite akin to those of the *wt* RGCs in corresponding types

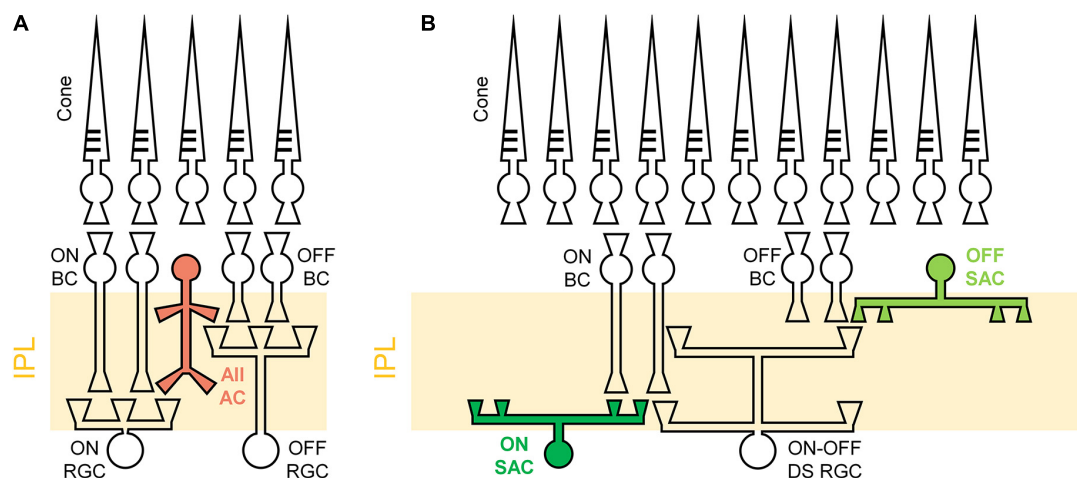


FIGURE 9

Schematic illustrations of different retinal circuits between non-DS and DS RGCs. (A) All amacrine cell (AC) has a narrow field of bistratified dendrites to ON and OFF RGCs. (B) Starburst amacrine cells (SACs) stratify their dendrites to a relatively wide area to modulate direction-selective light responses of DS RGCs. IPL, inner plexiform layer; BC, bipolar cell; RGC, retinal ganglion cell; All AC, all amacrine cell; SAC, starburst amacrine cell; DS RGC, directional selective retinal ganglion cell. Rod pathways are not illustrated for brevity.

(Figure 4). However, the populational characteristics of the electric responses were substantially different between the *rd8* and *wt* RGCs. In addition, those populational differences were distinct in each type (i.e., ON, OFF, and DS type) as summarized in Table 2. For example, in the cases of response magnitudes represented by PFR (Figure 5) of non-DS cells, ON RGCs in the *rd8* retinas maintained similar positive correlations like *wt* ON RGCs while OFF RGCs showed opposite correlation polarities compared to *wt* OFF RGCs (see “Response magnitude correlation with light responses” of ON and OFF RGCs in Table 2).

The opposite response characteristics between the *rd8* and *wt* retinas were also observed in DS RGCs. We examined non-DS as well as DS cells because they have different physiological functions and morphology. ON-OFF DS RGCs process the dynamic visual features in mammalian retinas, which would be critical for the survival of small animals. In non-human primate retinas, the recursive bistratified RGCs seems to have ON-OFF direction selective response features (Detwiler et al., 2019). In contrast to non-DS which have monostratified dendrites, DS RGCs stretch their dendrites to two sublaminae in the IPL layer. Moreover, since DS cells are known to have complex retinal circuits (Famiglietti, 1992; Fried et al., 2002; Borst and Euler, 2011; Vaney et al., 2012; Mauss et al., 2017; Wei, 2018), we expected that electrical responses of DS RGCs could sensitively reflect the remodeling of the neural circuits even in an early stage of retinal degeneration. Since starburst amacrine cells (SACs) are highly likely to strongly involve in the spiking activities of DS RGCs as inhibitory presynaptic neurons, electric responses (spike count) of the *wt* mice were weaker with bigger DSI_{AVG} of their light responses ($r = -0.90$ in Table 2) (Otgondemberel et al., 2021). However, the DS RGCs in the *rd8* retina showed proportionally stronger electric responses as DSI_{AVG} increased ($r = 0.40$ in Figure 6Aiii and Table 2), suggesting the inhibitory components may be affected by the degeneration. Besides, different from the *wt* DS cells, the spike counts of electric responses arising in the *rd8* DS RGCs were not positively correlated with those of light responses to white bars moving in preferred direction (Figure 6 and see “Response magnitude correlation with light responses” of ON-OFF DS RGCs in Table 2). The negative correlation between the light and the electric responses was observed in the *rd8* retinas for both ON and OFF preferred responses (Figures 6B, C and Table 2), which is a sharp contrast to the positive correlation between those in the *wt* retinas (Table 2; Otgondemberel et al., 2021). It may be helpful for the retinal prosthetic community to thoroughly investigate RGC responses to electric stimulation as a function of degeneration levels because it can offer some insights regarding critical implantation time window for maximal clinical efficacy (Yoon et al., 2020). Also, it must be crucial to uncover the underlying mechanism(s) of our findings observed even at the early stage of retinal degeneration more successful clinical outcomes of retinal implants. For example, it seems important to identify neuronal component(s) altering the populational response features in the OFF pathway, which may require early intervention before any irreversible molecular change(s) happen over the course of retinal degeneration.

Our results may be explained by the retinal foldings caused by *Crb1* mutation, which implies remodeling of the retinal circuit, especially close to the photoreceptor and bipolar cell layers. It is well known that we can selectively stimulate ganglion cells, bipolar cells, or photoreceptors by modulating electrical stimulus duration (Fried et al., 2006; Freeman et al., 2010). In detail, ganglion cells that have voltage-gated sodium channels are rapidly activated in less

than 1 ms (Fohlmeister and Miller, 1997). However, voltage-gated calcium channels are slowly activated in several milliseconds and are located at photoreceptors and synaptic terminals of bipolar cells (Protti and Llano, 1998; Thoreson, 2007; Hu et al., 2009). Since we stimulate the retinal tissue with a 4-ms-long monophasic cathodal current ($-100 \mu A$), it was sufficient stimulus duration to activate indirect responses from bipolar cells and photoreceptors. Therefore, we thought partial retinal foldings of *rd8* retinas may have resulted in the quite different indirect responses compared to healthy retinas. But, it is still unclear how those changes were not uniform across RGC types.

These differences in electric response features across RGC types may be caused by the different retinal neural circuits including types of inhibitory presynaptic neurons. For example, the AII amacrine cells (ACs) are known to stratify their dendrites in both ON and OFF sublaminae (Figure 9A), modulating responses of non-DS ON and OFF RGCs (Strettoi et al., 1992; MacNeil and Masland, 1998; MacNeil et al., 1999; Tsukamoto and Omi, 2017). For DS RGCs, the SACs are known to play a critical role in the generation of directionally-selective responses by suppressing responses to null-direction motions (Famiglietti, 1992; Fried et al., 2002; Borst and Euler, 2011; Vaney et al., 2012; Mauss et al., 2017; Wei, 2018). One notable point is that SACs have relatively wider dendritic fields than AII ACs (Figure 9B) (MacNeil et al., 1999; Lin and Masland, 2006), suggesting that it is more likely that the sporadic foldings in the *rd8* retinas affect DS circuits more than non-DS circuits. Moreover, due to the remarkable complexity in the retinal neural circuits of DS RGCs (Famiglietti, 1992; Fried et al., 2002; Borst and Euler, 2011; Vaney et al., 2012; Mauss et al., 2017; Wei, 2018), it is likely that even small remodeling of the retina creates a critical influence to not only light responses but also electrically-evoked responses. Certainly, the *rd8* and *wt* DS cells showed contrasting populational characteristics of electric responses in comparisons with both DSI_{AVG} and light response magnitudes (Figure 6).

4.2. Populational electric responses of ON and OFF RGCs may confound the brain of retinal prosthetic users with CRB1 gene mutation

In the earlier clinical trials of retinal prosthetic systems, the subjects perceived bright sensations, so called “phosphenes,” when electrical stimulation was applied (Humayun et al., 1996, 2003; Fujikado et al., 2007; Naycheva et al., 2012). However, it was not clear how those prosthetic users perceive electrically-evoked neural activities as the bright stimuli because the ON and OFF pathways of the retina are non-selectively activated near any electric stimulation site, which would be much different from the exclusive activation of either pathway during natural viewing (Dan et al., 1996; Marc et al., 2003; David et al., 2004; Touryan et al., 2005). In our previous study using the healthy rabbit retinas, we reported more physiological spiking patterns arose in response to identical electric stimulation in the ON pathway than the OFF counterpart (Im and Fried, 2015). Accordingly, even if electric pulses indiscriminately activate the two pathways, the downstream visual centers may better understand the electric responses from ON RGCs but misinterpret/ignore those from OFF RGCs, resulting in preferential reports of “bright” phosphenes. Consistent with this earlier work, the *wt* mouse retinas of the present

TABLE 2 Summary of populational electric response feature comparisons between *rd8* and wild-type (*wt*) retinas.

RGC types	Electric responses properties	<i>rd8</i>		<i>wt</i>		Related Figure
ON	Response magnitude correlation with light responses	$r = 0.82$		$r = 0.36$		Figure 5
	Response consistency (STTC)	Early response: No statistical significance Late response: $p < 0.001$ (lower in <i>rd8</i>)				Figure 7
OFF	Response magnitude correlation with light responses	$r = 0.64$		$r = -0.34$		Figure 5
	Response consistency (STTC)	Early response: No statistical significance Late response: $p < 0.01$ (lower in <i>rd8</i>)				Figure 7
DS	Response magnitude correlation with DSI_{AVG}	$r = 0.40$		$r = -0.90$		Figure 6
	Response magnitude correlation with light responses	ON preferred	$r = -0.34$	ON preferred	$r = 0.40$	Figure 6
		OFF preferred	$r = -0.26$	OFF preferred	$r = 0.45$	
		Response consistency (STTC)	Early response: No statistical significance Late response: No statistical significance			

Data of ON-OFF DS in *wt* retina from [Otgondemberel et al. \(2021\)](#). For brevity, r -value indicating the level of correlation is shown for total response only.

study showed more physiological spiking magnitudes in response to electric stimulation in ON than OFF RGCs: positive/negative correlations with light responses were observed in ON/OFF RGCs, respectively (**Figures 5C** vs. **5D**). However, in the *rd8* mouse retinas, the electric responses of both ON and OFF RGCs were positively correlated with their light responses (compare **Figures 5A** vs. **5B**), indicating that populational OFF responses were similarly physiological (i.e., natural). Therefore, the electric responses of the ON and OFF channels in the *rd8* mice may confound the brain as to the luminance level (i.e., bright or dark) of the stimulation site. If that is the case, it is even more critical to explore novel stimulation strategies for increasing the response ratio between ON versus OFF responses ([Tsai et al., 2009](#); [Freeman et al., 2010](#); [Twyford et al., 2014](#), [Lee and Im, 2018](#), [Lee and Im, 2019](#)).

Given that retinal prostheses periodically deliver electric pulses, the trial-to-trial spiking consistency of individual RGCs is likely to be crucial for stable/consistent visual percepts ([Yoon et al., 2020](#)). Accordingly, it would be another downside of the *rd8* retinas that the consistencies of the late responses were significantly decreased in both ON and OFF RGCs ($p < 0.001$ and $p < 0.01$ for ON and OFF RGC, respectively; **Figure 7B** and **Table 2**), even though the consistency was not altered in DS RGCs (see 'Response consistency (STTC)' of ON-OFF DS RGC in **Table 2**). Since the ON and OFF pathways are known to be crucial in forming visual percepts ([Im and Fried, 2015](#); [Lee and Im, 2019](#)), our results suggest the increased response variability of the two types of RGCs may hinder the precise perception of artificial vision. Instead of the inconsistent late responses in the degenerate retinas, it may be preferred to rely on the early responses which did not display any substantial changes in the spiking consistency. Although short electric pulses had long been thought to evoke direct spikes without late responses, it has recently been reported that late responses can be elicited with short pulses at high current amplitudes in the range of clinical use ([Roh et al., 2022](#)). Moreover, the early responses appeared less natural than the late responses ([Im and Fried, 2015](#)), remaining another challenge as to how to make overall artificial spiking activities as physiological as possible. Taken together, our results raise a possibility that retinal prosthetic users with *CRB1* gene mutation may experience

more challenges to discern any bright spots or perceive somewhat sophisticated patterns.

4.3. The quality of prosthetic vision may vary substantially across different genotypes

Even though identical retinal prostheses were implanted, some prosthetic users did not experience any artificial vision ([Stingl et al., 2015](#)). Due to the lack of genotyping before the implantations, subjects might have various genetic mutations and resulting considerable performance variations across the users. To explore any dependence on the RP genotypes, our earlier work ([Yoon et al., 2020](#)) and the present study have thoroughly analyzed electric responses of the major RGC types in the *rd10* and *rd8* mice which have *Pde6b* and *Crb1* mutations. However, in terms of prevalence, *PDE6B* and *CRB1* genes only takes 4–5% and 1% of the population of ARRP, respectively ([Hartong et al., 2006](#)). It is also worth noting that there are still plenty genes that cause blindness (see **Figure 1B**). Thus, it is somewhat doubtful whether experimental results obtained from both *rd10* and *rd8* mouse models can be effectively translational to the whole RP population. Also, there is a possibility that different clinical outcomes of retinal prostheses ([Stingl et al., 2015](#)) might be occurred by different types of mutated genes causing RP due to its genetic diversity. Therefore, additional RP animal models with different genotypes are highly likely to contribute for the future success of not only retinal prosthetics but also other sight restoration approaches such as optogenetics. In the case of rat models which have much bigger eyeballs than mouse models, the Royal College of Surgeons (RCS) rats are most widely used, which has a mutation in *Mertk* gene ([Vollrath et al., 2001](#)). *Mertk* is the orthologue of human *MERTK* gene which is responsible for less than 1% of autosomal recessive RP ([Hartong et al., 2006](#)). To represent bigger population of RP patients, there have been recent endeavors to develop new models such as *Pde6b* gene knockout rats ([Yeo et al., 2019](#); [Yang et al., 2021](#)).

Although it has not received much attention so far, we may need to pay extra considerations on both genotype and phenotype of

patients for the further improvement of retinal implants (Kuehlewein et al., 2022). For example, although the progression of retinal degeneration seems to reduce artificial visual information (Kang et al., 2021), it may be possible that certain genotype(s) minimizes the reduction in prosthetic neural information, raising a necessity to compute the artificial visual information transmitted from RGC populations (Kim et al., 2022). Also, the field of retinal prosthetics would need fundamental neuroscience research to reveal the underlying mechanisms of our findings reported here.

4.4. Limitations of this study

The present study has several limitations to be considered. First, we just classified the RGCs into three physiological types according to their light responses (i.e., non-DS ON, non-DS OFF, and DS ON-OFF cells). Since the retina is a very complex and sophisticated sensory organ, which has a tremendous number of RGC types including several subtypes in both ON and OFF pathways. Previous researches reported that RGCs can be divided into more than ~42 subtypes based on their genetic, morphological, and functional features (Boycott and Wässle, 1974; Baden et al., 2016; Kim et al., 2021; Goetz et al., 2022). Therefore, there is a possibility that some of the subtype-dependent characteristics might have been missed in our analyses. In the future follow-up study, it seems necessary to precisely subdivide RGC types using more advanced techniques. Second, our study has not considered the effect of aging which not only changes the morphology of RGCs but also cause loss of the RGCs (Neufeld and Gachie, 2003; Bell et al., 2020; Lee et al., 2022). Moreover, there is a risk of developing glaucoma which is another representative age-related disease that damages the function of RGCs (Chrysostomou et al., 2010; Bell et al., 2020).

5. Conclusion

In the present work, for the first time, we have reported the distinct electric responses of RGCs in ON, OFF, and DS types from the *rd8* mice (PW8-18) which carry *Crb1* mutation, and compared those of the *wt* mice in each type. In each RGC type of the *rd8* retinas, the electrically-evoked spiking responses seemed quite similar to those arising in the corresponding type of the healthy retina. It was somehow expected since our histological analyses showed, other than sporadic retinal folds, the relatively well-maintained retinal structures, suggesting that the *rd8* mice we used in this work were at the early-stage RP. However, populational characteristics were differently altered across the RGC types in terms of the correlations between the electric vs. light response features: both DS and non-DS RGCs of the *rd8* retinas showed much distinct correlation levels/tendencies contrary to those appeared in the *wt* retinas (Table 2). Also, the consistencies of electric responses significantly decreased in both ON and OFF RGCs of the *rd8* retinas, which is one of the hallmarks of degenerate retinas compared to the *wt* retinas; but the similar reduction was not observed in DS RGCs of the *rd8* retinas. All in all, for the enhanced performance of retinal prostheses in clinical use, it seems vital to perform comparative studies of key physiological types of RGCs across animal models with various genotypes.

Data availability statement

The original contributions presented in this study are included in the article/supplementary material, further inquiries can be directed to the corresponding author.

Ethics statement

This animal study was reviewed and approved by Institutional Animal Care and Use Committees of the Korea Institute of Science and Technology.

Author contributions

HR and YO conducted the cell-attached patch clamping experiments and analyzed the data. JE performed the H&E staining and summarized the histological characteristics. DK investigated the previous literatures regarding genotypes of outer retinal degenerative diseases and wrote the relevant texts. HR drafted the figures and manuscript. MI designed the study, supervised the all experiments and data analyses, and revised the figures and manuscript. All authors reviewed and approved the final manuscript before submission.

Funding

This work was supported in part by a KIST (Korea Institute of Science and Technology) institutional grant (2E31821) and the National R&D Program through the National Research Foundation (NRF) of Korea funded by the Ministry of Science and ICT (Nos. 2020R1C1C1006065, 2021M3F3A2A01037366, and 2022M3E5E8017395).

Acknowledgments

We would like to thank Seulgi Yang and Minho Nam for their technical assistance in H&E staining of this study.

Conflict of interest

The authors declare that the research was conducted in the absence of any commercial or financial relationships that could be construed as a potential conflict of interest.

Publisher's note

All claims expressed in this article are solely those of the authors and do not necessarily represent those of their affiliated organizations, or those of the publisher, the editors and the reviewers. Any product that may be evaluated in this article, or claim that may be made by its manufacturer, is not guaranteed or endorsed by the publisher.

References

- Ahuja, A. K., Dorn, J. D., Caspi, A., McMahon, M. J., Dagnelie, G., DaCruz, L., et al. (2011). Blind subjects implanted with the Argus II retinal prosthesis are able to improve performance in a spatial-motor task. *Br. J. Ophthalmol.* 95, 539–543. doi: 10.1136/bjo.2010.179622
- Aleman, T. S., Cideciyan, A. V., Aguirre, G. K., Huang, W. C., Mullins, C. L., Roman, A. J., et al. (2011). Human CRB1-associated retinal degeneration: Comparison with the rd8 Crb1-mutant mouse model. *Investig. Ophthalmol. Vis. Sci.* 52, 6898–6910. doi: 10.1167/iovs.11-7701
- Aredo, B., Zhang, K., Chen, X., Wang, C. X. Z., Li, T., and Ufret-Vincenty, R. L. (2015). Differences in the distribution, phenotype and gene expression of subretinal microglia/macrophages in C57BL/6N (Crb1rd8/rd8) versus C57BL6/J (Crb1wt/wt) mice. *J. Neuroinflammation*. 12:6. doi: 10.1186/s12974-014-0221-4
- Baden, T., Berens, P., Franke, K., Román Rosón, M., Bethge, M., and Euler, T. (2016). The functional diversity of retinal ganglion cells in the mouse. *Nature* 529, 345–350. doi: 10.1038/nature16468
- Battu, P., Sharma, K., Thangavel, R., Singh, R., Sharma, S., Srivastava, V., et al. (2022). Genotyping of clinical parameters in age-related macular degeneration. *Clin. Ophthalmol. (Auckland, N.Z.)* 16, 517–529. doi: 10.2147/OPTH.S318098
- Bell, K., Rosignol, I., Sierra-Filardi, E., Rodriguez-Muela, N., Schmelter, C., Cecconi, F., et al. (2020). Age related retinal Ganglion cell susceptibility in context of autophagy deficiency. *Cell Death Discov.* 6:21. doi: 10.1038/s41420-020-0257-4
- Berger, W., Kloeckener-Gruissem, B., and Neidhardt, J. (2010). The molecular basis of human retinal and vitreoretinal diseases. *Prog. Retin. Eye Res.* 29, 335–375. doi: 10.1016/j.preteyeres.2010.03.004
- Black, J. R. M., and Clark, S. J. (2016). Age-related macular degeneration: Genome-wide association studies to translation. *Genet. Med.* 18, 283–289. doi: 10.1038/gim.2015.70
- Borst, A., and Euler, T. (2011). Seeing things in motion: Models, circuits, and mechanisms. *Neuron* 71, 974–994. doi: 10.1016/j.neuron.2011.08.031
- Boycott, B. B., and Wässle, H. (1974). The morphological types of ganglion cells of the domestic cat's retina. *J. Physiol.* 240, 397–419. doi: 10.1113/jphysiol.1974.sp010616
- Bravo-Gil, N., González-Del Pozo, M., Martín-Sánchez, M., Méndez-Vidal, C., Rodríguez-De La Rúa, E., Borrego, S., et al. (2017). Unravelling the genetic basis of complex retinitis pigmentosa cases. *Sci. Rep.* 33, 306–315. doi: 10.1038/srep41937
- Bujakowska, K., Audo, I., Mohand-Said, S., Lancelot, M. E., Antonio, A., Germain, A., et al. (2015). CRB1 mutations in inherited retinal dystrophies. *Hum. Mutat.* 33, 306–315. doi: 10.1002/humu.21653
- Chang, B., Hawes, N. L., Hurd, R. E., Davisson, M. T., Nusinowitz, S., and Heckenlively, J. R. (2002). Retinal degeneration mutants in the mouse. *Vis. Res.* 42, 517–525. doi: 10.1016/S0042-6989(01)00146-8
- Chang, S., Vaccarella, L., Olatunji, S., Cebulla, C., and Christoforidis, J. (2011). Diagnostic challenges in retinitis pigmentosa: Genotypic multiplicity and phenotypic variability. *Curr. Genomics*. 12, 267–275. doi: 10.2174/138920211795860116
- Chrysostomou, V., Trownc, I. A., and Crowston, J. G. (2010). Mechanisms of retinal ganglion cell injury in aging and glaucoma. *Ophthalmic Res.* 44, 173–178. doi: 10.1159/000316478
- Churchland, M. M., Yu, B. M., Cunningham, J. P., Sugrue, L. P., Cohen, M. R., Corrado, G. S., et al. (2010). Stimulus onset quenches neural variability: A widespread cortical phenomenon. *Nat. Neurosci.* 13, 369–378. doi: 10.1038/nn.2501
- Cutts, C. S., and Egle, X. S. J. (2014). Detecting pairwise correlations in spike trains: An objective comparison of methods and application to the study of retinal waves. *J. Neurosci.* 34, 14288–14303. doi: 10.1523/JNEUROSCI.2767-14.2014
- da Cruz, L., Coley, B. F., Dorn, J., Merlino, F., Filley, E., Christopher, P., et al. (2013). The Argus II epiretinal prosthesis system allows letter and word reading and long-term function in patients with profound vision loss. *Br. J. Ophthalmol.* 97, 632–636. doi: 10.1136/bjophthalmol-2012-301525
- Dan, Y., Atick, J. J., and Reid, R. C. (1996). Efficient coding of natural scenes in the lateral geniculate nucleus: Experimental test of a computational theory. *J. Neurosci.* 16, 3351–3362. doi: 10.1523/jneurosci.16-10-03351.1996
- David, S. V., Vinje, W. E., and Gallant, J. L. (2004). Natural stimulus statistics alter the receptive field structure of V1 neurons. *J. Neurosci.* 24, 6991–7006. doi: 10.1523/JNEUROSCI.1422-04.2004
- Detwiler, P. B., Crook, J., Packer, O., Robinson, F., and Dacey, D. M. (2019). The recursive bistratified ganglion cell type of the macaque monkey retina is ON-OFF direction selective. *Investig. Ophthalmol. Vis. Sci.* 60:3884. doi: 10.1002/cne.25258
- Famiglietti, E. V. (1992). Dendritic Co-stratification of ON and ON-OFF directionally selective ganglion cells with starburst amacrine cells in rabbit retina. *J. Comp. Neurol.* 324, 322–335. doi: 10.1002/cne.903240303
- Fohlmeister, J. F., and Miller, R. F. (1997). Impulse encoding mechanisms of ganglion cells in tiger salamander retina. *J. Neurophysiol.* 78, 1935–1947. doi: 10.1152/jn.1997.78.4.1935
- Freeman, D. K., Eddington, D. K., Rizzo, J. F., and Fried, S. I. (2010). Selective activation of neuronal targets with sinusoidal electric stimulation. *J. Neurophysiol.* 104, 2778–2791. doi: 10.1152/jn.00551.2010
- Fried, S. I., Hsueh, H. A., and Werblin, F. S. (2006). A method for generating precise temporal patterns of retinal spiking using prosthetic stimulation. *J. Neurophysiol.* 95, 970–978. doi: 10.1152/jn.00849.2005
- Fried, S. I., Münch, T. A., and Werblin, F. S. (2002). Mechanisms and circuitry underlying directional selectivity in the retina. *Nature* 420, 411–414. doi: 10.1038/nature01179
- Fujikado, T., Morimoto, T., Kanda, H., Kusaka, S., Nakauchi, K., Ozawa, M., et al. (2007). Evaluation of phosphene elicited by extraocular stimulation in normals and by suprachoroidal-transretinal stimulation in patients with retinitis pigmentosa. *Graefes Arch. Clin. Exp. Ophthalmol.* 245, 1411–1419. doi: 10.1007/s00417-007-0563-z
- Gargini, C., Terzibasi, E., Mazzoni, F., and Strettoi, E. (2007). Retinal organization in the retinal degeneration 10 (rd10) mutant mouse: A morphological and ERG study. *J. Comp. Neurol.* 500, 222–238. doi: 10.1002/cne.21144
- Goetz, J., Jessen, Z. F., Jacobi, A., Mani, A., Cooler, S., Greer, D., et al. (2022). Unified classification of mouse retinal ganglion cells using function, morphology, and gene expression. *Cell Rep.* 40:111040. doi: 10.1016/j.celrep.2022.111040
- Hartong, D. T., Berson, E. L., and Dryja, T. P. (2006). Retinitis pigmentosa. *Lancet* 368, 1795–1809. doi: 10.1016/S0140-6736(06)69740-7
- Hawes, N. L., Chang, B., Hageman, G. S., Nusinowitz, S., Nishina, P. M., Schneider, B. S., et al. (2000). Retinal degeneration 6 (rd6): A new mouse model for human retinitis punctata albescens. *Investig. Ophthalmol. Vis. Sci.* 41, 3149–3157.
- Hippert, C., Graca, A. B., Barber, A. C., West, E. L., Smith, A. J., Ali, R. R., et al. (2015). Müller glia activation in response to inherited retinal degeneration is highly varied and disease-specific. *PLoS One* 10:e0120415. doi: 10.1371/journal.pone.0120415
- Hu, C., Bi, A., and Pan, Z. (2009). Differential expression of three T-type calcium channels in retinal bipolar cells in rats. *Vis. Neurosci.* 26, 177–187. doi: 10.1017/S0952523809000026
- Humayun, M. S., De Juan, E., Dagnelie, G., Greenberg, R. J., Propst, R. H., and Phillips, D. H. (1996). Visual perception elicited by electrical stimulation of retina in blind humans. *Arch. Ophthalmol.* 114, 40–46. doi: 10.1001/archoph.1196.01100130038006
- Humayun, M. S., Weiland, J. D., Fujii, G. Y., Greenberg, R., Williamson, R., Little, J., et al. (2003). Visual perception in a blind subject with a chronic microelectronic retinal prosthesis. *Vis. Res.* 43, 2573–2781. doi: 10.1016/S0042-6989(03)00457-7
- Im, M., and Fried, S. I. (2015). Indirect activation elicits strong correlations between light and electrical responses in ON but not OFF retinal ganglion cells. *J. Physiol.* 593, 3577–3596. doi: 10.1113/JP270606
- Im, M., and Fried, S. I. (2016a). Directionally selective retinal ganglion cells suppress luminance responses during natural viewing. *Sci. Rep.* 6:35708. doi: 10.1038/srep35708
- Im, M., and Fried, S. I. (2016b). Temporal properties of network-mediated responses to repetitive stimuli are dependent upon retinal ganglion cell type. *J. Neural. Eng.* 13:025002. doi: 10.1088/1741-2560/13/2/025002
- Im, M., Werginz, P., and Fried, S. I. (2018). Electric stimulus duration alters network-mediated responses depending on retinal ganglion cell type. *J. Neural. Eng.* 15:036010. doi: 10.1088/1741-2552/aaadcl
- Jacobson, S. G., Cideciyan, A. V., Aleman, T. S., Pianta, M. J., Sumaroka, A., Schwartz, S. B., et al. (2003). Crumbs homolog 1 (CRB1) mutations result in a thick human retina with abnormal lamination. *Hum. Mol. Genet.* 12, 1073–1078. doi: 10.1093/hmg/ddg117
- Jager, R. D., Mieler, W. F., and Miller, J. W. (2008). Age-related macular degeneration. *N. Engl. J. Med.* 358, 2606–2617. doi: 10.1056/NEJMra0801537
- Kang, J. H., Jang, Y. J., Kim, T., Lee, B. C., Lee, S. H., and Im, M. (2021). Electric stimulation elicits heterogeneous responses in ON but not OFF retinal ganglion cells to transmit rich neural information. *IEEE Trans. Neural. Syst. Rehabil. Eng.* 29, 300–309. doi: 10.1109/TNSRE.2020.3048973
- Kim, S., Roh, H., and Im, M. (2022). Artificial visual information produced by retinal prostheses. *Front. Cell Neurosci.* 16:911754. doi: 10.3389/fncel.2022.911754
- Kim, U. S., Mahroo, O. A., Mollon, J. D., and Yu-Wai-Man, P. (2021). Retinal ganglion cells-diversity of cell types and clinical relevance. *Front. Neurol.* 12:661938. doi: 10.3389/fneur.2021.661938
- Kuehlewein, L., Straßer, T., Blumenstock, G., Stingl, K., Fischer, M. D., Wilhelm, B., et al. (2022). Central visual function and genotype-phenotype correlations in PDE6A-associated retinitis pigmentosa. *Invest. Ophthalmol. Vis. Sci.* 63:9. doi: 10.1167/iovs.63.5.9
- Lee, J.-I., and Im, M. (2018). Non-rectangular waveforms are more charge-efficient than rectangular one in eliciting network-mediated responses of on type retinal ganglion cells. *J. Neural. Eng.* 15:055004. doi: 10.1088/1741-2552/aad416
- Lee, J.-I., and Im, M. (2019). Optimal electric stimulus amplitude improves the selectivity between responses of ON versus OFF types of retinal ganglion cells. *IEEE Trans. Neural. Syst. Rehabil. Eng.* 27, 2015–2024. doi: 10.1109/TNSRE.2019.2939012
- Lee, P. Y., Zhao, D., Wong, V. H. Y., Chrysostomou, V., Crowston, J. G., and Bui, B. V. (2022). The effect of aging on retinal function and retinal ganglion cell morphology following intraocular pressure elevation. *Front. Aging Neurosci.* 14:859265. doi: 10.3389/fnagi.2022.859265

- Lin, B., and Masland, R. H. (2006). Populations of wide-field amacrine cells in the mouse retina. *J. Comp. Neurol.* 499, 797–809. doi: 10.1002/cne.21126
- MacNeil, M. A., and Masland, R. H. (1998). Extreme diversity among amacrine cells: Implications for function. *Neuron* 20, 971–982. doi: 10.1016/S0896-6273(00)80478-X
- MacNeil, M. A., Heuss, J. K., Dacheux, R. F., Raviola, E., and Masland, R. H. (1999). The shapes and numbers of amacrine cells: Matching of photofilled with Golgi-stained cells in the rabbit retina and comparison with other mammalian species. *J. Comp. Neurol.* 413, 305–326. doi: 10.1002/(SICI)1096-9861(19991018)413:2<305::AID-CNE10<3.0.CO;2-E
- Marc, R. E., and Jones, B. W. (2003). Retinal remodeling in inherited photoreceptor degenerations. *Mol. Neurobiol.* 28, 139–147. doi: 10.1385/MN:28:2:139
- Marc, R. E., Jones, B. W., Watt, C. B., and Strettoi, E. (2003). Neural remodeling in retinal degeneration. *Prog. Retin. Eye Res.* 22, 607–655. doi: 10.1016/S1350-9462(03)00039-9
- Mauss, A. S., Vlasits, A., Borst, A., and Feller, M. (2017). Visual circuits for direction selectivity. *Annu. Rev. Neurosci.* 40, 211–230. doi: 10.1146/annurev-neuro-072116-031335
- Mehalow, A. K., Kameya, S., Smith, R. S., Hawes, N. L., Denegre, J. M., Young, J. A., et al. (2003). CRB1 is essential for external limiting membrane integrity and photoreceptor morphogenesis in the mammalian retina. *Hum. Mol. Genet.* 12, 2179–2189. doi: 10.1093/hmg/ddg232
- Mori, K., Horie-Inoue, K., Gehlbach, P. L., Takita, H., Kabasawa, S., Kawasaki, I., et al. (2010). Phenotype and genotype characteristics of age-related macular degeneration in a Japanese population. *Ophthalmology* 117, 928–938. doi: 10.1016/j.ophtha.2009.10.001
- Murphy, G. J., and Rieke, F. (2006). Network variability limits stimulus-evoked spike timing precision in retinal ganglion cells. *Neuron* 52, 511–524. doi: 10.1016/j.neuron.2006.09.014
- Naycheva, L., Schatz, A., Röck, T., Willmann, G., Messias, A., Bartz-Schmidt, K. U., et al. (2012). Phosphene thresholds elicited by transcorneal electrical stimulation in healthy subjects and patients with retinal diseases. *Investig. Ophthalmol. Vis. Sci.* 53, 7440–7448. doi: 10.1167/iovs.12-9612
- Neufeld, A. H., and Gachie, E. N. (2003). The inherent, age-dependent loss of retinal ganglion cells is related to the lifespan of the species. *Neurobiol. Aging* 24, 167–172. doi: 10.1016/S0197-4580(02)00059-3
- Otgondemberel, Y., Roh, H., Fried, S. I., and Im, M. (2021). Spiking characteristics of network-mediated responses arising in direction-selective ganglion cells of rabbit and mouse retinas to electric stimulation for retinal prostheses. *IEEE Trans. Neural. Syst. Rehabil. Eng.* 29, 2445–2455. doi: 10.1109/TNSRE.2021.3128878
- Palanker, D., Le Mer, Y., Mohand-Said, S., and Sahel, J. A. (2022). Simultaneous perception of prosthetic and natural vision in AMD patients. *Nat. Commun.* 13:513. doi: 10.1038/s41467-022-28125-x
- Palanker, D., Le Mer, Y., Mohand-Said, S., Muqit, M., and Sahel, J. A. (2020). Photovoltaic restoration of central vision in atrophic age-related macular degeneration. *Ophthalmology* 127, 1097–1104. doi: 10.1016/j.ophtha.2020.02.024
- Pang, J. J., Gao, F., and Wu, S. M. (2003). Light-evoked excitatory and inhibitory synaptic inputs to ON and OFF α ganglion cells in the mouse retina. *J. Neurosci.* 23, 6063–6073. doi: 10.1523/jneurosci.23-14-06063.2003
- Protti, D. A., and Llano, I. (1998). Calcium currents and calcium signaling in rod bipolar cells of rat retinal slices. *J. Neurosci.* 18, 3715–3724. doi: 10.1523/JNEUROSCI.18-10-03715.1998
- Rizzo, J. F., Wyatt, J., Loewenstein, J., Kelly, S., and Shire, D. (2003). Perceptual efficacy of electrical stimulation of human retina with a microelectrode array during short-term surgical trials. *Investig. Ophthalmol. Vis. Sci.* 44, 5362–5369. doi: 10.1167/iovs.02-0817
- Roh, H., Otgondemberel, Y., and Im, M. (2022). Short pulses of epiretinal prostheses evoke network-mediated responses in retinal ganglion cells by stimulating presynaptic neurons. *J. Neural. Eng.* 19:055006. doi: 10.1088/1741-2552/ac8ed7
- Stingl, K., Bartz-Schmidt, K. U., Besch, D., Chee, C. K., Cottrell, C. L., Gekeler, F., et al. (2015). Subretinal visual implant Alpha IMS - clinical trial interim report. *Vis. Res.* 111, 149–160. doi: 10.1016/j.visres.2015.03.001
- Strettoi, E., Raviola, E., and Dacheux, R. F. (1992). Synaptic connections of the narrow-field, bistratified rod amacrine cell (AII) in the rabbit retina. *J. Comp. Neurol.* 325, 152–168. doi: 10.1002/cne.903250203
- Thoreson, W. B. (2007). Kinetics of synaptic transmission at ribbon synapses of rods and cones. *Mol. Neurobiol.* 36, 205–223. doi: 10.1007/s12035-007-0019-9
- Touryan, J., Felsen, G., and Dan, Y. (2005). Spatial structure of complex cell receptive fields measured with natural images. *Neuron* 45, 781–791. doi: 10.1016/j.neuron.2005.01.029
- Tsai, D., Morley, J. W., Suaning, G. J., and Lovell, N. H. (2009). Direct activation and temporal response properties of rabbit retinal ganglion cells following subretinal stimulation. *J. Neurophysiol.* 102, 2982–2993. doi: 10.1152/jn.00545.2009
- Tsukamoto, Y., and Omi, N. (2017). Classification of mouse retinal bipolar cells: Type-specific connectivity with special reference to rod-driven AII amacrine pathways. *Front. Neuroanat.* 11:92. doi: 10.3389/fnana.2017.00092
- Twynford, P., Cai, C., and Fried, S. (2014). Differential responses to high-frequency electrical stimulation in on and off retinal ganglion cells. *J. Neural. Eng.* 11:025001. doi: 10.1088/1741-2560/11/2/025001
- van de Pavert, S. A., Kantardzhieva, A., Malysheva, A., Meuleman, J., Versteeg, I., Levelt, C., et al. (2004). Crumbs homologue 1 is required for maintenance of photoreceptor cell polarization and adhesion during light exposure. *J. Cell Sci.* 117, 4169–4177. doi: 10.1242/jcs.01301
- van de Pavert, S. A., Meuleman, J., Malysheva, A., Aartsen, W. M., Versteeg, I., Tonagel, F., et al. (2007). A single amino acid substitution (Cys249Trp) in Crb1 causes retinal degeneration and deregulates expression of pituitary tumor transforming gene Pttg1. *J. Neurosci.* 27, 564–573. doi: 10.1523/JNEUROSCI.3496-06.2007
- Vaney, D. I., Sivyer, B., and Taylor, W. R. (2012). Direction selectivity in the retina: Symmetry and asymmetry in structure and function. *Nat. Rev. Neurosci.* 13, 194–208.
- Verbakel, S. K., van Huet, R. A. C., Boon, C. J. F., den Hollander, A. I., Collin, R. W. J., Klaver, C. C. W., et al. (2018). Non-syndromic retinitis pigmentosa. *Prog. Retin. Eye Res.* 66, 157–186. doi: 10.1016/j.preteyeres.2018.03.005
- Vollrath, D., Feng, W., Duncan, J. L., Yasumura, D., D'Cruz, P. M., Chappelow, A., et al. (2001). Correction of the retinal dystrophy phenotype of the RCS rat by viral gene transfer of Mertk. *Proc. Natl. Acad. Sci. U.S.A.* 98, 12584–12589. doi: 10.1073/pnas.221364198
- Wei, W. (2018). Neural mechanisms of motion processing in the mammalian retina. *Annu. Rev. Vis. Sci.* 4, 165–192. doi: 10.1146/annurev-vision-091517-034048
- Yang, J. M., Chung, S., Yun, K. A., Kim, B., So, S., Kang, S., et al. (2021). Long-term effects of human induced pluripotent stem cell-derived retinal cell transplantation in Pde6b knockout rats. *Exp. Mol. Med.* 53, 631–642. doi: 10.1038/s12276-021-00588-w
- Yeo, J. H., Jung, B. K., Lee, H., Baek, I. J., Sung, Y. H., Shin, H. S., et al. (2019). Development of a Pde6b gene knockout rat model for studies of degenerative retinal diseases. *Investig. Ophthalmol. Vis. Sci.* 60, 1519–1526. doi: 10.1167/iovs.18-25556
- Yoon, Y. J., Lee, J. I., Jang, Y. J., An, S., Kim, J. H., Fried, S. I., et al. (2020). Retinal degeneration reduces consistency of network-mediated responses arising in ganglion cells to electric stimulation. *IEEE Trans. Neural. Syst. Rehabil. Eng.* 28, 1921–1930. doi: 10.1109/TNSRE.2020.3003345
- Zrenner, E., Bartz-Schmidt, K. U., Benav, H., Besch, D., Bruckmann, A., Gabel, V. P., et al. (2011). Subretinal electronic chips allow blind patients to read letters and combine them to words. *Proc. R. Soc. B Biol. Sci.* 278, 1489–1497. doi: 10.1098/rspb.2010.1747



OPEN ACCESS

EDITED BY

Günther Zeck,
Vienna University of Technology, Austria

REVIEWED BY

Stefan Gahbauer,
University of California, San Francisco,
United States
Chelsea Deleon,
University of North Carolina at Chapel
Hill, United States

*CORRESPONDENCE

Sonja Kleinlogel,
✉ sonja.kleinlogel@roche.com

†PRESENT ADDRESS

Sonja Kleinlogel,
Translational Medicine Neuroscience, F.
Hoffmann-La
Roche Ltd, Basel, Switzerland; Roche
Pharma Research and Early
Development, Neuroscience and Rare
Diseases, Roche Innovation Center Basel,
F. Hoffmann-La Roche Ltd., Basel,
Switzerland

SPECIALTY SECTION

This article was submitted to Signaling,
a section of the journal
Frontiers in Cell and
Developmental Biology

RECEIVED 28 September 2022

ACCEPTED 14 February 2023

PUBLISHED 01 March 2023

CITATION

Leemann S and Kleinlogel S (2023),
Functional optimization of light-
activatable Opto-GPCRs: Illuminating the
importance of the proximal C-terminus in
G-protein specificity.
Front. Cell Dev. Biol. 11:1053022.
doi: 10.3389/fcell.2023.1053022

COPYRIGHT

© 2023 Leemann and Kleinlogel. This is
an open-access article distributed under
the terms of the [Creative Commons
Attribution License \(CC BY\)](https://creativecommons.org/licenses/by/4.0/). The use,
distribution or reproduction in other
forums is permitted, provided the original
author(s) and the copyright owner(s) are
credited and that the original publication
in this journal is cited, in accordance with
accepted academic practice. No use,
distribution or reproduction is permitted
which does not comply with these terms.

Functional optimization of light-activatable Opto-GPCRs: Illuminating the importance of the proximal C-terminus in G-protein specificity

Siri Leemann and Sonja Kleinlogel*†

Translational Optogenetic Research Group, Institute of Physiology, University of Bern, Bern, Switzerland

Introduction: G-protein coupled receptors (GPCRs) are the largest family of human receptors that transmit signals from natural ligands and pharmaceutical drugs into essentially every physiological process. One main characteristic of G-protein coupled receptors is their ability to specifically couple with different families of G-proteins, thereby triggering specific downstream signaling pathways. While an abundance of structural information is available on G-protein coupled receptor interactions with G-proteins, little is known about the G-protein coupled receptor domains functionally mediating G-protein specificity, in particular the proximal C-terminus, the structure which cannot be predicted with high confidentiality due to its flexibility.

Methods: In this study, we exploited OptoGPCR chimeras between lightgated G-protein coupled receptors (opsins) and ligand-gated G-protein coupled receptors to systematically investigate the involvement of the C-terminus steering G-protein specificity. We employed rhodopsin-beta2-adrenoceptor and melanopsin-mGluR6 chimeras in second messenger assays and developed structural models of the chimeras.

Results: We discovered a dominant role of the proximal C-terminus, dictating G-protein selectivity in the melanopsin-mGluR6 chimera, whereas it is the intracellular loop 3, which steers G-protein tropism in the rhodopsin-beta2-adrenoceptor. From the functional results and structural predictions, melanopsin and mGluR6 use a different mechanism to bovine rhodopsin and b2AR to couple to a selective G-protein.

Discussion: Collectively, this work adds knowledge to the G-protein coupled receptor domains mediating G-protein selectivity, ultimately paving the way to optogenetically elicited specific G-protein signaling on demand.

KEYWORDS

OptoGPCR, optogenetics, rhodopsin, beta2-adrenoceptor, chimeric GPCR design, G protein selectivity, melanopsin, mGluR6

1 Introduction

Heterotrimeric, guanine-nucleotide binding G-protein coupled receptors (GPCRs) represent the largest family of membrane receptors in humans and play a principal role in physiology and pathology by transforming extracellular signals into intracellular responses. Therefore, drugs targeting GPCRs account for the largest portion of pharmaceuticals on the global market (Hauser et al., 2017).

GPCRs can be classified into five families (Class A-F) (Rosenbaum et al., 2009) and possess a highly conserved structure characterized by seven transmembrane alpha helices (TMs) with alternating extra- and intracellular loops (ILs), an extracellular N-terminus and an intracellular C-terminal tail (C-terminus) of highly variable length. GPCRs exert their downstream signaling by binding and activating heterotrimeric G-proteins. While the G α subunit is the main mediator of downstream signaling and triggers second messengers, the G β and G γ subunits can influence diverse effectors, amongst them membrane ion channels. In humans, there are at least 16 known G α subunits, 6 G β , and 13 G γ subunits, which can be assembled in a large variety of different combinations (Oldham and Hamm, 2008). The G α subunits are subdivided into four main families, each with a specific signaling pathway: the stimulatory Gs-proteins, which activate adenylyl cyclase and thereby increase the intracellular cAMP levels; the inhibitory Gi/o family, which can be further classified into Gi, Go, Gz and Gt proteins and which contrarily decrease levels of cAMP by inhibiting adenylyl cyclase; the Gq/11 family, which acts through phospholipase and includes the Gq, G11 and G15 proteins, and finally, the G12/13 group that stimulates Rho kinases (Neves et al., 2002; Milligan and Kostenis, 2006). Since these proteins trigger distinct downstream signaling pathways, selective binding of a particular GPCR to a specific G-protein is critical for accurate signal transduction (Flock et al., 2017).

While GPCRs have been extensively studied structurally, adding immensely to our understanding of their workings, it remains rather elusive how they selectively activate specific G-proteins. The structural components and molecular processes of GPCR-G-protein interactions were first elucidated at the structural level in bovine rhodopsin (bRhod) (Salom et al., 2006) and the beta2-adrenoceptor (b2AR) (Rosenbaum et al., 2009; Rasmussen et al., 2011b), whereas mGluR structures were only recently resolved (Seven et al., 2021) and the crystal structure of melanopsin remains to be elucidated. From the structural studies it became obvious that the intracellular loop 3 (IL3) (Rasmussen et al., 2011b; Ma et al., 2020), the intracellular loop 2 (IL2) (Kang et al., 2018; Tsai et al., 2019; Qiao et al., 2020; Seven et al., 2021) as well as the C-terminus (Bertheleme et al., 2013; Tsai et al., 2018; Tsai et al., 2019; Seven et al., 2021) contact the G-protein. However, contact to the G-protein does not necessarily indicate that the domain mediates G-protein selectivity, since the multiple ionic interaction networks also comprising the GPCR core structure could mediate specific conformational differences required to accommodate a particular G-protein (Venkatakrisnan et al., 2016). In group A GPCRs, the displacement of TM6 upon activation creates a cleft between TM3, TM5 and TM6 for insertion of the G-protein's C-terminus. IL3 as a main contact point of the G-protein's

C-terminus is therefore considered to play a major role in G-protein selectivity (Rasmussen et al., 2011b; Tsai et al., 2019; Zhou et al., 2019). This assumption was supported by functional studies with engineered chimeric Opto-GPCRs (Kim et al., 2005; Airan et al., 2009; Siuda et al., 2015; van Wyk et al., 2015). It also became obvious that the helical extensions of TM5 and TM6, protruding intracellularly and framing IL3 are dynamically involved in G-protein binding (Xu et al., 2011; Rose et al., 2014; Rose et al., 2015), rotating and extending to provide the binding pocket for the C-terminus of the G-protein (Choe et al., 2011; Lebon et al., 2011; Rosenbaum et al., 2011; Standfuss et al., 2011; Xu et al., 2011; Wang et al., 2013). However, in mGluRs—and in particular in mGluR2 (Seven et al., 2021)—cytosolic TM6 opening was not observed, but instead the G-protein's C-terminus was stabilized by a pocket formed by IL2 and the C-terminus of mGluR2 (Seven et al., 2021). While IL3 orchestrates receptor rearrangement, it remains unclear whether it is equally implicated in the determination of G-protein specificity in mGluR2. In particular, a C-terminal region between V826-S833 was shown to affect mGluR2's G-protein tropism (Seven et al., 2021) (Supplementary Figure S1). Opsins and other Class A GPCRs possess a conserved amphipathic helix 8 (H8) that folds into an α -helix and is arranged parallel to the cell membrane with a distal palmitoylation site. H8 holds a crucial position towards the intracellular side, where G-protein coupling occurs, and was shown to actively promote G-protein binding as well as stabilizing conformational states of the GPCR (Palczewski et al., 2000; Bruno et al., 2012). Importantly, the short stretch between TM7 and H8 and the proximal C-terminus beyond H8 were structurally shown to be in close contact with the G-protein and predicted to determine selective G protein activation in bovine rhodopsin (Tsai et al., 2018; Tsai et al., 2019).

To functionally define the involvement of these GPCR-G-protein contact regions, mutational studies were conducted, but the focus was on single residues and mutation most likely perturbed conformational and biophysical properties of the GPCR. Others compared the differences in active states of a GPCR known to bind to different G-proteins (Ma et al., 2020; Qiao et al., 2020). For example, b2AR binds primarily to the Gs-protein but can also stimulate the Gi/o pathway (Xiao, 2001; Alegre et al., 2021). These structures provided some insights into the residues involved in G-protein binding and potentially also G-protein selectivity, although the main differences were found to be different interaction modes of the GPCR with the G-protein (Sandhu et al., 2019; Alegre et al., 2021).

In this study, we functionally explored the involvement of the proximal C-terminal domain in G-protein selectivity. We employed engineered chimeric Opto-GPCRs, proteins based on an opsin GPCR with specific intracellular domains exchanged by those of a selected ligand-gated target receptor (Kleinlogel, 2016). Pioneering studies were performed with bovine rhodopsin (bRhod), where all intracellular domains were swapped by analogues of ligand-gated target receptors and the chimeras were tested functionally for their G-protein binding selectivity (Yamashita et al., 2001; Kim et al., 2005). However, as shown in recent work, engineering all intracellular domains results in poorer expression and functionality in *in vivo* experiments (Kralik et al., 2022). Thus, the second aim of this study was to determine which intracellular domains were crucial to replace to

induce the desired downstream signaling. For this, we engineered a systematic assortment of chimeras between the structurally and functionally best known receptors, namely, bovine rhodopsin [Gt and Gi selective (Terakita et al., 2002)] and the beta2-adrenoceptor (b2AR) [primarily Gs, secondarily Gi selective (Xiao, 2001; Hasseldine et al., 2003; Rasmussen et al., 2011b)], as well as a set of chimeras between the not yet crystallized melanopsin [mainly Gq, partially Gi/o selective (Bailes and Lucas, 2013)] and mGluR6 [mainly Go selective, minimally Gi selective (Tian and Kammermeier, 2006)], two proteins with potentially different G-protein activation mechanisms (Spoida et al., 2016; Valdez-Lopez et al., 2020; Seven et al., 2021). We found that exchanging the proximal C-terminus was simultaneously crucial and sufficient to shift G-protein tropism in the melanopsin-mGluR6 chimera, whereas it was the known TM5-IL3-TM6 domain in the bRhod-b2AR chimera that induced the desired signaling.

2 Materials and methods

2.1 Sequences and cloning

The following GenBank sequences were used to engineer the opsin-target receptor chimeras: human melanopsin (AF147788.1), mGluR6 (U82083.1), bovine rhodopsin (AH001149.2), and beta2-adrenergic receptors (AY136741.1). Additionally, mouse melanopsin (AF147789.1) was used.

All chimeric opsin versions were designed as described in the main text, first cloned in pIRES_opsin_TurboFP635 plasmids and then modified to contain the fluorescent proteins mKate or mScarlet. To create the plasmids of the melanopsin-mGluR6 (pIRES_melanopsin-mGluR6_TurboFP635) and bRhod-b2AR chimeras (pIRES_rhodopsin-b2AR_TurboFP635), the respective domains of the intracellular loops and the C-terminus from mGluR6 or b2AR, respectively, were synthesized as primer overhangs and introduced using overlap extension PCR with EcoRI and BamHI restriction sites.

In the modified variants containing the fluorescent proteins, the Kir2.1 trafficking sequence (TS; KSRITSEGEYIPLDQIDINV) was inserted, as well as the 1D4 sequence from the C-terminus of bovine rhodopsin (TETSQVAPA), to create the final chimeras in pIRES_hMelanopsin-mGluR6_TS-1D4-mScarlet and pIRES_bRhod-b2AR_TS-1D4-mKate, respectively. All constructs were verified by Sanger sequencing (MicroSynth).

2.2 Cell culture

HEK293 wildtype cells were cultured in Dulbecco's modified Eagle medium (DMEM) in an incubator at 37 °C with 5% CO₂ atmosphere. DMEM was supplemented with 10% fetal calf serum (FCS; Seraglob, S70500), 1X glutamine (Seraglob, K8701), 1% penicillin/streptomycin (Sigma, P0781). Cells were seeded in 24- or 96-well plates (Greiner) at a density of 40,000 or 15,000 cells per well, respectively, and transiently transfected after 24 h using the TransIT[®]LI 1 reagent (MirusBio, MIR2300) according to the manufacturer's instructions. Briefly, the DNA and the transfection reagent were mixed in OptiMem medium (Sigma, 31,985,062) and incubated at room temperature for 20 min

before transferring it to the cells. For 24-well plates, 0.5 µg of plasmid DNA and 1.5 µL of reagent was mixed in 50 µL of OptiMem. For 96-well plates, 0.1 µg of plasmid and 0.3 µL of Mirus was mixed in 10 µL of OptiMem. After transfection, all further steps were carried out under dim red light.

2.3 Plate reader assays

To test for specificity, we performed a variety of plate reader assays, including the aequorin assay to test for Gq-coupling, the GloSensor assay to test for Gi/o- and Gs-coupling, as well as the GsX assay to specify Gi/o- and Gq-coupling more precisely.

2.3.1 Aequorin Ca²⁺ assay

To test for Gq-selectivity, we performed a standard Ca²⁺ assay using aequorin, a calcium-sensitive bioluminescent reporter protein, that is used extensively in GPCR assays as a calcium indicator. The measured luminescence is directly proportional to the Ca²⁺ concentration. For transfection, cells were transiently transfected with a 2:1 ratio of GPCR chimera plasmid and reporter DNA. Cells were incubated in the transfection reagent for 3–4 h and then supplemented by complete medium containing 1 µg/mL doxycyclin and 1 µM 9-cis retinal. The following day, the cells were incubated for 1 hour in the dark at room temperature in phenol-free Leibovitz (L-15) medium containing penicillin/streptomycin, 10% FCS, and L-glutamine (Gibco), 1 µM 9-cis retinal and 10 µM coelenterazine-h. For the measurements, 100 µL of cell suspension was added to a single well of a white 96-well plate. Luminescence was measured using an Infinite 200Pro Tecan plate reader (Männedorf, Switzerland). Raw luminescence was measured every 15 s. After letting the cells adapt for 1 minute and measuring baseline luminescence for six cycles, the plate was ejected, the cells were subjected to the stimulus, and recording resumed for a minimum of 15 additional cycles. Cells were stimulated by a single light flash. Data was collected in i-control (Tecan) from three replicates for each construct and condition during each assay.

2.3.2 GloSensor cAMP assay

To test for Gs and Gi signaling, we performed a standard cAMP assay using GloSensor, a bioluminescent cAMP reporter. Cells were seeded at a density of 15,000 the day before or at 40,000 the day of transfection in solid white 96-well plates and co-transfected overnight or for at least 6 h as above with a 2:1 ratio of GPCR plasmid and GloSensor reporter DNA. Cells were incubated at 37° and 5% CO₂ in the transfection reagent for 1–2 h before supplementing with medium containing 1 µg/mL doxycyclin and 1 µM 9-cis retinal and, where appropriate, 100 ng pertussis toxin. Pertussis toxin was added to inhibit endogenous Gi signaling. The following day, 1–2 h before taking the measurements, the cells were incubated at room temperature in the dark in phenol-red free Leibovitz media containing FBS, penicillin/streptomycin and L-glutamine, with 1 µM 9-cis retinal and 4 mM beetle luciferin. Beetle luciferin potassium salt (Promega) was reconstituted in 10 mM HEPES with a p.H. of 6.9.

For the Gs second messenger assay, a baseline luminescence was measured for every 15 s for 12 cycles, then the plate was ejected, and the cells were subjected to the stimulus. For the Gi assay, 50 µL of 3 µM forskolin was added to the cells directly

prior to beginning the assay to raise cAMP levels before exposing the cells to the stimulus. Here, raw luminescence was measured every 15 s for 60 cycles to allow for cAMP levels to rise high enough in order for proper measurement of the cAMP decrease following the light stimulus. Cells were stimulated with a single 470 nm light flash from a custom-built LED array. Data was collected from three replicates for each construct and condition during each assay. To evaluate the Gs to Gi signaling ratio for bRhod-b2AR chimeras, pertussis toxin (PTX) was added to the Gs assay, blocking Gi responses. Subtracting the Gs response during PTX block from the Gs response without PTX was used as a proxy for the pure Gi response.

2.3.3 GsX assay

The GsX assay was established according to the protocol by Ballister and R. Lucas (Ballister et al., 2018). GsX plasmids (AddGene) are Gs subunit chimeras that transform the coupling of receptors to specific G proteins into increases in cAMP levels. Therefore, this assay can be used to test a greater variety of G protein coupling more precisely within one assay. Since the C-termini of the G proteins are known to be crucial in coupling selectivity, chimeric Gs subunits were designed by the Lucas group, in which the 13 most distal residues are replaced with different Galpha C-terminal sequences. Consequently, a GPCR that hypothetically couples to Gi, Gt, and G15 would activate the GsX chimeras with a Gi, Gt or G15 tail (termed Gsi, Gst, and Gs15), leading to downstream Gs signaling and an increase in cAMP levels. The assays were executed analogously to the GloSensor cAMP assays described above. For transfection, cells were transfected with a 1:2 ratio of GloSensor reporter and plasmid DNA. Additionally, 50 ng of GsX chimera DNA was added to the transfection reagent, resulting in a final ratio of 10:5:1 of plasmid, reporter and GsX DNA. We found the 10:1 ratio of plasmid:GsX to be optimal when tested with human rhodopsin and Gsi (see [Supplementary Figure S2](#)).

2.4 Immunofluorescence

For immunohistochemistry, cells were transiently transfected in 24-well plates at a density of 40,000 cells as described above. Cells were then seeded onto coated Superfrost™ Plus Adhesion Microscope slides (Eppredia, J1800AMNZ) and incubated at 37° overnight.

Sections were analyzed either under a Zeiss inverted microscope, equipped with Axiocam 712 mono-camera and ZEISS-Blue software, or under an ANA_Zeiss_LSM 880 confocal microscope (equipment supported by the Microscopy Imaging Center (MIC), University of Bern, Switzerland). Images were then processed and analyzed using ImageJ. The fluorescence intensity was measured across the cell membrane by drawing a line across the membrane and plotting the intensity profile in ImageJ, and was consecutively normalized in Excel. Fluorescence values were first normalized to the maximum average fluorescence along the radial line of the cells and, secondly, normalized to the wildtype opsins, which were set to 1.

2.5 Data processing and statistics

For the second messenger plate reader assays, raw luminescence was first normalized by dividing by the measured mKate2 fluorescence of each well, normalizing for the number of cells and subtracting the baseline luminescence signal. In the standard second messenger assays, the luminescence signal was normalized to baseline and then normalized to the wildtype opsin for the Gs and Gq assays, which was set to 1. For the Gi assays, luminescence was normalized to the maximum fold decrease in cAMP levels and then analogously normalized to the wildtype opsin. This is shown as the normalized luminescence in the time-course graphs in [Supplementary Figures S3, S4, S5, S7](#). For the GsX assays, the maximum fold increase in the cAMP level was calculated and normalized to baseline. The wildtype opsin was analogously set to 1. In general, the analyses were performed on averaged, pooled data from the individual replicates. Given N values represent the number of triplets tested.

In the standard cAMP and Ca²⁺ second messenger assays, Gi activation efficacy was calculated by dividing maximum Gi signaling by maximum Gq signaling. G-protein signaling efficacy was calculated by adding the maximum Gi- and Gq responses and dividing by two. In the GsX assay, the relative activation efficacies of the different G-protein subtypes were calculated by dividing the maximum response of each GsX chimera by the sum of the maximum responses of all chimeras tested. The Gi activation efficacy was calculated by dividing the sum of Gsi, Gso and Gst responses by the sum of the Gsq and Gs15 responses. The G-protein signaling efficacy was calculated by dividing the sum of all maximum responses by 5.

All statistical analyses were performed either by Excel or using Graphpad Prism 9 software. In the figures the different levels of significance are indicated by * for $p < 0.05$, ** for $p < 0.01$, *** if $p < 0.001$, and **** if $p < 0.0001$. Average values are indicated with \pm standard deviation.

2.6 Structural AlphaFold2 models

Alphafold-predicted structural models of our chimeras were calculated with ColabFold (Jumper et al., 2021; Mirdita et al., 2022) under default settings, alone and complexed with their G-proteins, with three recycling iterations and using MMseqs2 to search environmental and UniRef sequences. The protein structures were visualized, and images were captured using UCSF ChimeraX (Pettersen et al., 2021).

3 Results

3.1 Bovine rhodopsin—Beta2 adrenoceptor chimeras (bRhod-b2ARs)

3.1.1 Design and engineering

We started by exploring chimeras between bRhod (GenBank accession number: AH001149.2) and b2AR (GenBank accession number: AY136741.1), since 1) the proximal C-terminus of bRhod was hypothesized to be involved in G-protein selectivity (Tsai et al.,

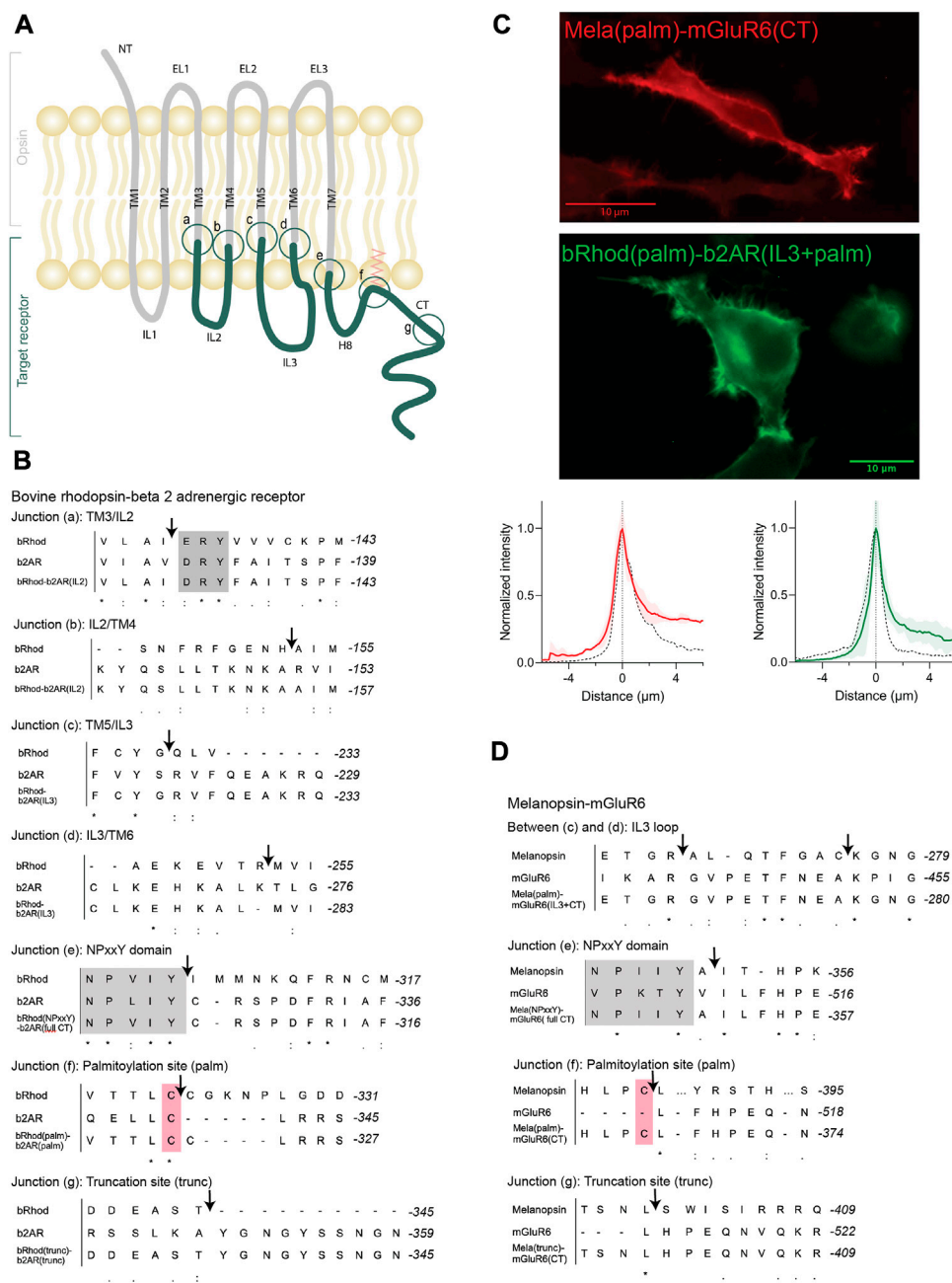
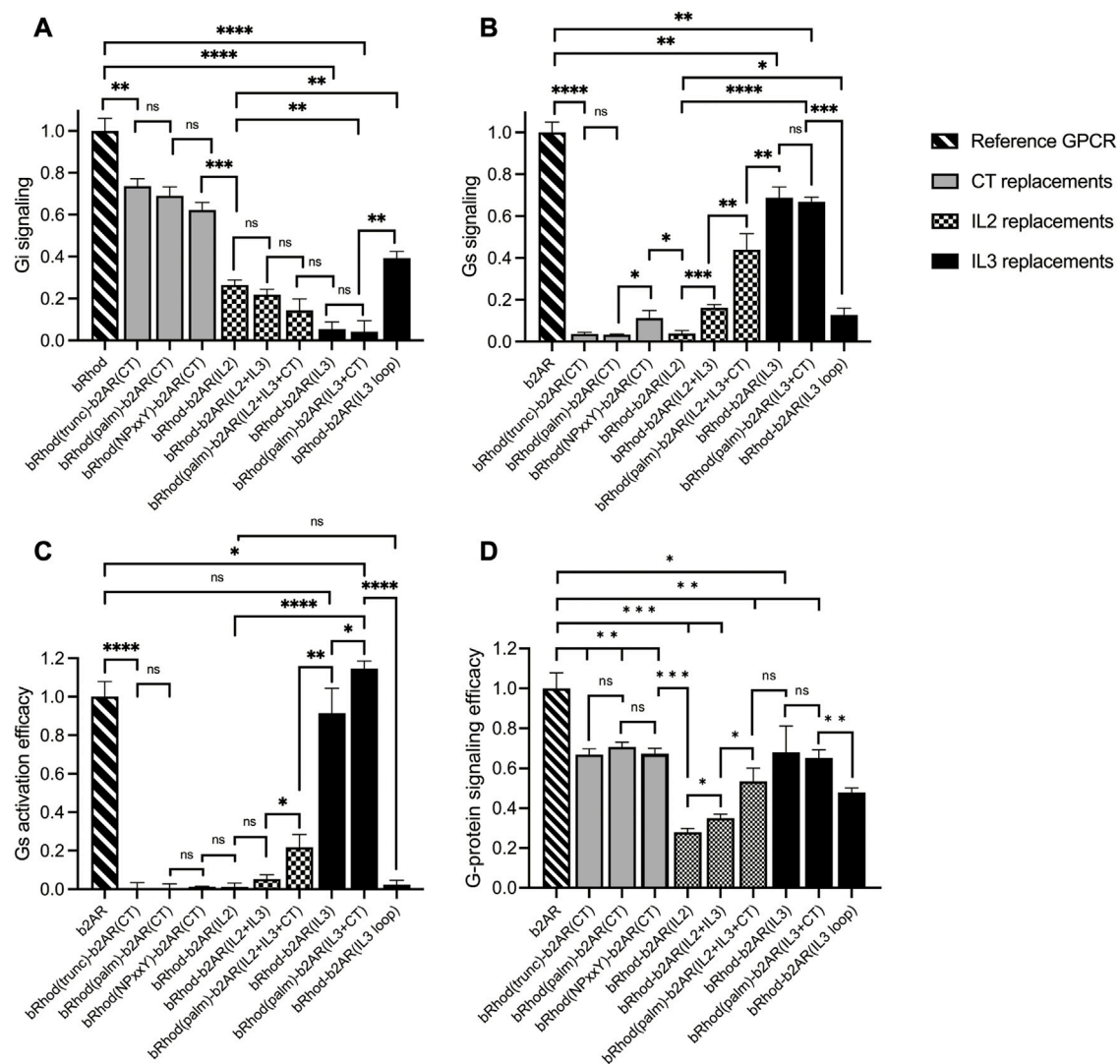


FIGURE 1

OptoGPCR engineering and expression in HEK293 cells. **(A)** Schematic representation of an Opto-GPCR chimera. The opsin domains are drawn in grey, the domains of the ligand-gated target receptor in dark green. Sites A-G highlight the chimeric recombination sites, detailed in panels B and (D) **(B,D)** Sequence alignments of bovine rhodopsin with the beta-2 adrenergic receptor **(B)** and melanopsin with the mGluR6 receptor **(D)** around the chimeric fusion sites shown in **(A)**. Conserved reference sites are highlighted in grey (NPxxY) and pink (palmitoylated cysteine). **(C)** Example photomicrographs and cross-sectional expression profiles of HEK293 cells expressing Mela(palm)-mGluR6(CT)-mKate2 and bRhod(palm)-b2AR(IL3+CT)-mKate2 fusion proteins, nicely trafficked to the cell membrane. The fluorescence intensity profiles are compared to their respective wildtype opsins (black dashed line), which were set to 1. Please refer to [Supplementary Figure S4](#) for all other chimeras and the wildtype opsins.

2019), 2) abundant structural data is available, 3) both belong to Class A GPCRs facilitating sequence alignment (Kleinlogel, 2016) and 4) since functional rhodopsin chimeras with all intracellular domains exchanged have previously been successfully engineered (Yamashita et al., 2001; Kim et al., 2005; Airan et al., 2009; Tichy et al., 2022). Using the available structures as templates, we

successively replaced IL2, IL3 and the C-terminus of rhodopsin by homologous domains of b2AR (Figures 1A, B; all sequences are provided in [Supplementary Data S1](#); an overview over all chimeras is given in [Supplementary Table S1](#)). In addition, the known G-protein contacts of bRhod and b2AR ([Supplementary Figures S3A, B](#)) were considered when defining the chimeric exchange points. In line with

**FIGURE 2**

Shift from Gi to Gs activation of bRhod-b2AR chimeras determined with the GloSensor second messenger assay. **(A,B)** Normalized cAMP decrease indicative of Gi activation **(A)** and normalized increase indicative of Gs activation **(B)**. The reporter luminescence values of the chimeras were normalized to WT bRhod **(A)** and WT b2AR **(B)** values, respectively (N = 9). IL3 replacements, without and with the C-terminus additionally replaced at the palmitoylation site shifted bRhod-b2AR chimera signalling clearly to Gs. **(C)** Gs activation efficacy was calculated by dividing max. Gs value by the max. Gi value for each opsin variant. WT b2AR was normalized to 1, all other variants were normalized to WT b2AR (N = 3). bRhod-b2AR(IL3) activated Gs as efficiently as WT b2AR, bRhod(palm)-b2AR(IL3+CT) significantly exceeded WT b2AR activity. **(D)** Overall G-protein signaling efficacy was calculated by dividing the sum of Gi and Gs activation by 2. Light stimulus: 5×10^{16} photons/cm²/s. Raw data traces can be found in [Supplementary Figure S6](#).

previous work (Kim et al., 2005; Airan et al., 2009), we included the intracellular ends of the TM5 and TM6 in the IL3 replacements as structural research has shown these regions to include important G-protein contact sites (Supplementary Figures S3A, B) (Rasmussen et al., 2011b; Zhou et al., 2019).

The aim of the chimera design was to adapt G-protein specificity from that of bRhod to that of b2AR while maintaining functionality of the receptor. Since we were mainly interested in the functional contributions of the proximal C-terminus (from helix 8 to AA335 in bRhod), which was recently hypothesized from structure of bRhod (Tsai et al., 2019), we created three bRhod-b2AR chimeras that only contained b2AR domains within the C-terminus: 1)

bRhod(trunc)-b2AR(CT), which retained rhodopsin's C-terminus up to AA335, reported to modulate the signaling kinetics (Phillips and Cerione, 1994; Herrmann et al., 2006) and Gi-binding in rhodopsin (Tsai et al., 2019), 2) bRhod(palm)-b2AR(CT), retaining the palmitoylation site of rhodopsin at the end of helix 8 (H8) that anchors H8 into the cell membrane and mediates conformational stability of the receptor (Palczewski et al., 2000) and 3) bRhod(NPxxY)-b2AR(CT), where the whole C-terminus from the NPxxY motif at the distal end of TM7 was replaced. For a graphical view of the chimeric exchange sites refer to [Figures 1A–C](#) and [Supplementary Figures S3A, B](#).

All chimeric constructs were C-terminally tagged with the fluorescent mKate2 protein and cloned behind a CMV promoter

for transient transfection of HEK293 cells. Fluorescent microscopy for mKate2 confirmed expression and correct membrane localization (Figure 1C; Supplementary Figure S4).

3.1.2 Shifting G-protein selectivity from bRhod (Gi) to that of b2AR (Gs)

To test which chimeric design maximally shifts the response from the physiological Gi response of bRhod (Figure 2A; Supplementary Figure S5) to the Gs response of b2AR (Figure 2B; Supplementary Figure S5), we performed a standard bioluminescent cAMP plate reader assay in HEK293 cells (Bailes et al., 2012) to quantify the Gi-mediated decrease vs. the Gs-mediated increase in intracellular cAMP after light stimulation. As opposed to the findings by Tsai and colleagues, neither exchanging the full C-terminus [bRhod(NPxxY)-b2AR(CT)] (Tsai et al., 2018) nor exchanging the proximal C-terminus after H8 [bRhod(palm)-b2AR(CT)] (Tsai et al., 2019) in rhodopsin by that of b2AR changed G-protein tropism (Figures 2A, B) from Gi to Gs, leading to Gs-activation (Figure 2C). However, both C-terminal replacements decreased Gi-protein signaling ($p = 0.0016$, $p = 0.0026$, Figure 2A). As expected, also replacing the full distal C-terminus beyond AA335 of bRhod [bRhod(trunc)-b2AR(CT)] did not change G-protein tropism ($p = 0.0053$).

However, exchanging the full IL3, including the TM5 and TM6 helical cytoplasmic domains almost completely shifted G-protein selectivity to Gs ($p < 0.0001$, Figure 2; Supplementary Figure S6), confirming existing literature that IL3 is the major mediator of G-protein selectivity (Rasmussen et al., 2011b; Flock et al., 2017). Additionally exchanging the proximal C-terminus in bRhod(palm)-b2AR(IL3+CT) did not enhance Gs tropism (Figure 2B), but significantly increased Gs activation (Figure 2C; $p = 0.0423$), corroborating a synergistic interaction of the proximal C-terminus with IL3 also in b2AR, as proposed by Tsai and colleagues for rhodopsin (Tsai et al., 2019). However, exchanging only the hypervariable loop region of IL3 was not as effective at changing G-protein tropism and reduced G-protein activation efficacy. This confirms the findings by the Kobilka group (Rasmussen et al., 2011a; Rasmussen et al., 2011b) that the distal part of TM5 and the proximal part of TM6, extending well into the cytoplasmic space and comprising multiple G-protein contacts (Supplementary Figure S3) actively support G-protein selection. Exchanging only the TM5 and TM6 cytoplasmic helical regions killed, as expected, the function of the chimera (Supplementary Figure S6) (Deupi and Kobilka, 2007).

Finally, since IL2 is also in close contact with the G-protein (Rasmussen et al., 2011b), we additionally created three chimeras in which we exchanged IL2. IL2 exchange alone did not adapt tropism to Gs and significantly reduced G-protein signaling (Figures 2B, D; $p < 0.0001$). However, if the IL2 was exchanged together with IL3, tropism shifted to Gs (Figure 2B; $p = 0.0005$) and G-protein signaling was significantly improved (Figure 2D; $p = 0.0136$). Additional replacement of the C-terminus after the palmytoilation site further increased Gs tropism ($p = 0.0036$) and G-protein signaling (Figure 2D; $p = 0.0102$). Although not highly significant, these results may point towards a synergistic role of IL2, IL3 and the proximal C-terminus in G-protein selectivity, however, the Gs tropism and the Gs activation efficacy of bRhod-b2AR(IL2+IL3+palm) was significantly decreased compared to

bRhod-b2AR(IL3) (Figures 2B, C, $p < 0.0001$ and $p = 0.0038$), suggesting that too much engineering may impact functioning of the bRhod-b2AR receptor.

Conclusively, IL3 appears to dictate G-protein selectivity in the bRhod-b2AR chimera.

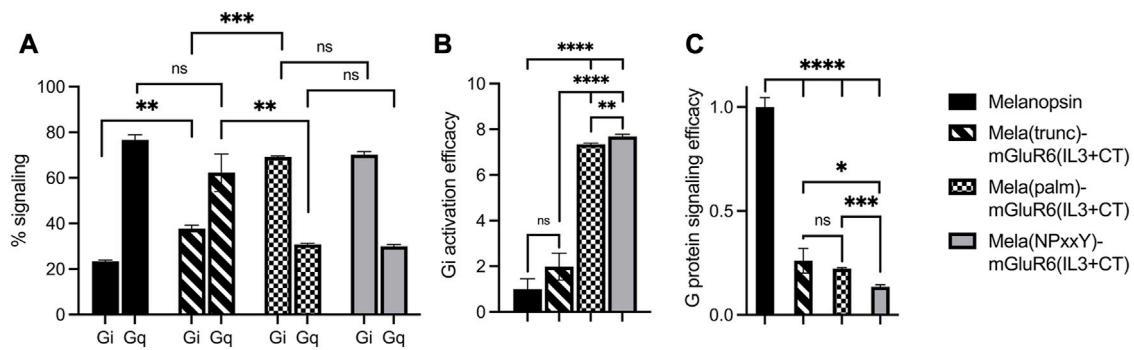
3.2 Melanopsin-mGluR6 chimeras

3.2.1 Design and engineering

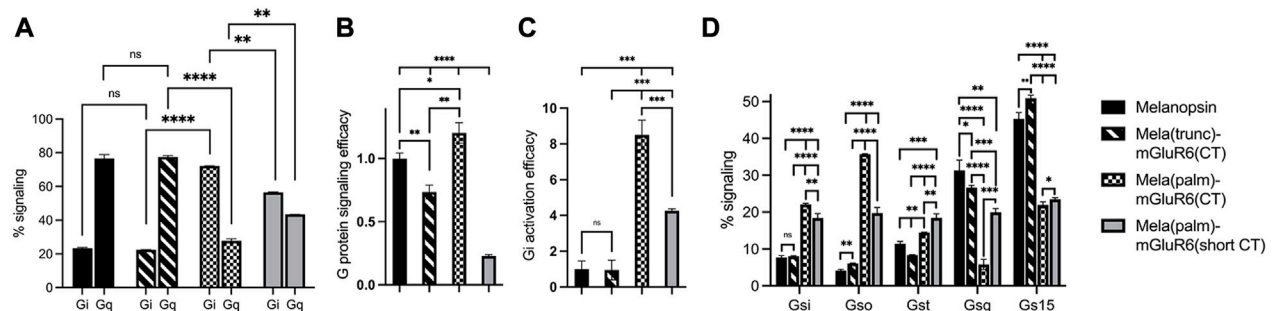
Based on the sequences of melanopsin (GenBank accession number: AF147788) and mGluR6 (GenBank accession number: NM_000843.4), we designed chimeric Mela-mGluR6 variants, wherein different parts of the C-terminus—analogue to the bRhod-b2AR chimeras—were replaced without and together with IL3 of the corresponding regions of mGluR6 (Figure 1D, sequences provided in Supplementary Data S1; chimera overview provided in Supplementary Table S1). Chimeric design of Mela-mGluR6 variants is complicated by the fact that melanopsin belongs to the class A GPCRs, whereas mGluR6 belongs to class C GPCRs, showing marked differences in structure and sequence [(Pin et al., 2003), Figure 1D; Supplementary Figure S3]. Nevertheless, the well-preserved domains, including the E/DRY motif, the ionic lock and the NPxxY domain, can be used as reference points for sequence alignment (Kleinlogel, 2016; Supplementary Figure S3). However, alignment of the C-terminal sequence is difficult, since mGluRs possess neither a palmytoilation site, nor an ordered H8 (Bruno et al., 2012). Further, melanopsin and other Class A GPCRs possess a long IL3 and a short IL2, whereas this arrangement is swapped in mGluR6 and other Class C GPCRs, with a short IL3 and a long IL2. We were therefore forced to only replace the hypervariable IL3 loop region (Matos-Cruz et al., 2011) of melanopsin with the short IL3 of mGluR6 (Figure 1D; Supplementary Figures S3, S8).

Since the most effective bRhod-b2AR chimera in terms of Gs activation was the combined IL3+CT exchange variant, we combined the three different C-terminal replacements in the Mela-mGluR6 chimeras directly with IL3 loop replacements (Figures 1A, D; Supplementary Figure S3): 1) a Mela(trunc)-mGluR6(IL3+CT) chimera, where the C-terminus was exchanged at AA400 of melanopsin, comprising the analogous part of the proximal C-terminus of melanopsin reported to bind to the G-protein in bovine rhodopsin (Tsai et al., 2019), 2) a Mela(palm)-mGluR6(IL3+CT) chimera, where the C-terminus was exchanged just distal to H8 of melanopsin after the palmytoilation site at AA367 and 3) a fully truncated Mela(NPxxY)-mGluR6(IL3+CT) variant where the whole C-terminus of melanopsin distal to TM7 was replaced by that of mGluR6. In all three chimeras, the whole mGluR6 C-terminus, starting just distal to the NPxxY (VPKTY in mGluR6) motif was included (Supplementary Figures S1, S3). Since previous studies indicated that the C-terminus of mGluRs is involved in direct coupling with G-proteins (Rondard et al., 2011; Seven et al., 2021), we additionally designed a Mela(palm)-mGluR6(short CT) chimera that comprised a shorter mGluR6 C-terminus not including the proximal C-terminus of mGluR6 (Supplementary Figure S2).

The chimeric constructs were C-terminally tagged with mKate2 and cloned behind a CMV promoter for transient transfection of HEK-293 cells. Fluorescent microscopy for

**FIGURE 3**

Shift from Gq to Gi activation of Mela-mGluR6 chimeras with combined IL3 and C-terminus replacements determined by the GsX second messenger assay. HEK293 cells transfected with the respective OptoGPCR plasmids, GloSensor reporter and the C-terminal mutated Gs_q, Gs₁₅, Gs_i, Gs_o, or Gs_t G-proteins were subjected to a Gs cAMP assay. The maximum cAMP levels were divided by the sum of all values and normalized to 1 for each GsX protein. **(A)** The total Gq and Gi signaling was calculated by adding the max. cAMP value of Gs_q and Gs₁₅, and Gs_i, Gs_o, and Gs_t, respectively, and dividing by the sum of all GsX responses to determine the percentage of each G-protein in total signalling. **(B)** The Gi activation efficacy was calculated to quantify the shift from Gq to Gi signaling. This was calculated by dividing the summed max. Gi values by the summed max. Gq value for each opsin variant. **(C)** The total G-protein signalling efficacy was calculated to determine the signaling functionality by calculating $(Gi_{total} + Gq_{total})/2$. WT melanopsin was normalized to 1, all other variants were normalized to WT melanopsin. Replacing the proximal C-terminus in melanopsin shifted G-protein specificity from Gq to Gi. However, disrupting the TM7-H8 domain of melanopsin in the Mela(NPxxY) variant significantly impacted the G-protein signalling efficacy. N = 3; light stimulus: 470 nm, 5×10^{16} photons/cm²/s. Raw data traces can be found in [Supplementary Figure S9](#).

**FIGURE 4**

The role of the proximal C-terminus in Mela-mGluR6 chimeras in shifting tropism from Gq to Gi determined by the GsX second messenger assay. **(A)** The proximal C-terminus is responsible for G protein selectivity in the Mela-mGluR6 chimera and the analogue region steers G-protein selectivity also in mGluR6. The percentual proportion of each G-protein subfamily in total Gq and Gi signaling (100%) was calculated by dividing the max. cAMP response of each GsX-protein by the total sum of all max. GsX values. **(B)** The total G-protein signaling efficacy was determined by calculating $[Gi_{total} + Gq_{total}]/2$. This was performed to quantify the functionality of the chimeric constructs. **(C)** The Gi activation efficacy ratio was calculated by dividing the summed max. Gi values by the summed max. Gq values indicating the shift from Gq to Gi signaling. WT melanopsin was normalized to 1, all other variants were normalized to WT melanopsin. **(D)** The percentage of each G-protein in total signaling (100%) was calculated by dividing the max. cAMP response of each GsX-protein by the total sum of all GsX-proteins resulting in a fingerprint of the Gi and Gq signaling profiles of these variants. N = 3; light stimulus: array of 3×8 LEDs, 470 nm, 5×10^{16} photons/cm²/s.

mKate2 confirmed expression and correct membrane localization (Figure 1C; [Supplementary Figure S4](#)).

3.2.2 Shifting G-protein selectivity from melanopsin (Gq) to that of mGluR6 (Gi)

We first compared the different C-terminal replacement melanopsin variants that also had the IL3 loop region exchanged in the standard cAMP and Ca²⁺ GloSensor bioluminescent assays ([Supplementary Figure S9](#)) (Bailes and Lucas, 2013). As expected, none of the variants activated Gs (not shown), but Gq (indicative of melanopsin) and Gi (indicative predominantly for mGluR6) at different ratios (Figure 3;

[Supplementary Figure S9](#)). Mela(trunc)-mGluR6(IL3+CT) still dominantly activated Gq ($62.3\% \pm 8.2\%$ Gq, $37.7\% \pm 1.5\%$ Gi), similar to wildtype melanopsin ($76.6\% \pm 2.3\%$ Gq, $23.4\% \pm 0.4\%$ Gi), albeit with a significant increase in Gi tropism, which we attribute to the additional IL3 exchange and confirmed in the next set of experiments (see Figure 3B). However, once the proximal part of the C-terminus of melanopsin was exchanged, the G-protein tropism switched to Gi [Mela(palm)-mGluR6(IL3+CT): Gi $69.2\% \pm 0.5\%$, Gq $30.8\% \pm 0.5\%$; Mela(NPxxY)-mGluR6(IL3+CT): Gi $70.1\% \pm 1.3\%$, Gq $29.9\% \pm 0.8\%$] and the Gi activation efficacy increased approximately 8-fold compared to WT melanopsin (Figure 3B).

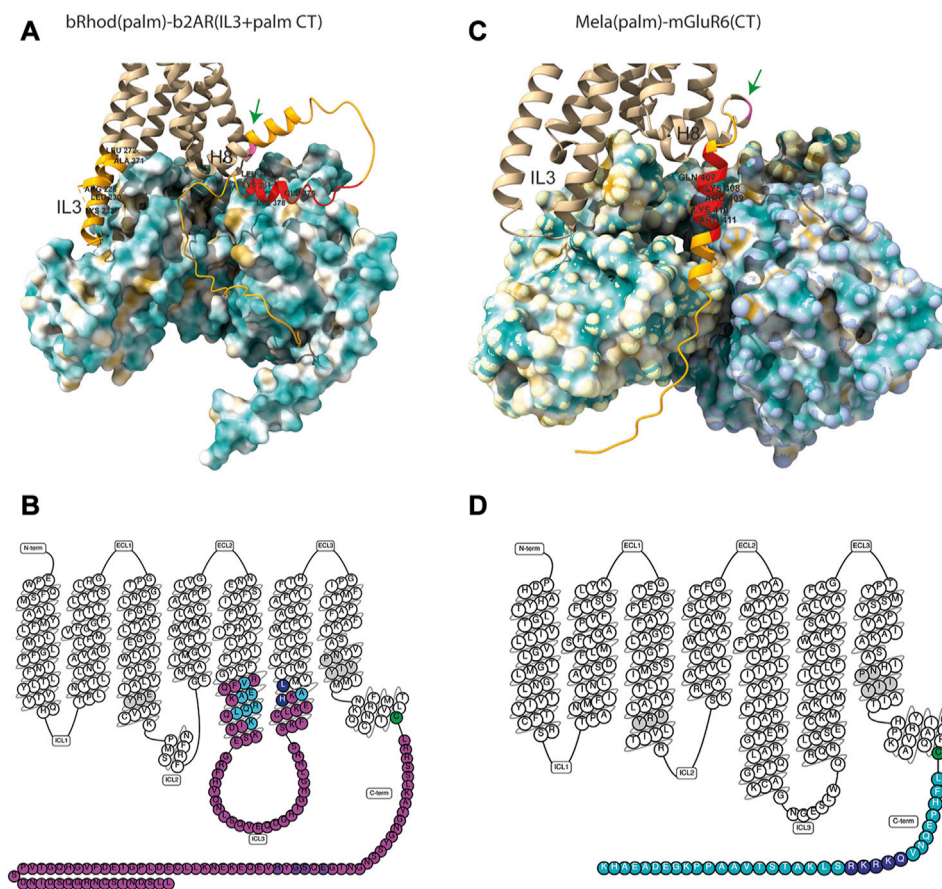


FIGURE 5

Structures of the bRhod(palm)-b2AR(IL3+CT) and Mela(palm)-mGluR6(CT) chimeras. **(A,B)** AlphaFold-predicted structural models of the chimeras with hydrophobicity surface maps of their respective G-proteins. **(A)** Structural model of the bRhod(palm)-b2AR(IL3+CT) chimera with the Gs-α and Gβ subunits. Highlighted in light orange are the b2AR domains. The residues highlighted additionally in red are the analogues to the residues that form contacts with the Gβ subunit in rhodopsin (Tsai et al., 2019). The palmitoylation site is indicated in pink (green arrow). **(B)** Structural model of the Mela(palm)-mGluR6(CT) construct with the Gi-α and Gβ subunits. Highlighted in orange is the C-terminal domain of mGluR6. The residues highlighted in addition in red are analogous to the residues in mGluR2 that have been shown to form contacts with the Gα subunit (Seven et al., 2021). **(C,D)** Snakeplots of the chimeras. **(C)** Snakeplot of the bRhod(palm)-b2AR(IL3+CT) construct. Shown in pink are the b2AR domains, which were inserted in bRhod. The residues that form contacts with the G-protein [light blue (Rasmussen et al., 2011b) and dark blue (Zhou et al., 2019)] are highlighted, as well as the residues that are analogous to the residues that form contacts with the Gβ subunit in rhodopsin [purple (Tsai et al., 2019)]. **(D)** Snakeplot of Mela(palm)-mGluR6(CT). Shown in light blue is the C-terminus of mGluR6, which was added following H8 and the palmitoylation site (green). The residues that are analogous to the residues that form contacts with the G-protein in mGluR2 [dark blue (Seven et al., 2021)] are highlighted. In grey are the highly conserved DRY and NPxxY motifs.

Evaluating the specific G-protein subtype activation profiles in a GsX assay (Ballister et al., 2018) (Supplementary Figure S10) confirmed that the proximal C-terminus of melanopsin, from the NPxxY motif to AA400, dominantly determines G-protein selectivity in the Mela-mGluR6 chimera (Figure 3; Supplementary Figure S10). Interestingly, the increase in Gi-protein tropism affected all three Gi-protein subtypes (Gi, Go and Gt) equally, hinting towards the fact that mGluR6 may not only activate Go and Gi (Tian and Kammermeier, 2006), but also Gt. However, the G-protein signaling efficacy of the Mela(NPxxY)-mGluR6(IL3+CT) chimera was significantly reduced compared to the Mela(palm)-mGluR6(IL3+CT) chimera (Figure 3C; $p < 0.0001$). We hypothesize that the lack of the amphipathic H8 in Mela(NPxxY)-mGluR6(IL3+CT) may

destabilize conformational states and reduce G-protein activation upon light stimulation, an effect previously described for truncated rhodopsin (Krishna et al., 2002).

We went on to test another set of chimeras devoid of the IL3 loop replacement to investigate the explicit role of the proximal C-terminus in G-protein tropism. The results corroborated our findings above: while the Mela(trunc)-mGluR6(CT) version did not shift G-protein tropism, the Mela(palm)-mGluR6(CT) chimera shifted G-protein tropism from Gq to Gi ($72.2\% \pm 0.2\%$ Gi, $27.8\% \pm 1.1\%$ Gq) almost identical to the Mela(palm)-mGluR6(IL3+CT) chimera (Figure 4A). Consequently, the main determinant of G-protein specificity in melanopsin is the proximal C-terminus, with a subordinate role of IL3. It should also be noted that the

Mela(palm)-mGluR6(CT) was significantly more effective in activating the G-proteins compared to the Mela(palm)-mGluR6(IL3+CT), additionally comprising the IL3 of mGluR6 (Figures 3C, 4B). This may be partially due a slightly reduced expression of Mela(palm)-mGluR6(IL3+CT) (approx. 85%) compared to Mela(palm)-mGluR6(CT) (Supplementary Figure S4B), however, the reduction of G-protein activation is significantly larger.

The seemingly mechanical difference of the Mela-mGluR6 chimera to the bRhod-b2AR chimera is remarkable. To visualize differences in the arrangement of the proximal C-terminus and IL3 in relation to the G-protein in the bRhod(palm)-b2AR(IL3+CT) and the Mela(palm)-mGluR6(CT) chimeras, we created structural AlphaFold models (Figure 5A). Since no crystal structures are available for melanopsin or mGluR6, we modeled melanopsin on bovine rhodopsin (PDB: 6QNO) and mGluR6 on mGluR2 in complex with Gi (PDB: 7MTS). The bRhod-b2AR model shows proximity of the proximal C-terminus (residues AA375-AA382) to the Gbeta subunit as described previously (Tsai et al., 2019). The proximal C-terminus of the Mela-mGluR6 chimera, however, shows a very different, much more extended and tighter interface with the G-protein, starting immediately distal to H8 and lying within a cleft between the Galpha and Gbeta subunits with opposing hydrophobic (yellow) and hydrophilic (blue) surfaces. This defined placement and tight interaction with both, not only the Gbeta, but in particular also the Galpha subunit, may be the structural determinant of its involvement in G-protein selectivity. On the other hand, the IL3 of bRhod is in much closer proximity to the Galpha subunit, as this is the case in the Mela-mGluR6 chimera, hinting towards the dominant role of IL3 in G-protein selectivity.

To investigate if the proximal C-terminus of mGluR6 is also involved in G-protein tropism, we next created an additional Mela(palm)-mGluR6(short CT) variant, where a truncated version of the mGluR6 C-terminus, commencing 3 AA downstream of the putative H8 considered devoid of G-protein interactions was employed (Rai et al., 2021) (Supplementary Figure S3). Indeed, Gi activation was significantly reduced (Figure 4C; $p = 0.0009$) in this short CT variant in favor of Gq activation when compared to the full CT Mela(palm) version, although the overall tropism of the chimera remained shifted to Gi (Figure 4A; $56.6\% \pm 0.2\%$ Gi, $43.4\% \pm 0.04\%$ Gq). Defining the Gi-protein subtype specificity of Mela(palm)-mGluR6(short CT) and Mela(palm)-mGluR6(full CT) in more detail with the GsX assay clearly showed a shift predominantly to Go of mGluR6 (Tian and Kammermeier, 2006) only in the full CT version (Figure 4D), proving that the proximal C-terminus is also the mediator of G-protein selectivity in mGluR6.

While we established the GsX assay, we found varying G-protein tropisms for murine and human melanopsin: human melanopsin had a significantly lower Gq specificity, but an elevated Gi specificity compared to murine melanopsin (Supplementary Figure S11; murine: Gq $67.8\% \pm 0.8\%$, Gi $32.2\% \pm 1.07\%$; human: Gq 63.2 ± 0.4 , Gi 36.8 ± 0.2). Interestingly, human melanopsin also possessed a significantly increased G15 vs. Gq tropism, which was not found in murine melanopsin (Supplementary Figure S11). Intriguingly, when comparing the sequences of human and murine melanopsin, they deviated from each other exactly in the proximal C-terminus between H8 and the truncation site in Mela(trunc) (AA400), as

well as the IL3, but not in the IL2 (Supplementary Figure S11). This corroborates our findings that the proximal C-terminus and the IL3 influence G-protein selectivity in melanopsin.

Taken together, our results unravel the dominant role of the proximal C-terminus in G-protein selectivity in melanopsin and mGluR6.

4 Discussion

Selective coupling of GPCRs to specific G-protein subtypes is critical to transform signals from light, neurotransmitters, and drugs into intracellular responses throughout the body. In the past 30 years, the field has tried to understand the molecular and structural underpinnings in GPCRs responsible for G-protein selectivity, however, they remain largely elusive. The recent surge in resolved GPCR-G-protein structures, including structures in the active and inactive states, has expanded our understanding of G-protein recognition and GPCR-mediated signal transduction. However, since structural data only provide snapshots of particular GPCR-G-protein states and since the intracellular G-protein interacting domains on the GPCR (ILs and CT) are flexible, largely unordered domains, deferring functional involvement in G-protein selectivity remains a challenge (Deupi and Kobilka, 2007). Fab fragments (Rasmussen et al., 2007), mini G-proteins (Carpenter et al., 2016; Tsai et al., 2018) and nanobodies (Bertheleme et al., 2013) have been employed to immobilize these flexible domains to promote crystallization, which may, however, partially perturb dynamic movements of the GPCR and cast a distorted picture on GPCR/G-protein interactions. Opto-GPCRs present a powerful tool to add temporally longitudinal functional data of G-protein coupling signatures to the existing structural knowledge.

The first structure of the b2AR was obtained in the presence of a Fab fragment bound to IL3 (Rasmussen et al., 2007) and the first active state crystal structure was derived from rhodopsin (Palczewski et al., 2000). Most of the insights of GPCR-G-protein interactions have been derived from these two proteins and the residues described to be involved in G-protein contacts are similar (Supplementary Figure S3) (Rasmussen et al., 2011a; Rasmussen et al., 2011b; Tsai et al., 2018). With well-defined contacts to the G-protein (Rasmussen et al., 2011b; Flock et al., 2017; Kang et al., 2018; Tsai et al., 2019; Zhou et al., 2019) and supporting functional data (Kim et al., 2005; Airan et al., 2009; Siuda et al., 2015; Ma et al., 2020), the IL3 is considered the main determinant of G-protein selectivity, at least in Class A GPCRs. Here, we were mainly interested in elucidating the potential involvement of the proximal C-terminus, which was also predicted to be involved in G-protein activation and selectivity in recent structural studies (Tsai et al., 2019; Seven et al., 2021). Tsai and colleagues showed the TM7/H8 joint of rhodopsin (Kang et al., 2018; Tsai et al., 2018; Gao et al., 2019) to AA(T/A335) (Tsai et al., 2019) to closely contact the G-protein and suggested a role in G-protein activation and potentially also selectivity. While we could not confirm a role in selectivity of the proximal C-terminus in our bRhod-b2AR chimeras, we found a significant decrease of Gi activation the more of the C-terminus of rhodopsin was replaced by that of b2AR, which corroborates the suggested importance of the

proximal carboxyl terminus (from NPxxY to AA335) specifically in Gi-protein binding and activation. Our structural model of the bRhod(palm)-b2AR(palm + IL3) chimera visualizes the proximity of the proximal C-terminus to the G β subunit, specifically of amino acids 375–382 (Figure 5A), underscoring the supportive role of this domain in G-protein activation.

IL3 is one of the most diverse regions in GPCRs and is often structurally not completely resolved. For instance, b2AR has a much longer and extremely flexible IL3 compared to rhodopsin. IL3 exchange in our bRhod-b2AR chimera almost completely shifted G-protein selectivity to Gs. These findings agree with the common assumption that IL3 is the major mediator of G-protein specificity in bRhod and b2AR (Rasmussen et al., 2011b; Flock et al., 2017). Exchanging only the hypervariable loop region of IL3 was not as effective as exchanging the entire intracellular IL3 domain including the intracellular TM5 and TM6 protrusions. This confirms the findings by the Kobilka group (Rasmussen et al., 2011a; Rasmussen et al., 2011b) that the distal part of TM5 and the proximal part of TM6, extending into the cytoplasmic space and comprising multiple G-protein contact sites, actively support G-protein selection (Supplementary Figure S3). However, only replacing TM5 and TM6 did not suffice to induce a Gs signal. Therefore, we conclude that the entire TM5-IL3-TM6 region is necessary for optimal Gs coupling of the bRhod-b2AR chimera. Exchanging the C-terminus in addition to IL3 in the bRhod-b2AR chimera [bRhod(palm)] had no significant effect on G-protein selectivity, but significantly increased Gs activation, confirming a supportive role of the proximal C-terminus in G-protein activation, probably by the hypothesized interactions with IL3 (Tsai et al., 2019).

Similarly, we did not find IL2 to promote Gs selectivity on its own, albeit shown to be in close contact to the G-protein in rhodopsin (Kang et al., 2018; Tsai et al., 2018), in b2AR (Rasmussen et al., 2011b) and in our bRhod-b2AR model (Figure 5A). In fact, replacement of IL2 in the bRhod-b2AR chimera reduced the G-protein activation efficacy, suggesting that too much engineering in Opto-GPCRs may disturb the conformational states of the GPCR and/or hamper G-protein binding. A previous study on b1AR, a related receptor to b2AR also coupling to Gs, suggested that PIP2 lipid binding to the distal IL2 (cytoplasmic end of TM4) stabilizes the active state of b1AR by forming a PIP2 bridging interaction specifically to Gs (Yen et al., 2018). However, our bRhod-b2AR(IL2) chimera was still mainly sensitive to Gi. Potentially, the surrounding membrane environment may have affected PIP2 lipidation of IL2 leading to an underestimated Gs binding in our experiments.

While the results obtained with the bRhod-b2AR chimera are in good agreement with existing structural and mutational data (Rasmussen et al., 2011b; Kang et al., 2018; Tsai et al., 2019; Zhou et al., 2019), we obtained novel results with the melanopsin-mGluR6 chimera. We discovered that the proximal C-termini of melanopsin (from the palmitoylation site at C367 to AA400) and of mGluR6 (AA846-AA864) act as main mediators of G-protein selectivity. It has to be noted, that neither the melanopsin nor the mGluR6 crystal structures are known.

The most effective variant to shift tropism from Gq to Gi/o was the Mela(palm)-mGluR6(CT) chimera. The fully truncated Mela(NPxxY)-mGluR6 variant was much less effective in

G-protein activation, assumingly due to the lack of the amphipathic H8 shown to stabilize conformational states in rhodopsin, and potentially other opsins (Krishna et al., 2002). Valdez-Lopez and colleagues (Valdez-Lopez et al., 2020) suggested ionic interactions between the proximal melanopsin C-terminus (C367–Y382) and IL3, specifically within the helical intracellular extensions of TM5 (R259, R262, R266, R277) and in the IL3 loop region (R280, Q281, W282, Q283, R284, L285), forming a stable conformation critical for initiating G-protein signaling. However, in our study, additionally replacing IL3 of melanopsin by that of mGluR6 significantly reduced the capacity of the chimera to activate the G-protein, hinting towards conformational disturbances. It has to be noted that IL3 exchange was not trivial in the melanopsin-mGluR6 chimera, since melanopsin belongs to Class A GPCRs, whereas mGluR6 belongs to Class C GPCRs. Melanopsin and other Class A GPCRs possess a long IL3 and a short IL2, whereas mGluR6 and other Class C GPCRs possess a short IL3 and a long IL2 (Pin et al., 2003). We were therefore forced to only replace the hypervariable IL3 loop region of melanopsin with the short IL3 of mGluR6, which potentially disturbed the suggested ionic network between IL3 and the proximal C-terminus. According to the sequence differences between human and murine melanopsin IL3, including the TM5 and TM6 extensions (Supplementary Figure S11), for which we also found differences in G-protein selectivity, we suggest that Gi/o selectivity of the Mela(palm)-mGluR6(IL3+CT) chimera may be further enhanced by including the TM5 and TM6 protrusions into the IL3 replacement.

It is interesting that Valdez-Lopez also pointed towards this same proximal C-terminal region in Gq-coupled melanopsin, as residues on the proximal C-terminus are quite conserved across Gs and Gi proteins (Tsai et al., 2019), but not Gq proteins. Our structural model of the Mela(palm)-mGluR6(CT) chimera shows a very different arrangement of the C-terminus compared to the bRhod-b2AR chimera (Figure 5). While in the bRhod-b2AR model, the proximal C-terminus contacts solely the G β subunit, in the Mela(palm)-mGluR6(CT) model, the whole C-terminus is nested into a cleft between the G α and the G β subunits. This difference in arrangement, and potentially the additional contact to the G α subunit, may explain the strong involvement of the proximal C-terminus in G-protein selectivity in the Mela(palm)-mGluR6(CT) chimera. The fact that the bRhod-b2AR chimera has a much closer contact of IL3 to the G α subunit corroborates that the contact to the G α subunit determines G-protein selectivity.

Already in the 1990s it was suggested from mGluR chimeras that the C-terminal segment located downstream of TM7 is necessary for specific G-protein activation (Pin et al., 1994). This was recently confirmed in mGluR2 by cryo-EM studies (Seven et al., 2021), which show a binding between the proximal C-terminus of mGluR2 and the Gi-protein. To study the involvement of the proximal C-terminus of mGluR6 in G-protein selectivity, we compared Mela(palm)-mGluR6(CT)-mGluR6 chimeras comprising the whole mGluR6 C-terminus (cut after the NPxxY motif) and a short C-terminus (Mela(palm)-mGluR6(short CT)), lacking the mGluR6 analog of the proximal C-terminus to melanopsin. Albeit definition of the proximal mGluR6 C-terminus is not trivial due to the lack of a palmitoylation site and an ordered H8 (Bruno et al., 2012) (see Supplementary Figure S3), we could functionally confirm that the proximal C-terminus of mGluR6

(Q849-R856) comprising the analogue amino acid stretch mentioned by Seven and colleagues in mGluR2 (V826-S833) (Seven et al., 2021) (Supplementary Figure S1), is an important mediator of G protein selectivity.

Considering Opto-GPCR variants as optogenetic tools, we showed in our study that in contrast to most previous work with Opto-GPCRs, in which the IL2, IL3 and the full C-terminus were replaced, only certain domains need to be replaced to induce the required shift in G-protein coupling without compromising the G-protein coupling efficacy. While the bRhod-b2AR variant was optimally designed by introducing the b2AR TM5-IL3-IL6 and C-terminus after the palmitoylation site in bRhod, a proximal C-terminus replacement of melanopsin by the whole C-terminus of the mGluR6 receptor, including the proximal C-terminus, sufficed to retarget to the Gi/o protein class. Overall, the Mela(palm)-mGluR6(CT) seems to be the favorable chimera for functional applications since it activates G-proteins with high efficacy and shows a strong tropism towards Gi/o (Kralik et al., 2022). Of course, since Cryo-EM studies on mGluR2 showed that the G-protein's C-terminus is stabilized by a pocket formed by IL2 and the C-terminus (Seven et al., 2021), IL2 may also be involved in Gi/o-selectivity together with the proximal C-terminus of mGluR6, which was, however, not investigated in this study. Interestingly, Gi-protein subtype specificity (Gi, Go and Gt) was increased the more of the melanopsin C-terminus was replaced by that of mGluR6, hinting toward the fact that mGluR6 may not only activate Go and Gi (Tian and Kammermeier, 2006), but also Gt. This could be the reason why middle-wave cone opsin (Gaub et al., 2014) and rhodopsin (Cehajic-Kapetanovic et al., 2015), which both naturally bind to Gt (transducin), were efficient in activating ON-bipolar cells of the retina and restoring some vision. We also showed that bovine rhodopsin binds not only to Gt, but equally well to Gi and to a lesser degree (approx. 10%) to Go (Supplementary Figure S5). This further explains why rhodopsin functioned well as an optogenetic tool in retinal-ON bipolar cells (Cehajic-Kapetanovic et al., 2015), since rhodopsin and mGluR6 both activate Gi, Go and Gt, just with different efficacies. Overall, it appears that GPCRs are far more promiscuous than generally believed.

Our study highlights the complexity and individuality of G-protein selectivity in GPCRs and with that the challenge to design Opto-GPCRs targeting a specific G-protein. From the limited results we generated with the bRhod-b2AR and Mela-mGluR6 chimeras, we suggest that GPCR interactions with the Galpha interface may trigger G-protein specificity, while interactions with the Gbeta protein support G-protein activation. From our results, no single blueprint can be created that would be applicable to all opsins and target receptors. Rather, there is a need to consider each opsin-target receptor pair separately to achieve efficient and optimized Opto-GPCR chimeric receptor function. To further corroborate these results and propose potential general schemes for different classes of GPCRs and for GPCRs that couple to different G-proteins, additional chimeras should be created and investigated. In the future, the gained knowledge will assist the

design and functionality of Opto-GPCRs and drugs that promote specific signaling pathways and avoid unwanted side effects (Hauser et al., 2017).

Data availability statement

The datasets presented in this study can be found in online repositories. The names of the repository/repositories and accession number(s) can be found in the article/Supplementary Material.

Author contributions

SL performed and analyzed the experiments and wrote the first draft of the manuscript. SK supervised the project, designed the experiments, helped with the analysis and writing of the manuscript as well as provided funding for the project.

Funding

This research was funded by grants from the Swiss National Science Foundation (310030E_188991 and 31003A_176065) to SK.

Acknowledgments

We would like to thank Sabine Schneider for assistance in cloning, immunohistochemistry and the plate reader assays and Michiel van Wyk for the fruitful discussions about GPCRs and G-proteins.

Conflict of interest

The authors declare that the research was conducted in the absence of any commercial or financial relationships that could be construed as a potential conflict of interest.

Publisher's note

All claims expressed in this article are solely those of the authors and do not necessarily represent those of their affiliated organizations, or those of the publisher, the editors and the reviewers. Any product that may be evaluated in this article, or claim that may be made by its manufacturer, is not guaranteed or endorsed by the publisher.

Supplementary material

The Supplementary Material for this article can be found online at: <https://www.frontiersin.org/articles/10.3389/fcell.2023.1053022/full#supplementary-material>

References

- Airan, R. D., Thompson, K. R., Fenno, L. E., Bernstein, H., and Deisseroth, K. (2009). Temporally precise *in vivo* control of intracellular signalling. *Nature* 458 (7241), 1025–1029. doi:10.1038/nature07926
- Alegre, K. O., Paknejad, N., Su, M., Lou, J. S., Huang, J., Jordan, K. D., et al. (2021). Structural basis and mechanism of activation of two different families of G proteins by the same GPCR. *Nat. Struct. Mol. Biol.* 28 (11), 936–944. doi:10.1038/s41594-021-00679-2
- Bailes, H. J., and Lucas, R. J. (2013). Human melanopsin forms a pigment maximally sensitive to blue light ($\lambda_{\text{max}} \approx 479$ nm) supporting activation of G(q/11) and G(i/o) signalling cascades. *Proc. Biol. Sci.* 280 (1759), 20122987. doi:10.1098/rspb.2012.2987
- Bailes, H. J., Zhuang, L. Y., and Lucas, R. J. (2012). Reproducible and sustained regulation of Gas signalling using a metazoan opsin as an optogenetic tool. *PLoS One* 7 (1), e30774. doi:10.1371/journal.pone.0030774
- Ballister, E. R., Rodgers, J., Martial, F., and Lucas, R. J. (2018). A live cell assay of GPCR coupling allows identification of optogenetic tools for controlling Go and Gi signaling. *BMC Biol.* 16 (1), 10. doi:10.1186/s12915-017-0475-2
- Bertheleme, N., Chae, P. S., Singh, S., Mossakowska, D., Hann, M. M., Smith, K. J., et al. (2013). Unlocking the secrets of the gatekeeper: Methods for stabilizing and crystallizing GPCRs. *Biochim. Biophys. Acta* 1828 (11), 2583–2591. doi:10.1016/j.bbmem.2013.07.013
- Bruno, A., Constantino, G., de Fabritiis, G., Pastor, M., and Selent, J. (2012). Membrane-sensitive conformational states of helix 8 in the metabotropic Glu2 receptor, a class C GPCR. *PLoS One* 7 (8), e42023. doi:10.1371/journal.pone.0042023
- Carpenter, B., Nehme, R., Warne, T., Leslie, A. G., and Tate, C. G. (2016). Structure of the adenosine A(2A) receptor bound to an engineered G protein. *Nature* 536 (7614), 104–107. doi:10.1038/nature18966
- Cehajic-Kapetanovic, J., Eleftheriou, C., Allen, A. E., Milosavljevic, N., Pienaar, A., Bedford, R., et al. (2015). Restoration of vision with ectopic expression of human rod opsin. *Curr. Biol.* 25 (16), 2111–2122. doi:10.1016/j.cub.2015.07.029
- Choe, H. W., Kim, Y. J., Park, J. H., Morizumi, T., Pai, E. F., Krauss, N., et al. (2011). Crystal structure of metarhodopsin II. *Nature* 471 (7340), 651–655. doi:10.1038/nature09789
- Deupi, X., and Kobilka, B. (2007). Activation of G protein-coupled receptors. *Adv. Protein Chem.* 74, 137–166. doi:10.1016/S0065-3233(07)74004-4
- Flock, T., Hauser, A. S., Lund, N., Gloriam, D. E., Balaji, S., and Babu, M. M. (2017). Selectivity determinants of GPCR-G-protein binding. *Nature* 545 (7654), 317–322. doi:10.1038/nature22070
- Gao, Y., Hu, H., Ramachandran, S., Erickson, J. W., Cerione, R. A., and Skiniotis, G. (2019). Structures of the rhodopsin-transducin complex: Insights into G-protein activation. *Mol. Cell* 75 (4), 781–790.e3. doi:10.1016/j.molcel.2019.06.007
- Gaub, B. M., Berry, M. H., Holt, A. E., Reiner, A., Kienzler, M. A., Dolgova, N., et al. (2014). Restoration of visual function by expression of a light-gated mammalian ion channel in retinal ganglion cells or ON-bipolar cells. *Proc. Natl. Acad. Sci. U. S. A.* 111 (51), E5574–E5583. doi:10.1073/pnas.1414162111
- Hasseldine, A. R., Harper, E. A., and Black, J. W. (2003). Cardiac-specific overexpression of human beta2 adrenoceptors in mice exposes coupling to both Gs and Gi proteins. *Br. J. Pharmacol.* 138 (7), 1358–1366. doi:10.1038/sj.bjp.0705191
- Hauser, A. S., Attwood, M. M., Rask-Andersen, M., Schioth, H. B., and Gloriam, D. E. (2017). Trends in GPCR drug discovery: New agents, targets and indications. *Nat. Rev. Drug Discov.* 16 (12), 829–842. doi:10.1038/nrd.2017.178
- Herrmann, R., Heck, M., Henklein, P., Kleuss, C., Wray, V., Hofmann, K. P., et al. (2006). Rhodopsin-transducin coupling: Role of the Galpha C-terminus in nucleotide exchange catalysis. *Vis. Res.* 46 (27), 4582–4593. doi:10.1016/j.visres.2006.07.027
- Jumper, J., Evans, R., Pritzel, A., Green, T., Figurnov, M., Ronneberger, O., et al. (2021). Highly accurate protein structure prediction with AlphaFold. *Nature* 596 (7873), 583–589. doi:10.1038/s41586-021-03819-2
- Kang, Y., Kuybeda, O., de Waal, P. W., Mukherjee, S., Van Eps, N., Dutka, P., et al. (2018). Cryo-EM structure of human rhodopsin bound to an inhibitory G protein. *Nature* 558 (7711), 553–558. doi:10.1038/s41586-018-0215-y
- Kim, J. M., Hwa, J., Garriga, P., Reeves, P. J., RajBhandary, U. L., and Khorana, H. G. (2005). Light-driven activation of beta 2-adrenergic receptor signaling by a chimeric rhodopsin containing the beta 2-adrenergic receptor cytoplasmic loops. *Biochemistry* 44 (7), 2284–2292. doi:10.1021/bi048328i
- Kleinlogel, S. (2016). Optogenetic user's guide to Opto-GPCRs. *Front. Biosci. (Landmark Ed.)* 21 (4), 794–805. doi:10.2741/4421
- Kralik, J., Wyk, M. v., Stocker, N., and Kleinlogel, S. (2022). Bipolar cell targeted optogenetic gene therapy restores parallel retinal signaling and high-level vision in the degenerated retina. *Commun. Biol.* 5, 1116. doi:10.1038/s42003-022-04016-1
- Krishna, A. G., Menon, S. T., Terry, T. J., and Sakmar, T. P. (2002). Evidence that helix 8 of rhodopsin acts as a membrane-dependent conformational switch. *Biochemistry* 41 (26), 8298–8309. doi:10.1021/bi025534m
- Lebon, G., Warne, T., Edwards, P. C., Bennett, K., Langmead, C. J., Leslie, A. G., et al. (2011). Agonist-bound adenosine A2A receptor structures reveal common features of GPCR activation. *Nature* 474 (7352), 521–525. doi:10.1038/nature10136
- Ma, X., Hu, Y., Batebi, H., Heng, J., Xu, J., Liu, X., et al. (2020). Analysis of β_2 AR-Gs and β_2 AR-Gi complex formation by NMR spectroscopy. *Proc. Natl. Acad. Sci. U. S. A.* 117 (37), 23096–23105. doi:10.1073/pnas.2009786117
- Matos-Cruz, V., Blasic, J., Nickle, B., Robinson, P. R., Hattar, S., and Halpern, M. E. (2011). Unexpected diversity and photoperiod dependence of the zebrafish melanopsin system. *PLoS One* 6 (9), e25111. doi:10.1371/journal.pone.0025111
- Milligan, G., and Kostenis, E. (2006). Heterotrimeric G-proteins: A short history. *Br. J. Pharmacol.* 147 (1), S46–S55. doi:10.1038/sj.bjp.0706405
- Mirdita, M., Schutze, K., Moriwaki, Y., Heo, L., Ovchinnikov, S., and Steinegger, M. (2022). ColabFold: Making protein folding accessible to all. *Nat. Methods* 19 (6), 679–682. doi:10.1038/s41592-022-01488-1
- Neves, S. R., Ram, P. T., and Iyengar, R. (2002). G protein pathways. *Science* 296 (5573), 1636–1639. doi:10.1126/science.1071550
- Oldham, W. M., and Hamm, H. E. (2008). Heterotrimeric G protein activation by G-protein-coupled receptors. *Nat. Rev. Mol. Cell Biol.* 9 (1), 60–71. doi:10.1038/nrm2299
- Palczewski, K., Kumasaka, T., Hori, T., Behnke, C. A., Motoshima, H., Fox, B. A., et al. (2000). Crystal structure of rhodopsin: A G protein-coupled receptor. *Science* 289 (5480), 739–745. doi:10.1126/science.289.5480.739
- Petersen, E. F., Goddard, T. D., Huang, C. C., Meng, E. C., Couch, G. S., Croll, T. I., et al. (2021). UCSF ChimeraX: Structure visualization for researchers, educators, and developers. *Protein Sci.* 30 (1), 70–82. doi:10.1002/pro.3943
- Phillips, W. J., and Cerione, R. A. (1994). A C-terminal peptide of bovine rhodopsin binds to the transducin alpha-subunit and facilitates its activation. *Biochem. J.* 299 (2), 351–357. doi:10.1042/bj2990351
- Pin, J.-P., Galvez, T., and Pr zeau, L. (2003). Evolution, structure, and activation mechanism of family 3/C G-protein-coupled receptors. *Pharmacol. Ther.* 98 (3), 325–354. doi:10.1016/S0163-7258(03)00038-X
- Pin, J. P., Joly, C., Heinemann, S. F., and Bockaert, J. (1994). Domains involved in the specificity of G protein activation in phospholipase C-coupled metabotropic glutamate receptors. *EMBO J.* 13 (2), 342–348. doi:10.1002/j.1460-2075.1994.tb06267.x
- Qiao, A., Han, S., Li, X., Li, Z., Zhao, P., Dai, A., et al. (2020). Structural basis of Gs and Gi recognition by the human glucagon receptor. *Science* 367 (6484), 1346–1352. doi:10.1126/science.aaz5346
- Rai, D., Akagi, T., Shimohata, A., Ishii, T., Gangi, M., Maruyama, T., et al. (2021). Involvement of the C-terminal domain in cell surface localization and G-protein coupling of mGluR6. *J. Neurochem.* 158 (4), 837–848. doi:10.1111/jnc.15217
- Rasmussen, S. G., Choi, H. J., Fung, J. J., Pardon, E., Casarosa, P., Chae, P. S., et al. (2011a). Structure of a nanobody-stabilized active state of the $\beta(2)$ adrenoceptor. *Nature* 469 (7329), 175–180. doi:10.1038/nature09648
- Rasmussen, S. G., Choi, H. J., Rosenbaum, D. M., Kobilka, T. S., Thian, F. S., Edwards, P. C., et al. (2007). Crystal structure of the human beta2 adrenergic G-protein-coupled receptor. *Nature* 450 (7168), 383–387. doi:10.1038/nature06325
- Rasmussen, S. G., DeVree, B. T., Zou, Y., Kruse, A. C., Chung, K. Y., Kobilka, T. S., et al. (2011b). Crystal structure of the β_2 adrenergic receptor-Gs protein complex. *Nature* 477 (7366), 549–555. doi:10.1038/nature10361
- Rondard, P., Goudet, C., Kniazeff, J., Pin, J. P., and Prezeau, L. (2011). The complexity of their activation mechanism opens new possibilities for the modulation of mGlu and GABAB class C G protein-coupled receptors. *Neuropharmacology* 60 (1), 82–92. doi:10.1016/j.neuropharm.2010.08.009
- Rose, A. S., Elgeti, M., Zachariae, U., Grubmuller, H., Hofmann, K. P., Scheerer, P., et al. (2014). Position of transmembrane helix 6 determines receptor G protein coupling specificity. *J. Am. Chem. Soc.* 136 (32), 11244–11247. doi:10.1021/ja5055109
- Rose, A. S., Zachariae, U., Grubmuller, H., Hofmann, K. P., Scheerer, P., and Hildebrand, P. W. (2015). Role of structural dynamics at the receptor G protein interface for signal transduction. *PLoS One* 10 (11), e0143399. doi:10.1371/journal.pone.0143399
- Rosenbaum, D. M., Rasmussen, S. G., and Kobilka, B. K. (2009). The structure and function of G-protein-coupled receptors. *Nature* 459 (7245), 356–363. doi:10.1038/nature08144
- Rosenbaum, D. M., Zhang, C., Lyons, J. A., Holl, R., Aragao, D., Arlow, D. H., et al. (2011). Structure and function of an irreversible agonist- $\beta(2)$ adrenoceptor complex. *Nature* 469 (7329), 236–240. doi:10.1038/nature09665
- Salom, D., Lodowski, D. T., Stenkamp, R. E., Le Trong, I., Golczak, M., Jastrzebska, B., et al. (2006). Crystal structure of a photoactivated deprotonated intermediate of rhodopsin. *Proc. Natl. Acad. Sci. U. S. A.* 103 (44), 16123–16128. doi:10.1073/pnas.0608022103
- Sandhu, M., Touma, A. M., Dysthe, M., Sadler, F., Sivaramakrishnan, S., and Vaidehi, N. (2019). Conformational plasticity of the intracellular cavity of GPCR-G-protein

complexes leads to G-protein promiscuity and selectivity. *Proc. Natl. Acad. Sci. U. S. A.* 116 (24), 11956–11965. doi:10.1073/pnas.1820944116

Seven, A. B., Barros-Alvarez, X., de Lapeyriere, M., Papasergi-Scott, M. M., Robertson, M. J., Zhang, C., et al. (2021). G-protein activation by a metabotropic glutamate receptor. *Nature* 595 (7867), 450–454. doi:10.1038/s41586-021-03680-3

Siuda, E. R., McCall, J. G., Al-Hasani, R., Shin, G., Il Park, S., Schmidt, M. J., et al. (2015). Optodynamic simulation of beta-adrenergic receptor signalling. *Nat. Commun.* 6, 8480. doi:10.1038/ncomms9480

Spoida, K., Eickelbeck, D., Karapinar, R., Eckhardt, T., Mark, M. D., Jancke, D., et al. (2016). Melanopsin variants as intrinsic optogenetic on and off switches for transient versus sustained activation of G protein pathways. *Curr. Biol.* 26 (9), 1206–1212. doi:10.1016/j.cub.2016.03.007

Standfuss, J., Edwards, P. C., D'Antona, A., Fransen, M., Xie, G., Oprian, D. D., et al. (2011). The structural basis of agonist-induced activation in constitutively active rhodopsin. *Nature* 471 (7340), 656–660. doi:10.1038/nature09795

Terakita, A., Yamashita, T., Nimbari, N., Kojima, D., and Shichida, Y. (2002). Functional interaction between bovine rhodopsin and G protein transducin. *J. Biol. Chem.* 277 (1), 40–46. doi:10.1074/jbc.M104960200

Tian, L., and Kammermeier, P. J. (2006). G protein coupling profile of mGluR6 and expression of G alpha proteins in retinal ON bipolar cells. *Vis. Neurosci.* 23 (6), 909–916. doi:10.1017/S0952523806230268

Tichy, A. M., So, W. L., Gerrard, E. J., and Janovjak, H. (2022). Structure-guided optimization of light-activated chimeric G-protein-coupled receptors. *Structure* 30, 1075–1087.e4. doi:10.1016/j.str.2022.04.012

Tsai, C. J., Marino, J., Adaixo, R., Pamula, F., Muehle, J., Maeda, S., et al. (2019). Cryo-EM structure of the rhodopsin-Gai- $\beta\gamma$ complex reveals binding of the rhodopsin C-terminal tail to the g β subunit. *eLife* 8, e46041. doi:10.7554/eLife.46041

Tsai, C. J., Pamula, F., Nehme, R., Muhle, J., Weinert, T., Flock, T., et al. (2018). Crystal structure of rhodopsin in complex with a mini-Go sheds light on the principles of G protein selectivity. *Sci. Adv.* 4 (9), eaat7052. doi:10.1126/sciadv.aat7052

Valdez-Lopez, J. C., Petr, S. T., Donohue, M. P., Bailey, R. J., Gebreeziabher, M., Cameron, E. G., et al. (2020). The C-terminus and third cytoplasmic loop cooperatively activate mouse melanopsin phototransduction. *Biophys. J.* 119 (2), 389–401. doi:10.1016/j.bpj.2020.06.013

van Wyk, M., Pielecka-Fortuna, J., Lowel, S., and Kleinlogel, S. (2015). Restoring the on switch in blind retinas: Opto-mGluR6, a next-generation, cell-tailored optogenetic tool. *PLoS Biol.* 13 (5), e1002143. doi:10.1371/journal.pbio.1002143

Venkatakrisnan, A. J., Deupi, X., Lebon, G., Heydenreich, F. M., Flock, T., Miljus, T., et al. (2016). Diverse activation pathways in class A GPCRs converge near the G-protein-coupling region. *Nature* 536 (7617), 484–487. doi:10.1038/nature19107

Wang, C., Jiang, Y., Ma, J., Wu, H., Wacker, D., Katritch, V., et al. (2013). Structural basis for molecular recognition at serotonin receptors. *Science* 340 (6132), 610–614. doi:10.1126/science.1232807

Xiao, R. P. (2001). Beta-adrenergic signaling in the heart: Dual coupling of the beta2-adrenergic receptor to G(s) and G(i) proteins. *Sci. STKE* 2001 (104), re15. doi:10.1126/stke.2001.104.re15

Xu, F., Wu, H., Katritch, V., Han, G. W., Jacobson, K. A., Gao, Z. G., et al. (2011). Structure of an agonist-bound human A2A adenosine receptor. *Science* 332 (6027), 322–327. doi:10.1126/science.1202793

Yamashita, T., Terakita, A., and Shichida, Y. (2001). The second cytoplasmic loop of metabotropic glutamate receptor functions at the third loop position of rhodopsin. *J. Biochem.* 130 (1), 149–155. doi:10.1093/oxfordjournals.jbchem.a002954

Yen, H. Y., Hoi, K. K., Liko, I., Hedger, G., Horrell, M. R., Song, W., et al. (2018). PtdIns(4,5)P2 stabilizes active states of GPCRs and enhances selectivity of G-protein coupling. *Nature* 559 (7714), 423–427. doi:10.1038/s41586-018-0325-6

Zhou, X. E., Melcher, K., and Xu, H. E. (2019). Structural biology of G protein-coupled receptor signaling complexes. *Protein Sci.* 28 (3), 487–501. doi:10.1002/pro.3526



OPEN ACCESS

EDITED BY

Maesoon Im,
Korea Institute of Science and Technology
(KIST), Republic of Korea

REVIEWED BY

Zhijie Charles Chen,
Stanford University, United States
Gengxi Lu,
University of Southern California, United States

*CORRESPONDENCE

Kyungsik Eom
✉ kseom@pusan.ac.kr

RECEIVED 13 April 2023

ACCEPTED 17 July 2023

PUBLISHED 27 July 2023

CITATION

Rahmani A and Eom K (2023) Computational analysis of efficient organic solar cell-based retinal prosthesis using plasmonic gold nanoparticles.
Front. Cell. Neurosci. 17:1205048.
doi: 10.3389/fncel.2023.1205048

COPYRIGHT

© 2023 Rahmani and Eom. This is an open-access article distributed under the terms of the [Creative Commons Attribution License \(CC BY\)](#). The use, distribution or reproduction in other forums is permitted, provided the original author(s) and the copyright owner(s) are credited and that the original publication in this journal is cited, in accordance with accepted academic practice. No use, distribution or reproduction is permitted which does not comply with these terms.

Computational analysis of efficient organic solar cell-based retinal prosthesis using plasmonic gold nanoparticles

Ali Rahmani^{1,2} and Kyungsik Eom^{1*}

¹Department of Electronics Engineering, College of Engineering, Pusan National University, Busan, Republic of Korea, ²Department of Electronics, College of Electrical and Computer Engineering, Yadegar-e-Imam Khomeini (RAH) Shahre-e-Rey Branch, Islamic Azad University, Tehran, Iran

Introduction: Photovoltaic restoration of vision, especially in conjunction with the use of silicon photodiodes, has gained attention for use in patients affected by blindness due to retinal layer disease. Although the use of silicon photodiodes offers miniaturization of the implant unit and increase in the stimulation channel, the implant unit may suffer from the fracture of these brittle photodiodes when mechanical pressure exerted.

Methods: We present an organic solar cell (OSC)-based retinal prosthesis in which spherical gold nanoparticles (AuNPs) are embedded into the active layer to increase the efficiency of the bioelectric interface.

Results: We demonstrate computationally that a modeled OSC incorporating spherical AuNPs has three times higher efficiency than that of a bare OSC presented before for retinal prostheses. Our AuNP based OSC was able to activate the neuron at the minimum light intensity of 0.26 mW/mm², which is lower than that of the bare OSC.

Discussion: The use of AuNPs in OSC allows device miniaturization or lowering of the light exposure required for neural activation using a photovoltaic retinal prosthesis, which can generally be applied in a broad range of neural prostheses.

KEYWORDS

organic solar cell, spherical gold nanoparticles, localized surface plasmon resonance, photovoltaic retinal prosthesis, neural interface

1. Introduction

Age-related macular degeneration and retinitis pigmentosa are the most prevalent incurable eye diseases leading to photoreceptor degeneration and irreversible blindness (Wong et al., 2014). Age-related macular degeneration is the primary cause of irreversible vision loss in the elderly affecting 1.5% of Americans over 40 to >15% of those over 80, while retinitis pigmentosa affects younger people and leads to more vision loss

Abbreviations: OSC, organic solar cell; AuNP, gold nanoparticle; P₃HT, poly(3-hexylthiophene-2,5-diyl); PEDOT:PSS, poly(3,4-ethylenedioxythiophene)-polystyrene sulfonate; PC₆₁BM, [6,6]-phenyl-C₆₁-butyric acid methyl ester; BHJ, bulk heterojunction; PCE, power conversion efficiency; f_s, filling fraction.

(Palanker et al., 2022). Retinal prostheses provide a way to restore vision in blind patients suffering from retinal diseases by artificially stimulating the surviving retinal neural networks, such as bipolar cells and retinal ganglion cells (RGCs) (Lorach et al., 2015).

Microelectrode arrays inserted into the epiretinal and subretinal spaces have been extensively studied for the electrical activation of retinal neurons to restore light sensation (Mandel et al., 2013). Argus II (Second Sight Medical Products, Inc., CA, United States) was the first epiretinal implant approved by the Food and Drug Administration that targeted RGCs with a visual acuity below 20/1,260 (Arevalo et al., 2021). Implantation of a large implant unit and the unavoidable connection from the receiver coil to the electrode array require sophisticated surgical procedures and increase the likelihood of adverse effects (DeMarco et al., 2007). In addition, perceived vision is entirely dependent on the camera's direction rather than on eye movement. The Alpha IMS (Retina Implant AG, Reutlingen, Germany) is one of the most successful subretinal implants that stimulate the inner nuclear layer of the retina (Stingl et al., 2015). In contrast to Argus II, data delivery via an inductive link is not required as silicon photodiodes are implanted to capture the external scene, thereby increasing the number of electrodes (Klauke et al., 2011). A subretinally implanted silicon photodiode was illuminated by a high-intensity stimulation light pattern projected outside the eye, which converted light energy to electrical current to stimulate the inner nuclear layer. The use of a photodiode in combination with an external light projection minimizes the size of the implanted unit. Moreover, the use of pixels with widths equal to 100 μm in the wireless photovoltaic retinal implant (PRIMA; Pixium Vision, Paris, France) allows improved visual acuity ranging from 20/550 to 20/460 (Palanker et al., 2022). Despite these remarkable accomplishments, current wireless photovoltaic retinal prostheses face significant challenges in terms of potential safety. Because these prostheses are fabricated on a silicon substrate, they may fracture when exposed to the mechanical pressure. Moreover, being implanted in a curved eyeball, these prostheses are continuously subjected to mechanical bending forces that damage the retinal layer. Therefore, thin, and flexible photovoltaic devices are desirable which have less concern to the exerted mechanical stress specially during the surgery and implanting the interface (Antognazza et al., 2016).

As effective photovoltaic devices in neuronal prostheses, organic materials have been proven to be successful in converting light signals to electrical voltage to stimulate neurons (Shim et al., 2020). In recent decades, many research groups have focused on improving the quality and efficiency of organic interfaces, thus making them more widely applicable and cost-effective (Ghezzi et al., 2011; Kelly et al., 2011; Hadjinicolaou et al., 2012). Organic materials maintain their activity when in contact with electrolyte solutions, and neurons can grow effectively on these materials (Antognazza et al., 2009). In addition, organic layers in the subretinal configuration can restore the light sensitivity of retinas extracted from retina-degenerated rats (Feyen et al., 2016). The use of organic materials offers many advantages over silicon devices, including low cost, lightweight, high flexibility, and bendability of neural interface to form in retinal curvature (Ghezzi et al., 2011). However, several issues remain unresolved. One crucial issue is that the low-photoconversion efficiency of these organic devices prevents them from shrinking, thus making it difficult for

them to achieve large channel densities (Pillai and Green, 2010). Another issue is the requirement for high-output light intensity to stimulate retinal neurons, which may damage the retinal tissue (Mathieson et al., 2012). Many researchers have developed some conjugated polymers, such as poly(3-hexylthiophene-2,5-diyl), P3HT; [poly(3,4-ethylenedioxythiophene)-polystyrene sulfonate], PEDOT:PSS, and other organic semiconductors ([6,6]-phenyl-C61-butyric acid methyl ester, PC₆₁BM) as photovoltaic subretinal prostheses to enhance visual acuity (Antognazza et al., 2016; Maya-Vetencourt et al., 2017). Other groups have presented epiretinal prostheses (POLYRETINA) using the P₃HT:PC₆₀BM bulk heterojunction (BHJ), which was able to activate RGCs (Ferlauto et al., 2018); however, given the poor photoconversion of organic solar cells (OSCs) made of pure BHJ, either the cell size or projected light intensity should be increased, limiting the stimulation resolution or safety issues, respectively (Rathbun et al., 2014).

The main factors limiting the power conversion efficiency (PCE) of the OSC are low-light absorption and low-photogenerated exciton extraction efficiency (Jung et al., 2015). To enhance the PCE of OSCs, numerous light-trapping materials, such as quantum dots (Wu et al., 2015) and nanowires (Christesen et al., 2012), and plasmonic nanoparticles (NPs) have been employed. The use of plasmonic metal nanoparticles is a practical strategy for boosting light absorption in an organic active layer without sacrificing the electrical properties or degrading the device structure (Tan et al., 2012). In some studies, plasmonic metal NPs were located both inside and outside the organic active layers (Wang et al., 2018).

In this study, we investigated theoretically an efficient photovoltaic retinal prosthesis based on organic materials, using spherical gold NPs (AuNPs) in an active P₃HT:PCBM layer. In contrast to the presented bare active layer solar cells which require high light intensity or have a low PCE, this type of solar cell exploits the lower light intensity or higher PCE. For this purpose, regarding the retinal prostheses considerations, several factors, such as the size and filling fraction (f_s) of the NPs and their effects on parameters, such as the current density, absorption, and scattering terms in the active layer, were investigated. The incident light was tuned to a wavelength of 610 nm, which caused high-light absorption due to the localized surface plasmon resonance (LSPR) wavelength of the AuNPs. We modeled the active layer cell of the BHJ as a mixed donor-acceptor layer intertwined in a comb shape. The cell interface was assumed to be curved to be closer to the actual structure. We considered both the absorption and scattering cross-sections of the NPs to estimate the entire effective region of exciton generation in the active layer in the COMSOL simulator. We computationally modeled the neuron and incorporated it into a NPs-embedded solar cell to determine the optical intensity threshold required to activate the neuron.

2. Materials and methods

2.1. Solar cell modeling

Organic solar cells usually include different organic or inorganic layers. The active absorbing layer is an organic material in which free charges are generated (Sompech et al., 2016). This

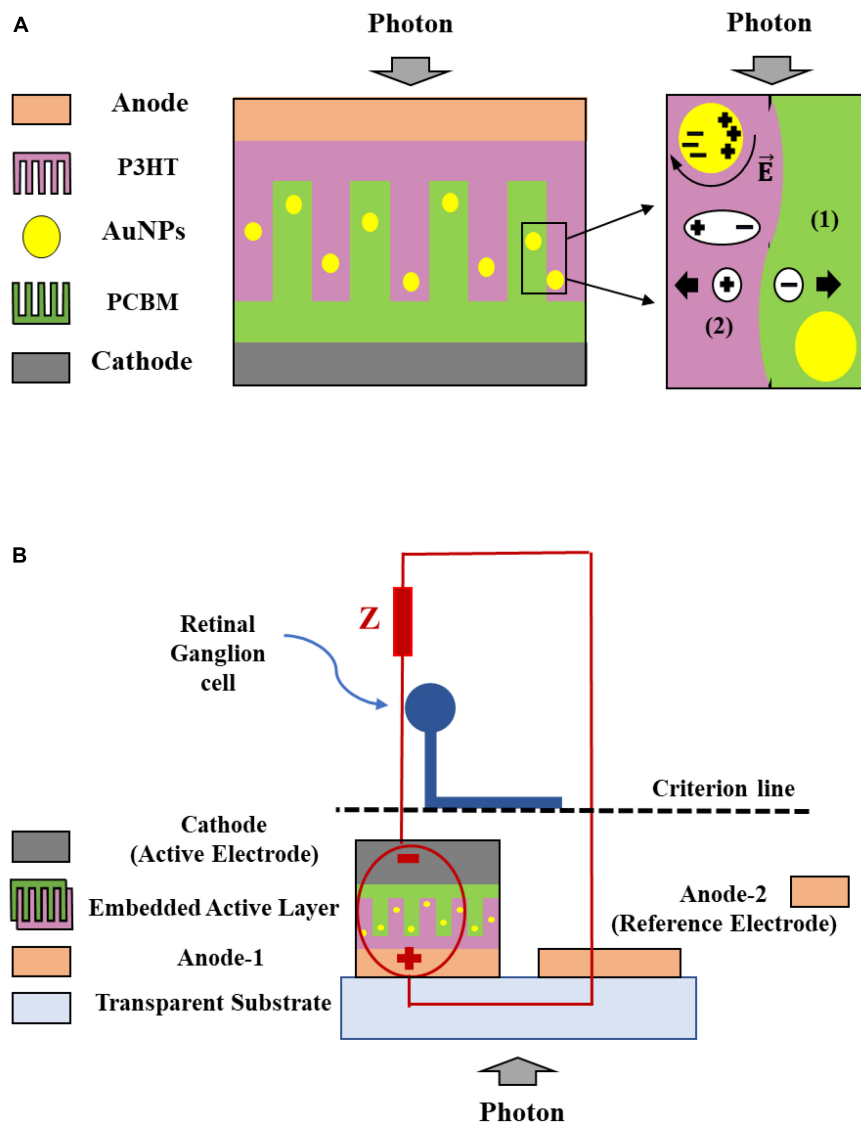


FIGURE 1

Gold nanoparticles (AuNPs)-embedded solar cell structure and the process of the exciton (1), and free carrier generation (2), considering the comb shape of the active layer with a curvature interface between the donor and acceptor (A). The solar cell was used as a voltage source to stimulate the unmyelinated neurons (circuit model) (B).

device comprises two electrodes on both sides of the active layer (anode and cathode), one of which is transparent (Fleetham et al., 2015). In inorganic materials, thermal energy ($K_B T \approx 26$ meV) is sufficient to dissociate excitons into free charges. However, in organic compounds, the binding energy is high (approximately 0.5 eV). Therefore, their separation requires the blend of the two materials with the necessary energy and the formation of a BHJ.

The performance of OSCs is based on the mechanism of the electron donor and acceptor, which utilizes the advantages of the BHJ structure to broaden the interface between the donor and acceptor in the active layer. An increased interface enhances the probability of charge-pair dissociation and prevents recombination phenomena that result in a high PCE (Shabani et al., 2022). Therefore, in contrast to other active-layer structures, such as single-layer, bilayer, and laminated layers, the BHJ is the optimal choice for a bare active layer (Zidan et al., 2021). Because of their

ability to stimulate the neurons, a mixture of P₃HT and PCBM has proven appealing compared with other organic materials (Zidan et al., 2021; Shabani et al., 2022). The charge carrier mobility and exciton diffusion length in organic semiconductors are much smaller than in inorganic crystalline materials (Longeaud et al., 2016). Thus, a trade-off between a high thickness for light absorption and a low thickness for exciton dissociation should be considered to enhance the photoconversion efficiency. The balanced thickness of the organic photoactive layers was in the range of 100 nm for the active layer (Ma et al., 2005).

The BHJ active layer was modeled in two dimensions (Figures 1A, B). The blended BHJ architecture can be modeled as a periodic comb shape in which the periodicity allows us to simulate only a segment of the structure (Raba et al., 2013). Because the contact surface of the donor and acceptor increases in the BHJ blend, and their boundaries intertwine with each other, the

comb shape is a suitable approximation for modeling the active layer. Herein, we assumed that the interface between the two domains was non-flat and considered the curvature form to be closer to the actual structure. L , W_d , and W_a denote the active-layer thickness, and mean width of the donor and acceptor domains, respectively. The donor to acceptor ratio (D/A) is determined by considering the densities of P₃HT and PCBM (Prosa et al., 1992). For the blend of P₃HT:PCBM with a 1:0.8 weight ratio, the volume ratio was approximately 1.4. Considering the mechanism governing the generation and diffusion of excitons toward the interface and charge transfer states, and using the mathematical description of the system, the main parameters of the modeled structure can be determined (Raba et al., 2013). Accordingly, the mean widths of the donor and acceptor were 14 and 10 nm, respectively, and the thickness of the active layer, L , was assumed to be 100 nm.

The photovoltaic structure was simulated using the finite element analysis software COMSOL Multiphysics (COMSOL Inc., Burlington, MA, USA). In the simulation, we used two-dimensional domain, semiconductor module, and fine meshing. The simulated structure is the active layer cell (Figure 1A) that includes two layers of P₃HT and PCBM as the donor and acceptor layers, respectively, with a curved interface. In this simulation, all materials were selected from the COMSOL library, and the complex refractive indices of the materials were inserted as a function of the incident light wavelength. Figure 1B shows the solar cell (circuit model) which stimulates the neurons as a voltage source.

2.2. Modeling of plasmonic AuNPs

Metal NPs have been employed in buffer layers, active layers, and at the interface of OSCs to enhance light absorption and increase current density (Su et al., 2012). The incorporation of NPs improves light harvesting through LSPR via two mechanisms: near-field plasmonic interactions and forward light scattering, thus resulting in an increase in the optical path length. When NPs are embedded in the active layer, strong local field enhancements occur in the vicinity of the NPs owing to resonant plasmon excitation. Excitons are generated in these strong fields, thus causing increased light absorption and high PCE. Among the various metals, gold was chosen because it is inert in biological tissues.

For metal NPs smaller than the wavelength of the incident light, the absorption (C_{abs}) and scattering (C_{sc}) cross-sectional areas from the quasi-static approximation are expressed by the following equations (Bohren, 1983):

$$C_{abs} = \frac{2\pi}{\lambda} \text{Im}[\alpha_{sp}] \quad (1)$$

$$C_{scat} = \frac{1}{6\pi} \left(\frac{2\pi}{\lambda} \right)^4 |\alpha_{sp}|^2 \quad (2)$$

$$\alpha_{sp} = 3V \frac{\epsilon_m - \epsilon_s}{\epsilon_m + 2\epsilon_s} \quad (3)$$

where α_{sp} is the polarizability of the NPs, V is the NP volume, r is the radius of NP, λ is the incident light wavelength, and ϵ_m and ϵ_s are wavelength dependent dielectric functions of the metal NPs and surrounding medium, respectively. The normalized absorption (Q_{abs}) and scattering cross-section (Q_{scat}) are calculated by the

ratio of their terms and the cross-sectional area of NPs, which is πr^2 , i.e., Q_{abs} is equal to $C_{abs}/\pi r^2$ and Q_{scat} is equal to $C_{scat}/\pi r^2$. The scattering efficiency is given by Bohren (1983),

$$Q_{sc} = \frac{C_{scat}}{C_{scat} + C_{abs}} \quad (4)$$

Scattering efficiency indicates the proportion of scattering relative to the absorption cross-sectional area. In resonance conditions, wherein the frequency of the incident light is close to the frequency of the surface plasmon resonance, the denominator (Equation 3) equals zero. This resulted in an increased polarizability of the NPs, enabling the incident light to interact with a larger area than the cross-section of the NP. Consequently, a thorough investigation of the impact of NPs on the absorption and scattering cross-sections, as well as the scattering efficiency, was conducted to improve the interaction between the incident light and the NPs.

We first set the geometry of the NPs, wavelength of the incident light, and material properties of the NPs and surrounding medium, as they determine the scattering and absorption cross-sections. Gold and P₃HT:PCBM were selected as materials for the NPs and their surroundings, respectively. Concerning the geometry of the AuNPs, a spherical shape was chosen because of its strong LSPR phenomenon when illuminated with visible light. The radius of the spherical AuNPs was constrained to 10 nm because the scattering effect was overwhelmed by their absorption for sizes beyond this limit. Moreover, exciton quenching and carrier recombination reduce the PCE of larger AuNPs (Li et al., 2020). Three different AuNP sizes (5, 7.5, and 10 nm) were designed and simulated.

2.3. Current generation in the solar-embedded AuNPs

Metal nanoparticles with nanoscale dimensions have significant effects on free-carrier generation owing to their unusual optoelectronic properties in OSCs (Su et al., 2012). When the AuNPs were under resonant light wavelength, strong interactions were observed between the free carriers in the AuNPs and the incident electromagnetic field. The collective oscillations of the free electrons were plasmons, followed by localized dipole production in the proximity of the AuNP surface. The fields created by these localized dipoles generate excitons in the active organic layer. Free electrons arising from these excitons at the interface cause higher current generation compared with the bare active layer (Wang et al., 2011).

The current density of the device was calculated by introducing the generation rate (G) of free carriers into the COMSOL simulator. The generation rate and short-circuit current density (J_{sc}) equations for the bare active layer are defined by Equations 5, 6, respectively (Wu et al., 2011; Piralae et al., 2020). The short-circuit current density (J_{sc}) of a solar cell is the current density in short-circuit conditions.

$$G(\lambda) = \alpha(\lambda)\lambda I_0 P/hc \quad (5)$$

$$J_{sc}(\lambda) = G(\lambda)qL \quad (6)$$

where α is the absorption coefficient and equals $\frac{4\pi}{\lambda} k(\lambda)$, k is the imaginary part of the medium refraction index, λ is the incident

TABLE 1 Modeling parameters and their values for the solar cell in COMSOL.

Parameter	Definition	Value	Unit
r	AuNPs radius	5, 7.5, and 10	nm
f_s	Filling fraction	10, 15, and 20%	–
I	Incident light intensity	0.26 and 0.38	mW/mm ²
A	Cell area	100 × 100	μm ²
D	Active layer thickness	100	nm
W _d	Donor thickness	14	nm
W _a	Acceptor thickness	10	nm

light wavelength, I_0 is light intensity, h is Planck's constant, c is the speed of the light, P is the probability of excitons dissociation at the interface, q is the electron charge, and L is the cell's height.

For the active layers with AuNPs, the total J_{sc} was modified to consider not only the free carrier generation in the bare active layer but also the effects of absorption and scattering of light at the AuNPs in the active layer. Using Equations 5, 6 and considering P in Equation 5 as the probability of exciton dissociation in the medium from the presented experimental works, this parameter is 79.2% for the bare active layer and 84.4% for AuNPs-embedded active layer (Wu et al., 2011); the short circuit current density equation is described as,

$$J_{sc}(\lambda) = (I_0 \lambda q L / hc) \left[(79.2\% \alpha_1(\lambda)(1 - f_s - v_1 f_s - v_2 f_s)) + (84.4\% \alpha_2(\lambda)(1 - Q_{sc})(v_1 f_s)) + (84.4\% \alpha_2(\lambda) Q_{sc}(v_2 f_s)) \right] \quad (7)$$

where α_1 and α_2 are absorption coefficients as a function of the incident light wavelength for the bare P₃HT:PCBM and AuNPs, respectively. Q_{sc} is the scattering efficiency, f_s , $v_1 f_s$, and $v_2 f_s$ show the fraction of NPs, absorption term, and the scattering term in the active layer volume, respectively. v_1 is the ratio of v_{abs} to v_{NP} , where v_{abs} is the volume of the absorption cross-section (near-field absorption region around the NP), and v_{NP} is the volume of the NP. In addition, v_2 is the ratio of v_{scat} to v_{NP} , where v_{scat} is the volume of the scattering cross-section (the scattering region around the NP). The first term of the generation rate of free carriers is the fraction of the generated free carriers in the active layer, whereas the second term represents the generated free carriers owing to the light absorption of AuNPs with a probability of $(1 - Q_{sc})$. The scattering efficiency (Q_{sc}) determines the ratio of the scattering and absorption cross-sections in free carrier generation. The third term generates free carriers owing to the scattering cross-section of AuNPs with the probability of Q_{sc} in the short-circuit current density. The modeling parameters of the solar cells and their values are listed in Table 1.

2.4. Plasmonic solar cell-based neural stimulation system

We intended to design an OSC and identify a way to increase its PCE by varying the size and filling fraction of AuNPs. We validated

TABLE 2 Modeling parameters and their values for neurons in SIM4LIFE LIGHT.

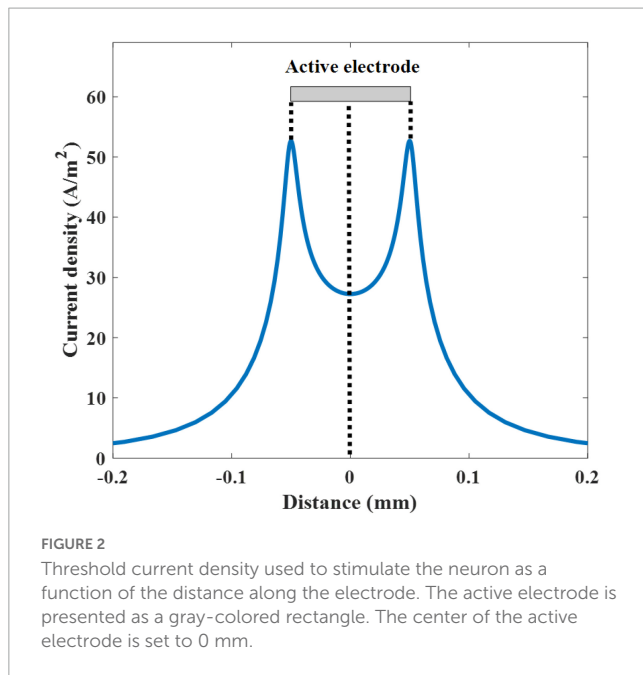
Parameter	Definition	Value	Unit
A	Electrode area	100 × 100	μm ²
t	Electrode thickness	150	nm
l	Neuron distance from electrode surface	5	μm
d	Axon diameter	1	μm

whether our modeled organic solar radiation could stimulate neurons and determined the required optical intensity for neural activation. To achieve this, we modeled a neuron with stimulating electrodes that could generate an electrical stimulation pulse generated by a solar cell using the neuronal dynamics simulator SIM4LIFE LIGHT [Zurich Medtech AG (ZMT), Switzerland].

The architecture of the neural stimulation system using a plasmonic solar cell in which the AuNPs were embedded in the active layer is shown in Figure 1. Following a previously demonstrated retinal prosthesis with an electrode size of 100 μm × 100 μm (Ferlauto et al., 2018), we designed a pixel with the same size (A). Each pixel included a cathode gate, a blend of P₃HT:PCBM semiconductor as the active layer with a thickness (D) of 100 nm, and an electron-blocking layer as the anode at the bottom part.

To model the unmyelinated neurons, a spatially extended stimulation model was employed. This neuroelectric model was used to simulate an effective electrical nerve stimulation. To inject current into the neuron using a voltage source with electrical characteristics identical to those of the designed solar cell, we modeled the electrodes and neuron. In this structure, the active and reference electrode areas (A) with a thickness (t) of 150 nm from titanium (Ti), a metal which primarily delivers charge through the capacitive process, is typical option used in many experimental studies (Ferlauto et al., 2018). The RGC was positioned precisely atop the central region of the active electrode, parallel to the electrode plate with a distance (l) of 5 μm from the surface of the electrode (Figure 1B). The axon's diameter (d) was deliberately chosen as 1 μm, falling within the diameter range observed in human retinal axons (FitzGibbon and Taylor, 2012; FitzGibbon and Nestorovski, 2013). Monophasic cathodic stimulation was employed, and the voltage magnitude was swept to determine the threshold voltage. The modeling parameters of the neurons and solar cells and their values are listed in Table 2.

As the electrode in the solar cell interfaces with the neuron, the current injected into the neuron at a given applied voltage is determined by the impedance of the electrode to the neuron (Figure 1B). In this case, the electrode is assumed as a perfect contact and thereby the steady state current is injected during the stimulation. The spatial distributions of the electric potential and current density were calculated at the frequency of 10 Hz. The calculated electric currents were then applied to the neuron with a cathodic duration of 50 ms, which is identical to the 10 Hz sinusoidal stimulus. The threshold current density is determined by increasing the input pulse until the neuron triggers an action potential. The threshold current density is plotted against the distance along the active electrode whose center was fixed at 0 mm. We measured the current density along the transverse direction



parallel to the surface of the electrode on the axonal trajectory (criterion line), 5 μm above the electrode surface (Figure 2). The average current density from edge to edge of the active electrode (-0.05 to $+0.05$ mm) was 33.63 A/m^2 . Two spikes (at -0.05 and $+0.05$ mm) were observed at the edge of the active electrode. Regarding the given threshold voltage and current density which are 0.065 V and 33.63 A/m^2 , respectively, the total impedance across the electrode-to neuron is calculated as V/I . The values of the total impedance in 10 and 100 Hz are 1.9 and $0.57 \text{ k}\Omega \text{ mm}^2$, respectively. This trend shows that increasing the simulation frequency reduces the total impedance. In this case, based on the SIM4LIFE material library, the tissue electric conductivity and relative permittivity values in 10 Hz are 0.027 S/m and 4.06×10^7 , and these values in 100 Hz are 0.089 S/m and 3.90×10^6 , respectively. The calculated total impedance was used to determine the optical threshold intensity for photovoltaic neural stimulation.

3. Results

3.1. Localized surface plasmon resonance of AuNPs

To enhance the light absorption and PCE of the conventional bare active layer (e.g., $\text{P}_3\text{HT}:\text{PCBM}$)-based solar cells, plasmonic spherical AuNPs were embedded in the active layer. These AuNPs serve as light-trapping centers that can enhance the photon absorption through the near-field absorption and far-field scattering via increasing the optical path length. The photon absorption and scattering spectra of solar cells with AuNPs in the active layer were investigated in terms of the wavelength of the incident light. The fractions of absorption and scattering in the light-trapping process are important for calculating the current generation parameters (i.e., v_1 and v_2 in Equation 7) and were assessed while the size of the AuNPs was varied. Other solar cell

properties, such as current generation, current and voltage (I - V) characteristics, and power-voltage relations for different sizes and f_s of AuNPs, were investigated to modify and determine the optical characteristics of the solar cell.

The normalized scattering and absorption cross-sections over the incident light wavelength revealed that the scattering and absorption reached a maximum value at a resonant frequency of 610 nm and minimum at approximately 500 nm (Figures 3A, B). The peak values of the scattering and absorption terms increased as the radius of the AuNPs increased. This is attributed to the dependence of these terms on the polarizability of the AuNPs, which is directly related to the AuNP volume (Equation 3). Interestingly, the normalized absorption cross-section overwhelms the scattering term for the entire simulated wavelength. The peak values of the normalized absorption cross-sections with AuNPs radii of 10, 7.5, and 5 nm were 2.3, 1.7, and 1.2, respectively, while the peaks of the normalized scattering term of 10, 7.5, and 5 nm were 0.0116, 0.0037, and 0.0008, respectively. These outcomes demonstrate that the contribution of light trapping by AuNPs is limited owing to their absorption. The scattering term was dominant only for AuNPs with radii larger than 25 nm (Li et al., 2020). In additional analyses that showed the variation of the scattering efficiency as a function of wavelength (Figure 3C), we also confirmed that the scattering efficiency, the portion of scattering over the total absorption and scattering term, was limited up to 0.016, which is the maximum value of the entire simulated case. The scattering efficiency decreased as the AuNP size decreased. Although total photon trapping can be boosted by the scattering of large AuNPs, this enhancement cannot compensate for the PCE reduction. This is owing to the fact that as the size of AuNPs increases in the active layer, exciton quenching and charge recombination deteriorate the PCE (You et al., 2014).

3.2. Effects of AuNPs on solar cell performance

Having found that AuNPs significantly promote light trapping by the LSPR phenomena, especially by means of absorption by the LSPRs effect, it is essential to validate whether light trapping via AuNPs can enhance current generation at the active layer. In this study, we evaluated the effect of the size of AuNPs and their relative concentration inside the active layer on the current generation of solar cells.

To evaluate the effects of AuNPs on the current generation, the short-circuit current densities of the solar cells with and without AuNPs were investigated. When a solar cell with a bare active layer was irradiated with a light intensity of 0.26 mW/mm^2 , the maximum short-circuit current density was found to be approximately 500 nm (Figure 4). Interestingly, another sharp current peak was observed near a wavelength of 610 nm for the solar cell with AuNPs, which originated from the LSPRs of the AuNPs, especially owing to light absorption. These current peaks at 610 nm increased as the size of the AuNPs or f_s increased, thus indicating that as the radius of the AuNPs increased, the short-circuit current density originating from absorption and scattering increased, but by different amounts (Equation 7). Unlike the case at 610 nm, an increase in f_s led to a decrease in the short-circuit

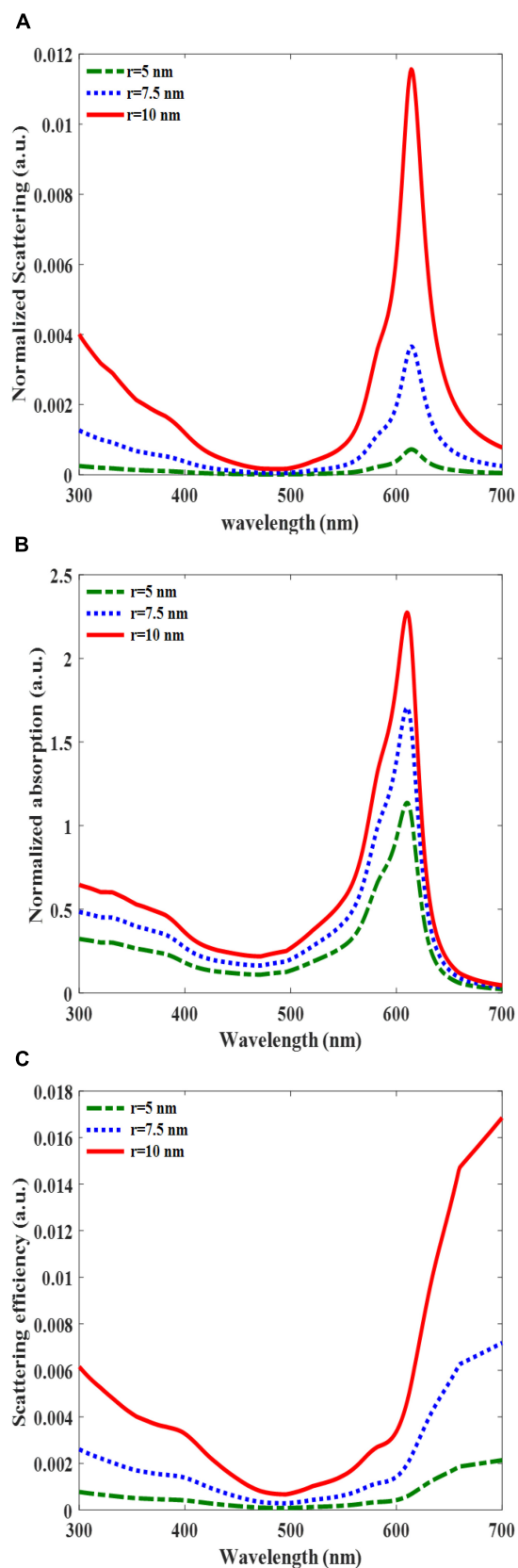


FIGURE 3
Normalized scattering (A), normalized absorption cross-section (B), and scattering efficiency (C), for embedded AuNPs in the active layer versus the incident light wavelength for different AuNP radii were all equal to 5, 7.5, and 10 nm.

current density at 500 nm. We conjecture that this change arises from a reduction in the volume fraction of the active layers as f_s increases.

An enhancement in the short-circuit current density at a wavelength of 610 nm relative to 500 nm was observed in both the 7.5 and 10 nm AuNP-incorporated solar cells for all f_s . Notably, we observed an increase in the short-circuit current density at 610 nm compared with that at 500 nm in both the 7.5 and 10 nm AuNP-integrated solar cells for all f_s values (Figures 4B, C).

However, for 5 nm AuNPs, only the f_s value of 20% yielded photocurrent at 610 nm which were larger by 1.1 times compared with those at 500 nm, while f_s values smaller than 20% yielded a lower photocurrent at 610 nm compared with that of 500 nm (Figure 4A). Taken together, these results suggest that to achieve the maximum photocurrent, it is advantageous to use AuNPs with sizes ≥ 7.5 nm and adjust the incident light wavelength to 610 nm. This is because of the higher absorption cross-section of larger AuNPs, and hence owing to the higher free carrier generation at the resonant wavelength.

After confirming the enhanced current generation with the aid of AuNPs, especially for the sizes of 7.5, and 10 nm, we then simulated the I–V response of solar cells with AuNPs for various f_s values (10, 15, and 20%) at the resonance condition and solar cells without AuNPs at the wavelengths of 500 and 610 nm (Figure 5). By altering the values of f_s to 10, 15, and 20% for AuNPs with a radius of 7.5 nm, we observed corresponding short-circuit current densities of 35, 50, and 67 A/m², respectively (Figure 5A). These values were higher than those without AuNPs at wavelengths of 500 and 610 nm which are 34 and 4.5 A/m², respectively. For AuNPs with a radius of 10 nm and light intensity of 0.26 mW/mm² for different values of f_s , 10, 15, and 20%, the short-circuit current densities were 35, 51, and 67 A/m², respectively. Likewise, these values were higher than those of the bare active layer at the wavelengths of 500 and 610 nm, which were equal to 22 and 3.1 A/m², respectively (Figure 5B).

The power–voltage relationship was investigated to determine the solar cell performance parameters (Figure 6). The power–voltage graph of the solar cell versus the anode voltage for various f_s is presented for two different active layers: one with a radius of 7.5 nm and a light intensity of 0.38 mW/mm² (Figure 6A), and the other with a radius of 10 nm and a light intensity of 0.26 mW/mm² (Figure 6B). Since the irradiated light wavelength is in visible range (610 nm), and threshold light intensities of our AuNPs OSC are higher than natural sunlight illumination on the retinal neurons, these light powers are not compatible with the patients who retain some natural light sensitivity. These intensities can be used only for the patients whose natural vision are completely degenerated and do not retain any light sensitivity (Leccardi et al., 2020). These figures demonstrate the significant impact of the AuNPs on the solar cell output power compared with the bare structure at wavelengths of 500 and 610 nm. The power generated by the solar cell increased from 16 to 32 W/m² as the f_s increased from 10 to 20%. This increase in power was attributed to the higher number of AuNPs, which led to higher light absorption and free carrier generation. The power curves reached their maximum values at the anode voltage of 0.53 V for each case. Using the related equations, the solar cell performance parameters were calculated, and are presented in Tables 3, 4. The filling factor was calculated as $P_{\max}/I_{sc} V_{sc}$ and the PCE was calculated as P_{\max}/P_{in} , where P_{in} is

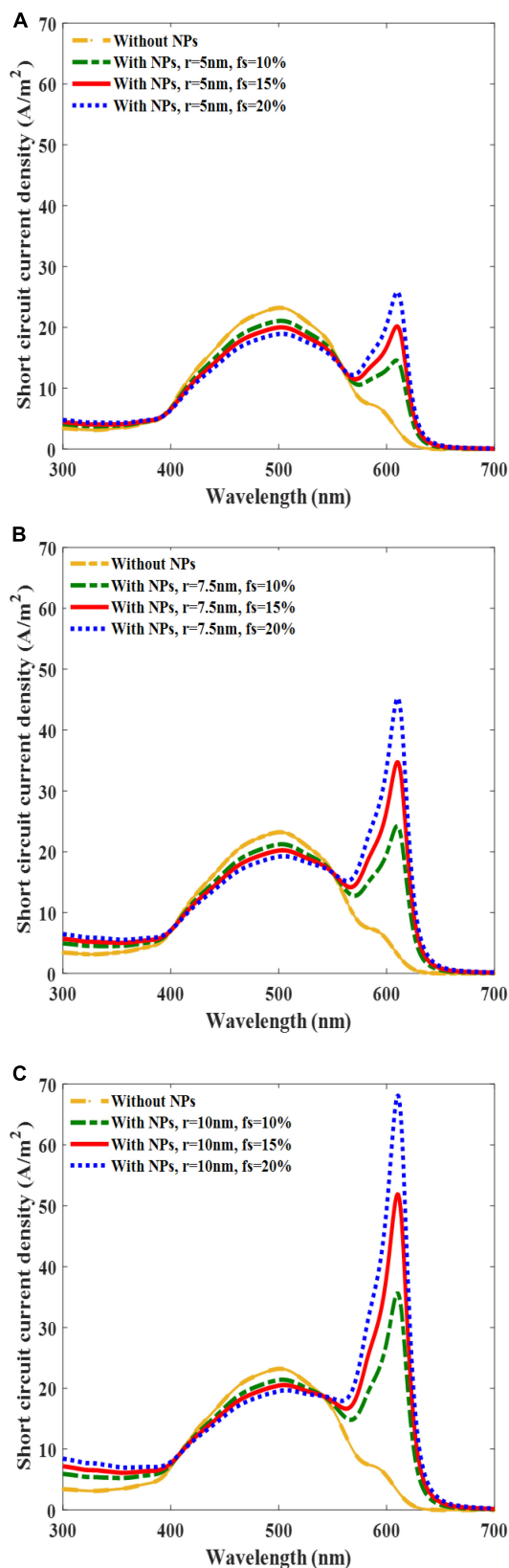


FIGURE 4
Plots of solar cell short-circuit current density versus incident light wavelength at the incident light intensity of 0.26 mW/mm^2 and at the different filling fraction (f_s) of gold in active layer volumes of 10, 15, and 20% and different radii equal to 5 nm (A), 7.5 nm (B), and 10 nm (C).

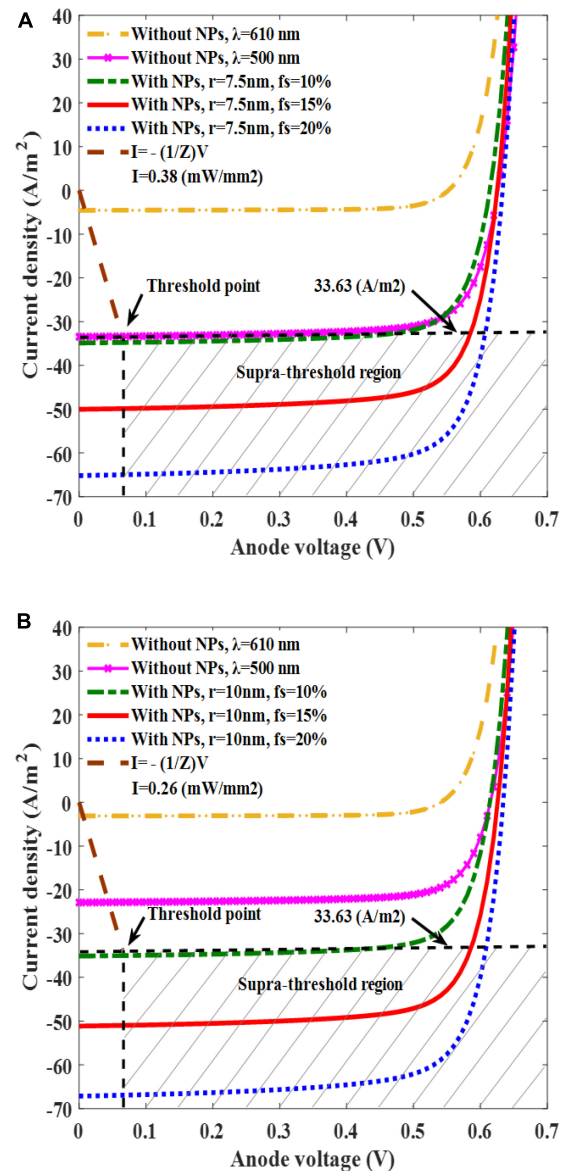


FIGURE 5
Plots of solar cell current density versus anode voltage for the filling fractions (f_s) of 10, 15, and 20% for a AuNP radius of 7.5 nm and light intensity of 0.38 mW/mm^2 (A), and for a AuNP radius of 10 nm and a light intensity of 0.26 mW/mm^2 (B).

$A \times I_{in}$, A is the cell area, I_{in} is the incident light intensity, and P_{max} is $I_{max} \times V_{max}$. The results in the tables show that the PCE of the solar cell increased as functions of the f_s and radius of the AuNPs owing to the increase in the overall absorption cross-section and current generation.

According to the performance parameters in both tables, the solar cells with active layers containing AuNPs had higher PCEs than those without AuNPs. **Table 3** shows that the ratio of PCE for the solar cell with an active layer with AuNPs and a radius of 7.5 nm and f_s values of 15 and 20% to the PCE of the bare active layer were 1.4 and 1.92, respectively. The ratios in **Table 4** for the active layer with AuNPs and radii of 10 nm and f_s of 15 and 20% to the bare layer were approximately 2.3 and 3, respectively. This demonstrates the importance of AuNPs in increasing the efficiency of solar cells.

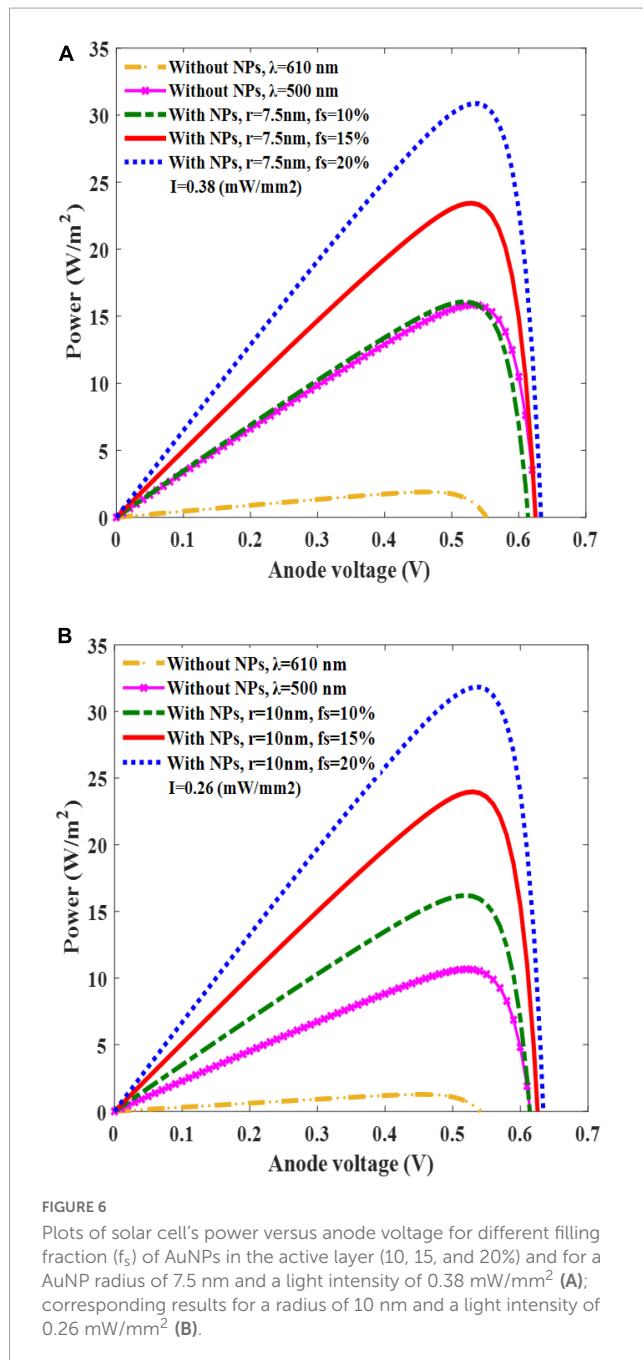


FIGURE 6

Plots of solar cell's power versus anode voltage for different filling fraction (f_s) of AuNPs in the active layer (10, 15, and 20%) and for a AuNP radius of 7.5 nm and a light intensity of 0.38 mW/mm² (A); corresponding results for a radius of 10 nm and a light intensity of 0.26 mW/mm² (B).

Between these cases, AuNPs with a radius of 10 nm and f_s values of 15 and 20% were the preferred options for designing the final intended solar cell structure because of their low-light intensity and high-PCE ratio.

3.3. AuNP-embedded solar cells can stimulate neurons efficiently

Incorporating AuNPs into solar cells enhances light absorption owing to LSPRs and free charge generation. Using AuNPs in the active layer of the solar cell, the current generation is enhanced; therefore, the neurons can be activated with a lower light intensity or reduced solar cell size. In this section, we investigate the optical

TABLE 3 Performance parameters for solar cells without and with AuNPs in the active layer with a radius of 7.5 nm and light intensity of 0.38 mW/mm².

Solar cell's structure	J_{SC} (A/m ²)	V_{OC} (V)	FF (%)	PCE (%)
Active layer without AuNPs, $\lambda = 610$ nm	4.5	0.55	76.5	0.5
Active layer without AuNPs, $\lambda = 500$ nm	34	0.63	74.7	4.2
Active layer with AuNPs, $r = 7.5$ nm, $f_s = 10\%$	35	0.61	75.4	4.2
Active layer with AuNPs, $r = 7.5$ nm, $f_s = 15\%$	50	0.63	73	6
Active layer with AuNPs, $r = 7.5$ nm, $f_s = 20\%$	67	0.64	72.2	8.1

TABLE 4 Performance parameters for solar cells without and with AuNPs in the active layer with a radius of 10 nm and light intensity of 0.26 mW/mm².

Solar cell's structure	J_{SC} (A/m ²)	V_{OC} (V)	FF (%)	PCE (%)
Active layer without AuNPs, $\lambda = 610$ nm	3.1	0.54	77.6	0.5
Active layer without AuNPs, $\lambda = 500$ nm	22	0.62	77	4
Active layer with AuNPs, $r = 10$ nm, $f_s = 10\%$	35	0.62	73.7	6.1
Active layer with AuNPs, $r = 10$ nm, $f_s = 15\%$	51	0.63	74.7	9.2
Active layer with AuNPs, $r = 10$ nm, $f_s = 20\%$	67	0.64	74.6	12.3

threshold intensity required to stimulate neurons in solar cells with and without AuNPs-embedded in their active layers. In addition, we confirmed the efficacy of the plasmonic solar cells as a neural stimulation system.

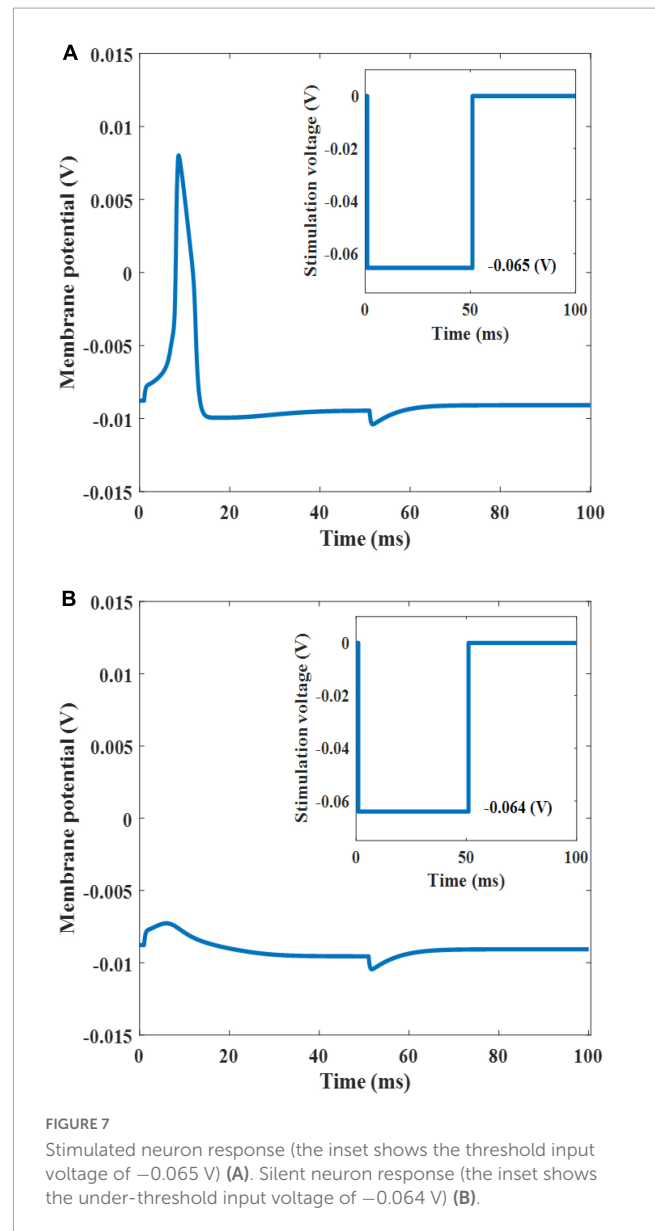
To demonstrate whether our plasmonic solar cell can trigger neural activation, we first defined a stimulation threshold for the targeted neuron, which represented the minimum electrical stimulation parameter required for activation. The threshold current density and its corresponding voltage were determined to be 33.63 A/m² and -0.065 V, respectively (Figures 5A, B). This point serves as a criterion, where the area above it is the suprathreshold region that can trigger neural activation, while the area below it is the subthreshold region that cannot activate the neuron. Using this threshold point, the threshold light intensity used to produce a threshold current for neural activation was determined for two types of solar cells (solar cells with 10 and 7.5 nm AuNPs with f_s values of 15 and 20%, respectively). Our findings indicate that a solar cell with 7.5 nm AuNPs requires a light intensity of 0.38 mW/mm², whereas a solar cell embedded with 10 nm AuNPs requires only 0.26 mW/mm², thus maintaining the wavelength of light fixed at 610 nm to maximize the photocurrent in both cases (Figure 5). Stimulating the neurons using the bare active layer requires a light intensity of 0.38 mW/mm² at a wavelength of 500 nm, which is higher than the light intensity of the 10 nm AuNP-embedded active layer.

When light is irradiated onto the plasmonic solar cell to produce a threshold cathodic voltage pulse (-0.065 V) with a duration of 50 ms, the neuron elicited an action potential (Figure 7A). However, when an input voltage of -0.064 V was applied (this value was slightly below the threshold level), the neuron remained silent (Figure 7B). As this threshold voltage lies within the water window, which is a potential range that does not induce water oxidation and reduction, stimulating neurons at this potential would not degrade the electrode (Boinagrov et al., 2016). Moreover, for our solar cell, the maximum voltage of the cathode was 0.64 V (which falls within the water window of 1.23 V) indicates that the voltage does not undergo electrolytic neural stimulation. To exclude this possibility, it is essential to determine accurately the actual voltage applied to the electrode and limit the voltage within the water window. First, using the impedance of the electrode–electrolyte interface (Z), the I–V relationship of the electrode was determined, as shown by the dotted purple in Figure 5. The intersection of the two I–V traces of the electrode and plasmonic solar cell represents the current and voltage that are actually applied to the neuron. For instance, when a light intensity of 0.26 mW/mm² is applied to the 10 nm AuNPs with a f_s of 15%, it could deliver a voltage of 0.065 V and 33.63 A/m² onto the neuron, which is within the water window.

In summary, our designed plasmonic solar cell efficiently stimulated neurons with a lower light intensity than solar cells without AuNPs. Moreover, we determined the maximum allowable optical intensity that would not induce water oxidation or reduction. We found that considering AuNPs with the radii of 7.5 or 10 nm using the light intensities of 0.38 and 0.26 mW/mm², respectively, with $f_s \geq 15\%$, neurons were activated. Our main option is the case in which the radius of 10 nm owing to its lower intensity. The f_s values higher than 20% are not allowed because of the deteriorating active layer. The PCE ratios of these two types of AuNP-embedded active layers to the bare one was 2.3 and 3, respectively, thus revealing the high efficiency of this solar cell, which enables us to use either low-power illumination or a miniaturized cell structure. The simulation results indicate that this technique is suitable for highly efficient solar-cell-based retinal prostheses.

4. Discussion

In this study, we demonstrated that solar cells using bare active layers are not efficient enough to exploit either low-power incident light or high-current density to stimulate neurons. A high-current density enables the miniaturization of the cell dimensions to reach a high-resolution interface or to use low-power light illumination. In this way, by using the SIM4LIFE LIGHT simulator, we determined the current and voltage threshold levels required to stimulate the neurons. These threshold levels aid in designing and determining the desired characteristics of the solar cell interface. Subsequently, the active layer was modeled as a comb-shaped structure. We simulated a solar cell with and without spherical AuNPs, extracted the I–V curves of the cells, and compared two different conditions to determine the suitable characteristics of the solar cell. Our results indicate that a larger radius or f_s creates a higher current density. We adjusted these conditions to fulfill the threshold conditions



of voltage and current density to stimulate the neurons. The power–voltage results are useful for calculating the performance parameters of the solar cells. The values of these parameters show that the preferred choices yield acceptable filling factor and PCE outcomes.

By comparing the absorption and scattering cross-sections, it was observed that for AuNPs with radii up to 10 nm, the absorption term is dominant, and the light absorption increases considerably. By increasing the radius of the AuNPs to values >10 nm, scattering is enhanced, but carrier trapping and exciton quenching increase and overcome scattering enhancement and reduce the PCE. The short-circuit current density data indicate that the resonant wavelength for AuNPs occurs at 610 nm and there is a discriminative enhancement for embedded active layers that have AuNPs with radii higher than 7.5 and 10 nm. The obtained results for a radius of 5 nm showed that either, (a) this size of AuNPs has weak resonance and could not stimulate neurons, or (b) required high-light intensities. In these simulations, we considered

different AuNP radii (7.5 and 10 nm), which were illuminated at 0.38 and 0.26 mW/mm², respectively. These are the optimum amounts used to fulfill the neuron activation conditions and are placed in the suprathreshold region of the I–V graph. The f_s value of 15% is the minimum filling fraction that satisfies the threshold point. f_s values >20% are not suitable and cause damage to the active layer. In contrast to the case with a radius of 7.5 nm and an intensity of 0.38 mW/mm², the preferred case for embedded AuNPs corresponded to a radius of 10 nm and f_s values of 15 and 20% with an intensity of 0.26 mW/mm², owing to its lower light intensity. In the preferred case, the ratios of PCE for the active layers with f_s values of 15 and 20% to the PCE of the bare active layer are 2.3 and 3, respectively, which allows us to miniaturize the device. These results show that these types of embedded AuNPs are suitable for solar cell design owing to their high PCE ratios and low intensities. Overall, this design is a modified structure for an efficient solar cell interface used as a retinal prosthesis.

5. Conclusion

The main purpose of this work was to improve the performance efficiency of solar cell-based retinal prostheses using embedded spherical AuNPs in the active layer and achieving higher power and current densities. The extracted outcomes showed that by illuminating the solar cells with incident light tuned to an LSPR wavelength of 610 nm, the photon absorption of the active layer was increased; this resulted in higher efficiency outcomes. This efficiency enhancement can be exploited to decrease the solar cell dimensions, which increases the retinal prosthesis resolution or decreases the light power. Our preferred values for the final structure are the AuNP radius of 10 nm, filling fractions of 15 and 20%, and a light intensity of 0.26 mW/mm², which should be tuned to 610 nm. As discussed, with these values, the ratios of the PCE of the AuNP-embedded active layer in contrast to the bare one are 2.3 and 3, respectively, which can increase the solar cell efficiency and resolution by these proportions. The simulation results demonstrate that this structure can improve the resolution of the interface cells, which is a useful solution for enhanced solar cell-based retinal prosthesis performance.

References

- Antognazza, M. R., Di Paolo, M., Ghezzi, D., Mete, M., Di Marco, S., Maya-Vetencourt, J. F., et al. (2016). Characterization of a polymer-based fully organic prosthesis for implantation into the subretinal space of the rat. *Adv. Healthc. Mater.* 5, 2271–2282. doi: 10.1002/adhm.201600318
- Antognazza, M. R., Ghezzi, D., Musitelli, D., Garbugli, M., and Lanzani, G. (2009). A hybrid solid-liquid polymer photodiode for the bioenvironment. *Appl. Phys. Lett.* 94, 92–95. doi: 10.1063/1.3153846
- Arevalo, J. F., Al Rashaed, S., Alhamad, T. A., Al Kahtani, E., Al-Dhibi, H. A., Mura, M., et al. (2021). Argus II retinal prosthesis for retinitis pigmentosa in the Middle East: The 2015 Pan-American Association of Ophthalmology gradle lecture. *Int. J. Retin. Vitr.* 7, 1–11. doi: 10.1186/s40942-021-00324-6
- Bohren, C. F. (1983). Absorption and scattering of light by small particles. *Physics Bulletin* 35:104. doi: 10.1088/0031-9112/35/3/025
- Boinagrov, D., Lei, X., Goetz, G., Kamins, T. I., Mathieson, K., Galambos, L., et al. (2016). Photovoltaic pixels for neural stimulation: Circuit models and performance. *IEEE Trans. Biomed. Circuits Syst.* 10, 85–97. doi: 10.1109/TBCAS.2014.2376528
- Christesen, J. D., Zhang, X., Pinion, C. W., Celano, T. A., Flynn, C. J., and Cahoon, J. F. (2012). Design principles for photovoltaic devices based on Si nanowires with axial or radial p-n junctions. *Nano Lett.* 12, 6024–6029. doi: 10.1021/nl303610m
- DeMarco, P. J., Yarbrough, G. L., Yee, C. W., McLean, G. Y., Sagdullaev, B. T., Ball, S. L., et al. (2007). Stimulation via a subretinally placed prosthetic elicits central activity and induces a trophic effect on visual responses. *Investig. Ophthalmol. Vis. Sci.* 48, 916–926. doi: 10.1167/iovs.06-0811
- Ferlauto, L., Airaghi Leccardi, M. J. I., Chenais, N. A. L., Gilliéron, S. C. A., Vagni, P., Bevilacqua, M., et al. (2018). Design and validation of a foldable and photovoltaic wide-field epiretinal prosthesis. *Nat. Commun.* 9:992. doi: 10.1038/s41467-018-03386-7
- Feyen, P., Colombo, E., Endeman, D., Nova, M., Laudato, L., Martino, N., et al. (2016). Light-evoked hyperpolarization and silencing of neurons by conjugated polymers. *Sci. Rep.* 6:22718. doi: 10.1038/srep22718

Data availability statement

The raw data supporting the conclusions of this article will be made available by the authors, without undue reservation.

Author contributions

KE and AR: conceptualization and generating the idea, data collection, and drafting and revising. AR: analysis and writing. KE: funding. Both authors contributed to the article and approved the submitted version.

Funding

This work was supported by 2022 BK21 FOUR Program of Pusan National University, by National Research Foundation of Korea (NRF) grant funded by the Korea Government (MSIT) (2020R1C1C1010505), and by BK21PLUS, Creative Human Resource Education and Research Programs for ICT Convergence in the 4th Industrial Revolution.

Conflict of interest

The authors declare that the research was conducted in the absence of any commercial or financial relationships that could be construed as a potential conflict of interest.

Publisher's note

All claims expressed in this article are solely those of the authors and do not necessarily represent those of their affiliated organizations, or those of the publisher, the editors and the reviewers. Any product that may be evaluated in this article, or claim that may be made by its manufacturer, is not guaranteed or endorsed by the publisher.

- FitzGibbon, T., and Nestorovski, Z. (2013). Human intraretinal myelination: Axon diameters and axon/myelin thickness ratios. *Indian J. Ophthalmol.* 61, 567–575. doi: 10.4103/0301-4738.121075
- FitzGibbon, T., and Taylor, S. F. (2012). Mean retinal ganglion cell axon diameter varies with location in the human retina. *Jpn. J. Ophthalmol.* 56, 631–637. doi: 10.1007/s10384-012-0185-9
- Fleetham, T., Choi, J. Y., Choi, H. W., Alford, T., Jeong, D. S., Lee, T. S., et al. (2015). Photocurrent enhancements of organic solar cells by altering dewetting of plasmonic Ag nanoparticles. *Sci. Rep.* 5:14250. doi: 10.1038/srep14250
- Ghezzi, D., Antognazza, M. R., Dal Maschio, M., Lanzarini, E., Benfenati, F., and Lanzani, G. (2011). A hybrid bioorganic interface for neuronal photoactivation. *Nat. Commun.* 2:1164. doi: 10.1038/ncomms1164
- Hadjinicolaou, A. E., Leung, R. T., Garrett, D. J., Ganesan, K., Fox, K., Nayagam, D. A. X., et al. (2012). Electrical stimulation of retinal ganglion cells with diamond and the development of an all diamond retinal prosthesis. *Biomaterials* 33, 5812–5820. doi: 10.1016/j.biomaterials.2012.04.063
- Jung, J. H., Aloni, D., Yitzhaky, Y., and Peli, E. (2015). Active confocal imaging for visual prostheses. *Vision Res.* 111, 182–196. doi: 10.1016/j.visres.2014.10.023
- Kelly, S. K., Shire, D. B., Chen, J., Doyle, P., Cogan, S. F., Gingerich, M. D., et al. (2011). A hermetic wireless subretinal neurostimulator for vision prostheses. *IEEE Trans. Biomed. Eng.* 58, 3197–3205. doi: 10.1109/TBME.2011.2165713
- Klauke, S., Goertz, M., Rein, S., Hoehl, D., Thomas, U., Eckhorn, R., et al. (2011). Stimulation with a wireless intraocular epiretinal implant elicits visual percepts in blind humans. *Investig. Ophthalmol. Vis. Sci.* 52, 449–455. doi: 10.1167/iops.09-4410
- Leccardi, M., Chenais, N., Ferlauto, L., Kawecki, M., Zollinger, E., and Ghezzi, D. (2020). Photovoltaic organic interface for neural stimulation in the near-infrared. *Comms. Materials* 1:21. doi: 10.1038/s43246-020-0023-4
- Li, Y. F., Kou, Z. L., Feng, J., and Sun, H. B. (2020). Plasmon-enhanced organic and perovskite solar cells with metal nanoparticles. *Nanophotonics* 9, 3111–3133. doi: 10.1515/nanoph-2020-0099
- Longeaud, C., Fath Allah, A., Schmidt, J., El Yaakoubi, M., Berson, S., and Lemaitre, N. (2016). Determination of diffusion lengths in organic semiconductors: Correlation with solar cell performances. *Org. Electron.* 31, 253–257. doi: 10.1016/j.orgel.2016.01.043
- Lorach, H., Goetz, G., Smith, R., Lei, X., Mandel, Y., Kamins, T., et al. (2015). Photovoltaic restoration of sight with high visual acuity. *Nat. Med.* 21, 476–482. doi: 10.1038/nm.3851
- Ma, W., Yang, C., Gong, X., Lee, K., and Heeger, A. J. (2005). Thermally stable, efficient polymer solar cells with nanoscale control of the interpenetrating network morphology. *Adv. Funct. Mater.* 15, 1617–1622. doi: 10.1002/adfm.200500211
- Mandel, Y., Goetz, G., Lavinsky, D., Huie, P., Mathieson, K., Wang, L., et al. (2013). Cortical responses elicited by photovoltaic subretinal prostheses exhibit similarities to visually evoked potentials. *Nat. Commun.* 4:2980. doi: 10.1038/ncomms2980
- Mathieson, K., Loudin, J., Goetz, G., Huie, P., Wang, L., Kamins, T. I., et al. (2012). Photovoltaic retinal prosthesis with high pixel density. *Nat. Photonics* 6, 391–397. doi: 10.1038/nphoton.2012.104
- Maya-Vetencourt, J. F., Ghezzi, D., Antognazza, M. R., Colombo, E., Mete, M., Feyen, P., et al. (2017). A fully organic retinal prosthesis restores vision in a rat model of degenerative blindness. *Nat. Mater.* 16, 681–689. doi: 10.1038/nmat4874
- Palanker, D., Le Mer, Y., Mohand-Said, S., and Sahel, J. A. (2022). Simultaneous perception of prosthetic and natural vision in AMD patients. *Nat. Commun.* 13:513. doi: 10.1038/s41467-022-28125-x
- Pillai, S., and Green, M. A. (2010). Plasmonics for photovoltaic applications. *Sol. Energy Mater. Sol. Cells* 94, 1481–1486. doi: 10.1016/j.solmat.2010.02.046
- Piralaee, M., Ebrahimpour, Z., and Asgari, A. (2020). The improved performance of BHJ organic solar cells by random dispersed metal nanoparticles through the active layer. *Curr. Appl. Phys.* 20, 531–537. doi: 10.1016/j.cap.2020.01.016
- Prosa, T. J., Winokur, M. J., Moulton, J., Smith, P., and Heeger, A. J. (1992). X-ray structural studies of poly(3-alkylthiophenes): An example of an inverse comb. *Macromolecules* 25, 4364–4372. doi: 10.1021/ma00043a019
- Raba, A., Cordan, A. S., and Leroy, Y. (2013). Two-dimensional simulation of organic bulk heterojunction solar cell: Influence of the morphology. *J. Nanosci. Nanotechnol.* 13, 5164–5169. doi: 10.1166/jnn.2013.7501
- Rathbun, S. D., Participants, S., Birch, D., Dowling, J., Ellis, E., Fitzke, F., et al. (2014). Restoring vision to the blind: The new age of implanted visual prostheses. *Transl. Vis. Sci. Technol.* 3:3. doi: 10.1167/tvst.3.7.3
- Shabani, L., Mohammadi, A., and Jalali, T. (2022). Numerical study of plasmonic effects of Ag nanoparticles embedded in the active layer on performance polymer organic solar cells. *Plasmonics* 17, 491–504. doi: 10.1007/s11468-021-01539-x
- Shim, S., Eom, K., Jeong, J., and Kim, S. J. (2020). Retinal prosthetic approaches to enhance visual perception for blind patients. *Micromachines* 11, 1–26. doi: 10.3390/mi11050535
- Sompech, S., Thaomola, S., and Dasri, T. (2016). Optical effects in the active layer of organic solar cells with embedded noble metal nanoparticles. *Orient. J. Chem.* 32, 85–91. doi: 10.13005/ojc/320108
- Stingl, K., Bartz-Schmidt, K. U., Besch, D., Chee, C. K., Cottriall, C. L., Gekeler, F., et al. (2015). Subretinal visual implant alpha IMS – Clinical trial interim report. *Vision Res.* 111, 149–160. doi: 10.1016/j.visres.2015.03.001
- Su, Y. H., Ke, Y. F., Cai, S. L., and Yao, Q. Y. (2012). Surface plasmon resonance of layer-by-layer gold nanoparticles induced photoelectric current in environmentally-friendly plasmon-sensitized solar cell. *Light Sci. Appl.* 1, 2–6. doi: 10.1038/lsa.2012.14
- Tan, H., Santbergen, R., Smets, A. H. M., and Zeman, M. (2012). Plasmonic light trapping in thin-film silicon solar cells with improved self-assembled silver nanoparticles. *Nano Lett.* 12, 4070–4076. doi: 10.1021/nl301521z
- Wang, D. H., Kim, D. Y., Choi, K. W., Seo, J. H., Im, S. H., Park, J. H., et al. (2011). Enhancement of donor – Acceptor polymer bulk heterojunction solar cell power conversion efficiencies by addition of Au nanoparticles. *Angew. Chemie – Int. Ed.* 50, 5519–5523. doi: 10.1002/anie.201101021
- Wang, J., Jia, S., Cao, Y., Wang, W., and Yu, P. (2018). Design principles for nanoparticle plasmon-enhanced organic solar cells. *Nanoscale Res. Lett.* 13:211. doi: 10.1186/s11671-018-2620-4
- Wong, W. L., Su, X., Li, X., Cheung, C. M. G., Klein, R., Cheng, C. Y., et al. (2014). Global prevalence of age-related macular degeneration and disease burden projection for 2020 and 2040: A systematic review and meta-analysis. *Lancet Glob. Heal.* 2, e106–e116. doi: 10.1016/S2214-109X(13)70145-1
- Wu, J., Yu, P., Susha, A. S., Sablon, K. A., Chen, H., Zhou, Z., et al. (2015). Broadband efficiency enhancement in quantum dot solar cells coupled with multispiked plasmonic nanostars. *Nano Energy* 13, 827–835. doi: 10.1016/j.nanoen.2015.02.012
- Wu, J. L., Chen, F. C., Hsiao, Y. S., Chien, F. C., Chen, P., Kuo, C. H., et al. (2011). Surface plasmonic effects of metallic nanoparticles on the performance of polymer bulk heterojunction solar cells. *ACS Nano* 5, 959–967. doi: 10.1021/nn102295p
- You, J., Leonard, K., Takahashi, Y., Yonemura, H., and Yamada, S. (2014). Effects of silver nanoparticles with different sizes on photochemical responses of polythiophene-fullerene thin films. *Phys. Chem. Chem. Phys.* 16, 1166–1173. doi: 10.1039/c3cp53331j
- Zidan, M. N., Ismail, T., and Fahim, I. S. (2021). Effect of thickness and temperature on flexible organic P3HT:PCBM solar cell performance. *Mater. Res. Express* 8:95508. doi: 10.1088/2053-1591/ac2773

Frontiers in Cellular Neuroscience

Leading research in cellular mechanisms underlying brain function and development

Part of the world's most cited neuroscience journal series that advances our understanding of the cellular mechanisms underlying cell function in the nervous system across all species.

Discover the latest Research Topics

[See more →](#)

Frontiers

Avenue du Tribunal-Fédéral 34
1005 Lausanne, Switzerland
frontiersin.org

Contact us

+41 (0)21 510 17 00
frontiersin.org/about/contact

